**Transactions of the ASME, Journal of Applied Mechanics** (ISSN 0021-8936) is published bimonthly (Jan., Mar., May, July, Sept., Nov.) The American Society of Mechanical Engineers, Three Park Avenue, New York, NY 10016. Periodicals postage paid at New York, NY and additional mailing office. POSTMASTER: Send address changes to Transactions of the ASME, Journal of Applied Mechanics, c/o THE AMERICAN SOCIETY OF MECHANICAL ENGINEERS, 22 Law Drive, Box 2300, Fairfield, NJ 07007-2300. **CHANGES OF ADDRESS** must be received at Society headquarters seven weeks before they are to be effective. Please send old label and new address. **STATEMENT from By-Laws.** The Society shall not be responsible for statements or opinions advanced in papers or . . . printed in its publications (B7.1, Para. 3).
 **INDEXED** by Applied Mechanics Reviews and Engineering Information, Inc. Canadian Goods & Services Tax Registration #126148048.

# Journal of Applied Mechanics

**Published Bimonthly by ASME**

**VOLUME 71 • NUMBER 1 • JANUARY 2004**

## TECHNICAL PAPERS



## BRIEF NOTES



(**Contents continued on inside back cover**)

This journal is printed on acid-free paper, which exceeds the ANSI Z39.48-1992 specification for permanence of paper and library materials. ♾™
♻ 85% recycled content, including 10% post-consumer fibers.

(**Contents continued**)

**Journal of Applied Mechanics** **Volume 71, Number 1** **JANUARY 2004**



## ERRATUM



The ASME Journal of Applied Mechanics is abstracted and indexed in the following:

*Alloys Index, Aluminum Industry Abstracts, Applied Science & Technology Index, AMR Abstracts Database, Ceramic Abstracts, Chemical Abstracts, Civil Engineering Abstracts, Compendex (The electronic equivalent of Engineering Index), Computer & Information Systems Abstracts, Corrosion Abstracts, Current Contents, EEA (Earthquake Engineering Abstracts Database), Electronics & Communications Abstracts Journal, Engineered Materials Abstracts, Engineering Index, Environmental Engineering Abstracts, Environmental Science and Pollution Management, Fluidex, Fuel & Energy Abstracts, GeoRef, Geotechnical Abstracts, INSPEC, International Aerospace Abstracts, Journal of Ferrocement, Materials Science Citation Index, Mechanical Engineering Abstracts, METADEX (The electronic equivalent of Metals Abstracts and Alloys Index), Metals Abstracts, Nonferrous Metals Alert, Polymers Ceramics Composites Alert, Referativnyi Zhurnal, Science Citation Index, SciSearch (Electronic equivalent of Science Citation Index), Shock and Vibration Digest, Solid State and Superconductivity Abstracts, Steels Alert, Zentralblatt MATH*

# A Geometrically Nonlinear Shear Deformation Theory for Composite Shells

**Wenbin Yu**[1]
Post Doctoral Fellow

**Dewey H. Hodges**
Professor
Mem. ASME

School of Aerospace Engineering,
Georgia Institute of Technology,
Atlanta, GA 30332-0150

*A geometrically nonlinear shear deformation theory has been developed for elastic shells to accommodate a constitutive model suitable for composite shells when modeled as a two-dimensional continuum. A complete set of kinematical and intrinsic equilibrium equations are derived for shells undergoing large displacements and rotations but with small, two-dimensional, generalized strains. The large rotation is represented by the general finite rotation of a frame embedded in the undeformed configuration, of which one axis is along the normal line. The unit vector along the normal line of the undeformed reference surface is not in general normal to the deformed reference surface because of transverse shear. It is shown that the rotation of the frame about the normal line is not zero and that it can be expressed in terms of other global deformation variables. Based on a generalized constitutive model obtained from an asymptotic dimensional reduction from the three-dimensional energy, and in the form of a Reissner-Mindlin type theory, a set of intrinsic equilibrium equations and boundary conditions follow. It is shown that only five equilibrium equations can be derived in this manner because the component of virtual rotation about the normal is not independent. It is shown, however, that these equilibrium equations contain terms that cannot be obtained without the use of all three components of the finite rotation vector.* [DOI: 10.1115/1.1640364]

## Introduction

For an elastic three-dimensional continuum, there are two types of nonlinearity: geometrical and physical. A theory is geometrically nonlinear if the kinematical (strain-displacement) relations are nonlinear but the constitutive (stress-strain) relations are linear. This kind of theory allows large displacements and rotations with the restriction that strain must be small. A physically (or materially) nonlinear theory is necessary for biological, rubber-like or inflatable structures where the strain cannot be considered small, and a nonlinear constitutive law is needed to relate the stress and strain. Although this classification seems obvious and clear for a structure modeled as a three-dimensional continuum, it becomes somewhat ambiguous to model dimensionally reducible structures—structures that have one or two dimensions much smaller than the other(s) such as beams, plates, and shells, [1]—using reduced one-dimensional or two-dimensional models. A nonlinear constitutive law for the reduced structural model can in some circumstances be obtained from the reduction of a geometrically nonlinear three-dimensional theory. For example, in the so-called Wagner or trapeze effect, [2–5], the effective torsional rigidity is increased due to axial force. This physically nonlinear one-dimensional model stems from a purely geometrically nonlinear theory at the three-dimensional level. On the other hand, the present paper focuses on a geometrically nonlinear analysis at the three-dimensional level which becomes a geometrically nonlinear analysis at the two-dimensional as well. That is, the two-dimensional generalized strain-displacement relations are nonlinear while the two-dimensional generalized stress-strain relations turn out to be linear.

A shell is a three-dimensional body with a relatively small thickness and a smooth reference surface. The feature of the small thickness attracts researchers to simplify their analyses by reducing the original three-dimensional problem to a two-dimensional problem by taking advantage of the thinness. By comparison with the original three-dimensional problem, an exact shell theory does not exist. Dimensional reduction is an inherently approximate process. Shell theory is a very old subject, since the vibration of a bell was attempted by Euler even before elasticity theory was well established, [6]. Even so, shell theory still receives a lot of attention from modern researchers because it is used so extensively in so many engineering applications. Moreover, many shells are now made with advanced materials that have only recently become available.

Generally speaking, shell theories can be classified according to *direct, derived*, and *mixed* approaches. The direct approach, which originated with the Cosserat brothers, [7], models a shell directly as a two-dimensional ''orientated'' continuum. Naghdi [8] provided an extensive review of this kind of approach. Although the direct approach is elegant and able to account for transverse and normal strains and rotations associated with couple stresses, it nowhere connects with the fact that a shell is a three-dimensional body and thus completely isolates itself from three-dimensional continuum mechanics. This could be the main reason that this approach has not been much appreciated in the engineering community. One of the complaints of these approaches that they are difficult for numerical implementation has been answered by Simo and his co-workers by providing an efficient formulation ''free from mathematical complexities and suitable for large scale computation,'' [9,10]. And more recently a similar theory was developed by Ibrahimbegovic [11] to include drilling rotations so that not-so-smooth shell structures can be analyzed conveniently. However, the main complaint remains that these approaches lack a meaningful way to find the constitutive models ''which can only be experienced and formulated properly in our three-dimensional real world,'' [12]. Reissner [13] developed a very general nonlin-

[1]Presently Assistant Professor, Department of Mechanical and Aerospace Engineering, Utah State University, Logan, UT 84322-4130.

Contributed by the Applied Mechanics Division of THE AMERICAN SOCIETY OF MECHANICAL ENGINEERS for publication in the ASME JOURNAL OF APPLIED MECHANICS. Manuscript received by the ASME Applied Mechanics Division, June 5, 2002; final revision, June 10, 2003. Associate Editor: D. A. Kouris. Discussion on the paper should be addressed to the Editor, Prof. Robert M. McMeeking, Journal of Applied Mechanics, Department of Mechanical and Environmental Engineering University of California–Santa Barbara, Santa Barbara, CA 93106-5070, and will be accepted until four months after final publication of the paper itself in the ASME JOURNAL OF APPLIED MECHANICS.

  

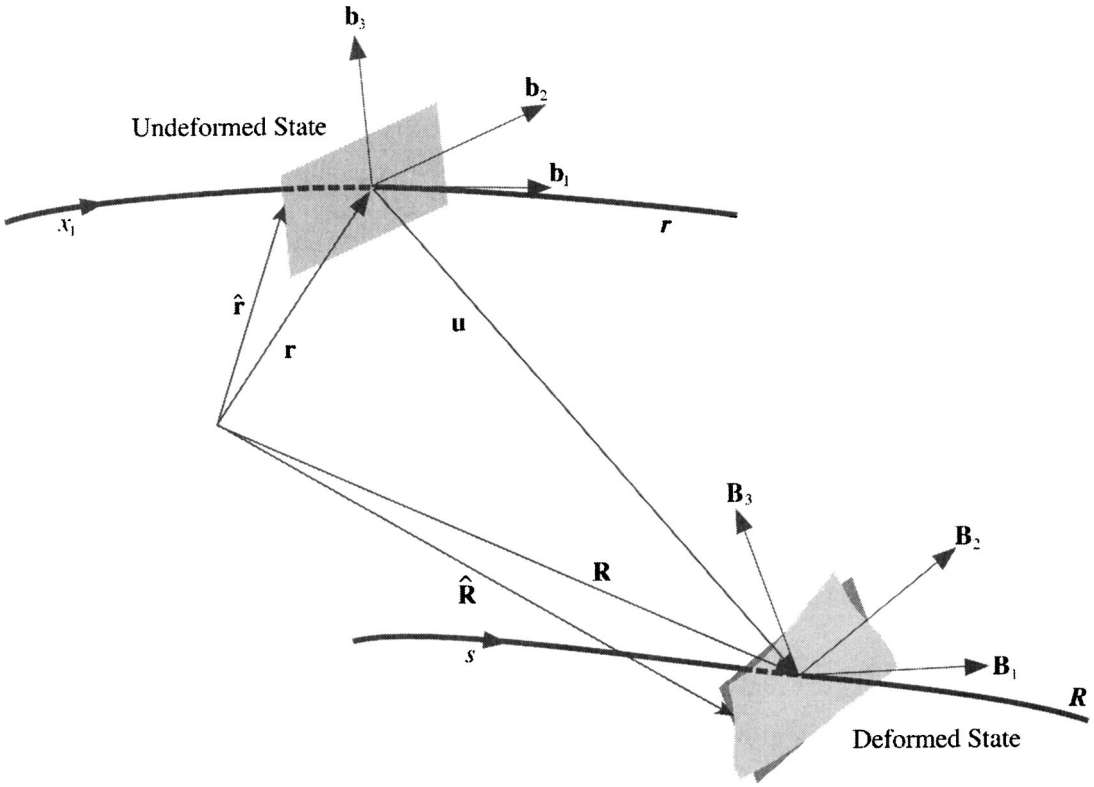


**Fig. 1 Schematic of shell deformation**

ear shell theory introducing 12 generalized strains by considering the dynamics of stress resultants and couples on the reference surface as the basis. He gracefully avoided the awkwardness of finding a proper constitutive model by pointing out two possible means to establish them. It is recommended in [13] that one could either design experiments to determine the constitutive constants without explicit reference to the three-dimensional nature of the structure or derive an appropriate two-dimensional model from the given knowledge of the constitutive relations for the real three-dimensional model of the structure.

Derived approaches reduce the original three-dimensional elasticity problem into a two-dimensional problem to be solved over the reference surface. Such reductions are usually carried out in one of two ways. The most common approach is to assume a priori the distribution of three-dimensional quantities through the thickness and then to construct a two-dimensional strain energy per unit area by integrating the three-dimensional energy per unit volume through the thickness. Remarkably, classical (also known as Kirchhoff-Love type theory), first-order shear deformation (also known as Reissner-Mindlin type theory), higher-order, and layer-wise shell theories all fall into this category, including the theories proposed by Reddy [14], for example. Another approach is to apply an asymptotic method to expand all quantities into an asymptotic series of the thickness coordinate, so that a sequence of two-dimensional problems can be solved according to the different orders.

The mixed approach is used in [15] based on the argument that all the three-dimensional elasticity equations except the constitutive relations are independent of the material properties, such as the kinematical relations, equilibrium of momentum and forces. The constitutive law must be determined experimentally, and hence it is avoidable that it is approximate. Libai and Simmonds [15] obtain exact shell equations for the balance of momentum, heat flow and an entropy inequality from the three-dimensional continuum mechanics via integration through the thickness. An analogous two-dimensional constitutive law is postulated due to the fact that even three-dimensional constitutive laws are inexact.

There is a sense in which the present approach can also be considered as mixed. The two-dimensional constitutive model is obtained by the variational asymptotic method (VAM), [16], such that the two-dimensional energy is as close to an asymptotic approximation of the original three-dimensional energy as possible, [17]. The process of constructing the constitutive model defines the reference surface and the kinematics of this surface are geometrically exact formulated in an intrinsic format. The two-dimensional equilibrium equations are obtained from the two-dimensional energy with the knowledge of the variations of the generalized strains. The only approximate part of our two-dimensional shell theory is the constitutive law which is not postulated but is mathematically obtained by VAM.

## Shell Kinematics

The equations of two-dimensional shell theory are written over the domain of the reference surface, on which every point can be represented by a position vector $\mathbf{r}$ in the undeformed configuration and $\mathbf{R}$ in the deformed configuration (see Fig. 1) with respect to a fixed point $O$ in the space. A set of two curvilinear coordinates, $x_\alpha$, are required to located a point on the reference surface. The coordinates are so-called *convected* coordinates such that every point of the configuration has the same coordinates during the deformation. (Here and throughout the paper Latin indices assume 1, 2, 3; and Greek indices assume values 1 and 2. Dummy indices are summed over their range except where explicitly indicated.) Without loss of generality, $x_\alpha$ are chosen to be the lines of curvatures of the surface to simplify the formulation. For the purpose of representing finite rotations, an orthonormal triad $\mathbf{b}_i$ is introduced for the initial configuration, such that

$$\mathbf{b}_\alpha = \mathbf{a}_\alpha / A_\alpha \quad \mathbf{b}_3 = \mathbf{b}_1 \times \mathbf{b}_2 \tag{1}$$

where $\mathbf{a}_\alpha$ is the set of base vectors associated with $x_\alpha$ and $A_\alpha$ are the Lamé parameters, defined as

$$\mathbf{a}_\alpha = \mathbf{r}_{,\alpha} \quad A_\alpha = \sqrt{\mathbf{a}_\alpha \cdot \mathbf{a}_\alpha}. \tag{2}$$

From the differential geometry of the surface and following [13] and [18], one can express the derivatives of $\mathbf{b}_i$ as

$$\mathbf{b}_{i,\alpha} = A_\alpha \mathbf{k}_\alpha \times \mathbf{b}_i \tag{3}$$

where $\mathbf{k}_\alpha$ is the curvature vector measured in $\mathbf{b}_i$ with the components

$$k_\alpha = \lfloor -k_{\alpha 2} \quad k_{\alpha 1} \quad k_{\alpha 3} \rfloor^T \tag{4}$$

in which $k_{\alpha\beta}$ refers to out-of-plane curvatures. We note that $k_{12} = k_{21} = 0$ because the coordinates are the lines of curvatures. The geodesic curvatures $k_{\alpha 3}$ can be expressed in terms of the Lamé parameters as

$$k_{13} = -\frac{A_{1,2}}{A_1 A_2} \quad k_{23} = \frac{A_{2,1}}{A_1 A_2}. \tag{5}$$

When the shell deforms, the particle that had position vector $\mathbf{r}$ in the undeformed state now has position vector $\mathbf{R}$ in the deformed shell. The triad $\mathbf{b}_i$ rotates to be $\mathbf{B}_i$. The rotation relating these two triads can be arbitrarily large and represented in the form of a matrix of direction cosines $C(x_\alpha)$ so that

$$\mathbf{B}_i = C_{ij}\mathbf{b}_j \quad C_{ij} = \mathbf{B}_i \cdot \mathbf{b}_j. \tag{6}$$

A definition of the two-dimensional generalized strain measures is needed for the purpose of formulating this problem in an intrinsic form. Following [13] and [18], they can be defined as

$$\mathbf{R}_{,\alpha} = A_\alpha(\mathbf{B}_\alpha + \epsilon_{\alpha\beta}\mathbf{B}_\beta + 2\gamma_{\alpha 3}\mathbf{B}_3) \tag{7}$$

and

$$\mathbf{B}_{i,\alpha} = A_\alpha(-K_{\alpha 2}\mathbf{B}_1 + K_{\alpha 1}\mathbf{B}_2 + K_{\alpha 3}\mathbf{B}_3) \times \mathbf{B}_i \tag{8}$$

where $\epsilon_{\alpha\beta}$ are the two-dimensional in-plane strains, and $K_{ij}$ are the curvatures of the deformed surface, which are the summation of curvatures of undeformed geometry $k_{ij}$ and curvatures introduced by the deformation $\kappa_{ij}$, and $\gamma_{\alpha 3}$ are the transverse strains because $\mathbf{B}_3$ is not constrained to be normal to the reference surface after deformation. Please note that the two-dimensional generalized strain measures are defined by Eqs. (7) and (8) in an intrinsic fashion, the symmetry of the inplane strain measures such that $\epsilon_{12} = \epsilon_{21}$ does not hold automatically. Nevertheless, one is free to set $\epsilon_{12} = \epsilon_{21}$, i.e.,

$$\frac{\mathbf{B}_1 \cdot \mathbf{R}_{,2}}{A_2} = \frac{\mathbf{B}_2 \cdot \mathbf{R}_{,1}}{A_1} \tag{9}$$

which is a constraint used in [17] to make the three-dimensional formulation unique.

At this point sufficient preliminary information has been obtained to develop a geometrically nonlinear shell theory.

## Compatibility Equations

It is well known that a rigid body in three-dimensional space has only six degrees-of-freedom. Thus, the kinematics of an element of the deformed shell reference surface can be expressed in terms of *at most* six independent quantities: three measures of displacement, say $\mathbf{u} \cdot \mathbf{b}_i$, and three measures of the rotation of $\mathbf{B}_i$ (since the global rotation tensor $\mathbf{C}$, which brings $\mathbf{b}_i$ into $\mathbf{B}_i$, can be expressed in terms of three independent quantities). However, we have the 11 two-dimensional strain measures $\epsilon_{11}$, $2\epsilon_{12}$, $\epsilon_{22}$, $2\gamma_{\alpha 3}$, $\kappa_{\alpha\beta}$, and $\kappa_{\alpha 3}$ as defined in Eqs. (7) and (8). Thus, they are not independent; there are some compatibility equations among these eleven quantities. In [19] and [13] appropriate compatibility equations are derived by first enforcing the equalities

$$\mathbf{R}_{,12} = \mathbf{R}_{,21} \tag{10}$$

and

$$\mathbf{B}_{i,12} = \mathbf{B}_{i,21}. \tag{11}$$

These two vector equations lead to six independent compatibility equations equivalent to a form of those found in [13]. These equations are rewritten here for convenience in the present notation. First, from the $\mathbf{B}_3$ components of Eq. (10), we obtain

$$(1+\epsilon_{22})\kappa_{12} - (1+\epsilon_{11})\kappa_{21} = \frac{(A_2 2\gamma_{23})_{,1}}{A_1 A_2} - \frac{(A_1 2\gamma_{13})_{,2}}{A_1 A_2} + \epsilon_{12}(K_{22} - K_{11}). \tag{12}$$

Next, from the $\mathbf{B}_\alpha$ components of Eq. (10) we obtain two equations for $\alpha = 1$ and 2, respectively, as

$$\begin{aligned}(1+\epsilon_{22})K_{13} - \epsilon_{12}K_{23} &= \frac{(A_2\epsilon_{12})_{,1}}{A_1 A_2} - \frac{[A_1(1+\epsilon_{11})]_{,2}}{A_1 A_2} - 2\gamma_{13}\kappa_{21} + 2\gamma_{23}K_{11} \\ (1+\epsilon_{11})K_{23} - \epsilon_{12}K_{13} &= \frac{[A_2(1+\epsilon_{22})]_{,1}}{A_1 A_2} - \frac{(A_1\epsilon_{12})_{,2}}{A_1 A_2} - 2\gamma_{13}K_{22} + 2\gamma_{23}\kappa_{12}.\end{aligned} \tag{13}$$

Finally, from the three components of Eq. (11) we have nine identities. However, there are only three independent equations, given by

$$\begin{aligned}&\frac{(A_1 K_{11})_{,2}}{A_1 A_2} - \frac{(A_2\kappa_{21})_{,1}}{A_1 A_2} + K_{13}K_{22} - \kappa_{12}K_{23} = 0 \\ &\frac{(A_1\kappa_{12})_{,2}}{A_1 A_2} - \frac{(A_2 K_{22})_{,1}}{A_1 A_2} + K_{23}K_{11} - \kappa_{21}K_{13} = 0 \\ &\frac{(A_2 K_{23})_{,1}}{A_1 A_2} - \frac{(A_1 K_{13})_{,2}}{A_1 A_2} + K_{11}K_{22} - \kappa_{12}\kappa_{21} = 0.\end{aligned} \tag{14}$$

There are now 11 quantities which are related by six compatibility equations. This means that these strain measures can be determined in terms of *only five* independent quantities—*not six*.

In the process of dimensional reduction of [17] to find an accurate constitutive model for composite shells, the authors encountered the question whether one should include $\kappa_{21}$ and $\kappa_{12}$ as two different generalized strain measures. This was determined by the following argument. Let us denote a new twist measure $2\omega = \kappa_{12} + \kappa_{21}$. From Eq. (12) the difference between $\kappa_{21}$ and $\kappa_{12}$ can be obtained as

$$\frac{\kappa_{12} - \kappa_{21}}{2} = \frac{\dfrac{(A_2 2\gamma_{23})_{,1} - (A_1 2\gamma_{13})_{,2}}{A_1 A_2} + \epsilon_{12}(K_{22} - K_{11}) + \omega(\epsilon_{11} - \epsilon_{22})}{(2 + \epsilon_{11} + \epsilon_{22})}. \tag{15}$$

This difference is clearly $O(\varepsilon h/\ell^2)$ or $O(\varepsilon/R)$ disregarding the nonlinear terms ($\varepsilon$ is the order of generalized strains, $h$ is the thickness of the shell, $l$ is the wavelength of in-plane deformation and $R$ is the characteristic radius of shell). One can show that it contributes terms that are $O(\varepsilon h^2/\ell^2 h/R)$ or $O(\varepsilon h^2/R^2)$ to the three-dimensional strains. Clearly, such terms will not be counted in a physically linear theory with only correction up to the order of $h/R$ and $(h/l)^2$.

Equations (13) can be solved for the in-plane curvatures $\kappa_{13}$ and $\kappa_{23}$, and Eq. (15) can be used to express $\kappa_{12}$ and $\kappa_{21}$ in terms of $\omega$. Now, using these expressions, one can rewrite the *three* Eqs. (14) entirely in terms of the *eight* strain measures $\epsilon_{11}$, $2\epsilon_{12}$, $\epsilon_{22}$, $2\gamma_{13}$, $2\gamma_{23}$, $\kappa_{11}$, $2\omega$, and $\kappa_{22}$. This confirms that *only five independent measures of displacement and rotation are necessary to define these strain measures* as we will demonstrate conclusively below by deriving such measures.

## Global Displacement and Rotation Variables

There is no unique choice for the global deformation variables. For this reason, the importance (not to mention the beauty) of an intrinsic formulation is widely appreciated. On the other hand, for the purpose of understanding the displacement field more fully, for practical computational algorithms, and for easy derivation of virtual strain-displacement relations, it is expedient to introduce a suitable set of displacement measures.

The displacement measures we choose are derived by expressing $\mathbf{R}$ in terms of $\mathbf{r}$ plus a displacement vector so that

$$\mathbf{R}(x_1,x_2)=\mathbf{r}(x_1,x_2)+u_i\mathbf{b}_i \tag{16}$$

Differentiating both sides of Eq. (16) with respect to $x_\alpha$, and making use of Eq. (7), one can obtain the identity

$$\mathbf{B}_\alpha+\epsilon_{\alpha\beta}\mathbf{B}_\beta+2\gamma_{\alpha3}\mathbf{B}_3=\mathbf{b}_\alpha+u_{i;\alpha}\mathbf{b}_i+u_i\mathbf{k}_\alpha\times\mathbf{b}_i \tag{17}$$

where $(\,)_{;\alpha}=1/A_\alpha\partial(\,)/\partial\alpha$. The above formula allows the determination of the strain measures $\epsilon_{\alpha\beta}$ and $2\gamma_{\alpha3}$ in terms of $C$, $u_i$ and the derivatives of $u_i$. Introducing column matrices $u=\lfloor u_1\ u_2\ u_3\rfloor^T$, $e_1=\lfloor1\ 0\ 0\rfloor^T$, $e_2=\lfloor0\ 1\ 0\rfloor^T$, $\gamma_1=\lfloor\epsilon_{11}\ \epsilon_{12}\ 2\gamma_{13}\rfloor^T$, and $\gamma_2=\lfloor\epsilon_{21}\ \epsilon_{22}\ 2\gamma_{23}\rfloor^T$, we can obtain the following identity in matrix form:

$$e_\alpha+\gamma_\alpha=C(e_\alpha+u_{;\alpha}+\widetilde{k_\alpha}u) \tag{18}$$

where $C$ is the matrix of direction cosines from Eq. (6), $k_\alpha$ is defined in Eq. (4), and $\widetilde{(\,)}_{ij}=-e_{ijk}(\,)_k$.

Rodrigues parameters, [20], can be used as rotation measures to allow a compact expression of $C$. These are derived based on Euler's theorem, which shows that any rotation can be represented as a rotation of magnitude $\Theta$ about a line parallel to a unit vector $\mathbf{e}$. Defining the Rodrigues parameters $\rho_i=2\mathbf{e}\cdot\mathbf{b}_i\tan(\Theta/2)$ and arranging these in a column matrix $\rho=\lfloor\rho_1\ \rho_2\ \rho_3\rfloor^T$, the matrix $C$ can simply be written as

$$C=\frac{\left(1-\dfrac{\rho^T\rho}{4}\right)I-\widetilde{\rho}+\dfrac{\rho\rho^T}{2}}{1+\dfrac{\rho^T\rho}{4}} \tag{19}$$

Let us also denote the direction cosines of $\mathbf{B}_3$ by

$$C_{3i}=\delta_{3i}+\theta_i \tag{20}$$

Hodges [21] has shown that, given the third row of $C$, the Rodrigues parameters can be uniquely expressed in terms of $\theta_i$ as

$$\rho_1=\frac{\rho_3\theta_1-2\theta_2}{2+\theta_3}$$

$$\rho_2=\frac{\rho_3\theta_2+2\theta_1}{2+\theta_3} \tag{21}$$

$$\rho_3=2\tan\left(\frac{\phi_3}{2}\right)$$

where $\rho_3$ can be understood as a change of variables to simplify later parts of the derivation. Later on we will discuss the meaning of $\phi_3$ for a special case. Finally, it is noted that the three rotational parameters $\theta_i$ are not independent but instead satisfy the constraint

$$\theta_1^2+\theta_2^2+(1+\theta_3)^2=1. \tag{22}$$

When Eq. (21) is substituted into Eq. (19), the resulting elements of $C$ can be expressed as functions of $\theta_i$ and $\phi_3$

$$C_{11}=\frac{(2+\theta_3-\theta_1^2)\cos\phi_3-\theta_1\theta_2\sin\phi_3}{2+\theta_3}$$

$$C_{12}=\frac{(2+\theta_3-\theta_2^2)\sin\phi_3-\theta_1\theta_2\cos\phi_3}{2+\theta_3}$$

$$C_{13}=-\theta_1\cos\phi_3-\theta_2\sin\phi_3$$

$$C_{21}=\frac{-(2+\theta_3-\theta_1^2)\sin\phi_3-\theta_1\theta_2\cos\phi_3}{2+\theta_3}$$

$$C_{22}=\frac{(2+\theta_3-\theta_2^2)\cos\phi_3+\theta_1\theta_2\sin\phi_3}{2+\theta_3} \tag{23}$$

$$C_{23}=\theta_1\sin\phi_3-\theta_2\cos\phi_3$$

$$C_{31}=\theta_1$$

$$C_{32}=\theta_2$$

$$C_{33}=1+\theta_3.$$

This representation reduces to those of [22] when considering small, finite rotations. There is an apparent singularity in the present scheme when $\theta_3=-2$ (i.e., when the shell deforms in such a way that $\mathbf{B}_3$ is pointed in the opposite direction of $\mathbf{b}_3$). This should pose no practical problem, however, since $\theta_1=\theta_2=0$ for that condition, and none of the kinematical relations become infinite in the limit as $\theta_3\to-2$.

When these expressions for the direction cosines are substituted into Eq. (18), explicit expressions for the strain measures can be found as

$$\epsilon_{11}=\left[\frac{(2+\theta_3-\theta_1^2)(1+u_{1;1}-k_{13}u_2+k_{11}u_3)-\theta_1\theta_2(u_{2;1}+k_{13}u_1)}{2+\theta_3}+\theta_1(k_{11}u_1-u_{3;1})\right]\cos\phi_3$$
$$+\left[\frac{(2+\theta_3-\theta_2^2)(u_{2;1}+k_{13}u_1)-\theta_1\theta_2(1+u_{1;1}-k_{13}u_2+k_{11}u_3)}{2+\theta_3}+\theta_2(k_{11}u_1-u_{3;1})\right]\sin\phi_3-1$$

$$\epsilon_{22}=\left[\frac{(2+\theta_3-\theta_2^2)(1+u_{2;2}+k_{23}u_1+k_{22}u_3)-\theta_1\theta_2(u_{1;2}-k_{23}u_2)}{2+\theta_3}-\theta_2(u_{3;2}-k_{22}u_2)\right]\cos\phi_3$$
$$+\left[\frac{(2+\theta_3-\theta_1^2)(k_{23}u_2-u_{1;2})+\theta_1\theta_2(1+u_{2;2}+k_{23}u_1+k_{22}u_3)}{2+\theta_3}+\theta_1(u_{3;2}-k_{22}u_2)\right]\sin\phi_3-1$$

$$\epsilon_{12}=\left[\frac{(2+\theta_3-\theta_2^2)(u_{2;1}+k_{13}u_1)-\theta_1\theta_2(1+u_{1;1}-k_{13}u_2+k_{11}u_3)}{2+\theta_3}+\theta_2(k_{11}u_1-u_{3;1})\right]\cos\phi_3$$
$$-\left[\frac{(2+\theta_3-\theta_1^2)(1+u_{1;1}-k_{13}u_2+k_{11}u_3)-\theta_1\theta_2(u_{2;1}+k_{13}u_1)}{2+\theta_3}+\theta_1(k_{11}u_1-u_{3;1})\right]\sin\phi_3$$

$$\epsilon_{21}=\left[\frac{(2+\theta_3-\theta_1^2)(u_{1;2}-k_{23}u_2)+\theta_1\theta_2(1+u_{2;2}+k_{23}u_1+k_{22}u_3)}{2+\theta_3}+\theta_1(u_{3;2}-k_{22}u_2)\right]\cos\phi_3$$
$$+\left[\frac{(2+\theta_3-\theta_2^2)(1+u_{2;2}+k_{23}u_1+k_{22}u_3)-\theta_1\theta_2(u_{1;2}-k_{23}u_2)}{2+\theta_3}-\theta_2(u_{3;2}-k_{22}u_2)\right]\sin\phi_3$$
$$2\gamma_{13}=\theta_1(1+u_{1;1}-k_{13}u_2+k_{11}u_3)+\theta_2(u_{2;1}+k_{13}u_1)+(1+\theta_3)(u_{3;1}-k_{11}u_1)$$
$$2\gamma_{23}=\theta_1(u_{1;2}-k_{23}u_2)+\theta_2(1+u_{2;2}+k_{23}u_1+k_{22}u_3)+(1+\theta_3)(u_{3;2}-k_{22}u_2). \tag{24}$$

These expressions explicitly depend on $\sin\phi_3$ and $\cos\phi_3$. It is evident that one can choose $\phi_3$ so that $\epsilon_{12}=\epsilon_{21}$, yielding

$$\tan\phi_3=\frac{n_1+\theta_2^2(u_{2;1}+k_{13}u_1)-\theta_1^2(u_{1;2}-k_{23}u_2)+\theta_1\theta_2[u_{1;1}-u_{2;2}+(k_{11}-k_{22})u_3-k_{23}u_1-k_{13}u_2]}{n_2+\theta_1^2(u_{1;1}+k_{11}u_3-k_{13}u_2)+\theta_2^2(u_{2;2}+k_{22}u_3+k_{23}u_1)+\theta_1\theta_2(u_{1;2}+u_{2;1}-k_{23}u_2+k_{13}u_1)} \tag{25}$$

where

$$n_1=(2+\theta_3)[u_{1;2}-u_{2;1}-\theta_1(u_{3;2}-k_{22}u_2)+\theta_2(u_{3;1}-k_{11}u_1)$$
$$-k_{13}u_1-k_{23}u_2] \tag{26}$$
$$n_2=(2+\theta_3)[\theta_1(u_{3;1}-k_{11}u_1)+\theta_2(u_{3;2}-k_{22}u_2)-u_{1;1}-u_{2;2}-2$$
$$-\theta_3-k_{23}u_1-(k_{22}+k_{11})u_3+k_{13}u_2]$$

It is now clear that once the functions $u_1$, $u_2$, $u_3$, $\theta_1$ and $\theta_2$ are known, the entire deformation is determined. Because of this, one should expect that a variational formulation would yield only five equilibrium equations–*not six*.

For small displacement and small strain, one can obtain $\phi_3$ as

$$\phi_3=\frac{(A_2u_2)_{,1}-(A_1u_1)_{,2}}{2A_1A_2} \tag{27}$$

which is half the angle of rotation about $\mathbf{B}_3$, the same as obtained in [23].

Although one can now find exact expressions for $\epsilon_{11}$, $2\epsilon_{12}$, $\epsilon_{22}$, $2\gamma_{13}$ and $2\gamma_{23}$ which are independent of $\phi_3$, such expressions are rather lengthy and are not given here. Alternatively, one could leave $\phi_3$ in the equations and regard Eq. (25) as a constraint. This would allow the construction of a shell finite element which would be compatible with beam elements which have three rotational degrees-of-freedom at the nodes.

Expressions for the curvatures can be found in terms of $C$ as

$$\widetilde{K_\alpha}=-C_{;\alpha}C^T+C\widetilde{k_\alpha}C^T \tag{28}$$

where

$$K_\alpha=\lfloor -k_{\alpha2}\ \ k_{\alpha1}\ \ k_{\alpha3}]^T+\lfloor -\kappa_{\alpha2}\ \ \kappa_{\alpha1}\ \ \kappa_{\alpha3}]^T \tag{29}$$

Following [24], the curvature vector can also be found using Rodrigues parameters

$$K_\alpha=\frac{I-\frac{\tilde{\rho}}{2}}{1+\frac{\rho^T\rho}{4}}\rho_{;\alpha}+Ck_\alpha. \tag{30}$$

Using the form of $C$ from Eqs. (23), the curvatures become

$$\kappa_{\alpha1}=\theta_{1;\alpha}\cos\phi_3+\theta_{2;\alpha}\sin\phi_3-\frac{\theta_{3;\alpha}(\theta_1\cos\phi_3+\theta_2\sin\phi_3)}{2+\theta_3}$$
$$+\hat{k}_{\alpha1}-k_{\alpha1}$$
$$\kappa_{\alpha2}=-\theta_{1;\alpha}\sin\phi_3+\theta_{2;\alpha}\cos\phi_3+\frac{\theta_{3;\alpha}(\theta_1\sin\phi_3-\theta_2\cos\phi_3)}{2+\theta_3}$$
$$+\hat{k}_{\alpha2}-k_{\alpha2} \tag{31}$$
$$\kappa_{\alpha3}=\phi_{3;\alpha}+\frac{\theta_{1;\alpha}\theta_2-\theta_1\theta_{2;\alpha}}{2+\theta_3}+\hat{k}_{\alpha3}$$

where

$$\hat{k}_{\alpha1}=\left(k_{\alpha3}-\frac{k_{\alpha2}\theta_1}{2+\theta_3}+\frac{k_{\alpha1}\theta_2}{2+\theta_3}\right)(\theta_1\sin\phi_3-\theta_2\cos\phi_3)+k_{\alpha2}\sin\phi_3$$
$$+k_{\alpha1}\cos\phi_3$$
$$\hat{k}_{\alpha2}=\left(k_{\alpha3}-\frac{k_{\alpha2}\theta_1}{2+\theta_3}+\frac{k_{\alpha1}\theta_2}{2+\theta_3}\right)(\theta_1\cos\phi_3+\theta_2\sin\phi_3)+k_{\alpha2}\cos\phi_3$$
$$-k_{\alpha1}\sin\phi_3 \tag{32}$$
$$\hat{k}_{\alpha3}=-k_{\alpha2}\theta_1+k_{\alpha1}\theta_2+k_{\alpha3}\theta_3.$$

As before, $\phi_3$ can be eliminated from these expressions, so that all six curvatures can be expressed in terms of five independent quantities. Note that $\kappa_{\alpha3}$ are not independent two-dimensional generalized strains. They will, however, appear in the equilibrium equations because of their appearance in the virtual strain-displacement relations derived later.

## Two-Dimensional Constitutive Law

To complete the analysis for an elastic shell, a two-dimensional constitutive law is required to relate two-dimensional generalized stresses and strains. As mentioned before the constitutive law can not be exact, however, one should try to avoid introducing any unnecessary approximation in addition to the already-approximate three-dimensional constitutive relations.

Among many approaches that have been proposed to deal with dimensional reduction, the approach in [17] stands out for its accuracy and simplicity. In that work, a simple Reissner-Mindlin type energy model is constructed that is as close as possible to being asymptotically correct. Moreover, the original three-dimensional results can be recovered accurately. The resulting model can be expressed as

$$2\Pi=\epsilon^TA\epsilon+\gamma^TG\gamma+2\epsilon^TF \tag{33}$$

where $\epsilon=\lfloor\epsilon_{11}\ 2\epsilon_{12}\ \epsilon_{22}\ \kappa_{11}\ \kappa_{12}+\kappa_{21}\ \kappa_{22}]^T$ and $\gamma=\lfloor 2\gamma_{13}\ 2\gamma_{23}]^T$. It is noticed that there is only one in-plane shear strain $\epsilon_{12}$ in Eq. (33). This is possible only after one uses the constraints in Eq. (9). Moreover, the strain energy is independent of $\kappa_{\alpha3}$ so that the rotation about the normal only appears algebraically, making it possible for it to be eliminated.

This simple constitutive model is rigorously reduced from the original three-dimensional model for multilayer shells, each layer of which is made with an anisotropic material with monoclinic symmetry. The variational asymptotic method [16] is used to guarantee the resulting two-dimensional shell model to yield the best approximation to the energy stored in the original three-dimensional structure by discarding all the insignificant contribu-

tion to the energy higher than the order of $(h/l)^2$ and $h/R$. The stiffness matrices $A$ and $G$ obtained through this process carry all the material and geometry information through the thickness (see Eqs. (63) and (73) in Ref. [17] for detailed expressions). The term containing the column matrix $F$ is produced by body forces in the shell structure and tractions on the top and bottom surfaces, and it is very important for the recovery of the original three-dimensional results. Interested readers can refer to Ref. [17] for details of constructing the model in Eq. (33) for multilayered composite shells.

Having obtained the two-dimensional constitutive law from three-dimensional elasticity, one can derive all the other relations over the reference surface of the shell, a two-dimensional continuum.

## Virtual Strain-Displacement Relations

In order to derive intrinsic equilibrium equations from the two-dimensional energy, it is necessary to express the variations of generalized strain measures in terms of virtual displacements and virtual rotations.

The variation of the energy expressed in Eq. (33) can be written as

$$\delta\Pi = \frac{\partial\Pi}{\partial\epsilon_{11}}\delta\epsilon_{11} + \frac{\partial\Pi}{\partial\epsilon_{12}}\delta\epsilon_{12} + \frac{\partial\Pi}{\partial\epsilon_{22}}\delta\epsilon_{22} + \frac{\partial\Pi}{\partial\gamma_{13}}\delta\gamma_{13} + \frac{\partial\Pi}{\partial\gamma_{23}}\delta\gamma_{23} + \frac{\partial\Pi}{\partial\kappa_{11}}\delta\kappa_{11} + \frac{\partial\Pi}{\partial\omega}\delta\omega + \frac{\partial\Pi}{\partial\kappa_{22}}\delta\kappa_{22}. \tag{34}$$

It is now obvious that one must express $\delta\epsilon_{11}, \ldots, \delta\kappa_{22}$, in terms of virtual displacements and rotations in order to obtain the final Euler-Lagrange equations of the energy functional in their intrinsic form. Following Ref. [24], we introduce measures of virtual displacement and rotation that are ''compatible'' with the intrinsic strain measures. For the virtual displacement, we note the form of Eq. (18) and choose

$$\overline{\delta q} = C\,\delta u. \tag{35}$$

Similarly, for the virtual rotation, we note the form of Eq. (28) and write

$$\widetilde{\overline{\delta\psi}} = -\,\delta C C^T \tag{36}$$

where $\overline{\delta\psi}$ is a column matrix arranged similarly as the curvature column matrix in Eq. (4) $\overline{\delta\psi} = \lfloor -\overline{\delta\psi}_2\ \overline{\delta\psi}_1\ \overline{\delta\psi}_3\rfloor^T$. The bars indicate that these quantities are not necessarily the variations of functions. Using these relations it is clear that

$$\delta u = C^T\overline{\delta q} \tag{37}$$

and

$$\delta C = -\,\widetilde{\overline{\delta\psi}}C. \tag{38}$$

Let us begin with the generalized strain-displacement relationship, Eq. (18). A particular in-plane strain element can be written as

$$\epsilon_{\alpha\beta} = e_\beta^T[C(e_\alpha + u_{;\alpha} + \widetilde{k}_\alpha u) - e_\alpha]. \tag{39}$$

Taking a straightforward variation, one obtains

$$\delta\epsilon_{\alpha\beta} = e_\beta^T[\,\delta C(e_\alpha + u_{;\alpha} + \widetilde{k}_\alpha u) + C(\delta u_{;\alpha} + \widetilde{k}_\alpha\delta u)]. \tag{40}$$

The right-hand side contains $u_{;\alpha}$ and $\delta u_{;\alpha}$, which must be eliminated in order to obtain variations of the strain that are independent of displacements. These are needed to derive intrinsic equilibrium equations.

Premultiplying both sides of Eq. (18) by $C^T$, making use of Eq. (36), and finally using a property of the tilde operator that, for arbitrary column matrices $Y$ and $Z$, $\widetilde{Y}Z = -\widetilde{Z}Y$, one can make the first term in brackets on the righthand side independent of $u_{;\alpha}$. After all this, one obtains

$$\delta C(e_\alpha + u_{;\alpha} + \widetilde{k}_\alpha u) = \delta C C^T(e_\alpha + \gamma_\alpha) = -\,\widetilde{\overline{\delta\psi}}(e_\alpha + \gamma_\alpha) = (\widetilde{e}_\alpha + \widetilde{\gamma}_\alpha)\overline{\delta\psi}. \tag{41}$$

An expression for the second term in brackets on the right-hand side of Eq. (40) can now be obtained by differentiating Eq. (37) with respect to $x_\alpha$ and premultiplying by $C$. This yields

$$C(\delta u_{;\alpha} + \widetilde{k}_\alpha\delta u) = C(C^T\overline{\delta q})_{;\alpha} + C\widetilde{k}_\alpha\delta u = \overline{\delta q}_{;\alpha} + \widetilde{K}_\alpha\overline{\delta q}. \tag{42}$$

Substituting Eqs. (41) and (42) into Eq. (40), one obtains an intrinsic expression for the variation of the in-plane strain components as

$$\delta\epsilon_{\alpha\beta} = e_\beta^T[\,\overline{\delta q}_{;\alpha} + \widetilde{K}_\alpha\overline{\delta q} + (\widetilde{e}_\alpha + \widetilde{\gamma}_\alpha)\overline{\delta\psi}] \tag{43}$$

where $e_\beta^T\widetilde{e}_\alpha$ vanishes when $\alpha = \beta$. This matrix equation can be written explicitly as four scalar equations:

$$\begin{aligned}
\delta\epsilon_{11} &= \overline{\delta q}_{1;1} - K_{13}\overline{\delta q}_2 + K_{11}\overline{\delta q}_3 - 2\gamma_{13}\overline{\delta\psi}_1 + \epsilon_{12}\overline{\delta\psi}_3\\
\delta\epsilon_{12} &= \overline{\delta q}_{2;1} + K_{13}\overline{\delta q}_1 + \kappa_{12}\overline{\delta q}_3 - 2\gamma_{13}\overline{\delta\psi}_2 - (1+\epsilon_{11})\overline{\delta\psi}_3\\
\delta\epsilon_{21} &= \overline{\delta q}_{1;2} - K_{23}\overline{\delta q}_2 + \kappa_{21}\overline{\delta q}_3 - 2\gamma_{23}\overline{\delta\psi}_1 + (1+\epsilon_{22})\overline{\delta\psi}_3\\
\delta\epsilon_{22} &= \overline{\delta q}_{2;2} + K_{23}\overline{\delta q}_1 + K_{22}\overline{\delta q}_3 - 2\gamma_{23}\overline{\delta\psi}_2 - \epsilon_{12}\overline{\delta\psi}_3.
\end{aligned} \tag{44}$$

The variations $\delta\epsilon_{12}$ and $\delta\epsilon_{21}$ should be equal due to Eq. (9); hence, one can solve for the virtual rotation component about $\mathbf{B}_3$ as

$$\overline{\delta\psi}_3 = \frac{\overline{\delta q}_{2;1} - \overline{\delta q}_{1;2} + K_{13}\overline{\delta q}_1 + K_{23}\overline{\delta q}_2 + (\kappa_{12} - \kappa_{21})\overline{\delta q}_3 - 2\gamma_{13}\overline{\delta\psi}_2 + 2\gamma_{23}\overline{\delta\psi}_1}{2 + \epsilon_{11} + \epsilon_{22}}. \tag{45}$$

It is now possible to write the variations of all strain measures in terms of three virtual displacement and two virtual rotation components as

$$\begin{aligned}
\delta\epsilon_{11} &= \overline{\delta q}_{1;1} - K_{13}\overline{\delta q}_2 + K_{11}\overline{\delta q}_3 - 2\gamma_{13}\overline{\delta\psi}_1 + \epsilon_{12}\overline{\delta\psi}_3\\
\delta\epsilon_{22} &= \overline{\delta q}_{2;2} + K_{23}\overline{\delta q}_1 + K_{22}\overline{\delta q}_3 - 2\gamma_{23}\overline{\delta\psi}_2 - \epsilon_{12}\overline{\delta\psi}_3
\end{aligned} \tag{46}$$

$$2\,\delta\epsilon_{12} = \overline{\delta q}_{2;1} + \overline{\delta q}_{1;2} + K_{13}\overline{\delta q}_1 - K_{23}\overline{\delta q}_2 + 2\,\omega\,\overline{\delta q}_3 - 2\gamma_{13}\overline{\delta\psi}_2 - 2\gamma_{23}\overline{\delta\psi}_1 + (\epsilon_{22} - \epsilon_{11})\overline{\delta\psi}_3$$

with $\overline{\delta\psi}_3$ taken from Eq. (45).

Let us now consider the transverse shear strains

$$2\gamma_{\alpha 3} = e_3^T[C(e_\alpha + u_{;\alpha} + \widetilde{k}_\alpha u) - e_\alpha]. \tag{47}$$

Following a procedure similar to the above, one can obtain the virtual strain-displacement equation for transverse shear strains as

$$2\,\delta\gamma_{\alpha 3}=e_3^T[\,\overline{\delta q}_{;\alpha}+\widetilde{K_\alpha}\overline{\delta q}+(\widetilde{e_\alpha}+\widetilde{\gamma_\alpha})\,\overline{\delta\psi}]. \tag{48}$$

Explicit expressions for the variations of the shear strain components are now easily written as

$$2\,\delta\gamma_{\alpha 3}=\overline{\delta q}_{3;\alpha}+\overline{\delta\psi}_\alpha+\epsilon_{\alpha\beta}\overline{\delta\psi}_\beta-K_{\alpha\beta}\overline{\delta q}_\beta. \tag{49}$$

Finally, variations of the curvatures are found. First, taking the straightforward variation of Eq. (28), one obtains

$$\delta\widetilde{\kappa_\alpha}=-\frac{\delta C_{,\alpha}C^T}{A_\alpha}-\frac{C_{,\alpha}\delta C^T}{A_\alpha}+\delta C\widetilde{k_\alpha}C^T+C\widetilde{k_\alpha}\delta C^T. \tag{50}$$

In order to eliminate $\delta C_{,\alpha}$, we differentiate Eq. (36) with respect to $x_\alpha$

$$\widetilde{\widetilde{\delta\psi}}_{,\alpha}=-\delta C_{,\alpha}C^T-\delta CC_{,\alpha}^T. \tag{51}$$

In order to eliminate $\delta C$, we can use Eq. (38). Then, Eq. (50) becomes

$$\delta\widetilde{\kappa_\alpha}=\widetilde{\widetilde{\delta\psi}}_{;\alpha}+\widetilde{K_\alpha}\widetilde{\widetilde{\delta\psi}}-\widetilde{\widetilde{\delta\psi}}\widetilde{K_\alpha}. \tag{52}$$

Using another tilde identity ($\widetilde{\widetilde{Y}Z}=\widetilde{Y}\widetilde{Z}-\widetilde{Z}\widetilde{Y}$) one can find the virtual strain-displacement relation as

$$\delta\kappa_\alpha=\overline{\delta\psi}_{;\alpha}+\widetilde{K_\alpha}\,\overline{\delta\psi}. \tag{53}$$

In explicit form

$$\begin{aligned}
\delta\kappa_{11}&=\frac{\overline{\delta\psi}_{1,1}}{A_1}-K_{13}\overline{\delta\psi}_2+\kappa_{12}\overline{\delta\psi}_3\\
\delta\kappa_{22}&=\frac{\overline{\delta\psi}_{2,2}}{A_2}+K_{23}\overline{\delta\psi}_1-\kappa_{21}\overline{\delta\psi}_3\\
2\,\delta\omega&=\frac{\overline{\delta\psi}_{1,2}}{A_2}+\frac{\overline{\delta\psi}_{2,1}}{A_1}+K_{13}\overline{\delta\psi}_1-K_{23}\overline{\delta\psi}_2+(K_{22}-K_{11})\,\overline{\delta\psi}_3
\end{aligned} \tag{54}$$

where $\overline{\delta\psi}_3$ can again be eliminated by using Eq. (45).

## Intrinsic Equilibrium Equations

In this section, we will make use of the virtual strain-displacement relations in the variation of the internal strain energy in order to derive the intrinsic equilibrium equations. Here we define the generalized forces as

$$\begin{aligned}
&\frac{\partial\Pi}{\partial\epsilon_{11}}=N_{11}\quad\frac{\partial\Pi}{\partial\epsilon_{22}}=N_{22}\quad\frac{1}{2}\frac{\partial\Pi}{\partial\epsilon_{12}}=N_{12}\\
&\frac{\partial\Pi}{\partial\kappa_{11}}=M_{11}\quad\frac{\partial\Pi}{\partial\kappa_{22}}=M_{22}\quad\frac{1}{2}\frac{\partial\Pi}{\partial\omega}=M_{12}\\
&\frac{1}{2}\frac{\partial\Pi}{\partial\gamma_{13}}=Q_1\quad\frac{1}{2}\frac{\partial\Pi}{\partial\gamma_{23}}=Q_2.
\end{aligned} \tag{55}$$

To use the principle of virtual work to derive the equilibrium equations, one needs to know the applied loads. In addition to the applied loads used in the modeling process, $\tau_i\mathbf{B}_i$ at the top surface, $\beta_i\mathbf{B}_i$ at the bottom surface and body force $\phi_i\mathbf{B}_i$ [17], one can also specify appropriate combinations of displacements, rotations (geometrical boundary conditions), running forces and moments (natural boundary conditions) along the boundary around the reference surface. It is trivial to apply the geometrical boundary conditions. Although it is possible in most cases that natural boundary conditions can be derived from Newton's law, the procedure is tedious and not easily applied here because the physical meanings for some of the generalized forces are not clear. Thus, natural boundary conditions are best derived from the principle of virtual work.

Suppose on boundary $\Gamma$ (see Fig. 2), we specify a force resultant $\hat{N}_{\nu\nu}$ and moment resultant $\hat{M}_{\nu\nu}$ along the outward normal of the boundary curve tangent to the reference surface $\nu$, $\hat{N}_{\nu\tau}$ and $\hat{M}_{\nu\tau}$ along the tangent of the boundary curve $\tau$, $\hat{N}_{\nu 3}$ along the normal of the reference surface. Then the principle of virtual work (strictly speaking, the principle of virtual displacements) can be stated as:

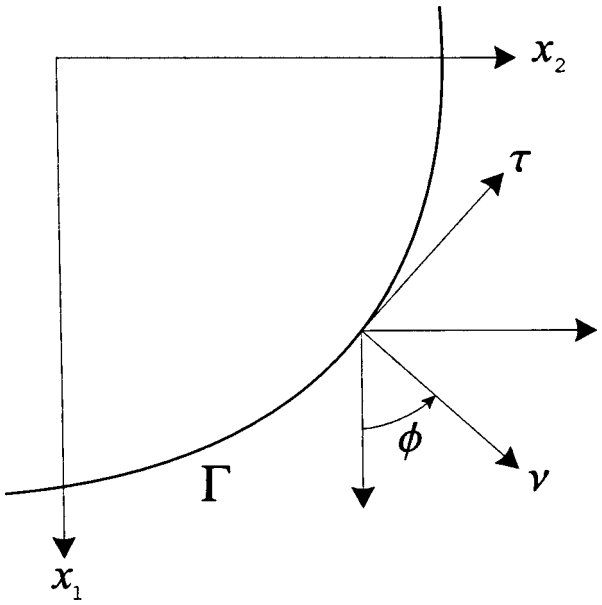


**Fig. 2 Schematic of an arbitrary boundary**

$$\begin{aligned}
\int\int_s(\delta\Pi-\overline{\delta q}_i f_i-\overline{\delta\psi}_\alpha m_\alpha)A_1A_2\mathrm{d}x_1\mathrm{d}x_2-\int_\Gamma(\hat{N}_{\nu\nu}\overline{\delta q}_\nu+\hat{N}_{\nu\tau}\overline{\delta q}_\tau\\
+\hat{N}_{\nu 3}\overline{\delta q}_3+\hat{M}_{\nu\nu}\overline{\delta\psi}_\nu+\hat{M}_{\nu\tau}\overline{\delta\psi}_\tau)\mathrm{d}\Gamma=0
\end{aligned} \tag{56}$$

where $f_i$ and $m_\alpha$ are taken directly from [17].

It is now possible to obtain intrinsic equilibrium equations and consistent edge conditions by use of the principle of virtual work and the virtual strain-displacement relations derived in the previous section. The equilibrium equations are

$$\begin{aligned}
&\frac{(A_2N_{11})_{,1}}{A_1A_2}+\frac{[A_1(N_{12}+\mathcal{N})]_{,2}}{A_1A_2}-K_{13}(N_{12}-\mathcal{N})\\
&\quad-K_{23}N_{22}+Q_1K_{11}+Q_2\kappa_{21}+f_1=0\\
&\frac{(A_1N_{22})_{,2}}{A_1A_2}+\frac{[A_2(N_{12}-\mathcal{N})]_{,1}}{A_1A_2}+K_{23}(N_{12}+\mathcal{N})\\
&\quad+K_{13}N_{11}+Q_1\kappa_{12}+Q_2K_{22}+f_2=0\\
&\frac{(A_2Q_1)_{,1}}{A_1A_2}+\frac{(A_1Q_2)_{,2}}{A_1A_2}-K_{11}N_{11}-K_{22}N_{22}\\
&\quad-2\,\omega N_{12}+(\kappa_{12}-\kappa_{21})\mathcal{N}+f_3=0\\
&\frac{(A_2M_{11})_{,1}}{A_1A_2}+\frac{(A_1M_{12})_{,2}}{A_1A_2}-Q_1(1+\epsilon_{11})-Q_2\epsilon_{12}+2\,\gamma_{13}N_{11}\\
&\quad+2\,\gamma_{23}(N_{12}+\mathcal{N})-M_{12}K_{13}-M_{22}K_{23}+m_1=0\\
&\frac{(A_2M_{12})_{,1}}{A_1A_2}+\frac{(A_1M_{22})_{,2}}{A_1A_2}-Q_2(1+\epsilon_{22})-Q_1\epsilon_{12}+2\,\gamma_{13}(N_{12}-\mathcal{N})\\
&\quad+2\,\gamma_{23}N_{22}+M_{11}K_{13}+M_{12}K_{23}+m_2=0
\end{aligned} \tag{57}$$

where

$$\mathcal{N}=\frac{(N_{22}-N_{11})\epsilon_{12}+N_{12}(\epsilon_{11}-\epsilon_{22})+M_{22}\kappa_{21}-M_{11}\kappa_{12}+M_{12}(K_{11}-K_{22})}{2+\epsilon_{11}+\epsilon_{22}}. \tag{58}$$

The associated natural boundary conditions on $\Gamma$ are

$$\begin{aligned}
\hat{N}_{\nu\nu}&=\nu_1^2N_{11}+2\nu_1\nu_2N_{12}+\nu_2^2N_{22}\\
\hat{N}_{\nu\tau}&=\nu_1\nu_2(N_{22}-N_{11})+(\nu_1^2-\nu_2^2)N_{12}-\mathcal{N}\\
\hat{N}_{\nu\nu}&=\nu_1^2N_{11}+2\nu_1\nu_2N_{12}+\nu_2^2N_{22}\\
\hat{N}_{\nu 3}&=\nu_1Q_1+\nu_2Q_2\\
\hat{M}_{\nu\nu}&=\nu_1^2M_{11}+2\nu_1\nu_2M_{12}+\nu_2^2M_{22}\\
\hat{M}_{\nu\tau}&=\nu_1\nu_2(M_{22}-M_{11})+(\nu_1^2-\nu_2^2)M_{12}
\end{aligned} \tag{59}$$

where $\nu_1=\cos\phi$, $\nu_2=\sin\phi$, and $\phi$ is the angle between the outward normal of the boundary and the $x_1$ direction as shown in Fig. 2. The terms containing $\mathcal{N}$ stem from consistent inclusion of the finite rotation from undeformed triad to deformed triad although the *nonzero* rotation about $\mathbf{B}_3$ is expressed in terms of other kinematical quantities. Similar terms are found in the shell equations derived by Berdichevsky [16] where only five equilibrium equations are derived.

In a mixed formulation, $\mathcal{N}$ can be shown to be the Lagrange multiplier that enforces Eq. (45). To further understand the nature of $\mathcal{N}$ one can undertake the following exercise: Setting $P_i=0$ and $\epsilon_{12}=\epsilon_{21}$ for the equilibrium equations given in [13], $(N_{21}-N_{12})/2$ can be solved from Reissner's sixth equilibrium equation. This shows that Reissner's $(N_{21}-N_{12})/2$ is the same as our $\mathcal{N}$, and Reissner's $(N_{21}-N_{12})/2$ is the same as our $N_{12}$. Finally, substitution of this sixth equation into the other five yields the five equilibrium equations given here in Eqs. (57). It is noted that Reissner's equilibrium equations are derived based on the basis of Newton's law of motion without consideration of either constitutive law or strain-displacement relations. However, the present derivation is purely displacement-based. The reproduction of those equilibrium equations by the present derivation illustrates that, as long as the formulation is geometrically exact, one can derive exact equilibrium equations.

A few investigators have noted an apparent conflict between the symmetry of the stress resultants and the satisfaction of moment equilibrium about the normal. In reality there is no conflict, but one must be careful. We have shown herein that the triad $\mathbf{B}_i$ can always be chosen so that $\epsilon_{12}=\epsilon_{21}$. If this relation is enforced strongly, there is only one in-plane shear stress resultant, $N_{12}$, that can be derived from the energy. In that case the physical quantity associated with the antisymmetric part of Reissner's in-plane stress resultants, while it is not available from the constitutive law, is nevertheless available as a reactive quantity from the moment equilibrium equation about the normal. However, it must be stressed that the moment equilibrium equation about the normal is not available from a conventional energy approach, in which the virtual displacements and rotations must be independent.

In a somewhat similar vein, not being able to obtain the antisymmetric part of the moment stress resultants from derivatives of the two-dimensional strain energy is a result of the approximate dimensional reduction process in which it was determined, based on asymptotic considerations and *geometrically* nonlinear three-dimensional elasticity, that the antisymmetric term $\kappa_{12}-\kappa_{21}$ does not appear as an independent generalized strain measure in the two-dimensional constitutive law with correction only to the order of $h/R$. However, if a more refined theory with respect to $h/R$ is required, then $\kappa_{12}-\kappa_{21}$ would appear as a generalized strain in the two-dimensional constitutive law and a new generalized moment would be defined based on the constitutive law.

For practical computational schemes, equilibrium equations and boundary conditions need to use the constitutive law to relate with the generalized two-dimensional strains. Finally a set of kinematical equations is needed. Depending on how this part is done, the analysis can be completed in either of two fundamentally different ways: a purely intrinsic form, relying on compatibility equations, and a mixed form relying on explicit strain-displacement relations.

In the intrinsic form we have five equilibrium equations, Eqs. (57); six compatibility equations, Eqs. (12)–(14); and the eight constitutive equations—a total of 19 equations. The 19 unknowns are the eight stress resultants, $N_{11}$, $N_{12}$, $N_{22}$, $Q_1$, $Q_2$, $M_{11}$, $M_{12}$, and $M_{22}$; and the 11 strain measures $\epsilon_{11}$, $2\epsilon_{12}$, $\epsilon_{22}$, $2\gamma_{13}$, $2\gamma_{23}$, $\kappa_{11}$, $2\omega_{12}$, and $\kappa_{22}$, along with $\kappa_{13}$, $\kappa_{23}$, and $\kappa_{12}-\kappa_{21}$. The last three strain measures appear in the equilibrium equations but not in the constitutive law.

In a mixed formulation one would use the same five equilibrium equations and eight constitutive equations. One would also need a set of strain-displacement relations among the 11 generalized strain measures $\epsilon_{11}$, $2\epsilon_{12}$, $\epsilon_{22}$, $2\gamma_{13}$, $2\gamma_{23}$, $\kappa_{11}$, $2\omega$, and $\kappa_{22}$, along with $\kappa_{13}$, $\kappa_{23}$, and $\kappa_{12}-\kappa_{21}$, and the five global displacement and rotational variables $u_1$, $u_2$, $u_3$, $\theta_1$, and $\theta_2$. One possible set of such equations is as follows: use five of Eqs. (24), using either $\epsilon_{12}$ or $\epsilon_{21}$; use the six Eqs. (31). There are also the two other rotational variables $\theta_3$ and $\phi_3$, which are governed by Eqs. (22) and (25), respectively. This way there are 26 equations and 26 unknowns. This mixed formulation is capable of handling boundary conditions on two-dimensional stress resultants and displacement/rotation variables. At least in principle, one could recover a displacement formulation by eliminating all the unknowns except the displacement and rotation variables.

Equations (57) and (58) contain terms that could be disregarded because of the original assumption of small strain. We will not undertake this simplification here, because it is out of the scope of the present study to actually implement the two-dimensional nonlinear theory. Therefore, our equilibrium equations and kinematical equations are geometrically exact; all approximations stem from the dimensional reduction process used to obtain the two-dimensional constitutive law.

The present work is a direct extension of [18] to treat shells. If one sets $k_{ij}=0$ and $A_\alpha=1$, all the formulas developed here will reduce to those in [18], which indirectly verifies that derivation.

## Conclusions

A nonlinear shear-deformable shell theory has been developed to be completely compatible with the modeling process in [17]. The compatibility equations, kinematical relations and equilibrium equations are derived for arbitrarily large displacements and rotations under the restriction that the strain must be small. The resulting formulas are compared with others in the literature. The following conclusions can be drawn from the present work:

1. The variational asymptotic method can be used to decouple the original three-dimensional elasticity problem of a shell into a one-dimensional, through-the-thickness analysis, [17], and a two-dimensional, shell analysis. The through-the-thickness analysis provides both an accurate two-dimensional constitutive law for the nonlinear shell theory and accurate through-the-thickness recovery relations for three-dimensional displacement, strain, and stress. This way, an intimate relation between the shell theory and three-dimensional elasticity is established.

2. A full finite rotation must be applied to fully specify the displacement field. However, since the strain energy on which the

formulation is based is independent of $\kappa_{\alpha 3}$, the rotation about the normal is not independent and can be expressed in terms of other quantities. Thus, it can be chosen so that the two-dimensional, in-plane shear strain measures are equal. This way all the strain measures can be expressed in terms of five independent quantities: three displacement and two rotation measures, and only one stress resultant for in-plane shear can be derived from the two-dimensional energy.

3. Only five equilibrium equations are obtainable in a displacement-based variational formulation. Moment equilibrium about the normal is satisfied implicitly. If one does not include the full finite rotation, but rather sets the rotation about the normal equal to zero, the correct equilibrium equations cannot be obtained. This should shed some light on the nature of ''drilling'' degrees of freedom.

## References


[1] Yu, W., 2002, ''Variational Asymptotic Modeling of Composite Dimensionally Reducible Structures,'' Ph.D. thesis, Aerospace Engineering, Georgia Institute of Technology, Atlanta, GA, May.

[2] Campbell, A., 1913, ''On Vibration Galvanometer With Unifilar Torsional Control,'' Proceedings of the Physical Society, **25**, pp. 203–205.

[3] Pealing, H., 1913, ''On an Anomalous Variation of the Rigidity of Phosphor Bronze,'' Philos. Mag., **25**(147), pp. 418–427.

[4] Buckley, J. C., 1914, ''The Bifilar Property of Twisted Strips,'' Philos. Mag., **28**, pp. 778–785.

[5] Wagner, H., 1936, ''Torsion and Buckling of Open Sections,'' Paper No. NACA TM 807.

[6] Love, A. E. H., 1944, *Mathematical Theory of Elasticity*, 4th Ed., Dover Publications, New York.

[7] Cosserat, B., and Cosserat, F., 1909, *Théorie des Corps Deformables*, Hermann, Paris.

[8] Naghdi, P. M., 1972, ''The Theory of Shells and Plates,'' *Handbuch der Physik*, Springer-Verlag, Berlin. **6**(a/2), pp. 425–640.

[9] Simo, J. C., and Fox, D. D., 1989, ''On a Stress Resultant Geometrically Exact Shell Model. Part I: Formulation and Optimal Parametrization,'' Comput. Methods Appl. Mech. Eng., **72**, pp. 267–304.

[10] Simo, J. C., and Fox, D. D., 1989, ''On a Stress Resultant Geometrically Exact Shell Model. Part II: The Linear Theory; Computational Aspects,'' Comput. Methods Appl. Mech. Eng., **73**, pp. 53–92.

[11] Ibrahimbegovic, A., 1994, ''Stress Resultant Geometrically Nonlinear Shell Theory With Drilling Rotations—Part I. A Consistent Formulation,'' Comput. Methods Appl. Mech. Eng., **118**, pp. 265–284.

[12] Kratzig, W. B., 1993, '''Best' Transverse Shearing and Stretching Shell Theory for Nonlinear Finite Element Simulations,'' Comput. Methods Appl. Mech. Eng., **103**(1–2), pp. 135–160.

[13] Reissner, E., 1974, ''Linear and Nonlinear Theory of Shells,'' *Thin Shell Structures*, Y. C. Fung and E. E. Sechler, eds., Prentice-Hall, Englewood Cliffs, NJ, pp. 29–44.

[14] Reddy, J. N., 1997, *Mechanics of Laminated Composite Plates: Theory and Analysis*, CRC Press, Boca Raton, FL.

[15] Libai, A., and Simmonds, J. G., 1998, *The Nonlinear Theory of Elastic Shells*, 2nd Ed., Cambridge University Press, Cambridge, UK.

[16] Berdichevsky, V. L., 1979, ''Variational-Asymptotic Method of Constructing a Theory of Shells,'' Prikl. Mat. Mekh., **43**(4), pp. 664–687.

[17] Yu, W., Hodges, D. H., and Volovoi, V. V., 2002, ''Asymptotic Generalization of Reissner-Mindlin Theory: Accurate Three-Dimensional Recovery for Composite Shells,'' Comput. Methods Appl. Mech. Eng., **191**(44), pp. 4971–5112.

[18] Hodges, D. H., Atilgan, A. R., and Danielson, D. A., 1993, ''A Geometrically Nonlinear Theory of Elastic Plates,'' ASME J. Appl. Mech., **60**, pp. 109–116.

[19] Simmonds, J. G., and Danielson, D. A., 1972, ''Nonlinear Shell Theory With Finite Rotation and Stress-Function Vectors,'' ASME J. Appl. Mech., **39**, pp. 1085–1090.

[20] Kane, T. R., Likins, P. W., and Levinson, D. A., 1983, *Spacecraft Dynamics*, McGraw-Hill, New York.

[21] Hodges, D. H., 1987, ''Finite Rotation and Nonlinear Beam Kinematics,'' Vertica, **11**(1/2), pp. 297–307.

[22] Reissner, E., 1986, ''On Finite Deflections of Anisotropic Laminated Elastic Plates,'' Int. J. Solids Struct., **22**(10), pp. 1107–1115.

[23] Axelrad, E. L., 1986, *Theory of Flexible Shells*, Elsevier, Amsterdam.

[24] Hodges, D. H., 1990, ''A Mixed Variational Formulation Based on Exact Intrinsic Equations for Dynamics of Moving Beams,'' Int. J. Solids Struct., **26**(11), pp. 1253–1273.

**T. R. Williams**
Department of Mechanical Engineering,
University of Alberta,
4–9 Mechanical Engineering Building,
Edmonton, Alberta T6G 2G8, Canada
e-mail: thomasw@ualberta.ca

**K. R. Fyfe**
Dynastream Innovations, Inc.,
228 River Avenue,
Cochrane, AB T4C 2C1, Canada
e-mail: ken.fyfe@dynastream.com

# Planar Accelerometer Configurations

*Numerous accelerometer configurations have been proposed and implemented by previous researches to determine parameters of the motion of the body to which the accelerometers are attached. To date, there has been no study of the geometric requirements of such configurations. This paper presents the requirements for minimal configurations for the case of general planar motion.* [DOI: 10.1115/1.1640365]

## 1 Introduction

As accelerometers become cheaper and smaller, a process driven by the application of the technology in mass-produced consumer items, the possibility of designing practical proprioceptive units (sensor combinations that are able to sense their own motion and position), is becoming a reality.

Even before accelerometers became cheap, researchers explored their use for determining parameters of motion such as angular velocities and accelerations, and employed integration schemes to determine body orientations and positions. An early example is the work of Schuler [1], who presented five accelerometer configurations of varying complexity to determine the rotational parameters of the spatial acceleration field, suggesting that it would be feasible to remove the gyroscopes from the traditional inertial navigation system. In 1973, Morris [2] presented a five-axis accelerometer scheme to assess human gait. This was closely followed by Kane et al. in 1974, [3], who used a 12-axis configuration to study the dynamics of a tennis racquet. This configuration was later used by Hayes et al. in 1983 to study human gait, [4]. Another configuration, this time composed of nine axes, was developed by Padgaonkar in 1975, [5], to determine angular and translational acceleration for general spatial motion. This configuration was used by Chou and Sinha [6] to study the kinematics of the head of a crash-test dummy. Later Mital and King [7] presented an integration scheme for the configuration that allowed the computation of spatial orientation. Also concerned with the kinematics of crash-test dummies, Nusholtz [8,9] presented schemes for planar (four axes) and spatial motion (with nine axes). A very similar system was used by Shea and Viano [10] for the same purpose. Recently, Chen et al. [11–13] have discussed a six-axis scheme that enables the determination of angular acceleration and, with numerical integration, translational acceleration. Schaecter [14] has considered the problem of designing accelerometer configurations that will yield the acceleration vector of a point on a rigid body with the condition that the configuration should still yield the desired information should one of the axes fail. This brief review indicates the interest in the use of accelerometers in determining parameters of rigid-body motion, and also the large range of configurations that have been used.

Up to a numerical limit, it is generally true that the more axes that are used, the more information that can be determined about the motion. Even below this limit, however, one can add axes that yield no additional information. It is the contribution of this paper to find the geometrical conditions on the minimal configurations of accelerometers that yield subsets of the possible information for the case of planar motion. Once similar analysis is completed for spatial motion, all feasible accelerometer configurations will be contained within a general framework. Rather than designing a configuration by trial and error, it will be possible to follow a set of design rules.

This paper proceeds by first developing a useful expression for the planar acceleration field in Sec. 2. Section 3 then presents configurations of single-axis accelerometers for the determination of angular motion parameters, either separately or together. The major problem of determining all possible information from the minimal number of axes is the subject of Sec. 4. All analysis is undertaken using simple vector geometry.

## 2 The Planar Acceleration Field

Consider a rigid body, $E$, undergoing planar motion relative to an inertial frame, $\Sigma$, as shown in Fig. 1. We identify $n+1$ points $R_i\ i=0,1,2,\ldots,n$ fixed within $E$. Position vectors $\mathbf{r}_{0i}$ from $R_0$ to $R_i$ ($\mathbf{r}_{0i}=R_i-R_0$) are used to identify each of the points. As $E$ moves, the points have non-zero velocity and acceleration relative to $\Sigma$. The position vectors of the points relative to an arbitrary point fixed in $\Sigma$ are denoted $\mathbf{R}_i$, thus

$$\mathbf{R}_i=\mathbf{R}_0+\mathbf{r}_{0i} \qquad i=1,2,\ldots,n. \tag{1}$$

The acceleration vector at $R_i$ is found by a double differentiation of Eq. (1):

$$\mathbf{A}_i=\mathbf{A}_0+\alpha\mathbf{s}_{0i}-\omega^2\mathbf{r}_{0i} \tag{2}$$

where $\omega$ is the angular velocity and $\alpha$ is the angular acceleration of body $E$ relative to $\Sigma$. The vector $\mathbf{s}_{0i}$ is obtained through a $+\pi/2$ rotation of $\mathbf{r}_{0i}$, and $\mathbf{A}_0$ is the acceleration vector at point $R_0$. Since there is an acceleration vector for every point in $E$, we have a time-varying vector field. It is easily confirmed that the choice of $R_0$ in $E$ is arbitrary, and this point is exploited in the analysis.

In the following, an accelerometer axis at a point $R_i$ parallel to unit vector $\boldsymbol{\sigma}_i$ is modeled as a perfect operator that gives as output, $m_i$, the scalar product of the total acceleration vector at $R_i$ with $\boldsymbol{\sigma}_i$.

The total acceleration vector at $R_i$, $\mathbf{T}_i$, is the vector sum of the inertial and gravitational acceleration vectors at the point, $\mathbf{T}_i=\mathbf{A}_i+\mathbf{g}$, thus the output of the $i$th axis can be written:

$$m_i=\boldsymbol{\sigma}_i\cdot(\mathbf{A}_0+\mathbf{g})+\alpha\boldsymbol{\sigma}_i\cdot\mathbf{s}_{0i}-\omega^2\boldsymbol{\sigma}_i\cdot\mathbf{r}_{0i}\,. \tag{3}$$

Since the accelerometers are fixed in the body, the coefficients $\boldsymbol{\sigma}_i\cdot\mathbf{s}_{0i}$ and $\boldsymbol{\sigma}_i\cdot\mathbf{r}_{0i}$ are time invariant. This paper shows how a minimal number of scalar measurements, $m_i$, can be used to find the parameters of the acceleration field.

Contributed by the Applied Mechanics Division of THE AMERICAN SOCIETY OF MECHANICAL ENGINEERS for publication in the ASME JOURNAL OF APPLIED MECHANICS. Manuscript received by the Applied Mechanics Division, July 4, 2002; final revision, June 9, 2003. Associate Editor: O. O'Reilly. Discussion on the paper should be addressed to the Editor, Prof. Robert M. McMeeking, Journal of Applied Mechanics, Department of Mechanical and Environmental Engineering, University of California–Santa Barbara, Santa Barbara, CA 93106-5070, and will be accepted until four months after final publication in the paper itself in the ASME JOURNAL OF APPLIED MECHANICS.

  

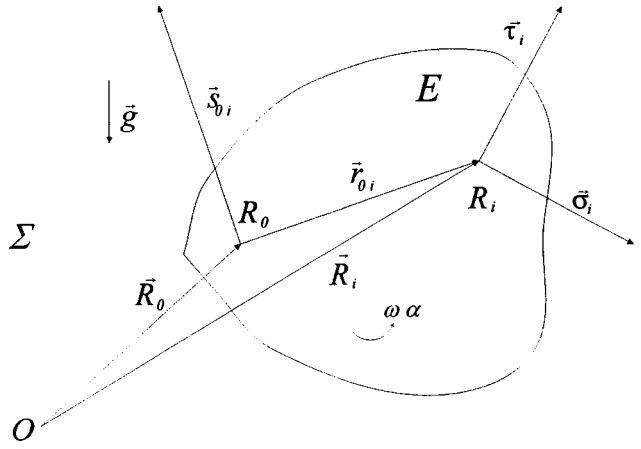


**Fig. 1 Definitions**

## 3 Finding Rotational Parameters

This section discusses simple configurations of scalar measurements that may be used to determine the rotational parameters of the acceleration field $(\alpha,\omega^2)$ first separately, then together, using the minimum number of measurements.

When determining a single parameter ($\alpha$ or $\omega^2$), the approach is to design configurations so that linear combinations of the outputs of the accelerometers result in an expression involving only the parameter of interest. To achieve this, one can alter the relative positions and orientations of the axes. In particular, since we are not for the moment interested in determining $\mathbf{T}_0=\mathbf{A}_0+\mathbf{g}$, the motion parameters which are independent of position, the orientations of the axes must be arranged so as to remove the effects from the outputs. A general linear combination of accelerometer outputs is of the form

$$\sum_{i=1}^{n}\lambda_i m_i=\sum_{i=1}^{n}\lambda_i\boldsymbol{\sigma}_i\cdot\mathbf{T}_0+\alpha\sum_{i=1}^{n}\lambda_i\boldsymbol{\sigma}_i\cdot\mathbf{s}_{0i}-\omega^2\sum_{i=1}^{n}\lambda_i\boldsymbol{\sigma}_i\cdot\mathbf{r}_{0i}\,. \tag{4}$$

Clearly for the combination to be free of $\mathbf{T}_0$, which is a time varying vector, the orientation vectors $\boldsymbol{\sigma}_i$ $i=1,2,\ldots,n$ must be such that it is possible to select $\lambda_i$ $i=1,2,\ldots,n$ such that

$$\sum_{i=1}^{n}\lambda_i\boldsymbol{\sigma}_i=\mathbf{0}. \tag{5}$$

The smallest configuration that may be used to this end is a parallel pair, $\boldsymbol{\sigma}_1=\boldsymbol{\sigma}_2$, with the outputs differenced, i.e., $\lambda_1=-\lambda_2$. Denoting the orientations of the two axes by $\boldsymbol{\sigma}$, the equation for their difference is

$$\begin{aligned} m_1-m_2&=\boldsymbol{\sigma}\cdot(\mathbf{T}_0+\alpha\mathbf{s}_{01}-\omega^2\mathbf{r}_{01})-\boldsymbol{\sigma}\cdot(\mathbf{T}_0+\alpha\mathbf{s}_{02}-\omega^2\mathbf{r}_{02})\\ &=\boldsymbol{\sigma}\cdot(\alpha(\mathbf{s}_{01}-\mathbf{s}_{02})-\omega^2(\mathbf{r}_{01}-\mathbf{r}_{02}))\\ &=\boldsymbol{\sigma}\cdot(\alpha\mathbf{s}_{21}-\omega^2\mathbf{r}_{21}) \end{aligned} \tag{6}$$

and it is seen that, since $\mathbf{s}_{21}$ and $\mathbf{r}_{21}$ are orthogonal, it is possible to select, for every $\boldsymbol{\sigma}$, relative positions for the two accelerometer axes so that the differences in the outputs is linearly proportional to $\alpha$ or $\omega^2$.

To determine $\alpha$ using two accelerometers, Eq. (6) states that we must have $\boldsymbol{\sigma}\cdot\mathbf{r}_{21}=0$, i.e., the line between the two accelerometer axes must be orthogonal to the sensing direction of the axes. Conversely, to determine $\omega^2$, the line between the two accelerometer axes must be collinear with the sensing directions.

To determine both $\alpha$ and $\omega^2$ it would be possible to use a combination of the configurations described above for $\omega^2$ and $\alpha$, requiring four accelerometer axes. It is possible, however, to use fewer than four axes, as is now demonstrated. Since two parameters are now desired, two linearly dependent equations are required. These equations must both be independent of $\mathbf{T}_0$. The minimum number of accelerometers that can be used to generate two such equations is three, where all have the same orientation $\boldsymbol{\sigma}$. To prove this, consider the following discussion. Assume that $\boldsymbol{\sigma}_1$ and $\boldsymbol{\sigma}_2$ are non-parallel, then for the equation

$$\lambda_1\boldsymbol{\sigma}_1+\lambda_2\boldsymbol{\sigma}_2+\lambda_3\boldsymbol{\sigma}_3=\mathbf{0} \tag{7}$$

to have a solution, $\lambda_3$ must be nonzero, in which case the equation can be rewritten as

$$\lambda_1'\boldsymbol{\sigma}_1+\lambda_2'\boldsymbol{\sigma}_2=\boldsymbol{\sigma}_3 \tag{8}$$

in which case there is only one solution to the equation (remember we are only working in two dimensions). Employing a parallel pair of axes $\boldsymbol{\sigma}_1=\boldsymbol{\sigma}_2$, with $\boldsymbol{\sigma}_3\neq\pm\boldsymbol{\sigma}_1$ has only the solution ($\lambda_1=-\lambda_2$, $\lambda_3=0$). Finally if three parallel axes are used, then there are two distinct solutions ($\lambda_1=-\lambda_2$, $\lambda_3=0$) and ($\lambda_1=-\lambda_3$, $\lambda_2=0$), the solution ($\lambda_1=0$, $\lambda_2=-\lambda_3$) being obtainable as a linear combination of these. The differences in outputs for the case of three parallel axes may be written as

$$\begin{aligned} m_1-m_2&=\alpha\boldsymbol{\sigma}\cdot(\mathbf{s}_1-\mathbf{s}_2)-\omega^2\boldsymbol{\sigma}\cdot(\mathbf{r}_1-\mathbf{r}_2)\\ m_1-m_3&=\alpha\boldsymbol{\sigma}\cdot(\mathbf{s}_1-\mathbf{s}_3)-\omega^2\boldsymbol{\sigma}\cdot(\mathbf{r}_1-\mathbf{r}_3). \end{aligned} \tag{9}$$

If $(\mathbf{r}_1-\mathbf{r}_2)\neq\lambda(\mathbf{r}_1-\mathbf{r}_3)$ these equations are linearly independent, and it is possible to solve for $\omega^2$ and $\alpha$. Geometrically, this means that the three parallel axes are positioned so that there is not a single line through their locations. Since it is not possible to use any less than three axes to generate two linearly independent equations without the effect of $\mathbf{T}_0$ present, the three parallel axes are the minimal configuration required to determine both $\alpha$ and $\omega^2$.

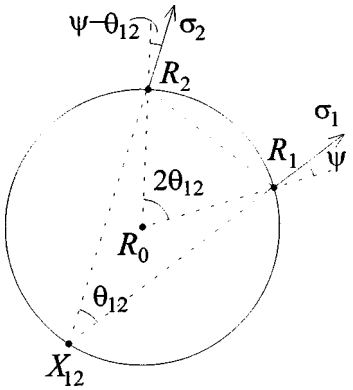


**Fig. 2 The construction of circle $\Psi_{12}$**

## 4 Planar Configurations

In this section, the configurations of accelerometers that yield the full set of motion parameters $(\alpha,\omega^2,\mathbf{T}_0)$ are discussed. As shown above, the *i*th measurement, i.e., the output of the accelerometer axis at $R_i$ with orientation $\boldsymbol{\sigma}_i$ is linear in the motion parameters:

$$m_i=\mathbf{T}_0\cdot\boldsymbol{\sigma}_i+\alpha(\boldsymbol{\sigma}_i\cdot\mathbf{s}_{0i})-\omega^2(\boldsymbol{\sigma}_i\cdot\mathbf{r}_{0i}) \tag{10}$$

thus yielding an equation in four unknowns, $\mathbf{T}_0$ comprising two of these. In order to solve for these unknowns, it is required that four measurements be taken such that the resulting equations, formed by multiple instances of Eq. (10) are linearly independent in the acceleration parameters, i.e., the only set of constants $\lambda_i$, $i=1$, 2, 3, 4 that satisfy the equation

$$\sum_{i=1}^{4}\lambda_i m_i=0 \tag{11}$$

for all possible motions are $\lambda_i=0$ $i=1, 2, 3, 4$. Equivalently we must demonstrate the non-singularity of the *configuration matrix* **C** with general row:

$$\mathbf{c}_i=[\boldsymbol{\sigma}_i^T \quad \boldsymbol{\sigma}_i^T\mathbf{s}_{0i} \quad \boldsymbol{\sigma}_i^T\mathbf{r}_{0i}]$$

where $(\boldsymbol{\sigma}_i,\mathbf{r}_{0i},\mathbf{s}_{0i})$ are coordinate matrices of $(\boldsymbol{\sigma}_i,\mathbf{r}_{0i},\mathbf{s}_{0i})$. Using **m** to denote the column matrix of measurements and $\mathbf{x}^T=[\mathbf{T}_0^T\ \alpha\ \omega^2]$ to describe the acceleration parameters, we can write the four measurement equations in the form $\mathbf{Cx}=\mathbf{m}$, which shows that we can only solve for **x** if **C** is nonsingular. The nonsingularity of the spatial analogue of this configuration matrix is the method that Tan et al. [12,13] used to prove the feasibility of their six-axis configuration. The advantage of the present approach over the use of a configuration matrix is the geometric insight offered.

In the following, rather than identify the conditions on $(R_i,\boldsymbol{\sigma}_i)$ $i=1, 2, 3, 4$ such that the equations are linearly independent, the converse is undertaken, i.e., the configurations for which at least one $\lambda_i\neq 0$ are found. This is performed incrementally. First the configurations of two axes which lead to linearly dependent equations are found. Next two axes are assumed to be placed so that the equations are linearly independent, and the positions and orientations of a third axis which yield three dependent equations are studied. Similar analysis is completed for four axes. Upon completion of each stage of this analysis, sets of configurations which yield linearly dependent equations for two, three and four axes can be identified. A configuration yielding linearly independent equations is any that is not a member of these sets.

A configuration of *n* axes which yields *n* linearly independent equations is defined as being a feasible *n*-axis configuration. If a particular position, $R_{n+1}$, of an axis $\boldsymbol{\sigma}_{n+1}$ renders a feasible *n*-axis configuration an infeasible $(n+1)$-axis configuration, then $R_{n+1}$ is referred to as an infeasible position for an axis of orientation $\boldsymbol{\sigma}_{n+1}$.

Before undertaking the analysis, some general equations that are useful in all the following cases are introduced. If we have a feasible *n*-axis configuration, then there are no non-zero constants that satisfy $\Sigma_{i=1}^{n}\lambda_i m_i=0$. In order for the $(n+1)$-axis configuration to be infeasible, there must be nonzero constants that satisfy $\Sigma_{i=1}^{n+1}\lambda_i m_i=0$. Since the *n*-axis configuration is feasible, the constant $\lambda_{n+1}$ associated with the measurement of the $n+1$ must be nonzero, and the equation may be rewritten

$$\sum_{i=1}^{n}\lambda_i m_i=m_{n+1} \tag{12}$$

where the $\lambda_i$ constants are different than those above. Allowing arbitrary variation in the motion parameters, and considering the form of Eq. (10), this scalar equation is seen to be equivalent to the following set of equations:

$$\sum_{i=1}^{n}\lambda_i\boldsymbol{\sigma}_i=\boldsymbol{\sigma}_{n+1} \tag{13}$$

$$\sum_{i=1}^{n}\lambda_i(\boldsymbol{\sigma}_i\cdot\mathbf{s}_{0i})=\boldsymbol{\sigma}_{n+1}\cdot\mathbf{s}_{0n+1} \tag{14}$$

$$\sum_{i=1}^{n}\lambda_i(\boldsymbol{\sigma}_i\cdot\mathbf{r}_{0i})=\boldsymbol{\sigma}_{n+1}\cdot\mathbf{r}_{0n+1}. \tag{15}$$

A given $\boldsymbol{\sigma}_{n+1}$ constrains the set of scalars $\{\lambda_i\}_{i=1}^{n}$ satisfying Eq. (13). Equations (14) and (15) are then used to solve for $\mathbf{r}_{0n+1}$ the infeasible position(s), relative to $R_0$, for the axis with orientation $\boldsymbol{\sigma}_{n+1}$. The method of solution for Eqs. (14) and (15) is to note that $\boldsymbol{\sigma}_j\cdot\mathbf{s}_{0j}=-\boldsymbol{\tau}_j\cdot\mathbf{r}_{0j}$, where $\boldsymbol{\tau}_j$ is the vector obtained by rotating $\boldsymbol{\sigma}_j$ $\pi/2$ radians counterclockwise. Then, since $\boldsymbol{\tau}_{n+1}$ and $\boldsymbol{\sigma}_{n+1}$ are orthogonal unit vectors, we have

$$\mathbf{r}_{0n+1}=\sum_{i=1}^{n}\lambda_i(\boldsymbol{\tau}_i\cdot\mathbf{r}_{0i})\boldsymbol{\tau}_{n+1}+\sum_{i=1}^{n}\lambda_i(\boldsymbol{\sigma}_i\cdot\mathbf{r}_{0i})\boldsymbol{\sigma}_{n+1}. \tag{16}$$

The general method of solution for each stage is to find $\{\lambda_i\}_{i=1}^{n}$ for a particular $\boldsymbol{\sigma}_{n+1}$ and then find the associated $\mathbf{r}_{0n+1}$. If the solution for $\{\lambda_i\}_{i=1}^{n}$ is unique for each $\boldsymbol{\sigma}_{n+1}$ then there is only one infeasible position for each axis. However, if there are an infinitude of solutions $\{\lambda_i\}_{i=1}^{n}$ that satisfy Eq. (13) then there is also an infinitude of infeasible positions for each axis. The results of the analysis are summarized at the end of each section.

**4.1 Infeasible Configurations for Two Axes.** For two axes to be arranged in an infeasible configuration, it is necessary that the measurements of the two axes be multiples of each other for all time and all possible motions. Considering Eq. (13) for the case $n=1$, the only possible solutions are $\lambda_1=1$ in which case $\boldsymbol{\sigma}_2=\boldsymbol{\sigma}_1$ or $\lambda_1=-1$ and $\boldsymbol{\sigma}_2=-\boldsymbol{\sigma}_1$. Substituting these two solutions into (16) gives

$$\mathbf{r}_{02}=(\boldsymbol{\tau}_1\cdot\mathbf{r}_{01})\boldsymbol{\tau}_1+(\boldsymbol{\sigma}_1\cdot\mathbf{r}_{01})\boldsymbol{\sigma}_1=\mathbf{r}_{01} \tag{17}$$

in both cases. The equivalence of axes at *R* with orientations $\boldsymbol{\sigma}$ and $-\boldsymbol{\sigma}$ leads us to identify them as identical in the following development.

**4.2 Infeasible Configurations for Three Axes.** If, as shown in Fig. 2, $\theta_{1j}$ is the angle of rotation between $\boldsymbol{\sigma}_1$ and $\boldsymbol{\sigma}_j$, i.e., $\boldsymbol{\sigma}_1$ must be rotated by $\theta_{1j}$ counterclockwise so that it is aligned with $\boldsymbol{\sigma}_j$, then

$$\boldsymbol{\sigma}_j=\cos\theta_{1j}\boldsymbol{\sigma}_1+\sin\theta_{1j}\boldsymbol{\tau}_1 \quad j=2,3. \tag{18}$$

Now, we can identify $\lambda_1$ and $\lambda_2$ such that $\boldsymbol{\sigma}_3=\lambda_1\boldsymbol{\sigma}_1+\lambda_2\boldsymbol{\sigma}_2$ from

$$\begin{aligned}\boldsymbol{\sigma}_3&=\lambda_1\boldsymbol{\sigma}_1+\lambda_2\boldsymbol{\sigma}_2=(\lambda_1+\lambda_2\cos\theta_{12})\boldsymbol{\sigma}_1+\lambda_2\sin\theta_{12}\boldsymbol{\tau}_1\\&=\cos\theta_{13}\boldsymbol{\sigma}_1+\sin\theta_{13}\boldsymbol{\tau}_1\end{aligned} \tag{19}$$

from which

$$\lambda_1=\cos\theta_{13}-\frac{\sin\theta_{13}}{\sin\theta_{12}}\cos\theta_{12} \tag{20}$$

$$\lambda_2=\frac{\sin\theta_{13}}{\sin\theta_{12}}. \tag{21}$$

Since there is only one pair of scalars $(\lambda_1,\lambda_2)$ for each $\boldsymbol{\sigma}_3$, we conclude from Eq. (16) that there is only one infeasible position $R_3(\boldsymbol{\sigma}_3)$ for each orientation $\boldsymbol{\sigma}_3$. Now the general equation, (16) for $\mathbf{r}_{03}(\boldsymbol{\sigma}_3)$, the vector from $R_0$ to the *unique* infeasible position, $R_3(\boldsymbol{\sigma}_3)$, for the axis with orientation $\boldsymbol{\sigma}_3$ can be written as

$$\mathbf{r}_{03}(\boldsymbol{\sigma}_3)=(\lambda_1\boldsymbol{\sigma}_1\cdot\mathbf{r}_{01}+\lambda_2\boldsymbol{\sigma}_2\cdot\mathbf{r}_{02})\boldsymbol{\sigma}_3+(\lambda_1\boldsymbol{\tau}_1\cdot\mathbf{r}_{01}+\lambda_2\boldsymbol{\tau}_2\cdot\mathbf{r}_{02})\boldsymbol{\tau}_3. \tag{22}$$

We place $R_0$ at the center of the circle, $\Psi_{12}$, of radius *r*, defined by the three points, $R_1$, $R_2$ and $X_{12}$, the point of intersection of the lines $L_i$ drawn through $R_i$ parallel to $\boldsymbol{\sigma}_i$ for $i=1, 2$ (we assume for now that $\boldsymbol{\sigma}_1$ and $\boldsymbol{\sigma}_2$ are not parallel). With such a choice of $R_0$, we know from a well known theorem on angles measured at the center and circumference of circles, [15], that the angle between the vectors $X_{12}R_1$ and $X_{12}R_2$, and hence $\boldsymbol{\sigma}_1$ and $\boldsymbol{\sigma}_2$ $(\theta_{12})$ is half that between $\mathbf{r}_{01}$ and $\mathbf{r}_{02}$, (see Fig. 2). Thus, defining $\psi$ to be the angle by which $\mathbf{r}_{01}$ must be rotated to bring it parallel to $\boldsymbol{\sigma}_1$, we immediately have $\psi-\theta_{12}$ as the angle between $\mathbf{r}_{02}$ and $\boldsymbol{\sigma}_2$. Thus Eq. (22) becomes

$$\mathbf{r}_{03}(\boldsymbol{\sigma}_3)=r(\cos(\psi-\theta_{13})\boldsymbol{\sigma}_3-\sin(\psi-\theta_{13})\boldsymbol{\tau}_3) \tag{23}$$

which demonstrates that the unique infeasible position $R_3(\boldsymbol{\sigma}_3)$ for the axis $\boldsymbol{\sigma}_3$ has the same relationship to $(R_1,\boldsymbol{\sigma}_1)$ as $(R_2,\boldsymbol{\sigma}_2)$ does, i.e., extending a line parallel to $\boldsymbol{\sigma}_3$ through $X_{12}$, the infeasible position for $\boldsymbol{\sigma}_3$ lies at the intersection of this line and the circle, $\Psi_{12}$, as is shown in Fig. 3. The infeasible position for an axis $\boldsymbol{\sigma}$ can therefore be found by extending the line through $X_{12}$ to $\Psi_{12}(\boldsymbol{\sigma})$ the point of intersection with the circle $\Psi_{12}$. Thus, in the case of three axes, at least two of which are non-parallel we know that the axes form an infeasible configuration if the lines drawn

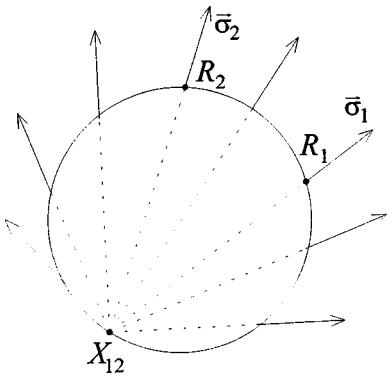


**Fig. 3 The infeasible positions and orientations of a third axis**

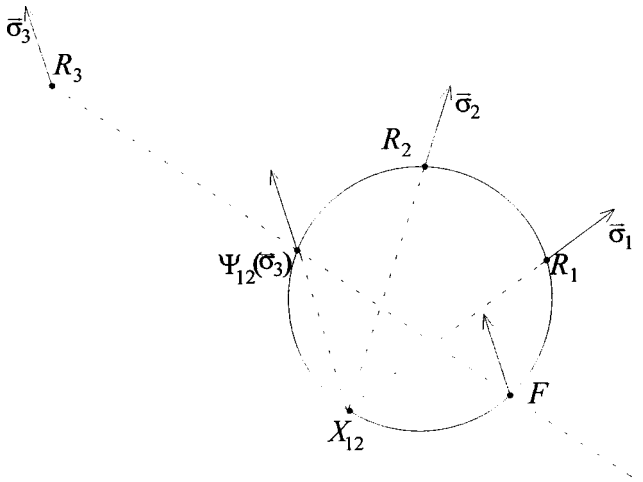


**Fig. 4 Construction of *F***

through the positions parallel to the axes intersect at a single point on the circle drawn through the positions of the axes.

Now we consider the special cases. We have already seen when considering the minimal configuration for the determination of $\alpha$ and $\omega^2$ that three parallel axes are infeasible if it is possible to draw a line through their locations. This line may be considered as the circle of infinite radius through the accelerometer positions and the point $X_{12}$ at infinity. It is also easily confirmed, using Eq. (16) that any three axes at a point are infeasible. In this case, $R_1$, $R_2$, $R_3$, and $X_{12}$ exist at a single point, which may be considered a circle of zero radius. Thus the above stated result on the infeasible configurations for three axes is seen to hold in all cases.

*Summary:* Three axes $(R_i, \boldsymbol{\sigma}_i)$ $i=1, 2, 3$ are in an infeasible configuration if the lines $L_i$ drawn through $R_i$ parallel to $\boldsymbol{\sigma}_i$ intersect at a single point, which is on the circle through $R_1$, $R_2$, and $R_3$.

**4.3 Infeasible Configurations for Four Axes.** Now we have to express $\boldsymbol{\sigma}_4$ as $\boldsymbol{\sigma}_4=\Sigma_{i=1}^{3}\lambda_i\boldsymbol{\sigma}_i$ where the constants for a given $\boldsymbol{\sigma}_4$ are no longer unique. We assume that $\boldsymbol{\sigma}_1$ and $\boldsymbol{\sigma}_2$ are nonparallel then we can find constants $(\mu_1,\mu_2)$ and $(\eta_1,\eta_2)$ such that

$$\mu_1\boldsymbol{\sigma}_1+\mu_2\boldsymbol{\sigma}_2=\boldsymbol{\sigma}_3 \tag{24}$$

$$\eta_1\boldsymbol{\sigma}_1+\eta_2\boldsymbol{\sigma}_2=\boldsymbol{\sigma}_4 \tag{25}$$

then Eq. (13) becomes

$$\boldsymbol{\sigma}_4=\lambda_1(\lambda_3)\boldsymbol{\sigma}_1+\lambda_2(\lambda_3)\boldsymbol{\sigma}_2+\lambda_3\boldsymbol{\sigma}_3 \tag{26}$$

where

$$\lambda_i(\lambda_3)=\eta_i-\lambda_3\mu_i. \tag{27}$$

Now, Eq. (16) for the determination of $\mathbf{r}_{04}(\boldsymbol{\sigma}_4)$, the vector from $R_0$ to the infeasible position of an axis with orientation $\boldsymbol{\sigma}_4$, becomes

$$\begin{aligned}\mathbf{r}_{04}(\boldsymbol{\sigma}_4,\lambda_3)=&\{(\eta_1\boldsymbol{\sigma}_1\cdot\mathbf{r}_{01}+\eta_2\boldsymbol{\sigma}_2\cdot\mathbf{r}_{02})\boldsymbol{\sigma}_4+(\eta_1\boldsymbol{\tau}_1\cdot\mathbf{r}_{01}\\&+\eta_2\boldsymbol{\tau}_2\cdot\mathbf{r}_{02})\boldsymbol{\tau}_4\}-\lambda_3(\mu_1\boldsymbol{\sigma}_1\cdot\mathbf{r}_{01}+\mu_2\boldsymbol{\sigma}_2\cdot\mathbf{r}_{02}\\&-\boldsymbol{\sigma}_3\cdot\mathbf{r}_{03})\boldsymbol{\sigma}_4-\lambda_3(\mu_1\boldsymbol{\tau}_1\cdot\mathbf{r}_{01}+\mu_2\boldsymbol{\tau}_2\cdot\mathbf{r}_{02}-\boldsymbol{\tau}_3\cdot\mathbf{r}_{03})\boldsymbol{\tau}_4\\=&\mathbf{r}_{04}(\boldsymbol{\sigma}_4,0)+\lambda_3\mathbf{v}(\boldsymbol{\sigma}_4).\end{aligned} \tag{28}$$

This is the equation of a line parametrized by $\lambda_3$. Using the analysis from the previous section, identifying $\eta_i$ with $\lambda_i$, we see that $\mathbf{r}_{04}(\boldsymbol{\sigma}_4,0)$ is the vector from $R_0$ to the point $\Psi_{12}(\boldsymbol{\sigma}_4)$, i.e., the intersection of the circle through $R_1$, $R_2$ and $X_{12}$ with the line through $X_{12}$ parallel to $\boldsymbol{\sigma}_4$. Thus, the infeasible positions for an axis with orientation $\boldsymbol{\sigma}_4$ lie on a line through $\Psi_{12}(\boldsymbol{\sigma}_4)$. Note that the coefficients of the vector $\mathbf{v}(\boldsymbol{\sigma}_4)$ are constants, fixed by the configuration of the first three axes. Consequently rotating $\boldsymbol{\sigma}_4$ causes an identical rotation of $\mathbf{v}(\boldsymbol{\sigma}_4)$ and knowledge of the vector for some $\boldsymbol{\sigma}$ is sufficient to specify $\mathbf{v}$ for all orientations. Choosing $\boldsymbol{\sigma}_4=\boldsymbol{\sigma}_3$, we get

$$\begin{aligned}\mathbf{v}(\boldsymbol{\sigma}_3)=&(\mu_1\boldsymbol{\sigma}_1\cdot\mathbf{r}_{01}+\mu_2\boldsymbol{\sigma}_2\cdot\mathbf{r}_{02})\boldsymbol{\sigma}_3+(\mu_1\boldsymbol{\tau}_1\cdot\mathbf{r}_{01}+\mu_2\boldsymbol{\tau}_2\cdot\mathbf{r}_{02})\boldsymbol{\tau}_3\\&-\mathbf{r}_{03}.\end{aligned} \tag{29}$$

Now, we can identify $\mu_i=\lambda_i$ from the previous section, so

$$\mathbf{v}(\boldsymbol{\sigma}_3)=\mathbf{r}_{04}(\boldsymbol{\sigma}_3,0)-\mathbf{r}_{03}=\Psi_{12}(\boldsymbol{\sigma}_3)-R_3 \tag{30}$$

and

$$R_4(\boldsymbol{\sigma}_3,\lambda_3)=\Psi_{12}(\boldsymbol{\sigma}_3)+\lambda_3(\Psi_{12}(\boldsymbol{\sigma}_3)-R_3) \tag{31}$$

i.e., the infeasible positions for an axis $\boldsymbol{\sigma}_3$ lie on the line through $R_3$, the position of the axis $\boldsymbol{\sigma}_3$, and $\Psi_{12}(\boldsymbol{\sigma}_3)$, the position deemed infeasible by the configuration of the first two axes. Since this relationship is valid for all $\lambda_3$ there is, unless $\boldsymbol{\sigma}_3$ is tangent to $\Psi_{12}$ at $\Psi_{12}(\boldsymbol{\sigma}_3)$, another point, $F$ on $\Psi_{12}$ at which it is infeasible to place an axis with orientation $\boldsymbol{\sigma}_3$, as is shown in Fig. 4. Now, writing $\boldsymbol{\sigma}_4(\theta)$ to mean the vector obtained by rotating $\boldsymbol{\sigma}_3$ by $\theta$ we know that $\mathbf{v}(\boldsymbol{\sigma}_4(\theta))$ is obtained by rotating $\mathbf{v}(\boldsymbol{\sigma}_3)$ by $\theta$ while $\mathbf{r}_{04}(\boldsymbol{\sigma}_4(\theta),0)$ is found by rotating $\mathbf{r}_{04}(\boldsymbol{\sigma}_3,0)$ by $2\theta$, hence we have the same geometry as was encountered in the previous section, and the lines of infeasible positions are seen to all pass through $F$. Thus the general expression for the infeasible positions for an axis with orientation $\boldsymbol{\sigma}_4$ is

$$R_4(\boldsymbol{\sigma}_4,\lambda_3)=\Psi_{12}(\boldsymbol{\sigma}_4)+\lambda_3(\Psi_{12}(\boldsymbol{\sigma}_4)-F). \tag{32}$$

This equation shows that there is a line of infeasible positions through $F$ for every orientation of axis $\boldsymbol{\sigma}_4$, as is shown in Fig. 5. Conversely for every point excluding $F$ in the plane, there is one infeasible orientation of axis $\boldsymbol{\sigma}_4$. Since every line of infeasible positions passes through $F$, any axis at $F$ will render the configuration infeasible. As was previously discussed, if $R_1=R_2$ $(\boldsymbol{\sigma}_1\neq\boldsymbol{\sigma}_2)$ then the circular distribution shrinks to a point, which is also $X_{12}$ and $F$. If a third axis is located at a distinct point, $R_3$, the three axis configuration is immediately feasible. A fourth axis may also be added at $R_3$ if it is not parallel to the third and we see that a configuration consisting of two pairs of nonparallel axes at two distinct points is always feasible. This is of interest since biaxial accelerometers are commercially available.

The assumption at the beginning of the analysis was that two of $\boldsymbol{\sigma}_i$ $i=1, 2, 3$ were nonparallel. These two non-parallel axes are required to generate the circular distribution of infeasible axes, then the third axis is used to find the point, $F$. If this is not the case, i.e., the three axes are parallel, and in a feasible configuration, it has already been shown that there must not be a line through $R_1$, $R_2$ and $R_3$. For a fourth axis to yield an infeasible configuration, it must be parallel to the first three, in which case there are two degrees-of-freedom in the selection of $(\lambda_1,\lambda_2,\lambda_3)$. For instance, $\lambda_1$ and $\lambda_2$ may be chosen arbitrarily, while $\lambda_3$ must satisfy $\lambda_3=1-\lambda_1-\lambda_2$. The equation for $\mathbf{r}_{04}$ in this case is

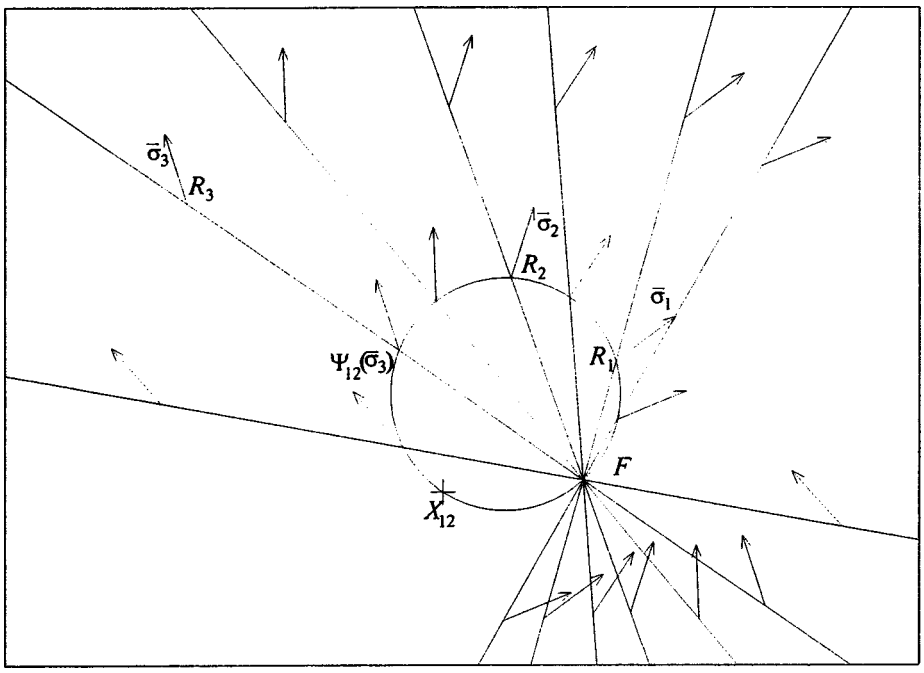


**Fig. 5 Some of the infeasible positions and orientations for a fourth axis given three axes, at least two of which are nonparallel. (The totality fill the plane.)**

$$\mathbf{r}_{04}(\boldsymbol{\sigma},\lambda_1,\lambda_2)=\boldsymbol{\sigma}\cdot(\lambda_1\mathbf{r}_{01}+\lambda_2\mathbf{r}_{02}+(1-\lambda_1-\lambda_2)\mathbf{r}_{03})\boldsymbol{\sigma}+\boldsymbol{\tau}\cdot(\lambda_1\mathbf{r}_{01}+\lambda_2\mathbf{r}_{02}+(1-\lambda_1-\lambda_2)\mathbf{r}_{03})\boldsymbol{\tau}$$
$$=\lambda_1(\mathbf{r}_{01}-\mathbf{r}_{03})+\lambda_2(\mathbf{r}_{02}-\mathbf{r}_{03})+\mathbf{r}_{03} \quad (33)$$

and since $\mathbf{r}_{01}-\mathbf{r}_{03}$ and $\mathbf{r}_{02}-\mathbf{r}_{03}$ are not parallel, it is seen that every point in the plane is an infeasible position for a fourth parallel axis, as would be expected.

*Summary:* No configuration of four parallel axes is feasible. Selecting any two non-parallel axes $(R_1,\boldsymbol{\sigma}_1)$ and $(R_2,\boldsymbol{\sigma}_2)$ from a feasible configuration of three axes we can draw a circle $\Psi_{12}$ through $R_1$, $R_2$ and $X_{12}$, the point of intersection of lines drawn through $R_1$ and $R_2$ parallel to $\boldsymbol{\sigma}_1$ and $\boldsymbol{\sigma}_2$. Every point $P$ on $\Psi_{12}$ is identified as an infeasible position for an axis parallel to the line $X_{12}-P$, and if $\boldsymbol{\sigma}$ is parallel to $X_{12}-P$ we write the infeasible position as $\Psi_{12}(\boldsymbol{\sigma})$. The line through $R_3$ and $\Psi_{12}(\boldsymbol{\sigma}_3)$ also intersects circle $\Psi_{12}$ at a point $F$. The lines, $\Lambda(\boldsymbol{\sigma})$, through $F$ are infeasible positions for axes with orientation $\boldsymbol{\sigma}$, where $\Psi_{12}(\boldsymbol{\sigma})$ lies at the intersection of $\Lambda$ and $\Psi_{12}$ that is not $F$.

## 5 Discussion

This paper has presented the infeasible configurations for two, three, and four accelerometer axes in the case of planar motion, four being the number required to extract as much information as possible about the motion of the configuration. The infeasible configurations were specified since they are less numerous than the feasible configurations and once infeasible configurations are known, any configuration that does not belong to this set must be feasible. The graphical means of finding the infeasible configurations may be used as a design tool if a general four-axis configuration is desired. Minimal configurations for finding $\alpha$, $\omega^2$ and both of these parameters together have also been presented. Since determining $\mathbf{A}_0$ from $\mathbf{T}_0$ requires either integration, and the knowledge of initial conditions, or some other sensing device, it may be that these configurations are the ones that are more directly useful.

A possible direction for future research is the extension to the spatial case which is obviously more generally applicable. Some results in spatial accelerometer configurations have been obtained by Tan et al. [13], although there is no geometric interpretation of the infeasibility configurations. Another interesting area of research is the determination of robust configurations; configurations that are least sensitive to placement errors and manufacturing errors in the accelerometers.

## References


[1] Schuler, A. R., Grammatikos, A., and Fegley, K. A., 1967, "Measuring Rotational Motion With Linear Accelerometers," IEEE Trans. Aerosp. Electron. Syst., **3**(3), pp. 465–472.

[2] Morris, J. R. W., 1973, "Accelerometry—A Technique for the Measurement of Human Body Movements," J. Biomech., **6**, pp. 729–736.

[3] Kane, T. R., Hayes, W. C., and Priest, J. D., 1974, "Experimental Determination of Forces Exerted in Tennis Play," *Biomechanics IV*, University Park Press, pp. 284–290.

[4] Hayes, W. C., Gran, J. D., Nagurka, M. L., Feldman, J. M., and Oatis, C., 1983, "Leg Motion Analysis During Gait by Multiaxial Accelerometry: Theoretical Foundations and Preliminary Validations," ASME J. Biomech. Eng., **105**, pp. 283–289.

[5] Padgaonkar, A. J., Krieger, K. W., and King, A. I., 1975, "Measurement of Angular Acceleration of a Rigid Body Using Linear Accelerometers," ASME J. Appl. Mech., **42**, pp. 552–556.

[6] Chou, C. C., and Sinha, S. C., 1976, "On the Kinematics of the Head Using Linear Acceleration Measurements," J. Biomech., **9**, pp. 607–613.

[7] Mital, N. K., and King, A. I., 1979, "Computation of Rigid-Body Rotation in Three-Dimensional Space From Body-Fixed Linear Acceleration Measurements," ASME J. Appl. Mech., **46**, pp. 925–930.

[8] Nusholtz, G. S., and Molinaro, R., 1991, "Force Deflection Curves for Air Bag Response," Exp. Tech., Mar./Apr., pp. 33–35.

[9] Nusholtz, G. S., 1993, "Geometric Methods in Determining Rigid-Body Dynamics," Exp. Mech., June, pp. 153–158.

[10] Shea, R. T., and Viano, D. C., 1994, "Computing Body Segment Trajectories in the Hybrid III Dummy Using Linear Accelerometer Data," ASME J. Biomech. Eng., **116**, pp. 37–43.

[11] Chen, J.-H., Lee, S.-C., and DeBra, D. B., 1994, "Gyroscope Free Strapdown Inertial Measurement Unit by Six Linear Accelerometers," J. Guid. Control Dyn., **17**(2), pp. 286–290.

[12] Tan, C.-W., Mostov, K., and Varaiya, P., 2000, "Feasibility of a Gyroscope-Free Inertial Navigations System for Tracking Rigid Body Motion," California PATH Research Report, May.

[13] Tan, C.-W., Park, S., Mostov, K., and Varaiya, P., 2001, "Design of Gyroscope-Free Navigation Systems," IEEE 4th International Conference on Intelligent Transportation Systems, Oakland, CA, Aug. IEEE Piscataway, NJ, pp. 286–291.

[14] Schaecter, D., 1999, "A Fully-Redundant Set of Single-Axis Accelerometers," 1999 AAS Astrodynamics, Conference, Girdwood, AK, Aug. 16–19.

[15] Audin, M., 2002, *Geometry*, Springer, Berlin.

# Elasticity Solutions Versus Asymptotic Sectional Analysis of Homogeneous, Isotropic, Prismatic Beams

**Wenbin Yu**[1]
Post Doctoral Fellow

**Dewey H. Hodges**
Professor
Mem. ASME

School of Aerospace Engineering,
Georgia Institute of Technology,
Atlanta, GA 30332-0150

*The original three-dimensional elasticity problem of isotropic prismatic beams has been solved analytically by the variational asymptotic method (VAM). The resulting classical model (Euler-Bernoulli-like) is the same as the superposition of elasticity solutions of extension, Saint-Venant torsion, and pure bending in two orthogonal directions. The resulting refined model (Timoshenko-like) is the same as the superposition of elasticity solutions of extension, Saint-Venant torsion, and both bending and transverse shear in two orthogonal directions. The fact that the VAM can reproduce results from the theory of elasticity proves that two-dimensional finite-element-based cross-sectional analyses using the VAM, such as the variational asymptotic beam sectional analysis (VABS), have a solid mathematical foundation. One is thus able to reproduce numerically with VABS the same results for this problem as one obtains from three-dimensional elasticity, but with orders of magnitude less computational cost relative to three-dimensional finite elements.*
[DOI: 10.1115/1.1640367]

## Introduction

The variational asymptotic method (VAM) is a mathematical approach applicable to any problem governed by an energy functional having one or more small parameters. Contrary to the formal asymptotic methods, VAM applies the asymptotic expansion to the energy functional instead of the system of differential equations, [1]. Hence, dropping a small term in the functional is equivalent to neglecting such quantities in several differential equations simultaneously. This implies that, when applicable, VAM is more compact and less cumbersome than standard asymptotic methods. The VAM includes the merits of both variational (systematic) and asymptotic (without ad hoc kinematic assumptions) methods. It allows one to replace a three-dimensional structural model with a reduced-order model in terms of an asymptotic series of certain small parameters inherent to the structure. Although there are different forms of this method, e.g., Ciarlet and Destuynder [2] and Berdichevsky [3], the method used in the present work is more closely aligned with the latter.

The application of the VAM to model beams with general geometry and material has been demonstrated in the theory associated with the computer program VABS (variational asymptotic beam sectional analysis). VABS was first mentioned in [4]. Its development over the past ten years is described in [5–10] and takes the variational asymptotic method (VAM), [3], as the mathematical basis. By means of the VAM, a general three-dimensional nonlinear elasticity problem for a beam-like structure is rigorously split into a two-dimensional linear cross-sectional analysis and a one-dimensional nonlinear beam analysis. It is interesting to know that Trabucho and Viano [11] applied the VAM of Ciarlet and Destuynder [2] to construct mathematical models for rods. Their work is oriented more toward mathematicians than engineers.

In accord with the theory behind it, VABS can perform a classical analysis for initially twisted and curved inhomogeneous, anisotropic beams with arbitrary geometry, material properties, and reference cross sections. It captures both trapeze and Vlasov effects, which are useful for specific beam applications. VABS is also able to calculate the one-dimensional stiffness matrix with transverse shear refinement for initially twisted and curved, inhomogeneous, anisotropic beams with arbitrary geometry and material properties. Finally, the three-dimensional stress and strain fields can be recovered, if required, for finding stress concentrations, interlaminar stresses, etc.

There are a lot of beam theories in the literature. However, almost all published work is of the ad hoc variety, especially in the area of modeling composite structures. Because VABS develops stiffness models that use the same fundamental types of deformation that appear in traditional beam theories (such as those of Euler-Bernoulli, Timoshenko, and Vlasov), some researchers may be tempted to believe that VABS is nothing more than a computerized adaptation of elementary theories. However, VABS is really very different from the traditional beam theories, and the assumptions behind it are far less restrictive. The fact that VABS uses the traditional types of deformation winds up creating a simple and smooth connection to traditional beam theories, so that the one-dimensional beam analyses will remain essentially the same. A large body of additional information regarding three-dimensional behavior of the beam, which need not be considered at all in a one-dimensional beam analysis, is actually taken into account by introducing three-dimensional warping functions that are subsequently calculated.

In view of this, the main purpose of the present work is to take the reader, who is presumed to have a basic understanding of elasticity and calculus of variations, through an analytical derivation and application of the equations used by VABS for a specialized case so that its relationship with traditional theories will be clearer and its mathematical basis (VAM) will appear less arcane. This paper is in essence an *analytical* validation of VABS against the well-established theory of elasticity. Although numerous nu-

[1]Presently, Assistant Professor, Department of Mechanical and Aerospace Engineering, Utah State University, Logan, UT 84322-4130.

Contributed by the Applied Mechanics Division of THE AMERICAN SOCIETY OF MECHANICAL ENGINEERS for publication in the ASME JOURNAL OF APPLIED MECHANICS. Manuscript received by the Applied Mechanics Division, Aug. 30, 2002; final revision, June 16, 2003. Associate Editor: D. A. Kouris. Discussion on the paper should be addressed to the Editor, Prof. Robert M. McMeeking, Journal of Applied Mechanics, Department of Mechanical and Environmental Engineering, University of California–Santa Barbara, Santa Barbara, CA 93106-5070, and will be accepted until four months after final publication in the paper itself in the ASME JOURNAL OF APPLIED MECHANICS.

  

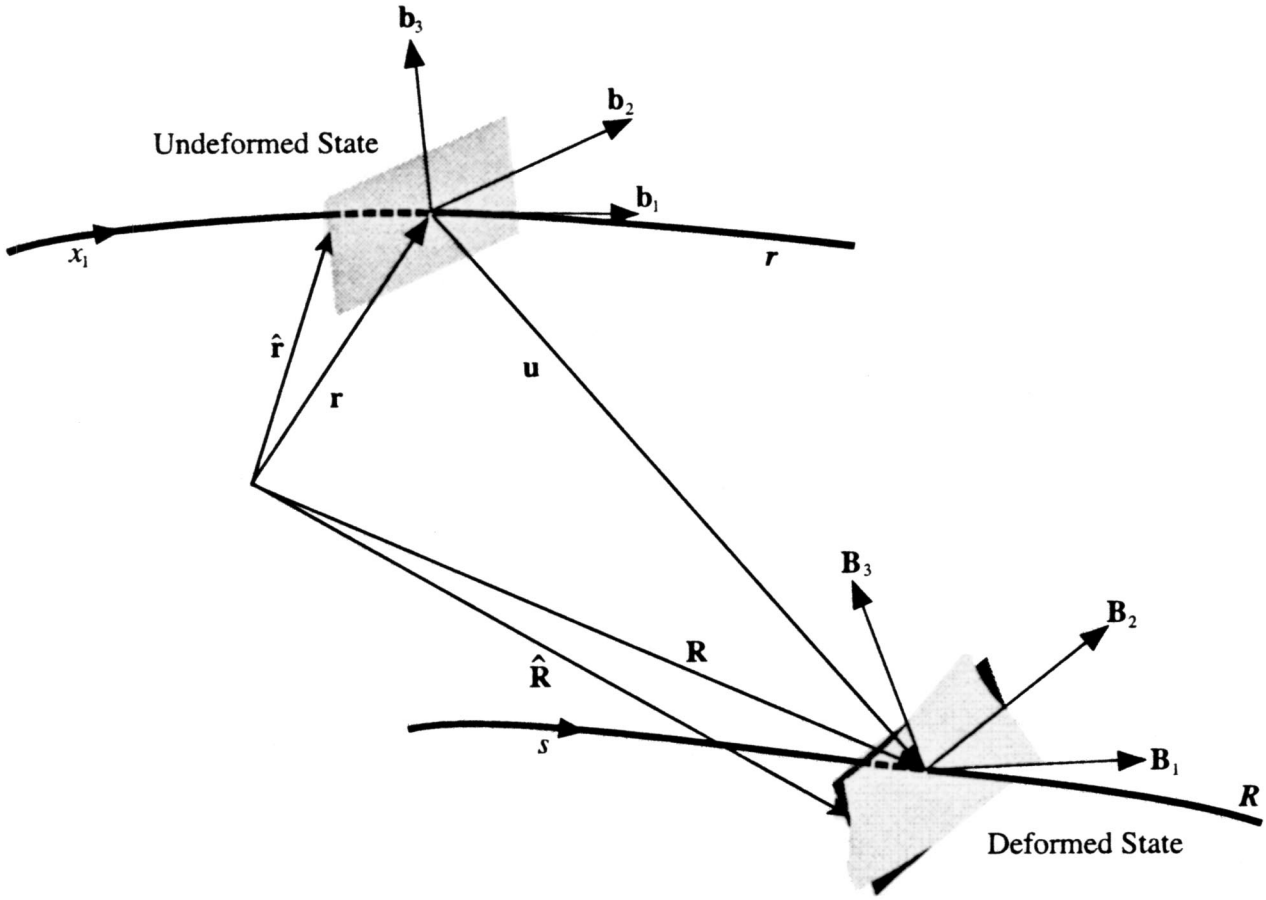


**Fig. 1 Schematic of beam deformation**

merical validation examples have been provided in [6,7,10,12], the present extensive and rigorous validation is required to demonstrate conclusively its versatility and accuracy. This paper then should increase the reader's confidence in results obtained from VABS.

To accomplish the above, the present work specializes the VABS general formulation for the analysis of isotropic, prismatic beams. Starting with the governing differential equations and associated boundary conditions of elasticity theory, we set out to prove (a) that the results from the classical model of VABS are the same as the superposition of elasticity solutions of extension, Saint-Venant torsion, and pure bending in two orthogonal directions; and (b) that the results from the Timoshenko-like model of VABS are the same as the superposition of the elasticity solutions of extension, Saint-Venant torsion, and both bending and transverse shear in two orthogonal directions.

## Three-Dimensional Formulation

As sketched in Fig. 1, a beam can be represented by a reference line $r$ measured by $x_1$, and a typical cross section $s$ with $h$ as its characteristic dimension and described by cross-sectional Cartesian coordinates $x_\alpha$. Note that here and throughout the paper, Greek indices assume values 2 and 3 while Latin indices assume 1, 2, and 3. Repeated indices are summed over their range except where explicitly indicated. For the convenience of comparing with elasticity solutions, the locus of all cross-sectional centroids along the beam is chosen as the reference line. An orthonormal triad $\mathbf{b}_i$ is chosen for the purpose of resolving tensorial quantities in component form for actual computation. For convenience, $\mathbf{b}_i$ is chosen to be tangent to $x_i$, respectively.

The spatial position vector $\hat{\mathbf{r}}$ of any point in the undeformed beam structure can be written as

$$\hat{\mathbf{r}}(x_1,x_2,x_3)=\mathbf{r}(x_1)+x_\alpha\mathbf{b}_\alpha \tag{1}$$

where $\mathbf{r}$ is the position vector of the points of the reference line. Note for a prismatic beam, the beam axis in the undeformed state is straight. Finally, $\mathbf{r}'=\mathbf{b}_1$ and $(\,)'$ means the partial derivative with respect to $x_1$.

After deformation, the particle that had position vector $\hat{\mathbf{r}}$ in the undeformed state now has the position vector $\hat{\mathbf{R}}$ in the deformed state. Another orthonormal triad $\mathbf{B}_i$ is introduced to express the deformed configuration, and the $\mathbf{B}_i$ unit vectors are not necessarily tangent to the deformed beam coordinates. However, for the convenience of applying VAM, we choose $\mathbf{B}_i$ to coincide with $\mathbf{b}_i$ in the case of zero deformation, $\mathbf{B}_1$ to be tangent to the deformed beam reference axis, and $\mathbf{B}_\alpha$ determined by a rotation about $\mathbf{B}_1$. Then $\mathbf{B}_i$ can be related to $\mathbf{b}_i$ by a rotation tensor which is called the global rotation tensor, [13], such that

$$\mathbf{C}^{Bb}=\mathbf{B}_i\mathbf{b}_i\,. \tag{2}$$

$\mathbf{C}^{bB}$ is the inverse rotation to bring $\mathbf{B}_i$ back to $\mathbf{b}_i$ which means

$$\mathbf{C}^{Bb}\cdot\mathbf{C}^{bB}=\mathbf{I} \tag{3}$$

where $\mathbf{I}$ is the identity tensor. Please note that we do *not* make any restrictive assumption here by choosing $\mathbf{B}_1$ to be tangent to $x_1$. Instead, the transverse shear deformation will be included in the warping functions introduced below and will be explicitly brought into evidence when we fit the asymptotic model into an engineering model that can account for this type of deformation, such as a Timoshenko-like model.

The position vector $\hat{\mathbf{R}}$ can be represented as

$$\hat{\mathbf{R}}(x_1,x_2,x_3)=\mathbf{R}(x_1)+x_\alpha\mathbf{B}_\alpha(x_1)+w_i(x_1,x_2,x_3)\mathbf{B}_i(x_1) \quad (4)$$

where $\mathbf{R}$ is the position vector to a point on the reference line of the deformed beam, and $w_i$ are the components of warping, both in and out of the cross-sectional plane. By introducing the unknown three-dimensional warping functions into the formulation, one takes into account all possible deformation.

One should note that Eq. (4) is four times redundant because of the way warping was introduced. One must impose four appropriate constraints on the displacement field to remove the redundancy. The four constraints applied here are

$$\langle w_i\rangle=0 \quad (5)$$

$$\langle x_2w_3-x_3w_2\rangle=0 \quad (6)$$

where the notation $\langle\ \rangle$ means integration over the reference cross section. The implication of Eq. (5) is that warping does not contribute to the rigid-body displacement of the cross section. This leads to one-dimensional displacement variables for extension and bending that have easily identifiable geometric meanings: they correspond to the measure numbers in the $\mathbf{b}_i$ basis of the average displacement of the cross section. Equation (6) implies the torsional rotation variable is the average rotation of the cross section about $\mathbf{B}_1$.

To formulate this problem in an intrinsic form, we need the definition of the one-dimensional generalized Lagrangean strains:

$$\boldsymbol{\gamma}=\mathbf{C}^{bB}\cdot\mathbf{R}'-\mathbf{b}_1 \quad (7)$$

$$\mathbf{B}_i'=\kappa_j\mathbf{B}_j\times\mathbf{B}_i \quad (8)$$

where the column matrices of the ''force-strain'' measures $\gamma=\lfloor\gamma_{11}\ 0\ 0\rfloor^T$ and $\kappa_i$ are the ''moment-strain'' measures. Based on the concept of decomposition of rotation tensor, [13], if the local rotation is small, which is the case for all the framework of VABS except the trapeze solution (not considered in this paper), the Jaumann-Biot-Cauchy strain components are given by

$$\Gamma_{ij}=\frac{1}{2}(F_{ij}+F_{ji})-\delta_{ij} \quad (9)$$

where $\delta_{ij}$ is the Kronecker symbol, and $F_{ij}$ the mixed-basis component of the deformation gradient tensor such that

$$F_{ij}=\mathbf{B}_i\cdot\mathbf{G}_k\mathbf{g}^k\cdot\mathbf{b}_j. \quad (10)$$

Here $\mathbf{G}_k=\partial\hat{\mathbf{R}}/\partial x_k$ is the covariant basis vector of the deformed configuration and $\mathbf{g}^k=\mathbf{b}_k$ for prismatic beams.

Because of the small strain assumption, which is applicable in the framework of a geometrically nonlinear formulation, we may neglect all terms that are products of the warping and the one-dimensional generalized strains. Thus, one obtains the three-dimensional strain field as

$$\begin{aligned}
\Gamma_{11}&=\gamma_{11}+x_3\kappa_2-x_2\kappa_3+w_1'\\
2\Gamma_{12}&=w_{1,2}-x_3\kappa_1+w_2'\\
2\Gamma_{13}&=w_{1,3}+x_2\kappa_1+w_3'\\
\Gamma_{22}&=w_{2,2}\\
2\Gamma_{23}&=w_{3,2}+w_{2,3}\\
\Gamma_{33}&=w_{3,3}
\end{aligned} \quad (11)$$

where $(\ )_{,\alpha}$ means the partial derivative with respect to $x_\alpha$. For an isotropic elastic body with Young's modulus $E$, shear modulus $G$ and Poisson's ratio $\nu$, twice the three-dimensional strain energy per unit length can be written as, [14],

$$\begin{aligned}
2\Pi=&E\langle\Gamma_{11}^2\rangle+4G\langle\Gamma_{12}^2+\Gamma_{13}^2+\Gamma_{23}^2\rangle\\
&+\frac{E}{(1+\nu)(1-2\nu)}\left\langle\begin{Bmatrix}\nu\Gamma_{11}+\Gamma_{22}\\ \nu\Gamma_{11}+\Gamma_{33}\end{Bmatrix}^T\begin{bmatrix}1-\nu & \nu\\ \nu & 1-\nu\end{bmatrix}\right.\\
&\left.\times\begin{Bmatrix}\nu\Gamma_{11}+\Gamma_{22}\\ \nu\Gamma_{11}+\Gamma_{33}\end{Bmatrix}\right\rangle.
\end{aligned} \quad (12)$$

From energy principles, we know that the exact warping functions satisfying the constraints, Eqs. (5) and (6), should minimize the strain energy in Eq. (12). However, the same difficulties as one finds in solving general three-dimensional elasticity problems will be encountered if one tries to solve this minimization problem directly. Fortunately, as demonstrated in publications related to VABS, the VAM can be used to solve for the unknown warping functions asymptotically to avoid the difficulty of the original three-dimensional formulation. This will be illustrated *analytically* in the following sections.

## Classical Model

Before applying the VAM, one must define the small parameters of the problem. It was mentioned above that products of the one-dimensional generalized strains and warping are assumed to be small because of the small-strain assumption. The assumption of small strain is adopted for the purpose of deriving a geometrically nonlinear beam formulation. It will be assumed and subsequently validated from the results that the warping is of the order of $h\varepsilon$ with $h$ as the characteristic dimension of the cross section. The smallness of the one-dimensional generalized strains is taken into account as follows. The stretching of the beam reference line is denoted by $\gamma_{11}$; the maximum strain induced by twist is of the order of $h\kappa_1$, while the maximum strain induced by bending is of the order of $h\kappa_\alpha$. This observation is consistent with the small local rotation assumption used to derive Eq. (9). Now, let us denote the order of the maximum strain as $\varepsilon=\max(\gamma_{11},h\kappa_i)$. This small parameter is then utilized when deriving the three-dimensional strain field, Eq. (11), so that the smallness of $\varepsilon$ need not be used in the rest of derivation. Another small parameter is $h/l$ where $l$ is the wavelength of beam axial deformation. This is the only small parameter one needs for prismatic beams for the purpose of solving the unknown warping functions asymptotically and obtaining a strain energy asymptotically correct up to a certain order.

The classical model of a prismatic beam is represented in terms of a strain energy per unit length that is asymptotically correct up to the order of $\mu\varepsilon^2$ where $\mu$ is of the order of the maximum material constant. All the prime terms in Eq. (11) are of order $h/l$ higher than the rest and do not contribute to such an energy. Then this energy, which is called the zeroth-order energy, can be obtained from Eq. (12) as

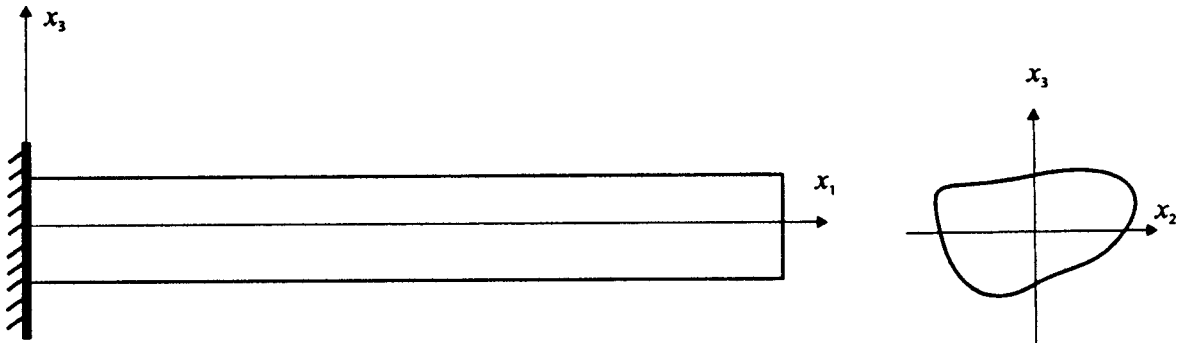


**Fig. 2 Sketch of a clamped prism**

$$2\Pi_0 = ES\gamma_{11}^2 + EI_\alpha \kappa_\alpha^2 + G\langle (w_{1,2} - x_3\kappa_1)^2 + (w_{1,3} + x_2\kappa_1)^2 + (w_{3,2} + w_{2,3})^2 \rangle + \frac{E}{(1+\nu)(1-2\nu)} \left\langle \begin{Bmatrix} \nu(\gamma_{11} + x_3\kappa_2 - x_2\kappa_3) + w_{2,2} \\ \nu(\gamma_{11} + x_3\kappa_2 - x_2\kappa_3) + w_{3,3} \end{Bmatrix}^T \begin{bmatrix} 1-\nu & \nu \\ \nu & 1-\nu \end{bmatrix} \begin{Bmatrix} \nu(\gamma_{11} + x_3\kappa_2 - x_2\kappa_3) + w_{2,2} \\ \nu(\gamma_{11} + x_3\kappa_2 - x_2\kappa_3) + w_{3,3} \end{Bmatrix} \right\rangle \tag{13}$$

with

$$S = \langle 1 \rangle \quad I_2 = \langle x_3^2 \rangle \quad I_3 = \langle x_2^2 \rangle \tag{14}$$

where $S$ is the cross-sectional area and $I_\alpha$ are the principal area moments of inertia about $x_\alpha$. The warping functions that minimize the above energy are governed by the Euler-Lagrange equations of this energy functional, given by

$$w_{1,22} + w_{1,33} = 0 \tag{15}$$

$$2(1-\nu)w_{2,22} + (1-2\nu)w_{2,33} + w_{3,23} - 2\nu\kappa_3 = 0 \tag{16}$$

$$2(1-\nu)w_{3,33} + (1-2\nu)w_{3,22} + w_{2,23} + 2\nu\kappa_2 = 0 \tag{17}$$

and the associated boundary conditions

$$n_3(x_2\kappa_1 + w_{1,3}) + n_2(w_{1,2} - x_3\kappa_1) = 0 \tag{18}$$

$$n_3(w_{2,3} + w_{3,2}) + \frac{2n_2}{1-2\nu}[\nu(\gamma_{11} + x_3\kappa_2 - x_2\kappa_3) + \nu w_{3,3} + (1-\nu)w_{2,2}] = 0 \tag{19}$$

$$n_2(w_{2,3} + w_{3,2}) + \frac{2n_3}{1-2\nu}[\nu(\gamma_{11} + x_3\kappa_2 - x_2\kappa_3) + \nu w_{2,2} + (1-\nu)w_{3,3}] = 0 \tag{20}$$

where $n_\alpha$ is the direction cosine of outward normal with respect to $x_\alpha$. Here, to maintain a simpler derivation, we do not use Lagrange multipliers to enforce the constraints of Eqs. (5) and (6). Instead, we keep these constraints in mind and check whether they can be satisfied by the solution. It can be observed that Eqs. (15) and (18) are just the equations of Saint-Venant warping $\psi(x_2, x_3)$ in elasticity textbooks such as, [15], except

$$w_1(x_1, x_2, x_3) = \hat{w}_1(x_1, x_2, x_3) = \psi(x_2, x_3)\kappa_1(x_1). \tag{21}$$

Hence the first approximation of the out-of-plane warping $\hat{w}_1$ can be solved by the methods given in elasticity books. According to the theory of elasticity, $\psi$ can be determined up to a constant, and one can choose the constant so that the constraint $\langle \hat{w}_1 \rangle = 0$ is satisfied. The following functions of $w_\alpha$ satisfy the other constraints as well as Eqs. (16), (17), (19), and (20):

$$w_2 = \hat{w}_2 = -\nu(x_2\gamma_{11} + x_2x_3\kappa_2) + \frac{\nu\kappa_3}{2}\left(x_2^2 - x_3^2 + \frac{I_2 - I_3}{S}\right)$$

$$w_3 = \hat{w}_3 = -\nu(x_3\gamma_{11} - x_2x_3\kappa_3) - \frac{\nu\kappa_2}{2}\left(x_2^2 - x_3^2 + \frac{I_2 - I_3}{S}\right). \tag{22}$$

Having obtained all the warping functions, the three-dimensional strain field can be recovered by Eq. (11) up to the zeroth order as

$$\Gamma_{11} = \gamma_{11} + x_3\kappa_2 - x_2\kappa_3$$

$$2\Gamma_{12} = w_{1,2} - x_3\kappa_1$$

$$2\Gamma_{13} = w_{1,3} + x_2\kappa_1$$

$$\Gamma_{22} = -\nu(\gamma_{11} + x_3\kappa_2 - x_2\kappa_3)$$

$$2\Gamma_{23} = 0$$

$$\Gamma_{33} = -\nu(\gamma_{11} + x_3\kappa_2 - x_2\kappa_3). \tag{23}$$

If one takes the definition of torsional rigidity from elasticity texts, which is

$$GJ = G\langle x_2^2 + x_3^2 + x_2\psi_{1,3} - x_3\psi_{1,2} \rangle \tag{24}$$

where $J$ is the Saint-Venant torsion constant, then the asymptotically correct three-dimensional energy, up to the order of $\mu\varepsilon^2$, can be written as

$$2\Pi_0 = ES\gamma_{11}^2 + GJ\kappa_1^2 + EI_2\kappa_2^2 + EI_3\kappa_3^2. \tag{25}$$

This energy coincides with the result of classical beam theory; however, it is obtained without any ad hoc kinematic assumptions whatsoever. Such ad hoc assumptions as assuming the cross section to be rigid in its own plane or setting $\nu = 0$ are common in the development of traditional beam theories in the literature.

For a straight beam clamped at $x_1 = 0$ and under the tip load $F_1$, $M_i$ at $x_1 = L$ (see Fig. 2), the one-dimensional strain measures can be solved with the help of the strain energy Eq. (25) as

$$\gamma_{11} = \frac{F_1}{ES} \quad \kappa_1 = \frac{M_1}{GJ} \quad \kappa_2 = \frac{M_2}{EI_2} \quad \kappa_3 = \frac{M_3}{EI_3}. \tag{26}$$

If a linear beam theory is used, the three-dimensional displacement field can be recovered as

$$u_1=\frac{F_1}{ES}x_1-\frac{M_3}{EI_3}x_2x_1+\frac{M_2}{EI_2}x_3x_1+\psi\frac{M_1}{GJ}$$

$$u_2=-\nu x_2\frac{F_1}{ES}-\nu x_2x_3\frac{M_2}{EI_2}+\frac{\nu M_3}{2EI_3}\left(x_2^2-x_3^2+\frac{I_2-I_3}{S}\right)+\frac{M_3}{EI_3}\frac{x_1^2}{2}$$

$$u_3=-\nu x_3\frac{F_1}{ES}+\nu x_2x_3\frac{M_3}{EI_3}+\frac{\nu M_2}{2EI_2}\left(x_2^2-x_3^2+\frac{I_2-I_3}{S}\right)-\frac{M_2}{EI_2}\frac{x_1^2}{2} \tag{27}$$

which is essentially the superposition of elasticity solutions for extension, pure bending in two directions and torsion. The only exception to this statement is that there is a difference of a constant from the elasticity solutions for $u_\alpha$ due to differences in the way the clamped boundary condition is handled. Published elasticity solutions enforce the clamped condition at the beam reference line. In our case, however, since the one-dimensional variables implied by the VAM solution are averages of the three-dimensional displacement, the most straightforward solution in our framework constrains the average displacement to be zero. Clearly, by enforcing a modified boundary condition in the one-dimensional beam theory, so as to mimic the clamped condition used in the elasticity solutions, the two solutions will become identical; in particular, the constant terms in $u_2$ and $u_3$ will simply drop out.

From the above, it is clearly shown that the above classical model stores the complete three-dimensional energy of prismatic beams due to uniform extension, uniform torsion, and pure bending in two directions obtained by elasticity theory. The linearized three-dimensional displacement field recovered by VABS is the same as that obtained from elasticity theory.

### Timoshenko-Like Model

Elasticity theory has another set of equations to solve for the so-called flexure problem, which involves both bending and transverse shear. For this VABS provides a Timoshenko-like model. Because a Timoshenko-like model can at most approximate the original three-dimensional energy up to the order of $\mu\varepsilon^2(h/l)^2$, a strain energy that is asymptotically correct to the second order of $h/l$ is sought first

$$2U_1=\boldsymbol{\epsilon}^TA\boldsymbol{\epsilon}+2\boldsymbol{\epsilon}^TB\boldsymbol{\epsilon}'+\boldsymbol{\epsilon}'^TC\boldsymbol{\epsilon}'+2\boldsymbol{\epsilon}^TD\boldsymbol{\epsilon}'' \tag{28}$$

where $A$, $B$, $C$, and $D$ are matrices carrying the geometry and material information of the cross section, elements of $\boldsymbol{\epsilon}=\lfloor\gamma_{11}\ \kappa_1\ \kappa_2\ \kappa_3\rfloor^T$ are the generalized one-dimensional strain measures of Euler-Bernoulli beam theory. For isotropic prismatic beams, in which the locus of cross-sectional centroids is taken as the reference line and cross-sectional principal axes are along $x_\alpha$, $A$ becomes a diagonal matrix with diagonal terms given by the extensional stiffness $ES$, the torsional stiffness $GJ$, and bending stiffnesses $EI_2$ and $EI_3$. A Timoshenko-like model is then created out of the energy, Eq. (28), as

$$2U=\boldsymbol{\epsilon}_t^TX\boldsymbol{\epsilon}_t+2\boldsymbol{\epsilon}_t^TF\boldsymbol{\gamma}+\boldsymbol{\gamma}^TG\boldsymbol{\gamma} \tag{29}$$

where $\boldsymbol{\epsilon}_t$ are the classical strain measures (but defined slightly differently because of the framework of Timoshenko-like model), and $\boldsymbol{\gamma}=\lfloor 2\gamma_{13}\ 2\gamma_{23}\rfloor^T$ transverse shear strains. The stiffness matrices $X$, $F$, and $G$ can be found by (see [9])

$$G=(Q^TA^{-1}CA^{-1}Q)^{-1}$$

$$F=B^TA^{-1}QG$$

$$X=A+FG^{-1}F^T \tag{30}$$

where

$$Q=\begin{bmatrix}0&0&0&1\\0&0&-1&0\end{bmatrix}^T. \tag{31}$$

$\boldsymbol{\epsilon}_t$ and $\boldsymbol{\epsilon}$ are related by $\boldsymbol{\epsilon}_t=\boldsymbol{\epsilon}-Q\boldsymbol{\gamma}$.

By a simple algebraic derivation, $F$ and $G$ can be expressed in terms of the components of $A$, $B$, and $C$ as

$$G=\frac{E^2}{C_{33}C_{44}-C_{34}^2}\begin{bmatrix}C_{33}I_3^2&C_{34}I_2I_3\\C_{34}I_2I_3&C_{44}I_2^2\end{bmatrix}$$

$$F=\frac{E}{C_{33}C_{44}-C_{34}^2}\begin{bmatrix}(B_{41}C_{33}-B_{31}C_{34})I_3&(B_{31}C_{44}-B_{41}C_{34})I_2\\(B_{42}C_{33}-B_{32}C_{34})I_3&(B_{32}C_{44}-B_{42}C_{34})I_2\\(B_{43}C_{33}-B_{33}C_{34})I_3&(B_{33}C_{44}-B_{43}C_{34})I_2\\(B_{44}C_{33}-B_{34}C_{34})I_3&(B_{34}C_{44}-B_{44}C_{34})I_2\end{bmatrix} \tag{32}$$

where the subscripted terms involving $B$ and $C$ are specified elements in those matrices. Here, one can conclude that $G$ is determined by the coefficients associated with $\kappa_\alpha'\kappa_\beta'$ in the asymptotic energy, and $F$ is determined by the coefficients associated with $\kappa_\alpha\gamma_{11}'$ and $\kappa_\alpha\kappa_i'$. This observation is very important because it leads to our finding a closed-form solution for the Timoshenko-like model for isotropic, prismatic beams. To obtain the second-order energy, we perturb the warping functions as

$$w_i=\hat{w}_i+V_i \tag{33}$$

where $V_i$ is of the order $\varepsilon h/l$. Substituting the perturbed warping functions back into Eq. (11), one obtains

$$\Gamma_{11}=\gamma_{11}+x_3\kappa_2-x_2\kappa_3+\underline{\hat{w}_1'+\underline{V_1'}}$$

$$2\Gamma_{12}=\hat{w}_{1,2}-x_3\kappa_1+\underline{V_{1,2}+\hat{w}_2'+\underline{V_2'}}$$

$$2\Gamma_{13}=\hat{w}_{1,3}+x_2\kappa_1+\underline{V_{1,3}+\hat{w}_3'+\underline{V_3'}}$$

$$\Gamma_{22}=\hat{w}_{2,2}+\underline{V_{2,2}}$$

$$2\Gamma_{23}=\hat{w}_{3,2}+\hat{w}_{2,3}+\underline{V_{3,2}+V_{2,3}}$$

$$\Gamma_{33}=\hat{w}_{3,3}+\underline{V_{3,3}} \tag{34}$$

where the underlined terms are of the order $\varepsilon h/l$, the double underlined terms are of the order $\varepsilon h^2/l^2$, and the rest of the terms are of the order $\varepsilon$. Substituting this perturbed strain field into the energy functional Eq. (12) and neglecting all the terms of order higher than $\mu(h/l)^2\varepsilon^2$, one obtains

$$2\Pi=2\Pi_0+2\Pi_1+2\Pi_2 \tag{35}$$

where $\Pi_0$ is the energy obtained for the classical model, Eq. (25) and

$$\Pi_1=E\langle\hat{w}_1'(\underline{\underline{\gamma_{11}}}+x_3\kappa_2-x_2\kappa_3)\rangle$$
$$+G[\underline{\langle(\hat{w}_{1,2}-x_3\kappa_1)V_{1,2}+(\hat{w}_{1,3}+x_2\kappa_1)V_{1,3}\rangle}$$
$$+\underline{\underline{\langle(\hat{w}_{1,2}-x_3\kappa_1)\hat{w}_2'+(\hat{w}_{1,3}+x_2\kappa_1)\hat{w}_3'\rangle}}]. \tag{36}$$

It is easy to prove that the underlined terms vanish for arbitrary $V_1$. According to Eq. (32), the double underlined terms will not affect the Timoshenko-like model constructed from the second-order energy. Thus, the only terms of interest are

$$\Pi_1=E\langle\hat{w}_1'(x_3\kappa_2-x_2\kappa_3)\rangle. \tag{37}$$

Note these terms will not necessarily vanish unless the Saint-Venant warping, for which we have already solved, possesses some kind of symmetry. Thus, the second-order energy becomes

$$2\Pi_2 = 2E\langle \underline{V_1'(\gamma_{11}+x_3\kappa_2-x_2\kappa_3)} + \hat{w}_1'^2\rangle + G\langle (V_{1,2}+\hat{w}_2')^2 + 2V_2'(\hat{w}_{1,2}-x_3\kappa_1)\rangle + G\langle (V_{1,3}+\hat{w}_3')^2 + 2V_3'(\hat{w}_{1,3}+x_2\kappa_1) + (V_{2,3}+V_{3,2})^2\rangle + \frac{E}{(1+\nu)(1-2\nu)}\left\langle \begin{Bmatrix} \nu\hat{w}_1'+V_{2,2} \\ \nu\hat{w}_1'+V_{3,3} \end{Bmatrix}^T \begin{bmatrix} 1-\nu & \nu \\ \nu & 1-\nu \end{bmatrix} \times \begin{Bmatrix} \nu\hat{w}_1'+V_{2,2} \\ \nu\hat{w}_1'+V_{3,3} \end{Bmatrix} \right\rangle. \tag{38}$$

The underlined terms create difficulty to solve this problem in the two-dimensional cross-sectional domain. However, our goal is to find an interior solution without consideration of boundary effects at the ends of the beam. Hence, integration by parts with respect to $x_1$ can be used, and the residual terms at the ends can be considered as having no effect on the interior solution. This argument can be illustrated mathematically if one constrains the warping $V_1$ in such a way that

$$\langle V_1(\gamma_{11}+x_3\kappa_2-x_2\kappa_3)|_{x_1=0}\rangle = \langle V_1(\gamma_{11}+x_3\kappa_2-x_2\kappa_3)|_{x_1=L}\rangle. \tag{39}$$

The effect of such a constraint will die out after a small distance from the ends according to the Saint-Venant principle. Then, the Euler-Lagrange equations for the functional $\Pi_2$ are

$$V_{1,22}+V_{1,33}+2(\gamma_{11}'+x_3\kappa_2'-x_2\kappa_3')=0 \tag{40}$$

$$2(1-\nu)V_{2,22}+(1-2\nu)V_{2,33}+V_{3,23}+(2\nu-1)x_3\kappa_1'+\hat{w}_{1,2}'=0 \tag{41}$$

$$2(1-\nu)V_{3,33}+(1-2\nu)V_{3,22}+V_{2,23}+(1-2\nu)x_2\kappa_1' + (1-2\nu)\hat{w}_{1,3}'=0 \tag{42}$$

and the associated boundary conditions given by

$$n_3(V_{1,3}+\hat{w}_3')+n_2(V_{1,2}+\hat{w}_2')=0 \tag{43}$$

$$n_3(\hat{w}_{2,3}+\hat{w}_{3,2})+\frac{2n_2}{1-2\nu}[\nu V_{3,3}+(1-\nu)V_{2,2}+\nu\hat{w}_1']=0 \tag{44}$$

$$n_2(\hat{w}_{2,3}+\hat{w}_{3,2})+\frac{2n_3}{1-2\nu}[\nu V_{2,2}+(1-\nu)V_{3,3}+\nu\hat{w}_1']=0. \tag{45}$$

It is observed that $V_\alpha$ is decoupled from $V_1$; $V_\alpha$ should be some function multiplying $\kappa_1'$ and $V_1$ will be a linear combination of $\gamma_{11}'$, and $\kappa_\alpha'$. The terms associated with $V_\alpha$ will not affect the Timoshenko-like model as shown in Eq. (32). (In fact these terms are related with the Vlasov theory and will be studied in later paper.) Hence, one can set $V_\alpha$ to be zero and drop all terms that have no effect on the Timoshenko-like model. Then, after recalculating $\Pi_2$, one finds

$$2\Pi_2 = 2E\langle V_1'(x_3\kappa_2-x_2\kappa_3)\rangle + G\left\langle \left[ V_{1,2}-\nu x_2x_3\kappa_2'+\frac{\nu\kappa_3'}{2}\left(x_2^2-x_3^2+\frac{I_2-I_3}{S}\right)\right]^2\right\rangle + G\left\langle \left[ V_{1,3}+\nu x_2x_3\kappa_3'+\frac{\nu\kappa_2'}{2}\left(x_2^2-x_3^2+\frac{I_2-I_3}{S}\right)\right]^2\right\rangle. \tag{46}$$

Then the corresponding Euler-Lagrange equation, Eq. (40), and boundary condition, Eq. (43), will be modified to

$$V_{1,22}+V_{1,33}=2(x_2\kappa_3'-x_3\kappa_2') \tag{47}$$

$$n_3\left[ V_{1,3}+\nu x_2x_3\kappa_3'+\frac{\nu\kappa_2'}{2}\left(x_2^2-x_3^2+\frac{I_2-I_3}{S}\right)\right] = -n_2\left[ V_{1,2}-\nu x_2x_3\kappa_2'+\frac{\nu\kappa_3'}{2}\left(x_2^2-x_3^2+\frac{I_2-I_3}{S}\right)\right]. \tag{48}$$

One can introduce a special function as

$$\begin{aligned} V_{1,2}-\nu x_2x_3\kappa_2'+\frac{\nu\kappa_3'}{2}\left(x_2^2-x_3^2+\frac{I_2-I_3}{S}\right) &= \phi_{,3}+(1+\nu)x_2^2\kappa_3'+f(x_3) \\ V_{1,3}+\nu x_2x_3\kappa_3'+\frac{\nu\kappa_2'}{2}\left(x_2^2-x_3^2+\frac{I_2-I_3}{S}\right) &= -\phi_{,2}-(1+\nu)x_3^2\kappa_2'+g(x_2) \end{aligned} \tag{49}$$

to satisfy Eq. (47) automatically, where $f(x_3)$ and $g(x_2)$ are arbitrary functions. The advantage of introducing $\phi$ is that Eq. (48) can be made much simpler based on the choice of $f(x_3)$ and $g(x_2)$. Using Eq. (49), the boundary condition, Eq. (48) becomes

$$\frac{\partial\phi}{\partial s} = -[f(x_3)+(1+\nu)x_2^2\kappa_3']n_2-[g(x_2)-(1+\nu)x_3^2\kappa_2']n_3 \tag{50}$$

where $s$ is the contour coordinate along the cross-sectional boundary. If the arbitrary functions are chosen such that on the boundary

$$f(x_3)=\begin{cases} -(1+\nu)x_2^2\kappa_3' & \text{if } n_2\neq 0, \\ \text{arbitrary} & \text{if } n_2=0 \end{cases} \qquad g(x_2)=\begin{cases} (1+\nu)x_3^2\kappa_2' & \text{if } n_3\neq 0, \\ \text{arbitrary} & \text{if } n_3=0 \end{cases} \tag{51}$$

then the right-hand side of Eq. (50) vanishes and $\phi$ is constant along the boundary. For simply connected domains, one can choose $\phi$ to vanish along the boundary. The governing differential equations for $\phi$ can be deduced from Eq. (49) as

$$\phi_{1,22}+\phi_{1,33}=-2\nu x_2\kappa_2'+\frac{dg(x_2)}{dx_2}-2\nu x_3\kappa_3'-\frac{df(x_3)}{dx_3}. \tag{52}$$

This equation is the same as that governing the flexure problem in both directions if one expresses $\kappa_\alpha'$ in terms of the tip transverse force and multiplies $\phi$ by the shear modulus $G$. Therefore, all flexure problems that are solvable by elasticity theory can also be solved analytically by the VAM (the procedure on which VABS is based). After $\phi$ is obtained, one can find $V_1$ up to a constant using Eq. (49), where the constant can be determined by the constraint $\langle V_1\rangle=0$. The portion of asymptotically correct energy Eq. (28) that is needed for constructing the Timoshenko-like model can be found from Eqs. (35) and (46).

Although it is necessary to carry out an integration by parts with respect to $x_1$ for the sets of terms in the first bracket of Eq. (46) to render the present problem as a purely cross-sectional problem, this operation should not be applied at the step where the strain energy is obtained. Previous publications, [7,9], are silent on this seemingly inconsistent practice because a reasonable explanation had not been formulated. However, for the present problem, the transverse shear energy is completely represented by the last two sets of terms and the first set of terms is part of the energy due to extension. If one integrates this first set of terms by parts, this energy represented by it will be transformed into transverse shear energy according to Eq. (32), which is at least physically inappropriate; and, in the worst case, the total transverse shear energy will turn out to be negative. Nevertheless, if one does the integration by parts and also keeps the residual terms at the ends, the fictitious transverse shear energy caused by integration by parts will be canceled by the residual terms at the boundaries, which means the final three-dimensional results will not be af-

fected by this operation. Based on this fact and Eq. (32), the first set of terms in Eq. (46) for the present problem will not affect the final Timoshenko-like model and will be discarded in later calculations.

After constructing the Timoshenko-like model using Eqs. (32) and (30) and using it to solve the one-dimensional beam problem, the three-dimensional strain field can be recovered using Eq. (34) and the displacement field can be recovered similarly as Eq. (27). This procedure will be given in detail for some example cross sections that follow.

## Example Cross Sections

In this section two typical examples listed in the elasticity text of Timoshenko and Goodier [15] are studied here using the analytical procedures formulated in previous sections.

**Elliptical Section.** For an elliptical cross section with semiaxes $a$ and $b$ in the directions of $x_2$ and $x_3$, respectively, and $\rho = a/b$ as the aspect ratio, the Saint-Venant warping is found to be

$$\psi = \frac{(b^2-a^2)x_2x_3}{a^2+b^2}. \tag{53}$$

If one chooses the $f(x_3)$ and $g(x_2)$ according to Eq. (51)

$$f(x_3) = -(1+\nu)x_2^2\kappa_3' = -(1+\nu)\left(1-\frac{x_3^2}{b^2}\right)a^2\kappa_3'$$

$$g(x_2) = (1+\nu)x_3^2\kappa_2' = (1+\nu)\left(1-\frac{x_2^2}{a^2}\right)b^2\kappa_2' \tag{54}$$

then both Eqs. (50) and (52) will be satisfied by

$$\phi = m\left(\frac{x_2^2}{a^2}+\frac{x_3^2}{b^2}-1\right)x_3 + n\left(\frac{x_2^2}{a^2}+\frac{x_3^2}{b^2}-1\right)x_2 \tag{55}$$

with

$$m = -\frac{\rho^2[\nu+(1+\nu)\rho^2]}{1+3\rho^2}b^2\kappa_3'$$

$$n = -\frac{[\nu\rho^2+(1+\nu)]}{3+\rho^2}b^2\kappa_2'. \tag{56}$$

Then one can obtain $V_1$ by Eq. (49) as

$$V_1 = p\frac{x_3\kappa_2'}{24(3+\rho^2)} + q\frac{x_2\kappa_3'}{24(1+3\rho^2)} \tag{57}$$

with

$$\begin{aligned} p &= -4x_3^2[4+\nu+(2-\nu)\rho^2] - 12x_2^2(2-\nu+\nu\rho^2) + 3b^2[16+8\rho^2 \\ &\quad +13\nu+2\nu\rho^2+\nu\rho^4)] \\ q &= 4x_2^2[(4+\nu)\rho^2+2-\nu] - 12x_3^2[(2-\nu)\rho^2+\nu] - 3b^2[16\rho^4 \\ &\quad +8\rho^2+13\nu\rho^4+2\nu\rho^2+\nu)]. \end{aligned} \tag{58}$$

Then the energy of the order $(h/l)^2$ excluding the terms that do not affect the final Timoshenko-like model can be computed as

$$\frac{2\Pi_2}{EAb^4} = \frac{[\rho^4\nu^2+2\rho^2(1+\nu)^2+5(1+\nu)^2]\kappa_2'^2}{12(3+\rho^2)(1+\nu)} + \frac{\rho^2[\nu^2+2\rho^2(1+\nu)^2+5\rho^4(1+\nu)^2]\kappa_3'^2}{12(1+3\rho^2)(1+\nu)}. \tag{59}$$

The final Timoshenko-like model can be expressed as

$$2U = \begin{Bmatrix} \gamma_{11} \\ \kappa_1 \\ \kappa_2 \\ \kappa_3 \end{Bmatrix}^T \begin{bmatrix} ES & 0 & 0 & 0 \\ 0 & GJ & 0 & 0 \\ 0 & 0 & EI_2 & 0 \\ 0 & 0 & 0 & EI_3 \end{bmatrix} \begin{Bmatrix} \gamma_{11} \\ \kappa_1 \\ \kappa_2 \\ \kappa_3 \end{Bmatrix} + \begin{Bmatrix} 2\gamma_{12} \\ 2\gamma_{13} \end{Bmatrix}^T \begin{bmatrix} S_2 & 0 \\ 0 & S_3 \end{bmatrix} \begin{Bmatrix} 2\gamma_{12} \\ 2\gamma_{13} \end{Bmatrix} \tag{60}$$

where

$$S = \pi ab \quad J = \frac{\pi a^3b^3}{a^2+b^2} \quad I_2 = \frac{\pi}{4}ab^3 \quad I_3 = \frac{\pi}{4}a^3b \tag{61}$$

and

$$S_2 = \frac{3a^2(3a^2+b^2)(1+\nu)^2GS}{2[b^4\nu^2+5a^4(1+\nu)^2+2a^2b^2(1+\nu)^2]}$$

$$S_3 = \frac{3b^2(a^2+3b^2)(1+\nu)^2GS}{2[a^4\nu^2+5b^4(1+\nu)^2+2a^2b^2(1+\nu)^2]}. \tag{62}$$

The results are the same as those in [10], but in that work the results are obtained by using the Ritz method and assuming a third-order polynomial which is of the exact form as shown here. This result is the same as what is in [16] which has been obtained through elasticity theory. However, the result provided in [17] is an approximation of the exact solution.

**Rectangular Section.** For a rectangular section of width $2a$ in $x_2$-direction and height $2b$ in $x_3$-direction (see Fig. 3), the Saint-Venant warping can be expressed in a form of infinite series such as

$$\psi = -x_2x_3 + \frac{32b^2}{\pi^3}\sum_{n=0}^{\infty}\frac{(-1)^n}{(2n+1)^3}\frac{\sinh\left(\frac{2n+1}{2}\frac{\pi x_2}{b}\right)}{\cosh\left(\frac{2n+1}{2}\frac{\pi a}{b}\right)}\sin\left(\frac{2n+1}{2}\frac{\pi x_3}{b}\right). \tag{63}$$

To solve for $\phi$, we should choose the arbitrary functions $f(x_3)$ and $g(x_2)$ first. Along $x_2 = \pm a$, $n_2 \neq 0$, so we can choose $f(x_3) = -(1+\nu)a^2\kappa_3'$ and $g(x_2)$ can be arbitrary. Along $x_3 = \pm b$, $n_3 \neq 0$, we can choose $g(x_2) = (1+\nu)b^2\kappa_2'$ and $f(x_3)$ can be arbitrary. Solving Eq. (52), one finds

$$\begin{aligned} \phi &= -\frac{\nu}{3}(x_2^2-a^2)x_2\kappa_2' \\ &\quad + \frac{4\nu a^3\kappa_2'}{\pi^3}\sum_{n=1}^{\infty}\frac{(-1)^n\cosh\left(\frac{n\pi x_3}{a}\right)\sin\left(\frac{n\pi x_2}{a}\right)}{n^3\cosh\left(\frac{n\pi b}{a}\right)} - \frac{\nu}{3}(x_3^2 \\ &\quad - b^2)x_3\kappa_3' + \frac{4\nu b^3\kappa_3'}{\pi^3}\sum_{m=1}^{\infty}\frac{(-1)^m\cosh\left(\frac{m\pi x_2}{b}\right)\sin\left(\frac{m\pi x_3}{b}\right)}{m^3\cosh\left(\frac{m\pi a}{b}\right)}. \end{aligned} \tag{64}$$

Then one can derive $V_1$ to be

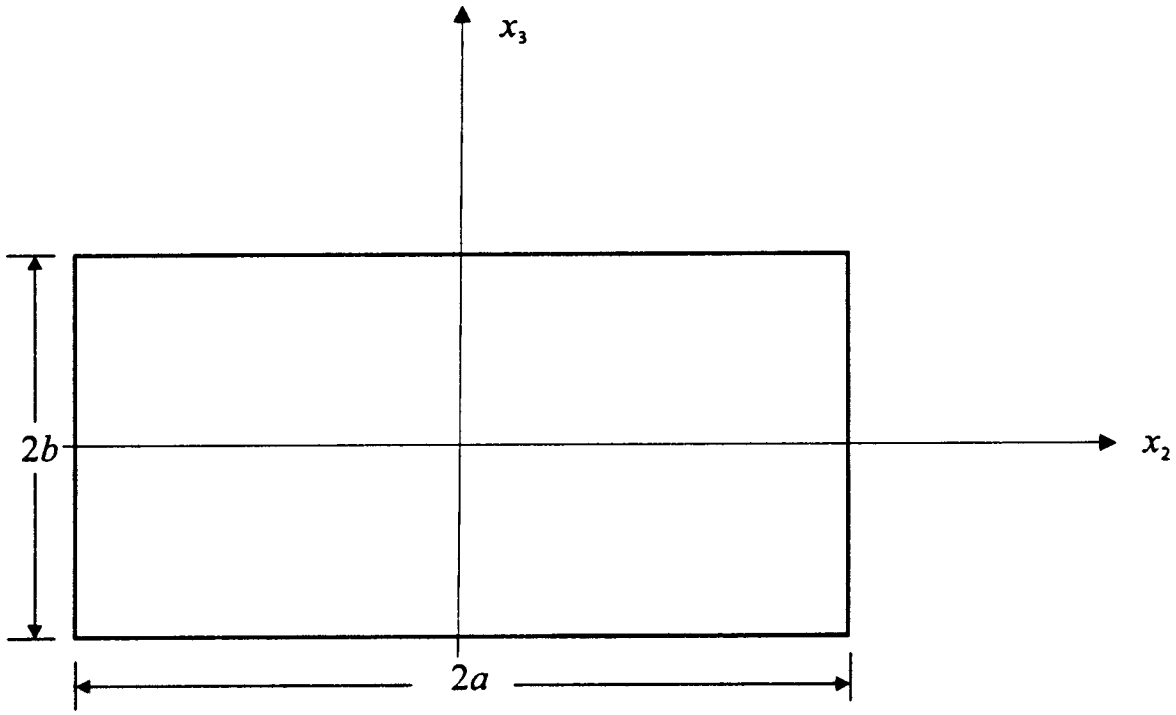


**Fig. 3 Sketch of a rectangular cross section**

$$V_1=-\frac{4a^3\nu\kappa_2'}{\pi^3}\sum_{n=1}^{\infty}\frac{(-1)^n\sinh\left(\frac{n\pi x_3}{a}\right)\cos\left(\frac{n\pi x_2}{a}\right)}{n^3\cosh\left(\frac{n\pi b}{a}\right)}$$
$$+\frac{4\nu b^3\kappa_3'}{\pi^3}\sum_{m=1}^{\infty}\frac{(-1)^m\sinh\left(\frac{m\pi x_2}{b}\right)\cos\left(\frac{m\pi x_3}{b}\right)}{m^3\cosh\left(\frac{m\pi a}{b}\right)}$$
$$+\left[\left(\frac{\nu}{6}+\frac{1}{3}\right)x_2^3-\left(a^2+\frac{5a^2\nu}{6}-\frac{b^2\nu}{6}\right)x_2-\frac{\nu x_2x_3^2}{2}\right]\kappa_3'$$
$$-\left[\left(\frac{\nu}{6}+\frac{1}{3}\right)x_3^3-\left(b^2+\frac{5b^2\nu}{6}-\frac{a^2\nu}{6}\right)x_3-\frac{\nu x_2^2x_3}{2}\right]\kappa_2'. \tag{65}$$

Then the energy of the order $(h/l)^2$ excluding the terms that do not affect the final Timoshenko-like model can be computed as

$$\frac{2\Pi_2}{G}=\left[\frac{16\nu^2ba^5+96b^5a(1+\nu)^2}{45}-\frac{32\nu^2a^6}{\pi^5}\times\sum_{n=1}^{\infty}\frac{\tanh\left(\frac{bn\pi}{a}\right)}{n^5}\right]\kappa_2'^2$$
$$+\left[\frac{16\nu^2b^5a+96a^5b(1+\nu)^2}{45}-\frac{32\nu^2b^6}{\pi^5}\sum_{m=1}^{\infty}\frac{\tanh\left(\frac{am\pi}{b}\right)}{m^5}\right]\kappa_3'^2. \tag{66}$$

The final Timoshenko-like model can be expressed as Eq. (60) with

$$S=4ab\quad J=\beta ab^3\quad I_2=\frac{4}{3}ab^3\quad I_3=\frac{4}{3}a^3b\quad S_\alpha=\frac{GS}{k_\alpha} \tag{67}$$

where $\beta$ can be found in elasticity textbooks such as [15] and $k_\alpha$ are the so-called shear correction factors, given by

$$k_2=\frac{6}{5}+\left(\frac{\nu}{1+\nu}\right)^2\rho^{-4}\left[\frac{1}{5}-\frac{18}{\rho\pi^5}\sum_{m=1}^{\infty}\frac{\tanh(m\pi\rho)}{m^5}\right]$$
$$k_3=\frac{6}{5}+\left(\frac{\nu}{1+\nu}\right)^2\rho^4\left[\frac{1}{5}-\frac{18}{\pi^5}\sum_{n=1}^{\infty}\frac{\tanh(n\pi\rho^{-1})}{n^5}\right]. \tag{68}$$

Although the form of the shear correction factors are different from those of Renton [16], the numerical values for different aspect ratios are the same. The reason the two results are of different form is because in [16] the flexure problem is solved by using a double trigonometric series while here hyperbolic series are used along with the trigonometric series which converge to a fixed value more rapidly. Please note that although [17] is also based on the VAM, the shear correction factors presented therein for the rectangular section are approximations of the elasticity solution.

## Conclusions

The variational asymptotic method, on which the finite-element-based cross-sectional analysis VABS (variational asymptotic beam sectional analysis) is based, has been used to analytically solve the isotropic prismatic beam problem. The same governing equations for Saint-Venant warping and the general flexure problem have been shown to correspond with those of the theory of elasticity. Identical results have been found between elasticity and VAM solutions for beams with elliptical and rectangular cross sections. It has been proven mathematically that for an isotropic prismatic bar with an arbitrary cross section the classical model of VABS is the same as the superposition of elasticity solutions for extension, pure bending in two directions and tor-

sion. Moreover, the Timoshenko-like model of VABS consists of these plus the solution for the general flexure problem in both directions.

The fact that the numerical procedure in VABS reproduces the results of elasticity theory clearly demonstrates that the VAM, the mathematical foundation of VABS, is a valid methodology that can be used to avoid the difficulties of dealing with three-dimensional elasticity while obtaining results that are coincident with the exact solutions. Although it may not be possible to validate the general theory of VABS for anisotropic beams in this same way, it is a natural deduction from the above demonstrations to conclude that the results for generally anisotropic beams should be the same as those calculated by methods based on three-dimensional elasticity theory, such as three-dimensional finite elements. Indeed, as three-dimensional finite elements allow one to go beyond the limitations of three-dimensional elasticity, VABS may also be considered as a means for going beyond those limits when considering the cross-sectional analysis of beams.

## References


[1] Le, K. C., 1999, *Vibrations of Shells and Rods*, 1st Ed., Springer, Berlin.

[2] Ciarlet, P. G., and Destuynder, P., 1979, ''A Justification of a Nonlinear Model in Plate Theory,'' Comput. Methods Appl. Mech. Eng., **17/18**, pp. 227–258.

[3] Berdichevsky, V. L., 1979, ''Variational-Asymptotic Method of Constructing a Theory of Shells,'' Prikl. Mat. Mekh., **43**(4), pp. 664–687.

[4] Hodges, D. H., Atilgan, A. R., Cesnik, C. E. S., and Fulton, M. V., 1992, ''On a Simplified Strain Energy Function for Geometrically Nonlinear Behavior of Anisotropic Beams,'' Composites Eng., **2**(5–7), pp. 513–526.

[5] Cesnik, C. E. S., and Hodges, D. H., 1993, ''Stiffness Constants for Initially Twisted and Curved Composite Beams,'' Appl. Mech. Rev., **46**(11, Part 2), pp. S211–S220.

[6] Cesnik, C. E. S., and Hodges, D. H., 1997, ''VABS: A New Concept for Composite Rotor Blade Cross-Sectional Modeling,'' J. Am. Helicopter Soc., **42**(1), pp. 27–38.

[7] Popescu, B., and Hodges, D. H., 1999, ''On Asymptotically Correct Timoshenko-Like Anisotropic Beam Theory,'' Int. J. Solids Struct., **37**(3), pp. 535–558.

[8] Popescu, B., Hodges, D. H., and Cesnik, C. E. S., 2000, ''Obliqueness Effects in Asymptotic Cross-Sectional Analysis of Composite Beams,'' Comput. Struct., **76**(4), pp. 533–543.

[9] Yu, W., Hodges, D. H., Volovoi, V. V., and Cesnik, C. E. S., 2002, ''On Timoshenko-Like Modeling of Initially Curved and Twisted Composite Beams,'' Int. J. Solids Struct., **39**(19), pp. 5101–5121.

[10] Yu, W., Volovoi, V. V., Hodges, D. H., and Hong, X., 2002, ''Validation of the Variational Asymptotic Beam Sectional Analysis,'' AIAA J., **40**(10), pp. 2105–2112.

[11] Trabucho, L., and Viano, J., 1996, ''Mathematical Modeling of Rods,'' *Handbook of Numerical Analysis*, *Vol. IV*, P. Ciarlet and J. Lions, eds., Elsevier, New York, pp. 487–974.

[12] Volovoi, V. V., Hodges, D. H., Cesnik, C. E. S., and Popescu, B., 2001, ''Assessment of Beam Modeling Methods for Rotor Blade Applications,'' Math. Comput. Modell., **33**(10–11), pp. 1099–1112.

[13] Danielson, D. A., and Hodges, D. H., 1987, ''Nonlinear Beam Kinematics by Decomposition of the Rotation Tensor,'' ASME J. Appl. Mech., **54**(2), pp. 258–262.

[14] Hodges, D. H., 1999, ''Non-linear Inplane Deformation and Buckling of Rings and High Arches,'' Int. J. Non-Linear Mech., **34**(4), pp. 723–737.

[15] Timoshenko, S. P., and Goodier, J. N., 1970, *Theory of Elasticity*, McGraw-Hill, Maidenhead, UK.

[16] Renton, J. D., 1991, ''Generalized Beam Theory Applied to Shear Stiffness,'' Int. J. Solids Struct., **27**(15), pp. 1955–1967.

[17] Berdichevsky, V. L., and Kvashnina, S. S., 1976, ''On Equations Describing the Transverse Vibrations of Elastic Bars,'' Prikl. Mat. Mekh., **40**, pp. 120–135.

**Z. Suo**[1]
**Y. F. Gao**[2]

Mechanical and Aerospace Engineering Department
and Princeton Materials Institute,
Princeton University,
Princeton, NJ 08544

**G. Scoles**
Chemistry Department and
Princeton Materials Institute,
Princeton, University,
Princeton, NJ 08544

# Nanoscale Domain Stability in Organic Monolayers on Metals

*Certain organic molecules, such as alkanethiols, can adsorb on metals to form monolayers. Sometimes domains appear in the monolayers. For example, an incomplete monolayer may form islands, and a mixed-composition monolayer may separate into distinct phases. During annealing, the molecules diffuse on the metal surface. The domain boundary energy drives the domains to coarsen. The contact potential between the dissimilar domains drives the domains to refine. On the basis of existing experimental information, we suggest that the competition between coarsening and refining should stabilize certain domain patterns. We formulate a free energy functional to include the effects of mixed species, domain boundary, and contact potential. An approximate energy minimization estimates the equilibrium domain size. We derive a diffusion equation consistent with the free energy functional. The numerical solution of the diffusion equation follows the evolution of the monolayers from a random initial concentration field to patterns of dots and stripes. We also discuss the practical implications of the theory and, in particular, the possibility of guided self-assembly.* [DOI: 10.1115/1.1640366]

## 1 Introduction

An alkanethiol molecule, $HS(CH_2)_nX$, consists of a thiol group HS at one end, an alkyl chain $(CH_2)_n$ in the middle, and a tail group X at the other end. As illustrated in Fig. 1, when a clean gold substrate is in contact with an alkanethiol solution, the molecules adsorb on the gold surface to form a self-assembled monolayer (SAM), [1–3]. The thiol groups bond to the gold surface, the alkyl chains attract one another through the van der Waals force, and the tail groups are exposed at the surface. Alkanethiol monolayers have been used as a model system to study many phenomena, [4–7]. For instance, SAMs can control surface properties (e.g., adhesion and wetting), [4]. Patterned SAMs (e.g., by microcontact printing) are used to fabricate devices, and to confine cells and biomolecules in desired regions on a substrate, [5–7].

Under certain conditions, a SAM spontaneously forms domains. For example, for an incomplete monolayer, patches of the monolayer coexist with patches of the bare metal, [8–10]. (The ''bare metal'' can actually be covered by the lying-down phase, [1].) Also, when a monolayer of dissimilar alkanethiols fully covers the metal surface, different phases may coexist, [9–12]). Unless the distinction is important, we will refer to the patches as domains, be they standing-up phase, lying-down phase, or bare metal. The domains observed so far have sizes ranging from nanometers to micrometers, and do not form any regular pattern. Is the domain size set by thermodynamic equilibrium, or by kinetics? Can the domains be guided to form some regular patterns, such as an array of stripes or a lattice of dots? Within the alkanethiol family, properties vary considerably with the alkyl chain length and the tail group, giving rise to a large parameter space, which can be used to tailor experiments. Regular domain patterns of a controllable size would open new applications of theses systems. Consequently, it is significant to consider these questions theoretically, even though definitive experiments are lacking. A predictive theory will point to fruitful experiments with alkanethiols on gold, as well as with other molecule-substrate systems.

This study was also prompted by the observation of equilibrium domain pattern formation in monolayers of several types. Examples include atomic monolayers on solid surfaces, [13–19], and molecular monolayer at the air-water interface, i.e., Langmuir films, [2,20–23]. The adsorbed atoms or molecules are mobile. Domains *coarsen* to reduce the total length of the domain boundaries. The residual stresses, or the presence of electric dipoles in a monolayer, induce an elastic or electrostatic field, so that the domains may *refine* to reduce the free energy associated with the field. It is the competition between the domain boundary energy and the field energy that leads to the equilibrium domain patterns, [23–30]. The observed domain sizes range from nanometers to hundreds of micrometers.

Domains in a Langmuir film change by viscous flow in the monolayer and water, although molecules may also diffuse on the surface, [21,31,32]. Domains in a SAM on a metal change by molecular diffusion. Electronic transport in the metal is much faster than molecular diffusion on the surface. Consequently, as molecules diffuse on the surface, electrons flow in the metal rapidly, the electric potential in the metal equalizes, and the electrostatic field in the space above the monolayer adjusts accordingly.

Section 2 discusses phase separation, domain coarsening, and domain refining, drawing on experimental data of alkanethiols on gold. Section 3 formulates a free energy functional to describe the effects of mixed species, domain boundaries, contact potential, and electrostatic field. In Section 4, we minimize the free energy by assuming sinusoidal concentration fields, arriving at an estimate of the equilibrium domain size. In Section 5, we derive a diffusion equation compatible with the free energy functional, and numerically simulate the annealing process.

## 2 Phase Separation, Domain Coarsening, and Domain Refining

When a gold substrate is in contact with an alkanethiol solution, two kinds of mass transport, i.e., adsorption-desorption and diffusion, proceed simultaneously. First consider the case that the solution contains a single species of alkanethiol. Initially molecules adsorbed on the surface form islands. As more molecules adsorb, the islands connect, and the remaining bare gold surface appears as monolayer-deep vacancy islands. Further adsorption causes the vacancy islands to shrink and disappear. Finally a monolayer com-

[1]To whom correspondence should be address. Present address: Division of Engineering and Applied Sciences, Harvard University, Cambridge, MA 02138. e-mail: suo@deas.harvard.edu

[2]Present address: Division of Engineering, Brown University, Providence, RI 02912.

Contributed by the Applied Mechanics Division of THE AMERICAN SOCIETY OF MECHANICAL ENGINEERS for publication in the ASME JOURNAL OF APPLIED MECHANICS. Manuscript received by the Applied Mechanics Division, Sept. 4, 2002; final revision, July 8, 2003. Associate Editor: H. Gao. Discussion on the paper should be addressed to the Editor, Prof. Robert M. McMeeking, Journal of Applied Mechanics, Department of Mechanical and Environmental Engineering, University of California–Santa Barbara, Santa Barbara, CA 93106-5070, and will be accepted until four months after final publication in the paper itself in the ASME JOURNAL OF APPLIED MECHANICS.

  

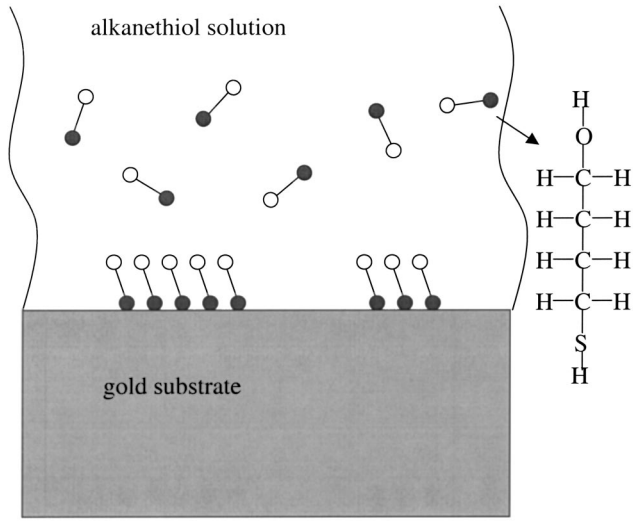


**Fig. 1 When a metal is in contact with an alkanethiol solution, the alkanethiol molecules adsorb on the metal surface to form a monolayer. The structure of a $HS(CH_2)_4OH$ molecule is illustrated.**

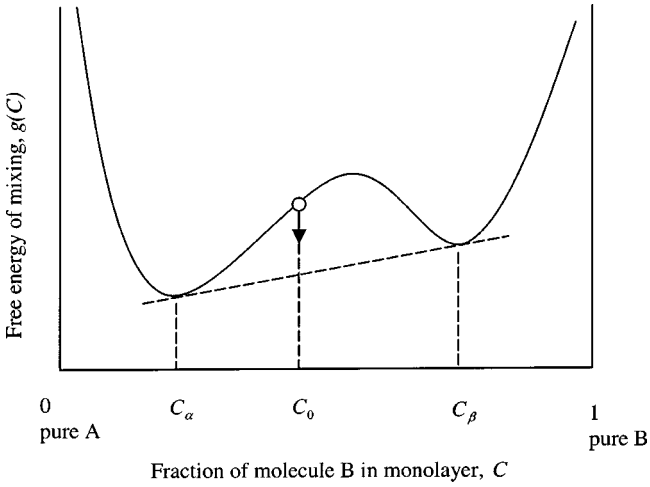


**Fig. 2 The free energy of mixing for a monolayer composed of two molecular species, A and B. The pair has a large enthalpy of mixing, so that the free energy of mixing has two wells at $C_\alpha$ and $C_\beta$, corresponding to two phases. When the average concentration of the monolayer, $C_0$, is between the two wells, to reduce the free energy, the monolayer separates into the two phases.**

pletely covers the gold surface. A necessary condition to form an equilibrium domain pattern of an incomplete monolayer is to break the contact between the solution and the metal before the monolayer completes. In subsequent annealing, molecules diffuse on the surface to change the domain patterns.

Similar considerations apply to the case that the solution contains two alkanethiol species, A and B. As pointed out by Folkers et al., [32], if gold is kept in contact with the solution, allowing the molecules on gold to exchange with those in the solution, in equilibrium the monolayer will have a single phase. Again, a necessary condition to stabilize two phases in a monolayer is to break the contact between the solution and the metal at some point. The monolayer covers the entire surface, and the amount of the two components in the monolayer has a suitable ratio. For the two phases to equilibrate in annealing, the enthalpy of mixing has to overcome the entropy of mixing. Let $C$ be the concentration of the monolayer, namely, the fraction of surface sites on gold occupied by B-alkanethiols. During annealing, the molecules can diffuse on the surface, but the amount of either species remains constant, so that the average concentration of the monolayer, $C_0$, remains invariant. Figure 2 illustrates the free energy of mixing $g(C)$ for a homogeneous monolayer. The two wells at $C_\alpha$ and $C_\beta$ correspond to the two phases. When $C_\alpha < C_0 < C_\beta$, the monolayer separates into the two phases in equilibrium.

Alkanethiol molecules form strong bonds to gold surface, and are not very mobile at room temperature. The diffusivity of alkanethiols on gold is estimated to be $D = 10^{-21}\,\mathrm{m}^2/\mathrm{s}$, [33]. For the concentration field to change over a length scale $L$, the time needed scales as $t \sim L^2/D$. For example, if the domain size is 10 nm, the time scale is $\sim 10^5$ s. It has been observed that nanoscale islands in an incomplete monolayer under atmospheric conditions coarsen at room temperature in days, [8]. To accelerate pattern formation, the monolayer can be annealed above room temperature, as long as the molecules do not evaporate appreciably, and the phases are still stable.

The excess free energy of the domain boundaries, i.e., the line tension, drives coarsening. For domains to be stable, a refining action must exist to prevent domains from growing too large. We now examine how the contact potential drives domains to refine. Regard the monolayer and a few top layers of gold atoms as an interfacial system. Across the thickness of this system, the positive and the negative electric charges are unevenly distributed, resulting in an electric dipole normal to the surface. Now consider two gold substrates, one covered with a monolayer of phase $\alpha$, and the other with a monolayer of phase $\beta$. When the two substrates are connected, electrons flow from one substrate to the other, until the chemical potentials of electrons in the two substrates are equilibrated. Due to the difference in the two monolayers, the electric potential in space near $\alpha$ differs from that near $\beta$, say $\phi_\alpha < \phi_\beta$. The difference, $U = \phi_\beta - \phi_\alpha$, is known as the contact potential, and can be measured by the Kelvin method, [34–36]. The contact potential sets up an electrostatic field in the space, and a charge density field on the metal surface, [37].

Figure 3 illustrates a monolayer composed of two kinds of domains, $\alpha$ and $\beta$. The period $\lambda$ represents the domain size. The metal occupies the lower half space $x_3 < 0$, and the monolayer coincides with the $(x_1, x_2)$ plane. The space above the monolayer is occupied by air. The electrostatic energy stored in the space depends on the magnitude of the contact potential, but not on how

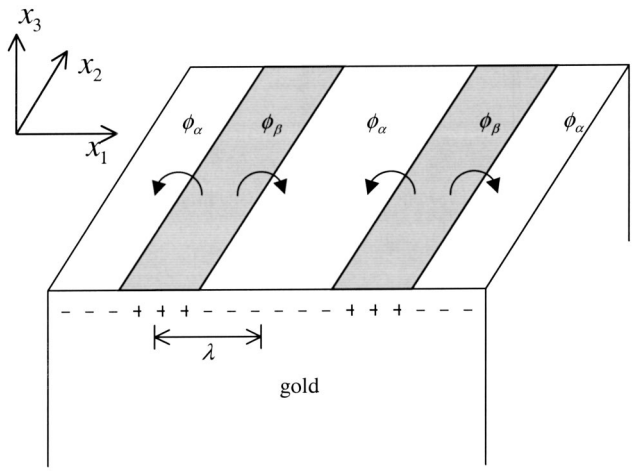


**Fig. 3 The contact potential $U = \phi_\beta - \phi_\alpha$ causes an electrostatic field in the air, a positive charge on the metal surface under domain $\beta$, and a negative charge under domain $\alpha$. Represent the domain size by the period $\lambda$.**

the contact potential is set up. Imagine that the contact potential can be varied from zero to its final magnitude $U$. This can be accomplished, for example, by starting with a pure $\alpha$-phase monolayer, and gradually converting some patches into the $\beta$-phase. When the contact potential is zero, the charge on the metal surface is zero. As the contact potential increases, electrons flow in the metal, setting up a net positive charge $+Q$ on the metal surface under the $\beta$ domains, and a net negative charge $-Q$ under the $\alpha$ domains. Because the electrostatic field equations in the space are all linear, $Q$ is linear in $U$ (Fig. 4($a$)). The slope of the line is the inverse of the capacitance of the system. When the contact potential changes from 0 to $U$, the electrostatic energy stored in the space above the monolayer is $1/2QU$. It is always a positive quantity.

In reality, the contact potential $U$ is held constant by the molecular difference between the two domains. The contact potential acts like a battery, and the $\beta$ and $\alpha$ domains act like two electrodes. The metal substrate serves as a wire connecting the electrodes. When transporting an amount of charge $Q$ from the $\alpha$ domains to the $\beta$ domains, the constant voltage $U$ does work $QU$. Having done this work, the ''battery'' reduces the free energy. Consequently, the electric free energy, of the combined system, is the electrostatic energy in space minus the work done by the constant contact potential, namely, $1/2QU-QU=-1/2QU$. The electric free energy is always a negative quantity. At a constant voltage, the higher the capacitance, the larger the charge, and the lower the free energy. That is, to reduce the electric free energy at the constant contact potential $U$, the system evolves toward a configuration of high capacitance.

We can now understand the refining action due to the contact potential. In the discussion above, we kept the domain pattern fixed. Now allow the domain pattern to change by molecular diffusion. In this process, $U$ is constant, but both the charge $Q$ on the metal surface and the electrostatic field in space change. As the domain size decreases from $\lambda_2$ to $\lambda_1$, the capacitance increases (Fig. 4($b$)). The trend is analogous to a parallel-electrode capacitor (Fig. 4($c$)). The charge $Q$ increases as the domain size decreases. The electric free energy is reduced if the domain size decreases, so that the contact potential drives the domains to refine.

## 3 Free Energy as a Functional of the Concentration Field

Similar to the Cahn-Hilliard model [38], we represent a polydomain monolayer by a continuum concentration field, $C(x_1,x_2)$, and a domain boundary by a gradient in the concentration field. First consider a surface of gold covered with a homogenous monolayer of concentration $C$. Denote $\phi$ as the contact potential between this surface and a reference surface, say, a gold surface covered with a monolayer of pure A. We assume that the contact potential is linear in the concentration:

$$\phi=\zeta C. \tag{1}$$

That is, the dipole moment of an individual molecule, either A or B, is assumed to be unaffected by the presence of other molecules on the substrate. The metal is covered by pure A at $C=0$, and by pure B at $C=1$. Consequently, the slope $\zeta$ in (1) equals the contact potential between a substrate covered by pure B and another substrate covered by pure A.

Figure 5 illustrates the interface between the air and the metal. We assume that the thickness of the interfacial system is small compared to the domain size, and is negligible in calculating the electrostatic field. Denote the electric potential in the space by $\Psi(x_1,x_2,x_3)$. The electric potential in the bulk of the metal is constant, taken to be zero. In the space, at a point immediately above the monolayer, $x_3=0^+$, the electric potential equals the contact potential:

$$\Psi(x_1,x_2,0)=\phi(x_1,x_2)=\zeta C(x_1,x_2). \tag{2}$$

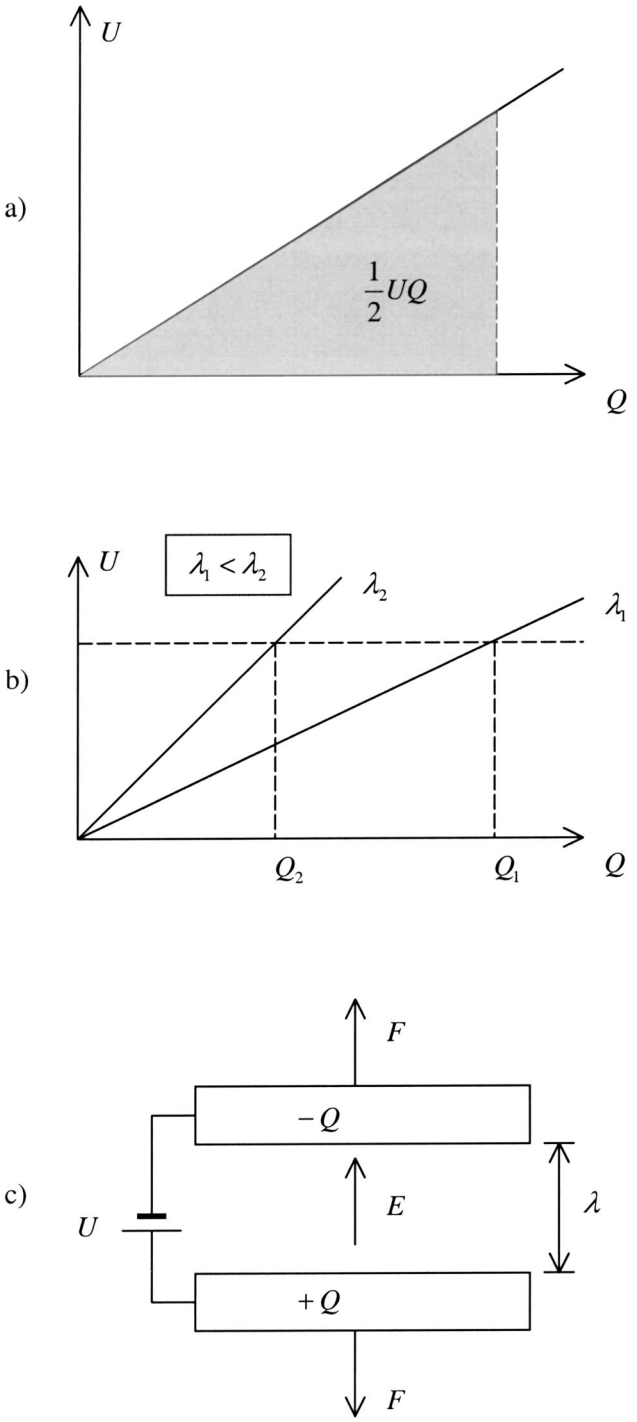


**Fig. 4** (*a*) **The charge $Q$ accumulated under either domain increases linearly with the contact potential between the two domains, $U=\phi_\beta-\phi_\alpha$. The area of the triangle is the electrostatic energy stored in the space occupied by the air. The slope of the line is inverse of the capacitance of the system.** (*b*) **The $Q$-$U$ lines for two domain sizes, $\lambda_1<\lambda_2$. At a constant voltage, the smaller the domain size, the larger the charge, namely, $Q_1>Q_2$.** (*c*) **In a parallel-electrode capacitor, the electric interaction causes the attraction between two electrodes. To keep the two electrodes in place, one has to apply a pair of forces to pull the electrodes apart.**

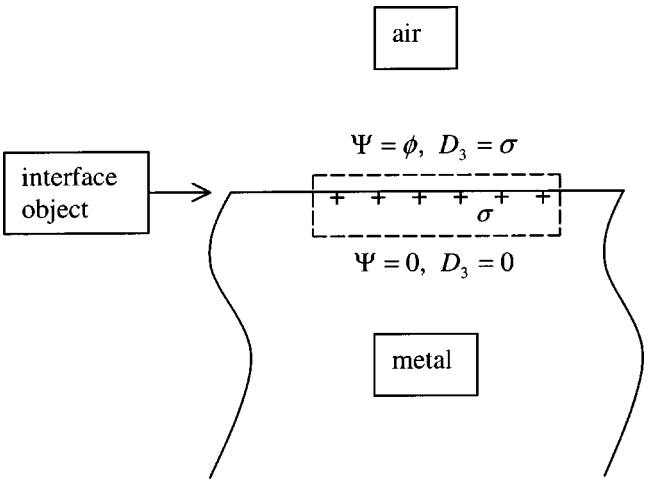


**Fig. 5 The boundary conditions at the interfacial object between the air and the bulk of the metal**

Let the electric charge per unit area on the metal surface be $\sigma(x_1,x_2)$. Applying Gauss's law to a small volume containing an element of the interfacial system, one confirms that the electric displacement component in the space immediately above the monolayer is $D_3(x_1,x_2,0)=\sigma(x_1,x_2)$. Consequently, the surface charge density relates to the electric potential in space as

$$\sigma(x_1,x_2)=-\varepsilon_0\frac{\partial\Psi}{\partial x_3},\quad x_3=0. \tag{3}$$

The field equations are standard. The electric field relates to the gradient of the electric potential as $\mathbf{E}=-\nabla\Psi$. The electric displacement is linear in the electric field, namely, $\mathbf{D}=\varepsilon_0\mathbf{E}$. We assume that the upper half space is free of charges, so that the electric displacement is divergence-free, $\nabla\cdot\mathbf{D}=0$. Consequently, the electric potential in the air satisfies the Laplace equation:

$$\nabla^2\Psi=0. \tag{4}$$

The electrostatic energy stored in the space is the same as the work done in building up the contact potential from zero to $\phi$, namely,

$$\int\frac{1}{2}\mathbf{E}\cdot\mathbf{D}dV=\int\frac{1}{2}\phi\sigma dA. \tag{5}$$

The integral on the left-hand side extends over the volume of the half space above the surface, and the integral on the right-hand side extends over the area of the surface. Equation (5) can also be confirmed by using the field equations and the divergence theorem. We assume that the system as a whole is neutral, $\int\sigma dA=0$. Equation (5) shows that the electrostatic energy in the space above the monolayer vanishes when the contact potential is uniform over the surface, as expected.

Next we examine the free energy of the interfacial system. The interfacial energy density, $\Gamma$, takes an unusual from. Assume that $\Gamma$ is a function of the concentration $C$, the concentration gradient $\nabla C$, and the surface charge density $\sigma$. Expanding the function into the Taylor series to the leading order terms in $\nabla C$ and $\sigma$, we have

$$\Gamma=g+h|\nabla C|^2-\phi\sigma, \tag{6}$$

where $g$, $h$, and $\phi$ are in general functions of $C$. The term $g(C)$ is the surface energy density when the concentration is uniform and the surface charge vanishes. Indeed, the function $g(C)$ is the free energy of mixing (Fig. 2), taken to be an input of the model. Because the interfacial energy density is independent of the direction of the concentration gradient, the leading term in $\nabla C$ is quadratic, with $h$ being a positive constant. In the expansion (6), we keep the third term linear in $\sigma$, but neglect terms which are higher order in $\sigma$. As discussed in Section 2, when $\phi$ is held a constant for the interfacial element, the work done by $\phi$ to add charge $\sigma$ to the element is $\sigma\phi$, which reduces the free energy.

The excess free energy of the interfacial object is the integral of $\Gamma$ over the area of the surface. The free energy $G$ of the system—the SAM on metal and the space above—is the sum of the electrostatic energy stored in the space, Eq. (5), and the excess free energy of the interfacial object, namely,

$$G=\int\left(g+h|\nabla C|^2-\frac{1}{2}\phi\sigma\right)dA. \tag{7}$$

In summary, this section defines a thermodynamic system by prescribing a procedure to calculate its free energy. The free energy is a functional of the concentration field. Given a concentration field $C(x_1,x_2)$, one determines the electric potential $\Psi(x_1,x_2,x_3)$ by solving the Laplace Eq. (4) subject to the boundary condition (2), and then calculates the surface charge density $\sigma(x_1,x_2)$ according to (3). Equation (7) gives the free energy of the system. The concentration field evolves to minimize this free energy.

## 4 An Approximate Analysis of Equilibrium Domain Sizes

An equilibrium domain pattern corresponds to a concentration field that minimizes the free energy functional (7). To estimate the equilibrium domain size, we minimize the free energy over a particular family of concentration fields:

$$C(x_1,x_2)=C_0+C_1\sin\left(\frac{2\pi x_1}{\lambda}\right). \tag{8}$$

This family represents an array of periodic stripes oriented along the $x_2$ direction. During annealing, the metal is no longer in contact with the alkanethiol solution, so that the average concentration of the monolayer, $C_0$, is fixed. The amplitude of fluctuation, $C_1$, and the period, $\lambda$, are varied to minimize the free energy.

A combination of (1) and (8) gives the contact potential

$$\phi=\zeta C_1\sin\left(\frac{2\pi x_1}{\lambda}\right). \tag{9}$$

Matching this boundary condition, the solution to the Laplace equation gives the electric potential in the upper half-space:

$$\Psi=\zeta C_1\sin\left(\frac{2\pi x_1}{\lambda}\right)\exp\left(-\frac{2\pi x_3}{\lambda}\right). \tag{10}$$

The electric potential decays exponentially as $x_3\to\infty$, the decay length being $\lambda/2\pi$. The surface charge is calculated according to (3), giving

$$\sigma=\varepsilon_0\zeta C_1\left(\frac{2\pi}{\lambda}\right)\sin\left(\frac{2\pi x_1}{\lambda}\right). \tag{11}$$

The surface charge is in phase with the contact potential (9), as expected.

The average energy per unit area is the integral (7) over one period, divided by the period. The calculation gives

$$\overline{G}=\overline{g}+\frac{C_1^2}{4}\left[2h\left(\frac{2\pi}{\lambda}\right)^2-\varepsilon_0\zeta^2\left(\frac{2\pi}{\lambda}\right)\right]. \tag{12}$$

The average energy of mixing, $\overline{g}$, is independent of the wavelength. The two terms in the bracket result from, respectively, the domain boundary and electrostatics. The trends discussed in Section 2 can now be seen clearly in (12). The domain boundary energy reduces when the wavelength increases, and drives the domains to coarsen. The electrostatic energy reduces when the wavelength decreases, and drives the domains to refine.

The free energy is quadratic in $(2\pi/\lambda)$, and reaches its minimum at the wavelength

$$\lambda_0 = \frac{8\pi h}{\varepsilon_0 \zeta^2}. \tag{13}$$

Using $\varepsilon_0 = 8.85\times 10^{-12}$ F/m, $h = 10^{-21}$ J and $\zeta = 0.5$ V, we find that $\lambda_0 = 11$ nm. Before taking this estimate seriously, we should discuss the validity of the analysis, and the field of variability of the parameters.

In reaching (13), we have sought the energy minimizer among candidates of a very small family of concentration fields, Eq. (8). The sinusoidal concentration profile is a reasonable approximation when the domain size is not too large compared to the domain boundary width. This happens when the refining action is strong, or when the coarsening action is weak (e.g., when the binary monolayer is held just below the critical temperature). When the domain size is, say, more than ten times the domain boundary width, however, the concentration profile is close to a square wave, which should be represented by a Fourier series of many wavelengths. An analysis following this line of thought shows that the equilibrium domain size is larger than that given by (13), [39]. In the limit that the domain size is much larger than the domain boundary width, the line tension model is appropriate, giving another estimate of the equilibrium domain size, [25,26]:

$$\lambda_\infty = 2\pi a \exp\left(\frac{2\pi\gamma}{\varepsilon_0 U^2} + 1\right), \tag{14}$$

where $a$ is a cutoff radius (close to molecular dimensions, $a \sim 1$ nm), $\gamma$ the line tension, and $U$ the contact potential between the two domains. The step jump of the contact potential at the domain boundary makes the electrostatic energy unbounded, and the cutoff radius is introduced to regularize the problem. Taking $\gamma = 10^{-12}$ N and $U = 0.5$ V, we find that $\lambda_\infty = 292$ nm.

Next we discuss the variability field of the parameters that determine the equilibrium domain size. We have assumed that the space above the monolayer is occupied by air. If a high-permittivity dielectric fluid lies above the monolayer during annealing, the equilibrium domain size will reduce accordingly. Of course, the presence of a dielectric fluid, rather than the air, may modify the contact potential and the domain boundary energy somewhat. Independent measurements of these quantities have to be made. Similarly, if one places a high-permittivity dielectric solid at a small gap above the monolayer during annealing, one can, in principle, even tune the equilibrium domain size by adjusting the gap.

Contact potentials have been measured for alkanethiols on gold, [35,36]. The potential increases linearly with the alkyl chain length by 0.0093 V per $CH_2$ unit. The potential changes also when the tail group changes; variation between $-0.75$ V to $+0.60$ V has been reported. One can even incorporate polar groups in the middle of the alkyl chain to increase the contact potential without compromising the functionality of the tail group.

We are unaware of any measurement of the domain boundary energy in alkanethiol monolayers. The line tension of the phase boundary in Langmuir films has been measured experimentally, a representative order of magnitude being $\gamma = 10^{-12}$ N, [22]. Considering the similarity of the inter-molecular forces involved in Langmuir films and in SAMs, we expect that the magnitude of the line tension should be comparable in the two systems. Note that the line tension decreases as the temperature increases, and vanishes above the critical temperature. Because the inter-molecular forces are weak, the critical temperature is not too high, and is typically within experimental reach.

Given the large variability in the parameters, one should expect very different equilibrium domain sizes in different systems. That is, the equilibrium domain size should be tunable.

When both the surface stress and contact potential are present, a combination of the above analysis and that in [28] gives the equilibrium domain size:

$$\lambda_0 = \frac{8\pi h}{\varepsilon_0 \zeta^2 + \dfrac{(1-\nu)\xi^2}{\mu}}, \tag{15}$$

where $\mu$ is the shear modulus, $\nu$ is Poisson's ratio, and $\xi$ is the slope of the surface stress as a function of the concentration. The relative importance of the electrostatic and elastic interaction is quantified by a dimensionless ratio

$$R = \frac{\mu\varepsilon_0\zeta^2}{(1-\nu)\xi^2}. \tag{16}$$

The surface stress has been measured for alkanethiols on gold, giving 0.017 N/m per $CH_2$ unit, [40]. The available data indicate that the effect of the surface stress and that of the contact potential are comparable for alkanethiols on gold. However, if one introduces high-permittivity dielectrics in the space above the monolayer, and incorporates polar groups into the molecules, the electrostatic interaction can be altered by orders of magnitude.

## 5 Diffusion Equation and the Need to Break Symmetry

In this section, we consider the diffusion process, in which the monolayer starts from an arbitrary initial concentration field, and evolves to a stable domain pattern. We derive a diffusion equation, following a standard procedure in nonequilibrium thermodynamics, [28,38]. Imagine a curve on the substrate surface. When some number of A-molecules crosses this curve, to maintain the integrity of the monolayer, an equal number of B-molecules must cross the curve in the opposite direction. Denote the unit vector lying in the surface normal to the curve by **m**. Let **I** be a vector field in the surface, such that **I**·**m** is the number of B-molecules across a unit length of the curve.

When the concentration on an element of the surface varies by $\delta C$, the same number of B-molecules must move into the element from the neighboring regions on the surface, namely,

$$\Lambda\,\delta C = -\nabla\cdot(\delta\mathbf{I}), \tag{17}$$

where $\Lambda$ is the number of surface sites per unit area. Combining (7) and (17), we find the variation of the free energy:

$$\delta G = \frac{1}{\Lambda}\int (\delta\mathbf{I})\cdot\nabla\left(\frac{\partial g}{\partial C} - 2h\nabla^2 C - \zeta\sigma\right) dA. \tag{18}$$

In deriving (18), we have used the fact that the term $\phi\sigma$ in (7) is quadratic in $C$. We have also discarded integrals along curves on the surface, assuming periodic boundary conditions.

Define the diffusion driving force **f** as the free-energy reduction associated with a molecule relocating by a unit distance. Comparing this definition and (18), we obtain an expression for the diffusion driving force:

$$\mathbf{f} = -\frac{1}{\Lambda}\nabla\left(\frac{\partial g}{\partial C} - 2h\nabla^2 C - \zeta\sigma\right). \tag{19}$$

When the diffusion driving force vanishes, the free energy variation vanishes, and the concentration field reaches equilibrium. The quantity in the parenthesis is a chemical potential. A concentration field is in equilibrium when the chemical potential is constant over the surface. Obviously, a homogeneous monolayer is an equilibrium state, which can be unstable. We are interested in stable, inhomogeneous equilibrium states.

In general, for an arbitrary concentration field, the driving force does not vanish—it drives the diffusion flux. Assume that the diffusion flux, **J**, is linearly proportional to the driving force, namely, $\mathbf{J} = M\mathbf{f}$, where $M$ is the mobility of the molecules on the

surface. The conservation of molecules requires that $\Lambda \partial C/\partial t = -\nabla \cdot \mathbf{J}$. These considerations lead to the diffusion equation

$$\frac{\partial C}{\partial t} = \frac{M}{\Lambda^2}\nabla^2\left(\frac{\partial g}{\partial C} - 2h\nabla^2 C - \zeta\sigma\right). \tag{20}$$

To evolve the concentration field numerically, we need to specify the free energy of mixing $g(C)$. Any function with two wells, as shown in Fig. 2, will serve the purpose. To be specific, we assume that the binary monolayer is a regular solution, with the free energy of mixing given by

$$g(C) = \Lambda k_B T[C\log C + (1-C)\log(1-C)] + \Lambda\omega C(1-C), \tag{21}$$

where $k_B$ is Boltzmann's constant, and $T$ the absolute temperature. The parameter $\omega$ measures the magnitude of the enthalpy of mixing. When $\omega/k_BT<2$, the entropy of mixing prevails, and $g(C)$ has a single well. When $\omega/k_BT>2$, the enthalpy of mixing prevails, and $g(C)$ has two wells.

A comparison of the first two terms in (20) leads to a length:

$$b = \left(\frac{h}{\Lambda k_B T}\right)^{1/2}. \tag{22}$$

This length scales the distance over which the concentration changes from the level of one phase to that of the other. From (20) and (21), we note that the diffusivity scales as $D \sim Mk_BT/\Lambda$. To resolve events occurring over the length scale $b$, the time scale is $b^2/D$. This consideration defines a time scale

$$\tau = \frac{h}{M(k_BT)^2}. \tag{23}$$

To evolve the concentration field according to (20), at each time-step, for a given concentration field, we need to solve the electrostatic boundary value problem, and calculate the surface charge field. This can be done by an area integral of a Green's function. The integral is singular, and extends over the entire surface. This approach would take a great deal of computation time. Rather, we will solve the electrostatic boundary value problem in the Fourier space. Consider the Fourier transform

$$C(x_1,x_2,t) = \int_{-\infty}^{+\infty}\int_{-\infty}^{+\infty}\hat{C}(k_1,k_2,t)\exp(ik_1x_1 + ik_2x_2)dk_1dk_2. \tag{24}$$

To ensure that $C(x_1,x_2,t)$ is real-valued, the two Fourier components $\hat{C}(k_1,k_2,t)$ and $\hat{C}(-k_1,-k_2,t)$ must be complex conjugate. Because the electrostatic field is governed by linear equations, we only need to determine the electrostatic field for an individual Fourier component, and then superimpose all the components. For a pair of components, $\hat{C}(k_1,k_2,t)$ and $\hat{C}(-k_1, -k_2,t)$, the concentration field is

$$C = 2\,\mathrm{Re}[\hat{C}(k_1,k_2,t)\exp(ik_1x_1 + ik_2x_2)], \tag{25}$$

where Re stands for the real part of a complex number. The contact potential is

$$\phi = 2\zeta\,\mathrm{Re}[\hat{C}\exp(ik_1x_1 + ik_2x_2)]. \tag{26}$$

This prescribes the boundary condition at $x_3=0$ for the electrostatic field in the upper half-space. One can readily confirm that the solution to the Laplace equation is

$$\Psi = 2\zeta\,\mathrm{Re}[\hat{C}\exp(ik_1x_1 + ik_2x_2 - kx_3)], \tag{27}$$

where $k=\sqrt{k_1^2+k_2^2}$. This electric potential matches the boundary condition (26), and vanishes as $x_3\to+\infty$. The surface charge density is

$$\sigma = 2\varepsilon_0 k\zeta\,\mathrm{Re}[\hat{C}\exp(ik_1x_1 + ik_2x_2)]. \tag{28}$$

Normalizing the time by $\tau$ and the spatial coordinates by $b$ in (20), and taking the Fourier transform on both sides, we obtain

$$\frac{\partial \hat{C}}{\partial t} = -k^2\hat{P} - 2k^4\hat{C} + \rho k^3\hat{C}, \tag{29}$$

where $\rho = 8\pi b/\lambda_0$ is a dimensionless parameter, and $\hat{P}(k_1,k_2)$ is a Fourier component of the function

$$P(C) = \log\left(\frac{C}{1-C}\right) + \frac{\omega}{k_BT}(1-2C), \tag{30}$$

which comes from the derivative of the free energy of mixing (21).

Remarkably, Eq. (29) is identical to that of a monolayer on an isotropic elastic substrate, where the surface stress drives domain refining, [29]. We will use the same numerical method to evolve the concentration field. The function $P(C)$ is nonlinear in $C$, so that $\hat{P}$ at a given point in the $(k_1,k_2)$ plane depends on $\hat{C}$ at all points in the $(k_1,k_2)$ plane. Consequently, (29) evolves $\hat{C}$ at all points in the $(k_1,k_2)$ planes simultaneously, in a coupled manner. Numerical simulation proceeds as follows. Start with a known concentration field $C(x_1,x_2,t_0)$ at time $t_0$. Calculate $P$ according to (30), and $\hat{P}$ by using the fast Fourier transform (FFT). Also obtain $\hat{C}$ by FFT. Equation (29) updates the field $\hat{C}$ for a small time step. Take an inverse FFT to obtain the updated $C$ field. Repeat the procedure for many time steps to evolve the concentration field over a long period of time. More details of numerical implementation can be found in [29,41].

In numerical simulations, we take $\omega/k_BT=2.2$, so that $g(C)$ has two wells at $C_\alpha=0.249$ and $C_\beta=0.751$. We take $\rho=2$, so that $\lambda_0 = 4\pi b$, and the equilibrium domain size is about one order of magnitude larger than the domain wall width. We restrict the calculation within a $256b\times256b$ square cell, and choose $b$ as the grid size. Periodic boundary conditions are used to replicate the cell to the entire monolayer. Figure 6 shows two simulation results taken from [29], which was originally intended for patterns stabilized by surface stress. Now if we interpret $\lambda_0$ by (15), the same simulation describes pattern evolution under combined actions of surface stress and contact potential.

Figure 6(*a*) shows the concentration field after the annealing time $t=10^5\tau$. The initial concentration field randomly fluctuates around the average value $C_0=0.5$. At around $t=10^2\tau$, the concentration field has already separated into two phases of meandering stripes. The pattern and the feature size hardly change between $10^2\tau$ to $10^5\tau$.

Figure 6(*b*) shows a pattern at time $t=4\times10^6\tau$, initiated from a concentration field randomly fluctuated around the average value $C_0=0.4$. The dots are established around $t=10^2\tau$. Further annealing does not change the size of the dots appreciably, but improves the spatial ordering of the dots. At $t=4\times10^6\tau$ shown in Fig. 6(*b*), the pattern consists of grains, each grain being a triangular lattice consisting of fewer than ten dots across.

Both meandering stripes and disordered dots have been observed in alkanethiol monolayers, [8–12]. Some of these experiments were carried out with the monolayers in contact with the alkanethiol solution at room temperature, so that the adsorption process affected the domain patterns. Alkanethiol molecules diffuse slowly on gold at room temperature, so that the observed domains may not be of the equilibrium size.

Figure 6 also clearly shows the effect of symmetry on pattern formation. The model is isotropic, with no preferred orientation in the plane of the monolayer. Consequently, stripes of all orientations are equally possible, so are lattices of all orientations. Improving the long-range order by annealing alone takes a long time. A powerful way to form patterns with long-range ordering is to break the symmetry. In a series of papers, [39,42–44], we have studied the effect of symmetry breaking of various modes on domain patterns, assuming surface stress stabilizes the domains. Do-

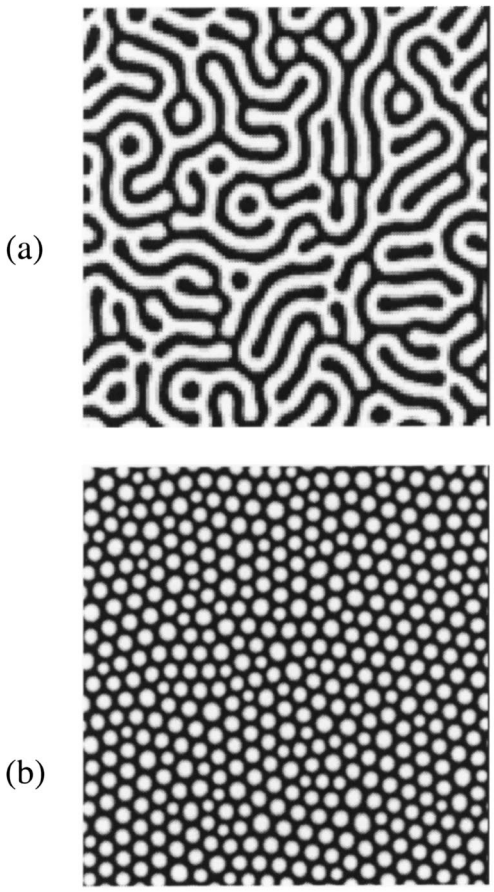


**Fig. 6 (*a*) The concentration field initially fluctuates with small amplitude around the average concentration $C_0=0.5$, and evolves into a pattern of meandering stripes. (*b*) The concentration field initially fluctuates with small amplitude around the average concentration $C_0=0.4$, and evolves into a pattern of dots.**

mains stabilized by contact potential offer additional opportunities. For example, during annealing, one can place an anisotropic dielectric crystal at a small distance above the monolayer. The presence of the crystal affects the electrostatic field, and can set a preferred orientation to guide the pattern. Similarly, one can make a metal pattern on a solid using lithography, and then place the patterned solid over the monolayer. During annealing, this lithographic pattern can guide the pattern formation in the monolayer. The concept is analogous to the lithographically-induced self-assembly (LISA), [45–47]. We will report details of these intriguing possibilities in subsequent papers [48,49].

## 6 Concluding Remarks

On the basis of available experimental data and theories, we suggest that alkanethiol SAMs on gold should form domain patterns under certain conditions. Upon annealing, alkanethiol molecules diffuse on the gold surface, and the domain pattern may evolve into an equilibrium state. The domain boundary energy drives the domains to coarsen, and the contact potential drives the domains to refine. The competition sets an equilibrium domain size, which can be varied by varying the alkyl chain length, by incorporating polar groups into the molecules, by placing a high-permittivity dielectric liquid above the monolayer, and by changing the temperature. In an isotropic system, the domain patterns are not organized over a long distance. Various modes of symmetry breaking may guide domains into periodic lattices. SAMs with ordered domains of controllable sizes would open new possibilities for applications. Further experiments and theoretical work need to be carried out to ascertain the premises, and to explore new opportunities, particularly those of guided self-assembly. The concepts are also applicable to monolayers of other molecules. Provided molecules on surfaces are mobile, the combined effects of surface stress and contact potential may be strong enough to stabilize domains of desired sizes.

## Acknowledgments

The work is supported by the Department of Energy through grants DE-FG02-99ER45787 and DE-FG02-93ER45503, and by the National Science Foundation through a Materials Research Science and Engineering Center at Princeton. We gratefully acknowledge helpful discussions with D. J. Srolovitz, K. Vanderlick, and Y. Hu.

## References

[1] Schreiber, F., 2000, ''Structure and Growth of Self-Assembling Monolayer,'' Prog. Surf. Sci., **65**, pp. 151–256.
[2] Ulman, A., 1991, *An Introduction to Ultrathin Organic Films: From Langmuir-Blodgett to Self-Assembly*, Academic Press, Boston.
[3] Dubois, L. H., and Nuzzo, R. G., 1992, ''Synthesis, Structure, and Properties of Model Organic-Surfaces,'' Annu. Rev. Phys. Chem., **43**, pp. 437–463.
[4] Bain, C. D., and Whitesides, G. M., 1989, ''Formation of Monolayers by the Coadsorption of Thiols on Gold-Variation in the Length of the Alkyl Chain,'' J. Am. Chem. Soc., **111**, pp. 7164–7175.
[5] Kumar, A., Biebuyck, H. A., and Whitesides, G. M., 1994, ''Patterning Self-Assembled Monolayers—Applications in Materials Science,'' Langmuir, **10**, pp. 1498–1511.
[6] Delmarche, E., Schmid, H., Bietsch, A., Larsen, N. B., Rothuizen, H., Michel, B., and Biebuyck, H., 1998, ''Transport Mechanisms of Alkanethiols During Microcontact Printing on Gold,'' J. Phys. Chem. B, **102**, pp. 3324–3334.
[7] Xia, Y., Rogers, J.A., Paul, K. E., and Whitesides, G. M., 1999, ''Unconventional Methods for Fabricating and Patterning Nanostructures,'' Chem. Rev., **99**, pp. 1823–1848.
[8] Barrena, E., Ocal, C., and Salmeron, M., 1999, ''Evolution of the Structure and Mechanical Stability of Self-Assembled Alkanethiol Islands on Au (111) due to Diffusion and Ripening,'' J. Chem. Phys., **111**, pp. 9797–9802.
[9] Tamada, K., Hara, M., Sasabe, H., and Knoll, W., 1997, ''Surface Phase Behavior of n-Alkanethiol Self-Assembled Monolayers Adsorbed on Au (111): An Atomic Force Microscope Study,'' Langmuir, **13**, pp. 1558–1566.
[10] Stranick, S. J., Parikh, A. N., Tao, Y. T., Allara, D. L., and Weiss, P. S., 1994, ''Phase-Separation of Mixed-Composition Self-Assembled Monolayers Into Nanometer-Scale Molecular Domains,'' J. Phys. Chem., **98**, pp. 7636–7646.
[11] Stranick, S. J., Atre, S. V., Parikh, A. N., Wood, M. C., Allara, D. L., Winograd, N., and Weiss, P. S., 1996, ''Nanometer-Scale Phase Separation in Mixed Composition Self-Assembled Monolayers,'' Nanotechnology, **7**, pp. 438–442.
[12] Hobara, D., Ota, M., Imabayashi, S., Niki, K., and Kakiuchi, T., 1998, ''Phase Separation of Binary Self-Assembled Thiol Monolayers Composed of 1-Hexadecanethiol and 3-Mercaptopropionic Acid on Au (111) Studied by Scanning Tunneling Microscopy and Cyclic Voltammetry,'' J. Electroanal. Chem., **444**, pp. 113–119.
[13] Kern, K., Niehus, H., Schatz, A., Zeppenfeld, P., Goerge, J., and Comsa, G., 1991, ''Long-Range Spatial Self-Organization in the Adsorbate-Induced Restructuring of Surfaces: Cu {110}-(2×1)O,'' Phys. Rev. Lett., **67**, pp. 855–858.
[14] Leibsle, F. M., Flipse, C. F. J., and Robinson, A. W., 1993, ''Structure of the Cu {100}-(2×2)N Surface: A Scanning-Tunneling-Microscopy Study,'' Phys. Rev. B, **47**, pp. 15,865–15,868.
[15] Parker, T. M., Wilson, L. K., Condon, N. G., and Leibsle, F. M., 1997, ''Epitaxy Controlled by Self-Assembled Nanometer-Scale Structures,'' Phys. Rev. B, **56**, pp. 6458–6461.
[16] Brune, H. M., Giovannin, K., Bromann, K., and Kern, K., 1998, ''Self-Organized Growth of Nanostructure Arrays on Strain-Relief Patterns,'' Nature (London), **394**, pp. 451–453.
[17] Pohl, K., Bartelt, M. C., de la Figuera, J., Bartelt, N. C., Hrbek, J., and Hwang, R. Q., 1999, ''Identifying the Forces Responsible for Self-Organization of Nanostructures at Crystal Surfaces,'' Nature (London), **397**, pp. 238–241.
[18] Plass, R., Last, J. A., Bartelt, N. C., and Kellogg, G. L., 2001, ''Self-Assembled Domain Patterns,'' Nature (London), **412**, pp. 875–875.
[19] Ellmer, H., Repain, V., Rousset, S., Croset, B., Sotto, M., and Zeppenfeld, P., 2001, ''Self-Ordering in Two Dimensions: Nitrogen Adsorption on Copper (100) Followed by STM at Elevated Temperature,'' Surf. Sci., **476**, pp. 95–106.
[20] Petty, M. C., 1996, *Langmuir-Blodgett Films*, Cambridge University Press, Cambridge, UK.
[21] McConnell, H. M., 1991, ''Structures and Transitions in Lipid Monolayers at the Air-Water Interface,'' Annu. Rev. Phys. Chem., **42**, pp. 171–195.
[22] Benvegnu, D. J., and McConnell, H. M., 1992, ''Line Tension Between Liquid Domains in Lipid Monolayers,'' J. Phys. Chem., **96**, pp. 6820–6824.
[23] Andelman, D., Brochard, F., and Joanny, J.-F., 1987, ''Phase-Transitions in

Langmuir Monolayers of Polar-Molecules,'' J. Phys. Chem., **86**, pp. 3673–3681.
[24] Seul, M., and Andelman, D., 1995, ''Domain Shapes and Patterns: The Phenomenology of Modulated Phases,'' **267**, pp. 476–483.
[25] Alerhand, O. L., Vanderbilt, D., Meade, R. D., and Joannopoulos, J. D., 1988, ''Spontaneous Formation of Stress Domains on Crystal Surfaces,'' Phys. Rev. Lett., **61**, pp. 1973–1976.
[26] Ng, K.-O., and Vanderbilt, D., 1995, ''Stability of Periodic Domain Structures in a Two-Dimensional Dipolar Model,'' Phys. Rev. B, **52**, pp. 2177–2183.
[27] Hannon, J. B., Tersoff, J., and Tromp, R. M., 2002, ''Surface Stress and Thermodynamic Nanoscale Size Selection,'' Science, **295**, pp. 299–301.
[28] Suo, Z., and Lu, W., 2000, ''Composition Modulation and Nanophase Separation in Binary Epilayer,'' J. Mech. Phys. Solids, **48**, pp. 211–232.
[29] Lu, W., and Suo, Z., 2001, ''Dynamics of Nanoscale Pattern Formation of an Epitaxial Monolayer,'' J. Mech. Phys. Solids, **49**, pp. 1937–1950.
[30] Mate, C. M., Kao, C.-T., and Somorjai, G. A., 1988, ''Carbon-Monoxide Induced Ordering of Adsorbates on the Rh (111) Crystal—Surface—Importance of Surface Dipole-Moments,'' Surf. Sci., **206**, pp. 145–168.
[31] Stone, H. A., and Ajdari, A., 1998, ''Hydrodynamics of Particles Embedded in a Flat Surfactant Layer Overlying a Subphase of Finite Depth,'' J. Fluid Mech., **369**, pp. 151–173.
[32] Folkers, J. P., Laibinis, P. S., Whitesides, G. M., and Deutch, J., 1994, ''Phase-Behavior of 2-Component Self-Assembled Monolayers of Alkanethiolates on Gold,'' J. Phys. Chem., **98**, pp. 563–571.
[33] Imabayashi, S., Hobara, D., and Kakiuchi, T., 2001, ''Voltammetric Detection of the Surface Diffusion of Adsorbed Thiolate Molecules in Artificially Phase-Separated Binary Self-Assembled Monolayers on a Au (111) Surface,'' Langmuir, **17**, pp. 2560–2563.
[34] Ashcroft, N. W., and Mermin, N. D., 1976, *Solid State Physics*, Saunders College Publications, Philadelphia, PA.
[35] Evans, S. D., and Ulman, A., 1990, ''Surface-Potential Studies of Alkyl-Thiol Monolayers Adsorbed on Gold,'' Chem. Phys. Lett., **170**, pp. 462–466.
[36] Evans, S. D., Urankar, E., Ulman, A., and Ferris, N., 1991, ''Self-Assembled Monolayers of Alkanethiols Containing a Polar Aromatic Group—Effects of the Dipole Position on Molecular Packing, Orientation, and Surface Wetting Properties,'' J. Am. Chem. Soc., **113**, pp. 4121–4131.
[37] Landau, L. D., Lifshitz, E. M., and Pitaevskii, L. P., 1984, *Electrodynamics of Continuous Media*, 2nd Ed., Butterworth Heinemann, New York.
[38] Cahn, J. W., and Hilliard, J. E., 1958, ''Free Energy of a Nonuniform System. 1. Interfacial Free Energy,'' J. Chem. Phys., **28**, pp. 258–267.
[39] Gao, Y. F., Lu, W., and Suo, Z., 2002, ''A Mesophase Transition in a Binary Monolayer on a Solid Surface,'' Acta Mater., **50**, pp. 2297–2308.
[40] Berger, R., Delamarche, E., Lang, H. P., Gerber, C., Gimzewski, J. K., Meyer, E., and Güntherodt, H.-J., 1997, ''Surface Stress in Self-Assembly of Alkanethiols on Gold,'' Science, **276**, pp. 2021–2024.
[41] Chen, L. Q., and Wang, Y. Z., 1996, ''The Continuum Field Approach to Modeling Microstruct. Evol.,'' JOM **48**, pp. 13–18.
[42] Lu, W., and Suo, Z., 2002, ''Symmetry Breaking in Self-Assembled Monolayers on Solid Surface. I. Anisotropic Surface Stress,'' Phys. Rev. B, **65** Paper No. 085401.
[43] Lu, W., and Suo, Z., 2002, ''Symmetry Breaking in Self-Assembled Monolayers on Solid Surface. II. Anisotropic Substrate Elasticity,'' Phys. Rev. B, **65** Paper No. 205418.
[44] Gao, Y. F., and Suo, Z., 2003, ''The Orientation of the Self-Assembled Monolayer Stripes on a Crystalline Substrate,'' J. Mech. Phys. Solids, **51**, pp. 147–167.
[45] Chou, S. Y., and Zhuang, L., 1999, ''Lithographically Induced Self-Assembly of Periodic Polymer Micropillar Arrays,'' J. Vac. Sci. Technol. B, **17**, pp. 3197–3202.
[46] Schäffer, E., Thurn-Albrecht, T., Russell, T. P., and Steiner, U., 2000, ''Electrically Induced Structure Formation and Pattern Transfer,'' Nature (London), **403**, pp. 874–877.
[47] Suo, Z., and Liang, J., 2001, ''Theory of Lithographically Induced Self-Assembly,'' Appl. Phys. Lett., **78**, pp. 3971–3973.
[48] Gao, Y.F., and Suo, Z., 2003, ''Guided Self-Assembly of Molecular Dipoles on a Substrate Surface,'' J. Appl. Phys., **93**, pp. 4276–4282.
[49] Suo, Z., and Hong, W., 2004, ''Programmable Motion and Assembly of Molecules on Solid Surfaces,'' publication 150, www.deas.harvard.edu/suo.

# Mechanical Modeling of Fabrics in Bending

**T. J. Lahey**

**G. R. Heppler**

Systems Design Engineering,
University of Waterloo,
Waterloo, ON N2L 3G1, Canada

*A fabric bending model that includes contributions from nonlinear elasticity, and viscous and Coulomb friction with hysteretic effects is presented. The model allows the recovery of the loading, unloading and hysteresis behaviors observed in the Kawabata evaluation system (KES) bending tests and provides the ability to simulate a continuum of property curves and to extrapolate to loading conditions not covered in the KES regimen. Model results are compared to experimental results. It is found that hysteretic behavior is observed due to friction between the yarns, and that nonlinear elastic behavior arises from jamming of the yarns and their subsequent compression.* [DOI: 10.1115/1.1629757]

## Introduction

Characterization of fabric bending remains an unresolved problem in that there is no clear ''best'' experimental protocol to establish the values of the set of parameters that uniquely define the material model. Nor is the parameter set defined and agreed upon. Abbott [1] have compared five different bending stiffness tests: the cantilever test, the heart loop test, the Schiefer Flexometer, the Planoflex, and the M.I.T. Drapemeter. The cantilever test was preferred to the other tests due to its simplicity and its high correlation to the subjective measurements. Subsequently, Grosberg and Abbott [2] discussed the apparatus of Livesey and Owen [3] and proposed an alternative apparatus based on the Instron Tensile Tester. In a contemporaneous paper, [4], they discussed the significant contribution that friction makes during the bending process and noted that large errors are present if a linear bending approximation is used.

The effect of friction was modeled by Grosberg [5] and by Grosberg and Swani [6] as a Coulomb-type frictional restraint moment at the yarn intersections. Once this frictional moment was overcome the yarns could be bent and that bending was modeled with a linear moment-curvature relationship. The inclusion of cyclic bending behavior was presented by Zhou and Ghosh [7] in a more developed model of fabric bending which used a piecewise linear model of the bending behavior that included hysteresis. This model is illustrated in Fig. 1. Illustrated in Fig. 2 is the more recent model of Shi et al. [8] who used a rheological model that included curvature-spring and curvature-friction elements. These elements allow for the inclusion of friction and hysteresis effects in the fabric model. Other investigations of bending include the linear bending model of Hu and Chung [9] which examined the effect of vertical seams on bending stiffness and the work of Hu et al. [10] which examined the effect that orientation plays in bending hysteresis.

The Kawabata, evaluation system fabric bending (KES-FB) test, [11], is perhaps the most frequently encountered and cited test used to determine the bending characteristics of fabric. In the KES-FB test the test sample is mounted vertically, to eliminate the effect of gravity, and the bending moment is measured as the sample is bent, at a constant rate of 0.5 $\mathrm{cm}^{-1}$/s, forward and backward through a range of curvatures $\kappa \in [-2.5, 2.5] \mathrm{cm}^{-1}$ as shown in Fig. 3. The apparatus used to conduct the KES-FB test has been designed to ensure, that over this range of curvatures, the sample is in pure bending, [11]. The characteristic values recorded by the system are: $B$, the bending rigidity per unit length, and $2HB$, the moment of hysteresis per unit length. Note that in addition to measuring these values for the weft and warp directions, they are also measured in the forward and backward directions.

Contributed by the Applied Mechanics Division of THE AMERICAN SOCIETY OF MECHANICAL ENGINEERS for publication in the ASME JOURNAL OF APPLIED MECHANICS. Manuscript received by the ASME Applied Mechanics Division, September 9, 2002; final revision, June 23, 2003. Associate Editor: D. A. Kouris. Discussion on the paper should be addressed to the Editor, Prof. Robert M. McMeeking, Department of Mechanical and Environmental Engineering University of California–Santa Barbara, Santa Barbara, CA 93106-5070, and will be accepted until four months after final publication of the paper itself in the ASME JOURNAL OF APPLIED MECHANICS.

## Fabric Bending Friction and Hysteresis

There are a number of mechanisms that influence the bending behavior of fabric. As illustrated in Fig. 4 it is generally the case that hysteresis is exhibited in KES-FB test results and that the loading and unloading portions of the curve are seldom linear. The absence of linear loading and unloading paths implies that a linear spring model is not an adequate for the ''elastic'' part of the fabric response. The shapes of the loading and unloading portions of the bending curve indicate that there is more than a linear elastic behavior present so an additional cubic spring element is included in the model.

The hysteresis loop implies that friction and rate effects should be included in the constitutive model yet there is a paucity of work on modeling hysteretic effects in fabric. It is clearly necessary to include this effect in a model for it to be able to accurately reproduce fabric bending behavior. Lindberg et al. [12] introduced both friction and rate (damping) elements in their load-deformation model of fabric with limited success. The current techniques used in fabric simulations are unable to capture all (or even most) of the characteristics of the mechanical property curves.

The friction model used here is based on a modification to the Bliman and Sorine friction model, [13–15]. This model is depicted in Fig. 5 and the governing equation for the model is

$$m\ddot{\kappa} = -d\dot{\kappa} - k_1\kappa - k_3\kappa^3 - M_f(\kappa) - M_{\mathrm{ext}} \tag{1}$$

The frictional moment term $M_f(\kappa)$ is defined by, [15],

$$\dot{\mathbf{x}} = A\mathbf{x} + B\dot{\kappa}, \quad \mathbf{x}(0) = 0 \tag{2}$$

$$M_f(\kappa)(t) = C\mathbf{x}(t) \tag{3}$$

where

$$\mathbf{x} = \begin{bmatrix} x_1 \\ x_2 \end{bmatrix}, \quad A = -\frac{|\dot{\kappa}|}{\varepsilon_f}\begin{bmatrix} \frac{1}{\eta} & 0 \\ 0 & 1 \end{bmatrix}, \quad B = \frac{1}{\varepsilon_f}\begin{bmatrix} \frac{f_1}{\eta} \\ -f_2 \end{bmatrix}, \quad C = [1 \;\; 1]. \tag{4}$$

The state vector $\mathbf{x}$ contains internal system variables that define the friction behavior. To ensure a dissipative system it is necessary that, [15],

$$f_1 > f_2 \geqslant 0 \tag{5}$$

$$\varepsilon_f > 0 \quad \text{and} \quad 0 < \eta < 1 \tag{6}$$

  

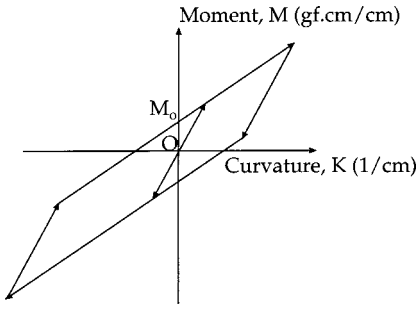


**Fig. 1 Zhou and Ghosh (1999) bending model**

be satisfied. The model can represent both dynamic and static friction through the selection of $f_1$, $f_2$, $\eta$, and $\varepsilon_f$. With reference to Fig. 6, the static friction threshold is given by

$$M_s = M_k + f_2\left(\frac{\eta f_2}{f_1}\right)^{\eta/(1-\eta)}(1-\eta) \tag{7}$$

where the steady-state kinetic friction is

$$M_k = f_1 - f_2. \tag{8}$$

The value of the curvature at the peak static friction is

$$s_e = \frac{\varepsilon_f \eta}{1-\eta}\log\left(\frac{f_1}{\eta f_2}\right) \tag{9}$$

while the 5% settling curvature (defined to be the curvature where the friction moment is within, and stays within, 5% of the steady-state dynamic friction value $M_k$) is given by

$$s_p = 3\varepsilon_f. \tag{10}$$

The minimum slope of the moment versus curvature curve is given by, [16],

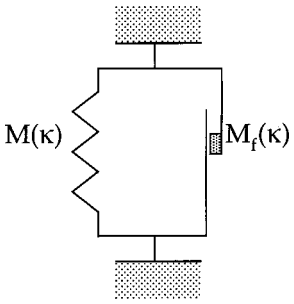


**Fig. 2 Shi et al. (2000) bending model**

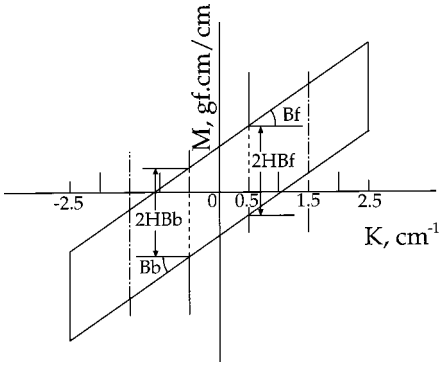


**Fig. 3 KES: bending measurements**

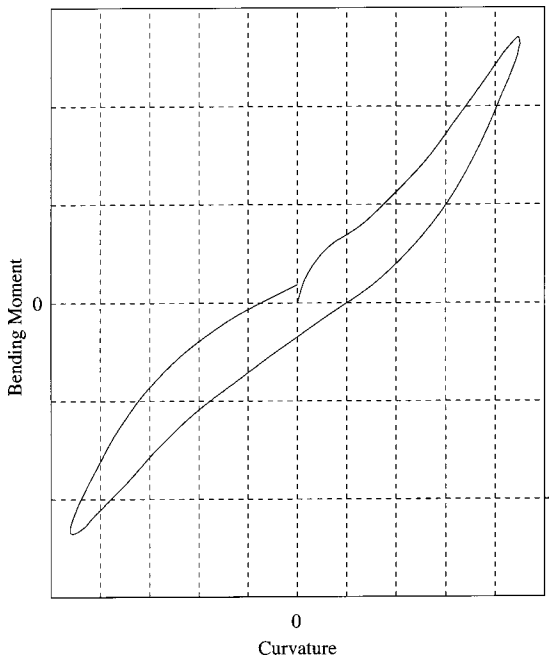


**Fig. 4 A representative KES-FB result**

$$\kappa_F^- = \frac{f_2}{\varepsilon_f}\left(\frac{\eta^2 f_2}{f_1}\right)^{\eta/(1-\eta)}(1-\eta) \tag{11}$$

and the maximum slope of the moment versus curvature curve is given by, [16],

$$\kappa_F^+ = \frac{f_1 - f_2\eta}{\eta\varepsilon_f}. \tag{12}$$

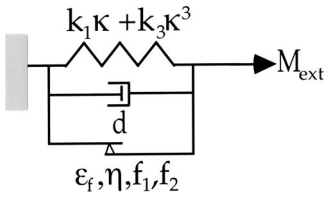


**Fig. 5 Model of fabric bending**

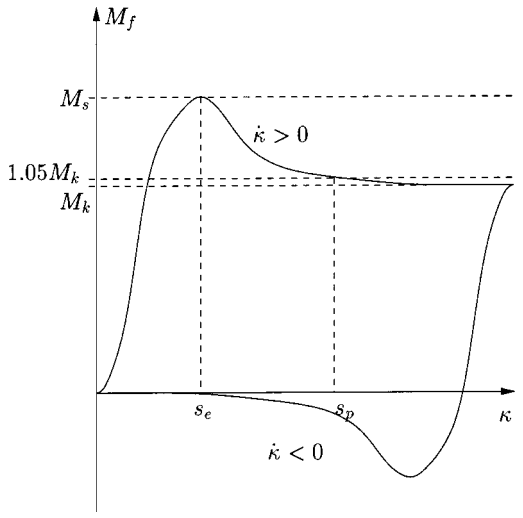


**Fig. 6 Bliman and Sorine second-order model**

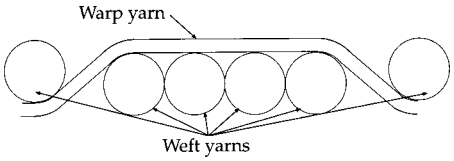


**Fig. 7 Warp-float satin (4×1) weave cross section**

Further discussion of this friction model can be found in Lahey [16].

The differential equation form of the friction model, as given by Eq. (2), is useful if the curvature history is to be calculated. The integral form, found by solving the differential equation, is useful if the curvature history is known. If it is assumed (or known) that there is no initial curvature at rest the frictional bending restraint can be modeled by

$$M_f(\kappa)(t) = (f_1 - f_2)\,\mathrm{sign}(\dot{\kappa}(t)) + \mathrm{sign}(\dot{\kappa}(0))(e^{-s(t)/\varepsilon_f} f_2 - e^{-s(t)/\eta\varepsilon_f} f_1). \quad (13)$$

This integral form is useful here because, during the KES-FB test, the curvature is prescribed over time. The quantity $s(t)$ in Eq. (13) is the total curvature that the fabric has experienced at time $t$ and is given by

$$s(t) = \int_0^t |\dot{\kappa}|\,dt. \quad (14)$$

## Determining the Model Parameters

It is necessary to find the best set of parameter values for the model to agree with the experimental results obtained from a KES-FB test. The curvature is prescribed by the test and is therefore known throughout the duration of the experiment. Hence the task is to find the set of model parameters that yields the best agreement between the model computed external moment and the experimental external moment. Looking at the problem differently to that in Eq. (1), the new problem can be written as

$$M_{\mathrm{ext}} = m\ddot{\kappa} + k_1\kappa + d\dot{\kappa} + k_3\kappa^3 + M_f(\kappa) \quad (15)$$

where $M_f(\kappa)$ is determined by Eq. (13). The KES-FB test prescribes a constant curvature rate of 0.5 $\mathrm{cm}^{-1}$/s, [11], but fails to specify, the acceleration profile that is needed to go from rest to the constant rate, the deceleration/acceleration profile needed when the curvature rate changes sign, and the deceleration profile that is needed to come to a stop at the end of the test. These regions of non-constant curvature rate are referred to as transition regions. The present model depends on the curvature acceleration, curvature velocity, and curvature value; this makes the transition regions important. The acceleration profiles in the transition regions are modeled by quadratic polynomials which are chosen to satisfy the velocity and acceleration continuity conditions at the beginning and end of each region.

**Model Parameter Identification.** Because the equipment necessary to perform the experimental tests was not available to the authors a digitization of Deng's, [17], experimental data was used for the purpose of illustration. The data is for a 100% polyester satin fabric that was bleached, dyed, and pre-shrunk in a resin finish. More specific details of the weave and finishing process were not available to us but it is likely that the fabric is a warp float satin similar to that illustrated in Figs. 7 and 8. Figure 7 shows a cross section of a 4×1 warp-float satin weave while Fig. 8 shows the pattern. The warp is represented in gray while the weft is represented in white.

The values of the model parameters that produce a model that best approximates the experimental results were found by applying a simulated annealing optimization method to a nonlinear least squares minimization problem. The curvature, velocity, and acceleration for the experiment were precalculated to facilitate the optimization procedure. The parameters that need to be identified are $f_1$, $f_2$, $\varepsilon_f$, $\eta$, $k_1$, $d$, and $k_3$. It was assumed that the duration of each acceleration/deceleration phase is a constant for the test equipment and was set a priori to a value of one second.

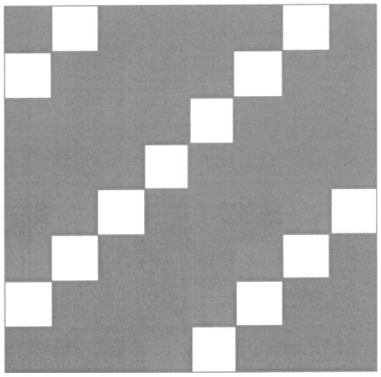

**Fig. 8 Warp-float satin (4×1) weave pattern**

The objective function to be minimized is

$$R(\kappa) = \sum (M_{\mathrm{model}}(\kappa) - M_{\mathrm{exp}}(\kappa))^2. \quad (16)$$

Because $M_{\mathrm{exp}}$ was not available as a continuous function, separate fourth-order polynomials were fit (in a least-squares sense) to the digitized experimental loading, unload/reverse loading, and reloading paths. These polynomial approximations to each of the $M_{\mathrm{exp}}$ paths were used because the simulation results are calculated through a time-stepping procedure and it is necessary to be able to evaluate the experimental results at points that lie between the digitized data. The model and the experiment approximating polynomials were sampled at intervals of one millisecond.

Results are presented in detail for the weft direction of this fabric, with some warp results presented for comparison purposes. Additional results for the warp direction of this fabric are given in detail in Lahey and Heppler [18]. The parameters and plots of the results for the full model for a cotton twill are also presented herein. Full details on the results for the cotton twill fabric are given in [16].

The parameters determined through the optimization procedure are given in Table 1. Comparing the weft direction parameters to those of the warp, we see a number of interesting results. First, the value of the weft damping parameter $d$ is less than half of the damping parameter value for the warp, the value of the weft linear spring constant $k_1$ is roughly three-quarters of the warp value, and the cubic spring constant $k_3$ is five times greater in the warp direction than in the weft. If the cubic spring behavior is caused by jamming of the yarns (i.e., the yarns are in a compressive configuration with no space to move), this could be explained by a greater spacing of yarns in the warp direction than in the weft.

Examining the friction model parameters in Table 2 we see that the maximum frictional moment $M_s$ in the weft direction occurs at a curvature value of $s_e = 10.49\ \mathrm{m}^{-1}$ which is approximately halfway through the loading path while the curvature value $s_p$ required to reach within 5% of the kinematic friction threshold $M_k$ is only approached at the end of the initial loading path. The pronounced difference between these two values demonstrates the utility of using a friction model that incorporates both static and kinematic friction. The friction in the warp direction, where only dynamic friction is encountered, is considerably different to that encountered in the weft direction.

Figure 9 shows the frictional contribution, for both the warp and the weft directions, throughout the KES test. Region 1 is the loading portion of the test, here we see, for the weft direction, that

**Table 1 Model parameters**

| Parameter (Units) | Satin Weft Value | Satin Warp Value, [18] | Twill Weft Value | Twill Warp Value |
|---|---|---|---|---|
| $f_1$ (N-m/m) | $4.450\times10^{-1}$ | $6.064\times10^{-1}$ | $4.291\times10^{-1}$ | $4.266\times10^{-1}$ |
| $f_2$ (N-m/m) | $4.438\times10^{-1}$ | $6.045\times10^{-1}$ | $4.291\times10^{-1}$ | $4.240\times10^{-1}$ |
| $\eta$ | $9.939\times10^{-1}$ | $9.998\times10^{-1}$ | $9.969\times10^{-1}$ | $9.908\times10^{-1}$ |
| $\varepsilon_f$ ($m^{-1}$) | 7.316 | 7.302 | $1.009\times10^{-1}$ | 7.207 |
| $d$ (N-m-s) | $2.094\times10^{-5}$ | $5.681\times10^{-5}$ | $5.506\times10^{-5}$ | $1.445\times10^{-4}$ |
| $k_1$ (N-m) | $4.473\times10^{-5}$ | $6.257\times10^{-5}$ | $3.582\times10^{-5}$ | $1.133\times10^{-4}$ |
| $k_3$ (N-$m^3$) | $1.587\times10^{-10}$ | $8.489\times10^{-10}$ | $5.520\times10^{-10}$ | $1.069\times10^{-9}$ |

the maximum static frictional moment ($M_s=1.849\times10^{-3}$ N-m/m) occurs at the curvature $s_e=10.49\ m^{-1}$ as given in Table 2. The unloading region is marked as region 2. Here we see that when the experiment passes through zero curvature there is no frictional moment. Region 3 consists of bending the fabric in the opposite direction. Note that due to the characteristics of the test, we do not see any static frictional effects in this region. Finally, region 4 consists of unloading from this negative curvature. Here, once again we see the static and kinematic friction behavior with a final frictional set in the fabric. The material behaves differently in the warp direction. The warp friction parameters in Table 2 show that the curvature value $s_e$ corresponding to the maximum static friction value $M_s$ is greater than the value $s_p$ required to reach the kinematic friction threshold $M_k$. This would, in view of Fig. 6, appear to be counterintuitive but it should also be noted that there is no difference between the static and dynamic friction values. This can be interpreted to mean that the friction model is behaving in a manner that is analogous to an overdamped system and that there is no "overshoot" behavior of the form shown for the weft direction in Fig. 9.

Figures 10–13 each show a comparison of three different curves. The dash-dotted line is the digitized version of experimental results from Deng [17]. The dotted line is constructed from three separate fourth-order polynomial fits to the digitized data. One polynomial is fit to the loading path, another to the unloading/reverse loading path, and the third to the reverse unloading path. The solid line shows the model simulation results.

It is of interest to examine the contribution of each of the parts of the model to the overall system response. To begin, consider Fig. 10 which shows the model behavior that would be obtained if a linear viscoelastic material were assumed such that

**Table 2 Supplementary friction results**

| Parameter (Units) | Satin Weft Value | Satin Warp Value, [18] | Twill Weft Value | Twill Warp Value |
|---|---|---|---|---|
| $s_e$ ($m^{-1}$) | 10.49 | 83.98 | $1.007\times10^{-1}$ | 11.76 |
| $s_p$ ($m^{-1}$) | 21.95 | 21.85 | $3.027\times10^{-1}$ | 21.62 |
| $M_k$ (N-m/m) | $1.200\times10^{-3}$ | $1.986\times10^{-3}$ | $3.708\times10^{-8}$ | $2.512\times10^{-3}$ |
| $M_s$ (N-m/m) | $1.849\times10^{-3}$ | $1.986\times10^{-3}$ | $4.983\times10^{-4}$ | $3.276\times10^{-3}$ |

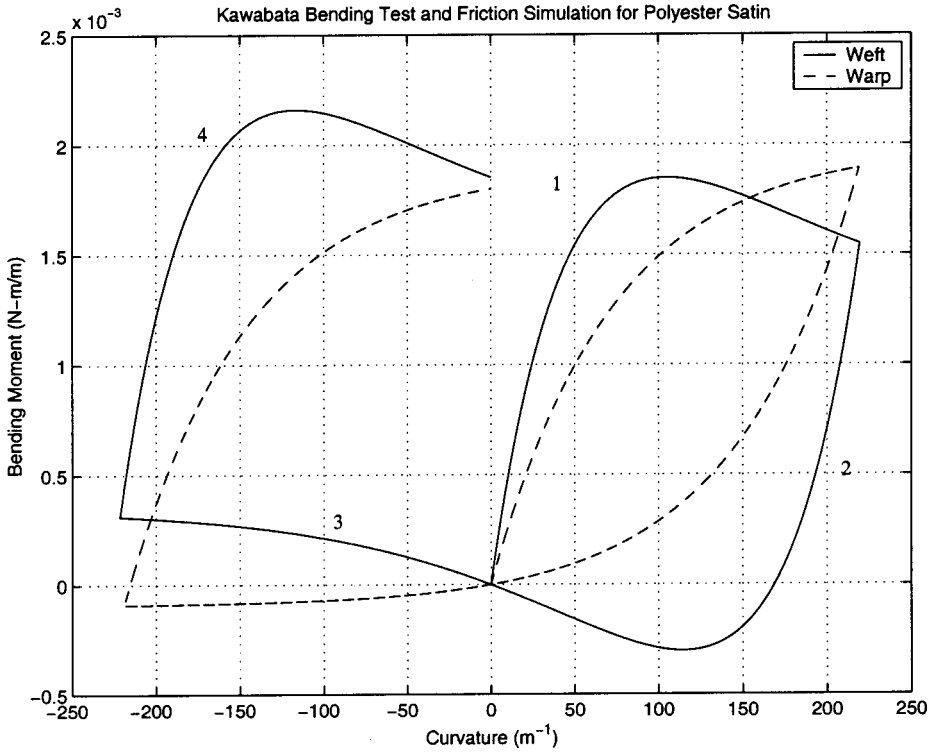


**Fig. 9 Polyester satin–frictional contribution to the bending moment**

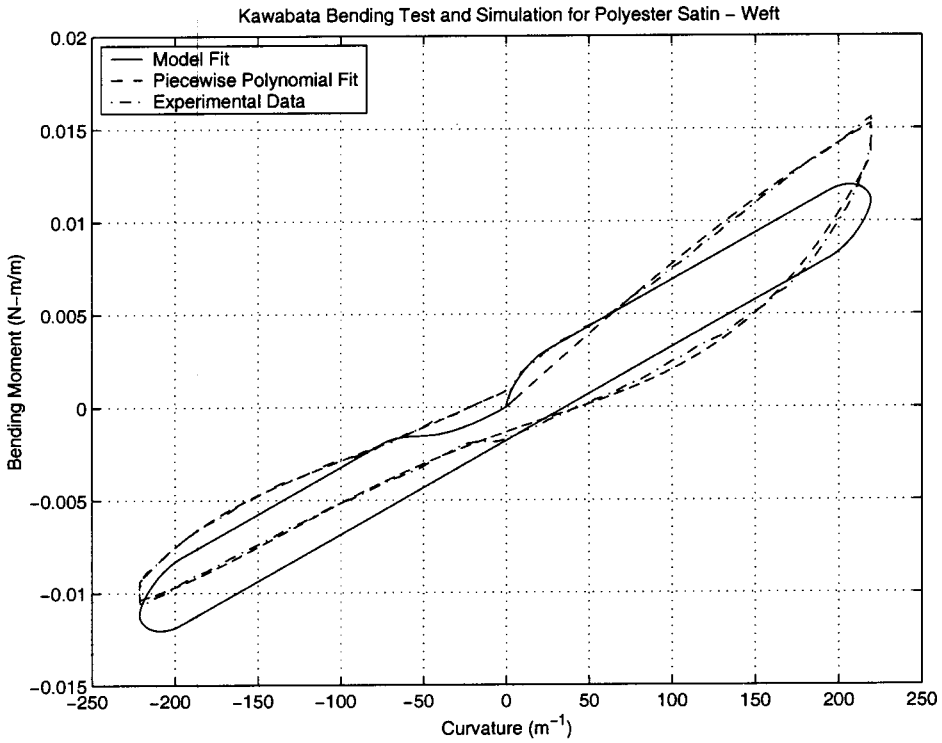


**Fig. 10 Polyester satin–weft direction (no friction and no cubic)**

$$M_{\text{ext}} = m\ddot{\kappa} + k_1\kappa + d\dot{\kappa}. \tag{17}$$

Of particular note is the straightness of the unloading portion of the response predicted by the model and its poor fit in the regions where the direction of bending is changing or where the test is coming to a stop. The slope given by the model does not match the experimental results due to optimization over the entire experimental procedure. Also in Fig. 10, one can see that the experimental results demonstrate a different slope and loop width which makes fitting the model difficult, as the model does not include different material properties for positive and negative loading directions.

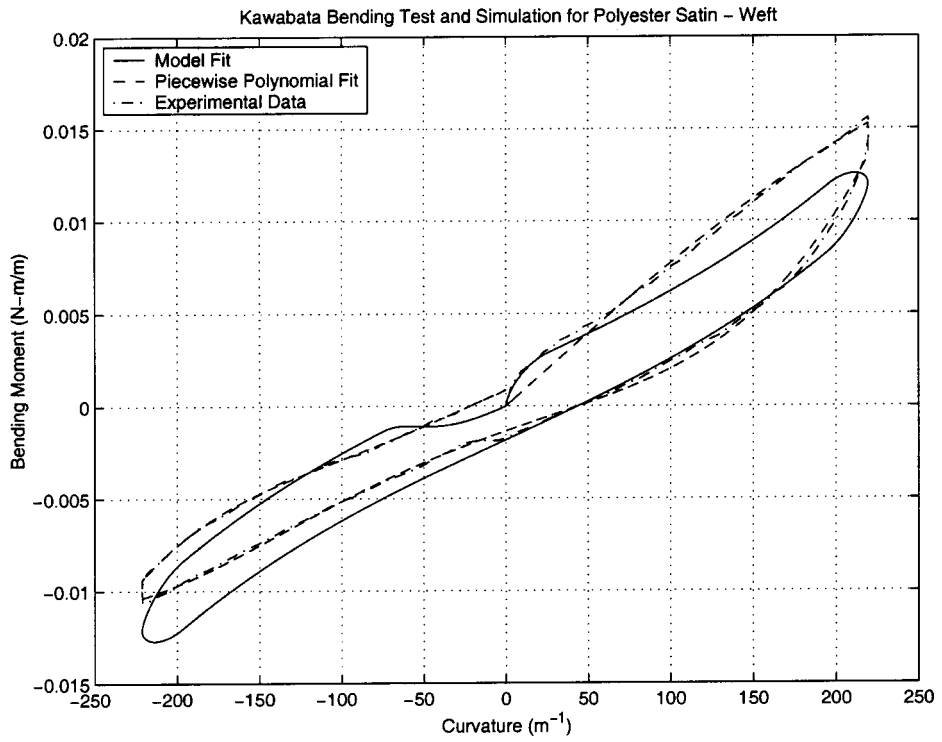


**Fig. 11 Polyester satin–weft direction (no friction)**

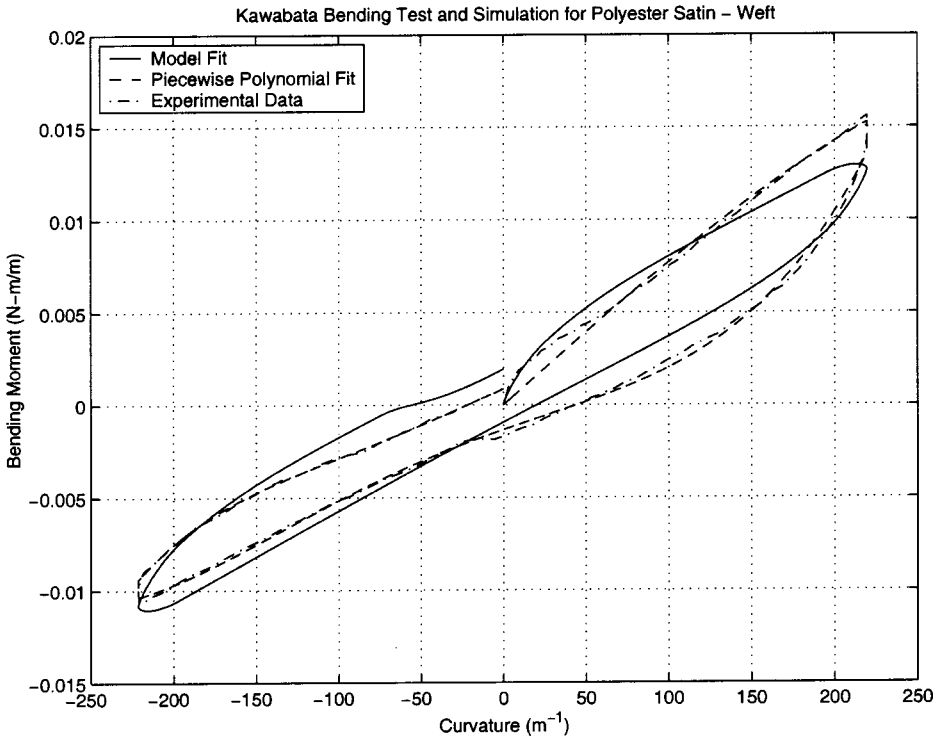


**Fig. 12 Polyester satin–weft direction (no cubic)**

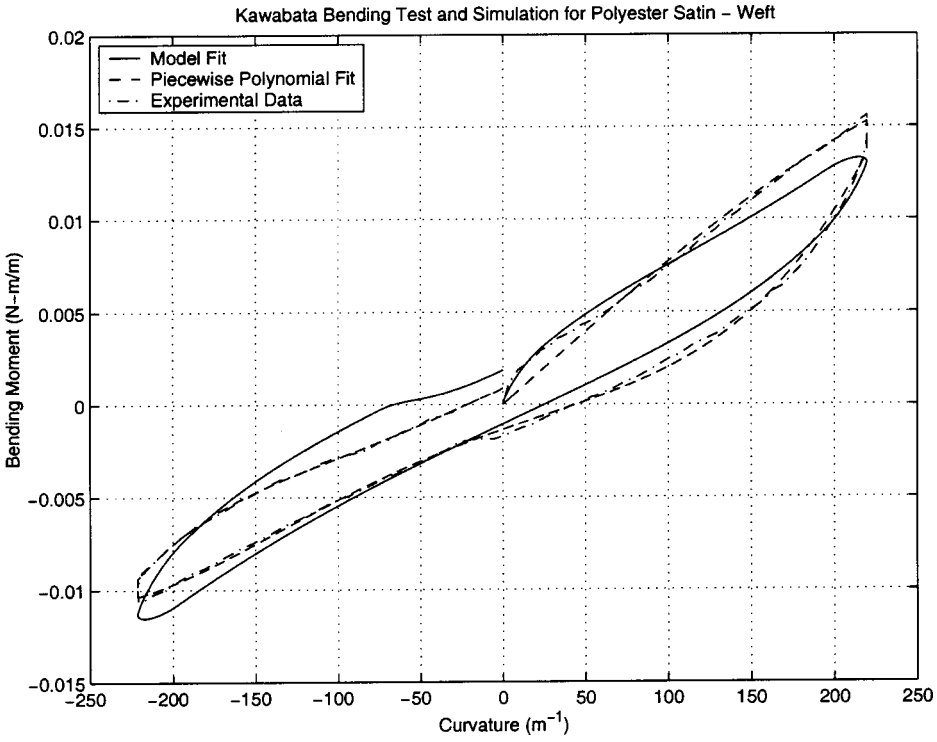


**Fig. 13 Polyester satin–weft direction full model**

**Table 3 Polyester satin-weft direction: model comparison**

| Test Case | Residual (N-m/m)$^2$ |
|---|---|
| Full model | $1.898 \times 10^{-2}$ |
| No friction term | $3.730 \times 10^{-2}$ |
| No cubic term | $2.056 \times 10^{-2}$ |
| No friction or cubic term | $4.303 \times 10^{-2}$ |

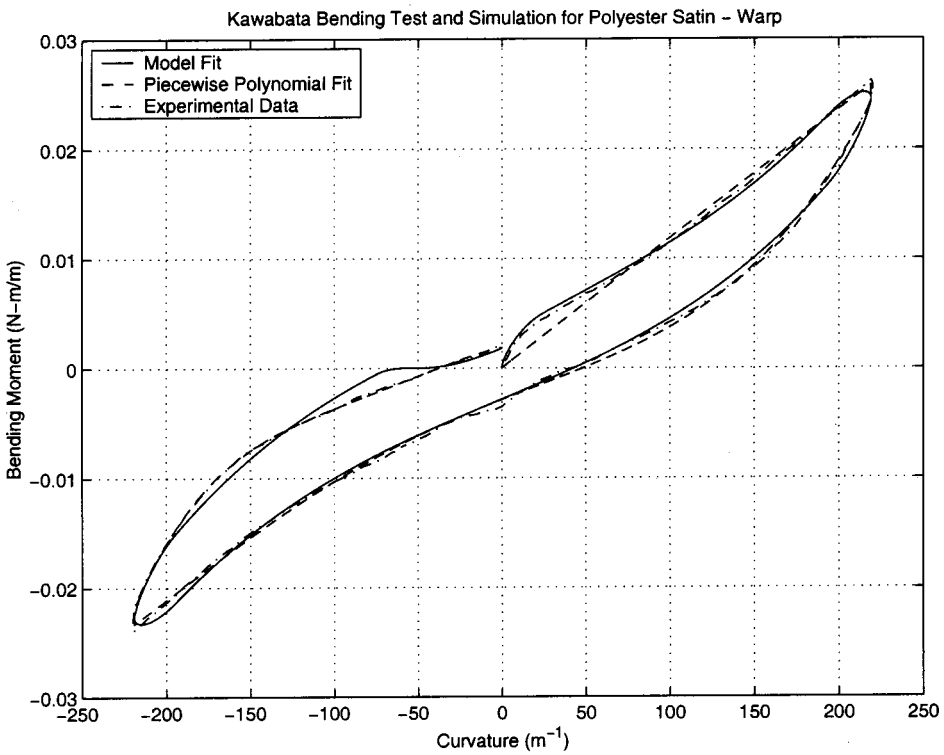


**Fig. 14 Polyester satin–warp direction full model**

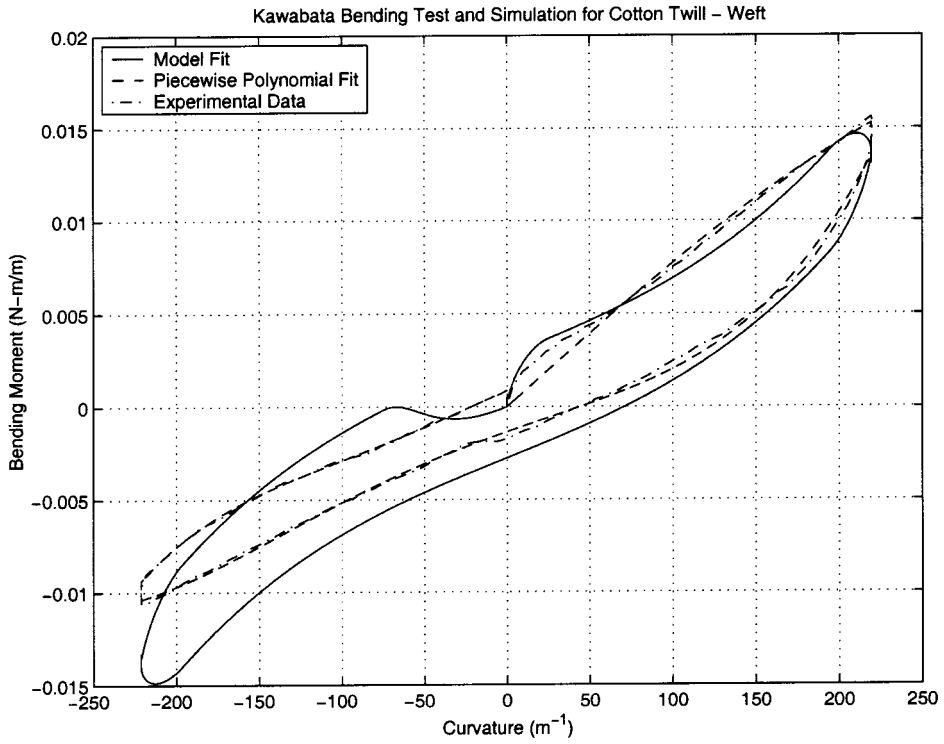


**Fig. 15 Cotton twill–weft direction full model**

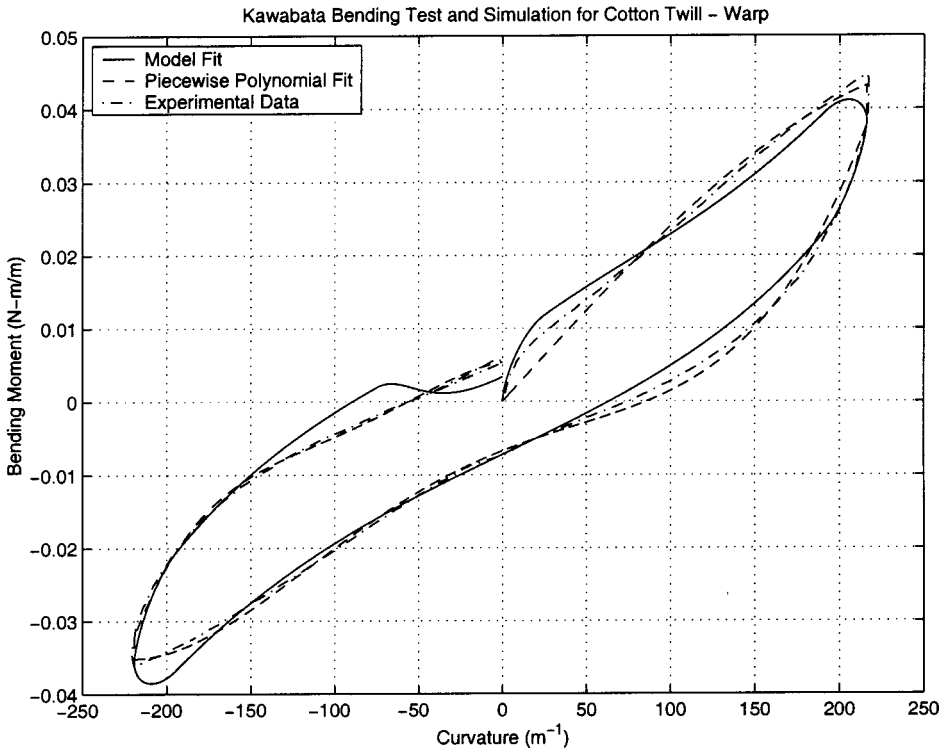


**Fig. 16 Cotton twill–warp direction full model**

In contrast to Fig. 10 consider Fig. 11 where the viscous damping as been retained and a cubic spring has been added to the model so that in this case

$$M_{\text{ext}} = m\ddot{\kappa} + k_1\kappa + d\dot{\kappa} + k_3\kappa^3. \tag{18}$$

The addition of the cubic spring does little to improve the overall fit, although it does improve the fit in the initial unloading phase from 150 $m^{-1}$ to 0 $m^{-1}$.

In Fig. 12 is shown the model behavior that is obtained when the Bliman and Sorine friction model, [13–15] is included but the cubic spring is not (Eq. (19)).

$$M_{\text{ext}} = m\ddot{\kappa} + k_1\kappa + d\dot{\kappa} + M_f(\kappa) \tag{19}$$

This case shows a noticeable improvement over both of the previous cases. We now see a closer approximation everywhere, except for the initial acceleration region from 0 $m^{-1}$ to 50 $m^{-1}$, and there is a final set at the end of the test that was not exhibited in the previous cases.

The results obtained from each of these three partial models suggests that by combining them together a single, superior model should result. This is the case, as may be seen in Table 3 where we can compare the quality of the model fit, as measured by the size of the residual for each of the different test cases. The complete model provides the best fit and the importance of the friction term is evident by comparing the magnitude of the residual for the cases that include it to those that do not.

The results obtained when all the above features are combined are illustrated in Fig. 13 where it may be observed that there is only a marginal improvement over the last case. Considering that the cubic term contributed little to the improvement of the fit, this result is not surprising.

While the results for the weft direction are not as close as one might prefer, the complete model provides an excellent fit for the warp direction as shown in Fig. 14.

The parameters for a 100% cotton twill fabric that has been bleached, dried and pre-shrunk in a pure finish are given in Tables 1 and 2. The resulting simulation for the weft direction is shown in Fig. 15. Note that only static friction is present in the model and as such does not fit the final frictional moment. As with the weft direction of the satin fabric, the model has a poor fit in the negative curvature region, but a fair fit to the positive loading region. This is in contrast to the fit to the warp direction given in Fig. 16 which gives a good fit throughout.

## Conclusions

It is believed that the friction arises due to the slipping of the yarns with respect to each other and therefore comes into play once larger curvatures (displacements) are reached. Since this fabric is comprised of a monofilament yarn it is assumed that the friction internal to the yarn is small. However, in some fabrics the friction seen is more likely to be a combination of both intrayarn and interyarn friction. The cubic term is believed to arise from the jamming of the yarns and their subsequent compression because the cubic contribution is greater in the negative curvature region where (with reference to Fig. 7) the weft yarns will be forced together as a result of the negative bending moment. Some of the response may also be due to a nonlinear yarn bending response.

The model provides the ability to simulate a continuum of property curves and to extrapolate to loading conditions not covered in the KES regimen.

## Nomenclature

$A$, $B$, $C$ = state-space friction model matrices
$d$ = material damping coefficient
$f_1$ = friction model property
$f_2$ = friction model property
$k_1$ = linear spring curvature stiffness
$k_3$ = cubic spring curvature-stiffness
$m$ = rotatory inertia parameter
$M_{\text{ext}}$ = external moment calculated by model
$M_f$ = friction moment generated by the internal friction model

$M_k$ = steady-state kinematic friction moment
$M_{\text{model}}$ = external moment calculated by model
$M_{\text{exp}}$ = KES-FB measured moment
$M_s$ = static friction threshold moment
$s_e$ = curvature at the maximum static friction
$s_p$ = curvature for 5% settling of $M_f$ to $M_k$
$\mathbf{x}$ = friction model state vector
$\varepsilon_f$ = friction model property
$\eta$ = friction model property
$\kappa$ = curvature
$\dot{\kappa}$ = curvature rate
$\ddot{\kappa}$ = curvature acceleration

## References


[1] Abbott, N. J., 1951, ''The Measurement of Stiffness in Textile Fabrics,'' Text. Res. J., **21**, pp. 435–444.
[2] Grosberg, P., and Abbott, G. M., 1966, ''Measurement of Fabric Stiffness and Hysteresis in Bending,'' Text. Res. J., **36**, pp. 928–930.
[3] Livesey, R. G., and Owen, J. D., 1964, ''Cloth Stiffness and Hysteresis in Bending,'' J. Text. Inst., **55**, pp. T516–T530.
[4] Grosberg, P., and Abbott, G. M., 1966, ''The Fabric Cantilever,'' Text. Res. J., **36**, pp. 930–932.
[5] Grosberg, P., 1966, ''The Mechanical Properties of Woven Fabric—Part II: The Bending of Woven Fabrics,'' Text. Res. J., **36**, pp. 205–211.
[6] Grosberg, P., and Swani, N. M., 1966, ''The Mechanical Properties of Woven Fabric—Part IV: The Determination of the Bending Rigidity and Frictional Restraint in Woven Fabrics,'' Text. Res. J., **36**, pp. 338–345.
[7] Zhou, Naiyue, and Ghosh, Tushar K., 1999, ''On-Line Measurement of Fabric Bending Behavior—Part III: Dynamic Considerations and Experimental Implementation,'' Text. Res. J., **69**(3), pp. 176–184.
[8] Shi, Fengjun, Hu, Jinlian, and Yu, Tongxi, 2000, ''Modeling the Creasing Properties of Woven Fabrics,'' Text. Res. J., **70**(3), pp. 247–255.
[9] Hu, Jinlian, and Chung, Siuping, 2000, ''Bending Behavior of Woven Fabrics With Vertical Seams,'' Text. Res. J., **70**(2), pp. 148–153.
[10] Hu, J. L., Lo, W. M., and Lo, M. T., 2000, ''Bending Hysteresis of Plain Woven Fabrics in Various Directions,'' Text. Res. J., **70**(3), pp. 237–242.
[11] Kawabata, Sueo, 1986, *The Standardization and Analysis of Hand Evaluation*, 2nd Ed., The Textile Machinery Society of Japan, Osaka, Japan.
[12] Lindberg, J., Behre, B., and Dahlberg, B., 1961, ''Mechanical Properties of Textile Fabrics—Part III: Shearing and Buckling of Various Commerical Fabrics,'' Text. Res. J., **31**, pp. 99–122.
[13] Bliman, P. A., and Sorine, M., 1993, ''Friction Modeling by Hysteresis Operators. Application to Dahl, Sticktion, and Stribeck Effects,'' *Models of Hysteresis*, Longman Scientific and Technical, London.
[14] Bliman, P. A., and Sorine, M., 1993, ''A System-Theoretic Approach of Systems With Hysteresis. Application to Friction Modelling and Compensation,'' *Proceedings of the 2nd European Control Conference*, Gronigen, Netherlands, European Union Control Association (EUCA), pp. 1844–1849.
[15] Bliman, P. A., and Sorine, M., 1995, ''Easy-to-Use Realistic Dry Friction Models for Automatic Control,'' *Proceedings of the 3rd European Control Conference*, Rome, Sept., European Union Control Association (EUCA), pp. 3788–3794.
[16] Lahey, T. J., 2002, ''Modelling Hysteresis in the Bending of Fabrics,'' Master's thesis, University of Waterloo, Waterloo, ON.
[17] Deng, Shigan, 1994, ''Nonlinear Fabric Mechanics Including Material Nonlinearity, Contact, and an Adaptive Global Solution Algorithm,'' Ph.D. thesis, North Carolina State University.
[18] Lahey, T. J., and Heppler, G. R., 2002, ''Mechanical Modeling of Fabrics in Bending,'' *Proceedings of the Symposium on Recent Advances in Solids and Structures*, ASME, New York, IMECE2002-PVP-32312.

# Predicting Oscillatory Fluid-Elastic Instability of a Tongue-in-Groove Leakage Joint

**David J. Manko**

**Myron M. Sussman**

Bechtel Bettis Corporation,
Bettis Atomic Power Laboratory,
P.O. Box 79,
West Mifflin, PA 15122-0079

*This paper describes the application of the small boundary displacement model (SBDM) of fluid-structure coupling for predicting oscillatory fluid-elastic instability of a tongue-in-groove leakage joint. This coupling model extends structural small displacement theory to fluid-structure interfaces, eliminating the need for temporally changing meshes when structural motion is small compared with joint dimensions. The SBDM algorithm accurately predicts the onset of oscillatory instability for a tongue-in-groove leakage joint when compared with experimental data. Even though the methodology is specifically applied to a tongue-in-groove joint, the approach is equally suitable for evaluating the fluid-elastic stability of leakage joints in general.* [DOI: 10.1115/1.1640368]

## 1 Introduction

Mechanical fluid-structure interactions arise from the transfer of mechanical energy across the fluid-structure interface where the generated fluid forces deflect the structural boundary. As the structure displaces, the fluid experiences a change in boundary velocity which affects the fluid forces and the cycle continues. Coupling of fluid and structural systems in an analytical model involves applying the appropriate structural motions to the fluid boundary while concurrently imposing the fluid boundary forces onto the adjacent structural surface. Although simple in concept, coupling the structural equations of motion and the Navier-Stokes fluid equations is difficult because the governing equations have fundamentally different forms. Displacements are the primary solution variables for the structural problem while velocities and pressures are the unknowns for the fluid problem. Therefore, the resulting discretized equations are not immediately compatible. A fluid-structure coupling algorithm is needed to enforce compatibility between the fluid and structural equations.

The study of fluid-structure interaction has long been of interest to engineers, and treatments based on simple models appear in textbooks such as Blevins [1]. More fundamental approaches, based on the equations of motion, appear in journal articles and conferences such as Ziada and Staubli [2]. This paper first presents a model based on loop pressure drops that is used to identify the critical components, and then a finite difference model for the fluid coupled to rigid structural motion and pressure drops for the rest of the loop.

The small boundary displacement model (SBDM) is a stable and efficient algorithm formulated to couple the fluid and structural representations, [3]. It extends structural small displacement theory to the fluid-structure interface by assuming that fluid and structural velocities agree at the interface but that net structural displacement is small compared with structural dimensions. Fluid forces at the interface contribute to the structural motion. Both fluid and structural meshes are stationary in time, and the fluid and structural equations are simultaneously solved without iteration. The SBDM has been shown, [3], to mathematically conserve energy at the fluid-structure interface, making it a good candidate method for predicting the onset of unstable oscillation.

Leakage joints, [4], are a mechanical design feature that minimize unintentional flow around components that have necessary clearances to enable installation and removal. Examples of leakage joints include a tube-in-tube slip joint, a piston ring and a tongue-in-groove joint. In service, leakage joints have exhibited unstable behavior that is a function of flow through the joint. This fluid-elastic instability behavior can occur in an excursive or oscillatory manner.

Excursive instability is characterized by a steady growth, usually rapid, of a structural displacement without oscillation. For an excursive instability, the destabilizing fluid force overwhelms the restoring structural force to produce the abrupt deflection. Unstable numerical techniques can result in excursive behavior where the destabilizing force is a numerical artifact.

Oscillatory instability is typified by vibrations of the structure with steadily increasing amplitude. In this case, the energy input to the structure by the destabilizing fluid forces exceeds the mechanical energy dissipated in the system (e.g., damping, viscous dissipation). From a design perspective, identification and avoidance of an unstable response is essential for a component or system to function properly.

Prediction of oscillatory instability is more difficult than prediction of excursive behavior because excessive numerical damping can contribute to system damping and can artificially suppress an otherwise unstable oscillatory response. Numerical damping can also shift the onset conditions of an oscillatory instability to require higher than observed flow rates. Accurate simulation of oscillatory instability requires that numerical damping be minimized, at least near fluid-structure interfaces.

This paper describes the application of the SBDM for predicting the onset of oscillatory fluid-elastic instability. Experimental results are available for a tongue-in-groove leakage joint which is characterized by a simple two-dimensional geometry. The test setup is described in Section 2. A stability model based on a hydraulic representation of joint flow is analyzed in Section 3. The hydraulic model of joint flow is replaced with an SBDM representation and results from this simulation based on first principles are provided in Section 4. Some technical details in implementing the SBDM are discussed in the Appendix. Even though the methodology is specifically applied to a tongue-in-groove joint, the approach is equally suitable for evaluating the fluid-elastic stability of leakage joints in general.

Contributed by the Applied Mechanics Division of THE AMERICAN SOCIETY OF MECHANICAL ENGINEERS for publication in the ASME JOURNAL OF APPLIED MECHANICS. Manuscript received by the ASME Applied Mechanics Division, September 18, 2002; final revision, June 10, 2003. Associate Editor: D. A. Siginer. Discussion on the paper should be addressed to the Editor, Prof. Robert M. McMeeking, Journal of Applied Mechanics, Department of Mechanical and Environmental Engineering, University of California–Santa Barbara, Santa Barbara, CA 93106-5070, and will be accepted until four months after final publication of the paper itself in the ASME JOURNAL OF APPLIED MECHANICS.

  

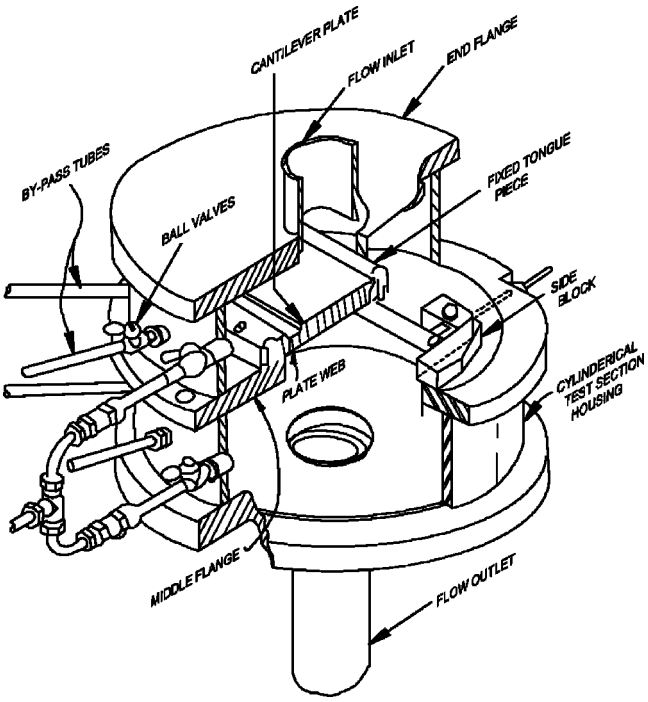


**Fig. 1 Tongue-in-groove leakage joint bench test section**

## 2 Problem Description

The test section shown in Fig. 1 consists of a 0.305 m×0.127 m (12 in×5 in nominal) rectangular plate made of aluminum ($\rho = 2768$ kg/m$^3$) that is clamped at one end with a tongue-in-groove joint at the opposite end (see Fig. 2). The dry natural frequency of the plate was measured by impulse testing, [5], to be 270 Hz with 0.4% material damping.

This plate configuration was chosen to ensure two-dimensional flow of de-aerated water ($\rho = 1000$ kg/m$^3$ and $\nu = 0.984 \cdot 10^{-6}$ m$^2$/sec) through the joint. Dependent on loop conditions, the plate experiences either oscillatory or excursive behavior when flow is increased. Prediction of oscillatory instability is the more demanding case and this case is investigated below.

The loop was configured for the bench test with an accumulator to maintain the pump inlet pressure at 482.65 kPa (gauge) (70 psig) and heat exchangers to keep the loop temperature below 65.6°C (150°F). The loop was connected to the test section with a flexible 63.5 mm (2.5 in) fire hose to mitigate the transmission of mechanical vibrations. Flow was generated by a 2.24 kW (3 hp) DC variable speed pump and the loop flow was controlled by pump speed. Loop flow was redundantly measured with Rotometer and Annubar flow meters, and venturis upstream of the test section.

The tongue-in-groove joint geometry is shown in Fig. 3. Leakage flow around the sides of the plate was restricted by placement of side blocks so that the side leakage flow was negligible compared to flow through the tongue-in-groove joint. As a result, flow through the test section was essentially two-dimensional and is appropriately simulated using a two-dimensional fluid dynamics code.

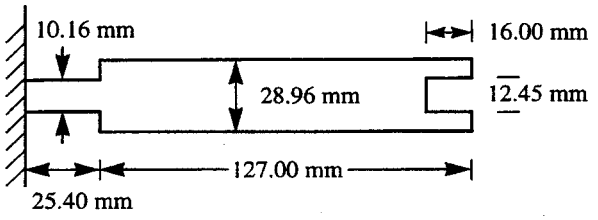


**Fig. 2 Plate geometry (schematic)**

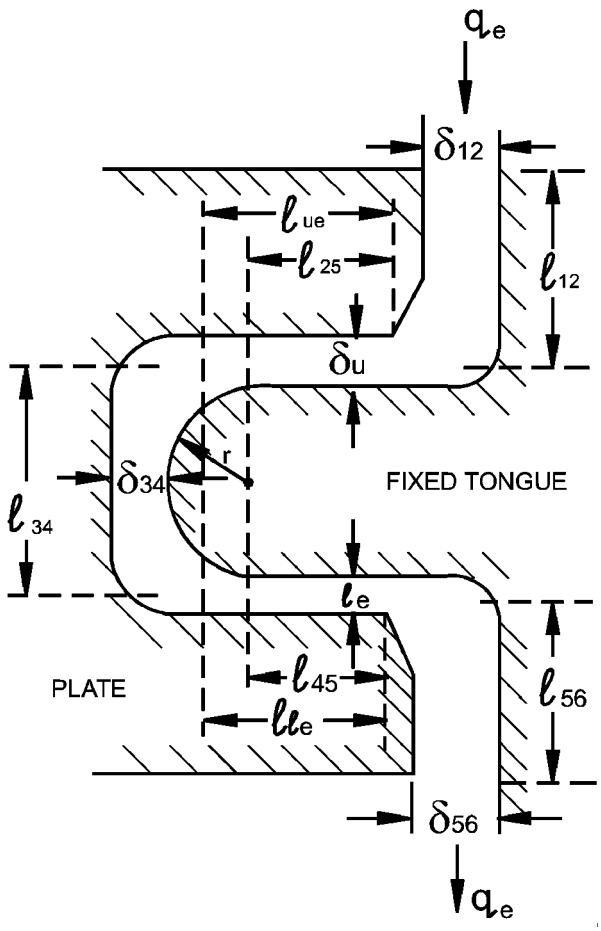


**Fig. 3 Curtiss-Wright tongue-in-groove joint geometry. This joint can be regarded as five channels in sequence: (1) vertical channel indicated by $l_{12}$; (2) horizontal channel indicated by $l_{ue}$; (3) vertical channel indicated by $l_{34}$; (4) horizontal channel indicated by $lle$; and (5) vertical channel indicated by $l_{56}$.**

The plate was positioned so that the upper gap spacing ($\delta_u$ in Fig. 3) was 0.401 mm (15.8 mils) for zero joint flow. As the pump speed was increased, the pressure drop across the joint and the edge flow increased, causing the upper gap spacing to decrease due to the increasing force on the plate. The joint exhibited an oscillatory instability for the set of test conditions defined by a 21.65 kPa (3.14 psi) pressure drop, a 0.316 l/sec (5 gpm) edge flow and a 0.232 mm (9.15 mil) upper gap spacing for a speed controlled pump without bypass flow. At these conditions, the plate oscillated at a frequency of 2.5 Hz.

## 3 Hydraulic-Based Stability Model

This section discusses the modeling and hydraulic-based stability analysis of the tongue-in-groove joint described in the previous section. The point of this model is to show that the destabilizing fluid force is associated with hydraulic conditions within the joint and it is not attributed to details exterior to the test section, thus setting the stage for the fluid-structure interaction model in the next section. The stability analysis accounts for the joint pressure drop-flow relationship, plate structural characteristics, pump head-flow, loop resistance, and loop inertia. Fluid compressibility is neglected since water is essentially incompressible at subcritical flows.

The approach taken here is to use the analytical models discussed below to generate a closed-form symbolic representation in Mathematica. Once assembled, the eigenvalues (i.e., stability) of the system are evaluated for the range of test parameters. Symbolic analysis enables detailed assessment of the conditions that lead to joint instability. Once the instability mechanism is understood, the hydraulic model of joint flow (see Eq. (2) below) is replaced with an SBDM representation and a first principles-based simulation conducted as described in Section 4.

Cross-sectional dimensions of the 0.305 m (12 in) wide plenum separating plate are shown in Fig. 2. The 10.16 mm (0.40 in) thick section acts as an elastic hinge and the remainder of the plate is essentially rigid. As a result, the plate responds as a cantilevered rigid body.

The generalized coordinate chosen to describe the plate motion is the displacement of its free end, characterizing the position of the tongue-in-groove joint. The generalized mass for this variable definition and plate geometry is derived to be $M=1.03$ kg ($M=0.0059$ lb-sec$^2$/in). Once the mass is defined, a stiffness value of $K=2.97\cdot 10^6$ N/m ($K=1.70\cdot 10^4$ lb/in) and damping coefficient of $C=14.0$ N-sec/m ($C=0.08$ lb-sec/in) are determined from the measured frequency and damping values, respectively. The pressure difference between the plena results in an equivalent force acting on the plate where the generalized force is half the plate area times the pressure drop across the plate or $F=0.194\cdot 10^{-1}\,\Delta P_{\text{joint}}$. The plate equation of motion is

$$M\ddot{x}+C\dot{x}+Kx=0.194\cdot 10^{-1}\Delta P_{\text{joint}} \tag{1}$$

where $x$ is the displacement of the plate tip.

The following joint pressure drop versus flow relationship, corresponding to the joint description in Fig. 3, is based on hydraulic theory, and accounts for transitional and friction losses in the joint.

$$\frac{\Delta P_{\text{joint}}}{q_e^2\rho}=\frac{K_{11}}{2\,\delta_{12}^2}+\frac{K_{12}+K_{23}}{2\,\delta_u^2}+\frac{K_{33}}{2\,\delta_{34}^2}+\frac{K_{34}+K_{45}}{2\,\delta_l^2}+\frac{K_{55}}{2\,\delta_{56}^2}+\frac{f}{4}\left(\frac{l_{12}}{\delta_{12}^3}+\frac{l_{34}}{\delta_{34}^3}+\frac{l_{56}}{\delta_{56}^3}+\frac{l_{ue}}{\delta_u^3}+\frac{l_{le}}{\delta_l^3}\right) \tag{2}$$

where $Q_{\text{joint}}$ is joint flow m$^3$/sec,

$q_e$ is volumetric joint flow per unit width$=Q_{\text{joint}}/0.305$ m$^2$/sec,

$\rho$ is fluid density, $\rho=1000$ kg/m$^3$,

$\delta_u$ is upper gap spacing$=0.401\cdot 10^{-3}-y_3$ m,

$K_{11}=0.50$,

$$K_{12}=0.47,$$

$$K_{23}=\left(1+\frac{0.401\cdot 10^{-3}}{\delta_u}\right)^{-2},$$

$$K_{33}=\left(1+\frac{0.226\sin^2 22^\circ}{2\,\delta_{34}}\right)^{-2}$$

$$K_{34}=0.30,$$

$$K_{45}=1.10,$$

$K_{55}=1.0$,

$$\delta_{12}=0.140\cdot 10^{-2}\ \text{m},$$

$$\delta_{34}=0.279\cdot 10^{-3}\ \text{m},$$

$$\delta_l=0.117\cdot 10^{-2}-\delta_u\ \text{m},$$

$$\delta_{56}=0.140\cdot 10^{-2}\ \text{m},$$

$$f \text{ is friction factor}=\begin{cases}96/\text{Re} & \text{Re}\leqslant 2042\\ 0.316/\text{Re}^{0.25} & \text{Re}>2042\end{cases}$$

$$l_{12}=0.848\cdot 10^{-2}\ \text{m},$$

$$l_{34}=0.404\cdot 10^{-2}\ \text{m},$$

$$l_{56}=0.848\cdot 10^{-2}\ \text{m},$$

$$l_{ue}=0.848\cdot 10^{-2}+0.631\cdot 10^{-1}\sqrt{\delta_u}\ \text{m},$$

and

$$l_{le}=0.848\cdot 10^{-2}+0.631\cdot 10^{-1}\sqrt{\delta_l}\ \text{m}.$$

The joint pressure drop equation was obtained by idealizing the tongue-in-groove joint as five connected channels shown in Fig. 3 with transition and friction losses for each channel. The $K_{ij}$ term represents the loss transitioning from channel $i$ to channel $j$ while $K_{11}$ and $K_{55}$ represent the entrance and exit losses for the joint, respectively. Friction losses were modeled by the Darcy-Weisbach relationship, [6], for laminar flow where the channel lengths were adjusted for the expansion and contraction regions for each channel. The friction factor changes from the laminar relationship to the Blasius relationship for turbulent flow, [6], at Re$\geqslant$2042.

The transitional loss coefficients $K_{ij}$ were initially estimated using handbook values, [7], for idealized channel geometries. The coefficient $K_{33}$ represents a smooth contraction plus an expansion in a lossless channel. This is similar to the treatment of a U-bend by Idelchik [7]. Results from the joint pressure drop equation (Eq. (2)) using the frictional losses and the estimated transitional losses were compared to CFD calculations to produce improved values for the $K_{12}$, $K_{34}$, and $K_{45}$ transitional loss coefficients. The frictional loss contributions were assumed to be sufficiently accurate and these terms were not altered.

The pump head-flow characteristics were determined by measuring the pressure head produced by the pump for several flow rates. The fitted pump head-flow equation (Eq. (3)) is applicable for different speed control settings.

$$\Delta P_{\text{pump}}=0.0777(\text{rpm})^2-0.138\cdot 10^4(\text{rpm})Q_{\text{loop}}-0.288\cdot 10^{10}Q_{\text{loop}}^2 \tag{3}$$

where rpm is rpm of speed controlled pump, and $Q_{\text{loop}}$ is loop flow m$^3$/sec. The pump head was measured in combination with loop flow to produce the following expression for loop hydraulic resistance:

$$\Delta P_{\text{loop}}=\frac{\rho}{2}\frac{K}{A^2}Q_{\text{loop}}^2 \tag{4}$$

where $K/A^2=0.649\cdot 10^7$ m$^{-4}$. The loop inertia was determined from a transient test where the main throttle valve was initially closed, then rapidly opened and the loop flow was measured as a function of time. The test section was replaced with a short length of pipe that had a negligible pressure drop for the loop inertia test because the joint pressure drop would otherwise dominate the response. The calibrated loop inertia is given below.

$$\Delta P_{\text{inertia}}=\rho\frac{L}{A}\frac{dQ_{\text{loop}}}{dt} \tag{5}$$

where $L/A=0.113\cdot 10^5$ m$^{-1}$.

The loop equilibrium equation is obtained by summing the pressure losses around the loop as follows:

$$\Delta P_{\text{pump}}=\Delta P_{\text{joint}}+\Delta P_{\text{loop}}+\Delta P_{\text{inertia}}.$$

It is important to note that the total loop flow is equal to the joint leakage flow plus a contribution to account for plate motions with the corresponding swept volume of fluid.

$$Q_{\text{loop}}=Q_{\text{joint}}+0.194\cdot 10^{-1}\dot{x} \tag{6}$$

where $\dot{x}$ is the velocity of the plate tip. The relationships for pump head-flow, loop resistance, and loop inertia (Eqs. (3), (4), and (5)) are functions of the total loop flow $Q_{\text{loop}}$ while the joint pressure drop versus flow representation (Eq. (2)) is a function of joint flow $Q_{\text{joint}}$. Substituting the equation for loop inertia (i.e., Eq. (5)) and

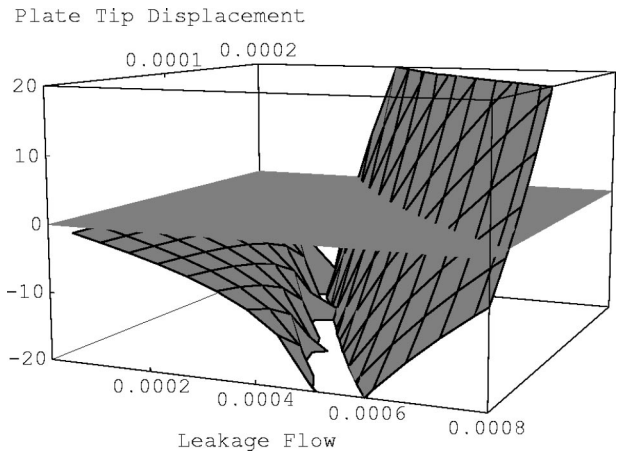


**Fig. 4 Stability map showing the structural eigenvalue's real component as a function of flow rate and upper gap spacing. Negative and positive components indicate stable and unstable conditions, respectively, while the neutral stability point is identified by a zero value. (Joint flow is given in $m^3$/sec and plate position in m.)**

the above expression for total flow into the loop equilibrium equation results in the following loop equilibrium equation.

$$\dot{Q}_{\text{joint}} + 0.194 \cdot 10^{-1} \ddot{x} = \frac{g}{\rho} \frac{A}{L} [\Delta P_{\text{pump}}(Q_{\text{loop}}) - \Delta P_{\text{joint}}(Q_{\text{joint}}) - \Delta P_{\text{loop}}(Q_{\text{loop}})] \quad (7)$$

where $\Delta P_{xxx}(Q_{yyy})$ denotes $\Delta P_{xxx}$ as a function of $Q_{yyy}$. The plate equation of motion (Eq. (1)) and the loop equilibrium equation (Eq. (7)) comprise the governing equations for the coupled plate/loop system.

The stability of the nonlinear system given by Eqs. (1)–(7) for a particular joint leakage flow and plate position can be determined by fixing the pressure drops at that joint leakage flow and plate position and then computing the eigenvalues of the resulting linear differential system. This procedure can be carried out using a symbolic manipulation package such as Mathematica [8]. Figure 4 is a plot of the structural eigenvalue's real component as a function of flow rate and upper gap spacing. Negative and positive components indicate stable and unstable conditions, respectively, while the neutral stability point is identified by a zero value.

For the test conditions of 0.316 l/sec (5 gpm) and an upper gap spacing of 0.232 mm ($\delta_u = 9.15$ mils) (see Fig. 3), the real part of the structural eigenvalue is equal to 0.047 which indicates very slow growth at the stability point, as expected. The true worth of this symbolic approach is the ability to isolate the instability mechanism by explicitly evaluating changes in system stability when system parameters are changed.

The most significant result obtained from the symbolic evaluation of the hydraulic-based stability analysis is identification of the second to last term, $f l_{ue}/4\delta_u^3$, in the joint pressure drop-flow relationship (Eq. (2)) to be the destabilizing fluid force. This term represents the frictional loss in the narrow section of the tongue-in-groove joint characterized by the upper gap spacing $\delta_u$ (see Fig. 3). This frictional loss accounts for 45% of the joint pressure drop and elimination of the corresponding term in the hydraulic-based stability analysis results in a stable system. The effect would be the same if the system losses (e.g., structural damping, fluid convection) exceeded this destabilizing term in magnitude. Additional system damping, although it may be insufficient itself to preclude an oscillatory instability, will shift the point of instability to a higher flow rate for a given gap spacing. The potential for an excursive instability increases under these conditions and the onset of an oscillatory instability may be superseded.

A second result of this study is the conclusion that the reduction of plate frequency from an air to a water environment (i.e., 270 Hz versus 2.5 Hz) is due to the swept volume (or added mass) contribution described above. The loop inertia couples the swept volume of water and the structural motion causing the frequency reduction.

The natural frequency of the immersed plate predicted by the hydraulic-based stability analysis is greater than the measured frequency (i.e., 4.23 Hz versus 2.5 Hz). This over-prediction of immersed frequency is attributed to neglecting the hydrodynamic mass of unrepresented water in the loop that is external to the plena volume. Sensitivity studies were conducted with various swept volumes and it was concluded that the stability point is minimally affected by the over-prediction of frequency for the range of parameters evaluated.

To summarize, the symbolic evaluation of the hydraulic-based stability analysis identified the destabilizing fluid force in the joint pressure-drop flow relationship. This force is associated with hydraulic conditions within the joint and it is not attributed to details of the exterior loop, although a loop must be suitably represented before the instability can be observed. In the next section, a two-dimensional fluid-structure interaction analysis model for flow within the joint is presented. This model, which was developed from first principles, is seen to predict the same flow instability that was observed experimentally when the joint model is coupled with the loop representation described above.

## 4 SBDM Model

As mentioned above, if the system losses are greater than the destabilizing forces, then the system will remain stable. Excessive numerical damping, which contributes to the system damping, can artificially suppress an otherwise unstable response. In any case, numerical damping will shift the onset conditions of an oscillatory instability to require higher than observed flow rates. This is why the successful prediction of the instability point of a self-excited vibration has been so elusive. The hallmark of the SBDM is elimination of numerical damping due to the coupling model itself. Other sources of numerical damping are well known and these sources are important in determining details of the steady flow prior to initiation of instability, but are less important in determining the onset of instability due to fluid-structure interaction. This application is an acid test for any fluid-structure interaction analysis capability.

The first step in replacing the hydraulic representation of loop flow (Eq. (2)) with an SBDM representation is to generate a sufficiently accurate fluid-only solution to serve as the starting point for the coupled solution. The channel model used for the calculation is shown in Fig. 5 where the plate is positioned so that the upper gap spacing $\delta_u = 0.232$ mm ($\delta_u = 9.15$ mils) (see Fig. 3) is consistent with a channel flow rate of 0.316 l/sec (5 gpm). The fluid mesh consisted of the union of quadrilaterals with 10 cells across the channel and 1076 cells along the length. Although the mesh details cannot be discerned in Fig. 5, the joint geometry is clearly depicted. A closeup of the mesh at the first inlet bend where the majority of the joint pressure drop occurs is provided in Fig. 6. The inlet and exit plena are not modeled because the block structured mesh requirements of the computer program makes it impractical to transition the mesh from the plena to the channel and vice versa. The inlet and exit pressure losses are represented with sufficient accuracy by hydraulic loss coefficients (see the $K_{11}$ and $K_{55}$ terms in Eq. (2)) because these features are not the source of the destabilizing fluid force.

Laminar flow is represented because at 0.316 l/sec (5 gpm) the channel flow is laminar everywhere other than the narrow section of the tongue-in-groove joint characterized by the upper gap spacing $\delta_u$ (see Fig. 3). The Reynolds number varies from 1050 at the inlet and exit regions to 6300 in the narrow section of the joint. No-slip wall conditions are specified and pressure forced boundary conditions are implemented to produce the 0.316 l/sec (5 gpm)

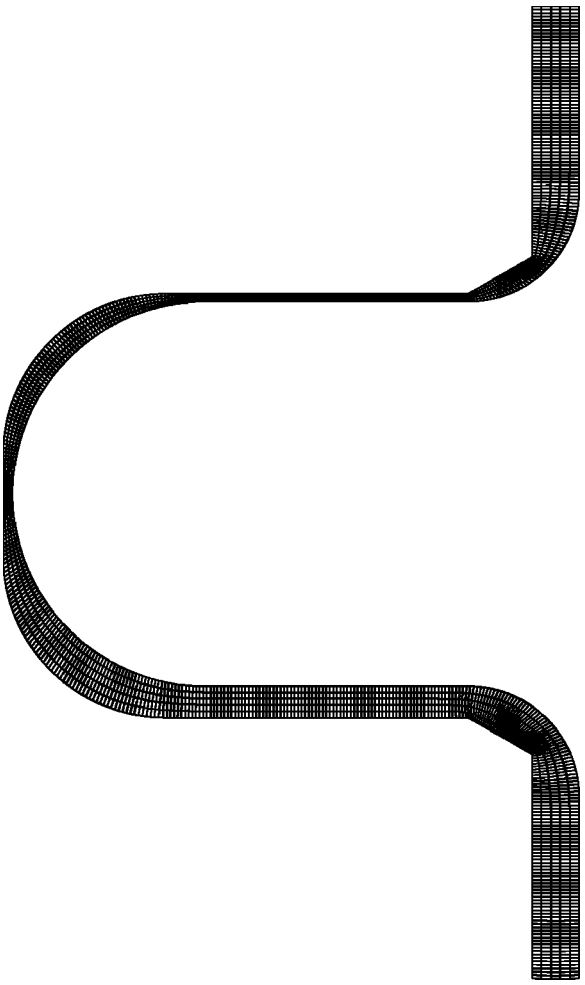

**Fig. 5 Channel model mesh. Half the mesh lines in each direction have been omitted for clarity.**

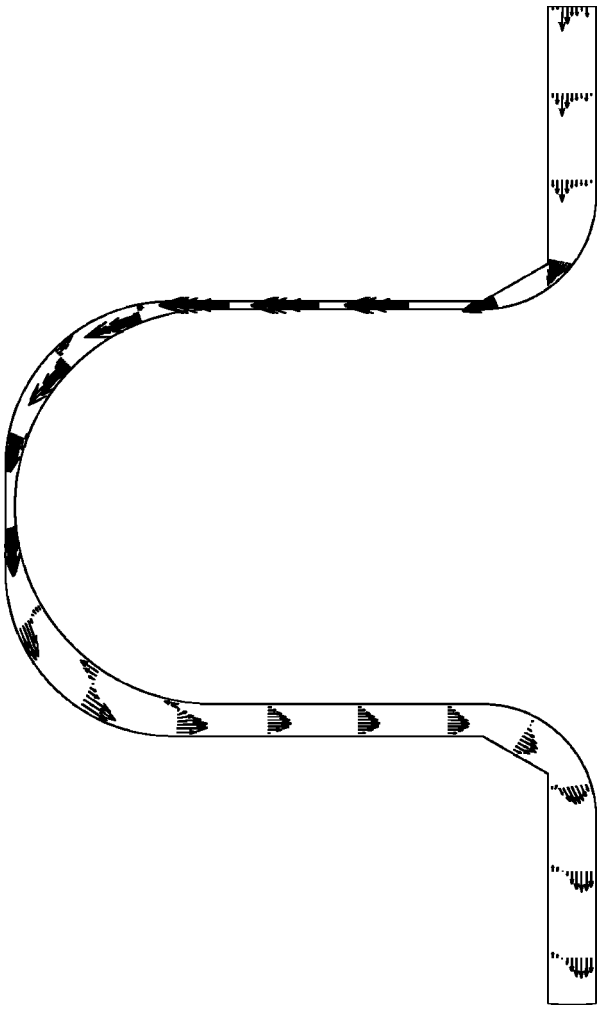

**Fig. 7 Velocity profile for the fluid-only solution**

flow rate. A constant time step of $1.25\times10^{-6}$ sec is used to produce a stable solution for the model shown in Fig. 5. Convection terms are discretized using a weighted average of 37.5% of donor-cell differencing and 62.5% centered differencing, values chosen to maintain as much accuracy as possible from centered differencing while maintaining a manageable time step size. Finally, the density and kinematic viscosity of the water were defined as 1000 kg/m$^3$ (0.0361 lb/in$^3$) and $0.984\cdot10^{-6}$ m$^2$/sec ($0.152\cdot10^{-2}$ in$^2$/sec), respectively.

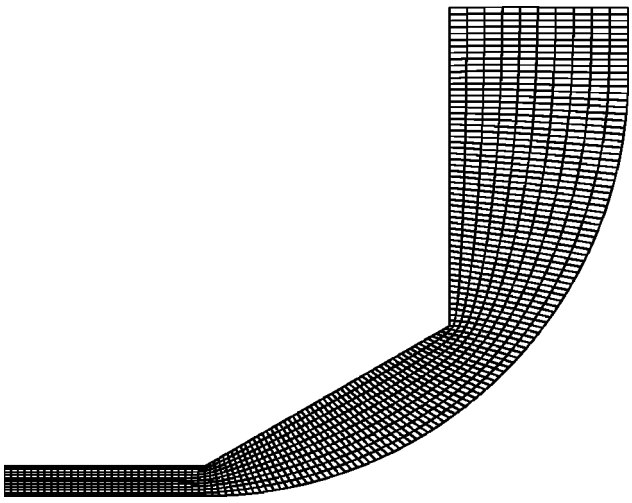

**Fig. 6 Mesh closeup of first inlet bend**

To establish a net pressure drop consistent with the discrete flow solution, a constant channel exit pressure of 482.65 kPa (70 psi) was specified and the inlet pressure was adjusted by trial and error until the desired flow rate of 0.316 l/sec (5 gpm) was achieved. The fluid-only solution was simulated for a total of 0.8 sec to establish steady-state flow conditions throughout the joint. The resulting channel pressure drop of 22.340 kPa (3.24 psi), combined with the 0.414 kPa (0.06 psi) inlet and exit channel losses, equals a 22.754 kPa (3.30 psi) pressure drop across the joint at a leakage flow of 0.317 l/sec (5.024 gpm). This analytical estimate is within 5% of the 21.650 kPa (3.14 psi) measured across the test section. Velocity and pressure profiles for the fluid-only solution are provided in Figs. 7 and 8, respectively. Note the effectiveness of the tongue-in-groove joint geometry of Fig. 3 in limiting leakage flow where the majority of pressure drop occurs on the inlet side of the joint.

The next phase of the effort is incorporation of the plate model into the SBDM fluid-structure interaction analysis to obtain a steady-state solution. The reason for taking this intermediate step and not directly analyzing the full system including loop conditions is that the latter approach can produce an excursive instability if the initial conditions do not represent equilibrium of the plate position and pressure drop. The SBDM coupled simulations

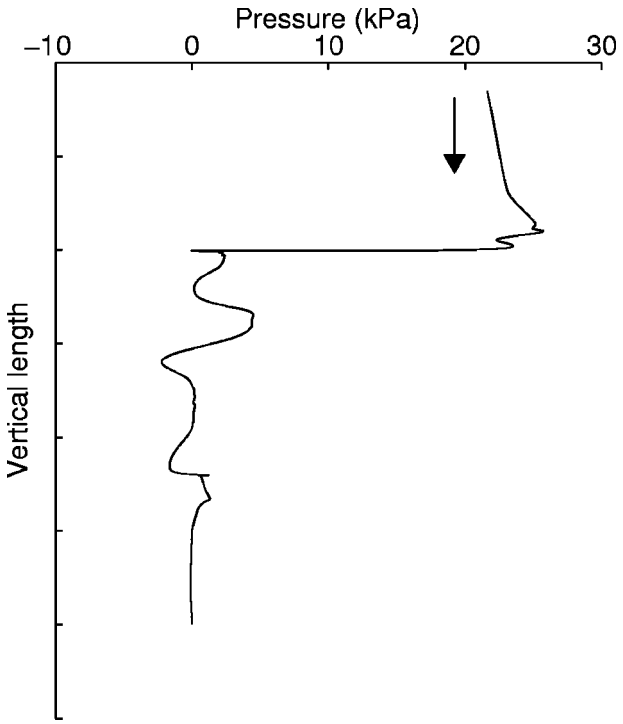


**Fig. 8 Centerline pressure profile for the fluid-only solution. Pressure is plotted versus vertical length, with channel geometry overlaid for clarity.**

(both with and without loop conditions modeled) used the same analysis parameters (e.g., laminar flow, time step) as previously described for the fluid-only solution.

The same plate representation used for the hydraulic-based stability analysis described in Section 3 was used here. A hydrodynamic mass of $0.422 \cdot 10^4$ kg (24.1 lb-sec$^2$/in) was added to the structural mass to account for the swept volume of water (see Eq. (6)) that is not represented because the inlet and outlet plena were not modeled as described above. The only additional representation required for SBDM implementation is specification of the geometrical relationship between fluid degrees-of-freedom on the plate and the generalized structural degree-of-freedom for the plate itself.

The coupled problem (without loop conditions) was run for a single time step to calculate the fluid force acting on the plate in the channel. A counterbalancing plate force was then specified to balance the fluid forces and this process was repeated until the plate was neutrally balanced in its nominal position. The coupled problem was simulated for 0.2 sec to assure the stability of the SBDM model. With the plate and fluid forces initially in balance, the plate did not experience an excursive instability.

The next step in the process is to introduce the representations for pump head-flow (Eq. (3)), loop hydraulic resistance (Eq. (4)), and loop inertia (Eq. (5)) into the SBDM coupled simulation. The first task is to determine the pump speed that corresponds to the loop flow and pump head in accordance with Eq. (3). The nominal loop flow was calculated at the beginning of the simulation prior to any time step calculations and this flow is the same flow as the end of the earlier SBDM simulation without the loop model for consistency. Using this value for loop flow, the pump head was determined by evaluating the equilibrium of the loop for steady-state conditions (i.e., $\Delta P_{\text{inertia}}=0$) as shown below.

$$\Delta P_{\text{pump}}=\Delta P_{\text{joint}}+\Delta P_{\text{loop}} \tag{8}$$

$$\Delta P_{\text{pump}}=0.223\cdot 10^5+\frac{q_e^2\rho}{2}\left(\frac{K_{11}}{\delta_{12}^2}+\frac{K_{55}}{\delta_{56}^2}\right)+\frac{\rho}{2}\frac{K}{A^2}Q^2$$

The joint pressure drop is represented above by contributions for the channel inlet and exit pressure losses (i.e., $K_{11}$ and $K_{55}$ terms of Eq. (2)) plus the channel pressure drop of 22.340 kPa (3.24 psi) that was imposed in the fluid-only solution to produce a leakage flow of 0.317 l/sec (5.024 gpm). Once the pump head was calculated, the corresponding pump speed was determined from Eq. (3). This pump speed was kept constant throughout the simulation and the pump head varied with loop flow according to Eq. (3). The counterbalancing plate force for the ''SBDM-with-loop'' simulation had to be redefined to account for the pressure drop across the joint in addition to the fluid force acting on the channel that was determined in the ''SBDM-without-loop'' simulation. Using the same representation for joint pressure drop described above and the initial joint leakage flow, the counterbalancing force was specified to neutrally balance the plate in its nominal position at the start of the ''SBDM-with-loop'' simulation.

The ''SBDM-with-loop'' simulation was driven by a channel inlet pressure that varied for each time step. The channel inlet pressure is implicitly dependent on the loop flow which requires treatment for incorporation into an explicit CFD code. The approach taken here was to estimate the loop flow for the next time step, then calculate the channel inlet pressure that was consistent with the estimated loop flow. Both the loop flow and corresponding inlet pressure were determined by evaluating unsteady loop equilibrium conditions as follows:

$$\Delta P_{\text{inertia}}+\Delta P_{\text{loop}}+\Delta P_{\text{joint}}-\Delta P_{\text{pump}}=0.$$

The first, second, and last terms of the above equilibrium equation are appropriately represented by Eqs. (5), (4), and (3), respectively. The joint pressure drop is a combination of channel inlet and exit pressure losses plus the pressure drop across the channel where the latter is an implicit function of loop flow and channel inlet pressure. The channel pressure drop was approximated by calculating a hydraulic loss for the channel based on the last SBDM time step and applying this estimate to the new time step. With this approximation and a central difference expression for loop flow rate in Eq. (5), the unsteady loop equilibrium equation becomes

$$0=\rho\frac{L}{A}\frac{2Q^{n+1}-Q^n-2Q^{n-1}+Q^{n-2}}{2dt}+\frac{\rho}{2}\frac{K}{A^2}(Q^{n+1})^2$$

$$+16.12\left(\frac{\rho}{2}\right)\left(\frac{Q^{n+1}}{\delta_{12}}\right)^2+\frac{P_{\text{inlet}}^n-0.483\cdot 10^6}{(Q^n)^2}(Q^{n+1})^2-0.195$$

$$\cdot 10^7\ \ (\text{rpm})^2+0.139\cdot 10^4(\text{rpm})Q^{n+1}+0.288\cdot 10^{10}(Q^{n+1})^2.$$

The above quadratic equation was solved to estimate the loop flow for the next time step $Q^{n+1}$. Once the loop flow was estimated, the channel inlet pressure for the next time step was calculated from the unsteady loop equilibrium equation as follows:

$$P_{\text{inlet}}^{n+1}=0.483\cdot 10^6+\Delta P_{\text{pump}}-\Delta P_{\text{I/O}}-\Delta P_{\text{loop}}-\Delta P_{\text{inertia}}$$

where $\Delta P_{\text{I/O}}$ is channel inlet and exit pressure losses.

$$P_{\text{inlet}}^{n+1}=0.483\cdot 10^6+0.0777(\text{rpm})^2-0.139\cdot 10^4(\text{rpm})(Q^{n+1})$$

$$-0.288\cdot 10^{10}(Q^{n+1})-0.161\cdot 10^{-2}\left(\frac{\rho}{2}\right)\left(\frac{Q^{n+1}}{\delta_{12}}\right)^2$$

$$-\rho\frac{K}{A^2}(Q^{n+1})^2-\rho\frac{L}{A}\frac{2Q^{n+1}-Q^n-2Q^{n-1}+Q^{n-2}}{2dt}$$

The above scheme proves to be an effective means of incorporating the loop conditions into the coupled SBDM simulation. A delicate point arises in devising a suitable numerical scheme to extrapolate the channel pressure drop to the $n+1$ time step. Alternate treatments, such as lagging the loop flow, result in excursive instabilities. The definition of a difference expression for the loop flow rate $\dot{Q}^{n+1}$ that preserved enough system energy to per-

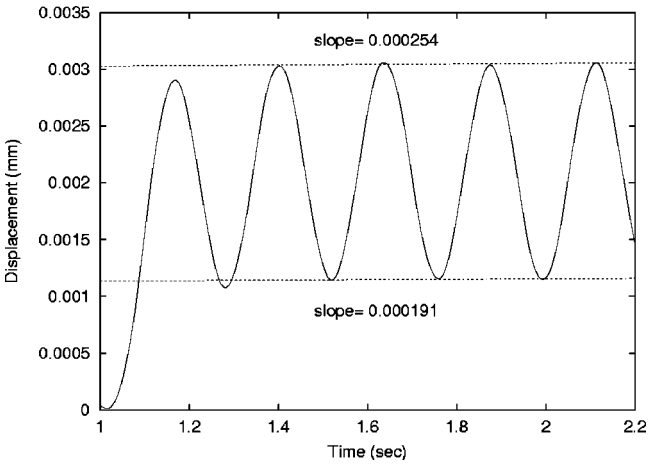


**Fig. 9 Results of SBDM coupled simulation with loop conditions modeled, $Q_{joint}=0.317$ l/sec**

mit oscillatory instability is an equally difficult task. Note that the contribution of the swept volume of water to the total loop flow was not considered in the SBDM analyses. This contribution is insignificant (amounting to less than 1% of the total flow) and successful incorporation of this term into an explicit analysis without dissipating excessive energy is difficult.

The coupled simulation with loop conditions was started from the steady-state solution for the coupled simulation without the loop modeled and run for a number of plate vibration cycles as shown in Fig. 9. The plate immediately began vibrating but the oscillations were centered around a nonzero plate position which indicated the counterbalancing plate force was slightly off. This perturbation generated a nonsteady plate motion that was most apparent in the first cycle of response. The plate displacements were an order of magnitude smaller than the channel gap size which confirmed that the small displacement assumption of the SBDM formulation is appropriate for this class of problem. Also, this example demonstrates that instabilities begin with small displacements that grow in time. The velocity and pressure profiles for the SBDM coupled simulation with loop conditions are essentially the same as the fluid-only results shown in Figs. 7 and 8.

The natural frequency of the SBDM simulation is equal to the hydraulic-based stability analysis result which, in turn, is higher than the measured frequency (4.23 Hz versus 2.5 Hz). Since the SBDM simulation accounts for the added mass of the water in the tongue-in-groove joint and the hydraulic-based model does not, it is concluded that this added mass is negligible because the predicted frequencies for the two approaches are virtually the same. The over-prediction of immersed frequency is attributed to neglecting the hydrodynamic mass of the water in the remainder of the loop.

Visual stability assessment of the results in Fig. 9 is clarified by least-squares fitting straight lines to the upper and lower peaks of oscillation (as shown in Fig. 9), respectively, after the first vibration cycle. Examination of the relative slopes of the fitted lines reveals the steady growth of an oscillatory instability. The growth is consistent but slow which indicates that the flow of 0.317 l/sec (5.024 gpm) appears to be the stability point.

To assess the stability point and demonstrate that the SBDM is not inherently unstable, the previously described simulations (i.e., fluid-only, coupled without loop conditions, and coupled with loop conditions) were conducted for the last experimental data point that was investigated prior to experiencing the instability. The last stable data point had a channel flow rate of 0.284 l/sec (4.5 gpm) corresponding to an upper gap spacing of $\delta_u = 0.250$ mm ($\delta_u = 9.86$ mils) (see Fig. 3). For the simulations of the 0.284 l/sec (4.5 gpm) case, the mesh refinement and all numerical treatments were kept the same as the parameters used for the unstable 0.316 l/sec (5 gpm) flow case.

The results of the 0.284 l/sec (4.5 gpm) simulation are shown in Fig. 10 attached, as before, straight lines were least-squares fit to the upper and lower peaks of response following the first vibration cycle. Examination of these lines clearly indicates a decaying or stable response. Therefore, the 0.317 l/sec (5.024 gpm) flow is shown to be the instability point consistent with the experimental data and the SBDM is shown to correctly predict the stability point in addition to the general phenomenon of oscillatory instability.

## 5 Summary

The fluid-elastic instability of a tongue-in-groove leakage joint was evaluated using the SBDM of fluid-structure coupling and compared to experimental results. The test configuration consists of a rectangular plate that is elastically hinged at one end with the tongue-in-groove joint at the opposite end. For a speed controlled pump, the plate experiences an oscillatory response when flow is increased.

A hydraulic-based stability analysis was executed symbolically using Mathematica to identify the frictional loss factor in the joint as the destabilizing force. Building on the lessons from the Mathematica model, a fluid-structure interaction analysis using the SBDM coupling algorithm was conducted for the test configuration.

1. A steady-state fluid-only solution was generated as a starting point for the coupled simulation.
2. The coupled model without loop conditions was simulated long enough to allow the joint to achieve an equilibrated position.
3. The coupled simulation with loop conditions was executed for a number of plate vibration cycles to demonstrate the growing oscillatory behavior.
4. The coupled simulation with loop conditions was executed for reduced flow conditions to correctly demonstrate a stable response, thus indicating the higher flow as the instability point.

The SBDM of fluid-structure coupling is demonstrated to correctly predict the oscillatory instability and instability point of a tongue-in-groove leakage joint from a first principles basis. This success has been made possible by the energy conserving feature of the SBDM coupling algorithm. Even though the methodology is specifically applied to a tongue-in-groove joint, the approach is equally suitable for evaluating the fluid-elastic stability of leakage joints in general.

## Appendix

The small boundary displacement model (SBDM) for fluid/structure coupling is based on explicit time differencing for both the fluid and structural equations that are solved simultaneously. Structural displacements are assumed small compared with problem dimensions. As implemented for this paper, the structure is modeled as a single degree-of-freedom, but the formulation can be applied to multiple structural degrees-of-freedom as well. Coupling between fluid and structure is accomplished by setting fluid velocity at fluid-structure interfaces equal to structural velocity, and by determining forces exerted on the structure from pressure and viscous forces generated within the fluid. Because displacements are assumed small, both fluid and structural meshes are stationary in time, avoiding difficulties arising from mesh motion. The authors' experience has shown that mesh motion can introduce ''numerical dissipation'' that is large enough to mask the initiation of physical instabilities.

Suppose that a spatial mesh and discretization method have been chosen, and denote by **U** the vector of fluid velocity degrees-of-freedom, by **P** the fluid pressure degrees-of-freedom, and by **X**

the structural displacement degrees-of-freedom. Suppose also that a uniform time step, $\Delta t$ is chosen and denote by a superscript the time level. The equations of motion can be schematically represented in the following way.

$$M_{\text{fluid}}\frac{\mathbf{U}^{n+1}-\mathbf{U}^{n}}{\Delta t}+G\mathbf{P}^{n+1}=\mathbf{S}^{n}, \tag{9}$$

$$G^{T}\mathbf{U}^{n+1}=0, \text{ and,} \tag{10}$$

$$M_{\text{struct}}\frac{\mathbf{X}^{n+1}-2\mathbf{X}^{n}+\mathbf{X}^{n-1}}{\Delta t^{2}}+K\mathbf{X}^{n}=\mathbf{F}^{n+1}, \tag{11}$$

where Eq. (9) is the discretized Navier-Stokes equation with **S** denoting all convective, viscous, and forcing terms; where Eq. (10) is the equation of the continuum; and where Eq. (11) is Newton's law of motion with **F** denoting all external forces, including fluid forces. Here, $M_{\text{fluid}}$ and $M_{\text{struct}}$ are the fluid and structural mass matrices, $K$ is the structural stiffness matrix, and $G$ is a matrix representing the discrete gradient operator. The discrete divergence operator is the transpose of the gradient, $G^{T}$.

At the fluid-structure interface, the equations are coupled together in the following way:

$$\mathbf{U}^{n+1}=\frac{\mathbf{X}^{n+1}-\mathbf{X}^{n}}{\Delta t}, \quad \text{and} \tag{12}$$

$$\mathbf{F}^{n+1}=-G\mathbf{P}^{n+1}+\mathbf{S}^{n}+\text{body forces} \tag{13}$$

Equation (12) equates the structural and fluid velocities at the interface and Eq. (13) indicates that the pressure force on the structure is the most important fluid force. It is essential that both Eqs. (12) and (13) be evaluated using consistent time levels.

The formulation sketched above, along with a stationary underlying mesh, yields a fixed linear system that must be solved at each time step in order to advance to the next time step. This linear system can be solved very efficiently. It should be noted that the marching procedure is not stable unless the time increment is limited in size. The limitation depends very strongly on the discrete treatment of the convection terms and usually requires some form of upwinding to maintain a reasonably sized time increment. For the current case, convection terms are discretized using a weighted average of 37.5% of donor-cell differencing and 62.5% centered differencing, values chosen to balance the inaccuracy of upwind differencing against its beneficial effect on time step size. System stability predictions are not sensitive to the choice of weighting because stability depends primarily on the rate of energy transfer across the fluid-structure interface, and not on dissipation mechanisms within the fluid and structure themselves.

The form of the discretized fluid equations is based on the method of Hirt, Amsden, and Cook [9]. This finite volume method employs mesh elements that are quadrilateral in shape, with velocity approximated as a bilinear function based on corner values, and constant pressure in each element. This element is neutrally stable in the Babuška-Brezzi-Ladyzhenzkaya sense, and spurious pressure modes are eliminated by specification of pressure in all elements at the exit of the flow region.

## References


[1] Blevins, R. D., 1994, *Flow-Induced Vibration*, Krieger Publishing Company, Melbourne, FL.

[2] Ziada, S., and Staubli, T., eds., 2000, *Flow-Induced Vibrations*, Proceedings of the Seventh International Conference on Flow-Induced Vibrations, Lucerne, Switzerland, June 19–22, A. A. Balkema, Rotterdam.

[3] Manko, D. J., and Sussman, M. M., 1998, "A Small Boundary Displacement Model of Fluid-Solid Coupling, Part 1—Theory," *Proc. 1st Symposium on Marine Applications of CFD*, McLean, VA, May 19–21.

[4] Mulcahy, T. M., 1983, "Leakage-Flow-Induced Vibration of Reactor Components," Shock Vib. Dig., **15**(9), pp. 11–18.

[5] Clough, R. W., and Penzien, J., 1975, *Dynamics of Structures*, McGraw-Hill, New York.

[6] Streeter, V. L., 1966, *Fluid Mechanics*, Fourth Ed., McGraw-Hill, New York.

[7] Idelchik, I. E., 1994, *Handbook of Hydraulic Resistance*, Third Ed., CRC Press, Ann Arbor, MI.

[8] Wolfram, S., 1999, *The Mathematica Book*, Fourth Ed., Cambridge University Press, New York.

[9] Hirt, C. W., Amsden, A. A., and Cook, J. L., 1974, "An Arbitrary Lagrangian-Eulerian Computing Method for All Flow Speeds," J. Comput. Phys., **14**, pp. 227–253.

**D. C. D. Oguamanam**
Assistant Professor,
Department of Mechanical, Aerospace and Industrial Engineering,
Ryerson University,
Toronto, ON M5B 2K3, Canada
Mem. ASME

**J. S. Hansen**
Professor,
Institute for Aerospace Studies,
University of Toronto,
4925 Dufferin Street,
Toronto, ON M3H 5T6, Canada

**G. R. Heppler**
Professor,
Systems Design Engineering,
University of Waterloo,
Waterloo, ON N2L 3G1, Canada

# Nonlinear Transient Response of Thermally Loaded Laminated Panels[1]

*The nonlinear response of a composite laminated panel that is suddenly exposed to a heat flux is examined using the finite element method. The panel is cantilevered onto a rigid hub, the rotation motion of which is either fully or partially restrained. The panel elastic deformations are assumed large and are modeled via the von Kármán strain-displacement relationship while the rigid-body angular rotation, for the case of a rotating rigid hub, is assumed small. The system of nonlinear governing equations is solved by the Newton-Raphson method in conjunction with the Newmark time integration scheme. The panel deformation is observed to be sensitive to the motion of the base.*
[DOI: 10.1115/1.1631033]

## 1 Introduction

The sudden application of a heat flux to a structure modeled as a beam, plate, or shell has the tendency to cause the structure to vibrate. This phenomenon is called thermal-induced vibration; it is dependent upon the relative magnitudes of the thermal time constant and the fundamental natural frequency of the structure. Tauchert [1] presents an extensive review of the subject. Another important survey study is by Thornton [2] which concentrates on the aerospace industry. The study by Heppler [3] is also worthy of mention; it examines the response of shells subject to thermal radiation from a nuclear burst.

Analysis of the response of both curved and flat panels that arises from exposure to a sudden heat flux finds application in industries such as aerospace, nuclear and manufacturing. The influence of thermomechanical loads on laminated plates is examined by Chandrashekhara and Tenneti [4]. A similar problem, but for the case involving only thermal loads, is investigated for laminated cylindrical panels by Chang and Shyong [5]. The study examines the issue of thermomechanical coupling and concludes that the degree of its relevance decreases with increasing panel radius of curvature. Feldman and Gilat [6] investigate the dynamic response of antisymmetric laminated plates and cylindrical panels for both temperature-dependent and independent material properties. The aforementioned studies consider fully restrained hub rotation.

The current study examines the nonlinear response of composite laminated panels that are suddenly exposed to heat flux. A typical panel is cantilevered onto a rigid hub, the rotation motion of which is fully or partially restrained. The responses of curved and flat panels with fully or partially tangential edge constraints under thermomechanical loads is the subject of the paper by Librescu and Win [7]. They include geometric imperfections and conclude that the panel response can be enhanced by varying the degree of the tangential edge restraints. The occurrence of snap-through buckling is also shown to be dependent upon the degree of the restraints.

The introduction of partial restraint on the hub rotation motion in present study makes the model the preferable choice in analyzing systems such as space-based pointing systems. Further, the added feature permits the use of the model in the investigation of thermal induced satellite attitude dynamics, [8]. Johnston and Thorton's [8] study on the attitude dynamics of a satellite is based on a linear strain-displacement relationship even though the determined elastic deformations are greater than the boom thickness by orders of magnitude.

The nonlinearity in the present study is geometric. It is modeled via the von Kármán strain-displacement relationship for moderately large deformations. A spatially uniform but time-dependent temperature distribution is assumed. The results obtained from the linearized governing equations are also presented, and a parametric study of the effects of: (1) geometric nonlinearity, (2) the magnitude of the inertia of the hub relative to that of the panel, and (3) the panel shallowness, is implemented.

## 2 Mathematical Formulation

The system of interest is depicted in Fig. 1. It comprises a laminated cylindrical panel, *ABCD* that is cantilevered onto a rigid circular cylindrical hub which can rotate about its geometric axis. The panel is assumed to be in a stress-free initial state when it is exposed to a sudden heat flux that results in a uniform temperature change over the surface of the panel. The temperature change $\Delta_T$ is constant through the thickness and is spatially uniform. It is taken after Johnson and Thornton [8] and is of the form

$$\Delta_T = \Delta_{Tss}(1 - e^{-t/T_t}) \tag{1}$$

where $\Delta_{Tss}$ is the steady-state temperature difference, $t$ is time, and $T_t$ is the thermal time constant.

It is also assumed that changes to the panel material properties are negligible within the operational temperature range. With reference to Fig. 1 the dynamics of the system are described with the aid of: an inertial frame located at *O* with the dexteral orthogonal basis vectors $[\hat{n}_1, \hat{n}_2, \hat{n}_3]$; a hub body-fixed rotating frame with dexteral basis vectors $[\hat{a}_1, \hat{a}_2, \hat{a}_3]$ also located at *O*; and a curvilinear panel-fixed frame with dexteral basis vectors $[\hat{e}_x, \hat{e}_\beta, \hat{e}_r]$.

[1]Part of this work was presented at the 5th International Conference on Dynamics and Control of Systems and Structures in Space, July 14–18, 2002, Cambridge.

Contributed by the Applied Mechanics Division of THE AMERICAN SOCIETY OF MECHANICAL ENGINEERS for publication in the ASME JOURNAL OF APPLIED MECHANICS. Manuscript received by the Applied Mechanics Division, September 18, 2002; final revision, May 1, 2003. Associate Editor: M.-J. Pindera. Discussion on the paper should be addressed to the Editor, Prof. Robert M. McMeeking, Chair, Department of Mechanics and Environmental Engineering, University of California–Santa Barbara, Santa Barbara, CA 93106-5070, and will be accepted until four months after final publication in the paper itself in the ASME JOURNAL OF APPLIED MECHANICS.

  

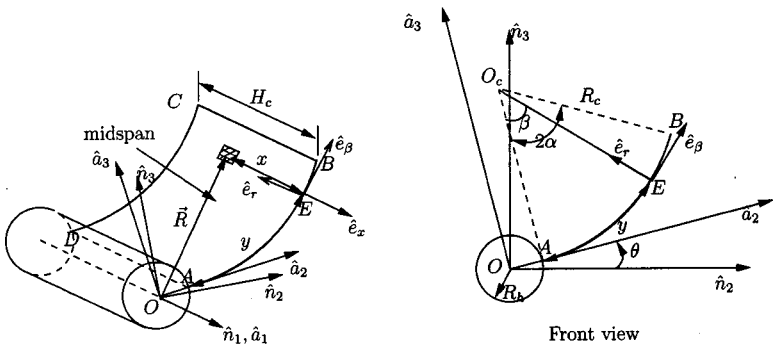


**Fig. 1 Cantilevered cylindrical panel**

The $\hat{a}_2$ basis vector is orientated such that it always passes through the point of attachment $A$ of the panel to the hub. It is rotated from the inertial basis vector $\hat{n}_2$ by angle $\theta$. It is also assumed that the radial line from the center of curvature of arc $AB$, or midsurface, to the point of attachment, i.e., $AO_c$, is always perpendicular to $\hat{a}_2$. The basis vectors $\hat{a}_1$ and $\hat{n}_1$ are coincident and are always parallel to the geometric axis of the rigid hub.

If the position vector from $O$ to a differential mass element of the panel is denoted by $\vec{R}$. This vector may be expressed by assuming that the arc length distance measured from $A$ along the curved edge $AB$ (or midsurface) is say $y=R_c\beta$. A local curvilinear panel-fixed frame is then attached at the point such that $\hat{e}_\beta$ is a tangential basis vector while $\hat{e}_r$ is an inward radial basis vector. The position of the differential mass element from this frame is $x$ units along the $\hat{e}_x$ basis vector. Hence $\vec{R}$ may be written as

$$\vec{R}=(R_h+R_c\sin\beta)\hat{a}_2+R_c(1-\cos\beta)\hat{a}_3-(x+\overline{u})\hat{e}_x+\overline{v}\hat{e}_\beta+\overline{w}\hat{e}_r \tag{2}$$

where $R_c$ and $R_h$ are the radii of the cylindrical panel and of the hub, respectively, and $\overline{u}$, $\overline{v}$, and $\overline{w}$ are the elastic deformations of the panel expressed in the curvilinear frame $[\hat{e}_x,\hat{e}_\beta,\hat{e}_r]$.

By denoting a first derivative with respect to time by $(\dot{\cdot})$ and the panel volume mass density by $\rho$, the kinetic energy of the system $\mathcal{T}$ is given as

$$\mathcal{T}=\frac{1}{2}I_h\dot{\theta}^2+\frac{1}{2}\rho\int_{v_p}\dot{\vec{R}}\cdot\dot{\vec{R}}dV_p. \tag{3}$$

The first term is due to the rotational inertia $I_h$ of the rigid hub and the second term is the contribution of the panel. The velocity $\dot{\vec{R}}$ is expanded in the hub body-fixed rotating frame as

$$\dot{\vec{R}}=\begin{Bmatrix}\hat{a}_1\\ \hat{a}_2\\ \hat{a}_3\end{Bmatrix}^T\begin{Bmatrix}\dot{u}\\ \dot{v}\cos\beta-\dot{w}\sin\beta-\dot{\theta}(R_c(1-\cos\beta)+(\overline{v}\sin\beta+\overline{w}\cos\beta))\\ \dot{v}\sin\beta+\dot{w}\cos\beta-\dot{\theta}(R_h+R_c\sin\beta+(\overline{v}\cos\beta-\overline{w}\sin\beta))\end{Bmatrix}. \tag{4}$$

The system potential energy $\mathcal{U}$ is due solely to the strain energy of the panel. This is written as

$$\mathcal{U}=\frac{1}{2}\int_{V_p}(\lfloor\underline{\epsilon}^T-\underline{\epsilon}_T^T\rfloor\underline{\sigma}+\underline{\gamma}^T\underline{\tau})dV_p \tag{5}$$

where $\underline{\epsilon}$ and $\underline{\epsilon}_T$ are vectors of the total in-plane and the thermal strains, respectively, $\underline{\sigma}$ is the vector of the in-plane stresses, and the transverse shear strains and stresses are, respectively, denoted by $\underline{\gamma}$ and $\underline{\tau}$. The Reissner-Mindlin plate theory displacement field is expressed as

$$\overline{u}(x,y,z,t)=u(x,y,t)-z\psi_x(x,y,t), \tag{6}$$

$$\overline{v}(x,y,z,t)=v(x,y,t)-z\psi_y(x,y,t), \tag{7}$$

$$\text{and}\quad \overline{w}(x,y,z,t)=w(x,y,t) \tag{8}$$

where $x$ and $y$ are as defined earlier, and $z$ is the position of the differential element along the normal to the midsurface. The von Kármán strain-displacement relations become

**Table 1 Material properties of graphite/epoxy**

| Parameter | Parameter Values |
|---|---|
| $E_{11}$ | 181.0 GPa |
| $E_{22}$ | 103.0 GPa |
| $G_{12}$ | 7.7 GPa |
| $G_{13}$ | 7.7 GPa |
| $G_{23}$ | 2.87 GPa |
| $\rho$ | $1.56\times10^3$ Kgm$^{-3}$ |
| $\nu_{12}$ | 0.28 |
| $\alpha_{11}$ | $2.08\times10^{-8}$ K$^{-1}$ |
| $\alpha_{22}$ | $22.5\times10^{-6}$ K$^{-1}$ |

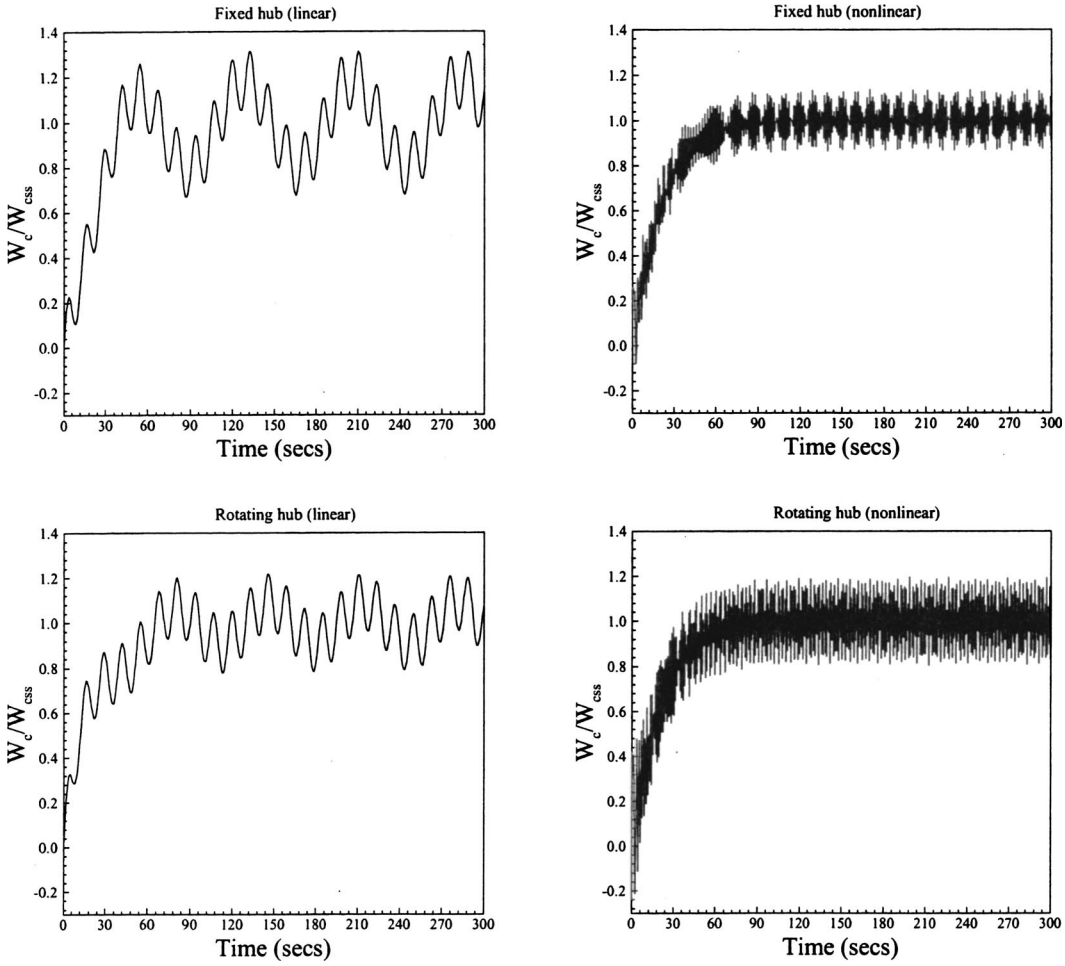


**Fig. 2 Effect of nonlinearity on elastic displacements $(0/90/0/90/0)_s$**

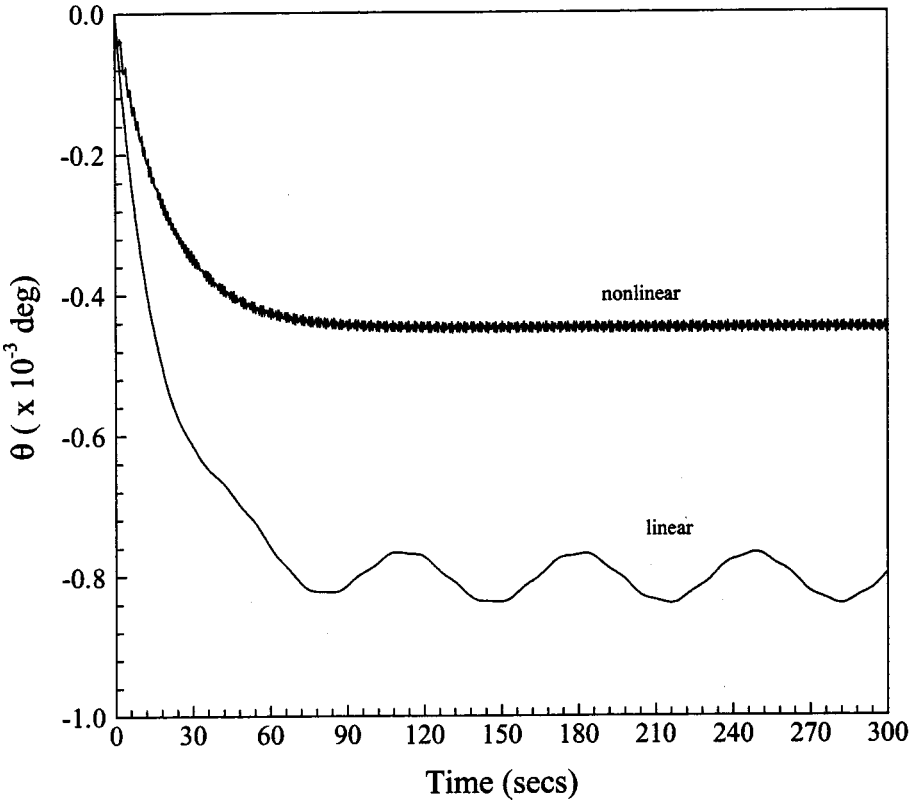


**Fig. 3 Effect of nonlinearity on hub angular rotation $(0/90/0/90/0)_s$**

$$\underline{\epsilon}=\begin{Bmatrix}\epsilon_{xx}\\ \epsilon_{yy}\\ \gamma_{xy}\end{Bmatrix}=\begin{Bmatrix}\dfrac{\partial u}{\partial x}\\ \dfrac{\partial v}{\partial y}+\dfrac{w}{R_c}\\ \dfrac{\partial u}{\partial y}+\dfrac{\partial v}{\partial x}\end{Bmatrix}-z\begin{Bmatrix}\dfrac{\partial \psi_x}{\partial x}\\ \dfrac{\partial \psi_y}{\partial y}\\ \dfrac{\partial \psi_x}{\partial y}+\dfrac{\partial \psi_y}{\partial x}\end{Bmatrix}+\frac{1}{2}\begin{Bmatrix}\left(\dfrac{\partial w}{\partial x}\right)^2\\ \left(\dfrac{\partial w}{\partial y}\right)^2\\ 2\dfrac{\partial w}{\partial x}\dfrac{\partial w}{\partial y}\end{Bmatrix}$$

$$\underline{\gamma}=\begin{Bmatrix}\gamma_{yz}\\ \gamma_{xz}\end{Bmatrix}\begin{Bmatrix}\dfrac{\partial w}{\partial y}-\psi_y-\dfrac{v}{R_c}\\ \dfrac{\partial w}{\partial x}-\psi_x\end{Bmatrix}. \tag{9}$$

With the direct correspondence to Eq. (9), the total in-plane strain vector $\underline{\epsilon}$ is rewritten as

$$\underline{\epsilon}=\underline{\epsilon}_L+z\underline{\kappa}+\underline{\kappa}_N$$

where the first term is the linear strain component, the second term denotes curvatures and the third term represents the nonlinear strains. The constitutive law relating the stresses and strains is, [9],

$$\underline{\sigma}=\overline{\mathbf{Q}}(\underline{\epsilon}-\underline{\epsilon}_T) \quad \text{and} \quad \underline{\tau}=\overline{\mathbf{Q}}_s\underline{\gamma}, \tag{10}$$

where all the components are referenced to the geometric or structural axes. Equation (10) is substituted into Eq. (5) and the expression resulting, after some algebra, can be written as

$$\begin{aligned}\mathcal{U}=&\frac{1}{2}\int_{\Omega_p}\begin{Bmatrix}\underline{\epsilon}_L\\ \underline{\kappa}\\ \underline{\gamma}\end{Bmatrix}^T\begin{bmatrix}\mathbf{A}&\mathbf{B}&0\\ \mathbf{B}&\mathbf{D}&0\\ 0&0&\mathbf{A}_s\end{bmatrix}\begin{Bmatrix}\underline{\epsilon}_L\\ \underline{\kappa}\\ \underline{\gamma}\end{Bmatrix}d\Omega_p\\ &-\int_{\Omega_p}\begin{Bmatrix}\underline{\epsilon}_L\\ \underline{\kappa}\end{Bmatrix}^T\begin{Bmatrix}\underline{N}_T\\ \underline{M}_T\end{Bmatrix}d\Omega_p\\ &+\frac{1}{2}\int_{\Omega_p}\begin{Bmatrix}\underline{\epsilon}_L\\ \underline{\kappa}\\ \underline{\epsilon}_N\end{Bmatrix}^T\begin{bmatrix}0&0&\mathbf{A}\\ 0&0&\mathbf{B}\\ \mathbf{A}&\mathbf{B}&\mathbf{A}\end{bmatrix}\begin{Bmatrix}\underline{\epsilon}_L\\ \underline{\kappa}\\ \underline{\epsilon}_N\end{Bmatrix}d\Omega_p\end{aligned} \tag{11}$$

where the thermal resultant forces and moments are denoted by $\underline{N}_T$ and $\underline{M}_T$, respectively. (Consult the Appendix for any matrix that is undefined in the text.) The component of the potential energy expression that is quadratic in the thermal strains is ignored since it does not contribute to the final variational form. The vector product of the nonlinear components of the total in-plane strains and the thermal strains is also ignored.

In anticipation of a finite element based formulation, the field variables of the system are identified as the rigid-body rotation $\theta$, and the displacements due to the panel flexibility $u$, $v$, $w$, $\psi_x$, $\psi_y$. A 16-node isoparametric Lagrange bicubic element is implemented, [10,11]. The variables are interpolated as

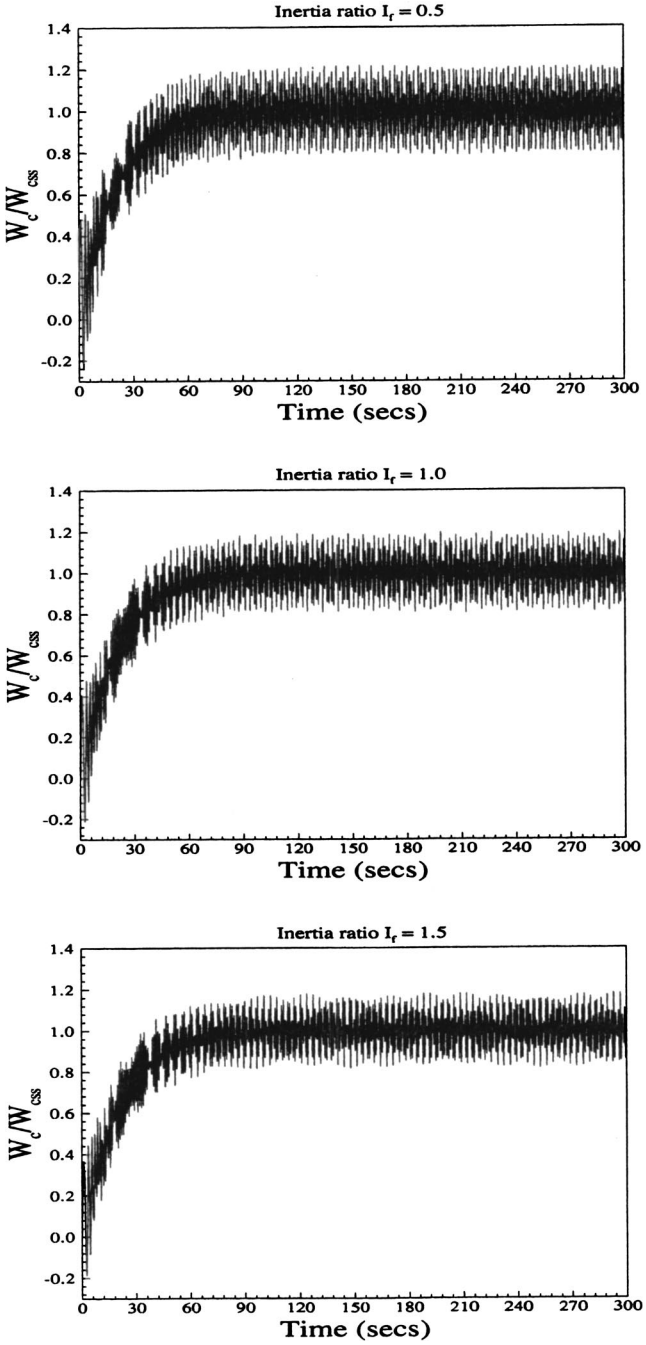


**Fig. 4 Effect of hub inertia on elastic displacements $(0/90/0/90/0)_s$**

$$\begin{Bmatrix}\theta\\ u^{(e)}\\ v^{(e)}\\ w^{(e)}\\ \psi_x^{(e)}\\ \psi_y^{(e)}\end{Bmatrix}=\begin{bmatrix}1&0&0&0&0&0\\ 0&\underline{N}^T&0&0&0&0\\ 0&0&\underline{N}^T&0&0&0\\ 0&0&0&\underline{N}^T&0&0\\ 0&0&0&0&\underline{N}^T&0\\ 0&0&0&0&0&\underline{N}^T\end{bmatrix}\begin{Bmatrix}\theta\\ \underline{u}^e\\ \underline{v}^{(e)}\\ \underline{w}^{(e)}\\ \underline{\psi}_x^{(e)}\\ \underline{\psi}_y^{(e)}\end{Bmatrix} \tag{12}$$

where $\underline{u}^{(e)}$ is a column vector of an element nodal axial displacements and the other entries are identified accordingly; $\underline{N}$ is a column vector of shape interpolation functions. In the sequel, the row vector of element nodal displacements $\lfloor \underline{u}^{(e)^T}\ \underline{v}^{(e)^T}\ \underline{w}^{(e)^T}\ \underline{\psi}_x^{(e)^T}\ \underline{\psi}_y^{(e)^T}\rfloor$ is denoted by $\underline{q}^{(e)^T}$.

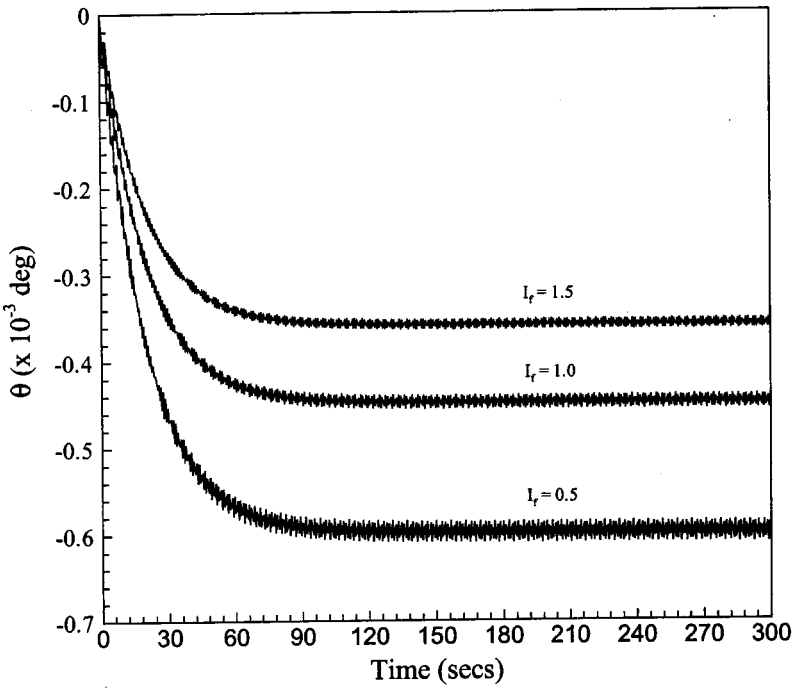


**Fig. 5 Effect of hub inertia on hub angular rotation $(0/90/0/90/0)_s$**

The kinetic energy of a finite element $\mathcal{T}^{(e)}$ is obtained by substituting the field variables approximations Eq. (12) into Eq. (4), and using the resulting expression in Eq. (3), where the rotatory inertia contribution of the hub is ignored for now, to obtain

$$\mathcal{T}^{(e)}=\frac{1}{2}\dot{\underline{q}}^{(e)^T}\mathbf{M}_{qq}^{(e)}\dot{\underline{q}}^{(e)}+\dot{\underline{q}}^{(e)^T}\underline{M}_{\theta_q}^{(e)}\dot{\theta} \tag{13}$$

with

$$\underline{M}_{\theta_q}^{(e)}=\rho\int_{V_p^{(e)}}\begin{Bmatrix}\underline{0}\\ \underline{N}(R_h\sin\beta+R_c(1-\cos\beta))\\ \underline{N}(R_h\cos\beta+R_c\sin\beta)\\ \underline{0}\\ \underline{0}\end{Bmatrix}dV_p^{(e)}.$$

Note that only terms that are quadratic in the field variables and their derivatives are retained in the kinetic energy expression. Hence terms involving $\dot{\theta}^2\overline{v}$, $\dot{\theta}^2\overline{w}$, $\dot{\theta}^2\overline{v}^2$, $\dot{\theta}^2\overline{w}^2$ are ignored. This ensures a time-independent inertia matrix.

The potential energy of an element $\mathcal{U}^{(e)}$ is derived by substituting Eq. (12) into Eq. (5). The nonlinear contributions are then expanded using the technique of Rajeskaran and Murray [12]. The method provides consistent matrices and is more general than that suggested by Mallet and Marcal [13,14]. The resulting potential energy of an element may be written as

$$\mathcal{U}^{(e)}=\frac{1}{2}\underline{q}^{(e)^T}\left(\mathbf{K}^{(e)}+\frac{1}{3}\mathbf{K}_1^{(e)}+\frac{1}{6}\mathbf{K}_2^{(e)}\right)\underline{q}^{(e)^T}-\underline{q}^{(e)^T}\underline{F}_T^{(e)} \tag{14}$$

where $\mathbf{K}^{(e)}$ is the usual displacement independent stiffness matrix obtained in a linear analysis, $\mathbf{K}_1^{(e)}$ is a component of the overall stiffness matrix that is linearly dependent upon displacements, $\mathbf{K}_2^{(e)}$ is the component that is quadratic in the displacements, and $\underline{F}_T^{(e)}$ is the vector of consistent thermal loads.

The governing equations for a typical element are obtained via Hamilton's principle by using the kinetic and potential energies, Eqs. (13) and (14). These are expressed in matrix notational format as

$$\begin{bmatrix}M_{\theta\theta}^{(e)} & \underline{M}_{\theta_q}^{(e)^T}\\ \underline{M}_{\theta_q}^{(e)} & \mathbf{M}_{qq}^{(e)}\end{bmatrix}\begin{Bmatrix}\ddot{\theta}\\ \ddot{\underline{q}}^{(e)}\end{Bmatrix}+\begin{bmatrix}0 & \underline{0}^T\\ \underline{0} & \mathbf{K}_{qq}^{(e)}\end{bmatrix}\begin{Bmatrix}\theta\\ \underline{q}^{(e)}\end{Bmatrix}=\begin{Bmatrix}0\\ \underline{F}_T^{(e)}\end{Bmatrix} \tag{15}$$

where

$$\mathbf{K}_{qq}^{(e)}=\mathbf{K}^{(e)}+\frac{1}{2}\mathbf{K}_1^{(e)}+\frac{1}{3}\mathbf{K}_2^{(e)}.$$

The above elemental governing equations are assembled in the usual finite element method manner (see Bathe [10]) to obtain the global system of governing equations which can be written as

$$\mathbf{M}_G\ddot{\underline{\mathbf{p}}}_G+\mathbf{K}_G\underline{\mathbf{p}}_G=\underline{\mathbf{F}}_G \tag{16}$$

where $\mathbf{M}_G$ and $\mathbf{K}_G$ are the global inertia and stiffness matrices, respectively, $\underline{\mathbf{F}}_G$ is the global force vector, and $\underline{\mathbf{p}}_G$ is the vector of global nodal field variables. The expanded form of the global equation Eq. (16) is identical to the governing equations for a finite element, Eq. (15). The difference is that the $M_{\theta\theta}$ term of the global inertia matrix includes the hub inertia. Hence

$$M_{\theta\theta}=I_h+\sum_{(e)}M_{\theta\theta}^{(e)}$$

The scenario in which the rotational motion of the hub is fully restrained is governed by an identical system of equations with the exclusion of rotation $(\theta,\ddot{\theta})$ contributions.

## 3 Numerical Simulation and Discussion

The numerical simulations are based on 10-ply laminates composed of graphite/epoxy laminae. The thickness of each lamina is 0.125 mm. The mechanical and thermal properties are given in Table 1. A typical system comprises a cylindrical panel of radius $R_c=10$ m and height $H_c=10$ m, a hub radius $R_h=1$ m, with an exponential time varying temperature profile with thermal time constant $T_t=20$ secs and steady-state temperature $\Delta T_{ss}=20$ K. The hub inertia is related to the inertia of the panel about the rotating axis of the hub (i.e., hub center) by a constant of propor-

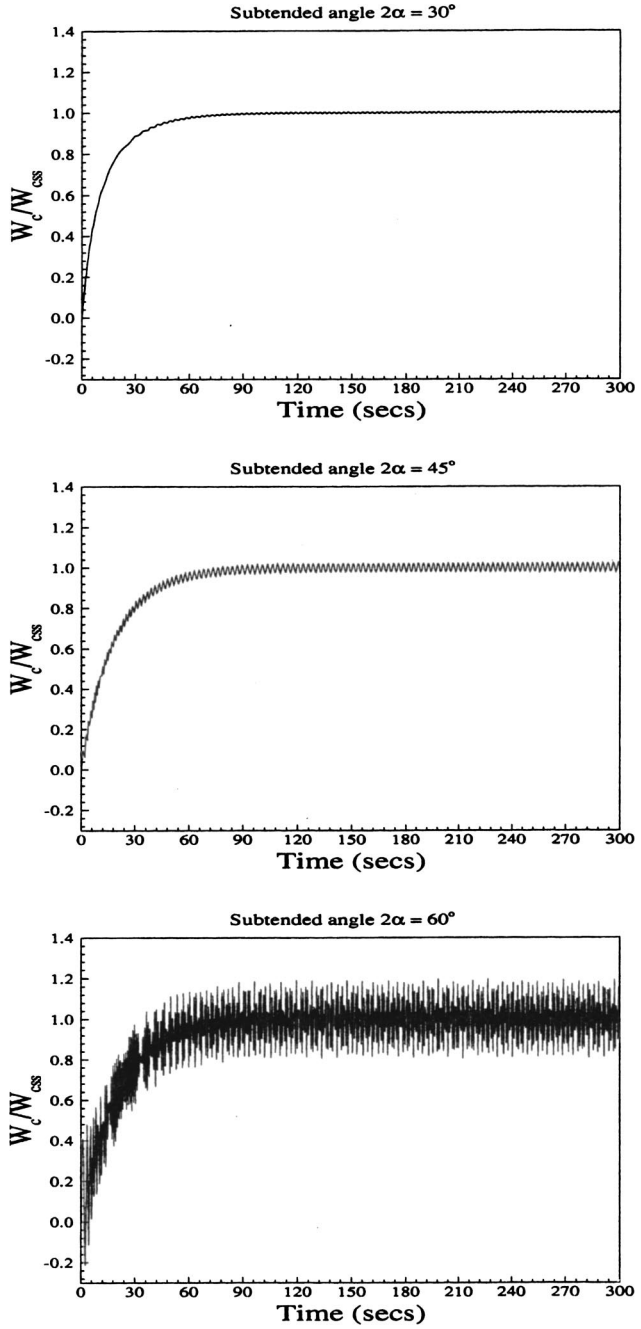


**Fig. 6 Effect of panel shallowness on elastic displacements $(0/90/0/90/0)_s$**

tionality $I_f$. The midspan linear (nonlinear) deformations are normalized with respect to the steady-state linear (nonlinear) quasi-static deformation.

**Effect of Geometric Nonlinearity and Hub Rotation.** The effects of hub rotation and geometric nonlinearity are investigated for a system with a cylindrical panel that has a subtended angle $2\alpha = 60°$ and a hub inertia constant of proportionality $I_f = 1.0$. The ply stacking sequence is $(0/90/0/90/0)_s$. Figure 2 depicts the normalized midspan (this location is identified on Fig. 1) deformation of the cylindrical panel for the fixed and rotating hub cases for both linear and nonlinear formulations. The linear plots show that the peak-to-peak steady-state deformation in the fixed hub case is higher than that of the rotating hub scenario. This observation is explained by the transfer of energy between the hub motion and the panel deformation. An FFT analysis of the fixed hub data reveals a dominant frequency of $1.270 \times 10^{-2}$ Hz, which is equivalent to the first mode of the panel. A similar analysis of the rotating hub data indicates a dominant rigid-body motion that is followed by a frequency of $7.714 \times 10^{-2}$ Hz. This frequency is the same as that of the second most dominant mode in the fixed hub scenario. The steady-state quasi-static deformation is 86.3 $\mu$m.

The inclusion of the geometric nonlinearity yields reduced deformation and increased frequency—0.951 Hz for the fixed hub scenario and 0.823 Hz for the rotating hub case—the higher frequencies are indicative of stiffening. The frequencies are provided to facilitate a more quantitative analysis even though an FFT is not advisable for nonlinear processes. The steady-state quasi-static deformation is 14.5 $\mu$m. Unlike the linear scenario, a higher peak-to-peak steady-state deformation is observed with the rotating hub. This is in accord with the FFT analysis results which show a lower frequency for the nonlinear rotating case; hence the fixed hub case is a stiffer scenario.

By defining dynamic amplification as the ratio of the maximum steady-state transient deformation to the steady-state quasistatic deformation, the linear fixed hub case is observed to yield the most amplification while the nonlinear fixed hub provides the least amplification. The amplification with the nonlinear rotating hub case is comparable to that of linear rotating hub. This implies that, for the present configuration, inertia effect is more pronounced in the fixed hub case.

The profile of the hub angle of rotation is depicted in Fig. 3. The hub rotation decreases while its frequency increases in the presence of the nonlinear formulation.

In summary, the inclusion of the geometric nonlinearity has a noticeable effect on the system vibration irrespective of whether the rotation motion of the hub is fully or partially restrained. Given that the hub may never really be fixed in the literal sense, it is advisable to use the rotating hub model. Based on these observations, the subsequent simulations are for a nonlinear analysis.

**Effect of Hub Inertia.** The influence of the magnitude of the hub inertia relative to the inertia of the panel about the hub axis is examined by varying $I_f$ over 0.5, 1.0, and 1.5, respectively. The nondimensional midspan deformation and the hub rotation angle are depicted in Figs. 4 and 5, respectively. These results are in excellent agreement with intuition and it is imperative that they are reflected by the analysis.

In particular, the higher the inertia factor, the better the chances that the hub motion can indeed be adequately modeled as fixed. This is because the rotation of the hub tends to zero. It is therefore expected that the effect on the elastic deformation is such that the elastic response approaches that of the fixed hub, as can be inferred from from the results with $I_f = 1.0$ and 1.5 (see Fig. 4). These observations on the role of the relative magnitude of the inertia of the hub on the overall system response are also confirmed by Johnston and Thornton [8].

**Effect of Panel Shallowness.** In order to examine the effect of the panel shallowness, the subtended angle of the cylindrical panel is varied as $2\alpha = 30$ deg, 45 deg, and 60 deg, respectively, while the hub inertia factor $I_f = 1.0$. The respective steady-state quasi-static displacements are 110.1 $\mu$m, 54.3 $\mu$m, and 14.5 $\mu$m. The elastic response is depicted in Fig. 6 and the rigid-body angular rotation is depicted in Fig. 7. The shallowest panel exhibits both the least dynamic amplification and the least angular rotation.

## 4 Conclusion

The response of laminated symmetric cross-ply cylindrical panels that are suddenly exposed to heat flux is examined. Structural nonlinearity in the form of geometric nonlinearity is considered and is modeled via the von Kármń strain-displacement formula. The nonlinear governing equations are solved via the use of Newmark time-integration scheme and the Newton-Raphson method.

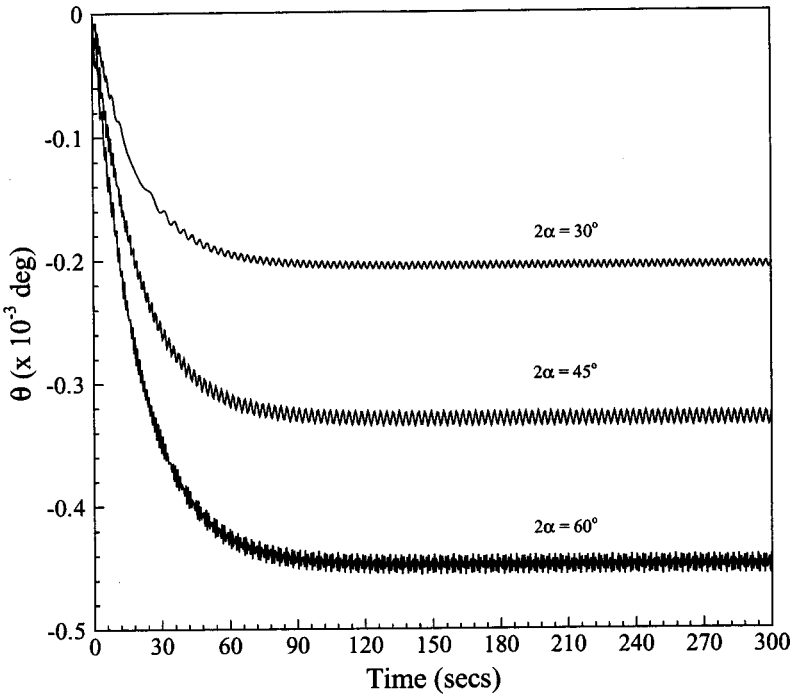


**Fig. 7 Effect of panel shallowness on hub angular rotation $(0/90/0/90/0)_s$**

It is observed that even though the angles rotated by the hub are small, the allowance for hub rotation significantly affects the response of the panel. The importance of this extra degree-of-freedom decreases, as expected, with increasing ratio of hub inertia to panel inertia. The shallowest panel investigated yields both the least dynamic amplification and the least hub rotation. It is instructive to implement nonlinear analysis in light of the enormous differences in response compared to the corresponding response from a linear analysis.

Finally, it is acknowledged that the results presented in this study are dependent upon laminate sequence. However, the investigation of this dependency is beyond the scope of this paper. This is primarily due to the numerous combinations of laminate sequence. The problem is perhaps best addressed in the context of optimization. To this end, an optimal laminate sequence is sought for appropriately defined objective function and constraints. While the $(0/90/0/90/0)_s$ laminate sequence is selected in this study in order to explore the simplifications associated with a symmetric, cross-ply laminate, it is easily manufactured with fabric.


## Acknowledgment

This work was partially funded by the Natural Sciences and Engineering Research Council (NSERC) of Canada. The authors are most grateful to the reviewers for their invaluable comments and suggestions.


## Appendix

$$\mathbf{M}_{qq}^{(e)} \overset{\Delta}{=} \int_A \begin{bmatrix} \mathcal{A}\underline{N}\underline{N}^T & 0 & 0 & -\mathcal{B}\underline{N}\underline{N}^T & 0 \\ 0 & \mathcal{A}\underline{N}\underline{N}^T & 0 & 0 & -\mathcal{B}\underline{N}\underline{N}^T \\ 0 & 0 & \mathcal{A}\underline{N}\underline{N}^T & 0 & 0 \\ -\mathcal{B}\underline{N}\underline{N}^T & 0 & 0 & \mathcal{D}\underline{N}\underline{N}^T & 0 \\ 0 & -\mathcal{B}\underline{N}\underline{N}^T & 0 & 0 & \mathcal{D}\underline{N}\underline{N}^T \end{bmatrix} dA \tag{A1}$$

$$(\mathcal{A},\mathcal{B},\mathcal{D}) = \rho \sum_{k=1}^{N} \int_{z_{k-1}}^{z_k} (1,z,z^2)\,dz$$

$$\mathbf{K}^{(e)} \overset{\Delta}{=} \int_A \mathbf{\Phi}^T \begin{bmatrix} \mathbf{A} & \mathbf{B} & 0 \\ \mathbf{B} & \mathbf{D} & 0 \\ 0 & 0 & \mathbf{A}_s \end{bmatrix} \mathbf{\Phi}\,dA \tag{A2}$$

$$(A_{ij},B_{ij},D_{ij}) = \sum_{k=1}^{N} \int_{z_{k-1}}^{z_k} \overline{Q}_{(k)_{ij}}(1,z,z^2)\,dz \quad \text{and}$$

$$\mathbf{A}_{s_{ij}} = \sum_{k=1}^{N} \int_{z_{k-1}}^{z_k} \overline{Q}_{s_{(k)ij}}\,dz$$

$$\mathbf{\Phi}^T \overset{\Delta}{=} \begin{bmatrix} \underline{N}_{,x} & 0 & \underline{N}_{,y} & 0 & 0 & 0 & 0 & 0 \\ 0 & \underline{N}_{,y} & \underline{N}_{,x} & 0 & 0 & 0 & -\dfrac{\underline{N}}{R_c} & 0 \\ 0 & \dfrac{\underline{N}}{R_c} & 0 & 0 & 0 & 0 & \underline{N}_{,y} & \underline{N}_{,x} \\ 0 & 0 & 0 & -\underline{N}_{,x} & 0 & -\underline{N}_{,y} & 0 & -\underline{N} \\ 0 & 0 & 0 & 0 & -\underline{N}_{,y} & -\underline{N},x & -\underline{N} & 0 \end{bmatrix} \tag{A3}$$

$$\mathbf{K}_1^{(e)} \overset{\Delta}{=} \int_A \left\{ \mathbf{G}_1^T \begin{bmatrix} \varphi_1+\varphi_2 & \zeta_1+\zeta_2 \\ \zeta_1+\zeta_2 & \varrho_1+\varrho_2 \end{bmatrix} \mathbf{G}_1 + \mathbf{G}_2^T[\mathbf{A}\ \mathbf{B}]\mathbf{G}_3 + \mathbf{G}_3^T[\mathbf{A}\ \mathbf{B}]^T\mathbf{G}_2 \right\} dA \tag{A4}$$

$$\mathbf{G}_1 \overset{\Delta}{=} \begin{bmatrix} 0 & 0 & \underline{N}_{,x}^T & 0 & 0 \\ 0 & 0 & \underline{N}_{,y}^T & 0 & 0 \end{bmatrix},$$

$$\mathbf{G}_2 \overset{\Delta}{=} \begin{bmatrix} 0 & 0 & w_{,x}\underline{N}_{,x}^T & 0 & 0 \\ 0 & 0 & w_{,y}\underline{N}_{,y}^T & 0 & 0 \\ 0 & 0 & w_{,x}\underline{N}_{,y}^T + w_{,y}\underline{N}_{,x}^T & 0 & 0 \end{bmatrix} \tag{A5}$$

$$\mathbf{G}_3 \overset{\Delta}{=} \begin{bmatrix} \underline{N}_{,x}^T & 0 & 0 & 0 & 0 \\ 0 & \underline{N}_{,y}^T & \dfrac{\underline{N}^T}{R_c} & 0 & 0 \\ \underline{N}_{,y}^T & \underline{N}_{,x}^T & 0 & 0 & 0 \\ 0 & 0 & 0 & -\underline{N}_{,x}^T & 0 \\ 0 & 0 & 0 & 0 & -\underline{N}_{,y}^T \\ 0 & 0 & 0 & -\underline{N}_{,y}^T & -\underline{N}_{,x}^T \end{bmatrix} \tag{A6}$$

$$\begin{Bmatrix} \varphi_1 \\ \varrho_1 \\ \zeta_1 \end{Bmatrix} \overset{\Delta}{=} \begin{Bmatrix} A_{11}u_{,x} + A_{12}\left(v_{,y} + \dfrac{w}{R_c}\right) + A_{16}(u_{,y} + v_{,x}) \\ A_{12}u_{,x} + A_{22}\left(v_{,y} + \dfrac{w}{R_c}\right) + A_{26}(u_{,y} + v_{,x}) \\ A_{16}u_{,x} + A_{26}\left(v_{,y} + \dfrac{w}{R_c}\right) + A_{66}(u_{,y} + v_{,x}) \end{Bmatrix} \tag{A7}$$

$$\begin{Bmatrix} \varphi_2 \\ \varrho_2 \\ \zeta_2 \end{Bmatrix} \overset{\Delta}{=} -\begin{Bmatrix} B_{11}\psi_{x,x} + B_{12}\psi_{y,y} + B_{16}(\psi_{x,y} + \psi_{y,x}) \\ B_{12}\psi_{x,x} + B_{22}\psi_{y,y} + B_{26}(\psi_{x,y} + \psi_{y,x}) \\ B_{16}\psi_{x,x} + B_{26}\psi_{y,y} + B_{66}(\psi_{x,y} + \psi_{y,x}) \end{Bmatrix} \tag{A8}$$

$$\mathbf{K}_2^{(e)} \overset{\Delta}{=} \int_A \left\{ \mathbf{G}_2^T \mathbf{A} \mathbf{G}_2 + \frac{1}{2}\mathbf{G}_1^T \begin{bmatrix} \chi_1 & \chi_3 \\ \chi_3 & \chi_2 \end{bmatrix} \mathbf{G}_1 \right\} dA \tag{A9}$$

$$\begin{Bmatrix} \chi_1 \\ \chi_2 \\ \chi_3 \end{Bmatrix} \overset{\Delta}{=} \begin{Bmatrix} A_{11}w_{,x}^2 + A_{12}w_{,y}^2 + 2A_{16}w_{,x}w_{,y} \\ A_{12}w_{,x}^2 + A_{22}w_{,y}^2 + 2A_{26}w_{,x}w_{,y} \\ A_{16}w_{,x}^2 + A_{26}w_{,y}^2 + 2A_{66}w_{,x}w_{,y} \end{Bmatrix} \tag{A10}$$

$$F_T^{(e)} \overset{\Delta}{=} \int_A \begin{bmatrix} \underline{N}_{,x} & 0 & \underline{N}_{,y} & 0 & 0 & 0 \\ 0 & \underline{N}_{,y} & \underline{N}_{,x} & 0 & 0 & 0 \\ 0 & \dfrac{\underline{N}}{R_c} & 0 & 0 & 0 & 0 \\ 0 & 0 & 0 & -\underline{N}_{,x} & 0 & -\underline{N}_{,y} \\ 0 & 0 & 0 & 0 & -\underline{N}_{,y} & -\underline{N},x \end{bmatrix} \begin{Bmatrix} \underline{N}_T \\ \underline{M}_T \end{Bmatrix} dA \tag{A11}$$

$$(\underline{N}_T, \underline{M}_T) = \sum_{k=1}^{N} \int_{z_{k-1}}^{z_k} \underline{\mathbf{Q}}_{(k)} \alpha_k \Delta T(1,z)\, dz$$

## References


[1] Tauchert, T. R., 1991, "Thermally Induced Flexure, Buckling, and Vibration of Plates," Appl. Mech. Rev., **44**(8), pp. 347–360.

[2] Thornton, E. A., 1992, "Thermal Structures: Four Decades of Progress," J. Aircr., **29**(3), pp. 485–498.

[3] Heppler, G. R., 1986, "On the Analysis of Shell Structures Subjected to a Blast Environment: A Finite Element Approach," University of Toronto Institute for Aerospace Studies Report No. 302, Feb.

[4] Chandrashekhara, K., and Tenneti, R., 1994, "Non-linear Static and Dynamic Analysis of Heated Laminated Plates: A Finite Element Approach," Compos. Technol., **51**, pp. 85–94.

[5] Chang, J-S. C., and Shyong, J-W., 1994, "Thermally Induced Vibration of Laminated Circular Cylinderical Shell Panels," Compos. Technol., **51**, pp. 419–427.

[6] Feldman, E., and Gilat, R., 1999, "On the Dynamic Response of Metal Matrix Composite Panels to Uniform Temperature Loading," Compos. Struct., **47**(1–4), pp. 619–624.

[7] Librescu, L., and Lin, W., 1997, "Vibration of Thermomechanically Loaded Flat and Curved Panels Taking Into Account Geometric Imperfections and Tangential Edge Restraints," Int. J. Solids Struct., **34**(17), pp. 2161–2181.

[8] Johnston, J. D., and Thornton, E. A., 1998, "Thermally Induced Attitude Dynamics of a Spacecraft With a Flexible Appendage," J. Guid. Control Dyn., **21**(4), pp. 581–587.

[9] Jones, R. M., 1975, *Mechanics of Composite Materials*, Scripta Book Company, Washington, DC.

[10] Bathe, K-J., 1996, *Finite Element Procedures*, Prentice-Hall, Englewood Cliffs, NJ.

[11] Heppler, G. R., and Hansen, J. S., 1986, "A Mindlin Element for Thick and Deep Shells," Comput. Methods Appl. Mech. Eng., **54**, pp. 21–47.

[12] Rajeskaran, S., and Murray, D. W., 1973, "Incremental Finite Element Matrices," J. Struct. Div. ASCE, **99**(ST12), pp. 2423–2438.

[13] Mallet, R. H., and Marcal, P. V., 1968, "Finite Element Analysis of Nonlinear Structures," J. Struct. Div. ASCE, **94**(ST9), pp. 2081–2105.

[14] Mallet, R. H., and Marcal, P. V., 1970, closure and errata to "Finite Element Analysis of Nonlinear Structures," J. Struct. Div. ASCE, **96**(ST1), pp. 132–133.

# Thermoelastic Instability of Two-Conductor Friction System Including Surface Roughness

**J. Y. Jang**

**M. M. Khonsari**[1]
Fellow ASME
Dow Chemical Endowed Chair in Rotating Machinery,
e-mail: khonsari@me.lsu.edu

Department of Mechanical Engineering,
Louisiana State University,
Baton Rouge, LA 70803

*A model is developed to investigate the mechanism of thermoelastic instability (TEI) in tribological components. The model consists of two thermally conducting bodies of finite thickness undergoing sliding contact. Appropriate governing equations are derived to predict the critical speed beyond which the TEI is likely to occur. This model takes into account the surface roughness characteristics of the contacting bodies as well as the thermal contact conductance at the interface. Analytical expressions are provided for the special cases neglecting the disk thickness and the thermal contact conductance. An extensive series of parametric simulations and discussion of the implication of the results are also presented. The simulations show that the difference in material properties and geometry of the two conducting bodies has a pronounced influence on the critical speed. A special case of the model shows that the threshold of TEI critical speed is pushed to a much higher level when the conducting bodies have identical material properties and are geometrically symmetric. It is also shown that the perturbed wave generally tends to move with the body with higher thermal conductivity.* [DOI: 10.1115/1.1629756]

## 1 Introduction

High-speed sliding contact between nominally flat surfaces is associated with thermoelastic instability (TEI) where pressure perturbation appears in the contact area. Such instability may lead to the formation of hot spots which are thought to be a consequence of local thermoelastic expansion and high contact pressures. TEI is commonly observed in mechanical seals, brakes, and clutches.

There is a rich volume of archival research publications dealing with TEI. Barber [1,2] first explained the thermoelastic instability and the formation of hot spots in railway brakes. Dow and Burton [3] used the perturbation method to determine the critical speed for TEI. Their work was extended by Burton et al. [4], Kilaparti and Burton [5], Banerjee and Burton [6], Lebeck [7], Barber et al. [8], Lee and Barber [9], Du et al. [10], Jang and Khonsari [11–13], and Yi et al. [14] in applications involving mechanical seals, braking systems, and wet clutch assemblies. In all of these applications, TEI manifests itself in the form of macroscopic hot spots.

Many applications are classified as the so-called conductor-insulator system where the stationary component (brake pad, mating ring in seals, and friction disk in clutches) has a low enough thermal conductivity to be classified as an insulator. In contrast, the rotating component (separator in wet clutches and primary ring in seals) possesses a much greater thermal conductivity. The conductor-insulator model simplifies the analysis because all of the heat generated goes directly into the conductor and nothing into the insulator.

Burton et al. [4] showed that the predicted critical speed based on the insulator-conductor assumption is in good agreement with that of the two-conductor system only for the case that one of the friction pair is made of glass. According to Lee and Barber [9] the critical speed based on Burton's semi-infinite analysis with plane-strain hypothesis yields a critical speed that is beyond what is observed experimentally in automotive disk brake systems. They attributed this phenomenon, in part, to neglecting the finite thickness of the conducting body.

Another important factor is surface roughness. Jang and Khonsari [11] showed that the critical speed is dependent upon the load applied on the system by considering the surface roughness. Consideration of surface roughness with proper thermal analysis enables one to account for the real area of contact between two surfaces. Therefore, to predict the realistic critical speed, a two-conductor system of finite thickness considering the surface roughness and the thermal contact resistance should be taken into account.

In this paper, we develop a TEI model for a friction pair consisting of two conducting bodies with rough surfaces. Each body has a finite thickness. The model is a two-dimensional problem where the lateral dimension is neglected. This paper concentrates on the theoretical development of a generalized TEI formulation of the problem. The appropriate governing equations are derived and solved for the critical speed and the wave speed. This paper also presents an extensive series of parametric simulations together with the implications of the results.

## 2 Theory

A schematic of the model is shown in Fig. 1. The model consists of two finite conducting bodies with rough surfaces. Both bodies are of finite thickness with isotropic surface roughness because most engineering surfaces are isotropic. The nominal surface separation between two bodies is $h_o$. The lower surface is stationary and the upper surface undergoes a sliding motion at a constant speed, $U$. It is assumed that the system is operating under the steady state condition. We seek to determine the critical speed, $U_{cr}$, beyond which TEI occurs. For this purpose, a small surface wave representing a disturbance is imposed to the system. If the resultant surface deformation is smaller than the imposed surface disturbance, the system will be thermoelastically stable. Assuming that the disturbance wave has an absolute speed $c$ in the moving direction, the relative wave speeds with respect to the upper and lower bodies are $c_H$ and $c_L$, respectively. Since the lower body is stationary, its relative wave speed is equal to the absolute wave speed, i.e., $c_L = c$. It follows that $c_H = c_L - U$.

When two rough surfaces are brought into contact, they touch only a small fraction of the nominal area. The remaining gap is

[1]To whom correspondence should be addressed.

Contributed by the Applied Mechanics Division of THE AMERICAN SOCIETY OF MECHANICAL ENGINEERS for publication in the ASME JOURNAL OF APPLIED MECHANICS. Manuscript received by the ASME Applied Mechanics Division, February 19, 2003; final revision, February 26, 2003. Associate Editor: J. R. Barber. Discussion on the paper should be addressed to the Editor, Prof. Robert M. McMeeking, Department of Mechanical and Environmental Engineering University of California—Santa Barbara, Santa Barbara, CA 93106-5070, and will be accepted until four months after final publication of the paper itself in the ASME JOURNAL OF APPLIED MECHANICS.

  

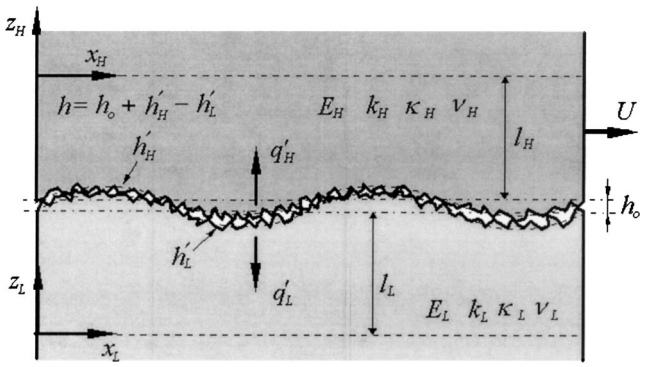


**Fig. 1 Schematic of the model**

filled with an interstitial fluid such as air with relatively low thermal conductivity, which tends to reduce the rate of heat conduction between the bodies. Because of this thermal resistance, the magnitude of the perturbed wave is changed and the wave is delayed at the interface. To characterize the behavior of the interface, a constant resistance is used.

**2.1 Temperature Distributions.** Let $T'$ denote the temperature perturbation brought about as a result of the imposed surface disturbance. To assess the effect of temperature disturbance on the thermoelastic behavior of the system, one must consider the transient heat conduction equation for each conducting body given below.

$$\frac{\partial^2 T'_i}{\partial x_i^2} + \frac{\partial^2 T'_i}{\partial z_i^2} = \frac{1}{\kappa_i}\frac{\partial T'_i}{\partial t}, \quad i = H, L \tag{1}$$

where $\kappa_i$ is the thermal diffusivity. The prime represents the perturbation. The subscript $i = H$ represents the upper body and the subscript $i = L$ represents lower body, respectively. Coordinate system $(x_i, z_i)$ is affixed in the midsection of body *i*. The proper boundary conditions for the temperature in each body are, [9]:

$$\frac{\partial T'_i}{\partial z_i} = 0 \quad \text{at } z_i = 0$$
$$T'_i = \mathrm{Im}[\,\theta_i e^{\beta t} e^{j\Omega(x_i - c_i t + \Delta_i)}] \quad \text{at the interface.} \tag{2}$$

The theory is based on the assumption of the symmetric mode, and this is particularly appropriate for a pair of disks in the multidisk clutch pack. Therefore, all properties are symmetric at the midplane of the disk thickness. Hence, adiabatic boundary condition at the midplane (at $z_i = 0$) is used in this analysis. In the circumferential direction, the periodic boundary condition is used. Parameter $\theta_i$ denotes the amplitude of the temperature disturbance at the surface of body *i*. Parameter $\Omega$ represents the wave number in the *x* direction. Parameter $\Delta_i$ is the wave phase shift of temperature between surfaces due to the thermal contact conductance $\mathfrak{I}_c$. The moving body has a phase shift of $\Delta_H = \Delta$ and that of the stationary body is $\Delta_L = 0$. Parameter $\beta$ represents the time exponent of growth of the temperature wave and is essentially the defining eigenvalue of the problem. If $\beta < 0$, the disturbance decays to zero and the system is stable, while for $\beta > 0$, the instability grows with time. The threshold of instability is defined by $\beta = 0$. The first adiabatic boundary condition in (2) takes advantage of the symmetry at $z_i = 0$. Therefore, inserting Eq. (2) into Eq. (1), the perturbed temperature distribution in each body is

$$T'_i = \mathrm{Im}\left[\theta_i \frac{\cosh b_i z_i}{\cosh b_i l_i} e^{\beta t} e^{j\Omega(x_i - c_i t + \Delta_i)}\right] \tag{3}$$

where

$$b_i = \xi_i + j a_i = \sqrt{\left(\Omega^2 + \frac{\beta}{\kappa_i}\right) - j\frac{\Omega c_i}{\kappa_i}}. \tag{4}$$

**2.2 Heat Generation at the Interface.** The frictional heat flux $q'_i$ at the interface entering either the upper or the lower body is given by

$$q'_i = \mathrm{Im}\left[\mp k_i \left.\frac{\partial T'_i}{\partial z_i}\right|_{z_i = \mp l_i}\right] = \Omega k_i \theta_i [\Re_{2i} \cos\Omega(x_i - c_i t + \Delta_i) + \Re_{1i} \sin\Omega(x_i - c_i t + \Delta_i)] e^{\beta t} \tag{5}$$

where $k_i$ represents the thermal conductivity and $l_i$ represents the half thickness of the body. In Eq. (5), the negative sign is for the upper body and the positive sign is for the lower body. The subscript $1i$ represents the amplitude of sine component, and the subscript $2i$ represents the amplitude of cosine component of body *i*, respectively. Dimensionless parameters $\Re_{1i}$ and $\Re_{2i}$ in Eq. (5) are

$$\Re_{1i} = \frac{\xi_i \sinh 2\xi_i l_i - a_i \sin 2a_i l_i}{\Omega(\cosh 2\xi_i l_i + \cos 2a_i l_i)}$$
$$\Re_{2i} = \frac{a_i \sinh 2\xi_i l_i + \xi_i \sin 2a_i l_i}{\Omega(\cosh 2\xi_i l_i + \cos 2a_i l_i)}. \tag{6}$$

Note that as discussed before the phase shift for the stationary body $\Delta_L = 0$. The total perturbed frictional heat generated due to the asperity contact pressure is

$$q' = q'_H + q'_L = f P'_H U = f P'_L U \tag{7}$$

where $f$ is a friction coefficient, and $P'_H$ and $P'_L$ are the perturbed contact pressure acting on the upper and lower surfaces, respectively. Equation (7) represents $P'_H = P'_L$ to satisfy equilibrium. Inserting Eq. (5) into (7), and solving for the sine and cosine amplitudes of the contact pressure acting on the lower surface, $P_{1L}$ and $P_{2L}$, yields

$$fUP_{1L} = [\Omega k_H \theta_H (\Re_{1H} \cos\Omega\Delta - \Re_{2H} \sin\Omega\Delta) + \Omega k_L \theta_L \Re_{1L}] e^{\beta t}$$
$$fUP_{2L} = [\Omega k_H \theta_H (\Re_{1H} \sin\Omega\Delta + \Re_{2H} \cos\Omega\Delta) + \Omega k_L \theta_L \Re_{2L}] e^{\beta t}. \tag{8}$$

For the special case that the thermal contact conductance is not considered, the phase shift becomes nil ($\Delta = 0$).

**2.3 Thermoelastic Deformations.** The particular solution of the thermoelastic problem for the plane strain can be obtained using the strain potential $\psi'_i$. To obtain a general solution that satisfies the boundary conditions, the isothermal solution should be superimposed on the particular solution, [15]. The isothermal solution can be obtained from the isothermal potentials $\phi'_i$ and $\omega'_i$. The boundary conditions for the elastic problem are

$$u_{zi}|_{z_i = 0} = 0$$
$$u_{zi}|_{z_i = \mp l_i} = h'_i$$
$$\sigma_{zi}|_{z_i = \mp l_i} = -P'_i$$
$$\tau_{xzi}|_{z_i = \mp l_i} = f P'_i \tag{9}$$

where $h'_i = h_{1i} \sin\Omega(x_i - c_i t + \Delta_i) + h_{2i} \cos\Omega(x_i - c_i t + \Delta_i)$ is the surface displacement perturbation of the each body. The functional form of $h'_i$ is assumed to have the amplitude of sine component, $h_{1i}$, and the amplitude of cosine component, $h_{2i}$. Using the boundary conditions (9) together with the functional form of the surface displacements, the displacements of the upper and lower surfaces are obtained. Combining all the equations above, the results of the displacement amplitudes of the upper and lower surfaces are

$$2G_H\Omega h_{1H}=\lambda_H(1-\Sigma_{2H})\Gamma_{2H}\theta_H e^{\beta t}+\lambda_H\Sigma_{1H}\Gamma_{4H}\theta_H e^{\beta t}+\Sigma_{1H}P_{1H}+f\Sigma_{2H}P_{2H}$$

$$2G_H\Omega h_{2H}=-\lambda_H(1-\Sigma_{2H})\Gamma_{1H}\theta_H e^{\beta t}+\lambda_H\Sigma_{1H}\Gamma_{3H}\theta_H e^{\beta t}+\Sigma_{1H}P_{2H}-f\Sigma_{2H}P_{1H}$$

$$2G_L\Omega h_{1L}=-\lambda_L(1-\Sigma_{2L})\Gamma_{2L}\theta_L e^{\beta t}-\lambda_L\Sigma_{1L}\Gamma_{4L}\theta_L e^{\beta t}-\Sigma_{1L}P_{1L}+f\Sigma_{2L}P_{2L}$$

$$2G_L\Omega h_{2L}=\lambda_L(1-\Sigma_{2L})\Gamma_{1L}\theta_L e^{\beta t}-\lambda_L\Sigma_{1L}\Gamma_{3L}\theta_L e^{\beta t}-\Sigma_{1L}P_{2L}-f\Sigma_{2L}P_{1L} \tag{10}$$

where

$$\lambda_i=\frac{\alpha_i E_i}{1-\nu_i};\quad \Sigma_{1i}=\frac{2(1-\nu_i)\sinh^2\Omega l_i}{\Omega l_i+\sinh\Omega l_i\cosh\Omega l_i};$$

$$\Sigma_{2i}=\frac{\Omega l_i-(1-2\nu_i)\sinh\Omega l_i\cosh\Omega l_i}{\Omega l_i+\sinh\Omega l_i\cosh\Omega l_i};$$

$$\Gamma_{1i}=\Omega\kappa_i\frac{(\beta a_i+\xi_i\Omega c_i)\sinh 2\xi_i l_i-(a_i\Omega c_i-\beta\xi_i)\sin 2a_i l_i}{(\beta^2+\Omega^2c_i^2)(\cosh 2\xi_i l_i+\cos 2a_i l_i)};\tag{11}$$

$$\Gamma_{2i}=\Omega\kappa_i\frac{(a_i\Omega c_i-\beta\xi_i)\sinh 2\xi_i l_i+(\beta a_i+\xi_i\Omega c_i)\sin 2a_i l_i}{(\beta^2+\Omega^2c_i^2)(\cosh 2\xi_i l_i+\cos 2a_i l_i)};$$

$$\Gamma_{3i}=\frac{\Omega^3\kappa_i c_i}{\beta^2+\Omega^2c_i^2};\quad \Gamma_{4i}=\frac{\Omega^2\kappa_i\beta}{\beta^2+\Omega^2c_i^2}.$$

The parameter $G_i$ represents the rigidity of the disks, and it is defined as $G_i=E_i/2(1+\nu_i)$. $\alpha_i$ is the coefficient of thermal expansion, $E_i$ is the elastic modulus, and $\nu_i$ is the Poisson's ratio, respectively.

**2.4 Asperity Contact Pressure.** The total surface separation therefore satisfies the following condition:

$$h=h_o+h'_H-h'_L \tag{12}$$

where $h'_H$ and $h'_L$ are the imposed surface disturbances on the upper and lower bodies, respectively. According to Natsumeda and Miyoshi [16], the mean pressure associated with an asperity contact $P_c$ is proportional to the ratio of the real area of contact to the nominal area, namely, $P_c=\mathcal{E}_c A_c$ where $\mathcal{E}_c$ is a proportionality constant, which we shall refer to as the "elastic modulus for contact." The real area of contact for two rough surfaces can be determined using the Greenwood-Tripp's theory, [17]. In this analysis, it is assumed that the model remains valid during sliding with presence of heat generation, and the asperities are distributed evenly leading to a uniform heat generation and surface deformation. Many engineering surfaces have a Gaussian or near-Gaussian height distribution. Using the polynomial density function, the real area of contact for $H\leqslant 3$ can be evaluated from

$$A_c=\frac{1}{128}(\pi\eta\gamma\sigma)^2\left[1-\left(\frac{H}{3}\right)\right]^6\left[64+69\left(\frac{H}{3}\right)+30\left(\frac{H}{3}\right)^2+5\left(\frac{H}{3}\right)^3\right] \tag{13}$$

where $H$ is the dimensionless surface separation, $H=h/\sigma$. For the case of $H>3$ the real area of contact becomes nil. The perturbed real area of contact, $A'_c$, is determined by inserting Eq. (12) into Eq. (13) and neglecting higher order terms. The result, using $H_o=h_o/\sigma$, is

$$A'_c=(\pi\eta\gamma\sigma)^2\varphi_c\frac{h'_H-h'_L}{h_o} \tag{14}$$

where

$$\varphi_c=\frac{1}{128}\left(\frac{H_o}{3}\right)\left[1-\left(\frac{H_o}{3}\right)\right]^5\left[315+423\left(\frac{H_o}{3}\right)+225\left(\frac{H_o}{3}\right)^2+45\left(\frac{H_o}{3}\right)^3\right]. \tag{15}$$

The perturbed asperity contact pressure is obtained from Eq. (14). The result is

$$P'_c=\chi\varphi_c\frac{h'_H-h'_L}{h_o} \tag{16}$$

where the surface characteristic parameter is defined as

$$\chi=(\pi\eta\gamma\sigma)^2\mathcal{E}_c \tag{17}$$

where $\eta$ is the asperity density, $\gamma$ is the asperity tip radius, and $\sigma$ is the surface roughness ($rms$). Equilibrium requires that $P'_c=P'_L=P'_H$. The relationships between the amplitudes of pressures and surface deformations are obtained.

$$P_{1H}=-\frac{\chi\varphi_c}{h_o}[h_{1H}-h_{1L}\cos\Omega\Delta-h_{2L}\sin\Omega\Delta]$$

$$P_{2H}=-\frac{\chi\varphi_c}{h_o}[h_{2H}+h_{1L}\sin\Omega\Delta-h_{2L}\cos\Omega\Delta] \tag{18}$$

In the coordinate system $(x,z)$ moving with the perturbed field, $P'_H$ and $P'_L$ obey the following relationship:

$$P_{1H}\sin\Omega(x+\Delta)+P_{2H}\cos\Omega(x+\Delta)=P_{1L}\sin\Omega x+P_{2L}\cos\Omega x. \tag{19}$$

After separating the sine and cosine components in Eq. (19), we obtain the following expressions for the amplitudes of $P'_H$ and $P'_L$.

$$P_{1H}=P_{1L}\cos\Omega\Delta+P_{2L}\sin\Omega\Delta$$

$$P_{2H}=-P_{1L}\sin\Omega\Delta+P_{2L}\cos\Omega\Delta \tag{20}$$

Note that if the two bodies were in perfect contact, then the thermal contact conductance would be nil and the corresponding temperature lag would vanish, i.e., $\Delta=0$. Equations (20) would reduce to simply $P_{1L}=P_{1H}$ and $P_{2L}=P_{2H}$, as expected.

**2.5 Thermal Contact Conductance.** It is assumed that all the heat generated is conducted into both surfaces by the thermal contact conductance, $\mathfrak{I}_c$. This parameter is simply the inverse of the thermal contact resistance. The relationship between the frictional heat and the temperature is

$$\mathfrak{I}_c(T'_H-T'_L)=q'_L-q'_H. \tag{21}$$

Inserting Eqs. (3) and (5) into Eq. (21) and separating sine and cosine terms, the following expressions are obtained:

$$\frac{\theta_L}{\theta_H}=\frac{\mathfrak{I}_c\cos\Omega\Delta+\Omega k_H(\mathfrak{R}_{1H}\cos\Omega\Delta-\mathfrak{R}_{2H}\sin\Omega\Delta)}{\mathfrak{I}_c+\Omega k_L\mathfrak{R}_{1L}}$$

$$\tan\Omega\Delta=\frac{\Omega k_L\mathfrak{R}_{2L}(\mathfrak{I}_c+\Omega k_H\mathfrak{R}_{1H})-\Omega k_H\mathfrak{R}_{2H}(\mathfrak{I}_c+\Omega k_L\mathfrak{R}_{1L})}{(\mathfrak{I}_c+\Omega k_L\mathfrak{R}_{1L})(\mathfrak{I}_c+\Omega k_H\mathfrak{R}_{1H})+\Omega^2k_Lk_H\mathfrak{R}_{2L}\mathfrak{R}_{2H}}. \tag{22}$$

Equations (22) represent the ratio of surface temperature amplitudes and the phase shift of the wave at the interface. If $\mathfrak{I}_c\to\infty$, then the two bodies are in "perfect" contact, and there is no thermal contact resistance. Therefore, the ratio of temperature amplitudes $\theta_L/\theta_H=1$ and the phase shift $\Delta=0$ leading to $T'_H=T'_L$. Contact resistance is indeed a difficult parameter to measure. In this paper, we present simulations over a wide range of contact resistance values in an attempt to cover different applications that one may be interested in. The results presented are also useful in

analyzing the limiting case, for example when $\Delta \to 0$ and $\theta^* \to 1$. Typically, for the seal the contact resistance is estimated as $10^4$ W/m$^2$ K, [7].

**2.6 Thermoelastic Instability.** Combining Eqs. (8), (10), (20), and (18) and separating the sine and cosine terms, we will obtain two equations to be solved for the critical speed and the wave speed. Before processing, we begin by defining the following set of dimensionless parameters:

$$\overline{U}=\frac{U}{\Omega\kappa_H};\quad \overline{c_i}=\frac{c_i}{\Omega\kappa_i};\quad \overline{\beta}=\frac{\beta}{\Omega^2\kappa_H};\quad \overline{\xi_i}=\frac{\xi_i}{\Omega};\quad \overline{a_i}=\frac{a_i}{\Omega}. \tag{23}$$

Using these dimensionless parameters, the following coupled equations are obtained:

$$\begin{aligned}
\Lambda_T\Bigg\{&[(\Gamma_{1H}\sin\Omega\Delta+\Gamma_{2H}\cos\Omega\Delta)(1-\Sigma_{2H})-(\Gamma_{3H}\sin\Omega\Delta\\
&-\Gamma_{4H}\cos\Omega\Delta)\Sigma_{1H}]\frac{1}{1-\nu_H}+\frac{\theta_L}{\theta_H}[\Gamma_{2L}(1-\Sigma_{2L})\\
&+\Gamma_{4L}\Sigma_{1L}]\frac{1+\nu_L}{1+\nu_H}\frac{\alpha_L}{\alpha_H}\frac{1}{1-\nu_L}\Bigg\}\overline{U}\\
&=-[(\cos\Omega\Delta+\Lambda_s\sin\Omega\Delta)]\Re_{1H}\\
&\quad+[(\sin\Omega\Delta-\Lambda_s\cos\Omega\Delta)]\Re_{2H}-\frac{\theta_L}{\theta_H}\frac{k_L}{k_H}(\Re_{1L}+\Lambda_s\Re_{2L})
\end{aligned} \tag{24}$$

$$\begin{aligned}
\Lambda_T\Bigg\{&[(\Gamma_{1H}\cos\Omega\Delta-\Gamma_{2H}\sin\Omega\Delta)(1-\Sigma_{2H})-(\Gamma_{3H}\cos\Omega\Delta\\
&+\Gamma_{4H}\sin\Omega\Delta)\Sigma_{1H}]\frac{1}{1-\nu_H}+\frac{\theta_L}{\theta_H}[\Gamma_{1L}(1-\Sigma_{2L})\\
&-\Gamma_{3L}\Sigma_{1L}]\frac{1+\nu_L}{1+\nu_H}\frac{\alpha_L}{\alpha_H}\frac{1}{1-\nu_L}\Bigg\}\overline{U}\\
&=[(\sin\Omega\Delta-\Lambda_s\cos\Omega\Delta)]\Re_{1H}\\
&\quad+[(\cos\Omega\Delta+\Lambda_s\sin\Omega\Delta)]\Re_{2H}-\frac{\theta_L}{\theta_H}\frac{k_L}{k_H}(\Lambda_s\Re_{1L}-\Re_{2L})
\end{aligned}$$

where

$$\Lambda_S=f\mathcal{D}^*=\frac{f}{\left[\dfrac{\Sigma_{1H}}{G_H}+\dfrac{\Sigma_{1L}}{G_L}+\dfrac{2\Omega h_o}{\chi\varphi_c}\right]}\left[\frac{\Sigma_{2H}}{G_H}-\frac{\Sigma_{2L}}{G_L}\right]$$

$$\Lambda_T=f\mathcal{H}^*=\frac{f}{\left[\dfrac{\Sigma_{1H}}{G_H}+\dfrac{\Sigma_{1L}}{G_L}+\dfrac{2\Omega h_o}{\chi\varphi_c}\right]}\left[\frac{2\alpha_H\kappa_H(1+\nu_H)}{k_H}\right]. \tag{25}$$

The parameter $\Lambda_S$ represents the coupling between the tangential and normal loading and we will refer to it as the *shear parameter*. Parameter $\mathcal{D}^*$ is a modified Dundurs' constant. At a high shear parameter, the effect of shear stress at the interface plays an important role and can not be neglected. When the surfaces are smooth and the bodies are treated as semi-infinite solids, the shear parameter reduces to the Dundurs' constant, $\mathcal{D}$, multiplied by the friction coefficient, i.e., $\Lambda_s=f\mathcal{D}$. The material parameter $\Lambda_T$ is related to the thermal deformation due to the frictional heat and we refer to it as the *material parameter*. Consider the special case where the upper body is semi-infinite, the lower body is rigid, and surfaces are both smooth, the material parameter reduces to the thermomechanical material parameter, $\mathcal{H}$, multiplied by the friction coefficient, i.e., $\Lambda_T=f\mathcal{H}$, [18]. Note that the thickness effect and the roughness effect are included in both the shear parameter $\Lambda_S$ and the material parameter $\Lambda_T$.

Mathematically, the stability parameter $\beta>0$ means that instability will grow unbounded with time and TEI is imminent. Therefore, the threshold of instability (i.e., the critical speed) is obtained by setting $\beta=0$ in the governing equations. This leads to $\Gamma_{1i}=\Re_{1i}/\overline{c_i}$, $\Gamma_{2i}=\Re_{2i}/\overline{c_i}$, $\Gamma_{3i}=1/\overline{c_i}$ and $\Gamma_{4i}=0$. Therefore, the following two dimensionless equations emerge from (24):

$$\begin{aligned}
\Lambda_T\Bigg\{&[(\Re_{1H}\sin\Omega\Delta+\Re_{2H}\cos\Omega\Delta)\coth\Omega l_H-\sin\Omega\Delta]\frac{\Sigma_H^*}{\overline{\xi_H}\,\overline{a_H}}\\
&+\theta^*\alpha^*\Re_{2L}\coth\Omega l_L\frac{\Sigma_L^*}{\overline{\xi_L}\,\overline{a_L}}\Bigg\}\overline{U_{cr}}\\
&=[(\cos\Omega\Delta+\Lambda_s\sin\Omega\Delta)]\Re_{1H}\\
&\quad-[(\sin\Omega\Delta-\Lambda_s\cos\Omega\Delta)]\Re_{2H}+\theta^*k^*(\Re_{1L}+\Lambda_s\Re_{2L})
\end{aligned} \tag{26}$$

$$\begin{aligned}
\Lambda_T\Bigg\{&[(\Re_{1H}\cos\Omega\Delta-\Re_{2H}\sin\Omega\Delta)\coth\Omega l_H-\cos\Omega\Delta]\frac{\Sigma_H^*}{\overline{\xi_H}\,\overline{a_H}}\\
&+\theta^*\alpha^*(\Re_{1L}\coth\Omega l_L-1)\frac{\Sigma_L^*}{\overline{\xi_L}\,\overline{a_L}}\Bigg\}\overline{U_{cr}}\\
&=-[(\sin\Omega\Delta-\Lambda_s\cos\Omega\Delta)]\Re_{1H}\\
&\quad-[(\cos\Omega\Delta+\Lambda_s\sin\Omega\Delta)]\Re_{2H}+\theta^*k^*(\Lambda_s\Re_{1L}-\Re_{2L})
\end{aligned}$$

where we have used the relationships $\overline{c_i}=-2\overline{a_i}\,\overline{\xi_i}$ and $1-\Sigma_{2i}=\Sigma_{1i}\coth\Omega l_i$ and

$$\alpha^*=\frac{1+\nu_L}{1+\nu_H}\frac{\alpha_L}{\alpha_H};\quad \theta^*=\frac{\theta_L}{\theta_H};\quad k^*=\frac{k_L}{k_H};$$

$$\kappa^*=\frac{\kappa_L}{\kappa_H}\quad\text{and}\quad \Sigma_i^*=\frac{\sinh^2\Omega l_i}{\Omega l_i+\sinh\Omega l_i\cosh\Omega l_i}. \tag{27}$$

There are three unknowns in (26): the critical speed $\overline{U_{cr}}$ and the wave speeds $\overline{c_H}$ and $\overline{c_L}$. Note that the third equation to solve unknowns is $\overline{c_H}=\kappa^*\overline{c_L}-\overline{U_{cr}}$. Equations (26) are derived based on the assumption that the problem is posed as a plane strain. Plane stress solutions can be obtained using the following conversions:

$$\nu\to\frac{\nu}{1+\nu};\quad \alpha\to\frac{1+\nu}{1+2\nu}\alpha\quad\text{and}\quad E\to\frac{1+2\nu}{(1+\nu)^2}E. \tag{28}$$

Examination of the governing equations reveals that the dimensionless critical speed is governed by eight independent dimensionless parameters. They are: $\Lambda_T$, $\Lambda_S$, $\alpha^*$, $k^*$, $\kappa^*$, $\Omega l_H$, $\Omega l_L$, and $\mathfrak{I}_c^*$. The parameter $\mathfrak{I}_c^*$ is the dimensionless thermal contact conductance defined as $\mathfrak{I}_c^*=\mathfrak{I}_c/\Omega k_H$. If both conducting bodies qualify as (a semi-infinite) half-space, the parameters $\Omega l_H$ and $\Omega l_L$ disappear in the governing equations. In the following sections, a series of special cases will be treated.

### 2.7 Special Cases

*2.7.1 System Without Thermal Contact Conductance.* The temperature ratio $\theta^*$ and phase shift $\Delta$ at the interface depend upon the thermal conductance $\mathfrak{I}_c^*$. Under an ''ideal contact'' condition the thermal conductance goes to infinity (zero resistance) and at the interface the temperature of both bodies match, i.e., $\theta^*=1$ and $\Delta=0$. Therefore, the governing equations for the system neglecting the thermal contact conductance become

$$\begin{aligned}
&\Lambda_T\left\{\frac{\Sigma_H^*\Re_{2H}\coth\Omega l_H}{\overline{\xi_H}\,\overline{a_H}}+\alpha^*\frac{\Sigma_L^*\Re_{2L}\coth\Omega l_L}{\overline{\xi_L}\,\overline{a_L}}\right\}\overline{U_{cr}}\\
&\quad=(\Re_{1H}+k^*\Re_{1L})+\Lambda_s(\Re_{2H}+k^*\Re_{2L})
\end{aligned}$$

$$\Lambda_T\left\{\frac{\Sigma_H^*(\Re_{1H}\coth\Omega l_H-1)}{\overline{\xi}_H\overline{a}_H}+\alpha^*\frac{\Sigma_L^*(\Re_{1L}\coth\Omega l_L-1)}{\overline{\xi}_L\overline{a}_L}\right\}\overline{U}_{cr}$$
$$=\Lambda_s(\Re_{1H}+k^*\Re_{1L})-(\Re_{2H}+k^*\Re_{2L}). \quad (29)$$

*2.7.2 System With Semi-Infinite Bodies.* Consider a system whose conducting members are thick enough so that the perturbed temperature penetrates a finite depth into body. For such a system it is reasonable to assume that the thickness of the conducting disks is semi-infinite. This would best describe a thick rotor.

Letting the half thickness $l_i\to\infty$, the dimensionless parameters are modified as follows:

$$\lim_{l_i\to\infty}\Sigma_i^*=1;\quad \lim_{l_i\to\infty}\Sigma_{1i}=2(1-\nu_i);\quad \lim_{l_i\to\infty}\Sigma_{2i}=-(1-2\nu_i);$$
$$\lim_{l_i\to\infty}\coth\Omega l_i=1;\quad \lim_{l_i\to\infty}\Re_{1i}=\overline{\xi}_i\quad\text{and}\quad \lim_{l_i\to\infty}\Re_{2i}=\overline{a}_i. \quad (30)$$

Equations (26) in conjunction with the modified parameters (30) give the critical speed for the system with semi-infinite disks. Moreover, if the thermal contact conductance is not considered, the governing equations reduce to

$$\Lambda_T\left(\frac{1}{\xi_H}+\alpha^*\frac{1}{\xi_L}\right)\overline{U}_{cr}=(\overline{\xi}_H+k^*\overline{\xi}_L)+\Lambda_s(\overline{a}_H+k^*\overline{a}_L)$$
$$\Lambda_T\left(\frac{\overline{\xi}_H-1}{\xi_H\overline{a}_H}+\alpha^*\frac{\overline{\xi}_L-1}{\xi_L\overline{a}_L}\right)\overline{U}_{cr}=\Lambda_s(\overline{\xi}_H+k^*\overline{\xi}_L)-(\overline{a}_H+k^*\overline{a}_L). \quad (31)$$

If surface roughness is neglected, Eqs. (31) reduce to the governing equations derived by Lee and Barber [18] for two semi-infinite bodies in contact, in the absence of a contact conductance. Furthermore, neglecting the shear stress effect ($\Lambda_s=0$), and converting equations for plane stress, the governing Eqs. (31) are identical to those derived by Burton et al. [4]. Replacing $L$ and $H$ by 1 and 2 in (31), the dimensional governing equations are

$$k_1\xi_1+k_2\xi_2=(c_1+|c_2|)\frac{fE_1E_2}{E_1+E_2}\left[\frac{\alpha_1\kappa_1|a_1|}{c_1}+\frac{\alpha_2\kappa_2a_2}{|c_2|}\right]$$
$$-k_1|a_1|+k_2a_2=(c_1+|c_2|)\frac{fE_1E_2}{E_1+E_2}\times\left[-\frac{\alpha_1\kappa_1(\Omega-\xi_1)}{c_1}+\frac{\alpha_2\kappa_2(\Omega-\xi_2)}{|c_2|}\right]. \quad (32)$$

Note that $|c_2|$ is used since the moving direction of $c_2$ in Burton's equations is opposite to that defined in this analysis.

*2.7.3 Insulator-Conductor System.* The so-called insulator-conductor system is an idealized model for treating TEI problems in a variety of engineering applications where all the heat generated at the interface is transferred to one of the bodies only. The stationary body is an insulator. For example, the friction pad in an automotive brake system may be represented as an insulator in contact with a conducting body, i.e., the rotor. Note that the thermal contact conductance is not needed. Taking the insulator positioned as the lower body, the governing Eqs. (26) reduce to

$$\Lambda_T'\frac{\Sigma_H^*\Re_{2H}\coth\Omega l_H}{\overline{\xi}_H\overline{a}_H}\overline{U}_{cr}=\Re_{1H}+\Lambda_s'\Re_{2H}$$
$$\Lambda_T'\frac{\Sigma_H^*(\Re_{1H}\coth\Omega l_H-1)}{\overline{\xi}_H\overline{a}_H}\overline{U}_{cr}=\Lambda_s'\Re_{1H}-\Re_{2H} \quad (33)$$

where

$$\Lambda_T'=\frac{2f\alpha_H\kappa_H(1+\nu_H)}{k_H\left[\frac{\Sigma_{1H}}{G_H}+\frac{2\Omega h_o}{\chi\varphi_c}\right]}$$
$$\Lambda_S'=\frac{f\Sigma_{2H}}{\Sigma_{1H}+\frac{2\Omega h_oG_H}{\chi\varphi_c}}. \quad (34)$$

If the conductor is semi-infinite, Eqs. (33) become

$$\frac{\Lambda_T'}{\overline{\xi}_H}\overline{U}_{cr}=\overline{\xi}_H+\Lambda_s'\overline{a}_H$$
$$\Lambda_T'\frac{(\overline{\xi}_H-1)}{\overline{\xi}_H\overline{a}_H}\overline{U}_{cr}=\Lambda_s'\overline{\xi}_H-\overline{a}_H. \quad (35)$$

If the shear stress at the interface is neglected, then the shear parameter $\Lambda_s$ disappears in the governing equations and the wave speed becomes zero, $\overline{c}_H=0$. Therefore, the governing Eqs. (35) reduce to the simple solution as follows:

$$\overline{U}_{cr}=\frac{1}{\Lambda_T'}=\frac{k_H}{2f\alpha_H\kappa_H(1+\nu_H)}\left[\frac{\Sigma_{1H}}{G_H}+\frac{2\Omega h_o}{\chi\varphi_c}\right]. \quad (36)$$

For the plane stress with semi-infinite conductor, Eq. (36) becomes, [11]:

$$\overline{U}_{cr}=\frac{2k_H}{f\alpha_H\kappa_HE_H}\left[1+\frac{2\Omega E_Hh_o}{\chi\varphi_c}\right]. \quad (37)$$

Neglecting the surface roughness, the most conservative critical speed for the insulator-conductor system is derived as follows, [4]:

$$\overline{U}_{cr}=\frac{2k_H}{f\alpha_H\kappa_HE_H}. \quad (38)$$

Comparison between the results of the prediction of the critical speed for the smooth surface model is much lower than that of the present theory, which includes provision for surface roughness. This is akin to the effect of a compliant layer. In the smooth surface model, the applied load does not appear as a direct parameter of the model and the model tacitly assumes that bodies are in perfect contact. In this paper, the critical speed is determined by the surface separation, which is a function of the applied load and the surface roughness. The critical speed increases with decreasing surface separation due to a heavy load or a large $\chi$. Accordingly, in this theory, it is assumed that there always exists surface separation and two surfaces are not under perfect contact.

## 3 Results and Discussion

We shall first focus our attention to a combination of different materials as shown in Table 1, [4]. Aluminum is a good conducting material and glass is an example of the insulator. A friction pair of graphite and cast iron is commonly used in seals as well as dry bearings.

Shown in Table 2 are the predictions of the critical speeds and the wave speeds corresponding to Table 1 based on the assumption of the plane stress. Roughness effect is not considered here, but will be covered in the next section. Case I is simulated based on the assumption that the effect of shear stress at the interface is nil. Therefore, Case I is governed by Eqs. (32) which are identical to those derived by Burton et al. [4]. The results in Table 2 match with Burton's critical speeds. It is shown that in Case I the wave speeds $c_H$ are very small and negative with comparison to the critical speed, which means that the perturbed wave is moving with the body with a high thermal conductivity, but at a slightly lower speed. An interesting material is the graphite for which the predictions of the critical speeds are very high. The reason is that the elastic modulus for graphite is much smaller than that of the

**Table 1 Material properties, [4]**

| Materials | 1 | 2 | 3 | 4 | 5 |
|---|---|---|---|---|---|
| Properties | Aluminum | Cast Iron | Silicon Carbide | Graphite | Glass |
| Elastic modulus, $E$ [GPa] | 68.9 | 124.1 | 89.6 | 6.9 | 89.6 |
| Poisson's ratio, $\nu$ | 0.33 | 0.3 | 0.15 | 0.3 | 0.16 |
| Coefficient of expansion, $\alpha$ [$10^{-5}$ K$^{-1}$] | 1.69 | 1.08 | 0.47 | 0.47 | 0.54 |
| Thermal diffusivity, $\kappa$ [$10^{-5}$ m$^2$/s] | 8.58 | 1.16 | 0.61 | 0.81 | 0.03 |
| Thermal conductivity, $k$ [W/mK] | 202 | 45 | 16 | 12 | 0.8 |

mating body. The low elastic modulus greatly reduces the pressure for a given amount of heat transferred into the body, thereby improving the thermoelastic behavior of the system. In fact, the critical speed for the pair of silicon carbide and graphite is far beyond the practical operating conditions and the system is thermoelastically stable.

Case II takes the effect of the shear stress at the interface into consideration. The critical speed does not vary much when one of the friction pairs has a low thermal conductivity. For example, the pair of aluminum and glass can be treated as an insulator-conductor system. For this friction pair, Table 2 shows the critical speed does not vary whether $\Lambda_S=0$ or not. Therefore, in an insulator-conductor system, the effect of the shear parameter is very small and can be neglected. However, the critical speeds vary significantly when the friction pair includes the graphite with a very low elastic modulus. Therefore, the elastic modulus plays an important role when $\Lambda_S\neq 0$. In addition to the significant change in the critical speed, the elastic modulus influences the wave speed $c_H$. As mentioned above, the wave is likely to move with the conducting body. Moreover, the wave tends to move with the body with a lower elastic modulus. This effect is turned on when $\Lambda_S\neq 0$. For graphite this effect of elastic modulus is more dominant than the effect of the thermal conductivity, and the wave speed is moving with the body made of graphite.

Case III shows the effect of the disk thickness. Compared to a semi-infinite body, a finite disk thickness tends to reduce the effect of the elastic modulus, thereby causing a significant change in the critical speed as well as the wave speed. In this case, the wave is moving with the conducting body even though the friction pair is made of graphite. Case IV shows the effect of the thermal contact conductance. It is shown that the thermal contact conductance does not significantly influence the critical speed for a friction pair when one member is made of glass. It should be mentioned that further investigation of thermal contact conductance shows that it also reduces the effect of the elastic modulus on the wave speed. At a small enough thermal contact conductance, the wave is moving with the conducting body. Case V shows the combined effect of the disk thickness and the thermal contact conductance. In most cases, the critical speed for Case V is similar to that for Case III. However, the critical speed for the pair of silicon carbide and graphite drops significantly due to the effect of the thermal contact conductance.

Results show that near the asymptote, the critical speed varies significantly even by a small change of the material properties and the disk thickness. For example, since the critical speed for the pair of silicon carbide and graphite changes significantly depending on the conditions, it is expected that the critical speed is located near the asymptote.

Secondly, in addition to comparing with Burton's predictions, we compare theoretical results with the experimental data by Dow and Stockwell [19]. Their experimental instrument consists of a rotating drum in contact with a stationary blade. The drum material is made of $Al_2O_3$-Ti and the blade materials are aluminum, brass and steel. The applied load is 44.5 N. The corresponding friction coefficient are $f=0.38$, 0.16 and 0.26, respectively. The experimentally observed critical speeds are 7.11 m/s, 8.13 m/s and 5.08 m/s for each friction pair, respectively. Their theoretical critical speeds are 0.66 m/s, 1.07 m/s and 0.4 m/s. Note that their theory is based on the simplified TEI model for the smooth surface, and their predicted critical speeds are roughly ten times lower than the observed critical speeds. Figure 2 shows the theoretical predictions of the critical speed as a function of the surface roughness for each friction pair. The observed critical speeds are also marked in the figure. Since all the input data is not given, some parameters are assumed in the simulations. The assumed parameters are $\chi=3$ MPa and $\mathfrak{I}_c=5\times 10^4$ W/m$^2$ K.

Figure 2 shows that TEI model for the rough surface predicts a higher critical speed than that for the smooth surface model. The surface roughness plays an important role, and for the range of surface roughness of 2–6 $\mu$m the results are close to experiments. Specially, the critical speeds at $\sigma=5.39$ $\mu$m for the aluminum blade, $\sigma=2.79$ $\mu$m for the brass blade, and $\sigma=2.14$ $\mu$m for the steel blade mach the observed critical speeds. The expected surface roughness is in the reasonable range in practice. However,

**Table 2 Critical speed for plane stress ($f=0.5$ and $\Omega=39.37$/m)**

| Condition | | CASE I | | CASE II | | CASE III | | CASE IV | | CASE V | |
|---|---|---|---|---|---|---|---|---|---|---|---|
| Friction Pair | | Semi-Infinite $\Lambda_s=0$ $\mathfrak{I}_c=\infty$ | | Semi-Infinite $\Lambda_s\neq 0$ $\mathfrak{I}_c=\infty$ | | $\Omega l_H=\Omega l_L=1$ $\Lambda_s\neq 0$ $\mathfrak{I}_c=\infty$ | | Semi-Infinite $\Lambda_s\neq 0$ $\mathfrak{I}_c=10^6$ W/m$^2$ K | | $\Omega l_H=\Omega l_L=1$ $\Lambda_s\neq 0$ $\mathfrak{I}_c=10^5$ W/m$^2$ K | |
| Upper Body | Lower Body | $U_{cr}$ [m/s] | $c_H$ [m/s] | $U_{cr}$ [m/s] | $c_H$ [m/s] | $U_{cr}$ [m/s] | $c_H$ [m/s] | $U_{cr}$ [m/s] | $c_H$ [m/s] | $U_{cr}$ [m/s] | $c_H$ [m/s] |
| 1 | 2 | 0.659 | −0.025 | 0.550 | −0.019 | 0.134 | −0.009 | 0.457 | −0.015 | 0.104 | −0.005 |
| | 3 | 0.143 | −0.005 | 0.143 | −0.005 | 0.055 | −0.004 | 0.143 | −0.005 | 0.057 | −0.003 |
| | 4 | 2.524 | −0.013 | 4.245 | −0.028 | 0.676 | −0.006 | 3.521 | −0.022 | 0.606 | −0.004 |
| | 5 | 0.058 | −0.001 | 0.058 | −0.001 | 0.028 | −0.001 | 0.058 | −0.001 | 0.028 | −0.001 |
| 2 | 3 | 0.421 | −0.006 | 0.625 | −0.010 | 0.079 | −0.002 | 0.490 | −0.007 | 0.059 | −0.001 |
| | 4 | 62.113 | −0.043 | 910.819 | −910.812 | 10.929 | −0.012 | 68.643 | −68.643 | 1.142 | −0.001 |
| | 5 | 0.020 | −0.001 | 0.021 | −0.001 | 0.009 | −0.000 | 0.021 | −0.000 | 0.009 | −0.000 |
| 3 | 4 | 139080 | −10 | 235.823 | −235.815 | 2520.861 | −0.329 | 47.508 | −47.506 | 4.169 | −0.001 |
| | 5 | 0.072 | −0.001 | 0.072 | −0.001 | 0.021 | −0.000 | 0.072 | −0.001 | 0.021 | −0.000 |
| 4 | 5 | 41.402 | −0.031 | 6.590 | −0.004 | 9.568 | −0.012 | 5.679 | −0.003 | 1.492 | −0.002 |

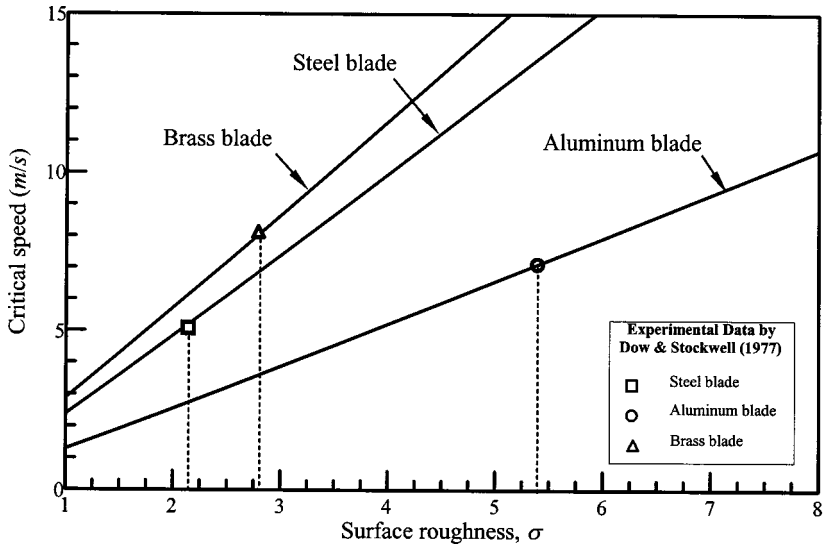


**Fig. 2 Comparison with experimental data**

the critical speed is very sensitive to some properties and geometry of the system and, therefore, the accurate input data is required.

**3.1 Effect of Surface Characteristic Parameter $\chi$.** The critical speed as a function of the film gap for a series of surface characteristics parameter $\chi$ is plotted in Fig. 3. This parameter can vary significantly depending on the application. For example, $\chi=0.5$ MPa for a mechanical face seal where the surfaces are polished within two helium light band. For a friction material in a clutch disk, $\chi$ is typically 9 MPa, [16]. The simulations presented are for a wide range $\chi$ of values to cover these applications. This parameter is directly proportional to the asperity radius $\gamma$, density $\eta$ and the surface roughness $\sigma$.

The critical speed decreases with increasing surface characteristic parameter since more frictional heat is generated at the interface for a relatively large $\chi$. Based on Greenwood and Tripp's theory, the surface separation increases as the applied load decreases. The surfaces are completely separated when $h_o \geqslant 3\sigma$, implying that the load on the system is removed and the system is no longer susceptible to TEI. Therefore, the critical speed increases with increasing surface separation, and tends to infinity when the gap approaches three standard deviations of the combined surface roughness.

**3.2 Effect of Material Parameter $\Lambda_T$.** Figure 4 shows the effect of material parameter $\Lambda_T$ on the critical speed for $-0.5 < \Lambda_S < 0.5$. This figure pertains to "perfect contact" between two bodies. It is also assumed that both bodies have identical dimensions and material properties, except their elastic modulus is different, i.e., $\alpha^*=\kappa^*=k^*=1$, $\Omega l_H=\Omega l_L=1$ and $\Im_c=\infty$. Physically, $\Lambda_T$ is directly proportional to the friction coefficient, $f$, and thermal expansion coefficient, $\alpha_H$. Therefore, as $\Lambda_T$ is reduced, the system's critical speed is pushed to a higher value. As mentioned above, the shear parameter $\Lambda_S$ represents the effect of the shear stresses at the interface. Figure 4 shows that neglecting the shear stress at the interface (i.e., $\Lambda_S=0$) results in a large error in prediction of the critical speed. Therefore when dealing with two conducting bodies in contact, the shear stress at the interface must not be neglected.

The shear parameter $\Lambda_S$ is nil when both conducting bodies

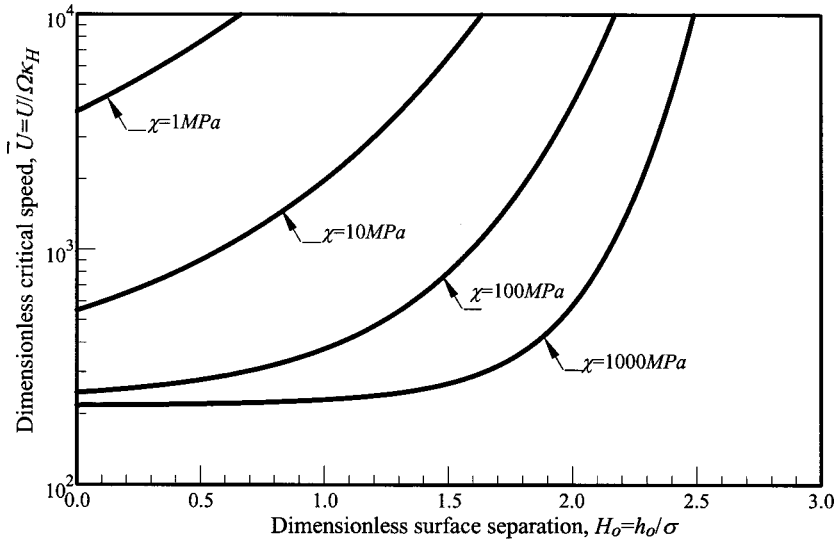


**Fig. 3 Effect of surface characteristic parameter on the critical speeds**

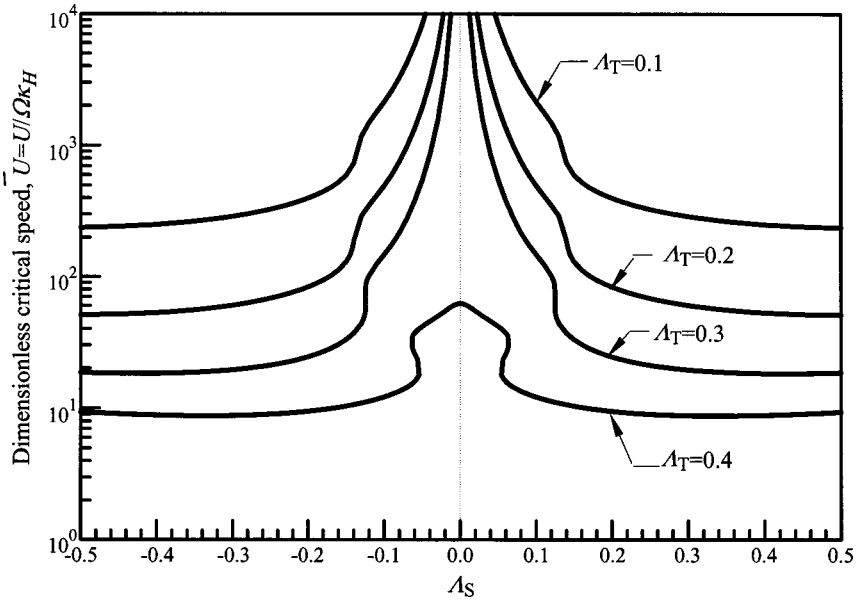


**Fig. 4 Critical speeds as a function of $\Lambda_S$ ($\alpha^*=\kappa^*=k^*=1$; $\Omega l_H=\Omega l_L=1$; $\Im_c=\infty$)**

have the same elastic modulus and Poisson's ratio. Therefore, in this simulation $\Lambda_S=0$ represents that the material properties and geometry of the upper disk are identical to those of the lower disk. The maximum critical speed occurs at $\Lambda_S=0$ due to the symmetry of the problem. Note that effect of the surface roughness appears in the definition of parameters $\Lambda_T$ and $\Lambda_S$. When $\Lambda_T$ is small enough ($\Lambda_T<0.4$), the critical speed approaches infinity as $\Lambda_s \rightarrow 0$. In other words, a system consisted of two identical conducting bodies (same material properties and dimensions) would be immune from TEI provided that $\Lambda_T$ is less than a certain value. This finding is in agreement with the results of Burton et al. [4].

It is also worthwhile to note that the sign of shear parameter $\Lambda_S$ does not affect on the critical speed and, therefore, the critical speed is symmetric about $\Lambda_S=0$. However, the wave speed is influenced by the sign of $\Lambda_S$. When $\Lambda_S$ is negative, the wave is moving at nearly the same speed of the moving disk. When $\Lambda_S$ is positive, the absolute wave speed is very small. In other words, the wave is likely to move together with the disk having a smaller elastic modulus when Poisson's ratios are the same and the roughness effect is neglected.

**3.3 Effect of Disk Thickness.** Figure 5 shows the effect of disk thickness when $\alpha^*=\kappa^*=k^*=1$, $\Lambda_T=0.2$ and $\Im_c=\infty$. The simulations show that when both of the disks are of identical thickness the critical speed tends to infinity at $\Lambda_S=0$, indicating that TEI does not occur. The asymptote at $\Lambda_S=0$ occurs because both disks have the same material properties and geometry. However, if the thickness of the disks are different, the asymptote is shifted. When the upper disk is thicker than the lower disk, the asymptote is shifted toward positive $\Lambda_S$ where the elastic modulus of the lower disk is relatively small. When the lower disk is thicker than the upper disk, the asymptote is shifted to the nega-

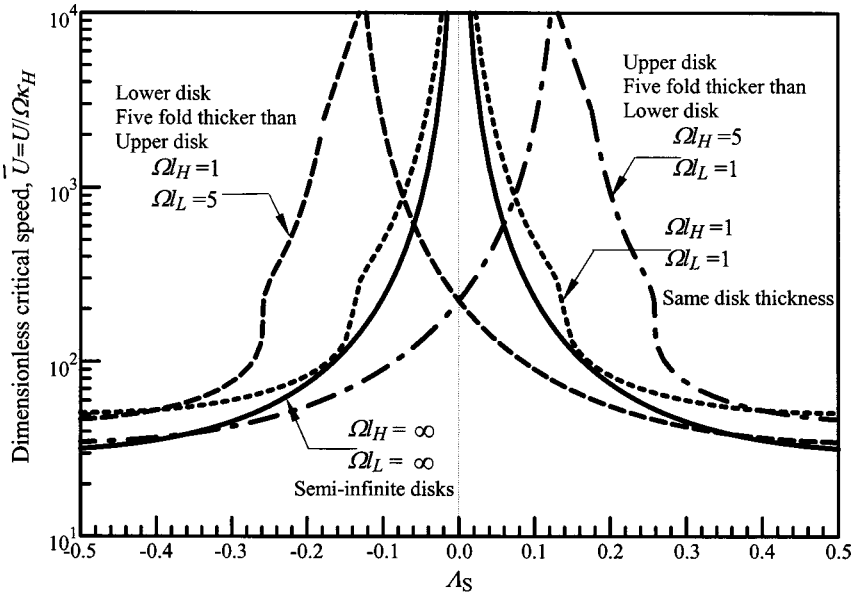


**Fig. 5 Effect of disk thickness on the critical speeds ($\alpha^*=\kappa^*=k^*=1$; $\Lambda_T=0.2$; $\Im_c=\infty$)**

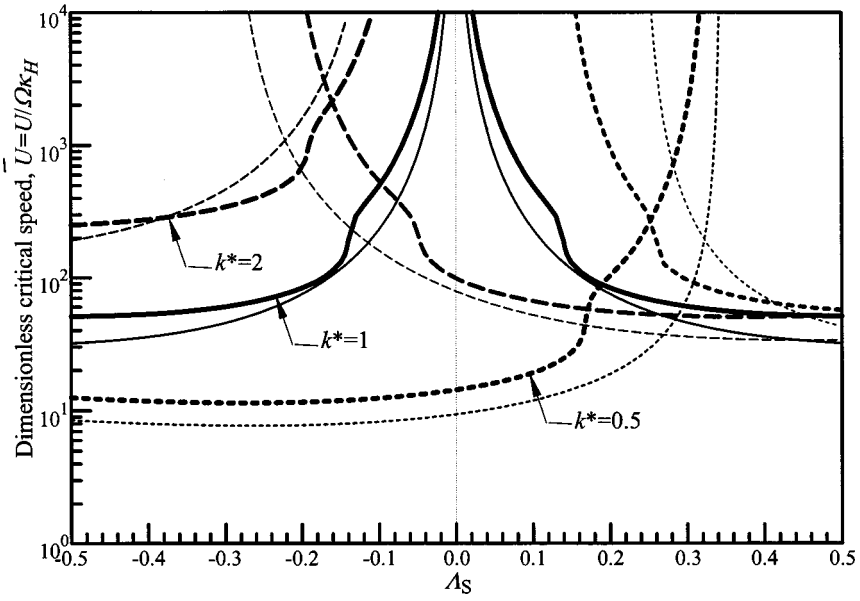


**Fig. 6 Effect of thermal conductivity ratio on the critical speeds ($\alpha^*=\kappa^*=1$; $\Lambda_T=0.2$; $\Omega l_H=\Omega l_L=\Im_c=\infty$)**

tive $\Lambda_S$ where the elastic modulus of the upper disk is relatively small. According to Fig. 4, if the elastic moduli of both bodies are identical, then the critical speed goes to the infinity. Figure 5 shows that to improve thermoelastic performance, it is advantageous to have a thicker disk with a higher elastic modulus.

Figure 5 shows that the dimensionless critical speed for $\Omega l_H=\Omega l_L=1$ is higher than the critical speed for $\Omega l_H=\Omega l_L=\infty$ for specified $\Lambda_T$ and $\Lambda_S$. Note that parameters $\Lambda_T$ and $\Lambda_S$ are functions of the disks' thickness parameters $\Omega l_H$ and $\Omega l_L$ and, therefore, in order to fix parameters $\Lambda_T$ and $\Lambda_S$ other material properties should be changed. If all material properties are fixed, the critical speed for the finite thickness is lower than the critical speed for the semi-infinite thickness, [9].

**3.4 Effect of Thermal Conductivity Ratio.** Figure 6 shows the effect of thermal conductivity ratio $k^*$ when $\alpha^*=\kappa^*=1$, $\Lambda_T=0.2$ and $\Im_c=\infty$. The thick lines represent the critical speed for $\Omega l_H=\Omega l_L=1$ and the thin lines represent the critical speed for $\Omega l_H=\Omega l_L=\infty$. The critical speed for $k^*=1$ goes to the infinity at $\Lambda_S=0$ since the material properties and the geometry of two bodies are identical. The simulations show that the asymptote at $\Lambda_S=0$ is shifted to negative $\Lambda_S$ when $k^*>1$, and to positive $\Lambda_S$ for $k^*<1$ since relatively large amount of frictional heat is transferred into the disk with higher thermal conductivity.

The simulations also show that at a given $\Lambda_T$ the critical speed has two different asymptotes for $k^*\neq 1$ due to the lack of symmetry in the thermal conductivity. Note that two asymptotes reduce to one as the material parameter $\Lambda_T$ becomes large, [18]. When $k^*\neq 1$, the system always has a finite value of critical speed and, therefore, an unconditionally stable condition does not exist. At a large positive $\Lambda_S$, the effect of $k^*$ on the critical speed is reduced.

**3.5 Effect of Thermal Diffusivity Ratio.** Figure 7 shows the effect of thermal diffusivity ratio $\kappa^*$ when $\alpha^*=k^*=1$, $\Lambda_T=0.2$ and $\Im_c=\infty$. The thick lines represent the critical speed for $\Omega l_H=\Omega l_L=1$ and the thin lines represent the critical speed for $\Omega l_H=\Omega l_L=\infty$. This plot is useful for determining the critical speed for a range of $\Lambda_s$ values. Note that in general the threshold of critical speed increases with decreasing thermal diffusivity ratio $\kappa^*$. Furthermore, the critical speed is sensitive to a range of $\Lambda_S$ from 0 to $\pm 0.3$ after which it does not change appreciably. Regardless of $\kappa^*$, in the range of $\Lambda_S>0.3$, the dimensionless critical speed for $\Omega l_H=\Omega l_L=\infty$ is predicted to be about 40. Note that parameter $\kappa^*$ appears in the relationship between the critical speed and the wave speed $\overline{c_H}=\kappa^*\overline{c_L}-\bar{U}$. At a positive $\Lambda_S$, the wave speed $\overline{c_L}$ tends to move with the lower body. As $\Lambda_S$ increases, $\overline{c_L}$ decreases. Therefore, at a larger $\Lambda_S$, the effect of $\kappa^*$ becomes very small. This effect is more significant for the system of $\Omega l_H=\Omega l_L=1$ and, therefore, the variation of the critical speed with the diffusivity ratio is small for $\Lambda_S>0$.

For $\kappa^*\neq 1$, the critical speed is not symmetric about $\Lambda_S=0$. The simulations show that for all thermal diffusivity ratios of $\kappa^*\leqslant 1.57$, the critical speed for $\Omega l_H=\Omega l_L=\infty$ goes to infinity at $\Lambda_S=0$, implying that TEI does not occur when $\Lambda_S=0$. Since $\overline{c_H}=\kappa^*\overline{c_L}-U$, the asymptote remains at $\Lambda_S=0$. However, under the conditions simulated for $\kappa^*\geqslant 1.57$, the critical speed has a finite value at any $\Lambda_S$. When $\Lambda_T$ decreases, this limiting value of $\kappa^*$ becomes larger than $\kappa^*=1.57$. Below the limiting value of $\kappa^*$, there exists a condition that makes the system immune from TEI depending upon the ratio of the elastic modulus. As $\kappa^*$ increases, the thermal expansion increases, and after the limiting value of $\kappa^*$ the thermal expansion is dominant over the role of the contact pressure to reduce TEI. As a result, the critical speed always has a finite value. However, simulation shows that the critical speed for $\Omega l_H=\Omega l_L=1$ goes to infinity at $\kappa^*=2$. It implies that the limiting value of $\kappa^*$ is much higher for the finite disk thickness.

**3.6 Effect of Thermal Expansion Coefficient Ratio.** Figure 8 shows the effect of thermal expansion coefficient ratio $\alpha^*$ on the critical speed. These results were obtained by setting $\kappa^*=k^*=1$, $\Lambda_T=0.2$ and $\Im_c=\infty$. The thick lines represent the critical speed for $\Omega l_H=\Omega l_L=1$ and the thin lines represent the critical speed for $\Omega l_H=\Omega l_L=\infty$. Consistent with previous results, the simulations show that the critical speed for $\alpha^*=1$ goes to infinity at $\Lambda_S=0$ due to the symmetry of the material properties and geometry. The asymptote is shifted to the negative $\Lambda_S$ for $\alpha^*=1.5$, and at the positive $\Lambda_S$ for $\alpha^*=0.5$. The simulations show that for $\alpha^*\geqslant 1.56$ the critical speed for $\Omega l_H=\Omega l_L=\infty$ has a finite value at any $\Lambda_S$ and, therefore, can not be unconditionally stable. Similar to the thermal diffusivity case, as $\alpha^*$ increases, the thermal expansion increases and overwhelms the role of the contact pressure to reduce TEI. When $\alpha^*$ exceeds the limiting value, the critical

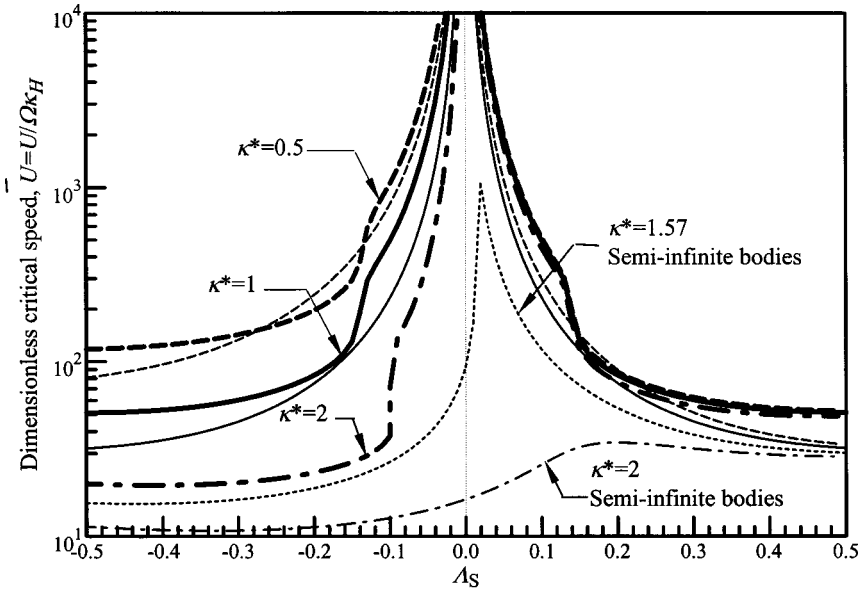


**Fig. 7 Effect of thermal diffusivity ratio on the critical speeds ($\alpha^*=k^*=1$; $\Lambda_T=0.2$; $\Omega l_H=\Omega l_L=\Im_c=\infty$)**

speed always has a finite value. However, for the case of $\Omega l_H=\Omega l_L=1$, the critical speed has an asymptote at $\alpha^*=2$.

**3.7 Effect of Thermal Contact Conductance.** Figure 9 shows the effect of thermal contact conductance $\Im_c^*$ when $\alpha^*=\kappa^*=k^*=1$, $\Omega l_H=\Omega l_L=\infty$, $\Lambda_T=0.2$. The simulations show that the critical speed is maximum at $\Lambda_S=0$ for any $\Im_c^*$ due to the symmetry of material properties and geometry. The sign of the shear parameter $\Lambda_S$ does not affect the critical speed. The critical speed increases with increasing thermal contact conductance. When the thermal contact conductance has a finite value, the surface temperature of the upper disk is different from that of the lower disk and the temperature wave is shifted at the interface. As the thermal contact conductance decreases, the temperature wave becomes more asymmetric, resulting in lowering the threshold of the critical speed.

Figure 10 shows the variation of surface temperature ratio $\theta^*$ and the temperature phase shift $\Omega\Delta$ corresponding to Figure 9. Note that the temperature ratio $\theta^*=1$ and $\Omega\Delta=0$ for $\Im_c^*=\infty$ since there is no thermal resistance. The simulations show that for $\Im_c^*\neq\infty$ the temperature ratio $\theta^*<1$ at the negative $\Lambda_S$, and $\theta^*>1$ for the positive $\Lambda_S$. In other words, the surface temperature of the disk with a small elastic modulus is higher than that of the surface with a large elastic modulus. The temperature difference between two disks increases as the thermal contact conductance decreases

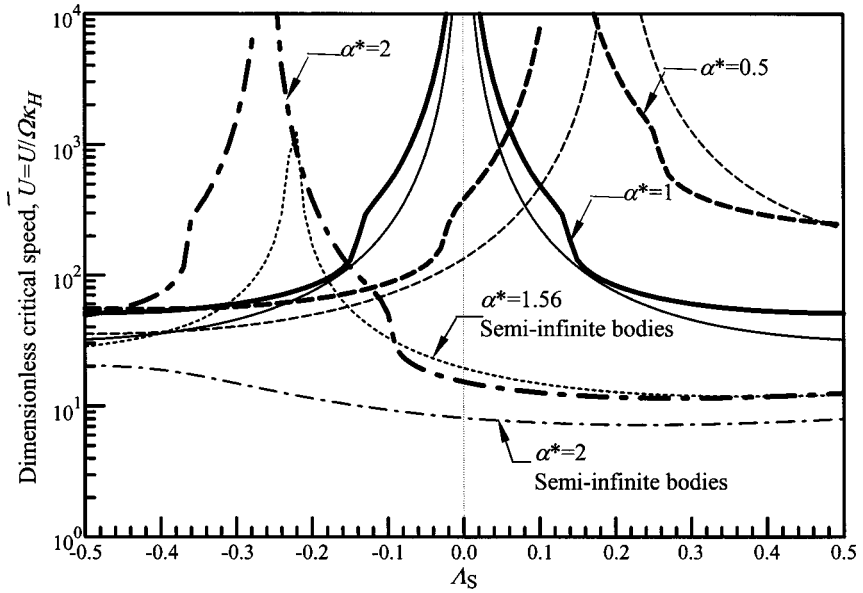


**Fig. 8 Effect of expansion coefficient ratio on the critical speeds ($\kappa^*=k^*=1$; $\Lambda_T=0.2$; $\Omega l_H=\Omega l_L=\Im_c=\infty$)**

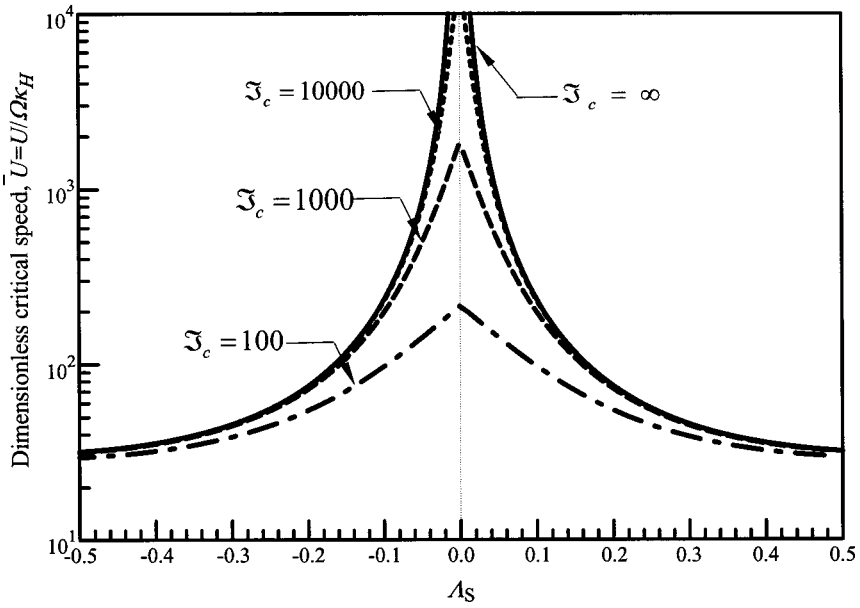


**Fig. 9 Effect of thermal contact conductance on the critical speeds ($\alpha^*=\kappa^*=k^*=1$; $\Lambda_T=0.2$; $\Omega l_H=\Omega l_L=\infty$)**

and the shear parameter $\Lambda_S$ goes to zero. For $\Im_c^* \neq \infty$ the phase shift has a negative value at any $\Lambda_S$, which implies that the wave of the moving body is delayed compared to the stationary body. The phase shift is symmetric about $\Lambda_S=0$. The minimum value of the phase shift occurs at $\Lambda_S=0$. In other words, when the elastic moduli of two bodies are identical, the phase shift becomes a maximum at a given $\Im_c^*$. The absolute value of the phase shift decreases with increasing thermal contact conductance, and becomes nil when $\Im_c^* \to \infty$ (no thermal resistance), as expected.

## 4 Concluding Remarks

An idealized model is developed to understand the mechanism of thermoelastic instability in a system consisting of two bodies of finite thickness and thermal conductivity. Appropriate governing equations are derived to solve the critical speed beyond which the TEI is likely to occur. This model takes into account the surface roughness characteristics of the contacting bodies, the influence of the disk thickness on the critical speed, and the effect of thermal contact conductance at the interface. Simple analytical expressions are provided for the special cases neglecting the disk thickness and the thermal contact conductance. The derived equations show that TEI is governed by eight dimensionless independent parameters. Three parameters are the ratios of thermal properties, one parameter is the thermal contact conductance, and two parameters are related to the thickness. The other two parameters are the shear parameter $\Lambda_S$ and the material parameter $\Lambda_T$. Roughness effect is included in the shear parameter and the material parameter. The shear parameter reduces to the Dundurs' constant multiplied by the friction coefficient for the simple case of the semi-

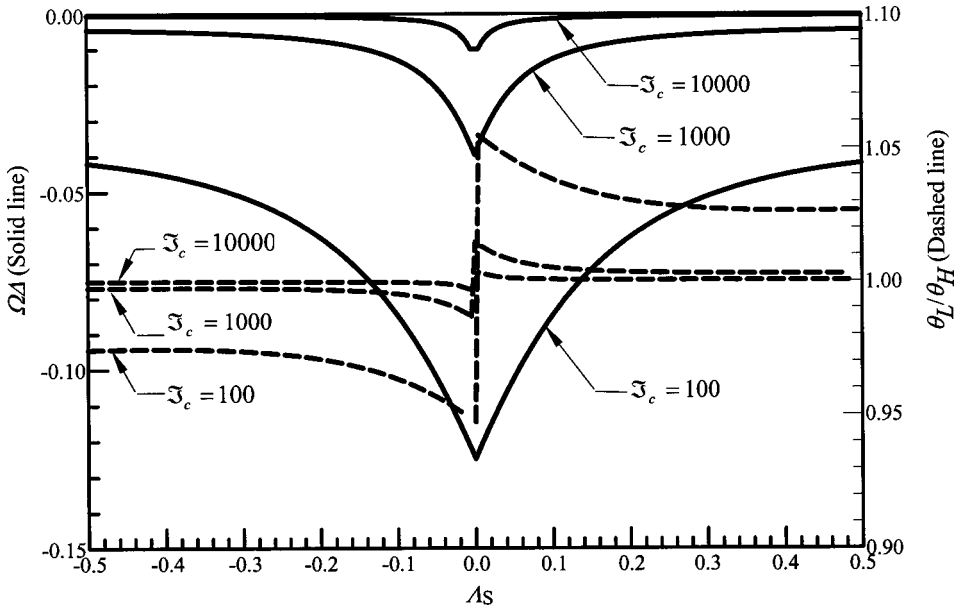


**Fig. 10 Effect of thermal contact conductance on the phase shift and the temperature ratio**

infinite bodies with smooth surfaces. The critical speed decreases with increasing material parameter since the material parameter is directly proportional to the friction coefficient.

The results of a series of simulations show that the critical speed increases when two bodies have identical properties and geometry. Ratios of material properties and geometry of two conducting bodies affect significantly the critical speed. The wave speed is strongly influenced by thermal conductivity and the elastic modulus. The wave is likely to move with the body of higher thermal conductivity or the lower elastic modulus. However, if the finite thickness of the body is considered, the effect of the elastic modulus on the wave speed is reduced considerably. The simulations show that critical speed increases with decreasing applied load leading to increasing surface separation. In most cases, there exist an asymptote where the critical speed goes to infinity. For the identical bodies, this asymptote is located at $\Lambda_S = 0$. This asymptote is shifted depending upon the ratios of thermal conductivities, thermal diffusivities and thermal expansion coefficients. The critical speed increases with increasing the thermal contact conductance (decreasing thermal resistance). At a small thermal contact conductance, the phase shift and the surface temperature ratio become larger. The results show that when parameters $\kappa^*$ or $\alpha^*$ exceeds a certain limiting value, the asymptote of the critical speed disappears and, therefore, cannot be unconditionally stable.

## References


[1] Barber, J. R., 1967, ''The Influence of Thermal Expansion on the Friction Wear Process,'' Wear, **10**, pp. 155–159.

[2] Barber, J. R., 1969, ''Thermoelastic Instabilities in the Sliding of Conforming Solids,'' Proc. R. Soc. London, Ser. A, **312**, pp. 381–394.

[3] Dow, T. A., and Burton, R. A., 1972, ''Thermoelastic Instability of Sliding Contact in the Absence of Wear,'' Wear, **19**, pp. 315–328.

[4] Burton, R. A., Nerlikar, V., and Kilaparti, R., 1973, ''Thermoelastic Instability in a Seal-Like Configuration,'' Wear, **24**, pp. 177–188.

[5] Kilaparti, R., and Burton, R. A., 1976, ''A Moving Hot-Spot Configuration for a Seal-Like Geometry, With Frictional Heating, Expansion and Wear,'' ASLE Trans., **20**, pp. 64–70.

[6] Banerjee, B. N., and Burton, R. A., 1976, ''An Instability for Parallel Sliding of Solid Surfaces Separated by a Viscous Liquid Film,'' J. Lubr. Technol., **98**, pp. 157–166.

[7] Lebeck, A. O., 1980, ''The Effect of Ring Defection and Heat Transfer on the Thermoelastic Instability of Rotating Face Seals,'' Wear, **59**, pp. 121–133.

[8] Barber, J. R., Beamond, T. W., Warning, J. R., and Pritchard, C., 1985, ''Implications of Thermoelastic Instability for the Design of Brakes,'' ASME J. Tribol., **107**, pp. 206–210.

[9] Lee, K., and Barber, J. R., 1993, ''Frictionally Excited Thermoelastic Instability in Automotive Disk Brakes,'' ASME J. Tribol., **115**, pp. 607–614.

[10] Du, S., Zagrodzki, J. R., Barber, J. R., and Hulbert, G. M., 1997, ''Finite Element Analysis of Frictionally Excited Thermoelastic Instability,'' J. Therm. Stresses, **20**, pp. 185–201.

[11] Jang, J. Y., and Khonsari, M. M., 1999, ''Thermoelastic Instability Including Surface Roughness Effects,'' ASME J. Tribol., **121**, pp. 648–654.

[12] Jang, J. Y., and Khonsari, M. M., 2000, ''Thermoelastic Instability With Consideration of Surface Roughness and Hydrodynamic Lubrication,'' ASME J. Tribol., **122**, pp. 725–732.

[13] Jang, J. Y., and Khonsari, M. M., 2002 ''On the Formation of Hot Spots in Wet Clutch Systems,'' ASME J. Tribol., **124**, pp. 336–345.

[14] Yi, Yun-Bo, Barber, J. R., and Zagrodzki, P., 2000, ''Eigenvalue Solution of Thermoelastic Instability Problems Using Fourier Reduction,'' Proc. R. Soc. London, Ser. A, **456**, pp. 2799–2821.

[15] Barber, J. R., 1992, *Elasticity*, Kluwer Academic Publishers, Dordrecht, The Netherlands, pp. 200–201.

[16] Natsumeda, S., and Miyoshi, T., 1994, ''Numerical Simulation of Engagement of Paper Based Wet Clutch Facing,'' ASME J. Tribol., **116**, pp. 232–237.

[17] Greenwood, J. A., and Tripp, J. H., 1970–1971, ''The Contact of Two Nominally Flat Rough Surfaces,'' Proc. Inst. Mech. Eng., **185**, pp. 625–633.

[18] Lee, K., and Barber, J. R., 1993, ''The Effect of Shear Tractions on Frictionally-Excited Thermoelastic Instability,'' Wear, **160**, pp. 237–242.

[19] Dow, T. A., and Stockwell, R. D., 1977, ''Experimental Verification of Thermoelastic Instabilities in Sliding Contact,'' J. Lubr. Technol., **99**, pp. 359–364.

# Direct Computational Simulations for Internal Condensing Flows and Results on Attainability/Stability of Steady Solutions, Their Intrinsic Waviness, and Their Noise Sensitivity

**A. Narain**[1]
Mem. ASME
e-mail: narain@mtu.edu

**Q. Liang**

**G. Yu**

**X. Wang**

Department of Mechanical Engineering–Engineering Mechanics, Michigan Technological University, 1400 Townsend Drive, Houghton, MI 49931

*The paper presents a new two-dimensional computational approach and results for laminar/laminar internal condensing flows. Accurate numerical solutions of the full governing equations are presented for steady and unsteady film condensation flows on a sidewall inside a vertical channel. It is found that exit conditions and noise sensitivity are important. Even for stable steady solutions obtained for nearly incompressible vapor phase flows associated with unconstrained exit conditions, the noise sensitivity to the condensing surface's minuscule transverse vibrations is high. The structure of waves, the underlying characteristics, and the "growth/damping rates" for the disturbances are discussed. A resonance condition for high "growth rates" is proposed and its efficacy in significantly enhancing wave motion and heat transfer rates is computationally demonstrated. For the unconstrained exit cases, the results make possible a separately reported study of the effects of shear, gravity, and surface tension on noise sensitive stable solutions.* [DOI: 10.1115/1.1641063]

## 1 Introduction

Accurate numerical solutions of the full governing equations are presented for steady and unsteady laminar/laminar film condensation flows on a sidewall inside a vertical channel. This is also a good geometry for addressing (see Liang et al. [1] and Liang [2]) the influence of shear over gravity—either by changing the channel inclination from vertical to horizontal (see Fig. 1) or by studying the flow in the absence of gravity (space applications). Such results are important in understanding qualitative phenomena and obtaining quantitative results (after suitable experimental validations of the computational tool for quasi-steady annular/stratified internal condensing flows) that are relevant to good design and performance of condensers in applications (see Krotiuk [3] and Faghri [4]) such as looped heat pipes, capillary pumped loops, thermal management systems, and electronic-cooling devices. These applications often involve pure vapors with none to negligible presence of noncondensable gases. Fundamental results reported in this paper address issues of annular/stratified condensing flows' heat transfer rates, flow realizability, stability, resonant and nonresonant noise sensitivity, and exit condition sensitivity.

This channel flow geometry is also a simple modification of the classical flat plate geometry associated with classical *external* film condensation flow studies over vertical, horizontal, and tilted walls (Nusselt [5], Rohsenow [6], Sparrow and Gregg [7], Koh et al. [8], Dhir and Lienhard [9], Rose [10], Tanasawa [11], Cess [12], Koh [13], etc.). Heat transfer correlations for laminar and wavy condensate situations for the vertical/inclined plate geometry are given by Kutateladze [14] and correlations for turbulent condensate, as proposed by Labuntsov [15], are given in Incropera and DeWitt [16]. For smooth-interface laminar/laminar condensing flows over a flat plate in vertical, horizontal, and tilted configurations; the computational approach developed in this paper yields results (see Yu [17]) in agreement with the relevant solutions of Nusselt [5] and Koh [14].

With regard to *internal* condensing flows, some qualitative understanding exists in papers by Chow and Parish [18], Narain et al. [19], etc. These analyses/predictions rely on integral control volume formulations that employ *models* for interfacial shear (e.g., Henstock and Hanratty [20]) and are typically available only for fast vapor motions requiring no exit condition specification (i.e., the vapor flow in Fig. 1 is ''parabolic''). To address laminar/laminar flow issues that cannot be addressed by the above approach, direct numerical simulations are undertaken here to better understand the wave phenomena and associated effects. Strictly speaking the results presented here are valid only for laminar vapor flows (i.e., inlet vapor Reynolds number based on channel height as characteristic length should be approximately less than 1400–2000) and laminar condensate flows (i.e., film Reynolds number as defined in Incropera and DeWitt [16] should be approximately less than 1400–1800). In practice, inlet vapor Reynolds number up to 7000 is allowed because of sufficiently thick laminar sub-layer in the vicinity of the interface. This is because vapor streamlines, as they approach the interface, are almost perpendicular to it (see Liang et al. [1]) and the velocity along the streamlines are very small. This allows the vapor streamlines to pierce the interface and drift downstream as liquid streamlines in an even slower motion of the *laminar* condensate. As a result, it is found that computational predictions of film thickness, heat transfer rates, etc. under laminar/laminar assumptions (though perhaps

[1]To whom correspondence should be addressed.

Contributed by the Applied Mechanics Division of THE AMERICAN SOCIETY OF MECHANICAL ENGINEERS for publication in the ASME JOURNAL OF APPLIED MECHANICS. Manuscript received by the Applied Mechanics Division, December 12, 2002; final revision, June 9, 2003. Associate Editor: T. E. Tezduyar. Discussion on the paper should be addressed to the Editor, Prof. Robert M. McMeeking, Journal of Applied Mechanics, Department of Mechanical and Environmental Engineering, University of California–Santa Barbara, Santa Barbara, CA 93106-5070, and will be accepted until four months after final publication of this paper in the ASME JOURNAL OF APPLIED MECHANICS.

  

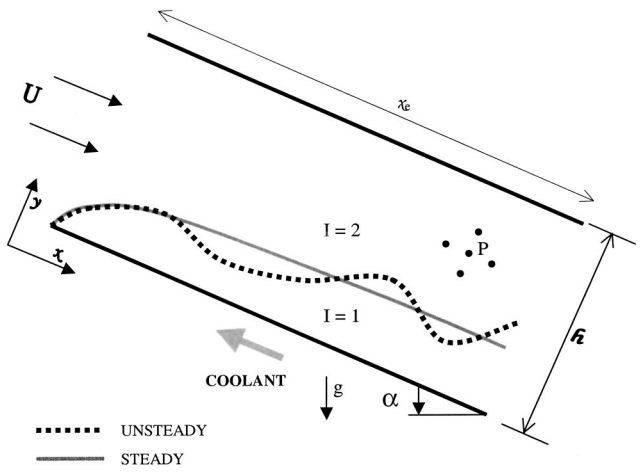


**Fig. 1 Flow geometry for simulations**

not the predictions of vapor velocity profile outside the laminar sublayer of the vapor surrounding the interface!) are in good agreement (see Liang et al. [1]) up to inlet Reynolds number as high as 8000, with relevant experimental results of Lu [21].

This paper proposes a novel and direct computational technique for steady and unsteady internal condensing flows in the annular/stratified regime. The unsteady laminar/laminar simulations employ a suitable adaptive grid and numerical solution of the appropriate hyperbolic *interface tracking equation* which is the same as the one used in level-set method (see Sussman et al. [22] and Son and Dhir [23]), VOF method (see Hirt and Nichols [24]), and other methods (Tezduyar [25], etc.). The numerical scheme used in this paper for the *interface tracking equation* exploits existing mathematical knowledge and experience for this equation (see Abbott and Basco [26]) to sidetrack the inaccuracy problems associated with reconstructing interface location within and around the *interface cells* predicted by VOF or related interface *capturing* techniques (see Tezduyar [25], Li and Renardy [27], etc.). The scheme used here ensures convergence and accuracy of both the amplitude and the phase of the interfacial waves. At each time step, the scheme locates the interface, solves the Navier-Stokes equation in each phase, satisfies the full nonlinear conditions at the phase-change interface, and satisfies the relevant inlet, outlet, and wall conditions. Since vapor in internal condensing flows slow down by the exit, the steady vapor flow equations are ''elliptic'' in the exit region (i.e., downstream points affect a flow variable's value at a representative point P in Fig. 1) and exit condition needs to be specified for a solution. Note that any condenser section of the type shown in Fig. 1 is, typically, just a *part* of a flow loop. A flow loop which maintains a constant pressure $p_0$ and constant flow rate of saturated vapor at the inlet may also be designed (see, e.g., Fig. 2) to provide: (a) an unconstrained exit condition (which is very often the case when exit pressure, or equivalently, exit vapor flow rate is free to adjust to any value it seeks) that allows the vapor to flow at nearly constant density (its density at the inlet), or (b) a constrained exit condition (this situation arises, when further downstream of the exit, there are natural constraints in the flow loop or, as in Fig. 2, there are active flow control devices) that forces non-negligible vapor density variations between the inlet and the outlet of the condenser section. For the constrained exit case not considered in this paper, the ''unsteady'' equations are also spatially ''elliptic'' near the exit and an exit condition can be prescribed if a nonconstant vapor density and an equation of state—of the type $\rho_2=\rho_2(p_2,\mathcal{T}_2)$— is incor-

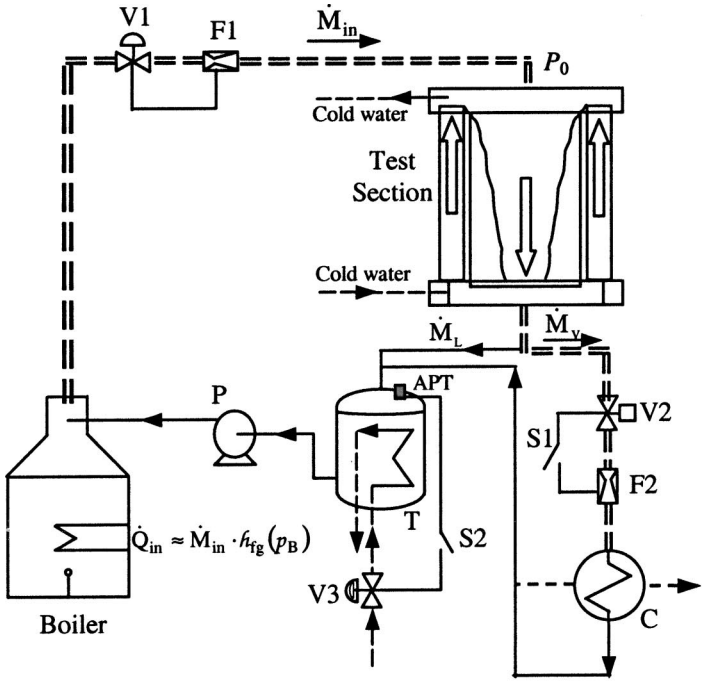


V1, V2: Solenoid Valve
V3: Pneumatic Valve
F1, F2: Flow Meter
S1, S2: Switch
P: Variable Head Pump
T: Sub cooled Tank
C: Auxiliary Condenser
APT: Absolute Pressure Transducer

Unconstrained Exit:
With fixed pressure and flow rate at the inlet of the test-section, valve V2 and pressure in T are not actively controlled (S1 and S2 open) and steady state is naturally achieved with tank T completely filled with liquid. The system finds natural values of exit vapor quality $Z_e = Z_e|_{Na}$ and pressure at APT.

Constrained Exit:
With fixed pressure and flow rate at the inlet of the test-section, valve V2 is controlled to a set point value in F2 while the pressure at APT in a partially filled T is held fixed at a value lower than its natural value for the unconstrained case. The flow can now be steady/quasi-steady at different exit vapor qualities (including $Z_e \neq Z_e|_{Na}$).

**Fig. 2 The solenoid valve *V*1 (actively controlled by flow meter *F*1) and constant heat input $\dot{Q}_{in} \approx \dot{M}_{in} \cdot h_{fg}(p_B)$ to the boiler fixes inlet pressure $p_0$ and inlet flow rate to the test section. The mass flow rate through pump *P* is adjusted to a value that matches the corresponding value at *F*1. A high flow rate of the coolant (water) flow around the test section fixes condensing surface temperature at a nearly uniform value of $\mathcal{T}_w$ while it still allows for different heat removed rates for different exit qualities $Z_e$.**

porated in the governing equations for the vapor phase. The unconstrained exit case, for which vapor compressibility is unimportant, is the focus of steady and unsteady simulations in this paper. For these simulations the ''unsteady'' equations for the unconstrained exit case are *not* spatially ''elliptic'' and an exit condition cannot be prescribed if a constant inlet vapor density $\rho_2=\rho_{20}$ is assumed in the governing equations. Constant vapor density assumption is valid for conditions involving $\Delta\rho_2/\rho_{20}\ll 1$ or, say, $\Delta\rho_2/\rho_{20}$ is less than 5% —this being the typical criteria for assuming incompressibility for gases that flow inside a duct and have Mach number values less than 0.3. For the unconstrained exit cases involving an assumed constant density for the vapor phase, it is shown in this paper that, if at $t=0$, one starts at *any* steady solution of the steady ''elliptic'' problem in Fig. 1 (under *any* reasonable and well-defined exit condition), then, over time (utilizing unconstrained unsteady simulation for $t\geqslant 0$), a natural steady solution and an associated natural exit condition is obtained at large times. This naturally determined value of the exit condition for prescribed inlet condition is very similar to the well-known behavior of other incompressible duct flows (single phase or air/water flows) which also exhibit well-defined pressure difference for given inlet pressure and flow rate. In fact, in Liang et al. [1], it is shown that the naturally selected quasi-steady computational solutions that are obtained for flow cases considered in the experimental runs of Lu [21] and Lu and Suryanarayana [28] yield values of film thickness, heat transfer rates, etc., that are in good agreement with experimentally obtained values. While this generates confidence in the proposed method of identifying stable steady solutions, these stable solutions are shown here to be sensitive to minuscule bottom plate noise that are typically almost always present. This makes the interface wavy for most situations. The reported determination of phase speeds and *characteristics curves* (along which disturbances propagate) for the waves improve our understanding of these flows and leads to a proposal of a new hitherto unknown resonance condition whose efficacy is also demonstrated in this paper. It is shown that specifically designed noise sources placed at suitably specified locations and specified variations in frequency satisfy the resonance criteria and enhance the wave energy and heat transfer rates significantly.

Unsteady simulations starting from steady solutions for the constrained exit cases are not considered here. In this case, compressibility effects on the stability and noise-sensitivity are expected to be important and these effects are one of the underlying causes behind various interesting experimental results (see Bhatt et al. [29], etc.) dealing with experiments whose exit conditions are constrained. The stability and flow oscillations issues associated with this case are also believed to arise in applications such as Looped Heat Pipes (Faghri [4]) where limits on the power of passive pumping (wicks, etc.) cause pressure variation constraints at the condenser exit while approximately constant values of pressure and flow rate is retained at the condenser inlet.

This paper restricts itself to consideration of single but arbitrary Fourier components of bottom plate noise (standing waves) and avoids discussions of wave interactions resulting from more complex random noises made up of several Fourier components. Within this limited context, we find that the front-steepening solitary wave patterns that are experimentally observed on air/water type vertical liquid films (see Liu and Gollub [30] and Alekseenko, et al. [31]) or the ones that are obtained by Miyara [32] in the reported computational simulations for the Nusslet [5] problem that deals with condensation on a vertical plate, occur much more gradually for the gravity dominated internal condensing flow cases considered here. Categorization of *typical noise levels* (with a random mix of amplitude, frequency, and wavelengths) and *typical responses* (or *strange attractors* as termed by Liu and Gollub [30]) requires separate study and is outside the scope of this paper. Furthermore, unlike gravity driven shallow or deep water waves (see Lighthill [33]), the reported waves, in their linearized limits, are nondispersive (i.e., phase speeds do not depend on the frequency or wavelengths of the disturbance). For the above reasons, neither a survey of results nor comparisons with results from the vast literature on noncondensing air/water type film flows (Alekseenko et al. [31]) is considered to be within the scope of this paper.

The results presented here underscore the importance of including the role of exit conditions and noise sensitivity in categorizing heat transfer correlations and flow regime maps. Therefore currently available heat transfer correlations (Traviss et al. [34]; Shah [35]; etc.) and flow regime maps (see Hewitt et al. [36], Carey [37], etc.) can be improved to address their reported deficiencies (see Palen et al. [38]). Therefore the reported results on exit conditions, noise sensitivity, and flow regime boundaries—in conjunction with proper experiments and use of computational tool such as the one proposed here—will eventually be of value in better categorization and development of relevant heat-transfer correlations and flow regime maps.

## 2 Governing Equations

The liquid and vapor phases in the flow (e.g., see Fig. 1) are denoted by a subscript $I$: $I=1$ for liquid and $I=2$ for vapor. The fluid properties (density $\rho$, viscosity $\mu$, specific heat $C_p$, and thermal conductivity $k$) with subscript $I$ are assumed to take their representative constant values for each phase ($I=1$ or 2). Let $\mathcal{T}_I$ be the temperature fields, $p_I$ be the pressure fields, $\mathcal{T}_s(p)$ be the saturation temperature of the vapor as a function of local pressure $p$, $\Delta$ be the film thickness, $\dot{m}$ be the local interfacial mass flux, $\mathcal{T}_w$ $(x)$ $(<\mathcal{T}_s(p))$ be a *known* temperature variation of the cooled bottom plate, and $\mathbf{v}_I=u_I\hat{\mathbf{i}}+v_I\hat{\mathbf{j}}$ be the velocity fields. Furthermore, let h be the channel height, $g_x$ and $g_y$ be the components of gravity along $x$ and $y$-axes, $p_0$ be the inlet pressure, $\Delta T\equiv\mathcal{T}_s(p_0)-\mathcal{T}_w(0)$ be a representative controlling temperature difference between the vapor and the bottom plate, $h_{fg}$ be the heat of vaporization at temperature $\mathcal{T}_s(p)$, and $U$ be the *average* inlet vapor speed determined by the inlet mass flux. With $t$ representing the actual time and $(x, y)$ representing physical distances of a point with respect to the axes in Fig. 1 ($x=0$ is at the inlet and $y=0$ is at the condensing surface), we introduce a new list of fundamental nondimensional variables—viz. $(x,y,t,\delta,u_I,v_I,\pi_I,\theta_I,\dot{m})$ —through the following definitions:

$$\{x,y,\Delta,u_I,\dot{m}\}\equiv\{h.x,h\cdot y,h\cdot\delta,U\cdot u_I,\rho_I\cdot U\cdot\dot{m}\}$$

$$\{v_I,\mathcal{T}_I,p_I,t\}\equiv\{U\cdot v_I,(\Delta\mathcal{T})\cdot\theta_I,p_0+\rho_I U^2\cdot\pi_I,(h/U)\cdot t\}. \tag{1}$$

**Interior Equations.** The nondimensional differential forms of mass, momentum ($x$ and $y$ components), and energy equations for incompressible flow in the interior of either of the phases are the well-known equations:

$$\frac{\partial u_I}{\partial x}+\frac{\partial v_I}{\partial y}=0$$

$$\frac{\partial u_I}{\partial t}+u_I\frac{\partial u_I}{\partial x}+v_I\frac{\partial u_I}{\partial y}=-\left(\frac{\partial\pi_I}{\partial x}\right)+\mathrm{Fr}_x^{-1}+\frac{1}{\mathrm{Re}_I}\left(\frac{\partial^2 u_I}{\partial x^2}+\frac{\partial^2 u_I}{\partial y^2}\right)$$

$$\frac{\partial v_I}{\partial t}+u_I\frac{\partial v_I}{\partial x}+v_I\frac{\partial v_I}{\partial y}=-\left(\frac{\partial\pi_I}{\partial y}\right)+\mathrm{Fr}_y^{-1}+\frac{1}{\mathrm{Re}_I}\left(\frac{\partial^2 v_I}{\partial x^2}+\frac{\partial^2 v_I}{\partial y^2}\right)$$

$$\frac{\partial\theta_I}{\partial t}+u_I\frac{\partial\theta_I}{\partial x}+v_I\frac{\partial\theta_I}{\partial y}\approx\frac{1}{\mathrm{Re}_I\,\mathrm{Pr}_I}\left(\frac{\partial^2\theta_I}{\partial x^2}+\frac{\partial^2\theta_I}{\partial y^2}\right), \tag{2}$$

where $\mathrm{Re}_I\equiv\rho_I Uh/\mu_I$, $\mathrm{Pr}_I\equiv\mu_I C_{pI}/k_I$, $\mathrm{Fr}_x^{-1}\equiv g_x h/U^2$ and $\mathrm{Fr}_y^{-1}\equiv g_y h/U^2$.

**Interface Conditions.** The nearly exact interface conditions (see Delhaye [39], etc.) for condensing flows are given in the Appendix (see Eqs. (*A*1)–(*A*8)). Utilizing a superscript "*i*" for values of flow variables at the interface $\mathcal{H}=y-\Delta(x,t)=0$, nondimensional forms of the interface conditions in the Appendix are as given below.

- The nondimensional form of the requirement of continuity of tangential component of velocities, as given by Eq. (*A*2), becomes
$$u_2^i = u_1^i - \delta_x (v_2^i - v_1^i), \tag{3}$$
where $\delta_x \equiv \partial\delta/\partial x$.
- The nondimensional form of the normal component of momentum balance at the interface, as given by Eq. (*A*3), becomes
$$\pi_1^i = \frac{\rho_2}{\rho_1}\pi_2^i - \frac{1}{\mathrm{We}}\left(\frac{\delta_{xx}}{[1+\delta_x^2]^{3/2}}\right) + \dot{m}^2\left(\frac{\rho_1}{\rho_2}-1\right), \tag{4}$$
where $\mathrm{We}\equiv\rho_1 U^2 h/\sigma$, and surface tension $\sigma$ is assumed to be nearly constant because of the nearly constant interface temperature. As reported elsewhere, results for $\sigma=\sigma(\mathcal{T}_s(p_2^i))$ in Eqs. (*A*3)–(*A*4), are nearly the same as the ones reported here for constant $\sigma$.
- The tangential component of momentum balance at the interface, as given by Eq. (*A*4), becomes
$$\left.\frac{\partial u_1}{\partial y}\right|^i = \frac{\mu_2}{\mu_1}\left.\frac{\partial u_2}{\partial y}\right|^i + [t], \tag{5}$$
where the term $[t]$ in Eq. (5) is defined in Eq. (*A*9) of the Appendix.
- The nondimensional form of mass fluxes $\dot{m}_{LK}$ and $\dot{m}_{VK}$ in Eq. (*A*5) become
$$\dot{m}_{LK} \equiv [u_1^i(\partial\delta/\partial x) - (v_1^i - \partial\delta/\partial t)]/\sqrt{1+(\partial\delta/\partial x)^2}, \quad \text{and}$$
$$\dot{m}_{VK} \equiv (\rho_2/\rho_1)[u_2^i(\partial\delta/\partial x) - (v_2^i - \partial\delta/\partial t)]/\sqrt{1+(\partial\delta/\partial x)^2} \tag{6}$$
- The nondimensional form of $\dot{m}_{\mathrm{Energy}}$ in Eq. (*A*6) becomes
$$\dot{m}_{\mathrm{Energy}} \equiv \mathrm{Ja}/(\mathrm{Re}_1\,\mathrm{Pr}_1)\{\partial\theta_1/\partial n|^i - (k_2/k_1)\partial\theta_2/\partial n|^i\}, \tag{7}$$
where $\mathrm{Ja}\equiv C_{p1}\Delta T/h_{fg}^0$, and $h_{fg}^0 \equiv h_{fg}(\mathcal{T}_s(p_o))$.
- Nondimensional form of interfacial mass balance in Eq. (*A*7) becomes
$$\dot{m}_{LK} = \dot{m}_{VK} = \dot{m}_{\mathrm{Energy}} \equiv \dot{m}. \tag{8}$$
- The nondimensional thermodynamic restriction on interfacial temperatures, as given by Eq. (*A*8), becomes
$$\theta_1^i \cong \theta_2^i = \mathcal{T}_s(p_2^i)/\Delta\mathcal{T} \equiv \theta_s(\pi_2^i). \tag{9}$$

Within the vapor phase, for the refrigerants considered here, changes in absolute pressure relative to the inlet pressure are typically small to affect temperatures. Therefore $\theta_s(\pi_2^i)\cong\theta_s(0)$.

**Boundary Conditions.** The problem posed by Eqs. (2)–(9) are computationally solved subject to boundary conditions that are

- at the inlet ($x=0, 0\leqslant y\leqslant 1$) at any time *t*:
$$u_2(0,y,t)=1 \quad v_2(0,y,t)=0$$
$$\pi_2(0,y,t)=0 \quad \theta_2(0,y,t)=\theta_s(0). \tag{10}$$
- at the bottom wall ($y=0, 0\leqslant x\leqslant x_e$) at any time *t*:
$$u_1(x,0,t)=0, \quad v_1(x,0,t)=0, \quad \theta_1(x,0,t)=\theta_w, \tag{11}$$
where $\theta_w\equiv\mathcal{T}_w(x)/\Delta\mathcal{T}$ is a constant unless it is otherwise specified. In case of flow in Fig. 2, this situation arises whenever, for a given heat load, the coolant flow rate is high enough to make the coolant its temperature rise negligible as it flows past the test section.
- at the top wall ($y=1, 0\leqslant x\leqslant x_e$) at any time *t*:
$$u_2(x,1,t)=0, \quad v(x,l,t)=0, \quad \theta_2(x,1,t)=\theta_s(0). \tag{12}$$

Furthermore, because of the nature of boundary conditions in Eqs. (10)–(12), $\theta_2(x,y,t)\cong\theta_s(0)$ is assumed/prescribed to limit the discussions in this paper to the flow of saturated vapor. This is done because, for the *pure* vapor flows considered here, it is easy to verify the well-known fact that the effects of superheat (commonly in the 5–10°C range) are negligible.

**Exit Conditions.** Any condenser section of the type shown in Fig. 1 is typically a *part* of a closed flow loop. A flow loop (see, e.g., Fig. 2), which maintains a constant flow rate and constant pressure $p_o$ (i.e. $\pi_2=0$) at the inlet, may also be designed to provide: (a) an unconstrained exit condition (which is very often the case), or (b) a constrained exit condition (this may arise from downstream constraints in the flow loop or active flow control of the downstream flow). An exit condition, at any time *t*, is specified by either specifying the value of the average cross-sectional pressure of the vapor at the exit or, equivalently (as seen later from results such as the one in Fig. 6), by specifying the exit vapor quality $Z_e(t)$. Exit vapor quality $Z_e(t)$ is the ratio of vapor mass flow rate at exit ($x=x_e$) to vapor mass flow rate at inlet.

For the case of *constrained* exit conditions, vapor compressibility effects cannot be ignored for unsteady simulations, and hence one cannot treat vapor density $\rho_2(x,y,t)$ to be a constant equal to its inlet value $\rho_{20}$. For these compressible cases, the "elliptic" equations for the vapor would require specification of the exit vapor quality $Z_e(t)$ defined as
$$Z_e(t) = \int_{\delta(x_e,t)}^{1} \{\rho_2(x_e,y,t)/\rho_{20}\} u_2(x_e,y,t)\cdot dy, \tag{13}$$
while allowing for nonconstant unsteady/steady vapor density values. This constrained exit case, though important in some cases because of the interesting compressibility effects on flow stability and noise sensitivity (see Bhatt et al. [27], etc.), is not considered here.

For the "elliptic" steady cases considered here for $t\leqslant 0$, the vapor density is assumed to be a constant with $\rho_2=\rho_{20}$ and exit condition is specified here by assigning a fixed value for the exit vapor quality $Z_e$ given by
$$Z_e = \int_{\delta_{\mathrm{steady}}(x_e)}^{1} u_{2\,\mathrm{steady}}(x_e,y)\cdot dy. \tag{14}$$

For unsteady cases under the assumption of constant vapor densities $\rho_2(x,y,t)=\rho_{20}$, the "unsteady" equations are not "elliptic" near the exit and unsteady exit vapor quality $Z_e(t)$ in Eq. (13) cannot be specified.

**Initial Conditions.** If $t=0$ is chosen to be the time when saturated vapor first comes in contact and condenses on a dry subcooled ($\mathcal{T}_w(x)<\mathcal{T}_s(p_0)$) bottom plate, the above described *continuum* equations do not apply at early times ($t\sim 0$) because they do not model and incorporate relevant intermolecular forces into the governing equations. These intermolecular forces are important in determining the evolution of very thin (approximately over 10–100 nm of film thickness) condensate film $\delta(x,t)$. Because of the above modeling limitations, the strategy here is to start at $t=0$, with *any* sufficiently thick *steady* solution of the *continuum* equations where all the governing equations clearly apply. That is, if $\phi(x,y,t)$ is any variable (such as $u_I$, $v_I$, $\pi_I$, $\theta_I$, etc.), the initial values of $\phi$ and film thickness $\delta(x,t)$ are such that
$$\phi(x,y,0)=\phi_{\mathrm{steady}}(x,y) \quad \text{and} \quad \delta(x,0)=\delta_{\mathrm{steady}}(x), \tag{15}$$
where $\phi_{\mathrm{steady}}$ and $\delta_{\mathrm{steady}}$ are solutions of the governing equations obtained by dropping all time dependencies in Eqs. (2)–(12) and solving the resulting steady equations (which are *elliptic* near exit) for *any* arbitrarily prescribed value of $Z_e(0)=Z_e$, where $Z_e$ is given by Eq. (14). The prescription of $Z_e$ within $0<Z_e<1$ is

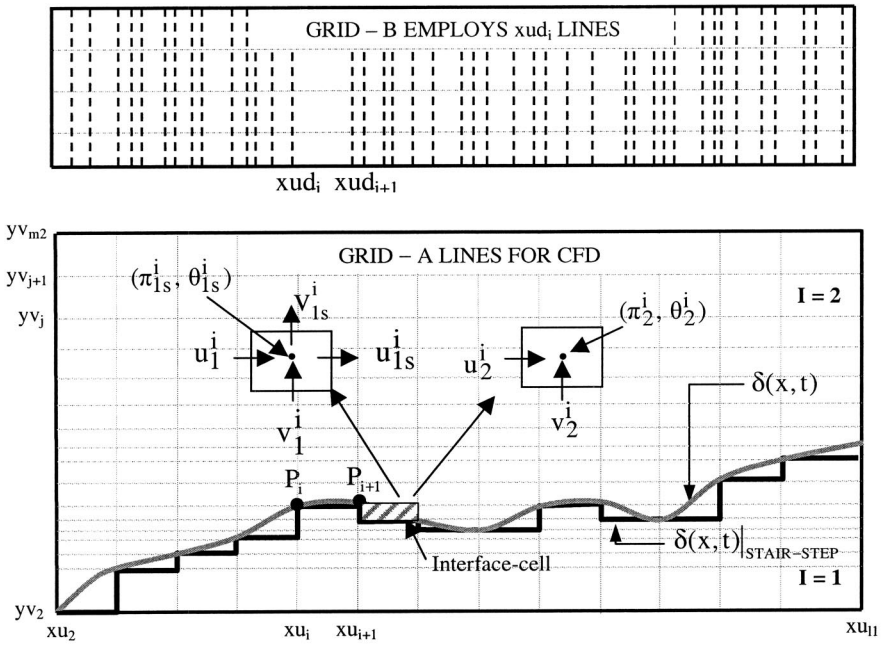


**Fig. 3 Computational grids for flow simulation. For chosen $xu_i$ lines, $yv_j$ lines in grid A are first generated by points $P_i$ on $\delta(x,t)$. Above the "highest" $yv_j$ line thus obtained, the remaining $yv_j$ lines are independently generated with suitable unequal spacings. Grid B lines at $x = xud_i$ are different from $xu_i$ lines and are used for tracking the interface $\delta(x,t)$.**

arbitrary except that it should be such that it should allow a steady computational solution in the stratified/annular regime indicated in Fig. 1. It is shown later that there exists a naturally selected value of $Z_e$ (denoted as $Z_e|_{\mathrm{Na}}$) which allows the steady solution to be stable and consistent with the chosen constant vapor density.

An inspection of all the non-dimensional governing equations, interface conditions, and boundary conditions reveal the fact that the flows considered here are affected by the following set of nondimensional parameters:

$$\left\{ \mathrm{Re}_{in}, \mathrm{Ja}, \mathrm{Fr}_x^{-1}, \frac{\rho_2}{\rho_1}, \frac{\mu_2}{\mu_1}, \mathrm{Pr}_1, x_e, Z_e(0), \mathrm{We}, \mathrm{Fr}_y^{-1} \right\}, \qquad (16)$$

where $\mathrm{Re}_{in} \equiv \rho_2 U h/\mu_2 \equiv \mathrm{Re}_2$. Here $\mathrm{Re}_{in}$, $\mathrm{Fr}_x^{-1}$, and Ja are control parameters associated with inlet speed $U$, inclination $\alpha$, and temperature difference $\Delta T$. For *unconstrained* exit conditions considered here, it is seen later that $Z_e(0)$ is not important because it does not affect the naturally selected steady solution and its associated exit vapor quality $Z_e|_{\mathrm{Na}}$. For *constrained* exit conditions not studied here, e.g., a prescription of time-averaged $Z_e(t) = Z_e(0)$ or $Z_e(t) = Z_e(0)$ for all $t \geq 0$, the value of the parameter $Z_e(0)$ becomes important. The density ratio $\rho_2/\rho_1$, viscosity ratio $\mu_2/\mu_1$, and Prandtl number $\mathrm{Pr}_1$ are passive fluid parameters. Also, for unsteady or quasi-steady wavy-interface situations, the above equations imply additional dependences on a surface tension parameter, Weber number $\mathrm{We} \equiv \rho_1 U^2 h/\sigma$, and a transverse gravity parameter $\mathrm{Fr}_y^{-1} \equiv g_y h/U^2$. For superheated vapors, there is a very weak dependence, through Eq. (7), on the thermal conductivity ratio $k_2/k_1$.

## 3 Computational Approach for Steady and Unsteady Solutions

For readers not interested in algorithm or code development, only a cursory reading of this section is recommended.

**Adaptive Grid and Computational Approach.** At each interface configuration, while solving the steady or unsteady problem, the fluid flow computational domains for each phase ($I = 1$ or 2) are defined by grid A in Fig. 3. A finite number of discrete points $P_i$ on the interface define a stair-step geometrical approximation for the interface $\delta(x,t)$. Use of this stair-step approximation still allows second-order ($O(\Delta x^2)$ and $O(\Delta t^2)$) accurate physical values of $\delta(x_{P_i}, t)$ because these values are used to generate higher order approximations to estimate intermediate physical values of $\delta(x,t)$ for discretization of the interface conditions (e.g., piecewise linear approximations for evaluation of the slope terms and cubic splines for evaluation of $\partial^2\delta/\partial x^2$ term appearing in the surface tension term of Eq. (4)). Each interface point $P_i$, at $x = xu\ (i)$, are marked by a tagging function "$xx\ (i)$" to identify whether the point belongs to an increasing ($xx\ (i) = 1$), flat ($xx\ (i) = 0$), or decreasing ($xx\ (i) = -1$) section of the interface. These points are also used to generate and define the $xu$ and $yv$ lines that are parallel to the coordinate axes (see Section 4.3 of Liang [2] for details). These lines also form the faces of the rectangular finite volume cells in the interior of each of the two phases.

For the *interiors* of the two fluid phases defined by grid A in Fig. 3, the chosen CFD approach is same as the SIMPLER approach of Patankar [40]. This makes the computations in the interior quite conservative because all balance laws are satisfied even for the coarser control volumes. However, at any time $t$ and location $(x, y)$ where the control volume (say of size $\Delta x_c \times \Delta y_c$) are near the interface cells, the truncation errors $\Delta\delta_T$ and $\Delta\phi_T$ in the discretizations for film thickness $\delta$ and any other flow variable $\phi$ are given by the relations

$$\Delta\varphi_T \approx \sqrt{\Delta\varphi_x^2 + \Delta\varphi_y^2 + \Delta\varphi_t^2} \quad \text{and} \quad \Delta\delta_T \approx \sqrt{\Delta\delta_x^2 + \Delta\delta_t^2}, \qquad (17)$$

where $\Delta\varphi_x \equiv \partial\varphi/\partial x \cdot \Delta x_c$, $\Delta\varphi_y \equiv \partial\varphi/\partial y \cdot \Delta y_c$, $\Delta\varphi_t \equiv \partial\varphi/\partial t \cdot \Delta t_c$, $\Delta\delta_x \equiv \partial^2\delta/\partial x^2 \cdot (\Delta x_c)^2$, and $\Delta\delta_t \equiv \partial^2\delta/\partial t^2 \cdot (\Delta t_c)^2$. The first order accuracy in $\phi$ above is due to second order discretization of $\delta$ and a mixed second-order and first-order discretizations for the remaining terms appearing in the interface conditions.

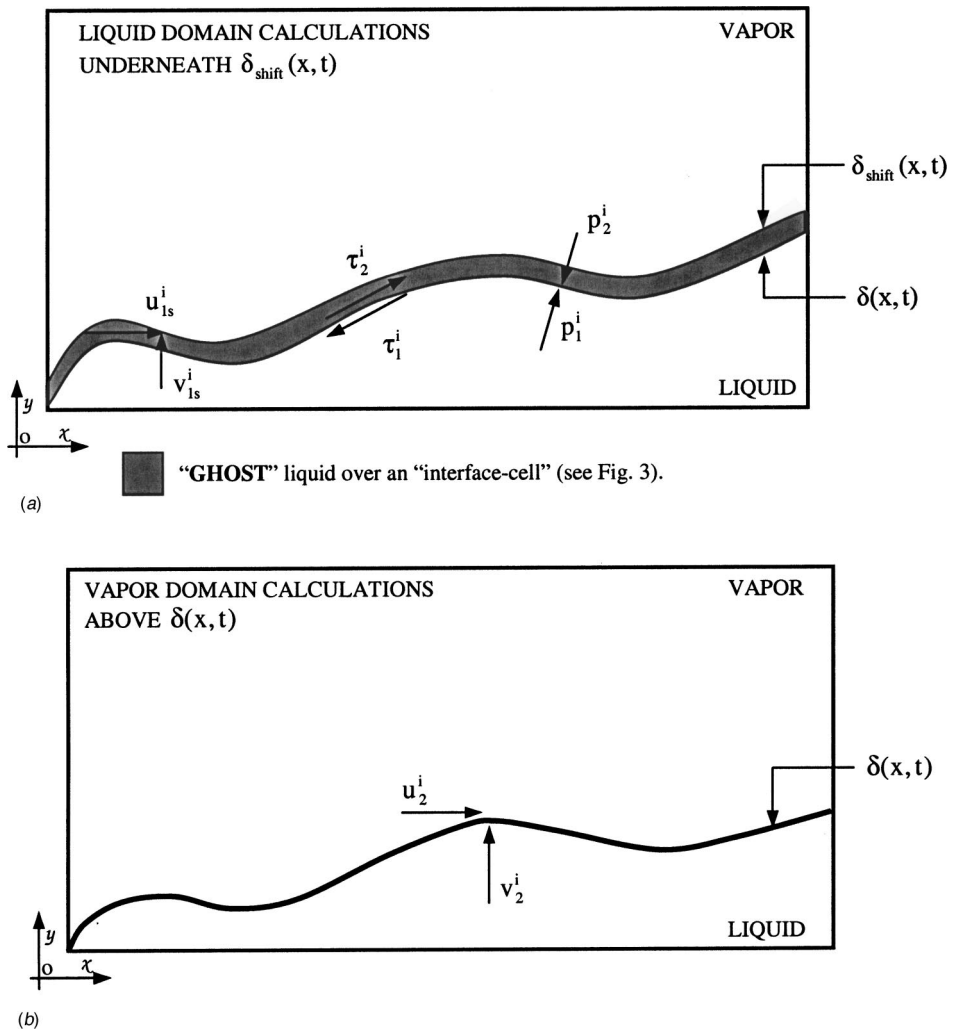


**Fig. 4 (*a*) The liquid domain calculations underneath $\delta_{shift}(x,t)$ with prescribed values of $(u_{1s}^i, v_{1s}^i, \theta_{1s}^i)$ on $\delta_{shift}(x,t)$ satisfy the shear and pressure condition on $\delta(x,t)$. (*b*) The vapor domain calculations above $\delta(x,t)$ with prescribed values of $(u_2^i, v_2^i, \theta_2^i)$ on $\delta(x,t)$ satisfy $\dot{m}_{VK} = \dot{m}_{Energy}$ and the requirement of continuity of tangential velocities.**

While consistent higher order discretizations of all the interface conditions can enhance accuracy, it is important to recall that the overall discretization errors in the solutions is best estimated by the convergence trends observed during refinement of the grids (see Section 3.10 of Ferziger and Peric [41]). Since the nonuniform grid A is very refined in the *y*-direction near the interface (i.e., small $\Delta y_c^i$) and acceptably coarse along the *x*-direction ($\Delta x_c^i$), the overall convergence trends (discussed in Section 6) are found to be good without excessive computational penalties in terms of memory and speed requirements (see Liang [2]).

With the help of known inlet and boundary conditions and standard CFD approach for single fluid flows, separate solutions for each domain is easy to obtain provided one has a correct guess of the interface $\delta(x,t)$ and correct values of $\{u_1^i, v_1^i, \theta_1^i\}$ on the interface in Fig. 4(*a*) (or, as depicted in the inset of Fig. 3, on a representative liquid interface cell in grid A), and, also, correct values of $\{u_2^i, v_2^i, \theta_2^i\}$ on the interface in Fig. 4(*b*) (or, as depicted in the inset of Fig. 3, on a representative vapor interface cell in grid A). In reality though, one has to make tentative guesses of these seven variables—viz: $\{u_1^i, v_1^i, \theta_1^i, u_2^i, v_2^i, \theta_2^i, \delta\}$—and then iteratively arrive at their correct values by repeatedly updating them with the help of the interface conditions, vapor domain solutions, and liquid domain solutions. Disregarding the two known and nearly constant temperatures $\theta_1^i$ and $\theta_2^i$ obtained through Eq. (9), the remaining *five* guesses are updated to their correct values with the help of *five* interface conditions—three from Eqs. (3)–(5) and two from Eq. (8). However, on use of the above described approach for obtaining a steady solution of the ''elliptic'' steady problem, it is found that such steady solutions are not *unique* and many liquid/vapor interface configurations are possible unless a suitable exit condition is specified. That is steady solutions carry the signature of the well-known degeneracy associated with saturated vapor's quality (i.e., any liquid/vapor interference configuration or all vapor or all liquid) under quiescent and equilibrium thermodynamic conditions. To find a unique steady solution, the exit vapor quality $Z_e$ is specified (this is equivalent to specifying exit pressure or the amount of heat removed) and only then a unique solution is obtained (this is accomplished by ''creating' a fictitious interface type condition described later in Eq. (19)). For unsteady simulations, if the exit conditions are unconstrained and the vapor flow is incompressible, one can start from one of these steady solutions at time $t=0$ and ascertain the real time evolution of this solution at $t>0$ without specifying the exit quality $Z_e(t)$. As $t\to\infty$, these unsteady solutions naturally seek out the right exit conditions that are consistent with the assumed constant value of the vapor density. For these unsteady solutions, the five values of

$\{u_1^i, v_1^i, u_2^i, v_2^i, \delta\}$ at any time "$t+\Delta t$" are obtained from the known values of these variables at time "$t$" and the *five* interface conditions (three from Eqs. (3)–(5) and two from Eq. (8)) discussed earlier. For the constrained exit case not considered in this paper, prescription of the value of $Z_e(t)$ at all times "$t$" (with the help of an equation of the type given in Eq. (19)) requires nonconstant vapor density $\rho_2$ and this changes the list of interfacial unknowns to eight: viz. $\{u_1^i, v_1^i, \theta_1^i, u_2^i, v_2^i, \theta_2^i, \delta, \rho_2^i\}$. Again this compressible case becomes solvable with eight conditions (the earlier seven interface conditions plus the eighth condition arising from the specified exit condition) for eight interfacial unknowns that need to be guessed for the unsteady equations governing condensing flows with compressible vapor.

To obtain separate calculations for the vapor domain in Fig. 4(*b*), the temporarily guessed values of $\{u_2^i, v_2^i, \theta_2^i\}$ on the interface are temporarily held fixed along the interface and the entire vapor flow field on grid A of Fig. 3 is obtained with the help of the inlet and the top wall conditions. After obtaining the full solution, the flow field values underneath the interface (the liquid domain!) is discarded because these values are neither sought nor do they affect the vapor domain values obtained for the well-posed vapor domain problem. The temporary fixing of $\{u_2^i, v_2^i, \theta_2^i\}$ on the interface $\delta(x,t)$ in Fig. 4(*b*) is accomplished by, respectively, adding terms called $t_{12}$, $t_{22}$, and $t_{32}$ to the right sides of the *x*-momentum, *y*-momentum, and the energy equations in Eq. (2) with $I=2$. These terms are defined as

$$t_{12} \equiv u_2 * A_1(\mathbf{x}_{\Sigma I}) * \breve{\delta}(|\mathbf{x}-\mathbf{x}_{\Sigma I}|) - u_2^i * A_1(\mathbf{x}_{\Sigma I}) * \breve{\delta}(|\mathbf{x}-\mathbf{x}_{\Sigma I}|)$$

$$t_{22} \equiv v_2 * A_2(\mathbf{x}_{\Sigma I}) * \breve{\delta}(|\mathbf{x}-\mathbf{x}_{\Sigma I}|) - v_2^i * A_2(\mathbf{x}_{\Sigma I}) * \breve{\delta}(|\mathbf{x}-\mathbf{x}_{\Sigma I}|)$$

$$t_{32} \equiv \theta_2 * A_3(\mathbf{x}_{\Sigma I}) * \breve{\delta}(|\mathbf{x}-\mathbf{x}_{\Sigma I}|) - \theta_2^i * A_3(\mathbf{x}_{\Sigma I}) * \breve{\delta}(|\mathbf{x}-\mathbf{x}_{\Sigma I}|). \tag{18}$$

In Eq. (18) above, $\breve{\delta}$ is a "delta function" (see Greenberg [42]) with $\mathbf{x}$ being the vectorial distance of any point from the origin. Also, in Eq. (18), $\mathbf{x}_{\Sigma I}$ is the position vector from the origin to any point on the interface. With the additional terms in Eq. (18) added to the appropriate equations on the right side of Eq. (2), the modified equations are discretized. The resulting equations and their treatment, with appropriate choices of the interfacial-cell constants $A_I$ $(I=1,2,3)$, lead (see Section 3.3 of Liang [2]) to the "source term method" and its results given in Eqs. (7.11)–(7.13) of Patankar [40]. The result of the above modifications is that the original equations in Eq. (2) continue to hold in the interior while the chosen values of $\{u_2^i, v_2^i, \theta_2^i\}$ get fixed on the interface $\delta(x,t)$.

To obtain separate calculations for the liquid domain in Fig. 4*a* and to keep the interface sensitive to the pressure and shear conditions (as given by Eqs. (4)–(5)) at the interface, instead of guessing and temporarily fixing values of $\{u_1^i, v_1^i, \theta_1^i\}$ on the interface $\delta(x,t)$ of Fig. 4(*a*), a scheme (described and termed the "$\tau$-$p$" method in Yu [17] and Liang [2]) is employed where $\{u_{1s}^i, v_{1s}^i, \theta_1^i\}$ are guessed and fixed on the shifted interface $\delta_{\text{shift}}(x,t)$ of Fig. 4(*b*). This extension of the liquid domain into the vapor domain by a single liquid *interface cell* (as depicted in the inset of Fig. 3 and shown as the gray region in Fig. 4(*a*)) is only for temporary computational convenience of fixing $\{u_{1s}^i, v_{1s}^i, \theta_1^i\}$ on $\delta_{\text{shift}}(x,t)$ by the "source term method." This method is identical to the one described earlier for fixing $\{u_2^i, v_2^i, \theta_2^i\}$ on $\delta(x,t)$ for the vapor domain calculations in Fig. 4(*b*). In this "$\tau$-$p$" method (see Liang [2]), the values of $u_{1s}^i$ are adjusted to ensure that the appropriate relationship between the tangential stresses, i.e., Eq. (5), is satisfied. Similarly $v_{1s}^i$ values are adjusted to ensure that the appropriate relationship between the normal stresses $\pi_1^i$ and $\pi_2^i$, i.e., Eq. (4), is satisfied. The values of $\theta_1^i$ are presented to satisfy Eq. (9). After the satisfaction of the pressure, shear, and temperature conditions on the actual interface $\delta(x,t)$, the entire solution underneath the actual liquid domain $\delta(x,t)$ is retained and the solution for the "ghost" liquid of Fig. 4(*a*) and the solution above $\delta_{\text{shift}}(x,t)$ are discarded. In short this method of fixing and adjusting $\{u_{1s}^i, v_{1s}^i, \theta_1^i\}$ on $\delta_{\text{shift}}(x,t)$ of Fig. 4(*a*) allows one to find and adjust $\{u_1^i, v_1^i, \theta_1^i\}$ on the actual interface $\delta(x,t)$ of Fig. 4(*a*) while concurrently satisfying the pressure (Eq. (4)), shear (Eq. (5)), and temperature (Eq. (9)) conditions on the actual interface.

It is important to note that the liquid and the vapor interface cells depicted in the inset of Fig. 3 are not used to *explicitly* satisfy mass, momentum (normal and tangential), energy, etc. restrictions on this cell. In this sense this approach is unlike some of the *interface capturing* and *interface tracking* approaches where balance laws are *explicitly* invoked for the interface cells. The interface cells (see insets in Fig. 3) are only *indirectly* used here to come up with a computational procedure where the values $\{u_1^i, v_1^i, \theta_1^i, u_2^i, v_2^i, \theta_2^i, \delta\}$ are so adjusted that their converged values satisfy the *discretized* form of all the seven interface conditions—viz. two for temperature (Eq. (9)), two for momentum (Eqs. (4)–(5)), two for mass (Eq. (8)), and one for continuity of tangential velocities (Eq. (3)). Recall that the aforementioned equations that are used were independently and analytically obtained to represent the restrictions imposed by various physical requirements at a sharp interface.

Between times "$t$" and "$t+\Delta t$," adaptive grids (termed grid A and grid B) are employed. At time *t*, grid A (as in Fig. 3) is based on the geometrical features of $\delta(x,t)$ as a function of *x*, and it changes whenever the liquid and the vapor flow variables need to be recomputed for a changed interfacial configuration $\delta(x,t)$. However, to make the best changes in $\delta(x,t)$ which leads to accurate prediction of $\delta$ at time "$t+\Delta t$," a different grid (grid B) is generally required for the variables ($\delta(x,t)$, etc.) appearing in the *interface tracking equation* (which results from one of the interface conditions and has one less spatial dimension as in Eq. (21) below) for this problem. Thus relevant variable values on grid A are mapped onto grid B, and the best predictions for changes in $\delta(x,t)$ are obtained on grid B. These predicted values of $\delta(x,t)$ are then interpolated back to obtain corresponding values on grid A. At any time *t*, linear interpolations are employed for the exchange of relevant flow variable values between grid A and grid B.

**Procedural Steps.** The final solution is obtained by solving the liquid and vapor domains *separately* and *iteratively* under repeated modifications of the interface configuration $\delta(x,t)$. The iterations modify, intimately connect, and converge the two solutions with the help of all the interface and boundary conditions. This convergence is accomplished through the following substeps:

(***a***) As described earlier, obtain grid A with the help of suitably selected points $P_i$ on an initial guess or a tentative intermediate prediction of the interface location.

(***b***) First extend the liquid domain by a single *interface cell* (depicted in Fig. 3 and shown as the gray region in Fig. 4(*a*)) to define $\delta_{\text{shift}}(x,t)$ as a *shifted extension* of $\delta(x,t)$. Utilizing the "$\tau$-$p$" method described above and using guessed values of $\{u_{1s}^i, v_{1s}^i, \theta_1^i\}$ on the estimate for shifted interface $\delta_{\text{shift}}(x,t)$ of Fig. 4(*a*), obtain a finite volume solution (SIMPLER technique of Patankar [40]) for the liquid domain underneath $\delta(x,t)$.

If unsteady solutions for $t>0$ are being sought, one skips the remaining operations described here in this paragraph and moves on to the next substep (c). However, for obtaining the steady solution at $t=0$, another liquid domain problem underneath the actual interface $\delta(x,t)$ is solved to *incorporate* the exit-condition prescription necessary for obtaining a *unique* steady solution. For this, the just obtained values of liquid velocity components $(u_1^i, v_1^i)$ and temperature $\theta_1^i$ from the "$\tau$-$p$" method (which involves $\delta_{\text{shift}}(x,t)$) are now temporarily fixed on the actual interface location $\delta(x,t)$. The values of *x*-component of interfacial velocity $u_1^i$ and temperature $\theta_1^i$ are retained as they are while the

$y$-component of interfacial velocity $v_1^i$ is modified to satisfy the current status of the equation $\dot{m}_{LK}=\dot{m}_{\text{Energy}}$. This is in preparation to achieve closure with the subsequent chain of mass flux equalities viz.: $\dot{m}_{VK}=\dot{m}_{\text{Energy}}$ in substep (c) below, and the exit condition restriction imposed as $(\dot{m}_{VK})_{\text{modified}}=\dot{m}_{\text{Energy}}$ in substeps (d)–(e) below.

(*c*) Making use of the vapor domain calculation method described earlier, obtain guesses for $\{u_2^i, v_2^i, \theta_2^i\}$ on the interface $\delta(x,t)$ in Fig. 4(*b*) and then solve the vapor domain flow problem by a finite volume technique (SIMPLER technique of Patankar [40]). Utilizing the liquid domain solution in substep (a) above; values of $u_2^i$ are obtained from a first order discretization of the *continuity of tangential velocities* condition in Eq. (3), values of $v_2^i$ are obtained from a discretization of the requirement $\dot{m}_{VK}=\dot{m}_{\text{Energy}}$ in Eq. (8), and values of $\theta_2^i$ are obtained from the thermodynamic restriction in Eq. (9).

(*d*) While obtaining unsteady solutions for $t>0$, this substep is skipped, and one moves on to the next substep (e). However, to obtain a steady solution at $t=0$, it is necessary to prescribe an exit vapor quality $Z_e$ at $x=x_e$. For this, a modified vapor mass flux $(\dot{m}_{VK})_{\text{modified}}\equiv\beta\cdot\dot{m}_{VK}$ is introduced. The parameter $\beta$ is then explicitly determined so as to make the total vapor mass transfer rate across the entire interface (computed as $\int_0^{x_e}\rho_1/\rho_2\cdot(\dot{m}_{VK})_{\text{modified}}\cdot\sqrt{1+\delta_x^2}\cdot dx$) consistent with the given value of exit quality $Z_e$ (i.e., it is made equal to $1-Z_e$). To account for changing vapor control volume and moving interface, suitable modifications of this approach is needed to specify exit conditions for compressible unsteady cases not considered in this paper. Once $\beta$ is obtained, the interfacial values of liquid velocity $v_1$ (denoted as $v_1^i$) are updated so as to satisfy, for steady flows, the additional exit constraint:

$$\dot{m}_{LK}=(\dot{m}_{VK})_{\text{modified}}. \tag{19}$$

The steady solution procedure then moves to the next substep (e) to update $\delta(x)$ values from Eq. (22) given below at the end of substep (e).

***(e)***. The only remaining interface condition $\dot{m}_{LK}=\dot{m}_{\text{Energy}}$ in Eq. (8) (which, for steady flow computations, because of Eq. (19) above, becomes $(\dot{m}_{VK})_{\text{modified}}=\dot{m}_{\text{Energy}}$) is satisfied in this substep. It should be noted that the physical variable form $\dot{m}_{LK}=\dot{m}_{\text{Energy}}$ of this equation arises from Eq. (*A*7) in the Appendix, and can be written in the following popular form for *tracking* the interface $\mathcal{H}(x,y,t)=0$:

$$\frac{\partial\mathcal{H}}{\partial t}+\mathbf{v}_1^i\cdot\nabla\mathcal{H}\cong\frac{-k_1}{\rho_1\cdot h_{fg}}\frac{\partial\mathcal{T}_1}{\partial n}\bigg|^i\cdot|\nabla\mathcal{H}|. \tag{20}$$

Focusing on locating the interface prior to any break up or pinch off, the interface $\mathcal{H}$ in Eq. (20) is represented by a simple single valued form given by $\mathcal{H}=y-\Delta(x,t)=0$. Nondimensionalizing the resulting Eq. (20) under Eq. (1), the following nonlinear and hyperbolic interface tracking equation is obtained:

$$\frac{\partial\delta}{\partial t}+\overline{u}(x,t)\frac{\partial\delta}{\partial x}=\overline{v}(x,t), \tag{21}$$

where $\overline{u}\equiv u_1^i+\{\text{Ja}/(\text{Re}_1\cdot\text{Pr}_1)\}\partial\theta_1/\partial x|^i$ and $\overline{v}\equiv v_1^i+\{\text{Ja}/(\text{Re}_1\cdot\text{Pr}_1)\}\partial\theta_1/\partial y|^i$ typically depend strongly, but indirectly, on $\delta$. While obtaining the steady solution at $t=0$, however, all time derivatives are set equal to zero, and the interface is updated by a simple numerical integration (trapezoid rule) of the *steady form* of Eq. (21), which is

$$d\delta/dx=\overline{v}(x)/\overline{u}(x)\quad\text{for}\quad x>0. \tag{22}$$

In this substep, Eq. (21) or Eq. (22) is solved to obtain new values of $\delta$. For the steady case, Eq. (22) yields new $\delta_{\text{steady}}(x)$ and for the unsteady case, Eq. (21) is solved to obtain new values of $\delta$ for the next time step "$t+\Delta t$" or is used merely to improve the existing estimates of $\delta$ and other flow variables for time "$t+\Delta t$." Whatever be the case, at each relevant $x$, all liquid and vapor flow variables are linearly mapped to the new liquid and vapor domains defined by each new prediction of the interface location.

Repetition of the steps (a)–(e) above with a starting guess $\delta_{\text{guess}}(x)$ for the interface location leads first to a convergent solution $\delta_{\text{steady}}(x)$ of the steady equations. This solution is consistent with the prescribed exit quality $Z_e$ because $\beta$ introduced and computed in substep (d) above satisfies the requirement of $\beta\to1$. Starting from this converged steady solution at $t=0$, steps (a)–(e) above are repeated a suitable number of times for each new time step, viz. $t=\Delta t$, $t=2\Delta t$, etc. This leads to a convergent unsteady solution consistent with the choice of initial and boundary data. The ability to improve the results at any time step by dwelling at that time step for repeated iterations between the time step under consideration and the previous time step makes the process of forward time marching *implicit* (or, more appropriately, *semi-explicit*).

The solution obtained by the above procedure not only satisfies the pressure, shear, temperature, and continuity of tangential velocity conditions at the interface, but also satisfies the various flow field restrictions that arise from having a nonzero interfacial mass flux $\dot{m}$. The *steady solutions* at $t=0$ satisfy $\dot{m}_{LK}=\dot{m}_{\text{Energy}}$ in substep (a), $\dot{m}_{VK}=\dot{m}_{\text{Energy}}$ in substep (b), and the exit condition restriction imposed as $(\dot{m}_{VK})_{\text{modified}}=\dot{m}_{\text{Energy}}$ in substeps (d)–(e). The *unsteady solutions* at $t>0$ satisfy $\dot{m}_{VK}=\dot{m}_{\text{Energy}}$ in substep (b) and $\dot{m}_{LK}=\dot{m}_{\text{Energy}}$ in substep (d).

**Discussions for the Interface Tracking Equation and Its Solution.** When the right side of Eq. (20) is zero, spatial extension of Eq. (20) leads to a color function $\mathcal{H}$ whose initial values $\mathcal{H}=0$ and $\mathcal{H}=1$ within each of the phases are retained for all times $t>0$, and this forms the basis of the popular VOF (volume of fluids) techniques (see Hirt and Nicholas [24], etc.) for air/water type flows. Similarly, a suitable spatial extension of Eq. (20), in conjunction with some other techniques, is used in the level-set method (Sussman et al. [22], etc.) for *capturing* the interface through iterative single domain (consisting of both the phases) calculations. For boiling related phase change flows, the level-set technique has recently been used by Son and Dhir [23]. In order to better understand and sidetrack some of the problems (see, e.g., Li and Renardy [27]) associated with interface *capturing* techniques (be it level-set, VOF, etc.) that utilize Eq. (20), we look at the existing knowledge base for the reduced form of Eq. (20) given in Eq. (21). Equation (21) is the *interface tracking equation* which, for $t>0$, defines the following *interface tracking problem:*

$$\frac{\partial\delta}{\partial t}+\overline{u}(x,t)\frac{\partial\delta}{\partial x}=\overline{v}(x,t)$$

$$\delta(0,t)=0$$

$$\delta(x,0)=\delta_{\text{steady}}(x)\quad or\quad\text{other prescriptions}. \tag{23}$$

The computational issues for discretization and numerical solution of Eq. (23) are well understood and extensively discussed in Abbott and Basco [26] with regard to various algorithms' stability and accuracy in determining both the amplitude and the phase of its often-wavy numerical solutions. It is known from there that among various possible discretizations for Eq. (23), the one that gives best results in marching from $(x,t)$ to $(x+\Delta x,t+\Delta t)$ has a Courant number Cr ($\text{Cr}\equiv\overline{u}(x,t)\cdot\Delta t/\Delta x$) equal to 1 (i.e., $\text{Cr}\cong1$) and the following discretizations:

$$\delta(x+\Delta x,t+\Delta t)=\delta(x,t)+\overline{v}(x,\tau)\cdot\Delta t$$

$$\partial\delta/\partial t=[\,\delta(x+\Delta x,t+\Delta t)-\delta(x+\Delta x,t)]/\Delta t$$

$$\partial\delta/\partial x=[\,\delta(x+\Delta x,t)-\delta(x,t)]/\Delta x. \tag{24}$$

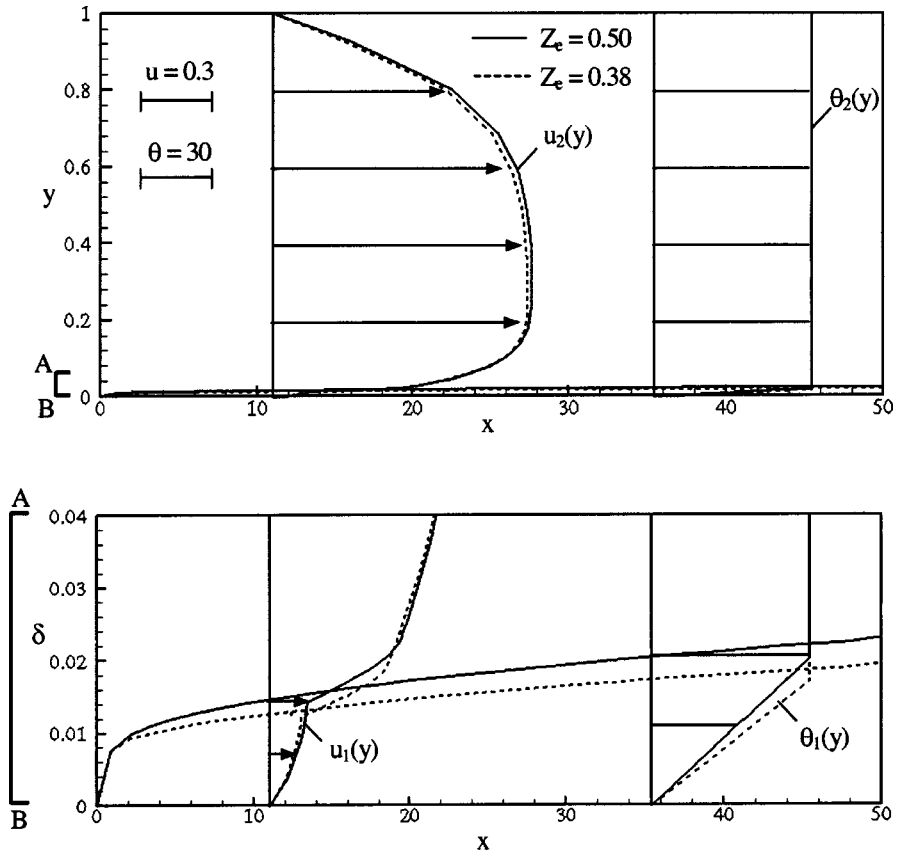


**Fig. 5 The above predictions are for vertical channel flows of saturated R-113 vapor. The flow cases are specified in Table 1 with $\alpha=90$ deg, $x_e=50$ and two different exit conditions, viz. $Z_{e_1}=0.5$ and $Z_{e_2}=0.38$.**

The intermediate time $\tau\,(t\leqslant\tau\leqslant t+\Delta t)$ in Eq. (24) above (appearing in the definition of Cr through $\overline{u}$ and in the first equation through $\overline{v}$) is chosen such that, by the end of iterations for this time interval, $\overline{u}$ and $\overline{v}$ satisfy $\overline{u}(x,\tau)=\{\overline{u}(x,t)+\overline{u}(x,t+\Delta t)\}/2$ and $\overline{v}(x,\tau)=\{\overline{v}(x,t)+\overline{v}(x,t+\Delta t)\}/2$. It should be noted that one can tentatively use any convenient and stable discretization for $\partial\delta/\partial x$ and $\partial\delta/\partial t$ in substeps (a)–(d) above, as long as the optimal discretizations in Eq. (24) are employed and satisfied *by the end* of repeated iterations of substeps (a)–(e) for any given time step.

The above requirement of $\mathrm{Cr}\equiv\overline{u}\Delta t/\Delta x\approx 1$ in Eq. (24) is handled by mapping the $xu(i)$ locations in grid A to $xud(i)$ locations in grid B (see Fig. 3). This is accomplished by setting, at any time $t$, $xud(3)=xu(3)=\varepsilon>0$ and sequentially finding all subsequent $xud(i)$ for $i\geqslant 4$ by the relation: $xud(i+1)=xud(i)+\overline{u}(xud(i),t)\cdot\Delta t$ where $\overline{u}(xud(i),t)$ values are also sequentially obtained from linear interpolations within the known set of values of $\overline{u}$ at $xu(i)$ locations. The $\delta$ values thus obtained from Eqs. (23)–(24) on grid B are then mapped back to grid A with the help of linear interpolations.

It is further noted that the discretizations in Eq. (24) are the same as the discretizations for the *method of characteristics* (see, e.g., Greenberg [42]). That is, evolution of $\delta(x,t)$ as a solution of Eq. (21) takes place along *characteristic curves* $x=x_c(t)$ given by

$$\frac{dx_c}{dt}=\overline{u}(x_c(t),t)$$

$$x_c(0)=x^* \quad \text{or} \quad x_c(t^*)=0, \tag{25}$$

where $x^*$ is any given value of $x$ between the inlet and the outlet

**Table 1 Specification of reported flow situations involving saturated R-113 vapor of the inlet. Properties of R-113 are taken from ASHRAE Handbook, [45].**

| Fig. # for flow | $p_o$ (kPa) | $\mathcal{T}_s(p_o)$ (°C) | $\Delta\mathcal{T}$ (°C) | $h$ (m) | U (m/s) | | | |
|---|---|---|---|---|---|---|---|---|
| | $\mathrm{Re_{in}}$ | Ja | $\mathrm{Fr^{-1}}_x$ | $\mathrm{Fr^{-1}}_y$ | $\rho_2/\rho_1$ | $\mu_2/\mu_1$ | We | $\mathrm{Pr_1}$ |
| 5, 6, 7, 8a, 8b, 10, 11a, 11b, 11c, 12, 13a, 13b, 14a, 14b, 15, 16, 17, 18 | 108.855 | 49.47 | 5 | 0.004 | 0.41 | | | |
| | 1200 | 0.0341 | 0.2379 | $0.32\times10^{-6}$ | 0.0053 | 0.0209 | 67.6335 | 7.2236 |

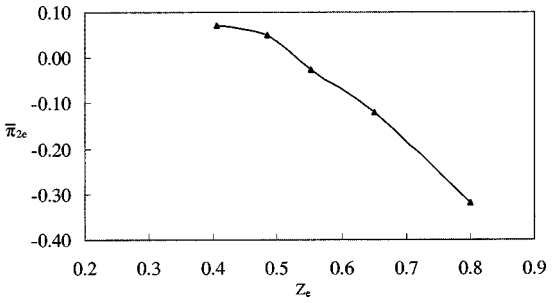


**Fig. 6 For the flow situations specified in Table 1 with $\alpha$=90 deg, $x_e$=50, the figure shows the equivalence of specifying exit vapor quality $Z_e$ or exit pressure $\bar{\pi}_e \equiv 1/(1-\delta)\int_\delta^1 \pi_2 dy$ to specify exit conditions. It is computationally more convenient to specify exit condition $Z_e$.**

in Fig. 1 and $t^*>0$. Equations (23) and (25) together imply that the evolution of $\delta(x,t)$ along the *characteristic curves* is governed by

$$\frac{d\hat{\delta}(t)}{dt} = \hat{\bar{v}}(t)$$

$$\hat{\delta}(0) = \delta_{\text{steady}}(x^*) \quad or \quad \text{other prescriptions}, \tag{26}$$

where $\hat{\delta}(t) \equiv \delta(x_c(t),t)$ and $\hat{\bar{v}}(t) \equiv \overline{v}(x_c(t),t)$.

It is found that the integrable singularity at $x \sim 0$ is such that replacement of the condition $\delta(0,t)=0$ in Eq. (23) by a condition of the type $\delta(\varepsilon_1,t)=\varepsilon_2$ for any suitably chosen $\varepsilon_1>0$ and $\varepsilon_2>0$ does not affect the solutions at $x \gg \varepsilon_1$. Therefore, unless one is interested in the singularity at $x=0$, the proposed approach works rather well for all cells except the first two to three cells at the leading edge corner (i.e., left corner of Fig. 2). This is because solution obtained away from the leading edge remains largely unaffected by changes in specific reasonable choices made for $\varepsilon_1$ and $\varepsilon_2$. Thus, as expected, integrability of this singularity in two or three-dimensional calculations poses no problem. However, resolution of the same singularity becomes more challenging for one-dimensional approaches (see Narain et al. [19]) that employ semi-empirical interfacial shear models.

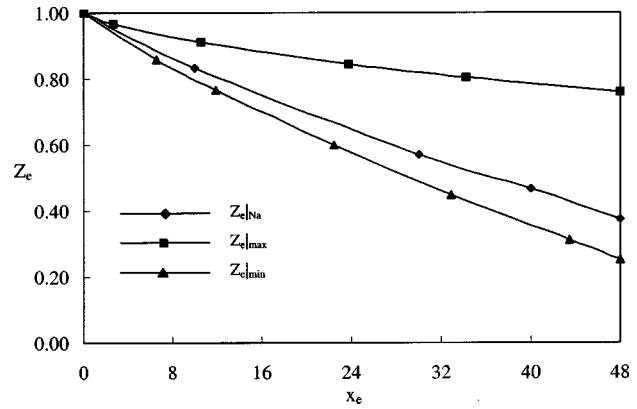


**Fig. 7 With all remaining flow parameters specified as in Table 1 with $\alpha$=90 deg, the above figure shows that exit condition specified by the number $Z_e$ at a given $x_e$ must lie within two well-defined values, viz. $Z_e|_{min}(x_e) \leq Z_e \leq Z_e|_{max}(x_e)$. This restriction, presumably, arises from the fact (see Carey [37]) that the assumed annular/stratified flows only occur within certain parameter ranges.**

## 4 Stability of Steady Solutions and the Role of Exit Conditions

For slow laminar/laminar internal condensing flows considered here, it is computationally shown in Fig. 5 that, for different exit conditions (i.e., exit vapor quality $Z_e=Z_e(0)$), one obtains different steady solutions for any given inlet pressure and inlet mass flow rate. In Fig. 6, we see that the prescription of a different exit vapor quality $Z_e$ is equivalent to a prescription of a different exit pressure $\bar{\pi}_{2e} \equiv 1/(1-\delta)\int_\delta^1 \pi_2 dy$. Because of the nonuniqueness of *steady* solutions in the absence of prescribed exit conditions, the following questions arise with regard to different solutions associated with different $Z_e$ values: (i) all else remaining the same, is there a range of $Z_e$ values that can be prescribed at a given $x=x_e$ for which a range of steady solutions can be obtained; (ii) is a particular steady solution for a given $Z_e$ stable or unstable in the *absence* of exit constraints for $t>0$ (i.e., if $Z_e(0)=Z_e$ but $Z_e(t)$ can take any value for $t>0$); and (iii) is a particular steady solution for a given $Z_e$ stable or unstable in the *presence* of exit constraints for $t>0$ (e.g., $Z_e(t)=Z_e$ for $t \geq 0$)?

Representative answer to question (i) above is given in Fig. 7 which computationally demarcates a range of $Z_e(0)=Z_e$ values for each $x_e$ while all other nondimensional parameters determining the flow are held fixed. The demarcation in Fig. 7 is of the type $Z_e|_{\min} \leq Z_e \leq Z_e|_{\max}$ where the lower and upper bounds are rather well defined. The parameter range shown in Fig. 7 changes as the remaining significant parameters (viz. $\text{Re}_{in}$, Ja, $\alpha$, $\rho_2/\rho_1$, $\mu_2/\mu_1$, and $\text{Pr}_1$) are changed.

Answer to question (ii) regarding stability of solutions for the unconstrained exit case follows from results given in Figs. 8–9. Based on two-dimensional *unsteady* simulations results shown in Fig. 8(*a*) for the idealized noise-free case and its noise-sensitive quasi-steady counterpart in Fig. 8(*b*), it is found that, for unconstrained exit conditions, as $t \to \infty$, there is an *attractive* solution (see Fig. 9) while the remaining steady solutions are *unstable*. All else being given, the final $Z_e$ value obtained for the attractive solution in Fig. 8(*a*), is denoted as $Z_e|_{\text{Na}}$ to indicate that it is *the* naturally selected value of $Z_e$ in the absence of exit constraints. This naturally selected attractive steady solution for unconstrained exit conditions is found to be *stable* (see definition of *stability* in Joseph [43]) because *initial* two-dimensional disturbances damp out over time. It should be noted that a solution might be *stable* and yet be difficult to realize in practice because of *sensitivity* to certain minuscule noises that are commonly present. To understand the stability and noise sensitivity issues, the problem in Eq. (23) and its solution along characteristics, as defined by Eqs. (25)–(26), is best rewritten in terms of the evolution of a disturbance $\delta'(x,t) \equiv \delta(x,t) - \delta_{\text{steady}}(x)$. Under this change of variables, the characteristics continue to be defined by Eq. (25) while Eq. (23) changes to

$$\frac{\partial \delta'}{\partial t} + \overline{u}(x,t)\frac{\partial \delta'}{\partial x} = \bar{\bar{v}}(x,t)$$

$$\delta'(0,t) = 0$$

$$\delta'(x,0) \quad or \quad \text{other prescriptions}, \tag{27}$$

where $\bar{\bar{v}}(x,t) \equiv [\overline{v}(x,t) - \overline{v}_{\text{steady}}(x) - \{\overline{u} - \overline{u}_{\text{steady}}\}(d\delta_{\text{steady}}/dx)]$ and Eq. (26) changes to

$$\frac{d\hat{\delta}'(t)}{dt} = \hat{\bar{\bar{v}}}(t)$$

$$\hat{\delta}'(0) = 0 \quad or \quad \text{other prescriptions}, \tag{28}$$

where $\hat{\delta}'(t) \equiv \delta'(x_c(t),t)$ and $\hat{\bar{\bar{v}}}(t) \equiv \bar{\bar{v}}(x_c(t),t)$. It should be noted that $|\overline{u} - \overline{u}_{\text{steady}}|$ and $|\bar{\bar{v}}(x,t)|$ are identically zero for steady solutions with $\delta'=0$ and are small for disturbances with small $\delta'$. The attractive solution in Figs. 8–9 is such that disturbances $\delta'(x,t)$ again propagate along characteristics curves given by Eq.

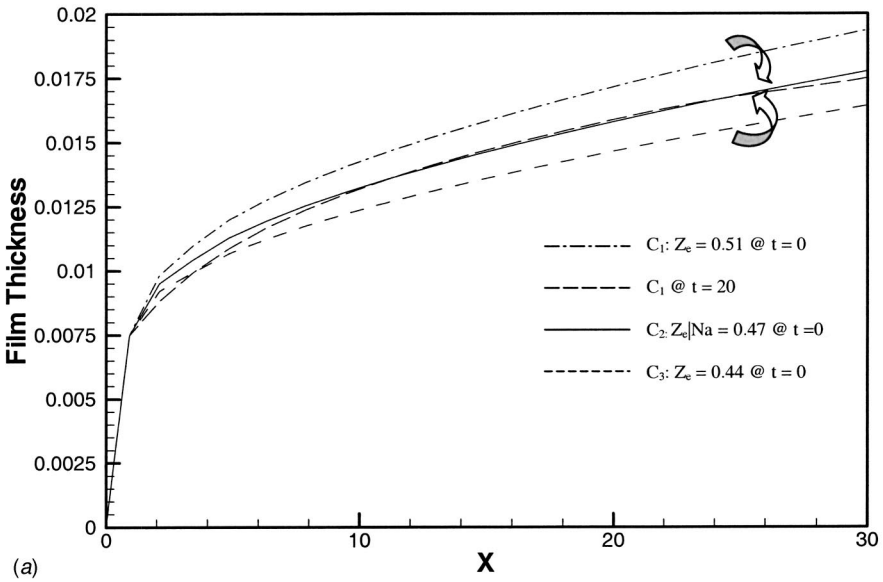


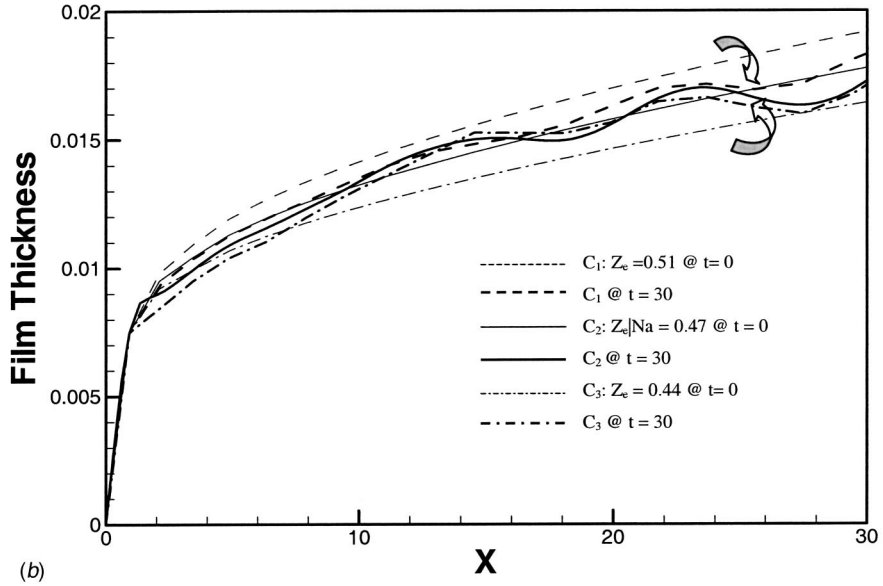


**Fig. 8 (*a*) For flow situation specified in Table 1 with $\alpha$=90 deg and $x_e$=30, the figure depicts two sets of $\delta(x,t)$ predictions for $t>0$. One curve *C*1 starts at $Z_e$=0.51 at $t$=0, and tends, as $t\to\infty$, to the solution for $Z_e|_{Na}$=0.47. The other curve *C*2 starts at $Z_e$=0.44 at $t$=0 and tends, as $t\to\infty$, to the same steady $Z_e|_{Na}$ solution. (*b*) For flow situations considered in Fig. 7(*a*), the above predictions for $t>0$ starts at $t$=0 from the same curves *C*1 and *C*2 in Fig. 7(*a*). However, at $t>0$, there is a condensing surface noise given by $v_1(x,0,t)=\varepsilon\cdot\sin(2\pi x/\lambda)\cdot\sin(2\pi t/T)$, with $\varepsilon$=0.3E-6, $\lambda$=10, and $T$=24. As $t\to\infty$, the mean part of wavy quasi-steady solutions coincides with the smooth solution, shown in Fig. 8(*a*) for $Z_e=Z_e|_{Na}$=0.47.**

(25). For the steady solution in Fig. 10, representative characteristics curves $C_1$, $C_2$, etc. are shown in Fig. 11(*a*). These curves are generated by numerical integration (fourth-order Runge Kutta) of Eq. (25) with the characteristic speed $\overline{u}(x,t)=\overline{u}_{\text{steady}}(x)$. Figure 11(*b*) shows that the characteristics speed for small initial disturbances (which, because of the nature and form of Eq. (27), is the same as phase speed) satisfies $\overline{u}(x,t)\cong\overline{u}_{\text{steady}}(x)$. For *intrinsic* waves induced by small initial disturbances, unlike gravity waves on water (see Lighthill [31]), the waves are nondispersive (i.e., wave speeds are nearly independent of wavelengths) and become somewhat dispersive only for large amplitude initial disturbances (see $\overline{u}$ for this case in Fig. 11(*b*)). For the steady and initial dis-

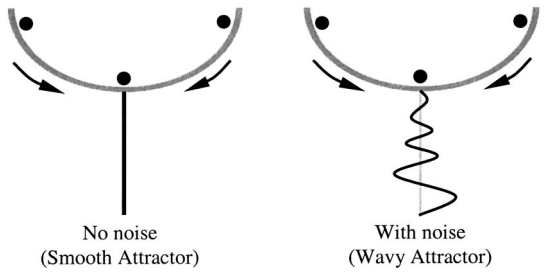


**Fig. 9 Qualitative nature of the stable, steady/quasi-steady solutions**

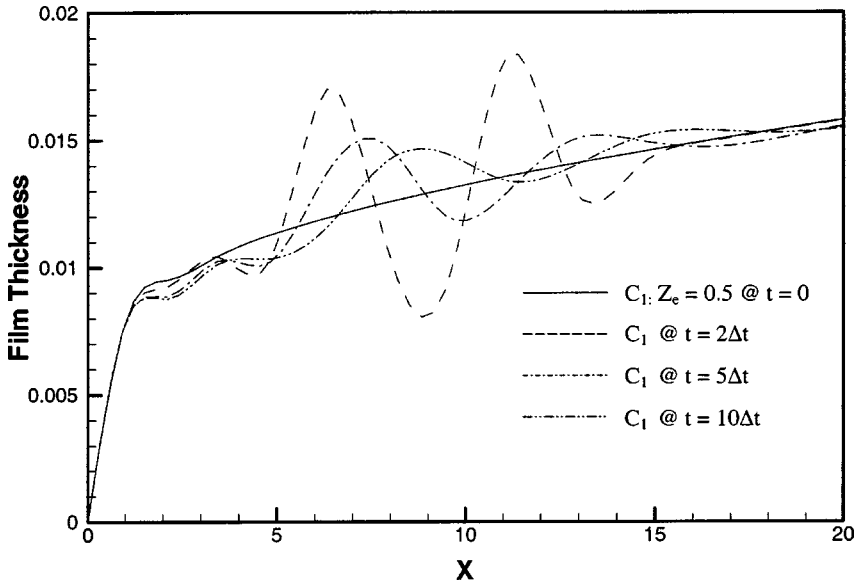


**Fig. 10 For flow situations specified in Table 1 with $\alpha$=90 deg and $x_e$=20, the above $\delta(x,t)$ predictions ($\Delta t$=2.5) are for initial data $\delta(x,0)=\delta_{steady}(x)+\delta'(x,0)$, where a nonzero disturbance $\delta'(x,0)$ has been superposed at $t$=0 on the steady solution $\delta_{steady}$ (shown as curve $C1$ above for $t<0$). The steady solution corresponds to $Z_e=Z_e|_{Na}$=0.5. Here $\delta'(x,0)=0$ except in the interval $x^*<x<x^*+10$, where $x^*$=3.5 and $\delta'(x,0)=0.5\cdot\delta_{steady}(x)\cdot\sin(2\pi x/5)$. It is clear that even this *large* a disturbance damps at later times.**

turbance cases shown in Fig. 10, Fig. 11($c$) shows values of the "growth/damping" factor $\hat{\bar{v}}(t)$ along a representative characteristic curve (such as $C_1$ in Fig. 11($a$)). The initial disturbance in Fig. 10 typically damps because, in Fig. 11($c$), we have a typical response of $\hat{\bar{v}}(t)<0$ for all sufficiently large $t$ and $\delta'(x_c(t),t)=\delta'(x^*,0)+\int_0^t\hat{\bar{v}}(\tau)\cdot d\tau$ tends to zero as $t\to\infty$ along characteristics originating on the $t=0$ line. Furthermore, besides damping of initial disturbances along the characteristics curves, disturbances leave the computational domain ($0\leqslant x\leqslant x_e$) with a forward phase speed of $\bar{u}>0$. As a result, in Fig. 11($a$)), at a fixed $x$ as $t\to\infty$, one would leave the solid line initial disturbance characteristics originating on the $t=0$ line and get on the characteristics originating on the $x=0$ line (these curves are over $t\geqslant t^*$ for any $t^*>0$). The values of $\delta'$ on these characteristics (over $t\geqslant t^*$ and $t^*>0$) are not affected by the nonzero initial disturbances since these characteristics only carry the nearly zero-noise information of $\delta'(0,t)\approx 0$ for all $t\geqslant t^*$. This stability of a natural steady solution associated with the exit condition $Z_e=Z_e|_{Na}$ is typically true for any initial disturbance (not just the large initial disturbance example used in Fig. 10) under unconstrained exit conditions. While the small intrinsic initial disturbance waves damp out as they propagate downstream with increasing wavelengths and increasing speed $\bar{u}\approx\bar{u}_{steady}(x)$. For the initial disturbance cases with initial wavelength $\lambda$, at later times $t$ the wavelengths $\bar{\lambda}(x,t)=\bar{\lambda}(x_c(t),t)$ with $\bar{\lambda}(x_c(0),0)=\lambda$. Here reciprocal of $\bar{\lambda}(x,t)$, as in Lighthill [33], is in terms of $x$-derivative of phase angles that are constant as they propagate along the characteristics curves. Since these derivatives get smaller with increasing $x$ because of the increasing $x$-separation among incrementally apart characteristics (this is also the case with finitely spaced characteristics $C_1$, $C_2$, etc. shown in Fig. 11($a$) the wavelengths $\bar{\lambda}(x,t)$ increase as the disturbances propagate forward under continued damping.

Earlier, in Fig. 5, it was shown that different steady solutions are possible for different exit constraints (i.e., different values of $Z_e$). With regard to stability of such steady solutions to initial disturbances while *exit conditions* are constrained to keep values of $Z_e$ fixed in the *immediate vicinity* of $Z_e|_{Na}$, stability, like the $Z_e=Z_e|_{Na}$ solutions, are expected. However, unsteady simulations for initial disturbances while retaining exit constraint at all times are outside the scope of this paper as such simulations require allowance of density fluctuations in the vapor phase and accounting for their interactions with fluctuations in other variables. It is, however, easily conjectured that many steady solutions with constrained the values (at all times) *sufficiently far* from $Z_e|_{Na}$, such as $Z_e=0.26$ case shown in Fig. 12 (with its unlikely liquid velocity profiles resulting from the inappropriate constant density assumptions), will have oscillatory *instability* in response to initial disturbances. This is because sustained density and other fluctuations/waves are expected.

## 5 Effects of Noise and Resonance Condition

The *natural* and *stable* solutions described in Fig. 9 and obtained in Fig. 8 were shown, in Fig. 10, to be *intrinsically wavy* to initial disturbances. It is shown in Fig. 13($a$) that, despite the *stability*, the interface is quite sensitive to even minuscule vibrations of the bottom plate. This is because transverse condensate velocity component $v_1$ is very small (e.g., if axial vapor velocity is $O(1)$, axial condensate velocity is often about $O(10^{-3})$, and transverse condensate velocity is often about $O(10^{-5})$) and yet it is a significant player in the forcing term on the right side of the interface tracking equation in Eq. (23). The small bottom plate noises considered in this paper correspond to a velocity $v_1(x,0,t)=\varepsilon\cdot\sin(2\pi x/\lambda)\cdot\sin(2\pi t/T)$ whose amplitude $\varepsilon$ is in the range of $1\times10^{-5}-3\times10^{-5}$. For the representative cases considered here (e.g., $T=12$, $\lambda=5$, $h=.004$ m, and $U=0.41$ m/s), the maximum displacement amplitude of the vibrations is about 0.25 $\mu$m, the maximum velocity amplitude is about 0.12 $\mu$m/s, and the maximum acceleration amplitude is about $6.25\times10^{-4}$ m/s$^2$ (which is less than $10^{-4}$ g, g$\cong$10 m/s$^2$). Such transverse condensing surface vibrations are typically induced by structural or coolant noise sources and are indeed commonly present in the 0–30 Hz range considered here. Thus these noise-induced waves

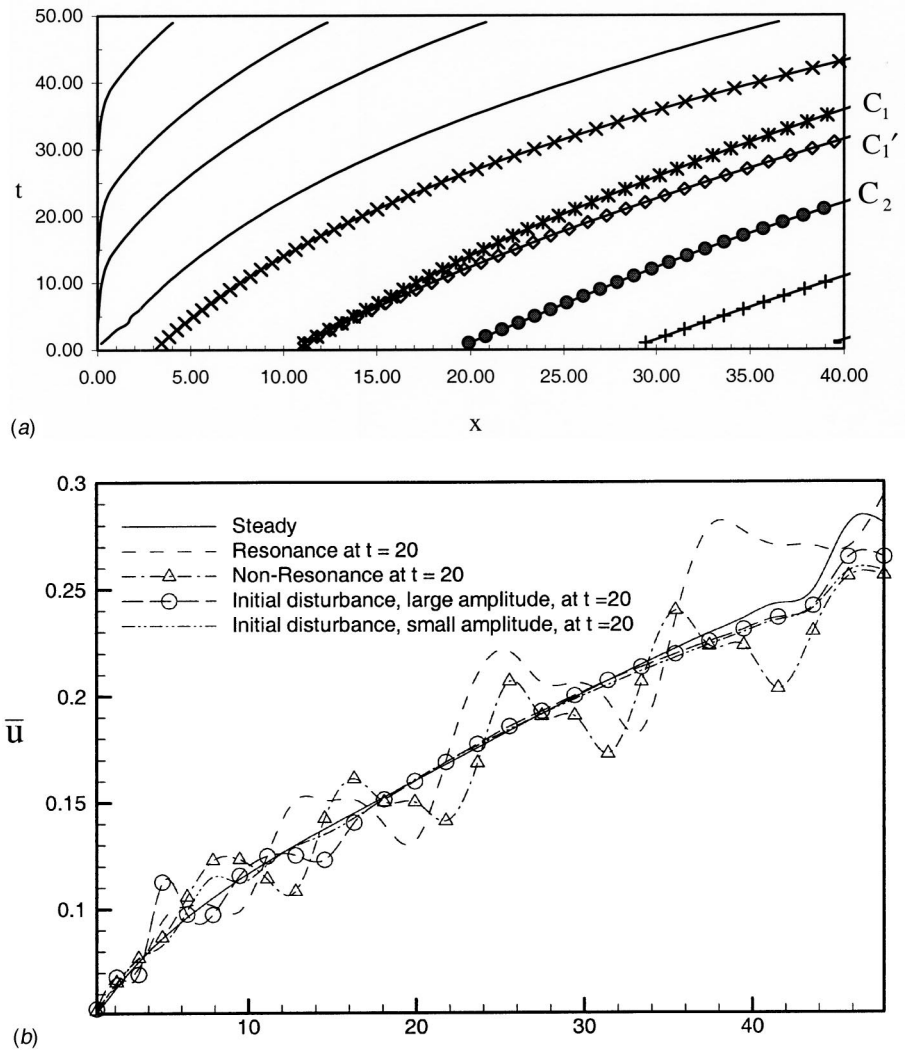


**Fig. 11** (*a*) **For flow situation specified in Table 1 with $\alpha$=90 deg and $x_e$=40, the characteristics curve $C_1$ denote curves along which infinitesimal initial disturbances naturally propagate on the stable steady solution. Curve $C_1'$ denotes characteristics along which finite disturbance arising from forced bottom wall noise actually propagate. On characteristics originating at $x$=0, $\delta(0,t)\cong 0$ implies $\delta'\cong 0$.** (*b*) **For flow situations defined in Table 1 with $\alpha$=90 deg and $x_e$=48, the above $\bar{u}(x,t)$ predictions for $t\geqslant 0$ are for** (i) **steady flow with $Z_e|_{Na}$=0.524,** (ii) **resonant case in Fig. 13,** (iii) **nonresonant case in Fig. 13,** (iv) **large initial disturbance of Fig. 10 and** (v) **small initial disturbance $\delta'(x,0)$ which is one-fifth of $\delta'(x,0)$ in Fig. 10.** (*c*) **For flow situations defined in Table 1 with $\alpha$=90 deg and $x_e$=50, the above $\bar{\bar{v}}(t)$ values are along actual characteristics curves like $C_1'$ in Fig. 11(*a*). The predictions are for** (*i*) **the steady and stable flow with $Z_e|_{Na}$=0.578,** (*ii*) **the resonant case of Fig. 13,** (*iii*) **the nonresonant case of Fig. 13, and** (iv) **the small initial disturbance case** (**scaled up and shown in the lower figure**) **in Fig. 11(*c*).**

discussed/studied here are the waves that appear as wavy interfacial oscillations in laminar/laminar condensing flows under unconstrained exit conditions.

The Fourier component of the standing-wave disturbance $v_1(x,0,t)$ used in Fig. 13(*a*) is equivalently written as the sum of two traveling waves. Denoting the forward traveling wave's phase angle as $\alpha_1 \equiv 2\pi\{x/\lambda - t/T\}$ and the backward traveling wave's phase angle as $\alpha_2 \equiv 2\pi\{x/\lambda + t/T\}$, the bottom plate noise is given as

$$v_1(x,0,t) = \frac{\varepsilon}{2}[\mathrm{Re}\{\exp(i\alpha_1(x,t)) - \exp(i\alpha_2(x,t))\}], \quad (29)$$

where "$i$" in the arguments of the exponential functions appearing in Eq. (29) denotes the complex number $\sqrt{-1}$ and "Re{ }" in Eq. (29) denotes real part of the expression within "{ }."

Furthermore, results in Figs. 13(*a*) are in accord with the expectation (see Miyara [32] for the Nusselt problem) that noise amplification is either sustained or increased with increasing downstream distances and film thickness values. For resonant or nonresonant condensing surface vibration considered in Fig. 13, the corresponding oscillatory "growth/damping" factor $\bar{\bar{v}}(t)$ values in Fig. 11(*c*) (computed along the actual unsteady characteristics such as $C_1'$ of Fig. 11(*a*)) are also, on average, either sustained or amplified. In Fig. 11(*b*), at large times, the noise-induced

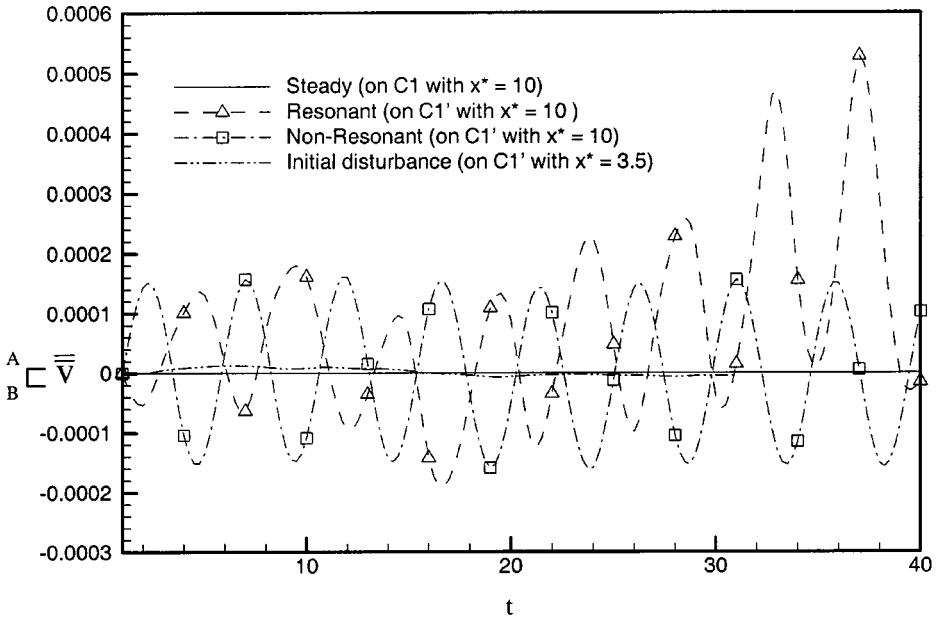


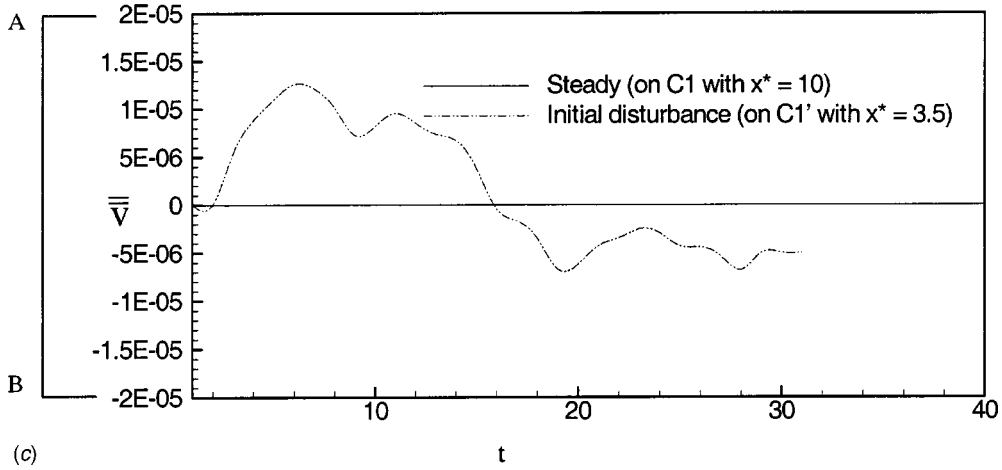


(*c*)

**Fig. 11** (***continued***)

waves' characteristics speed $\overline{u}(x,t)$ has a mean $\overline{u}_{\text{mean}}(x)$ (with $\overline{u}_{\text{mean}}(x) \cong \overline{u}_{\text{steady}}(x)$) and superposed oscillations/waves on $\overline{u}_{\text{mean}}(x)$. It is seen in Fig. 11(*a*) that the *integration* involved in obtaining the characteristics $C_1', C_2'$, etc. smooth out the effects of the fluctuating part of $\overline{u}(x,t)$ while its mean $\overline{u}_{\text{mean}}(x)$ mainly affects the *characteristics* at large *x*-locations where the noise effects are large and nonlinear effects associated with the size of $|\delta'(x,t)|$ play a role. For the nonresonant wall noise case in Fig. 13(*a*), both the "growth/damping" factor $\bar{v}(x,t)$ values (shown in Fig. 11(*c*) as $\hat{\bar{v}}(t)$ along $C_1$) and $\delta'(x,t)$ values have been computationally verified to sustain waves with approximately the same wavelength $\lambda$ and frequency $f_{\text{ext}} = 1/T$ as that of the external forcing noise. Thus the phase angles associated with these interfacial waves are same as those associated with the forcing noise in Eq. (29). To better understand the connection between these two variables in terms of the resulting phase speeds and the intrinsic phase speed for the flow, analytical implications of Eq. (23) are presented next for the case of small amplitude bottom wall noise.

For the purpose of identification of resonance conditions, it is assumed, as is the case in Fig. 11(*b*), that an amplitude "$\varepsilon$" for bottom wall noise can be found up to which (i.e., small to moderate values of $\varepsilon$) the approximation $\overline{u}(x,t) \cong \overline{u}_{\text{steady}}(x)$ holds. The above discussions for the bottom plate noise in Eq. (29) allow us to assume that the form of $\bar{v}(x,t)$ and the form of the associated $\delta'(x,t)$ are given by

$$\bar{v}(x,t) = \text{Re}\{v_{g1}(x,t)\exp(i\alpha_1(x,t) + v_{g2}(x,t)\exp(i\alpha_2(x,t)\}$$

$$\delta'(x,t) = \text{Re}\{\varsigma_{g1}(x,t)\exp(i\alpha_1(x,t) + \varsigma_{g2}(x,t)\exp(i\alpha_2(x,t)\}, \tag{30}$$

where the phase angles $\alpha_1$ and $\alpha_2$ are same as in Eq. (29). Furthermore *complex-valued* growth rates $v_{g1}$ and $v_{g2}$ for $\bar{v}(x,t)$ and $\varsigma_{g1}$ and $\varsigma_{g2}$ for $\delta'(x,t)$ are assumed to be non-oscillatory. Under this assumption of nonoscillatory $\overline{u}(x,t) \cong \overline{u}_{\text{mean}}(x)$, the relationships among the growth rates for $\bar{v}(x,t)$ and $\delta'(x,t)$ are found by substituting Eq. (30) in Eq. (27) and equating coefficients of the two exponentials. This gives

$$\frac{d\varsigma_{g1}}{dt} + i(D\Delta_1)\varsigma_{g1} = v_{g1}$$

$$\frac{d\varsigma_{g2}}{dt} + i(D\Delta_2)\varsigma_{g2} = v_{g2}, \tag{31}$$

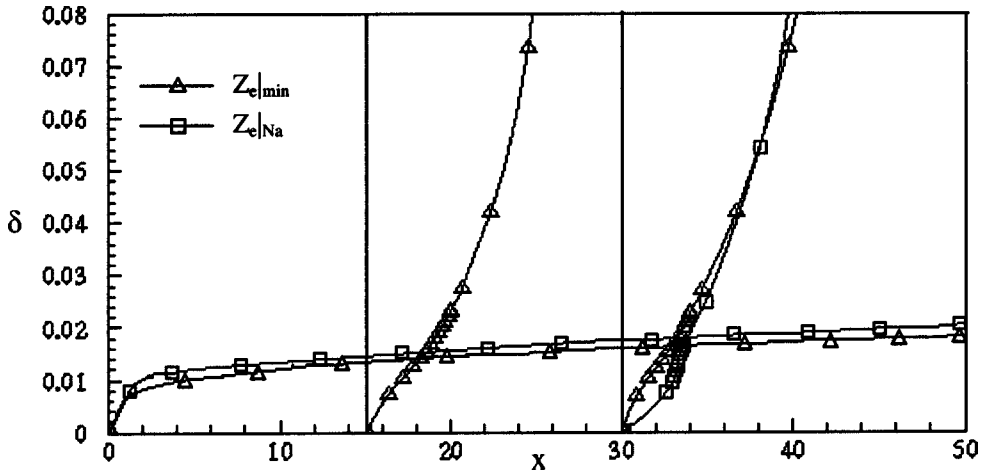


**Fig. 12 For the above flow situation specified in Table 1 with $\alpha$=90 deg and $x_e$=50, the steady solutions are obtained for $Z_e=Z_e|_{min}=0.26$ and $Z_e|_{Na}=0.36$**

where $D\Delta_1 \equiv (2\pi\overline{u}/\lambda - f_{ext})$, $D\Delta_2 \equiv (2\pi\overline{u}/\lambda + f_{ext})$, $f_{ext} \equiv 1/T$, and the *ordinary* time derivatives in Eq. (31) are taken along the characteristics $x = x_c(t)$ defined in Eq. (25). With $J=1$ or 2 denoting the numerical subscripts in Eq. (31), the solutions of the two equations in Eq. (31) subjected to the requirement of zero growth rates up to $t \leqslant 0$ are given by

$$\mathrm{s}_{gJ} = \exp(-i(D\Delta_J)t) \int_0^t v_{gJ}(\tau)\exp(i(D\Delta_J)\tau)\cdot d\tau. \quad (32)$$

From Eq. (32) it is easily inferred that, if $|D\Delta_J|$ values are significantly nonzero for $J=1$ and 2 (as in nonresonant cases), the growth rates $v_{gJ}$ for $\bar{v}(x,t)$ and $\mathrm{s}_{gJ}$ for $\delta'(x,t)$ are of the same order of magnitude. Thus the physical mechanisms inherent in Eq. (27) do not affect these growth rates in any *special* way. However, for $|D\Delta_1| \cong 0$ in Eq. (32), $\mathrm{s}_{g1}$ significantly starts growing as $|\mathrm{s}_{g1}| \cong |\int_0^t v_{g1}(\tau)d\tau| \approx t|v_{g1}(x_c(t),t)|_{av} \geqslant O(\varepsilon \cdot t)$. Therefore by choosing frequency $f_{ext} = f_{ext}(x) \equiv 1/T(x)$ to satisfy the resonance condition $|D\Delta_1| \cong 0$, i.e.,

$$\lambda f_{ext}(x) = \overline{u}(x,t) \cong \overline{u}_{steady}(x) \cong \overline{u}_{mean}(x), \quad (33)$$

one can match the phase speed $\lambda f_{ext}(x)$ of the bottom wall noise to the phase speed $\overline{u}_{steady}(x)$ of the *intrinsic initial disturbance waves*. It should be noted that, even for this case, $|D\Delta_2|$ is nonzero. Indeed, under these conditions, this resonance phenomenon is seen in Fig. 13(*a*). The fact that, in Fig. 13(*a*), interfacial waves' wavelengths only approximately equal wall-noise wavelength $\lambda$ and $\overline{u}(x,t)$ only approximately equal $\overline{u}_{steady}(x)$ is due to the fact that the amplitude of $\delta'(x,t)$ are not infinitesimal (as was assumed in the above analysis). All else being the same in Fig. 13(*a*), it is clear that the resonant case has significantly more wave energy than the same amplitude non-resonant noise. Thus whenever resonance condition in Eq. (33) is satisfied, the mechanisms represented by Eq. (27) imply that the forward moving component of the noise and the small amplitude *intrinsic interfacial waves* have the same phase speeds and this leads to phase reinforcements and significant increase in the amplitude of $\delta'$.

Although the results shown in Fig. 13 are for a sinusoidal standing wave on the condensing surface at $y=0$, more complex two-dimensional or three-dimensional patterns will arise from a more general noise that would *typically* be present. Furthermore, even if the noise itself is two-dimensional any three-dimensional imperfection in the geometry may cause the wave to become three-dimensional further downstream, and this is perhaps the reason why two-dimensional waves become three-dimensional in some of the known experiments (see, e.g., Lu [21]).

Although it is not presented here, effects of any *general* two-dimensional noise (as measured experimentally by accelerometers) can also be estimated by looking at the power density function of $v_1(x,0,t)$, through FFT, in the $k$-$\omega$ space (wave number $k \equiv 2\pi/\lambda$ and angular frequency $\omega \equiv 2\pi f$) and representing the disturbance $v_1(x,0,t)$ by a representative sum of Fourier components of wavelengths $\lambda$ and frequencies $f$.

The CFD simulation restrictions on wavelengths $\lambda$ that can be investigated is: $\Delta x^*/2 < \lambda < x_e/2$, where $\Delta x^*$ is of the order of magnitude of the largest $x$-width in grid A and grid B and $x_e$ is the distance between the inlet and the outlet. The smallest time step $\Delta t^*$ is the minimum of $(\Delta x/\overline{u})$ values due to $\mathrm{Cr} \cong 1$ restriction in Eq. (24). This restricts the maximum frequency $f = f_{max}$ that can be computationally studied to those that satisfy the Nyquist criteria $f_{max} < 1/(2\cdot\Delta t^*)$. Despite these restrictions on noise-sensitivity analyses, the *stability* results in Section 5 are true for all wavelengths $\lambda$. This is because the resulting interfacial wavelengths are increasing in nature and they increase to a value where it can be resolved by the refined grids employed in this paper.

With regard to noise sources other than the bottom plate noise, it was found that noise or fluctuations in the inlet velocity profile only leads to fluctuations in the vapor profile and has *little* impact on the interfacial waviness. In other words, under unconstrained exit conditions, only fluctuations in flow variables that significantly influence fluctuations in transverse liquid velocity $v_1(x,y,t)$ cause significant interfacial waviness. However, this paper can not account for density fluctuations that necessarily appear in the study of effects of superposed fluctuations in the exit conditions while the inlet conditions are being held fixed.

## 6 Convergence, Accuracy, and Other Regularities of the Solutions

For a computational solution to be accurate, it needs to satisfy the following criteria: (i) the convergence criteria in the interior of each fluid (i.e., smallness of "$b$" defined on p. 125 of Patankar [40]), (ii) the satisfaction of all the interface conditions, (iii) grid independent solutions for grids that are sufficiently refined, and (iv) unsteady simulation results for the sensitive interface locations should be free of computational noise in the absence of physical noise. The simulations presented here satisfy all the above criteria.

The satisfaction of the governing equations in the interior and all the conditions at the interface is demonstrated in Liang [2]. For sufficiently refined grid (i.e., both grid A and grid B described in Section 3) and sufficiently large (but not too large) number of

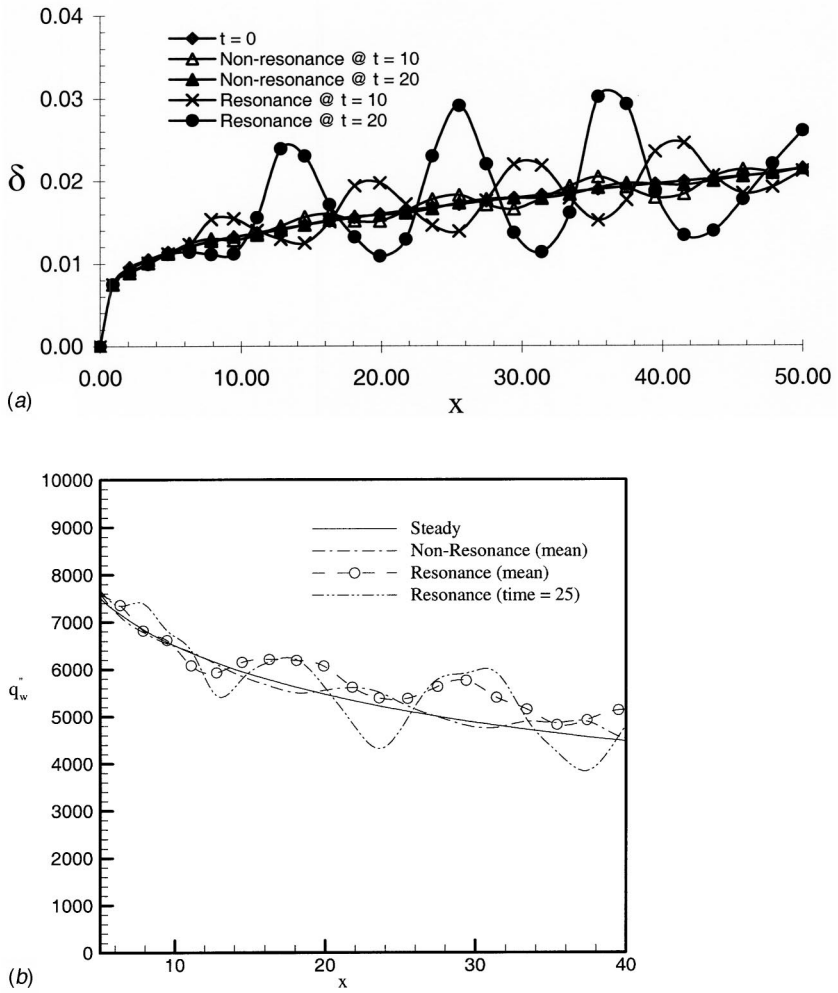


**Fig. 13 (*a*) For the flow situations specified in Table 1 with $\alpha$=90 deg, $x_e$=50 and $Z_e$=0.578; the above $\delta(x,t)$ predictions compare the nonresonant noise with a resonant noise of the same amplitude ($\varepsilon$=0.9E-4). The noise is given by: $v_1(x,0,t)=\varepsilon\cdot\sin(2\pi x/\lambda)\cdot\sin(2\pi t/T)$, where (i) $\lambda$=10 and $T$=24 for the nonresonant case, and (ii) $\lambda$=10 and $T=T(x)=\lambda/\bar{u}_{\text{steady}}(x)$. (*b*) For the flow situations considered in Fig. 13(*a*), the above depicts the wall heat flux $q''_w(x,t)$, in *W*, at $t$=25 for the resonant case, and its time-averaged values $\bar{q}''_w(x)$, in *W*, for all other cases.**

iterations, the combined sum of decreasing truncation and increasing roundoff errors are minimized to a plateau level and the solutions in Fig. 14(*a*) are grid independent to within 1–2%. The number of grid lines $n_i\times n_j|_L\times n_j|_v$ given in Fig. 14, respectively, indicate the number of grid lines over $0\leqslant x\leqslant x_e$, $0\leqslant y\leqslant\delta_{\text{steady}}(x)$, and $\delta_{\text{steady}}(x)\leqslant y\leqslant 1$ for the interface location at $t=0$. These numbers somewhat change with time. For grid II in Fig. 14(*a*), $(\Delta x)_{av}\equiv x_e/n_i=0.77$, $(\Delta y)_{avL}\equiv\delta(x_e)/n_j|_L=5.77\times10^{-4}$, $(\Delta y)_{avV}\equiv\{1-\delta(x_e)\}/n_j|_v=0.015$, and $\Delta t=5$. The corresponding representative grid spacing values in physical variables are $(\Delta x)_{av}=3.08$ mm, $(\Delta y)_{avL}=2.31$ $\mu$m, $(\Delta y)_{avV}=0.06$ mm, and $\Delta t=0.049$ s. For a technical estimate of total discretization error—Section 3.10 in Ferziger and Peric [41] is used for estimating error on a representative flow variable (say, film thickness in Fig. 14(*b*)) due to the coarseness of *x*-grid. On successive refinement of the *x*-grid, the results in Fig. 14(*b*) yield the error to be within 3%. Considering this and the refinement used in the time and in the *y*-direction, the total error of all reported results in this paper is about 6%.

*Smooth interface* unsteady solutions reported earlier in Fig. 8(*a*) establish that the highly sensitive interface predictions are free of computational noise whenever there is an absence of physical noise. In fact, in Liang [2], it is shown that inappropriate discretization schemes for the interface tracking equation or unsuitable choice of splines for mapping variable values between grid A and grid B can lead to wavy interface solutions even in the absence of physical noise. Such waves that are entirely due to computational noise have been eliminated from the present study.

Another regularity of the proposed computational approach is its ability to make steady predictions for the classical Nusselt [5] problem in agreement with its classical solution while allowing for improvements in it. This is shown in Fig. 15. The unsteady predictions for this classical problem will be discussed in a separate paper.

## 7 Trends of the Steady, Stable and Noise-Sensitive Solutions

The steady and stable solution (associated with $Z_e=Z_e|_{\text{Na}}$) in Fig. 8 for the vertical-channel case was found to be sensitive to noise in Fig. 13. Despite the waves, as seen in Fig. 13(*b*), there are no significant enhancements in heat transfer rates for the nonresonant case. This is because the oscillations around the mean film thickness are small and nearly symmetric, and temperature pro-

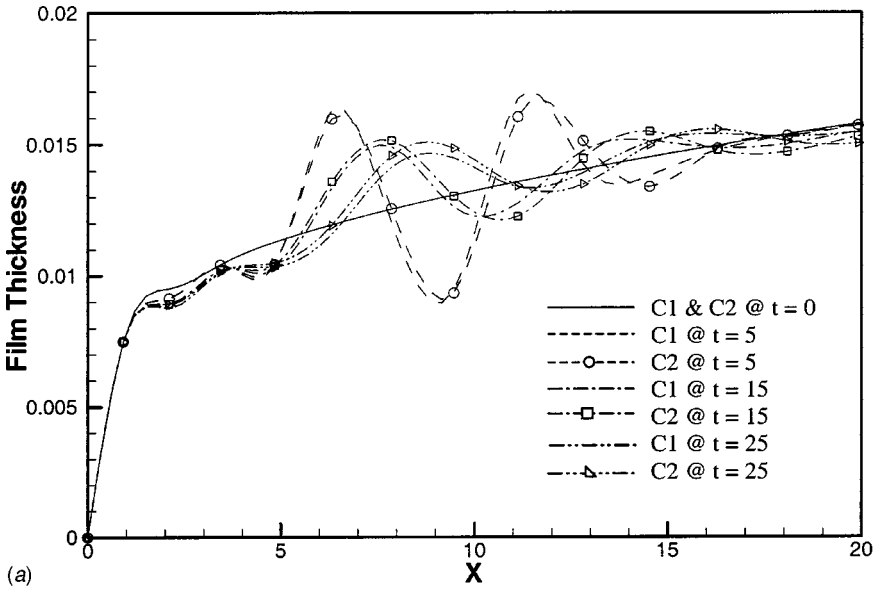


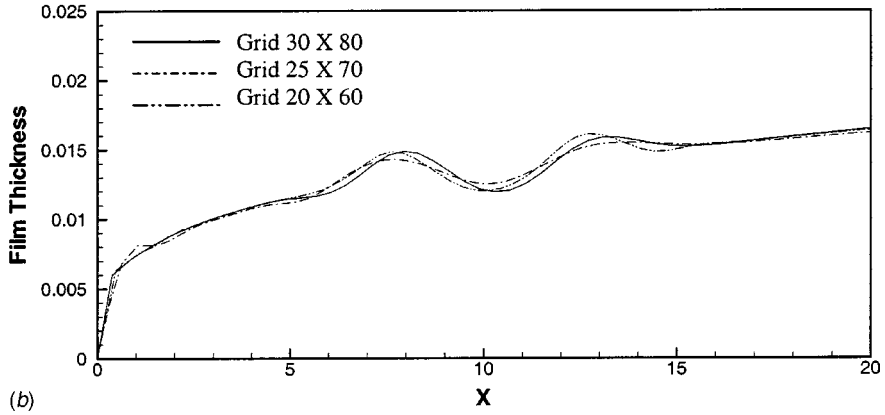


**Fig. 14 (*a*) The above $\delta(x,t)$ predictions for $t>0$ are for the steady solution curve $C1=C2$ at $t=0$ and initial noise specified in Fig. 10. The $t=0$ solutions are obtained on two grids I and II with $(n_i\times n_{j|L}\times n_{j|V})_I=(30\times30\times20)$ and $(n_i\times n_{j|L}\times n_{j|V})_{II}=(50\times50\times30)$. The $t>0$ solution are shown as curves $C1$ and $C2$ and are, respectively, obtained on grids that have: $(n_i\times n_{j|L}\times n_{j|V})_I\times\Delta t=(30\times30\times20)\times2.5$ and $(n_i\times n_{j|L}\times n_{j|V})_{II}\times\Delta t=(50\times50\times30)\times5$. At $t>0$, the number of grid lines $(n_i\times n_{j|L}\times n_{j|V})$ changes somewhat from their value at $t=0$.**

files are nearly linear. This yields heat flux $q''_w(x,t)\sim\Delta T/\delta(x,t)$ whose time-averaged values show no significant enhancement unless the wave amplitudes are large. As a result, for the larger amplitude resonant case in Fig. 13, there is a significant heat transfer enhancement of 10% or more in the downstream half of the channel. Therefore these stable and quasi-steady $Z_e=Z_e|_{\rm Na}$ solutions obtained in Fig. 8 are important in their own right for the purpose of estimating *typical* heat flux values. Hence it is good to ascertain the trends of these *natural* steady solutions as the inlet Reynolds number $\mathrm{Re}_{in}$ and the temperature difference $\Delta\mathcal{T}$ (or, equivalently, the parameter Ja) are changed. Figure 16 shows the effect of these changes on $Z_e=Z_e|_{\rm Na}$, Fig. 17 shows the effects on wall heat flux $\overline{q}''_w(x)$, and Fig. 18 shows the effects on flow fields ($\delta_{\rm steady}(x)$, etc.). Since the vertical channel configuration studied here is gravity-dominated, vapor motion does not significantly affect the condensate motion and, as expected, changes in inlet Reynolds number $\mathrm{Re}_{in}$ has no effects on mean film thickness $\delta_{\rm steady}(x)$ or wall heat flux $\overline{q}''_w(x)$. However, in Fig. 18, a thickening of $\delta_{\rm steady}(x)$ occurs due to an increase in temperature differ-

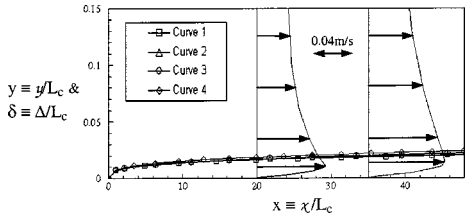


**Fig. 15 For the vertical plate situation specified in Table 1 with $\alpha=90$ deg, $x_e=48$ and $L_c=0.004$ m, Curve 1 is a plot of the analytical solution of $\delta(x)$ as given in Nusselt [5]. Curve 2 is the computational solution under the Nusselt assumption for stagnant vapor and zero liquid inertia. Curve 3 is the computational solution under the assumptions of stagnant vapor while allowing for liquid inertia. Curve 4 is the computational solution that allows vapor motion and liquid inertia (the vapor/liquid velocity profiles are shown only for this case). Though not shown above, vapor velocity tends to zero as $y\rightarrow\infty$.**

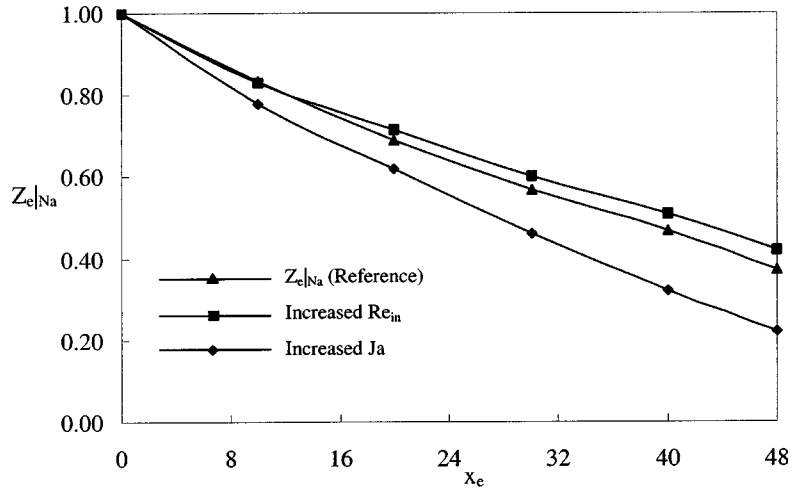


**Fig. 16 The above is a plot of natural values of $Z_{e|Na}$ for different $x_e$ values for a representative flow situation specified in Table 1 with $\alpha$=90 deg and $x_e$=48. The "Increased $Re_{in}$" case just changes $Re_{in}$ to a new value of 1300. The "Increased Ja" case just changes Ja to a new value of 0.0443 (i.e., $\Delta T$ =65°C).**

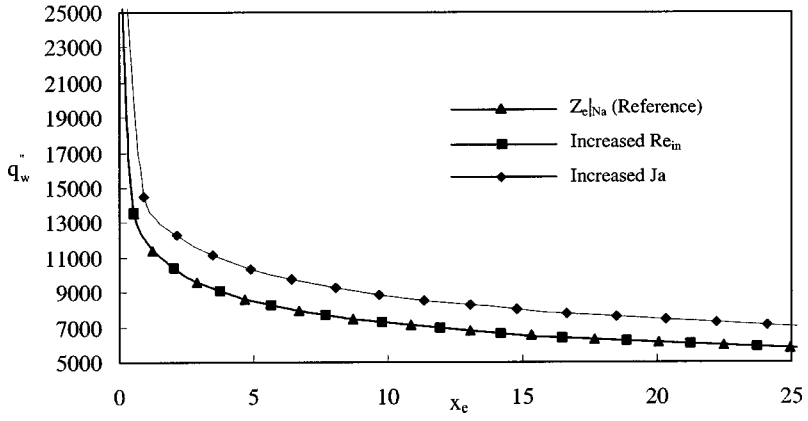


**Fig. 17 For the flow situations described in Fig. 16 and $x_e$=25.0, the above figure reports the representative wall heat flux values $q''_w(x)$, in *W*, as a function of $x$ with $0 \leq x \leq x_e$**

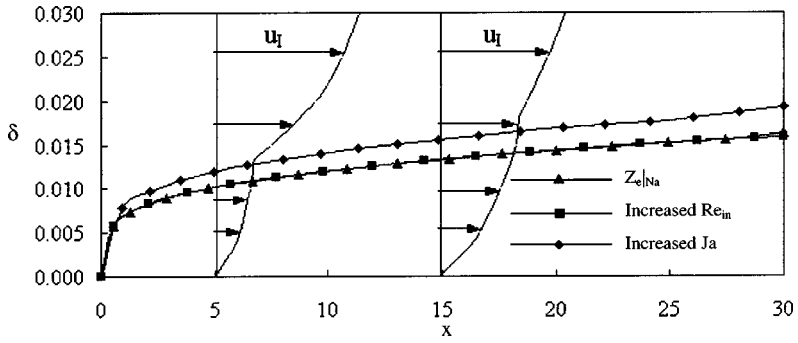


**Fig. 18 For the flow situations described in Figs. 16–17 and $x_e$=30.0, the above figure reports the values of $\delta_{steady}(x)$**

ence $\Delta\mathcal{T}$. This thickening occurs in a way so as to concurrently meet the requirements of increased heat flux values (see Fig. 17) and increased liquid flow rates.

Streamline patterns for the flow, effect of shear over gravity as tilt angle $\alpha$ is reduced from its 90 deg value, comparisons with experimental results for condensing flow simulations for a horizontal channel, effects of surface tension, effects of microgravity, negligible Marangoni effects, effects of fluctuations on the mean, etc., are not discussed here but are reported in Liang et al. [1].

## 8 Conclusions

- An algorithm for a successful computational approach capable of accurate simulation of unsteady wavy interface condensing flows has been presented.
- The "ellipticity" of the steady vapor flow equations and the role of exit conditions for steady and unsteady simulations have been discussed.
- For unconstrained exit conditions and nearly incompressible vapor flows, an unsteady noise-free simulation method for identifying and obtaining the *natural* and *stable* steady solutions has been presented and successfully used.
- The noise sensitivity of the *stable* steady or quasi-steady solutions to ubiquitous minuscule bottom plate vibrations has been demonstrated. To assist in quantitative noise-sensitivity studies, a method for obtaining the underlying *characteristics curves* and estimating "growth/damping" factors for interfacial disturbances has been presented.
- For design of smart condensers with actuators imbedded on the condensing surface, a new and hitherto unknown resonance condition has been proposed, and its efficacy in enhancing wave energy and heat transfer rates (up to 10% or more) has been demonstrated.
- For unconstrained exit situations, some trends of the *stable* steady or quasi-steady solutions have been discussed.


## Acknowledgment

This work was partially supported by the NSF grant CTS-0086988.


## Appendix

The interface conditions that apply at $\mathcal{H}(x,y,t)=y-\Delta(x,t)=0$, involve values of flow variables at the interface that are denoted by a superscript "*i*." The unit normal at any point on the interface, directed from the liquid towards the vapor, is denoted by $\hat{\mathbf{n}}$ and is equal to $\nabla\mathcal{H}/|\nabla\mathcal{H}|$. The unit tangent at any point on the interface, directed towards increasing $x$, is denoted by $\hat{\mathbf{t}}$. Each phase is modeled as a viscous and incompressible Newtonian fluid with stress tensor $\mathbf{T}=-p_I\mathbf{1}+\mathbf{S}_I$ where $\mathbf{S}_I=\mu_I\{(\text{grad}\cdot\mathbf{v}_I)+(\text{grad}\cdot\mathbf{v}_I)^T\}/2$ and $\mathbf{1}$ is the identity tensor.

- The surface velocity $\mathbf{v}_s^i$ of a point on the interface ($\mathcal{H}=0$) at time $t$ is associated with this point's movement to a new mapped position on the interface at time $t+\Delta t$. All such mappings must be such that the normal component of this $\mathbf{v}_s^i$ is given by

$$\mathbf{v}_s^i\cdot\hat{\mathbf{n}}=-(\partial\mathcal{H}/\partial t)/|\nabla\mathcal{H}|. \tag{A1}$$

- The tangential component of the vapor and liquid velocities at the interface must be continuous, i.e.,

$$\mathbf{v}_1^i\cdot\hat{\mathbf{t}}=\mathbf{v}_2^i\cdot\hat{\mathbf{t}}. \tag{A2}$$

- Ignoring normal component of $\nabla_s\sigma$ and viscous stresses, the normal component of momentum balance at a point on the interface is given by

$$\begin{aligned}p_1^i&=p_2^i+\dot{m}^2(1/\rho_2-1/\rho_1)+\sigma\nabla_s\cdot\hat{\mathbf{n}}-\nabla_s\sigma\cdot\hat{\mathbf{n}}+(\mathbf{S}_1^i-\mathbf{S}_2^i)\hat{\mathbf{n}}\cdot\hat{\mathbf{n}}\\&\cong p_2^i+\dot{m}^2(1/\rho_2-1/\rho_1)-(\sigma\Delta_{xx})/[1+\Delta_x^2]^{2/3}.\end{aligned} \tag{A3}$$

- The tangential component of momentum balance at any point on the interface, for nearly constant surface tension $\sigma$, reduces to

$$\mathbf{S}_1^i\hat{\mathbf{n}}\cdot\hat{\mathbf{t}}=\mathbf{S}_2^i\hat{\mathbf{n}}\cdot\hat{\mathbf{t}}+\nabla_s\sigma\cdot\hat{\mathbf{t}}\cong\mathbf{S}_2^i\hat{\mathbf{n}}\cdot\hat{\mathbf{t}}. \tag{A4}$$

- The mass fluxes $\dot{m}_{VK}$ and $\dot{m}_{LK}$ as determined by kinematic restrictions imposed by interfacial values of vapor and liquid velocities are

$$\dot{m}_{VK}\equiv-\rho_2(\mathbf{v}_2^i-\mathbf{v}_s^i)\cdot\hat{\mathbf{n}}\ \text{ and }\ \dot{m}_{LK}\equiv-\rho_1(\mathbf{v}_1^i-\mathbf{v}_s^i)\cdot\hat{\mathbf{n}}. \tag{A5}$$

- The energy balance at a point on the interface imposes a restriction on the interfacial mass flux $\dot{m}_{\text{Energy}}$, and this is given by

$$\begin{aligned}\dot{m}_{\text{Energy}}=1/h_{fg}\Bigg[&\{k_1\nabla\mathcal{T}_1|^i\cdot\hat{\mathbf{n}}-k_2\nabla\mathcal{T}_2|^i\cdot\hat{\mathbf{n}}\}+\frac{d\sigma}{dt}\Big|_s\\&+\frac{1}{2}\dot{m}\{|\mathbf{v}_1^i-\mathbf{v}_s^i|^2-|\mathbf{v}_2^i-\mathbf{v}_s^i|^2\}\\&+\{\mathbf{S}_1^i\hat{\mathbf{n}}\cdot(\mathbf{v}_1^i-\mathbf{v}_s^i)-\mathbf{S}_2^i\hat{\mathbf{n}}\cdot(\mathbf{v}_2^i-\mathbf{v}_s^i)\}\Bigg]\\\cong 1/h_{fg}\Bigg[&k_1\frac{\partial\mathcal{T}_1}{\partial n}\Big|^i-k_2\frac{\partial\mathcal{T}_2}{\partial n}\Big|^i\Bigg].\end{aligned} \tag{A6}$$

- Mass balance at any point on the interface requires single valuedness of the interfacial mass flux. That is

$$\dot{m}_{LK}=\dot{m}_{VK}=\dot{m}_{\text{Energy}}\equiv\dot{m}. \tag{A7}$$

- To account for the effects of nonzero interfacial mass flux $\dot{m}$, the interfacial pressures $p_1^i$ and $p_2^i$ (along with their difference $\Delta p^i\equiv p_1^i-p_2^i$) that appear in Eq. (*A*3) are often considered to be controlled by nonequilibrium thermodynamic effects that are represented by the functions: $p_1^i\equiv p_{1\,n\text{-}eq}^i(\mathcal{T}_1^i)$ and $p_2^i\equiv p_{2\,n\text{-}eq}^i(\mathcal{T}_2^i)$, where $\mathcal{T}_1^i$ is the liquid side interfacial temperature and $\mathcal{T}_2^i$ is the vapor side interfacial temperature. In the limit of zero mass flux $\dot{m}$, these thermodynamic pressures reach their equilibrium thermodynamic values and are denoted as $p_1^i\equiv p_{\text{sat}}(\mathcal{T}_1^i)$ and $p_2^i\equiv p_{\text{sat}}(\mathcal{T}_2^i)$, where $p_{\text{sat}}$ is the inverse function of the saturation temperature $\mathcal{T}_s(p)$. Respectively denoting the non-equilibrium and equilibrium values of the interfacial pressure differences as $(\Delta p^i)_{n\text{-}eq}$ and $(\Delta p^i)_{\text{sat}}$, it is common to *seek* or *model* a function $f$ such that $(\Delta p^i)_{n\text{-}eq}=f\{(\Delta p^i)_{\text{sat}},\dot{m}\}$, where $f$, be it *explicit* or *implicit* in form, allows the two pressure differences to become the same for zero mass flux $\dot{m}$. It is common to *model* $f$ by considerations (see, e.g., Plesset and Prosperetti [44] and Section 4.5 of Carey [37]) involving kinetic theory of gas for the vapor phase, the concept of accommodation coefficients, etc. The assumption that use of either $(\Delta p^i)_{n\text{-}eq}$ or $(\Delta p^i)_{\text{sat}}$ do not significantly affect the value of $\Delta\mathcal{T}^i\equiv\mathcal{T}_s(p_2^i+\Delta p^i)-\mathcal{T}_s(p_2^i)$ is well known and well justified in the present context where significantly larger thermal resistance is offered by the thin condensate at points away from $x\sim 0$ (see Section 4.5 of Carey [37] and Son and Dhir [22]). Furthermore, the computations in this paper also show that the solution further downstream is not affected by the nature of the singular solution at $x\sim 0$ and computed values in this zone always satisfy $\Delta\mathcal{T}^i\equiv\mathcal{T}_s(p_2^i+\Delta p^i)-\mathcal{T}_s(p_2^i)\cong 0$— in the sense that $\Delta\mathcal{T}^i\ll\Delta\mathcal{T}$, where $\Delta\mathcal{T}$ is the number defined in Eq. (1). Therefore, under negligible interfacial resistance approximation, the interfacial temperature values satisfy:

$$\mathcal{T}_1^i\cong\mathcal{T}_2^i=\mathcal{T}_s(p_2^i). \tag{A8}$$

- The term $[t]$ on the right side of Eq. (5) is given by

$$[t]=\left\{\frac{\mu_2}{\mu_1}\frac{\partial v_2}{\partial x}\bigg|^i-\frac{\partial v_1}{\partial x}\bigg|^i\right\}+\frac{2\delta_x}{[1-\delta_x^2]}\left\{\frac{\partial u_1}{\partial x}\bigg|^i-\frac{\partial v_1}{\partial y}\bigg|^i\right\}$$
$$-\frac{2\delta_x}{[1-\delta_x^2]}\frac{\mu_2}{\mu_1}\left\{\frac{\partial u_2}{\partial x}\bigg|^i-\frac{\partial v_2}{\partial y}\bigg|^i\right\}. \quad (A9)$$

## References


[1] Liang, Q., Wang, X., and Narain, A., 2004, ''Effects of Gravity, Shear, and Surface Tension in Internal Condensing Flows—Results from Direct Computational Simulations,'' (accepted for publication in the ASME *Journal of Heat Transfer*).

[2] Liang, Q., 2003, ''Unsteady Computational Simulations and Code Development for a Study of Internal Film Condensation Flows' Stability, Noise-Sensitivity, and Waviness,'' Ph.D. thesis, Michigan Technological University.

[3] Krotiuk, W. J., 1990, *Thermal-Hydraulics for Space Power, Propulsion, and Thermal Management System Design*, American Institute of Aeronautics and Aeronautics, Washington, DC.

[4] Faghri, A., 1995, *Heat Pipe Science and Technology*, Taylor and Francis, Washington, DC.

[5] Nusselt, W., 1916, ''Die Oberflächenkondesation des Wasserdampfes,'' Z. Ver. Dt. Ing., **60**(27), pp. 541–546.

[6] Rohsenow, W. M., 1956, Heat Transfer and Temperature Distribution in Laminar Film Condensation, Trans. ASME, **78**, pp. 1645–1648.

[7] Sparrow, E. M., and Gregg, J. L., 1959, ''A Boundary Layer Treatment of Laminar Film Condensation,'' ASME J. Heat Transfer, **81**, pp. 13–18.

[8] Koh, J. C. Y., Sparrow, E. M., and Hartnett, J. P., 1961, ''The Two-Phase ry Layer in Laminar Film Condensation,'' Int. J. Heat Mass Transfer, **2**, pp. 69–82.

[9] Dhir, V. K., and Lienhard, J. H., 1971, ''Laminar Film Condensation on Plane and Axisymmetric Bodies in Nonuniform Gravity,'' ASME J. Heat Transfer, **93**, pp. 97–100.

[10] Rose, J. W., 1988, ''Fundamentals of Condensation Heat Transfer: Laminar Film Condensation,'' JSME Int. J., **31**, pp. 357–375.

[11] Tanasawa, I., 1991, ''Advances in Condensation Heat Transfer,'' Adv. Heat Transfer, **21**, pp. 55–131.

[12] Cess, R. D., 1960, ''Laminar Film Condensation on a Flat Plate in the Absence of a Body Force,'' ZAMP, **11**, pp. 426–433.

[13] Koh, J. C. Y., 1962, ''Film Condensation in a Forced Convection Boundary Layer Flow,'' Int. J. Heat Mass Transfer, **5**, pp. 941–954.

[14] Kutateladze, S. S., 1963, *Fundamentals of Heat Transfer*, Academic Press, San Diego, CA.

[15] Labuntsov, D. A., 1957, ''Heat Transfer in Film Condensation of Pure Steam on Vertical Surfaces and Horizontal Tubes,'' Teploenergetica, **4**, p. 72. Also see (in Russian) ''Heat Transfer During Condensation of Steam on a Vertical Surface in Conditions of Turbulent Flow of a Condensate Film,'' 1960, Inghenerno-Fizicheski Zhurnal, **3**, pp. 3–12.

[16] Incropera, F. P., and DeWitt, D. P., 1996, *Fundamentals of Heat and Mass Transfer*, 4th Ed., John Wiley and Sons, New York.

[17] Yu, G., 1999, ''Development of a CFD Code for Computational Simulations and Flow Physics of Annular/Stratified Film Condensation Flows,'' *Ph.D. thesis*, ME-EM Department, Michigan Technological University.

[18] Chow, L. C., and Parish, R. C., 1986, ''Condensation Heat Transfer in Microgravity Environment,'' *Proceedings of the 24th Aerospace Science Meeting*, AIAA, New York.

[19] Narain, A., Yu, G., and Liu, Q., 1997, ''Interfacial Shear Models and Their Required Asymptotic Form for Annular/Stratified Film Condensation Flows in Inclined Channels and Vertical Pipes,'' Int. J. Heat Mass Transfer, **40**(15), pp. 3559–3575.

[20] Henstock, W. H., and Hanratty, T. J., 1976, ''The Interfacial Drag and the Height of the Wall Layer in Annular Flows,'' AIChE J., **22**, pp. 990–1000.

[21] Lu, Q., 1992, ''An Experimental Study of Condensation Heat Transfer With Film Condensation in a Horizontal Rectangular Duct,'' *Ph.D. thesis*, Michigan Technological University.

[22] Sussman, M., Smereka, P., and Osher, S., 1994, ''A Level Set Approach for Computing Solutions to Incompressible Two-Phase Flow,'' J. Comput. Phys., **114**, pp. 146–159.

[23] Son, G., and Dhir, V. K., 1998, ''Numerical Simulation of Film Boiling Near Critical Pressures with a Level Set Method,'' ASME J. Heat Transfer, **120**, pp. 183–192.

[24] Hirt, C. W., and Nichols, B. D., 1981, ''Volume of Fluid (VOF) Method for the Dynamics of Free Boundaries,'' J. Comput. Phys., **39**, pp. 201–255.

[25] Tezduyar, T. E., 2001, ''Finite Element Interface-Tracking and Interface-Capturing Techniques for Flows with Moving Boundaries and Interfaces,'' *Proceedings of the ASME Symposium on Fluid Physics and Heat Transfer for Macro and Micro-Scale Gas-Liquid and Phase-Change Flows*, HTD-Vol. 369-3, ASME, New York.

[26] Abbott, M. B., and Basco, D. R., 1989, *Computational Fluid Dynamics—An Introduction For Engineers*, Longman, pp. 86–88, Ch. 3, pp. 151–155, Ch. 5.

[27] Li, J., and Renardy, Y., 2000, ''Numerical Study of Flows of Two Immiscible Liquids at Low Reynolds Number,'' SIAM Rev., **42**(3), pp. 417–439.

[28] Lu, Q., and Suryanarayana, N. V., 1995, ''Condensation of a Vapor Flowing Inside a Horizontal Rectangular Duct,'' ASME J. Heat Transfer, **117**, pp. 418–424.

[29] Bhatt, B. L., Wedekind, G. L., and Jung, K., 1989, ''Effects of Two-Phase Pressure Drop on the Self-Sustained Oscillatory Instability in Condensing Flows,'' ASME J. Heat Transfer, **111**, pp. 538–545.

[30] Liu, J., and Gollub, J. P., 1994, ''Solitary Wave Dynamics of Film Flows,'' Phys. Fluids, **6**(5), pp. 1702–1712.

[31] Alekseenko, S. V., Nakoryakov, V. E., and Pokusaev, B. G., 1994, *Wave Flow of Liquid Films*, Begell House, New York.

[32] Miyara, A., 2001, ''Flow Dynamics and Heat Transfer of Wavy Condensate Film,'' ASME J. Heat Transfer, **123**, pp. 492–500.

[33] Lighthill, J., 1979, *Waves in Fluids*, Cambridge University Press, Cambridge, UK.

[34] Traviss, D. P., Rohsenow, W. M., and Baron, A. B., 1973, ''Forced Convection Condensation Inside Tubes: A Heat Transfer Equation for Condenser Design,'' ASHRAE Trans., **79**, Part 1, pp. 157–165.

[35] Shah, M. M., 1979, ''A General Correlation for Heat Transfer during Film Condensation inside Pipes,'' Int. J. Heat Mass Transfer, **22**, pp. 547–556.

[36] Hewitt, G. F., Shires, G. L., and Polezhaev, Y. V., eds., 1997, *International Encyclopedia of Heat and Mass Transfer*, CRC Press, Boca Raton, FL.

[37] Carey, V. P., 1992, *Liquid-Vapor Phase-Change Phenomena*, Series in Chemical and Mechanical Engineering, Hemisphere, Washington, DC.

[38] Palen, J. W., Kistler, R. S., and Frank Y. Z., 1993, ''What We Still Don't Know About Condensation in Tubes,'' *Condensation and Condenser Design* J. Taborek, J. Rose, and I. Tanasawa, eds., United Engineering Trustees, Inc. for Engineering Foundation and ASME, New York, pp. 19–53.

[39] Delhaye, J. M., 1974, ''Jump Conditions and Entropy Sources in Two Phase Systems: Local Instant Formulation,'' Int. J. Multiphase Flow, **1**, pp. 395–409.

[40] Patankar, S. V., 1980, *Numerical Heat Transfer and Fluid Flow*, Hemisphere, Washington DC.

[41] Ferziger, J. H., and Peric, M., 1997, *Computational Methods for Fluid Dynamics*, Springer, Berlin.

[42] Greenberg, M. D., 1978, *Foundations of Applied Mathematics*, Prentice-Hall, Englewood Cliffs, Jersey.

[43] Joseph, D. D., 1976, *Stability of Fluid Motions*, Vol. 1, Springer-Verlag, New York, pp. 7–8.

[44] Plesset, M. S., and Prosperetti, A., 1976, ''Flow of Vapor in a Liquid Enclosure,'' J. Fluid Mech., **78**(3), pp. 433–444.

[45] *ASHRAE Handbook*, 1985, Fundamentals SI Edition, American Society of Heating, Refrigeration and Air-Conditioning Engineers, Atlanta, GA.

# Three-Dimensional Instabilities in Flow Past a Rotating Cylinder

**S. Mittal**
Department of Aerospace Engineering,
Indian Institute of Technology,
Kanpur, UP 208 016, India
e-mail: smittal@iitk.ac.in

*Flow past a spinning circular cylinder placed in a uniform stream is investigated via three-dimensional computations. A stabilized finite element method is utilized to solve the incompressible Navier-Stokes equations in the primitive variables formulation. The Reynolds number based on the cylinder diameter and freestream speed of the flow is 200. The nondimensional rotation rate, $\alpha$, (ratio of the surface speed and freestream speed) is 5. It is found that although the two-dimensional flow for $\alpha=5$ is stable, centrifugal instabilities exist along the entire span in a three-dimensional set-up. In addition, a "no-slip" side-wall can result in separation of flow near the cylinder ends. Both these effects lead to a loss in lift and increase in drag. The end conditions and aspect ratio of the cylinder play an important role in the flow past a spinning cylinder. It is shown that the Prandtl's limit on the maximum lift generated by a spinning cylinder in a uniform flow does not hold.* [DOI: 10.1115/1.1631032]

## 1 Introduction

One of the earliest experiments for flow past a rotating cylinder were carried out by Prandtl [1]. He argued that the maximum lift generated by a spinning cylinder in a uniform flow is limited to $4\pi$ ($\sim$12.6). He also studied the effect of end conditions and aspect ratio. An increase in the overall lift coefficient was observed by utilizing end plates and using cylinders of higher aspect ratio. Since then, various studies have been conducted.

Recently, two-dimensional simulations for flow past a rotating cylinder have been presented by Mittal and Kumar [2]. The Reynolds number based on the cylinder diameter and freestream speed is 200 and various spin rates ($0\leqslant\alpha\leqslant5$) are considered. Here, $\alpha$ is the nondimensional rotation rate of the cylinder and is given as $\alpha=a\omega/U$ where $U$ is the freestream speed and $\omega$ is the angular velocity of the cylinder about its own axis. For $0\leqslant\alpha\leqslant1.9$ a von Karman street is seen in the wake behind the cylinder. For nonzero $\alpha$ the vortex street is deflected away from the center line. The wake becomes narrower and the Strouhal number for vortex shedding decreases with increase in rotation rate. Vortex shedding ceases beyond $\alpha\sim1.9$. At high rotation rates it is seen that the lift for purely two-dimensional flows can be very large. The values of the lift coefficient obtained in the present work exceed the maximum limit based on the arguments of Prandtl. The flow remains stable for $1.91\leqslant\alpha\leqslant4.34$ but looses its stability, again, for $\alpha\sim4.35$. For this rotation rate, unlike the shedding for lower $\alpha$, the cylinder sheds vortices of counterclockwise sense only from its lower surface. Vortex shedding continues for higher spin rates and the flow becomes stable, yet again, for $\alpha\geqslant4.8$. This was confirmed by carrying out a linear stability analysis of the flow. A possible cause for this interesting behavior of flow stability was also proposed.

One of the issues that remains unresolved is the maximum lift that can be generated by a rotating cylinder placed in a uniform flow. Researchers in the past have reported varied results on the magnitude of lift that can be generated via the Magnus effect. Goldstein [3], based on intuitive arguments by Prandtl, suggests that the maximum value of the lift coefficient that can be generated by a spinning cylinder is $4\pi$ ($\sim$12.6). The measurement of lift on a rotating cylinder is quite difficult due to the limitations posed by the rotation of the cylinder. Tokumaru and Dimotakis [4] devised a method to estimate the mean lift acting on a rotating cylinder in uniform flow. It is based on an inviscid point-vortex model and the transverse velocity that is measured, experimentally, ahead of the cylinder. Their results for $\mathrm{Re}=3.8\times10^3$ show that Prandtl's limit on lift coefficient ($C_{L_{\max}}=4\pi$) can be exceeded. For example, for $\alpha=10$ and a cylinder with span to diameter ratio of 18.7, they report an estimated lift coefficient that is more than 20% larger than this limit. Further, the trend of results suggests that $C_L$ can made larger for higher rotation rates and by taking cylinders of larger aspect ratio. They have suggested that perhaps it is the unsteady effects that weaken Prandtl's hypothesis and that the three-dimensional/end effects are responsible for lowering the value of lift coefficient that could be achieved in a purely two-dimensional flow. However, Chew et al. [5] have reported that their two-dimensional computations are in agreement with Prandtl's postulate. They find that for $\mathrm{Re}=1000$, the estimated mean lift coefficient approaches asymptotic values with increase in $\alpha$. At $\alpha=6$ they predict a mean lift coefficient of 9.1. Glauert [6] proposed a solution for a cylinder spinning at high rotation rates where the separation is suppressed. The solution of the flow in the boundary layer is obtained in the form of a power series and an expression for the circulation on the cylinder is obtained. Glauert found that Prandtl's limit can be exceeded and that the circulation increases indefinitely with $\alpha$. The assumed model for the flow is valid only for those values of $\alpha$ when the flow separation is suppressed.

Most of the other investigations have been limited to $\alpha\leqslant3.25$. Chen et al. [7] computed flow for $\mathrm{Re}=200$ and $\alpha\leqslant3.25$. Their computation for $\alpha=3.25$ does show $C_L$ whose instantaneous value exceeds $4\pi$, marginally. However, they report results only for $t\leqslant24$. Computations by Badr et al. [8] for $\alpha=3$ and $\mathrm{Re}=1000$ are limited to $t\leqslant22$. At $t=22$ $C_L$ is 8.8, approximately, and the trend of their results suggest higher $C_L$ for larger times. The drag coefficient, $C_D$, reaches almost a steady-state value of 5.2. The mean values for $C_D$ and $C_L$ for the fully developed flow reported by Chew et al. [5], for $\alpha=3$, are 2.8 and 8.7, respectively. Recently, Chou [9] has also reported computational results for this flow problem. The time histories of $C_D$ and $C_L$ from his computations, for $\mathrm{Re}=1000$ and $\alpha=3$, match quite well with those from Badr et al. [8] for early times. However, for $t>5$, he reports much larger values of $C_L$ and smaller values of $C_D$. It is interesting to observe that the streamline patterns from all the three sets of computations are quite similar and are in good agreement with the flow visualization results. Yet, the discrepancy

Contributed by the Applied Mechanics Division of THE AMERICAN SOCIETY OF MECHANICAL ENGINEERS for publication in the ASME JOURNAL OF APPLIED MECHANICS. Manuscript received by the Applied Mechanics Division, December 18, 2002; final revision, April 21, 2003. Associate Editor: T. E. Tezduyar. Discussion on the paper should be addressed to the Editor, Prof. Robert M. McMeeking, Chair, Department of Mechanics and Environmental Engineering, University of California–Santa Barbara, Santa Barbara, CA 93106-5070, and will be accepted until four months after final publication in the paper itself in the ASME JOURNAL OF APPLIED MECHANICS.

in the time histories of the aerodynamic coefficients is quite large. Our results for $\alpha=5$ for various Re, reported in earlier articles Mittal [10,11] result in large values of $C_L$. Recently, Stansby and Rainey [12] have reported computational results for Re=200 and $0\leqslant\alpha\leqslant5$. They observe an unsteady flow for lower rotation rates. For high rotation rates a steady flow with very large $C_L$ is realized.

Results are presented for three-dimensional computations past a finite cylinder for various aspect ratios and with different end conditions. One of the objectives of the computations is to investigate the existence of three-dimensional instabilities in the flow for $\alpha=5$. We also wish to study the effect of end conditions. It has been observed in experiments that the use of end plates can lead to a substantial increase in lift generated by the cylinder. The present

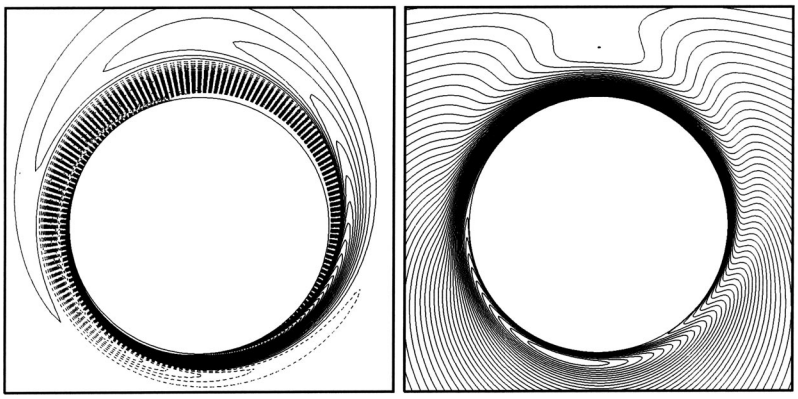

**Fig. 1 Re=200, $\alpha=5$ flow past a rotating cylinder: closeup view of the vorticity (left) and magnitude of velocity (right) for the fully developed two-dimensional flow. The freestream flow is from left to right and the cylinder is rotating in a counterclockwise sense. Solid lines denote positive while the broken lines show negative vorticity.**

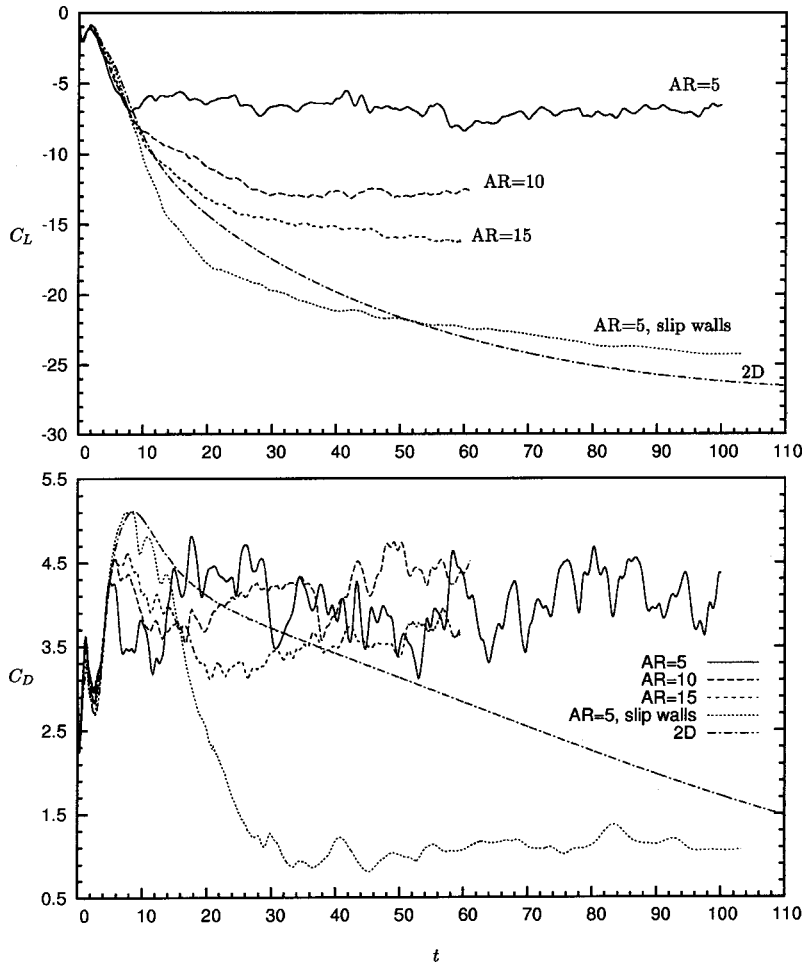


**Fig. 2 Re=200, $\alpha=5$ flow past a rotating cylinder: time histories of the lift and drag coefficients for two-dimensional and three-dimensional computations with cylinders of various aspect ratios (*AR*)**

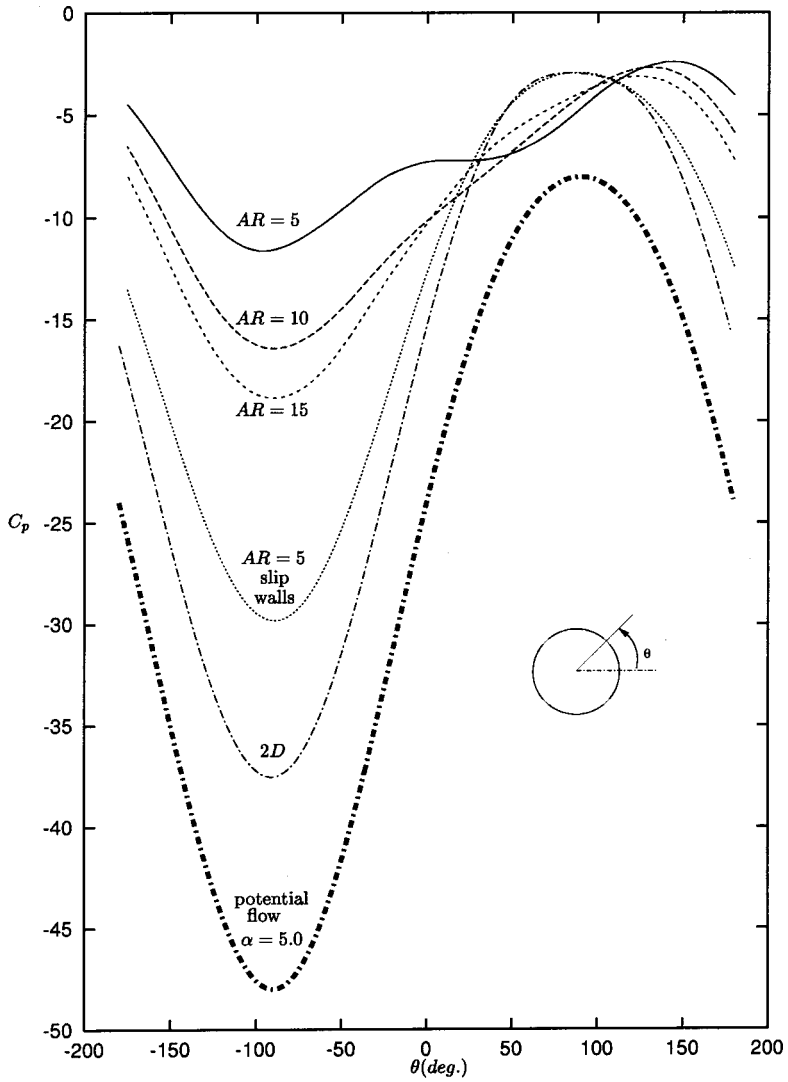


**Fig. 3 Re=200, $\alpha$=5 flow past a rotating cylinder for various aspect ratios: variation of the spanwise averaged pressure coefficient on the surface of cylinder**

computations show that flow for Re=200 and $\alpha=5$ is associated with centrifugal instabilities that exist along the span of the spinning cylinder. Further, in the presence of a "no-slip" side wall the flow near the wall separates leading to unsteadiness in the wake. As expected, the effect is more drastic for low aspect-ratio cylinders. It is the end wall and aspect-ratio effects that limit the lift generated via Magnus effect.

The outline of the rest of the article is as follows. We begin by reviewing the governing equations for incompressible fluid flow in Section 2. The problem setup is defined along with the boundary and initial conditions. The SUPG (streamline-upwind/Petrov-Galerkin) and PSPG (pressure-stabilizing/Petrov-Galerkin) stabilization technique, [13], is employed to stabilize our computations against spurious numerical oscillations and to enable us to use equal-order-interpolation velocity-pressure elements. Section 3 describes the finite element formulation incorporating these stabilizing terms. In Section 4 computational results for flows involving rotating cylinder are presented and discussed. In Section 5 a few concluding remarks are made.

## 2 The Governing Equations

Let $\Omega\subset\mathbb{R}^{n_{sd}}$ and $(0,T)$ be the spatial and temporal domains respectively, where $n_{sd}$ is the number of space dimensions, and let $\Gamma$ denote the boundary of $\Omega$. The spatial and temporal coordinates are denoted by $\mathbf{x}$ and $t$. The Navier-Stokes equations governing incompressible fluid flow are

$$\rho\left(\frac{\partial\mathbf{u}}{\partial t}+\mathbf{u}\cdot\nabla\mathbf{u}-\mathbf{f}\right)-\nabla\cdot\boldsymbol{\sigma}=0 \quad \text{on } \Omega \text{ for } (0,T), \tag{1}$$

$$\nabla\cdot\mathbf{u}=0 \quad \text{on } \Omega \text{ for } (0,T). \tag{2}$$

Here $\rho$, $\mathbf{u}$, $\mathbf{f}$, and $\boldsymbol{\sigma}$ are the density, velocity, body force, and the stress tensor, respectively. The stress tensor is written as the sum of its isotropic and deviatoric parts:

$$\boldsymbol{\sigma}=-p\mathbf{I}+\mathbf{T}, \quad \mathbf{T}=2\mu\boldsymbol{\varepsilon}(\mathbf{u}), \quad \boldsymbol{\varepsilon}(\mathbf{u})=\frac{1}{2}((\nabla\mathbf{u})+(\nabla\mathbf{u})^T), \tag{3}$$

where $p$ and $\mu$ are the pressure and coefficient of dynamic viscosity. Both the Dirichlet and Neumann-type boundary conditions are accounted for, represented as

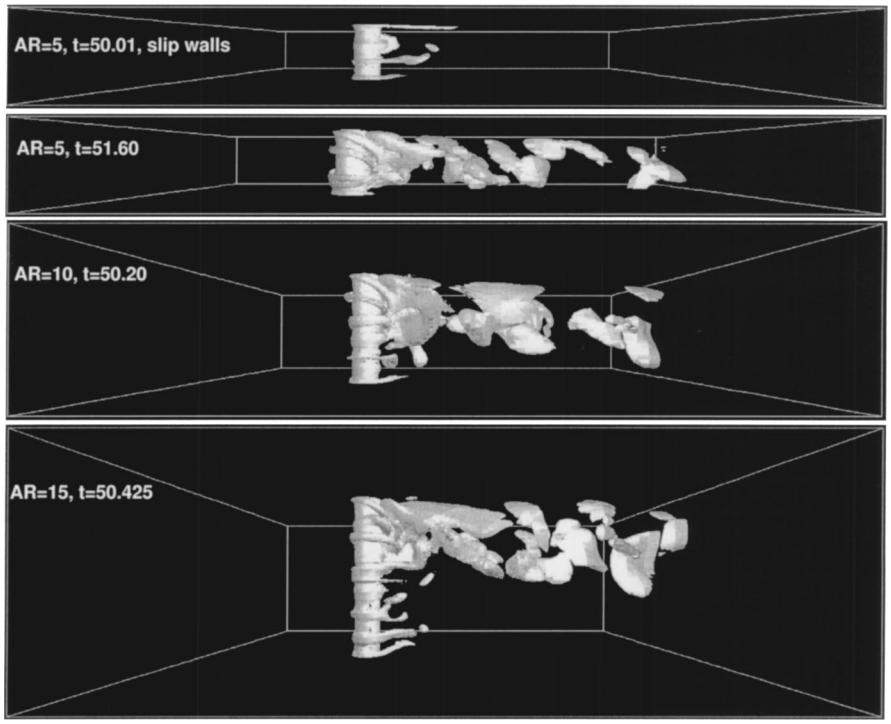


**Fig. 4 Re=200, $\alpha=5$ flow past a rotating cylinder: isosurfaces of the spanwise component of vorticity ($=0.4$) for various aspect ratios. The top frame corresponds to the simulation with slip walls as the end condition. For the other three frames, the upper wall is a no-slip wall.**

$$\mathbf{u}=\mathbf{g} \text{ on } \Gamma_g, \quad \mathbf{n}\cdot\boldsymbol{\sigma}=\mathbf{h} \text{ on } \Gamma_h, \tag{4}$$

where $\Gamma_g$ and $\Gamma_h$ are complementary subsets of the boundary $\Gamma$. The initial condition on the velocity is specified on $\Omega$:

$$\mathbf{u}(\mathbf{x},0)=\mathbf{u}_0 \quad \text{on } \Omega, \tag{5}$$

where $\mathbf{u}_0$ is divergence-free.

The force and moment coefficients are computed by carrying an integration, that involves the pressure and viscous stresses, around the circumference of the cylinder:

$$C_D=\frac{1}{\frac{1}{2}\rho U^2 2aL}\int_{\Gamma_{\text{cyl}}}(\boldsymbol{\sigma}\mathbf{n})\cdot\mathbf{n}_x d\Gamma, \tag{6}$$

$$C_L=\frac{1}{\frac{1}{2}\rho U^2 2aL}\int_{\Gamma_{\text{cyl}}}(\boldsymbol{\sigma}\mathbf{n})\cdot\mathbf{n}_y d\Gamma. \tag{7}$$

Here $\mathbf{n}_x$ and $\mathbf{n}_y$ are the Cartesian components of the unit vector $\mathbf{n}$ that is normal to the cylinder boundary $\Gamma_{\text{cyl}}$, $a$ is the radius of the cylinder, $L$ its spanwise length, $U$ the freestream speed, and $C_D$ and $C_L$ are the drag and lift coefficients, respectively.

The various parameters that influence this flow are Re, $\alpha$, $AR$ and end conditions. The Reynolds number is defined as $\text{Re}=2Ua/\nu$ where $a$ is the radius of cylinder, $U$ the freestream speed and $\nu$ is the coefficient of kinematic viscosity of the fluid. The rotation rate of the cylinder is nondimensionalized with respect to the freestream speed and is given as $\alpha=a\omega/U$ where $\omega$ is the angular velocity of the cylinder about its own axis. The aspect ratio, $AR$, of the cylinder is the ratio of its spanwise length and diameter. All the results presented in this article are with respect to the non dimensional time $\tau=Ut/a$, where $t$ is the actual time.

## 3 Finite Element Formulation

Consider a finite element discretization of $\Omega$ into subdomains $\Omega^e$, $e=1,2,\ldots,n_{\text{el}}$, where $n_{\text{el}}$ is the number of elements. Based on this discretization for velocity and pressure, we define the finite element trial function spaces $\mathcal{S}_{\mathbf{u}}^h$ and $\mathcal{S}_p^h$, and weighting function spaces $\mathcal{V}_{\mathbf{u}}^h$ and $\mathcal{V}_p^h$. These function spaces are selected, by taking the Dirichlet boundary conditions into account, as subsets of $[\mathbf{H}^{1h}(\Omega)]^{n_{sd}}$ and $\mathbf{H}^{1h}(\Omega)$, where $\mathbf{H}^{1h}(\Omega)$ is the finite-dimensional function space over $\Omega$. The stabilized finite element formulation of Eqs. (1)–(2) is written as follows: find $\mathbf{u}^h\in\mathcal{S}_{\mathbf{u}}^h$ and $p^h\in\mathcal{S}_p^h$ such that $\forall\mathbf{w}^h\in\mathcal{V}_{\mathbf{u}}^h$, $q^h\in\mathcal{V}_p^h$

$$\int_\Omega \mathbf{w}^h\cdot\rho\left(\frac{\partial\mathbf{u}^h}{\partial t}+\mathbf{u}^h\cdot\nabla\mathbf{u}^h-\mathbf{f}\right)d\Omega+\int_\Omega\boldsymbol{\varepsilon}(\mathbf{w}^h):\boldsymbol{\sigma}(p^h,\mathbf{u}^h)d\Omega$$
$$+\int_\Omega q^h\nabla\cdot\mathbf{u}^h d\Omega+\sum_{e=1}^{n_{\text{el}}}\int_{\Omega^e}\frac{1}{\rho}(\tau_{\text{SUPG}}\rho\mathbf{u}^h\cdot\nabla\mathbf{w}^h+\tau_{\text{PSPG}}\nabla q^h)\cdot$$

$$\left[\rho\left(\frac{\partial\mathbf{u}^h}{\partial t}+\mathbf{u}^h\cdot\nabla\mathbf{u}^h-\mathbf{f}\right)-\nabla\cdot\boldsymbol{\sigma}(p^h,\mathbf{u}^h)\right]d\Omega^e$$
$$+\sum_{e=1}^{n_{el}}\int_{\Omega^e}\tau_{\text{LSIC}}\nabla\cdot\mathbf{w}^h\rho\nabla\cdot\mathbf{u}^h d\Omega^e=\int_{\Gamma_h}\mathbf{w}^h\cdot\mathbf{h}^h d\Gamma. \tag{8}$$

The variational formulation given by Eq. (8), includes certain stabilization terms added to the basic Galerkin formulation to enhance its numerical stability. the first three terms and the right-hand side constitute the Galerkin formulation of the problem. De-

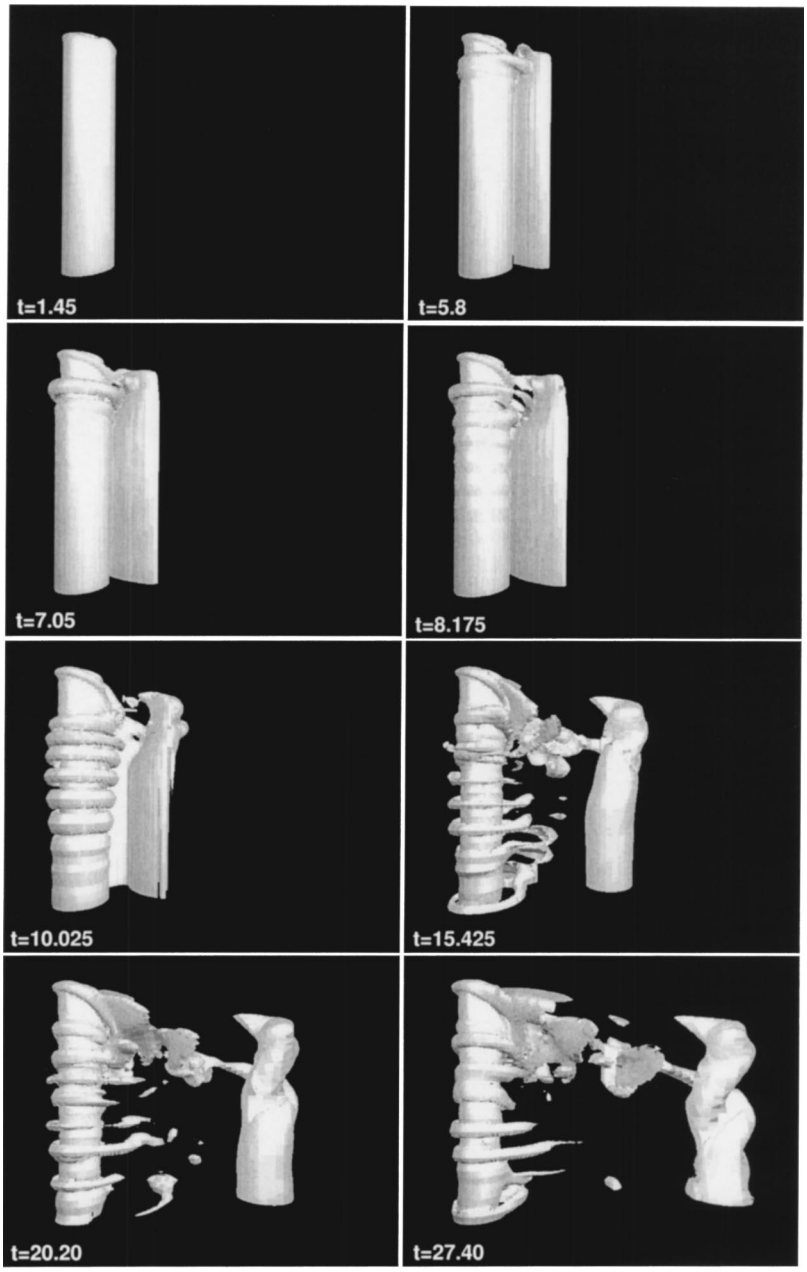


**Fig. 5 Re=200, $\alpha=5$, $AR=15$ flow past a rotating cylinder with a no-slip end wall: isosurfaces of the spanwise component of vorticity ($=0.4$) at various time instants following an impulsive start**

tails on the formulation can be found in references [13,14]. The stabilization terms involve the use of a characteristic ''element length.'' In the present computations this length is defined as the minimum edge length of an element, [13].

## 4 Results and Discussions

All the results in this article are for the Re=200 and $\alpha=5$ flow.

**4.1 Two-Dimensional Computations.** The cylinder resides in a rectangular domain and a flow velocity corresponding to the rotation rate, $\alpha$ is specified on the cylinder surface. The rotation is in the counterclockwise direction. A freestream value is assigned for the velocity at the upstream boundary while, at the downstream boundary, a Neumann-type boundary condition for the velocity is specified that corresponds to zero viscous stress vector. On the upper and lower boundaries, the component of velocity normal to and the component of stress vector along these boundaries is prescribed zero value. The initial condition for all the computations is an impulsive start, i.e., at $t=0$ the velocity is assigned value that corresponds to potential flow past a stationary cylinder. The outer boundaries are located at $100D$ from the center of the cylinder.

Figure 1 shows the fully developed solution obtained from the two-dimensional computations. Clockwise vorticity (negative) on the upper surface and counterclockwise vorticity (positive) on lower surface of the cylinder is generated. The high rotation rate of the cylinder causes this vorticity to move outward as tightly wound spirals. The stability of this flow has been ascertained via linear stability analysis, [2], and also by computing the flow for an eccentric cylinder [10]. Detailed results for $\alpha=5$ and other rotation rates have been presented in Mittal and Kumar [2].

**4.2 Three-Dimensional Computations.** Very large lift coefficients can be obtained for two-dimensional flows past a cylinder for high rotation rates. Tokumaru and Dimotakis [4] have reported a strong dependence of the lift coefficient on the aspect ratio of the cylinder (ratio of spanwise length to diameter) and its end conditions. To study the same, three-dimensional computations for flow past a rotating cylinder with an impulsive start are carried out for various end conditions and cylinder span-to-diameter ratio. Kalro and Tezduyar [15] used a very similar finite element formulation to study flow past a nonspinning cylinder.

In the three-dimensional simulations the cylinder extends along the entire span of the computational domain. One of the side boundaries, that intersects with the cylinder, is assumed to be a ''no-slip'' wall for the velocity while symmetry conditions are imposed on the other side wall. These boundary conditions simulate a rotating cylinder, without end plates, placed in a tunnel. Only one half of the tunnel is simulated. Mittal [16] investigated the flow past low aspect-ratio nonspinning cylinders in the presence of wall. The aspect ratios considered in the present work are 5, 10, and 15. A computation for $AR=5$ with ''slip'' side walls is also carried out to assess the effect of end conditions. The finite element mesh for the computation with $AR=15$ consists of 284,199 nodes and 270,000 hexahedral elements. At each time-step approximately 1.1 million nonlinear equations are solved iteratively. The time histories of the lift and drag coefficients for these simulations are shown in Fig. 2 along with the results from two-dimensional computations. It is observed that both the end conditions and the cylinder aspect ratio have a significant impact on the aerodynamic coefficients. Compared to the steady-state two-dimensional flow, the ''no-slip'' side wall results in lower lift and higher drag. The lift coefficient reduces with the decrease in aspect ratio of the cylinder. An increase in the aspect ratio of the cylinder reduces the effect of the ''no-slip'' wall. With the ''slip'' end conditions on the velocity on side walls, fairly high lift and low drag coefficients are obtained with a low aspect-ratio cylinder ($AR=5$). This study brings out the effect of end conditions in such flows. A similar observation was reported by Tokumaru and Dimotakis [4].

Shown in Fig. 3 are the spanwise averaged $C_p$ distributions for the various three-dimensional computations at approximately $t=50$. It is well known that for a stationary cylinder, the surface pressure distribution for the viscous and potential flows are qualitatively different. This is attributed to the flow separation in the case of a real fluid. However, for a rotating cylinder spinning at $\alpha=5$, it is interesting to observe that the pressure distributions for the two-dimensional and potential flows are very similar, qualitatively. As expected, compared to the two-dimensional flow, the three-dimensional effects tend to reduce the suction generated on the cylinder. Among all the cases, the $C_p$ variation for the $AR=5$ case with slip walls is the closest to that from the two-dimensional computations. The peak suction decreases as the $AR$ is reduced. It is also observed that the location of the peak value of $C_p$ moves towards the front of the cylinder as $AR$ is reduced and end effects become important.

Figure 4 shows the isosurfaces for the spanwise component of the vorticity for various cases at approximately $t=50$. In all the cases centrifugal instabilities, such as those observed in flows between two concentric rotating cylinders, exist along the span of the spinning cylinder. The spanwise wavelength of these centrifugal instabilities is, approximately, one cylinder diameter which is similar to that observed in Taylor instabilities. In addition, interaction of the rotating cylinder with the boundary layer on the ''no-slip'' side wall leads to flow separation. Both these effects contribute to a loss in lift and increase in drag. The effect of the side wall reduces as one moves away from it. For example, for $AR=15$, the flow on the lower half of the span appears quite similar to the $AR=5$ flow with slip walls. Therefore, for a cylinder with very large aspect ratio the aerodynamic coefficients may be quite close to those for the two-dimensional flows. However, the three-dimensional centrifugal instabilities would still be present and lead to loss of lift and increase in drag, compared to the two-dimensional flow.

Figure 5 shows the isosurfaces for spanwise vorticity at various time instants for $AR=15$. It is interesting to note that, as was the case with two-dimensional computations, only one spanwise vortex (the startup vortex) is shed for $\alpha=5$. The development of the centrifugal instabilities along the cylinder span can also be observed in the figure. Their initial development seems to be instigated by the end conditions. The shear generated by the boundary layer on the side wall is also responsible for the twisting of the startup vortex. The end effects can be eliminated/minimized by using end plates. Prandtl observed a value of $C_L \sim 3.2$ for a cylinder of $AR=4.7$ and at $\mathrm{Re}=5.2\times10^4$ (as reported by Tokumaru and Dimotakis [4] and Goldstein [3]). However, on using end plates of diameter 1.7 times the cylinder diameter, he observed that the value of the lift coefficient goes up to, approximately, 5.

Very high lift coefficients are observed for high rotation rates of the cylinder. The present results support the observation by Tokumaru and Dimotakis [4] that Prandtl's limit does not hold for large aspect-ratio cylinders. It certainly does not hold for the two-dimensional flows. The lift coefficient from the two-dimensional computations approach the values from the three-dimensional setup for large aspect-ratio cylinders.

## 5 Concluding Remarks

Three-dimensional flow past a cylinder, rotating in the counterclockwise sense, and placed in uniform stream ($\mathrm{Re}=200$) has been analyzed for a spin rate corresponding to $\alpha=5$. A stabilized finite element method is utilized to solve the incompressible Navier-Stokes equations in the primitive-variables formulation.

It is found that the aspect ratio of the cylinder (spanwise length/diameter) and its end conditions play an important role in determining the amount of lift generated by the rotating cylinder. While the two-dimensional flow for $\alpha=5$ is stable, the three-dimensional flow is associated with centrifugal instabilities. These instabilities are observed even for the case with ''slip walls'' and are quite similar to those observed in flow between rotating cylinders. The presence of a no-slip side wall (no end plates) results in flow separation. Both of these effects contribute to loss of lift and increased drag as compared to a purely two-dimensional flow. It is found that very large lift coefficients can be realized for large aspect-ratio cylinders via the Magnus effect and that Prandtl's limit does not hold.

## Acknowledgment

Partial support for this work has come from the Department of Science and Technology, India.

## References

[1] Prandtl, L., 1925, ''The Magnus Effect and Windpowered Ships,'' Naturwissenschaften, **13**, pp. 93–108.
[2] Mittal, S., and Kumar, B., 2003, ''Flow Past a Rotating Cylinder,'' J. Fluid Mech., **476**, pp. 303–334.
[3] Goldstein, S., 1938, *Modern Developments in Fluid Dynamics*, Clarendon Press, Oxford, UK.
[4] Tokumaru, P. T., and Dimotakis, P. E., 1993, ''The Lift of a Cylinder Executing Rotary Motions in a Uniform Flow,'' J. Fluid Mech., **255**, pp. 1–10.
[5] Chew, Y. T., Cheng, M., and Luo, S. C., 1995, ''A Numerical Study of Flow Past a Rotating Circular Using a Hybrid Vortex Scheme,'' J. Fluid Mech., **299**, pp. 35–71.
[6] Glauert, W. B., 1957, ''The Flow Past a Rapidly Rotating Circular Cylinder,'' Proc. R. Soc. London, Ser. A, **242**, pp. 108–115.
[7] Chen, Yen-Ming, Ou, Yuh-Roung, and Pearlstein, A. J., 1993, ''Development of the Wake Behind a Circular Cylinder Impulsively Started Into Rotary and Rectilinear Motion,'' J. Fluid Mech., **253**, pp. 449–484.
[8] Badr, H. M., Coutanceau, M., Dennis, S. C. R., and Menard, C., 1990, ''Unsteady Flow Past a Rotating Cylinder at Reynolds Numbers $10^3$ and $10^4$,'' J. Fluid Mech., **220**, pp. 459–484.
[9] Mo-Hong, Chou, 2000, ''Numerical Study of Vortex Shedding From a Rotating Cylinder Immersed in a Uniform Flow Field,'' Int. J. Numer. Methods Fluids, **32**, pp. 545–567.

[10] Mittal, S., 2001, ''Flow Past Rotating Cylinders: Effect of Eccentricity,'' ASME J. Appl. Mech., **68**, pp. 543–552.
[11] Mittal, S., 2001, ''Control of Flow Past Bluff Bodies Using Rotating Control Cylinders,'' J. Fluids Struct., **15(2)**, pp. 291–326.
[12] Stansby, P. K., and Rainey, R. C. T., 2001, ''A CFD Study of the Dynamic Response of a Rotating Cylinder in a Current,'' J. Fluids Struct., **15**, pp. 513–521.
[13] Tezduyar, T. E., Mittal, S., Ray, S. E., and Shih, R., 1992, ''Incompressible Flow Computations With Stabilized Bilinear and Linear Equal-Order-Interpolation Velocity-Pressure Elements,'' Comput. Methods Appl. Mech. Eng., **95**, pp. 221–242.
[14] Mittal, S., 2000, ''On the Performance of High Aspect-Ratio Elements for Incompressible Flows,'' Comput. Methods Appl. Mech. Eng., **188**, pp. 269–287.
[15] Kalro, V., and Tezduyar, T. E., 1997, ''Parallel 3D Computation of Unsteady Flows Around Circular Cylinders,'' Parallel Comput., **23**, pp. 1235–1248.
[16] Mittal, S., 2001, ''Computation of 3D Flows Past Circular Cylinders of Low Aspect Ratio,'' Phys. Fluids, **13**, pp. 177–191.

# Existence of Critical Wavelength for Gap Nucleation in Solidification on a Rigid Mold

**Faruk Yigit**
Department of Mechanical Engineering,
King Saud University,
P.O. Box 800,
Riyadh 11421, Saudi Arabia
e-mail: fyigit@ksu.edu.sa

*Previous theoretical models of pure metal solidification on a patterned mold surface neglected either the thermal capacitance of the solidifying shell material (which is equivalent to assume that thermal diffusivity is infinitely large) or interfacial coupling between the thermal and mechanical fields along the mold-shell interface. In the present work, however, we examine the combined effects of thermomechanical coupling at the mold-shell interface and non-negligible thermal capacitance (or finite thermal diffusivity) of the solidifying shell material during solidification of pure aluminum and iron shells on a rigid, perfectly conducting mold. It is assumed that the mold surface has a sinusoidal corrugation with a small aspect ratio, and the surface is perfectly wet by the molten metal which is initially at its melting temperature. The undulatory geometry of the mold surface lead to nonuniform heat extraction and hence initiated a nonuniform evolving distortion of the metal shell. This distortion produces a critical wavelength that corresponds to the situation where both the contact pressure and its time derivative simultaneously fall to zero. This critical mold surface wavelength serves as a cutoff between those wavelengths that lead to gap nucleation in the troughs and those that lead to gap nucleation in the crests. The conditions for gap nucleation in the mold surface troughs are examined since a corresponding increase in contact pressure at the crests signals the possibility of a growth instability in the metal shell at later stages in the process. Gap nucleation times, associated mean shell thicknesses, and critical wavelengths are calculated for pure aluminum and pure iron shells under identical process conditions. It is found that the iron shell nucleates gaps faster than an aluminum shell, with the associated critical wavelengths of iron being substantially larger than those for aluminum.*
[DOI: 10.1115/1.1641065]

## 1 Introduction

In the casting process, the mold surface topography has a great influence on cast surface quality, microstructure, and thickness uniformity, [1–3]. Therefore, considerable amount of effort has been directed towards the understanding of the effect of a patterned or ''textured'' mold surface on metallurgical structure of the cast product, where quality is either created or lost. Experimentalists have addressed the issue of shell thickness nonuniformity with a number process-related enhancements. One of the most common enhancements involves the application of a specific mold surface topography (see [4–12]). For example, periodic ''groove'' topographies that mimic the extended surface of a radiator, and hence allow for multidirectional heat flow at the mold-shell interface, have been routinely investigated with empirical methodologies. A qualitative observation made by most of these authors is that ingot contraction can be delayed due to the reduction in interfacial heat extraction. This leads to more uniform surface features, improved microstructural properties, and more uniform shell thickness. A similar observation can be made about the matte finish although the contact conditions differ due to wetting characteristics of the molten metal. Unfortunately, at present, there are no design criteria that might suggest how mold surface topographies can be ''tuned'' to a specific casting process and material.

Based upon existing experimental works on the mold surface topography effect on shell growth uniformity, Hector et al. [13] developed a model of pure metal solidification on a rigid, perfectly conducting mold with a sinusoidal surface of low aspect ratio. The total contact pressure along the mold-shell interface was calculated. Irregular distortion of the shell due to nonuniform heat extraction along mold-shell interface led to gap nucleation once the contact pressure dropped to zero. It was found that gaps always nucleate at the lowest points of the surface troughs, while the evolving distortion of the shell increased the contact pressure beyond the hydrostatic pressure at the highest points of the crests. They also found that gap nucleation time and the mean shell thickness were influenced by the topography wavelength such that gap nucleation was delayed or even prevented over the time frame of interest with increasing wavelength. Yigit and Hector [14,15] extended the theoretical model in [13] to include a deformable mold of finite thickness. The mold surfaces were again sinusoidal with low aspect ratios. The contact pressure at the lowest points of that surface of the mold in contact with the solidifying shell was calculated for systems where the mold and shell materials were combinations of pure aluminum, copper, iron, and lead. The theoretical results lead to the suggestion that for a given mold-shell material combination, a wavelength selection process occurs since a band of wavelengths for which the contact pressure always falls to zero at the lowest points of the troughs was identified. A band is delimited by two ''critical wavelengths'' which were defined as those wavelengths for which the interface pressure and its time derivative simultaneously fall to zero at positions of extreme surface curvature (i.e., the troughs). At the same time, the contact pressure increases at the surface crests. This signals the onset of a possible growth instability in which the initial shell nonuniformity becomes exaggerated to improve local heat transfer above the highest points on the mold surface. Wavelengths that lie outside of the band lead to gap nucleation at the highest points of the mold

Contributed by the Applied Mechanics Division of THE AMERICAN SOCIETY OF MECHANICAL ENGINEERS for publication in the ASME JOURNAL OF APPLIED MECHANICS. Manuscript received by the Applied Mechanics Division, January 3, 2003; final revision, July 16, 2003. Associate Editor: M.-J. Pindera. Discussion on the paper should be addressed to the Editor, Prof. Robert M. McMeeking, Journal of Applied Mechanics, Department of Mechanical and Environmental Engineering, University of California–Santa Barbara, Santa Barbara, CA 93106-5070, and will be accepted until four months after final publication in the paper itself in the ASME JOURNAL OF APPLIED MECHANICS.

  

surface, i.e., the crests, with a simultaneous increase in contact pressure in the troughs. The time to gap nucleation was largely dictated by the mold-shell material combination and its associated distortivity ratio which is indicative of the extent to which the materials deform at the interface, [16]. The bandwidth was largest for the iron-copper shell-mold combination. Much greater care would therefore have to be exercised in the selection of a mold wavelength. On the other hand, the bandwidths were smallest in those cases where a less distortive shell material (such as copper) solidified on a more distortive mold material (such as lead), or if the distortivity ratio of the two materials is near unity. The bandwidths predicted for solidification of a more distortive shell on a less distortive mold generally exceed those for a less distortive shell solidifying on a more distortive mold irrespective of the size of a selected process parameter. Yigit and Hector [17] recently reformulated the model presented in [13] to include the thermal diffusivity of the solidifying shell material. The thermal and mechanical fields were not fully coupled at the mold-shell interface since the thermal stress field is controlled by the temperature field but not vice versa. The mold was assumed to be a rigid, perfect conductor of heat, and the shell solidifies from the molten metal due to a prescribed constant heat flux at the mold-shell interface. Heat extraction through the mold-shell interface is mitigated by the sinusoidal geometry of the mold surface, and this leads to the evolution of a nonuniform stress field in the shell. The contact pressure profile at the shell/asperity interface, which is indicative of shell distortion due to the mold surface geometry, was obtained. The effects of the mold wavelength and shell thermal diffusivity on the contact pressure, temporal and spatial evolution of gap nucleation at the mold-shell interface, and mean shell thickness were examined in detail. It was subsequently concluded that (i) increasing the thermal capacitance (or decreasing the thermal diffusivity) of the shell leads to a decrease in the contact pressure perturbation due to nonuniform heat extraction at the sinusoidal mold surface. (ii) The diffusivity effect is negligible for small wavelengths. (iii) An increase in the mold surface wavelength increases the time to gap nucleation (or the time when the mold-shell contact pressure drops to zero) to form a separation. (iv) For a given mold wavelength and mean liquid pressure, an increase in the thermal capacitance of the shell leads to an increase in the time to gap nucleation. (v) For a given mold wavelength and mean liquid pressure, an increase in the thermal capacitance of the shell leads to a thicker shell at any time. As in [13], it was again found that gaps always nucleate at the lowest points of the surface troughs. Yigit and Hector [18] very recently reconsidered the problem developed in Yigit and Hector [14,15] removing the restriction that heat extraction through the mold-shell interface occurs across a pressure-dependent thermal contact resistance. The role of interfacial coupling between the thermal and mechanical fields along the mold-shell interface and the mechanical properties of the mold was examined via qualitative comparisons with the results presented in Yigit and Hector [14,15]. Perhaps the most significant feature of uncoupled physics was that the distortion of the mold material plays no role in the evolution of the contact pressure and the time and location of gap nucleation due to distortion of the shell material as it grows from the melt. However, when the thermal and mechanical problems are coupled through a pressure-dependent thermal contact resistance, and the mold is modeled as finite and deformable, the mold and shell interfacial distortions interact to produce two critical wavelengths as discussed earlier. Hence, it was concluded that in order to theoretically predict the critical wavelengths, it is necessary to model the mold as finite and deformable and to couple the thermal and mechanical problems at the mold-shell interface as in [14,15]. And yet, the critical wavelengths will not be predicted when a pure metal with infinitely large thermal diffusivity solidifying on a rigid, perfectly conducting mold with or without interfacial coupling as demonstrated by Hector et al. [13,19]. However, neither of these studies examined the combined effects of interfacial coupling between the thermal and mechanical fields along the mold-shell interface and finite thermal diffusivity of the solidifying shell material. Hence, the importance of the combined effects of thermomechanical coupling and nonzero (non-negligible) thermal capacitance of the shell material in solidification on a rigid mold has not been thoroughly delineated. For this reason, we extended the model presented in [17] to include coupling along the mold-shell interface through a pressure-dependent thermal contact resistance. This requires that the contact resistance be a functional of the contact pressure and hence can be smeared out along the mold-shell interface as a continuous function. This is a continuum representation of imperfect contact between the highest frequency components of the shell and mold surfaces due to microscopic gaps upon initial fluid wetting: It does not alter apparent wetting of the macroscale topography. Hence, the present model is a direct and logical continuation of the works by Hector et al. [13] and Yigit and Hector [17], in that we coupled the thermal and mechanical fields at the mold-shell interface and included the thermal diffusivity of the solidifying shell material.

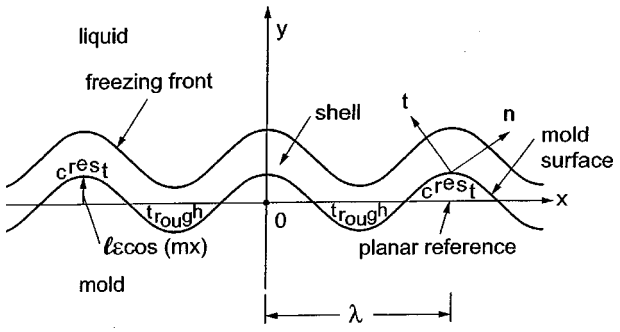


**Fig. 1 Pure metal shell solidifying on a sinusoidal mold surface**

The effects of the mold wavelength and shell thermal diffusivity on the contact pressure, temporal and spatial evolution of gap nucleation at the mold-shell interface, and mean shell thickness are examined for pure aluminum and iron shells. The impact of selected process parameters on the existence of the critical wavelength is explored through variation of the mean pressure of the molten metal, the pressure sensitivity of the thermal contact resistance, the amplitude of the mold surface, and the mean contact resistance. These results are qualitatively compared with comparable results presented in Yigit and Hector [15]. Finally, a discussion of the importance of surface wetting effects on the evolution of the shell thickness is presented.

## 2 Formulation of the Thermal Problem

A quiescent bath of molten liquid is assumed to perfectly wet the sinusoidal surface of a rigid mold at initial time as shown in Fig. 1. Molten material is initially at its melting temperature, $T_m$. The instantaneous location of the solidification front (relative to the mold surface) is given by $s(x,t)$. All material properties are assumed to be constant and independent of temperature. Relative to a planar reference, the mold surface is located at $y = a\cos(2\pi x/\lambda)$ where $a$ is the surface amplitude and $\lambda$ is the wavelength or center-to-center spacing between adjacent crests. The temperature field in the solidified shell, $T(x,y,t)$ is governed by the heat conduction equation

$$\nabla^2 T = \frac{1}{k}\frac{\partial T}{\partial t} \tag{1}$$

subject to the following boundary and initial conditions:

$$T(x,s,t) = T_m \tag{2}$$

$$K\frac{\partial T}{\partial y}(x,s,t)=L\rho\frac{\partial s}{\partial t}(x,t) \tag{3}$$

$$Q(x,t)=K\frac{\partial T}{\partial y}(x,y,t)=\frac{T(x,y,t)-T_{\text{mold}}}{R} \quad \text{at } y=l\epsilon\cos(mx) \tag{4}$$

$$s(x,0)=l\epsilon\cos(mx) \tag{5}$$

where $l=\lambda/2\pi=1/m$ and $\epsilon=a/l$ is the mold aspect ratio. The latter quantity is a convenient perturbation parameter since we assume $\epsilon\ll 1$. Justification of this assumption is discussed in Hector et al. [13]. Note that $k$, $K$, $L$, and $\rho$, are the thermal diffusivity, the thermal conductivity, the latent heat of fusion, and the density of the solidified shell, respectively. Equation (2) states that freezing front is isothermal at the melting temperature, while (3) defines the energy balance between heat conducted away from the moving interface into the shell and the latent heat released during solidification. Equation (5) implies that the thin shell is compliant to the sinusoidal mold surface at initial time. Heat extraction $Q(x,t)$ from the casting to the mold is opposed by a thermal contact resistance $R$, defined by Eq. (4). $T_{\text{mold}}$ is the temperature of the rigid mold, which can be taken to be zero without loss of generality.

Physical causes of the resistance $R$ include the presence of air gaps and inclusion materials of poor conductivity at the interface. Experimental and theoretical investigations of the conduction of heat between conducting solids show that contact resistance is very sensitive to the local contact pressure $P(x,t)$, probably because increased contact pressure increases the proportion of the interface over which the solids are in intimate contact. The resistance $R$ is therefore assumed to be a continuous and differentiable function of $P$, but no assumptions are made about the precise nature of this function.

Note that Eq. (4) is more appropriately written as

$$\mathbf{n}\cdot\nabla T=\frac{Q}{K} \tag{6}$$

where $\mathbf{n}$ is the unit normal vector to the mold surface at any point. However, the difference between Eqs. (4) and (6) can be shown to be $O(\epsilon^2)$ (this relies in part on the fact that the unperturbed solution is independent of $x$). A similar observation also applies to Eq. (3). The following perturbation analysis will only keep track of terms to $O(\epsilon)$, and hence we may retain Eq. (4) without loss of generality.

**2.1 Perturbation of the Thermal Problem.** When the moving solid-liquid interface is a plane $y=s_0(t)$, and temperatures and stresses depend only on $y$, $t$, the problem has a simple one-dimensional solution which is called the ''zeroth-order'' solution. However, if a very small spatial perturbation was introduced into the mold temperature or the thermal resistance $R$, the thermomechanical coupling associated with the boundary condition (4) might lead to unstable growth of an associated perturbation in temperature and stress fields. In particular, we assume the following forms for the temperature field, $T(x,y,t)$, the casting thickness, $s(x,t)$, the heat flux $Q(x,t)$ and thermal contact resistance $R$:

$$\begin{aligned} T(x,y,t)&=T_0(y,t)+T_1(y,t)\cos(mx)\\ s(x,t)&=s_0(t)+s_1(t)\cos(mx)\\ Q(x,t)&=Q_0(t)+Q_1(t)\cos(mx)\\ R(P(x,t))&=R_0+R_1(P(x,t))\cos(mx) \end{aligned} \tag{7}$$

where terms with suffix 1 are implicitly $O(\epsilon)$. We insert Eq. (7) into Eq. (1) and separate the zeroth-order and first-order governing thermal equations. We then expand Eqs. (2), (3), and (4) in a Taylor series about $y=s_0(t)$ and $y=0$ to $O(\epsilon)$, respectively. After grouping terms corresponding to the zeroth-order and first-order conditions, we separate expressions corresponding to the zeroth-order and first-order thermal problems, which are written as follows:

*The Zeroth-Order Problem.*

$$\frac{\partial^2 T_0}{\partial y^2}(y,t)=\frac{1}{k}\frac{\partial T_0}{\partial t}(y,t) \tag{8}$$

$$T_0(s_0,t)=T_m \tag{9}$$

$$L\rho\frac{ds_0(t)}{dt}=K\frac{\partial T_0}{\partial y}(s_0,t) \tag{10}$$

$$Q_0(t)=K\frac{\partial T_0}{\partial y}(0,t)=\frac{T_0(0,t)}{R_0} \tag{11}$$

*The First-Order Problem.*

$$\frac{\partial^2 T_1}{\partial y^2}(y,t)-m^2T_1(y,t)=\frac{1}{k}\frac{\partial T_1}{\partial t}(y,t) \tag{12}$$

$$s_1(t)\frac{\partial T_0}{\partial y}(s_0,t)+T_1(s_0,t)=0 \tag{13}$$

$$L\rho\frac{ds_1(t)}{dt}=K\left[\frac{\partial T_1(s_0,t)}{\partial y}+s_1(t)\frac{\partial^2 T_0(s_0,t)}{\partial y^2}\right] \tag{14}$$

$$Q_1(t)=K\frac{\partial T_1}{\partial y}(0,t)=\frac{1}{R_0}\left\{l\epsilon\frac{\partial T_0}{\partial y}(0,t)+T_1(0,t)-\frac{T_0(0,t)}{R_0}R'P_1(t)\right\} \tag{15}$$

where we have used the following equation for $R_1$:

$$R_1(P(x,t))=R'P_1(t) \tag{16}$$

which comes from the Taylor series expansion

$$R(P(x,t))=R(P_0(t)+P_1(t)\cos(mx)) \tag{17}$$

$$=R(P_0)+R'(P_0)P_1(t)\cos(mx) \tag{18}$$

and

$$R'=\frac{dR(P_0)}{dP}. \tag{19}$$

## 3 Determination of the Stress Field

To determine the stress field, we will follow the procedure outlined in [13], noting, however, that in his case the simplification $k\to\infty$ permitted the temperature field to be obtained in closed form, whereas in the present problem it is determined numerically and, therefore, is defined in discretized form. Since the analysis is closely related to that in [13], only the essential steps are presented in the following derivations, readers being referred to [13] for more details.

**3.1 The Zeroth-Order Solution.** Derivation of the zeroth-order solution is readily available in [20]. We therefore summarize only the final results:

$$\sigma_{xx_0}=-p+\frac{E\alpha}{1-\nu}[T_m-T_0(y,t)]; \quad \sigma_{yy_0}=-p; \quad \sigma_{xy_0}=0. \tag{20}$$

**3.2 The First-Order Solution.** We next consider the thermoelastic problem corresponding to the first order temperature field $T_1(y,t)\cos(mx)$. A suitable particular solution for the stress field can be defined in terms of a thermoelastic displacement potential $\phi$ (see [21]), where

$$\phi=\left[f(y,t)-\frac{\epsilon\alpha(1+\nu)}{m^2(1-\nu)}T_0(0,t)\sinh(my)\right]\cos(mx). \quad (21)$$

Equation (51) of [13] then requires that $f(y,t)$ satisfies the equation

$$\frac{\partial^2 f(y,t)}{\partial y^2}-m^2 f(y,t)=\frac{E\alpha}{(1-\nu)}T_1(y,t). \quad (22)$$

Note that this equation must be satisfied for all $t$, and hence it is essentially an ordinary differential equation for the function $f(y,t)$ in which $t$ appears only as a parameter. The first-order stress components corresponding to this potential are then obtained by substituting into Eqs. (52) of [13] in the form

$$\sigma^p_{xx_1}=-\left[f''(y,t)-\frac{E\alpha\epsilon}{(1-\nu)}T_0(0,t)\sinh(my)\right]\cos(mx) \quad (23)$$

$$\sigma^p_{xy_1}=-\left[mf'(y,t)+\frac{E\alpha\epsilon}{(1-\nu)}T_0(0,t)\cosh(my)\right]\sin(mx) \quad (24)$$

$$\sigma^p_{yy_1}=\left[m^2 f(y,t)-\frac{E\alpha\epsilon}{(1-\nu)}T_0(0,t)\sinh(my)\right]\cos(mx) \quad (25)$$

where $(')$ denotes differentiation with respect to $y$. To satisfy the boundary conditions of the problem, the particular solution must be supplemented by a homogeneous solution which we present in terms of the Airy stress function $\Phi$. Since the strain rates, but not strain, are required to be compatible (see [22]), it follows that the time derivative of $\Phi$ must be biharmonic and hence that the most general function of the appropriate sinusoidal form in $x$ is

$$\Phi=\{[a_1(t)+a_2(t)y]\cosh(my)+[a_3(t)+a_4(t)y]\sinh(my)+g(y)\}\cos(mx) \quad (26)$$

where the arbitrary time-dependent coefficients $a_1(t)-a_4(t)$ and the arbitrary time-independent function $g(y)$ are to be determined from the mechanical boundary conditions corresponding to the first-order problem.

Using Eqs. (23)–(26), and (69) of [13], we can construct the complete solution of the first-order problem in the form

$$\sigma_{xx_1}(x,y,t)=\left\{\left[a_1(t)+a_2(t)y+\frac{2a_4(t)}{m}\right]\cosh(my)+\left[a_3(t)+a_4(t)y+\frac{2a_2(t)}{m}\right]\sinh(my)+\frac{1}{m^2}[g''(y)-f''(y,t)]+\frac{E\alpha\epsilon}{m^2(1-\nu)}T_0(0,t)\sinh(my)\right\}m^2\cos(mx) \quad (27)$$

$$\sigma_{xy_1}(x,y,t)=\left\{\left[a_1(t)+a_2(t)y+\frac{a_4(t)}{m}\right]\sinh(my)+\left[a_3(t)+a_4(t)y+\frac{a_2(t)}{m}\right]\cosh(my)+\frac{1}{m}[g'(y)-f'(y,t)]+\frac{E\alpha\epsilon}{m^2(1-\nu)}T_0(0,t)\cosh(my)\right\}m^2\sin(mx) \quad (28)$$

$$\sigma_{yy_1}(x,y,t)=\left\{[a_1(t)+a_2(t)y]\cosh(my)-[a_3(t)+a_4(t)y]\sinh(my)-g(y)+f(y,t)-\frac{E\alpha\epsilon}{m^2(1-\nu)}T_0(0,t)\sinh(my)\right\}m^2\cos(mx). \quad (29)$$

Also, using the elastic constitutive relations for plane strain condition to determine the strain components and hence solve for the displacements, we obtain

$$\dot{u}_{y1}(x,y,t)=-\frac{1+\nu}{E}\left\{-\frac{1}{m}\dot{f}'(y,t)+\left[\dot{a}_1(t)+\dot{a}_2(t)y-\frac{1-\nu}{m}\dot{a}_4(t)\right]\sinh(my)+\left[\dot{a}_3(t)+\dot{a}_4(t)y-\frac{1-\nu}{m}\dot{a}_2(t)\right]\cosh(my)\right\}m\cos(mx) \quad (30)$$

where $(\dot{\cdot})$ denotes differentiation with respect to $t$.

We now consider the boundary conditions corresponding to the first order problem. Since the perturbation on the stress field is small, we can expand the stress field in the vicinity of the mean solid/melt interface position, $y=s_0(t)$ in a Taylor series. Then the first boundary condition in Eq. (49) of [13] can be written, dropping the higher order terms in small quantities, $\sigma_1$, $s_1$, as follows:

$$\sigma_{xx_0}(s_0,t)+\frac{\partial\sigma_{xx_0}(s_0,t)}{\partial y}s_1(t)\cos(mx)+\sigma_{xx_1}(s_0,t)=-p. \quad (31)$$

Separating periodic and uniform terms and using Eq. (20), we obtain the boundary condition for $\sigma_{xx_1}$ at $y=s_0(t)$, i.e.,

$$\sigma_{xx_1}(x,s_0(t),t)=\frac{E\alpha}{1-\nu}T_0'(s_0,t)s_1(t)\cos(mx). \quad (32)$$

The remaining boundary conditions in Eq. (49) of [13] can be obtained by applying the same procedure as follows:

$$\sigma_{xy_1}(x,s_0,t)=0; \quad \sigma_{yy_1}(x,s_0,t)=0. \quad (33)$$

The total shear stress on the mold surface given by Eq. (47) of [13] may be written in terms of the planar reference via

$$\sigma_{nt}(x,y,t)=\sigma_{xy}(\cos^2(\phi)-\sin^2(\phi))+(\sigma_{yy}-\sigma_{xx})\sin(\phi)\cos(\phi) \quad (34)$$

which, using Eq. (55) of [13], may be written as

$$\sigma_{nt}(x,y,t)=\sigma_{xy}-(\sigma_{yy}-\sigma_{xx})\epsilon\sin(mx) \quad (35)$$

and we obtain

$$\sigma_{xy_1}(0,t)=-\frac{E\epsilon\alpha}{1-\nu}[T_m-T_0(0,t)]\sin(mx) \quad (36)$$

where we have retained terms to $O(\epsilon)$. Also from Eq. (48) of [13], we have

$$\dot{u}^h_{y_1}(0,t)=0. \quad (37)$$

Applying boundary condition (36), using (28), we can obtain

$$a_3(t)=-\frac{a_2(t)}{m}+\frac{1}{m}[f'(0,t)-g'(0)]-\frac{E\alpha\epsilon}{m^2(1-\nu)}T_m. \quad (38)$$

Application of Eq. (37) gives

$$a_3(t)=\frac{1-2\nu}{m}a_2(t). \tag{39}$$

Solving the last two equations together, we get

$$a_2(t)=\frac{f'(0,t)}{2(1-\nu)}-\frac{E\alpha\epsilon T_m}{2m(1-\nu)^2} \tag{40}$$

$$a_3(t)=\frac{(1-2\nu)f'(0,t)}{2m(1-\nu)}-\frac{(1-2\nu)E\alpha\epsilon T_m}{2m^2(1-\nu)^2} \tag{41}$$

where we have imposed arbitrary condition $g'(0)=0$. Substituting for the stress components from Eqs. (27)–(29) into the remaining boundary conditions (32), (33), we obtain the equations

$$\begin{aligned}\cosh(ms_0)a_1(t)+\left[\frac{2}{m}\cosh(ms_0)+s_0\sinh(ms_0)\right]a_4(t)&\\ +\frac{1}{m^2}g''(s_0)&\\ =\frac{1}{m^2}f''(s_0,t)-\frac{E\alpha\epsilon T_0(0,t)}{m^2(1-\nu)}\sinh(ms_0)&\\ +\frac{E\alpha}{m^2(1-\nu)}T_0'(s_0,t)s_1(t)+\frac{E\alpha\epsilon T_m-m(1-\nu)f'(0,t)}{2m^2(1-\nu)^2}&\\ \times[ms_0\cosh(ms_0)+(3-2\nu)\sinh(ms_0)]&\end{aligned} \tag{42}$$

$$\begin{aligned}\sinh(ms_0)a_1(t)+\left[\frac{1}{m}\sinh(ms_0)+s_0\cosh(ms_0)\right]a_4(t)+\frac{1}{m}g'(s_0)&\\ =\frac{1}{m}f'(s_0,t)-\frac{E\alpha\epsilon T_0(0,t)}{m^2(1-\nu)}\cosh(ms_0)&\\ +\frac{E\alpha\epsilon T_m-m(1-\nu)f'(0,t)}{2m^2(1-\nu)^2}[ms_0\sinh(ms_0)&\\ +2(1-\nu)\cosh(ms_0)]&\end{aligned} \tag{43}$$

$$\begin{aligned}\cosh(ms_0)a_1(t)+s_0\sinh(ms_0)a_4(t)+g(s_0)&\\ =f(s_0,t)-\frac{E\alpha\epsilon T_0(0,t)}{m^2(1-\nu)}\sinh(ms_0)&\\ +\frac{E\alpha\epsilon T_m-m(1-\nu)f'(0,t)}{2m^2(1-\nu)^2}[ms_0\cosh(ms_0)&\\ +(1-2\nu)\sinh(ms_0)]&\end{aligned} \tag{44}$$

where we have used Eqs. (40), (41) to eliminate $a_2(t)$ and $a_3(t)$. These three equations must be satisfied for all values of $t$, and hence we can use them to eliminate $a_1(t)$ and $a_4(t)$. Let us define $\omega=\tanh(ms_0(t))$; therefore, we obtain

$$\begin{aligned}(\omega-ms_0\omega^2+ms_0)(g''(s_0)-f''(s_0,t))-2m(g'(s_0)-f'(s_0,t))&\\ +m^2(\omega+ms_0\omega^2-ms_0)(g(s_0)-f(s_0,t))&\\ =\frac{E\alpha}{(1-\nu)}(\omega-ms_0\omega^2+ms_0)s_1(t)T_0'(s_0,t)&\\ +\frac{2E\alpha\epsilon T_0(0,t)}{(1-\nu)\cosh(ms_0)}+\frac{ms_0\omega-2(1-\nu)}{(1-\nu)\cosh(ms_0)}&\\ \times\left[\frac{E\alpha\epsilon T_m}{(1-\nu)}-mf'(0,t)\right]&\end{aligned} \tag{45}$$

which serves to determine the unknown residual stress function $g(y)$. Once $g(y)$ is known, we can recover $a_1(t)$ and $a_4(t)$ by solving Eqs. (43), (44), with the result

$$\begin{aligned}a_1(t)=\frac{1}{\cosh(ms_0)}\Bigg\{\left[1+\frac{ms_0\omega}{2}\right]f(s_0,t)-\left[1+\frac{ms_0\omega}{2}\right]g(s_0)&\\ -\frac{E\alpha\epsilon T_0(0,t)}{m^2(1-\nu)}\sinh(ms_0)&\\ -\frac{ms_0\omega}{2}\left[\frac{E\alpha}{m^2(1-\nu)}s_1(t)T_0'(s_0,t)+\frac{1}{m^2}(f''(s_0,t)\right.&\\ \left.-g''(s_0))\right]+\frac{E\alpha\epsilon T_m-m(1-\nu)f'(0,t)}{2m^2(1-\nu)^2}\left[\frac{ms_0}{\cosh(ms_0)}\right.&\\ \left.+(1-2\nu)\sinh(ms_0)\right]\Bigg\}&\end{aligned} \tag{46}$$

$$\begin{aligned}a_4(t)=\frac{1}{2\cosh(ms_0)}\Bigg\{\frac{1}{m}\left[f''(s_0,t)-g''(s_0)\right]&\\ +m[g(s_0)-f(s_0,t)]+\frac{E\alpha}{m(1-\nu)}s_1(t)T_0'(s_0,t)&\\ -\frac{f'(0,t)}{(1-\nu)}\sinh(ms_0)+\frac{E\alpha\epsilon T_m}{m(1-\nu)^2}\sinh(ms_0)\Bigg\}.&\end{aligned} \tag{47}$$

Finally, we determine the perturbation in contact pressure $P_1(t)\cos(mx)$ at the casting-mold interface, from Eqs. (46) of [13] and (29) as

$$P_1(t)=m^2[a_1(t)-f(0,t)] \tag{48}$$

where we have imposed the arbitrary condition $g(0)=g'(0)=0$, since the free constants in the solution of Eq. (45) can be assigned to satisfy this condition.

## 4 Dimensionless Formulation

Before proceeding to the solution of the problem, it is convenient to define the following dimensionless parameters:

$$\begin{aligned}&Y=my;\quad S_0(\beta)=ms_0(t);\quad S_1(\beta)=\frac{m}{\epsilon}s_1(t);\quad \beta=\frac{m^2KT_m}{\rho L}t\\ &\overline{T}_0(Y,\beta)=\frac{T_0(y,t)}{T_m};\quad \overline{T}_1(Y,\beta)=\frac{T_1(y,t)}{\epsilon T_m};\quad \zeta=\frac{KT_m}{mk\rho L}\\ &\overline{Q}_0(\beta)=\frac{Q_0(t)}{mKT_m};\quad \overline{Q}_1(\beta)=\frac{Q_1(t)}{\epsilon mKT_m};\quad \overline{\omega}=\tanh(S_0)\\ &\overline{R}_0=mKR_0;\quad \overline{R}'=\frac{E\alpha T_m}{(1-\nu)R_0}R';\quad \overline{P}_1(\beta)=\frac{(1-\nu)K}{E\alpha\epsilon T_m}P_1(t)\\ &\overline{a}_1(\beta)=\frac{m^2(1-\nu)K}{E\alpha\epsilon T_m}a_1(t);\quad \overline{F}(Y,\beta)=\frac{m^2(1-\nu)K}{E\alpha\epsilon T_m}f(y,t)\\ &\overline{G}(Y)=\frac{m^2(1-\nu)K}{E\alpha\epsilon T_m}g(y).\end{aligned} \tag{49}$$

Hence, the governing Eqs. (8) and (12) for $\overline{T}_0(Y,\beta)$ and $\overline{T}_1(Y,\beta)$, then become

$$\frac{\partial^2\overline{T}_0(Y,\beta)}{\partial Y^2}=\zeta\frac{\partial\overline{T}_0(Y,\beta)}{\partial\beta} \tag{50}$$

$$\frac{\partial^2\overline{T}_1(Y,\beta)}{\partial Y^2}-\overline{T}_1(Y,\beta)=\zeta\frac{\partial\overline{T}_1(Y,\beta)}{\partial\beta}. \tag{51}$$

The boundary conditions (9)–(11), corresponding to the zeroth order temperature field $\bar{T}_0(Y,\beta)$ become

$$\bar{T}_0(S_0,\beta)=1 \tag{52}$$

$$\frac{dS_0(\beta)}{d\beta}=\frac{\partial \bar{T}_0(S_0,\beta)}{\partial Y} \tag{53}$$

$$\frac{\partial \bar{T}_0(0,\beta)}{\partial Y}=\frac{\bar{T}_0(0,\beta)}{R_0} \tag{54}$$

and the boundary conditions (13)–(15), corresponding to the first order temperature field $\bar{T}_1(Y,\beta)$, can be written as

$$S_1(\beta)\frac{\partial \bar{T}_0(S_0,\beta)}{\partial Y}+\bar{T}_1(S_0,\beta)=0 \tag{55}$$

$$\frac{dS_1(\beta)}{d\beta}=\frac{\partial \bar{T}_1(S_0,\beta)}{\partial Y}+S_1(\beta)\frac{\partial^2 \bar{T}_0(S_0,\beta)}{\partial Y^2} \tag{56}$$

$$\bar{Q}_1(\beta)=\frac{\partial \bar{T}_1(0,\beta)}{\partial Y}=\frac{1}{R_0}\left\{\frac{\partial \bar{T}_0(0,\beta)}{\partial Y}+\bar{T}_1(0,\beta)-\bar{T}_0(0,\beta)\bar{R}'\bar{P}_1(\beta)\right\}. \tag{57}$$

Thus, the heat conduction problem is reduced to the determination of two pairs of functions $\bar{T}_0(Y,\beta)$, $S_0(\beta)$ and $\bar{T}_1(Y,\beta)$, $S_1(\beta)$ in Eqs. (50) and (51), which satisfy the boundary conditions (52)–(54) and (55)–(57), respectively. These equations would completely define the temperature field if the heat flux $Q(x,t)$ of Eq. (7) were prescribed, as in [17], but, in the present problem, the heat flux is related to the temperature and the contact pressure through Eq. (57). The procedure here is to solve Eq. (22) for $f(y,t)$ and Eq. (45) for $g(y)$, after which we can find $a_1(t)$ from Eq. (46) and hence $P_1(t)$ from Eq. (48). The dimensionless form of these equations is

$$\frac{\partial^2 F(Y,\beta)}{\partial Y^2}-F(Y,\beta)=\bar{T}_1(Y,\beta) \tag{58}$$

$$\begin{aligned}(S_0\bar{\omega}^2-S_0-\bar{\omega})G''(S_0)+2G'(S_0)-(S_0\bar{\omega}^2+\bar{\omega}-S_0)G(S_0)\\ =(S_0\bar{\omega}^2-S_0-\bar{\omega})F''(S_0,\beta)+2F'(S_0,\beta)-(S_0\bar{\omega}^2+\bar{\omega}\\ -S_0)F(S_0,\beta)+(S_0\bar{\omega}^2-S_0-\bar{\omega})S_1(\beta)\bar{T}_0'(S_0,\beta)\\ -\frac{2T_0(0,\beta)}{\cosh(ms_0)}+\frac{S_0\bar{\omega}-2(1-\nu)}{(1-\nu)\cosh(S_0)}(F'(0,\beta)-\bar{T}_m)\end{aligned} \tag{59}$$

$$\begin{aligned}\bar{a}_1(\beta)=\frac{1}{\cosh(S_0)}\left\{\left[1+\frac{S_0\bar{\omega}}{2}\right]F(S_0,\beta)-\left[1+\frac{S_0\bar{\omega}}{2}\right]G(S_0)\right.\\ -T_0(0,\beta)\sinh(S_0)-\frac{S_0\bar{\omega}}{2}[S_1(\beta)T_0'(S_0,\beta)+(F''(S_0,\beta)\\ -G''(S_0))]+\frac{\bar{T}_m-F'(0,\beta)}{2(1-\nu)}\left[\frac{S_0}{\cosh(S_0)}+(1\right.\\ \left.\left.-2\nu)\sinh(S_0)\right]\right\}\end{aligned} \tag{60}$$

$$\bar{P}_1(\beta)=\bar{a}_1(\beta)-F(0,\beta). \tag{61}$$

## 5 Numerical Algorithm

Both zeroth-order and first-order problems require numerical solution, for which we use the algorithm developed in [17]. The zeroth-order solid phase $0<Y<S_0(t)$, is divided into a fixed number of elements $N$, so the space step size, $\delta=S_0/N$, increases with time due to the growth in $S_0(t)$. This permits the last node to be identified with the zeroth-order solid-liquid moving front at all times, but implies that the node locations move in time, necessitating the inclusion of convective terms in the updating algorithm for temperature. Thus, for example, the instantaneous zeroth-order temperature field is represented by the temperatures at the $N+1$ points $Y=(i-1)\delta$, $i=1,2,\ldots,N+1$. The increase of the shell thickness $S_0$ during the next time increment $\tau$ is determined from the finite difference form of Eq. (53)

$$S_0^{j+1}=S_0^j+\frac{\tau}{2\delta}(3T^j_{0_{N+1}}-4T^j_{0_N}+T^j_{0_{N-1}}), \tag{62}$$

after which the temperatures at the interior nodes $i=2,3,\ldots,N$ are updated using the finite difference form of the heat conduction Eq. (50)

$$\bar{T}^{j+1}_{0_i}=\bar{T}^j_{0_i}+\frac{\tau}{\zeta\delta^2}(\bar{T}^j_{0_{i+1}}-2\bar{T}^j_{0_i}+\bar{T}^j_{0_{i-1}});\quad i=2,3,\ldots,N \tag{63}$$

which can be corrected using convective terms through

$$\bar{T}^{j+1}_{0_i}=\bar{T}^{j+1}_{0_i}+(i-1)\frac{\delta^{j+1}-\delta^j}{\delta^j}(\bar{T}^{j+1}_{0_{i+1}}-\bar{T}^{j+1}_{0_i});\quad i=2,3,\ldots,N. \tag{64}$$

The temperatures at node $N+1$ remain at 1 for all times in view of Eq. (52) and that at node 1 is updated through Eq. (54), which determines the first difference in the first element.

Essentially, the same procedure is used to determine the evolution of the first-order temperature field, using Eqs. (51) and (55)–(57), except that $\bar{Q}_1(\beta)$ must be determined from Eq. (57) which necessitates the solution of the thermoelastic problem for $\bar{P}_1(\beta)$, using Eqs. (58)–(61). If the time increment $\tau$ is sufficiently small, the thermal and thermoelastic updating algorithms can be performed sequentially and hence explicitly.

The choice of an appropriate value for $\tau$ is motivated by the desire for computational efficiency, while retaining acceptable numerical convergence and stability. Extensive investigations were made into the effect of both space and time discretization to ensure that the final results are reliable. With the explicit scheme used here, the maximum time step for stability is proportional to $\zeta\delta^2$ and hence the stability requirement generally places the most severe restrictions on $\tau$ when good spatial accuracy is desired, necessitating small values of $\delta$. However, $S_0$ and hence $\delta$ increase during the process, permitting the time step to be increased as the system evolves, without loss of stability.

**5.1 Initial Conditions.** With the algorithm described above, it is clearly not possible to start at the instant of first solidification, since at $S_0=0$, all the nodes would coincide. Instead, we need to use an asymptotic solution of the problem at small times to provide a suitable initial condition for the numerical algorithm at finite time. Fortunately, the limiting solution (given in the appendix to verify that the present more general solution reduces to the result previously obtained in case of zero thermal capacity) due to Hector et al. [13], which assumes that diffusivity of the solidified shell material is infinitely large, becomes progressively more accurate at small times, since the temperature drop across the solidified layer is small at the very beginning of the process. We can therefore start the process with a small but finite thickness, using the limiting solution given in [13] to define the initial values for the temperature field in the solid layer.

## 6 Gap Nucleation Criterion

Determination of the conditions for gap nucleation can be achieved through examination of $P^{tr}$, which is the ratio of the

**Table 1 Material properties for pure aluminum and iron at the melting temperature**

| | MATERIAL | | |
|---|---|---|---|
| | Al | Fe | |
| PROPERTY | Value | Value | Fe Reference |
| $T_f$ (°C) | 660 | 1536 | [25] |
| $K\left(\frac{\mathrm{W}}{\mathrm{m}\cdot°\mathrm{C}}\right)$ | 229.4 | 36.2 | [26] |
| $\rho\left(\frac{\mathrm{kg}}{\mathrm{m}^3}\right)$ | 2650 | 7265 | [27] |
| $L\left(10^5\frac{\mathrm{J}}{\mathrm{kg}}\right)$ | 3.9 | 2.7 | [28] |
| $E(10^{10}\,\mathrm{Pa})$ | 6.0 | 14.4 | [29] |
| $\alpha(10^{-6}\,°\mathrm{C}^{-1})$ | 37.8 | 23.4 | [30] |
| $\nu$ | 0.33 | 0.33 | [29] |
| $k\left(10^{-5}\frac{\mathrm{m}^2}{\mathrm{s}}\right)$ | 8.2 | 16.1 | [31] |

total (dimensional) contact pressure at the lowest points of the troughs, $P$, to the mean pressure, $P_0$, at the mold surface troughs. Hence

$$P^{tr}=\frac{P}{P_0}=1-\frac{P_1}{P_0}. \tag{65}$$

Note that for $P_1/P_0\rightarrow 1$, the following condition, which is derived in [13] must be met:

$$-\frac{R'P_0}{R_0}\ll 1. \tag{66}$$

This limits the proposed gap nucleation analysis to weakly coupled systems. All other perturbation quantities are required to be much less than one.

Gap nucleation occurs when

$$P^{tr}=0. \tag{67}$$

If $P^{tr}>0$ during the time frame of interest, then gaps will not nucleate in the troughs. Gap nucleation at the troughs will indicate the possibility of irregular growth of the shell since contact will simultaneously increase at the crests. Beyond gap nucleation time, the present model is no longer valid since it cannot account for continued growth of the gaps and the shell.

As defined by Yigit and Hector [15], a wavelength is critical if it corresponds to

$$P^{tr}=\frac{dP^{tr}}{dt}=0. \tag{68}$$

Note that Yigit and Hector [15] found that wavelengths bands were delimited by upper and lower critical wavelengths. Wavelengths that fell between the two critical wavelengths led to the condition given by Eq. (68). Wavelengths that were either smaller than the lower critical wavelength, or larger than the upper critical wavelength led to gap nucleation at the highest points of the crests, instead of the lowest points in the troughs.

## 7 Results and Discussion

The material properties used in the calculations are listed in Table 1 along with pertinent references to those properties. Note that the properties for pure aluminum are taken from Richmond et al. [23]. The symbols $E$, $\alpha$, and $\nu$ denote Young's modulus, thermal expansion coefficient, and Poisson's ratio, respectively. Although it is assumed that each property is a temperature-independent constant, most of the reported values were measured close to the melting temperature of each material. For more information on the temperature-dependence of these materials, the reader is referred to Heinlein et al. [24]. The process parameters are chosen to be $R_0=10^{-5}\,\mathrm{m^2\,sec\,°C/J}$, $R'=0\,\mathrm{m^2\,sec\,°C/J\cdot Pa}$, $P_0=10{,}000\,\mathrm{Pa}$, and $a=1.0\,\mu\mathrm{m}$ (unless otherwise specified).

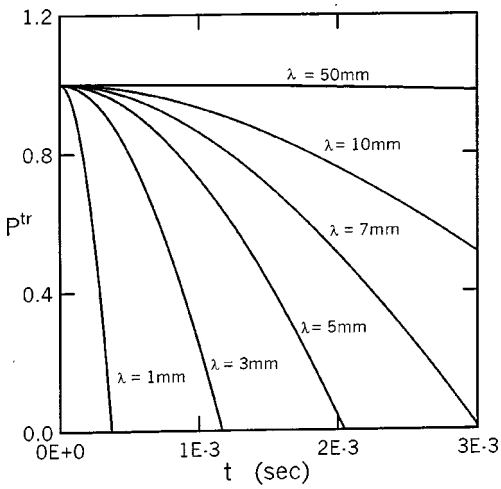


**Fig. 2 $P^{tr}$ versus $t$ for selected values of λ: pure aluminum shell. ($P_0=10000\,\mathrm{Pa}$, $R_0=10^{-5}\,\mathrm{m^2\,sec\,°C/J}$, $a=10^{-6}\,\mathrm{m}$, $R'=0\,\mathrm{m^2\,sec\,°C/J\cdot Pa}$).**

Figure 2 examines the evolution of the contact pressure at a trough in the mold surface for a pure aluminum shell. The six curves correspond to wavelengths of λ=1 mm, 3 mm, 5 mm, 7 mm, 10 mm, and 50 mm. The smaller wavelengths lead to faster gap nucleation, while the larger wavelengths, such as λ=50 mm, do not lead to gap nucleation over the time frame of interest.

Figure 3 shows the evolution of the contact pressure at a trough in the mold surface for a pure iron shell with the same process conditions used in Fig. 2. A comparison of Figs. 2 and 3 shows that the time to gap nucleation for pure iron is nearly an order-of-magnitude smaller than that for pure aluminum for any given value of λ. The controlling property that creates this distinction is the thermal capacity, $c=K/\rho k$. A pure iron shell has a smaller thermal capacity than a pure aluminum shell. Hence, the tendency of the aluminum shell to store latent heat liberated at the freezing

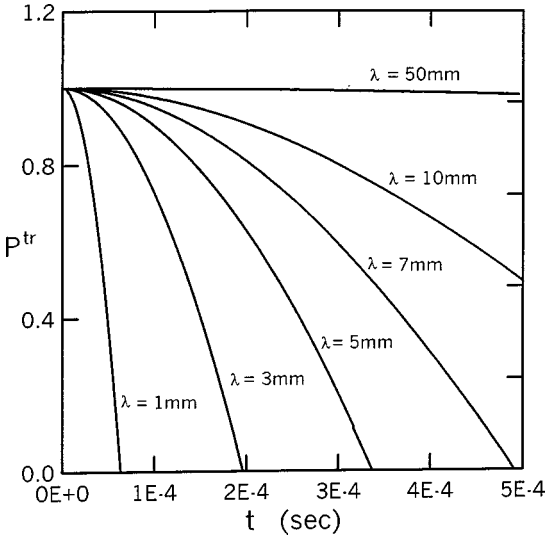


**Fig. 3 $P^{tr}$ versus $t$ for selected values of λ: pure iron shell. ($P_0=10000\,\mathrm{Pa}$, $R_0=10^{-5}\,\mathrm{m^2\,sec\,°C/J}$, $a=10^{-6}\,\mathrm{m}$, $R'=0\,\mathrm{m^2\,sec\,°C/J\cdot Pa}$).**

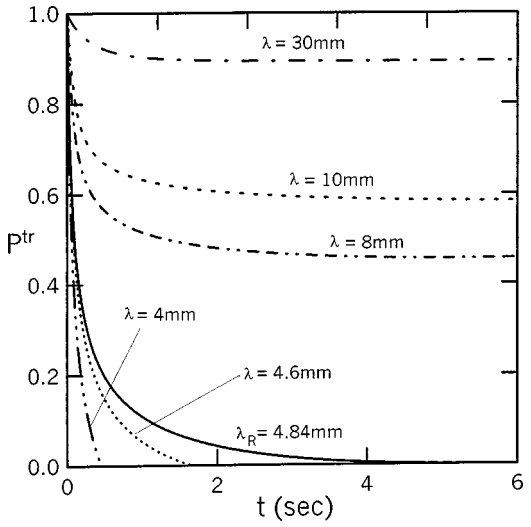


**Fig. 4 $P^{tr}$ versus $t$ variation for aluminum shell showing the critical wavelength at $\lambda_R = 4.84$ mm. ($P_0 = 2.0$ MPa, $R_0 = 10^{-5}$ m$^2$ sec °C/J, $a = 10^{-6}$ m, $R' = 0$ m$^2$ sec °C/J·Pa).**

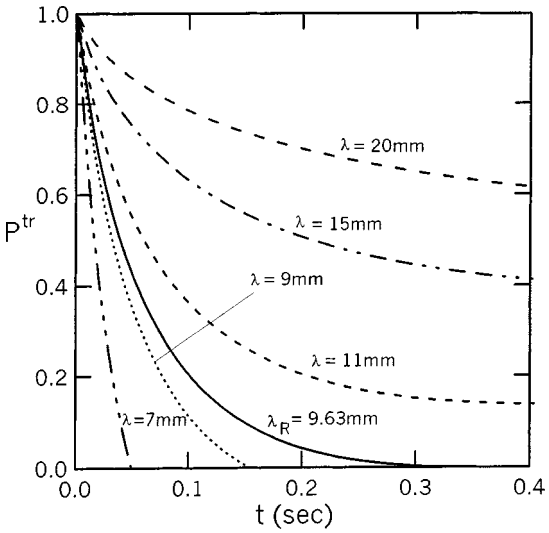


**Fig. 5 $P^{tr}$ versus $t$ variation for iron shell showing the critical wavelength at $\lambda_R = 9.63$ mm. ($P_0 = 2.0$ MPa, $R_0 = 10^{-5}$ m$^2$ sec °C/J, $a = 10^{-6}$ m, $R' = 0$ m$^2$ sec °C/J·Pa).**

front is greater than that for a pure iron shell. In other words, heat diffuses (propagates) more quickly through the iron shell than it does the aluminum shell, and the result is that the evolving thermomechanical distortion of the aluminum shell is less than that for the iron shell.

Solidification process conditions are not always conducive to gap nucleation. For example, Fig. 4 shows the evolution of $P^{tr}$ for solidification of a pure aluminum shell with the same process materials considered in Fig. 2, except that the nominal contact pressure has been increased to $P_0 = 2$ MPa. Six curves corresponding to wavelengths of 4 mm, 4.6 mm, 4.84 mm, 8 mm, 10 mm, and 30 mm are shown. Over the 6-sec time frame considered in Fig. 4, $P^{tr}$ due to 30-mm wavelength exhibits the smallest deviation from $P^{tr} = 1$. As the wavelengths are decreased, $P^{tr}$ decreases more rapidly at the earlier stages of solidification. This is evident from a comparison of the curves corresponding to $\lambda = 10$ mm and $\lambda = 30$ mm (for example). A larger value of $\lambda$ leads to a smaller value of the contact pressure perturbation $P_1$ over the earliest solidification times, and this causes the apparent ordering of the $P^{tr}$ curves in Fig. 4. Figure 4 shows that the wavelength denoted by $\lambda_R$ which is equal to 4.84 mm meets the critical wavelength criteria in Eq. (68). Gap nucleates at $t_R = 5.52$ sec. Wavelengths less than $\lambda_R$ lead to gap nucleation. Gap nucleation times for $\lambda = 4.0$ mm, 4.6 mm, and 4.84 mm are listed in Table 2 along with calculated gap nucleation times for the idealized case of zero thermal capacity material (i.e., material with infinitely large thermal diffusivity), $\zeta = 0$. For the $\lambda = 4$ mm, $t_R = 0.1549$ sec and 0.4523 sec for $\zeta = 0$ and $\zeta = 0.00114$, respectively, and hence the diffusivity effect does not significantly influence thermomechanical distortion of the shell. For $\lambda = 4.84$ mm, $t_R = 0.4495$ sec and 5.52 sec for $\zeta = 0$ and $\zeta = 0.00114$, respectively. Including thermal capacitance of the shell increases the gap nucleation time at a trough by more than 5.0 sec. This difference is further increased by increasing the wavelength to 5.0 mm, as shown in Table 2. Note that $t_R = 0.5856$ sec for $\zeta = 0$, however, gap never nucleates for $\zeta = 0.00114$. For small values of $\lambda$, the thermal diffusivity effect exerts little influence on the thermomechanical distortion of the shell since there is a small difference with the case in which the shell has infinitely large diffusivity. However, as the wavelength is increased, which means that the mold surface gradually becomes smoother, thermal diffusivity is much more significant since the time to gap nucleation increases rather dramatically, or gaps never nucleate for wavelengths that are larger than $\lambda_R$ when the thermal capacity of the solidifying material has been included.

Figure 5 shows the evolution of $P^{tr}$ for selected values of the mold surface wavelength, $\lambda$ for a pure iron shell. Note that the behavior observed in both Figs. 4 and 5 is the same. The gap nucleation time can be decreased by decreasing the mold surface wavelength. It is immediately apparent that gap nucleation time is over an order-of-magnitude faster for the iron shell than for the aluminum shell considered in Fig. 4. The critical wavelegth criteria has been met at $\lambda_R = 9.63$ mm which is larger than that the one observed in Fig. 4. Gap nucleates at $t_R = 0.342$ sec. Table 3 list the gap nucleation times for both $\zeta = 0$ and $\zeta = \zeta(\lambda)$ for the mold surface wavelenghts considered in Fig. 5. Note that the significance of finite thermal diffusivity for both pure aluminum and iron shell is evident in Tables 2 and 3 when the gap nucleation times for the $\zeta = 0$ and $\zeta = \zeta(\lambda)$ have been compared.

Although it cannot be established a quantitative comparison between the present formulation and that in Yigit and Hector [14,15], it is instructive to examine results from their model for the appropriate process parameters. Our intent here is reveal important qualitative differences between the present theoretical approach and that followed in [14,15]. For this purpose, we present Figs. 6 and 7 which examine the evolution of the contact pressure ratio due to selected mold-shell combinations. Note that the time

**Table 2 Thermal diffusivity effect on gap nucleation time for an aluminum shell**

| λ(mm) | $\zeta = 0.2843\times10^{-3}\,\lambda$ | $t_R$ (sec) for $\zeta = 0$ | $t_R$ (sec) for $\zeta = \zeta(\lambda)$ |
|---|---|---|---|
| 4.00 | 0.00114 | 0.1549 | 0.4523 |
| 4.60 | 0.00131 | 0.3168 | 1.6472 |
| 4.84 | 0.00138 | 0.4495 | 5.5200 |
| 5.00 | 0.00142 | 0.5856 | ⋯ |

**Table 3 Thermal diffusivity effect on gap nucleation time for an iron shell**

| λ (mm) | $\zeta = 0.0280\times10^{-3}\,\lambda$ | $t_R$ (sec) for $\zeta = 0$ | $t_R$ (sec) for $\zeta = \zeta(\lambda)$ |
|---|---|---|---|
| 7.00 | 0.000196 | 0.0289 | 0.0491 |
| 9.00 | 0.000252 | 0.0586 | 0.1493 |
| 9.63 | 0.000269 | 0.0729 | 0.3420 |
| 10.0 | 0.000280 | 0.0822 | ⋯ |

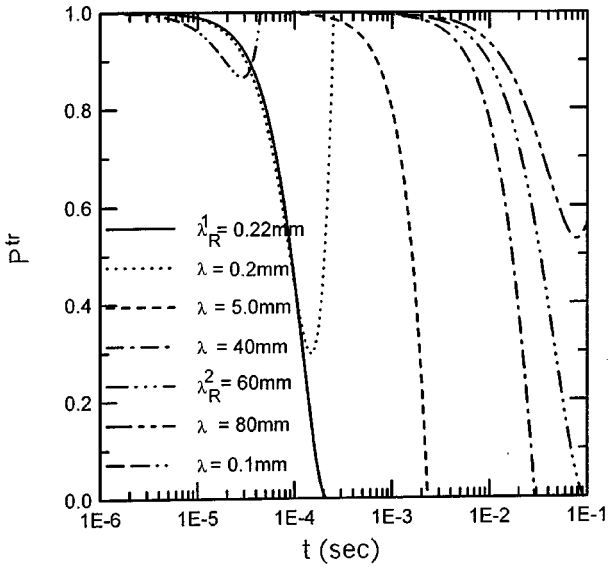


**Fig. 6** $P^{tr}$ **versus** $t$ **at** $t=t_R$ **for selected** $\lambda$**, aluminum solidifying on copper,** $P_0=10{,}000$ **Pa,** $h_0=0.5$ **mm,** $R_0=10^{-5}$ **m² sec °C/J, with critical wavelengths at** $\lambda_R^1=0.22$ **mm and** $\lambda_R^2=60.0$ **mm**

scale in each of the following two figures is logarithmic due to the large range of gap nucleation times for each combination. This required that we select different wavelength values for each combination. Figure 6 shows the evolution of $P^{tr}$ for an aluminum shell solidifying on a copper mold at the mold surface crests. Note that two wavelengths which meet the criteria established by Eq. (68) were identified as critical. These are $\lambda_R^1=0.22$ mm and $\lambda_R^2=60$ mm. Wavelengths that fall within the range delineated by the critical wavelengths (i.e., $\lambda=0.2$, 5, 40 mm) lead to gap nucleation at the crests in the mold surface. Wavelengths that lie outside of the range delineated by the critical wavelengths (i.e. $\lambda=0.1$, 80 mm) lead to gap nucleation in the troughs of the mold surface since the contact pressure in both cases achieves a minimum (nonzero) value and then turns around toward increasing values. Note that the gap nucleation times corresponding to the smaller and

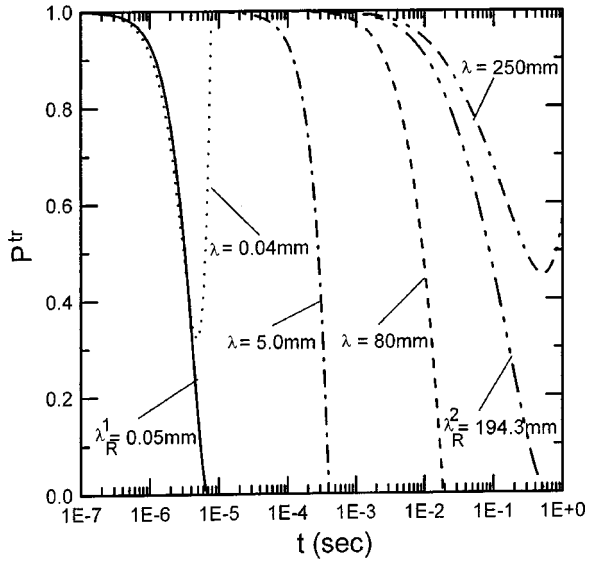


**Fig. 7** $P^{tr}$ **versus** $t$ **at** $t=t_R$ **for selected** $\lambda$**, iron solidifying on copper,** $P_0=10{,}000$ **Pa,** $h_0=0.5$ **mm,** $R_0=10^{-5}$ **m² sec °C/J, with critical wavelengths at** $\lambda_R^1=0.05$ **mm and** $\lambda_R^2=194.3$ **mm**

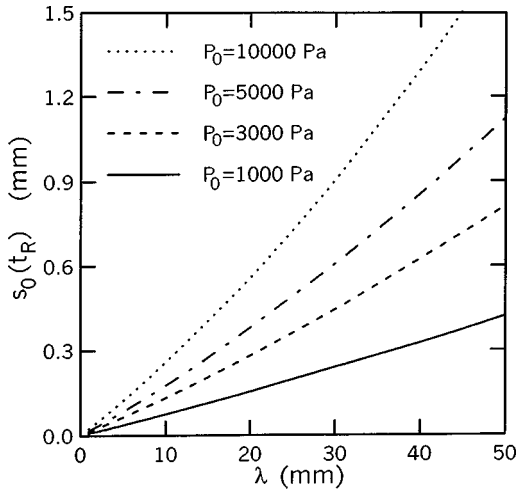


**Fig. 8** $s_0(t_R)$ **versus** $\lambda$ **for selected values of** $P_0$**: pure aluminum shell. (**$R_0=10^{-5}$ **m² sec °C/J,** $a=10^{-6}$ **m,** $R'=0$ **m² sec °C/J·Pa).**

larger critical wavelengths, are, respectively, $t_R=2.1\times10^{-4}$ sec, $t_R=9.22\times10^{-2}$ sec. Figure 7 shows the evolution of $P^{tr}$ for an iron shell solidifying on a copper mold at the surface crests. It is immediately apparent that gap nucleation is over an order-of-magnitude faster for the iron shell than for the aluminum shell in Fig. 6. The smaller critical wavelength, $\lambda_R^1=0.05$ mm corresponds to gap nucleation at $t_R=7.0\times10^{-6}$ sec. The larger critical wavelength, $\lambda_R^2=194.3$ mm corresponds to gap nucleation at $t_R=6.0\times10^{-1}$ sec. Clearly, the iron shell nucleates gaps faster than the aluminum shell and has a broader band of wavelengths that lead to gap nucleation at the mold crests.

Figures 8 and 9 show the mean thickness at gap nucleation time, $s_0(t_R)$, as a function of mold surface wavelength in mm for selected values of the mean contact pressure, $P_0$, for a pure aluminum and a pure iron shell. Increasing the mean pressure causes the shell to grow thicker in both figures. For any given wavelength, gaps nucleate more rapidly during solidification of an iron shell. For both cases, an increase in $P_0$ for fixed $\lambda$ leads to an increase in the mean thickness of the shell, $s_0$. It is interesting to note that and increase in $P_0$ for the solidification of pure iron leads to a shell thickness that is thinner than that for the aluminum. Clearly, the thermal conductivity for the iron shell is smaller

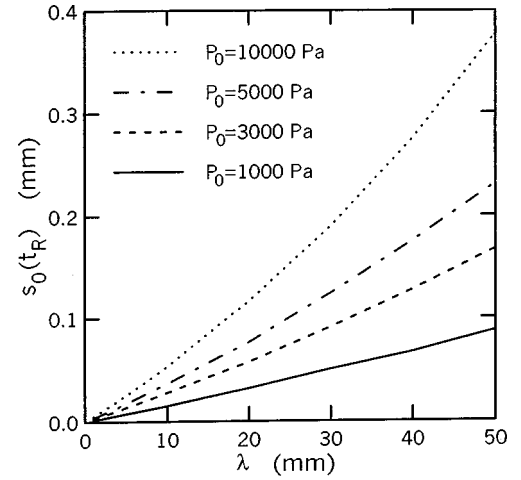


**Fig. 9** $s_0(t_R)$ **versus** $\lambda$ **for selected values of** $P_0$**: pure iron shell. (**$R_0=10^{-5}$ **m² sec °C/J,** $a=10^{-6}$ **m,** $R'=0$ **m² sec °C/J·Pa).**

**Table 4 Thermal diffusivity effect on mean shell growth at λ=5 mm and selected pressures**

| | $s_0(t_R)$ (mm) for $\zeta=0$ | | $s_0(t_R)$ (mm) | |
|---|---|---|---|---|
| $P_0$ (MPa) | Al | Fe | Al ($\zeta=0.56$) | Fe ($\zeta=0.15$) |
| 0.01 | 0.1158 | $2.5189\times10^{-2}$ | 0.1221 | $2.5425\times10^{-2}$ |
| 0.10 | 0.3987 | $8.5999\times10^{-2}$ | 0.4376 | $8.8331\times10^{-2}$ |
| 1.00 | 2.2027 | 0.3439 | 2.9841 | 0.3836 |
| 2.00 | 11.005 | 0.5752 | ⋯ | 0.6812 |

than that for the aluminum shell and this leads to slower growth of the former material. It is therefore not surprising to note that the pure iron is less sensitive to an increase in the mean pressure (for the chosen range of λ) when compared with the pure aluminum since the spread in the maximum values of $s_0$ for the former system is less than that for the latter system. Note that the influence of the mean contact pressure, $P_0$, on the mean shell thickness variation with the mold surface wavelength, i.e., $s_0$ vs. λ is almost linear for lower mean contact pressure, $P_0$ whereas the linearity gradually diminishes as the value of $P_0$ is increased.

Table 4 lists values of the $s_0(t_R)$ for the $P_0$, $\zeta$ combinations at $\lambda=5.0$ mm considered in Figs. 8 and 9. Increasing the mean pressure causes the shell to grow thicker. For any given value of $P_0$, a shell that stores latent heat liberated at the freezing front tends to grow thicker than one that does not. Figures 8 and 9 show that gap nucleation always occurs at the troughs on the mold surface. For any given wavelength, gaps nucleate more rapidly during solidification of an iron shell. The shell thickness increases very little through inclusion of the diffusivity effect at $P_0=1000$ Pa since $s_0(t_R)=0.1158$ mm and $2.5189\times10^{-2}$ mm for $\zeta=0$, and $s_0(t_R)=0.1221$ mm for $\zeta=0.001422$ and $\zeta=0.000140$ for a pure aluminum and a pure iron shell, respectively. However, this difference gradually becomes substantial as the mean pressure is increased. Note that $s_0(t_R)=11.005$ mm for the pure aluminum shell solidification with $P_0=2$ MPa and $\zeta=0$. However, gap never nucleates with the same process conditions when the thermal capacity has been included.

Figure 10 shows the variation of $\lambda_R$ with mean pressure, $P_0$. The remaining process parameters were fixed at $a=1.0\ \mu$m, $R_0=10^{-5}$ m$^2$ sec °C/J, and $R'=0$ m$^2$ sec °C/J·Pa. The smallest mean pressure evaluated in the figure is $P_0=10$ kPa. The $\lambda_R$ values for both mold materials are greatest at the smallest pressures.

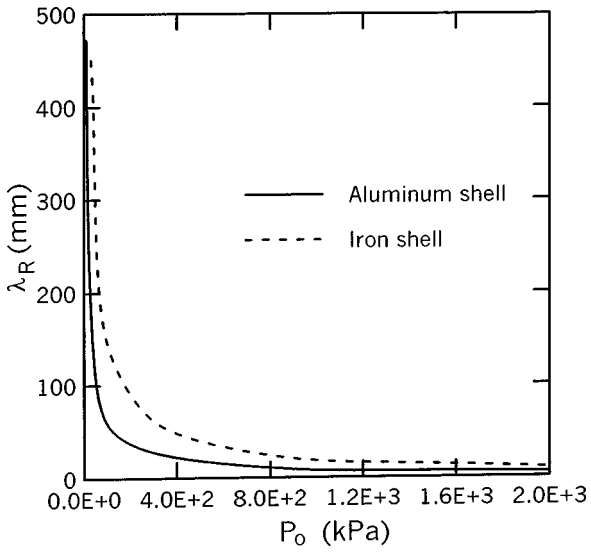


**Fig. 10 $\lambda_R$ variation with $P_0$. ($R_0=10^{-5}$ m$^2$ sec °C/J, $a=10^{-6}$ m, $R'=0$ m$^2$ sec °C/J·Pa).**

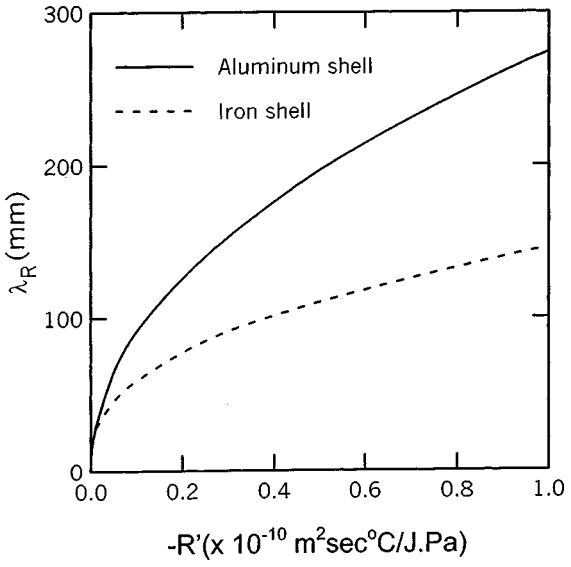


**Fig. 11 $\lambda_R$ variation with $R'$. ($P_0=1.0$ MPa, $R_0=10^{-5}$ m$^2$ sec °C/J, $a=10^{-6}$ m).**

As $P_0$ is increased, $\lambda_R$ decreases nonlinearly in both cases. Both systems give nearly constant values of $\lambda_R$ as further increase in $P_0$ has a diminishing effect. For all values of $P_0$ considered in Fig. 10, $\lambda_R$ for the pure aluminum is less than that for the pure iron. Hence, the wavelengths that lead to gap nucleation can be decreased by selecting casting material with higher thermal capacity at increased mean pressures.

Figure 11 shows the variation of $\lambda_R$ with pressure-sensitivity of the thermal contact resistance, $R'$ over the $0.0\ \text{m}^2\ \text{sec °C/J·Pa} < -\text{R}' < 1.0\times10^{-10}\ \text{m}^2\ \text{sec °C/J·Pa}$ range. The remaining process parameters were fixed at $P_0=1.0$ MPa, $R_0=10^{-5}$ m$^2$ sec °C/J, and $a=1.0\ \mu$m. Notice that $R'$ will generally be negative because the thermal contact resistance falls with increasing contact pressure. Figure 11 shows that $\lambda_R$ for both cases are always increased by a greater negative value of $R'$, implying that the interfacial coupling between the thermal and the mechanical problems promotes the possibility of undulatory growth of the shell in a very

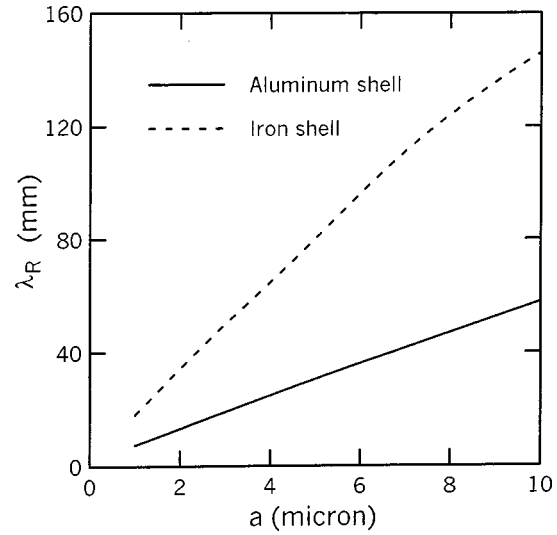


**Fig. 12 $\lambda_R$ variation with $a$. ($P_0=1.0$ MPa, $R_0=10^{-5}$ m$^2$ sec °C/J, $R'=0$ m$^2$ sec °C/J·Pa).**

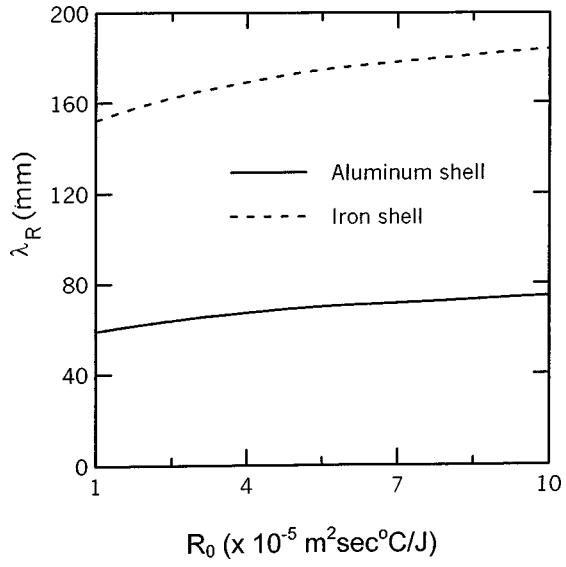


**Fig. 13 $\lambda_R$ variation with $R_0$. ($P_0$=100.0 kPa, $a$=$10^{-6}$ m, $R'$ = 0 $m^2$ sec °C/J·Pa).**

large range of the wavelength of the mold surface. This situation is enhanced for solidification of casting materials with higher thermal capacity.

Figure 12 shows the variation of $\lambda_R$ with amplitude, $a$, of the mold surface over the 1.0 $\mu$m$<a_1<$10.0 $\mu$m range. The remaining process parameters were fixed at $P_0=1.0$ MPa, $R_0=10^{-5}$ $m^2$ sec °C/J, and $R'=0$ $m^2$ sec °C/J·Pa. Variation of $a$ in the pure iron leads to a rapid increase in the $\lambda_R$, whereas a similar variation in the pure aluminum leads to much smaller $\lambda_R$. Hence, $\lambda_R$ for a shell with smaller thermal capacitance (or larger diffusivity) is more sensitive to changes in the mold surface amplitude than a corresponding shell material with higher thermal capacity.

Figure 13 shows the variation of $\lambda_R$ with mean contact resistance, $R_0$. The remaining process parameters were fixed at $a=1.0$ $\mu$m, $P_0=100.0$ kPa, and $R'=0$ $m^2$ sec °C/J·Pa. For both materials, variation of the mean resistance over the $1.0\times10^{-5}$ $m^2$ sec °C/J$<R_0<10.0\times10^{-5}$ $m^2$ sec °C/J range gives little variation in $\lambda_R$ since both curves are nearly horizontal.

## 8 Conclusions

The combined effects of thermomechanical coupling at the mold-shell interface and non-negligible thermal capacitance of the shell material during solidification of pure aluminum and iron shell on a rigid, perfectly conducting mold was presented. The evolution of the contact pressure at the lowest points of the mold surface troughs was examined. The mold surface was assumed to have a sinusoidal corrugation with a small aspect ratio. The undulatory geometry of the mold surface led to nonuniform heat extraction and hence initiated a nonuniform evolving distortion of the metal shell. This distortion produces the nucleation of gaps at the mold-shell interface wherein the contact pressure falls to zero. This implies the possibility of nonuniform or undulatory growth of the shell at later stages of the process since the contact pressure simultaneously increases at the highest points of the upper mold surface crests. The shell thickness above these points increases, whereas the shell thickness above the lowest points of the troughs diminishes. The critical wavelength was shown to exist for both pure aluminum and iron shells under specific process conditions. Those wavelengths that are larger than the critical wavelength do not promote gap nucleation in the troughs of the mold surface. They are more likely to cause gap nucleation at the crests of the mold surface and thereby promote planar growth of the shell at early times. Critical wavelengths and associated gap nucleation times were calculated for both pure aluminum and pure iron shells under identical process conditions. It was found that the iron shell nucleates gaps faster than an aluminum shell, with the associated critical wavelengths of iron being substantially larger than those for aluminum. Effects of important casting process parameters, such as pressure, pressure-sensitivity of contact resistance, the mold surface amplitude, and resistance, on the size of the critical wavelength were also examined in detail.

Perhaps the most significant result of the present model is that the coupling effect, when combined with the thermal capacitance effect considered in [17], leads to critical mold surface wavelength that surves as a cutoff between those wavelengths that lead to gap nucleation in the troughs and those that lead to gap nucleation in the crests. However, when the thermal and mechanical problems are uncoupled in the presence of thermal capacitance of the shell material, [17], or when the thermal and mechanical problems are coupled in the absence of thermal capacitance of the shell material, [13], critical wavelenghts were not predicted. Hence, in order to predict the critical wavelengths theoretically, it is necessary to model the system as one of the following: (i) to model the mold as finite and deformable and to couple the thermal and mechanical problems at the mold-shell interface without considering the effect of thermal diffusivity of the solidifying shell material, (ii) to model the mold as rigid, perfectly conducting and to couple the thermal and mechanical problems at the mold-shell interface including the effect of thermal diffusivity of the solidifying shell material. Table 5 summarizes the works done so far on the effects of three major features on the existence of critical wavelengths during solidification of pure metals. We observe that the problem defined in Case 5, where the mold is modeled as finite and deformable in the absence of interfacial coupling between the thermal and mechanical problems with finite thermal diffusivity of the solidifying shell material, must be solved to obtain a definitive conclusion about the prediction of a critical wavelength theoretically. Do two features among three (i.e., interfacial coupling, mold deformation, and thermal capacity of the shell) have to be included in the model to predict a critical wavelength or thermomechanical coupling along the mold-shell interface is necessary but not sufficient condition? This question is open at present, and is the subject of an ongoing investigation.

The perfect wetting assumption used in the present model is unlikely to be valid for sufficiently short mold surface wavelengths since surface tension effects tend to predominate the wetting process. Also, the interaction between imperfect wetting at

**Table 5 Effect of modeling on the existence of critical wavelength, $\lambda_R$, concept**

| Case | Coupling | Mold Distortivity | Thermal Capacity | Existence of $\lambda_R$ | Reference |
|---|---|---|---|---|---|
| 1 | Yes | Yes | Yes | Not yet investigated | ··· |
| 2 | Yes | No | Yes | $\lambda_R$ exists | [current work] |
| 3 | Yes | No | No | No $\lambda_R$ | [13] |
| 4 | Yes | Yes | No | $\lambda_R$ exists | [14], [15] |
| 5 | No | Yes | Yes | Not yet investigated | ··· |
| 6 | No | Yes | No | No $\lambda_R$ | [18] |
| 7 | No | No | Yes | No $\lambda_R$ | [17] |
| 8 | No | No | No | No $\lambda_R$ | [19] |

the microscale and macroscale roughness becomes important. The mechanical boundary conditions in the present model would need to be changed to include the effect of surface tension on the gap nucleation process and to delineate a possible surface tension-induced wavelength selection process for uniform shell growth.


## Acknowledgments

The author wish to express his gratitude to Dr. L. G. Hector, Jr. of GM R&D Center, Warren, MI, for his encouragement and continuous guidance during all phases of the work.


## Appendix

**Limiting Solution for Zero Thermal Capacity.** It can be demonstrated that the solution for $\zeta \to 0$ is a limiting case of the present more general theory. This simplification permits the predominantly analytical solution to be obtained.

The results of limiting case are useful in the development and checking of purely numerical solution of general case, as well as in providing a start-up solution for the general problem. In physical terms, this simplifying assumption is equivalent to the statement that the casting material has zero thermal capacity. In other words, the heat diffusivity of the casting is infinitely large. It then follows that Eq. (50) approximates Laplace's equation and in view of the condition, $\partial s/\partial x \ll 1$, that the temperature profile in the solidified layer is linear in $Y$. In this case Eq. (50) can easily be solved using the boundary conditions (52)–(54) with the result

$$\bar{T}_0(Y,\beta) = \frac{Y+\bar{R}_0}{S_0(\beta)+R_0}. \tag{A1}$$

Substituting (*A*1) into (53) and solving the ordinary differential equation for $S_0(\beta)$ we obtain the unperturbed solidification front as

$$S_0(\beta) = -\bar{R}_0 + \sqrt{R_0^2 + 2\beta}. \tag{A2}$$

Substituting (*A*1) into (54) gives the zeroth-order heat flux

$$Q_0(\beta) = \frac{1}{S_0(\beta)+R_0}. \tag{A3}$$

The governing Eq. (51) for the first-order temperature field can be solved using the remaining boundary conditions (55), (56) with the result

$$\bar{T}_1(Y,\beta) = \frac{1}{S_0+R_0}\{[S_1'(\beta)\cosh(S_0)+S_1(\beta)\sinh(S_0)]\sinh(Y) - [S_1'(\beta)\sinh(S_0)+S_1(\beta)\cosh(S_0)]\cosh(Y)\} \tag{A4}$$

where $(')$ denotes differentiation with respect to $S_0$. Once the first-order temperature profile has been determined the solution of Eq. (58) can also be obtained. We can then write Eq. (59) allowing $\zeta \to 0$ with the result

$$(S_0\bar{\omega}^2 - S_0 - \bar{\omega})G''(S_0) + 2G'(S_0) - (S_0\bar{\omega}^2 + \bar{\omega} - S_0)G(S_0) = -\frac{S_0\bar{\omega}}{S_0+R_0}S_1'(\beta) - \frac{S_0+\bar{\omega}}{S_0+R_0}S_1(\beta) + \frac{2(1-\nu)-S_0\bar{\omega}}{(1-\nu)\cosh(S_0)} - \frac{2\bar{R}_0}{(S_0+R_0)\cosh(S_0)}. \tag{A5}$$

Finally, substituting Eqs. (*A*1), (A4), and (61) into Eq. (57) we obtain

$$\left[\frac{S_0\bar{\omega}\bar{R}'}{2\cosh(S_0)}\right]\bar{G}''(S_0) - \frac{\bar{R}'}{\cosh(S_0)}\left[1+\frac{S_0\bar{\omega}}{2}\right]\bar{G}(S_0) = \frac{\bar{\omega}\bar{R}_0\bar{R}'}{S_0+\bar{R}_0} + \left\{\frac{\bar{R}'}{2\cosh(S_0)}\left(\frac{\cosh(S_0)\sinh(S_0)-S_0}{S_0+\bar{R}_0}\right) - \cosh(S_0) - \frac{\sinh(S_0)}{\bar{R}_0}\right\}S_1'(\beta) + \left\{\frac{\bar{R}'\bar{\omega}\sinh(S_0)}{2(S_0+\bar{R}_0)} - \sinh(S_0) - \frac{\cosh(S_0)}{\bar{R}_0}\right\}S_1(\beta) + \frac{1}{\bar{R}_0} - \frac{\bar{R}'}{2(1-\nu)}\left\{\frac{S_0}{\cosh^2(S_0)} + \bar{\omega}(1-2\nu)\right\} \tag{A6}$$

where we have set $\bar{G}(0) = \bar{G}'(0) = 0$ since these are arbitrary and will not affect the final results. Note that Eqs. (*A*4) and (*A*5) constitute a pair of coupled differential equations to determine the unknown quantities $\bar{G}(Y)$ and $S_1(\beta)$, given suitable initial conditions at $Y=0$. Once $\bar{G}(Y)$ and $S_1(\beta)$ are determined, contact pressure perturbation can be determined from

$$\bar{P}_1(\beta) = \frac{1}{2\cosh(S_0)}\left\{\left(\frac{1-2\nu}{1-\nu}\right)\left[\frac{S_0}{(1-2\nu)\cosh(S_0)} + \sinh(S_0)\right] + S_0\bar{\omega}[\bar{G}''(S_0) - \bar{G}(S_0)] - 2\bar{G}(S_0) - \frac{1}{S_0+\bar{R}_0}\left\{S_0\bar{\omega}S_1(\beta) + 2\bar{R}_0\sinh(S_0) + [S_1(\beta)\sinh(S_0) + S_1'(\beta)\cosh(S_0)] \times \left[\sinh(S_0) - \frac{S_0}{\cosh(S_0)}\right]\right\}\right\}. \tag{A7}$$

Note that Eqs. (*A*1)–(*A*6) are exactly equal to the results reported in [13].

## References


[1] Mizikar, E. A., Wojcik, W. M., and Li, K., 1967, "Method of Producing Steel Strip of Uniform Thickness by Direct Casting," United States Letters Patent #3,345,738.

[2] Morales, A., Glicksman, M. E., and Bilonia, H., 1977, "Influence of Mould Wall Microgeometry on Casting Structure," *Proc. Int. Conf. on Solidification*, Sheffield Metallurgical Eng. Ass'n., Univ. Sheffield and The Metals Society, Sheffield, UK, pp. 184–192.

[3] Wray, P. J., 1981, "Geometric Features of Chill-Cast Surfaces," Metall. Trans. B, **12B**, pp. 167–176.

[4] Buxmann, K., Boliger, M., and Gyongyos, I., 1981, "Mould With Roughened Surface for Casting Metals," U.S. Letters Patent #3,345,738.

[5] Laki, R. S., Beech, J., and Davies, G. J., 1985, "Surface Structures of Chill and Continuously Cast Stainless Steels," *Iron and Steelmaking*, **12**, pp. 233–241.

[6] Gaspar, T. A., 1987, "Textured Substrate and Method for the Direct, Continuous Casting of Metal Sheet Exhibiting Improved Uniformity," U.S. Letters Patent #4,705,095.

[7] Ostlund, A., and West, R., 1988, "Influence of Wheel Surface Roughness on Microstructure and Heat Transfer in Meltspun $Fe_{0.79}Si_{0.03}C_{0.04}B_{0.14}$," Int. J. Rapid Solidif., **3**, pp. 177–188.

[8] Bartlett, E., Maringer, R., and Rayment, J., 1989, "Direct Strip Casting on Grooved Wheels," U.S. Letters Patent #4,865,117.

[9] Murakami, H., Suzuki, M., Kitagawa, T., and Miyahara, S., 1992, "Control of Uneven Solidified Shell Formation of Hypo-Peritectic Carbon Steels in Continuous Casting Mold," *J. Iron and Steel Inst. Japan*, **78**, pp. 105–112.

[10] Haga, T., and Motomura, M., 1994, "Effect of Polishing Condition on the Roll of the Surface of Foils of Pure Aluminum and Al-Si Alloy Manufactured by Single Roll Rapid Solidification," J. Japan Inst. Light Metals, **44**, pp. 22–27.

[11] Sugitani, Y., Nakamura, M., Okuda, M., Kawasaki, M., and Miyahara, S., 1992, "Control of Uneven Solidified Shell Formation of Hypo-Peritectic Carbon Steels in Continuous Casting Mold," Trans. Iron Steel Inst. Jpn., **25**, pp. B–91.

[12] Weirauch, D. A., Jr., and Giron, A., 1998, "The Early Stages of Aluminum Solidification in the Presence of a Moving Meniscus," *Proceedings on the*

*Integration of Material, Process and Product Design—A Conference Dedicated to the 70th Birthday of Owen Richmond*, A. A. Balkema Publishers, Rotterdam, Netherlands, pp. 183–191.
[13] Hector, L. G., Jr., Howarth, J. A., Richmond, O., and Kim, W.-S., 1999, ''Mold Surface Wavelength Effect on Gap Nucleation in Solidification,'' ASME J. Appl. Mech., **67**, pp. 155–164.
[14] Yigit, F., and Hector, L. G., Jr., 2000, ''Critical Wavelengths for Gap Nucleation in Solidification. Part 1: Theoretical Methodology,'' ASME J. Appl. Mech., **67**, pp. 66–76.
[15] Yigit, F., and Hector, L. G., Jr., 2000, ''Critical Wavelengths for Gap Nucleation in Solidification. Part 2. Results for Selected Mold-Shell Material Combinations,'' ASME J. Appl. Mech., **67**, pp. 77–86.
[16] Dundurs, J., 1974, ''Distortion of a Body Caused by Free Thermal Expansion,'' Mech. Res. Commun., **1**, pp. 121–124.
[17] Yigit, F., and Hector, L. G., Jr., 2002, ''Solidification of a Pure Metal With Finite Thermal Capacitance on a Sinusoidal Mold Surface,'' J. Therm. Stresses, **25**, pp. 663–690.
[18] Yigit, F., Hector, L. G., Jr., and Richmond, O., 2002, ''A Theoretical Investigation of Pure Metal Solidification on a Deformable Mold in the Absence of Interfacial Coupling,'' J. Therm. Stresses, **25**, pp. 773–809.
[19] Hector, L. G., Jr., Kim, W.-S., and Howarth, J. A., 1999, ''Thermomechanical Models of Pure Metal Solidification on a Periodic Mold Surface,'' J. Therm. Stresses, **22**, pp. 125–158.
[20] Yigit, F., and Barber, J. R., 1994, ''Effect of Stefan Number on Thermoelastic Instabilities in Unidirectional Solidification,'' Int. J. Mech. Sci., **36**, pp. 707–723.
[21] Westergaard, H. M., 1964, *Theory of Elasticity and Plasticity*, Dover, New York.
[22] Li, N.-Y., and Barber, J. R., 1991, ''Thermoelastic Instability in Planar Solidification,'' Int. J. Mech. Sci., **33**, pp. 945–959.
[23] Richmond, O., Hector, L. G., Jr., and Fridy, J. M., 1990, ''Growth Instability During Non-Uniform Directional Solidification of Pure Metals,'' ASME J. Appl. Mech., **57**, pp. 529–536.
[24] Heinlein, M., Mukherjee, S., and Richmond, O., 1986, ''A Boundary Element Method of Analysis of Temperature Fields and Stresses During Solidification,'' Acta Mech., **59**, pp. 59–81.
[25] Boltz, R. E., and Tuve, G. L., 1984, *CRC Handbook of Tables for Applied Engineering and Science*, CRC Press, Boca Raton, FL.
[26] Touloukian, Y. S., Powell, R. W., Ho, C. Y., and Klemens, P. G., 1970, *Thermophysical Properties of Matter, Thermal Conductivity*, **1**, IFI/Plenum, New York.
[27] Lucas, L. D., 1972, ''Density of Metals at High Temperatures in the Solid and Molten States, Part 2,'' Mem. Sci. Rev. Metall., **69**(6), pp. 479–492.
[28] Baumeister, T., Avallone, E. A., and Baumeister III, T., 1978, *Marks' Standard Handbook for Mechanical Engineers*, 8th Ed., McGraw-Hill, New York.
[29] Wawra, H. H., 1974, ''The Elastomechanical Properties of Pure Iron and $FeS_2$ in Different Crystallographic Directions as a Function of Temperature and Pressure,'' Arch. Eisenhuettenwes., **45**(5), pp. 317–320.
[30] Touloukian, Y. S., Kirby, R. K., Taylor, R. E., and Desai, P. D., 1978, *Thermophysical Properties of Matter* (Vol. 12, Thermal Expansion), IFI/Plenum, New York.
[31] Zhang, R., and Barber, J. R., 1990, ''Effects of Material Properties on the Stability of Static Thermoelastic Contact,'' ASME J. Appl. Mech., **57**, pp. 365–369.

**Lingyuan Kong**
Graduate Student

**Robert G. Parker**[1]
Mem. ASME
e-mail: parker.242@osu.edu

Department of Mechanical Engineering,
The Ohio State University,
206 W. 18th Avenue,
Columbus, OH 43210

# Coupled Belt-Pulley Vibration in Serpentine Drives With Belt Bending Stiffness

*A method is developed to evaluate the natural frequencies and vibration modes of serpentine belt drives where the belt is modeled as a moving beam with bending stiffness. Inclusion of bending stiffness leads to belt-pulley coupling not captured in moving string models. New dynamic characteristics of the system induced by belt bending stiffness are investigated. The belt-pulley coupling is studied through the evolution of the vibration modes. When the belt-pulley coupling is strong, the dynamic behavior of the system is quite different from that of the string model where there is no such coupling. The effects of major design variables on the system are discussed. The spatial discretization can be used to solve other hybrid continuous/discrete eigenvalue problems.*
[DOI: 10.1115/1.1641064]

## Introduction

Serpentine belt drives with flat multi-ribbed belts are used to drive individual accessories of an automobile. Most of the models used in the literature only address the pulley rotational motion with the spans modeled as axial springs, [1–4]. These discrete models are relatively simple and have been used extensively. Many factors have been incorporated to describe the dynamic behavior such as damping, dry friction of the tensioner arm, slip between the pulley and belt, and so on. Its assumptions exclude the span transverse vibrations which may be large and interact strongly with the pulleys, as seen in experiments, [5], and communicated by automotive manufacturers and suppliers.

In contrast to the discrete model, more refined models include the span transverse vibrations, pulley rotational motions, and the interactions between these continuous and discrete components. Ulsoy et al. [6] considers the possibility of parametric instability and presented a mechanism which may cause large transverse span vibration due to tension fluctuations. Beikmann et al. [5,7] treats the belt as a moving string and studied a prototypical three-pulley model, which captured a linear coupling mechanism between the tensioner rotation and the transverse vibrations of the two spans adjacent to the tensioner (Fig. 1). Other spans are decoupled from pulley rotations in the linear model. Zhang et al. [8,9] build on this model by adding damping and give a complex modal analysis of the serpentine belt drive system. Parker [10] develops a spatial discretization of this model extended to $n$ pulleys.

By incorporating the belt bending stiffness, Kong and Parker [11] present another model. Each span is an Euler elastica, [12], moving with constant speed. Modeling the belt as a moving beam shows that transverse vibration of every span is linearly coupled with the rotations of the two adjacent pulleys at its ends. The degree of span-pulley coupling depends on the steady state curvature of the span. Further, a coupling indicator is defined for each span to quantify coupling strength. In [11], the attention is focused on analytical and numerical methods to calculate the steady motion and the effects of design parameters on the steady state and coupling indicator.

Belt-pulley coupling from bending stiffness is more consistent with observed automotive serpentine drive vibration problems than prior models. In these cases, span vibrations most commonly occur at low (engine idle) speeds and at the engine firing frequency from pulsations to the crankshaft pulley. This precludes belt or pulley runout as root causes because they lead to span vibrations at frequencies other than the firing frequency. Parametric instability from tension or speed fluctuations, [13–15], occurs in practice only at high engine speeds.

Based on the moving beam-pulley model, [11], this study investigates serpentine belt drive dynamic analysis. Computation of the natural frequencies and vibration modes is a central task. Serpentine belt drives belong to the class of hybrid continuous/discrete systems, and solving the eigenvalue problem for such a system is challenging. For the simpler case of a string model of the belt, three papers, [5,8,10], develop numerical methods to solve the serpentine drive eigenvalue problem. The first two methods, [5,8], fail when the spans are modeled as moving beams because both require the explicit solution form for axially moving continua while no such form exists for a traveling beam, [16]. Both methods retain the continuum model and seek roots of a numerically ill-behaved characteristic equation. The numerical singularities (see [10]) can lead to missing or false roots and significant computational expense to try to avoid these errors. To address these issues, the third method, [10], discretizes the two spans adjacent to the tensioner and uses Lagrange multipliers to enforce the geometric boundary conditions at the belt-tensioner interface. The method is presented for a general $n$-pulley drive.

One of the main developments of this paper is a spatial discretization to solve the serpentine belt drive eigenvalue problem with a moving beam model. Compared with characteristic equation methods, [5,8], the present approach can incorporate bending stiffness, is numerically economical with dramatic reduction in computation time, avoids numerical singularities, and does not require advance estimation of the natural frequency bandwidth. After a coordinate transformation and some mathematical modifications, the governing equations are rewritten into an extended operator form that retains the mathematical structure of a gyroscopic continuum. Galerkin discretization is readily applied in this extended operator context. Although the reformulation initially seems complicated, the key ideas are such that the method is straightforward to implement when devising code. The concepts can be naturally extended to other hybrid continuous/discrete systems.

[1]To whom correspondence should be addressed.

Contributed by the Applied Mechanics Division of THE AMERICAN SOCIETY OF MECHANICAL ENGINEERS for publication in the ASME JOURNAL OF APPLIED MECHANICS. Manuscript received by the ASME Applied Mechanics Division, Jan. 24, 2003; final revision, July 3, 2003. Associate Editor: O. O'Reilly. Discussion on the paper should be addressed to the Editor, Prof. Robert M. McMeeking, Journal of Applied Mechanics, Department of Mechanical and Environmental Engineering, University of California–Santa Barbara, Santa Barbara, CA 93106-5070, and will be accepted until four months after final publication of the paper itself in the ASME JOURNAL OF APPLIED MECHANICS.

  

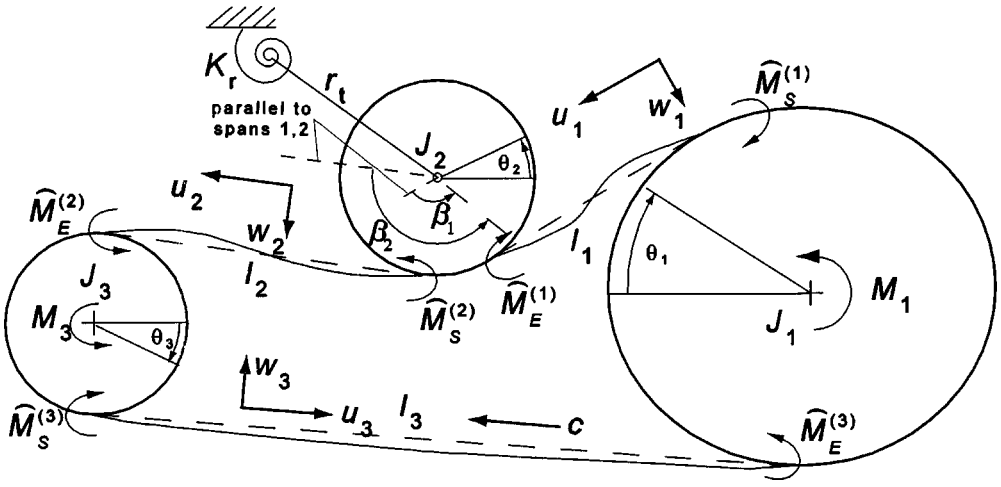


**Fig. 1 A prototypical three-pulley serpentine belt drive**

The three-pulley system in Fig. 1 is used to demonstrate the method and results. The method can be extended to multi-pulley serpentine drive systems. A comprehensive, multi-pulley analysis code based on the method has been developed for use in the automotive industry.

The relationship between belt-pulley coupling and bending stiffness is investigated from the perspective of evolution of the vibration modes. When the bending stiffness is appreciable, all the continuous (span) and discrete (pulley) components interact strongly with each other, and the former classification of the modes for the string model (pulley rotationally dominant vibration modes and span transversely dominant vibration modes, [5,8,10]) does not apply. When the bending stiffness is small, the dynamic behavior converges to that of string models. Finally, the effects of key design parameters on the natural frequencies are investigated.

## Linearization of Equations of Motion

Figure 1 depicts a prototypical three-pulley system that includes the primary components in automotive serpentine drives, [5,8,9]. The spans are modeled as Euler-Bernoulli beams translating with constant speed $c$. Each span is subjected to constant moments at its ends arising from the bending of the continuous belt around the pulleys. Movement of the belt-pulley contact point due to belt vibration is neglected, [17–19]. Detailed description of the model is given in [11]. Only essential equations and some key concepts are repeated here. Hamilton's principle applied to the prototypical serpentine belt drive leads to the equations of motion

$$m(w_{i,tt}-2cw_{i,xt}+c^2w_{i,xx})-[(P_i+\tilde{P}_i)w_{i,x}]_{,x}+EIw_{i,xxxx}=0 \qquad (1)$$

$$i=1,2,3$$

$$w_1(0,t)=0 \quad EIw_{1,xx}(0,t)=\frac{EI}{r_1}$$

$$w_1(l_1,t)=r_t\theta_t\cos\beta_1 \quad EIw_{1,xx}(l_1,t)=-\frac{EI}{r_2} \qquad (2)$$

$$w_2(0,t)=r_t\theta_t\cos\beta_2 \quad EIw_{2,xx}(0,t)=-\frac{EI}{r_2} \qquad (3)$$

$$w_2(l_2,t)=0 \quad EIw_{2,xx}(l_2,t)=\frac{EI}{r_3}$$

$$w_3(0,t)=0 \quad EIw_{3,xx}(0,t)=\frac{EI}{r_3} \quad w_3(l_3,t)=0 \qquad (4)$$

$$EIw_{3,xx}(l_3,t)=\frac{EI}{r_1}$$

$$J_1\ddot{\theta}_1+\tilde{P}_1r_1-\tilde{P}_3r_1=\tilde{M}_1 \qquad (5)$$

$$J_2\ddot{\theta}_2-\tilde{P}_1r_2+\tilde{P}_2r_2=0 \qquad (6)$$

$$J_3\ddot{\theta}_3-\tilde{P}_2r_3+\tilde{P}_3r_3=\tilde{M}_3 \qquad (7)$$

$$\begin{aligned}J_t\ddot{\theta}_t+k_r\theta_t+&[mcw_{1,t}(l_1)+(P_1-mc^2+\tilde{P}_1)w_{1,x}(l_1)\\&+EIw_{1,xxx}(l_1)]r_t\cos\beta_1+(mc^2-\tilde{P}_1)r_t\sin\beta_1\\&-[mcw_{2,t}(0)+(P_2-mc^2+\tilde{P}_2)w_{2,x}(0)\\&+EIw_{2,xxx}(0)]r_t\cos\beta_2\\&-(mc^2-\tilde{P}_2)r_t\sin\beta_2=0\end{aligned} \qquad (8)$$

where

$$\tilde{P}_1=\frac{EA}{l_1}\left(-r_2\theta_2+r_1\theta_1-r_t\theta_t\sin\beta_1+\int_0^{l_1}\frac{1}{2}w_{1,x}^2dx\right) \qquad (9)$$

$$\tilde{P}_2=\frac{EA}{l_2}\left(-r_3\theta_3+r_2\theta_2+r_t\theta_t\sin\beta_2+\int_0^{l_2}\frac{1}{2}w_{2,x}^2dx\right) \qquad (10)$$

$$\tilde{P}_3=\frac{EA}{l_3}\left(-r_1\theta_1+r_3\theta_3+\int_0^{l_3}\frac{1}{2}w_{3,x}^2dx\right) \qquad (11)$$

and $\tilde{M}_i(t)$ are dynamic accessory torques. All dynamic motions (pulley rotations $\theta_i$(t), tensioner arm rotation $\theta_t(t)$, transverse belt deflections $(w_i(x_i,t))$) are measured relative to the *reference* state corresponding to a stationary, string model system subject to any steady accessory torques, [11]. Different spans may have different reference tensions $P_i$ due to the accessory torques. $\beta_{1,2}$ are the orientation angles of the tensioner arm relative to the two spans adjacent to the tensioner in the reference state (Fig. 1).

The following nondimensional variables are introduced:

$$\hat{x}_i=\frac{x_i}{l_i}\quad \hat{w}_i=\frac{w_i}{l_i}\quad l=\frac{l_1+l_2+l_3}{3}\quad \hat{t}=t\sqrt{\frac{P_0}{ml^2}}\quad \hat{P}_i=\frac{P_i}{P_0}\quad \varepsilon^2=\frac{EI}{P_0l^2}$$

$$s=c\sqrt{\frac{m}{P_0}} \tag{12}$$

$$k_s=\frac{k_r}{P_0r_t}\quad \gamma=\frac{EA}{P_0}\quad m_i=\frac{J_i}{mr_il^2}\quad m_t=\frac{J_t}{mr_tl^2}\quad M_i=\frac{\tilde{M}_i}{P_0r_i}$$

where $P_0$ is the uniform tension at zero speed with no accessory torques using a string model, [11]. Substitution of (12) into (1)–(11) leads to the nondimensional *dynamic* equations of motion for the prototypical serpentine belt system, from which the equations governing the steady motion can be obtained by equating time derivative terms to zero. Methods to determine the steady motion and its properties are discussed in [11].

Linearization for small motions about the steady-state configuration yields the following nondimensional equations, where $\theta_i(t)$, $\theta_t(t)$, $w_i(x_i,t)$ now represent small vibrations about the steady motion (not about the reference state as in (1)–(11)); steady motion quantities are denoted by asterisks. The hats on dimensionless variables have been dropped. The span vibration equations are

$$\left(\frac{l_1}{r_t}\right)\left(\frac{l_1}{l}\right)^2 w_{1,tt}-2s\left(\frac{l_1}{l}\right)\left(\frac{l_1}{r_t}\right)w_{1,xt}-\left(\frac{l_1}{r_t}\right)\overline{P}_1w_{1,xx}+\varepsilon^2\left(\frac{l}{l_1}\right)^2\left(\frac{l_1}{r_t}\right)w_{1,xxxx}-\gamma\left(\frac{l_1}{r_t}\right)\left(-\frac{r_2}{l_1}\theta_2+\frac{r_1}{l_1}\theta_1-\frac{r_t}{l_1}\theta_t\sin\beta_1+\int_0^1 w_{1,x}w_{1,x}^*dx\right)w_{1,xx}^*=0 \tag{13}$$

$$w_1(0,t)=0\quad w_1(1,t)=\frac{r_t}{l_1}\cos\beta_1\theta_t\quad w_{1,xx}(0,t)=0\quad w_{1,xx}(1,t)=0 \tag{14}$$

$$\left(\frac{l_2}{r_t}\right)\left(\frac{l_2}{l}\right)^2 w_{2,tt}-2s\left(\frac{l_2}{l}\right)\left(\frac{l_2}{r_t}\right)w_{2,xt}-\left(\frac{l_2}{r_t}\right)\overline{P}_2w_{2,xx}+\varepsilon^2\left(\frac{l}{l_2}\right)^2\left(\frac{l_2}{r_t}\right)w_{2,xxxx}-\gamma\left(\frac{l_2}{r_t}\right)\left(-\frac{r_3}{l_2}\theta_3+\frac{r_2}{l_2}\theta_2+\frac{r_t}{l_2}\theta_t\sin\beta_2+\int_0^1 w_{2,x}w_{2,x}^*dx\right)w_{2,xx}^*=0 \tag{15}$$

$$w_2(0,t)=\frac{r_t}{l_2}\cos\beta_2\theta_t\quad w_2(1,t)=0\quad w_{2,xx}(0,t)=0\quad w_{2,xx}(1,t)=0 \tag{16}$$

$$\left(\frac{l_3}{r_t}\right)\left(\frac{l_3}{l}\right)^2 w_{3,tt}-2s\left(\frac{l_3}{l}\right)\left(\frac{l_3}{r_t}\right)w_{3,xt}-\left(\frac{l_3}{r_t}\right)\overline{P}_3w_{3,xx}+\varepsilon^2\left(\frac{l}{l_3}\right)^2\left(\frac{l_3}{r_t}\right)w_{3,xxxx}-\gamma\left(\frac{l_3}{r_t}\right)\left(-\frac{r_1}{l_3}\theta_1+\frac{r_3}{l_3}\theta_3+\int_0^1 w_{3,x}w_{3,x}^*dx\right)w_{3,xx}^*=0 \tag{17}$$

$$w_3(0,t)=0\quad w_3(1,t)=0\quad w_{3,xx}(0,t)=0\quad w_{3,xx}(1,t)=0 \tag{18}$$

$$\overline{P}_1=P_1-s^2+P_1^*, \tag{19}$$

$$P_1^*=\gamma\left[-\frac{r_2}{l_1}\theta_2^*+\frac{r_1}{l_1}\theta_1^*-\frac{r_t}{l_1}\theta_t^*\sin\beta_1+\int_0^1\frac{1}{2}(w_{1,x}^*)^2dx\right]$$

$$\overline{P}_2=P_2-s^2+P_2^*, \tag{20}$$

$$P_2^*=\gamma\left[-\frac{r_3}{l_2}\theta_3^*+\frac{r_2}{l_2}\theta_2^*+\frac{r_t}{l_2}\theta_t^*\sin\beta_2+\int_0^1\frac{1}{2}(w_{2,x}^*)^2dx\right]$$

$$\overline{P}_3=P_3-s^2+P_3^*, \tag{21}$$

$$P_3^*=\gamma\left[-\frac{r_1}{l_3}\theta_1^*+\frac{r_3}{l_3}\theta_3^*+\int_0^1\frac{1}{2}(w_{3,x}^*)^2dx\right].$$

The pulley and tensioner arm equations are

$$m_1\left(\frac{r_1}{r_t}\right)\theta_{1,tt}+\gamma\left(\frac{r_1}{r_t}\right)\left(-\frac{r_2}{l_1}\theta_2+\frac{r_1}{l_1}\theta_1-\frac{r_t}{l_1}\theta_t\sin\beta_1\right)+\gamma\left(\frac{r_1}{r_t}\right)\int_0^1 w_{1,x}w_{1,x}^*dx-\gamma\left(\frac{r_1}{r_t}\right)\left(-\frac{r_1}{l_3}\theta_1+\frac{r_3}{l_3}\theta_3\right)-\gamma\left(\frac{r_1}{r_t}\right)\int_0^1 w_{3,x}w_{3,x}^*dx=\left(\frac{r_1}{r_t}\right)M_1 \tag{22}$$

$$m_2\left(\frac{r_2}{r_t}\right)\theta_{2,tt}+\gamma\left(\frac{r_2}{r_t}\right)\left(-\frac{r_3}{l_2}\theta_3+\frac{r_2}{l_2}\theta_2+\frac{r_t}{l_2}\theta_t\sin\beta_2\right)+\gamma\left(\frac{r_2}{r_t}\right)\int_0^1 w_{2,x}w_{2,x}^*dx-\gamma\left(\frac{r_2}{r_t}\right)\left(-\frac{r_2}{l_1}\theta_2+\frac{r_1}{l_1}\theta_1-\frac{r_t}{l_1}\theta_t\sin\beta_1\right)-\gamma\left(\frac{r_2}{r_t}\right)\int_0^1 w_{1,x}w_{1,x}^*dx=0 \tag{23}$$

$$m_3\left(\frac{r_3}{r_t}\right)\theta_{3,tt}+\gamma\left(\frac{r_3}{r_t}\right)\left(-\frac{r_1}{l_3}\theta_1+\frac{r_3}{l_3}\theta_3\right)+\gamma\left(\frac{r_3}{r_t}\right)\int_0^1 w_{3,x}w_{3,x}^*dx-\gamma\left(\frac{r_3}{r_t}\right)\left(-\frac{r_3}{l_2}\theta_3+\frac{r_2}{l_2}\theta_2+\frac{r_t}{l_2}\theta_t\sin\beta_2\right)-\gamma\left(\frac{r_3}{r_t}\right)\int_0^1 w_{2,x}w_{2,x}^*dx=\left(\frac{r_3}{r_t}\right)M_3 \tag{24}$$

$$m_t\ddot{\theta}_t+s\left(\frac{l_1}{l}\right)\cos\beta_1 w_{1,t}(1)+\overline{P}_1\cos\beta_1 w_{1,x}(1)+\gamma\cos\beta_1\left(-\frac{r_2}{l_1}\theta_2+\frac{r_1}{l_1}\theta_1-\frac{r_t}{l_1}\theta_t\sin\beta_1+\int_0^1 w_{1,x}w_{1,x}^*dx\right)w_{1,x}^*(1)$$
$$-s\left(\frac{l_2}{l}\right)\cos\beta_2 w_{2,t}(0)-\overline{P}_2\cos\beta_2 w_{2,x}(0)-\gamma\cos\beta_2\left(-\frac{r_3}{l_2}\theta_3+\frac{r_2}{l_2}\theta_2+\frac{r_t}{l_2}\theta_t\sin\beta_2+\int_0^1 w_{2,x}w_{2,x}^*dx\right)w_{1,x}^*(0)$$
$$-\varepsilon^2\left(\frac{l}{l_1}\right)^2\cos\beta_1 w_{1,xxx}(1)+\varepsilon^2\left(\frac{l}{l_2}\right)^2\cos\beta_2 w_{2,xxx}(0)-\gamma\left(-\frac{r_2}{l_1}\theta_2+\frac{r_1}{l_1}\theta_1-\frac{r_t}{l_1}\theta_t\sin\beta_1+\int_0^1 w_{1,x}w_{1,x}^*dx\right)\sin\beta_1$$
$$+\gamma\left(-\frac{r_3}{l_2}\theta_3+\frac{r_2}{l_2}\theta_2+\frac{r_t}{l_2}\theta_t\sin\beta_2+\int_0^1 w_{2,x}w_{2,x}^*dx\right)\sin\beta_2+k_s\theta_t=0. \tag{25}$$

Equations (13)–(25) reveal that the transverse vibrations of *all* spans are coupled with the pulley rotational motions, in contrast to string models for the belt. Notice that Eq. (17) for span 3 shows that its transverse vibration is now coupled with the two adjacent pulleys' rotational motions and the degree of the span-pulley coupling is determined by its steady state curvature $w_{3,xx}^*$, [11]. If there is no bending stiffness, this span (and any others between fixed center pulleys in an $n$ pulley system) remains a straight line with $w_{3,xx}^*=0$ at steady state, meaning that its motion is completely decoupled from the rest of the system. This expanded coupling is the primary ramification of including belt bending stiffness.

## Extended Operator Formulation

The above system can be expressed in the extended operator form, [5,8,10],

$$\mathbf{M}\ddot{\mathbf{W}}+\mathbf{G}\dot{\mathbf{W}}+\mathbf{K}\mathbf{W}=\mathbf{F} \tag{26}$$

where the displacement vector, external force vector, and inner product are

$$\mathbf{W}=\{w_1,w_2,w_3,\theta_1,\theta_2,\theta_3,\theta_t\}^T \tag{27}$$

$$\mathbf{F}=\left\{0,0,0,\left(\frac{r_1}{r_t}\right)M_1,0,\left(\frac{r_3}{r_t}\right)M_3,0\right\}^T \tag{28}$$

$$\langle\mathbf{W},\mathbf{U}\rangle=\int_0^1 w_1\overline{u}_1dx+\int_0^1 w_2\overline{u}_2dx+\int_0^1 w_3\overline{u}_3dx+\sum_{i=1}^3\theta_i\overline{\sigma}_i+\theta_t\overline{\sigma}_t \tag{29}$$

and the overbar means complex conjugate. The differential operators **M** and **K** are symmetric while **G** is skew-symmetric. Therefore, the above linear model constitutes a conservative gyroscopic system. The factors $(l_i/r_t)$ in the span equations and $(r_i/r_t)$ in the pulley equations are necessary to preserve the symmetric/skew-symmetric properties of **M**, **G**, and **K**.

Although the above model is linear, solution of the corresponding eigenvalue problem is difficult because of the belt-pulley coupling in the differential equations, belt-tensioner coupling in the boundary conditions (see (14) and (16)), multiple spans, and gyroscopic character. Even for the simpler case of modeling the spans without bending stiffness, which eliminates the belt-pulley coupling, solution is difficult. In that case, the main obstacle lies in the inhomogeneous boundary conditions (14) and (16) that result from rotation of the tensioner arm moving the endpoints of the two adjacent spans.

Three distinct methods have been presented for the eigenvalue problem of the string model. The first one is by Beikmann et al. [5], who determine a boundary condition error function akin to a characteristic equation. The second approach is by Zhang and Zu [8], who established a closed-form characteristic equation, from which the eigenvalues for the belt drive system are numerically computed. The above two methods, however, cannot be used to attack the eigenvalue problem presented here because both methods require the explicit solution form for an axially moving string, [20]. For the present model, no such explicit solution exists, [16]. Furthermore, both of the two methods need a pre-specified bandwidth to search for roots of the characteristic equations. Singularities and numerical ill-behavedness of both characteristic equations complicate the root-finding process, [5,10], leading to time consuming calculations, especially when coded for general multi-pulley systems. Due to the numerical concerns, the accuracy and completeness of the calculated natural frequencies cannot be guaranteed (that is, some computed natural frequencies may be false and true natural frequencies in the specified range may be missed).

In [10], a third method is developed to solve the string model eigenvalue problem. There the spans adjacent to the tensioner (which are the only ones coupled to the pulleys) are expanded in a series of basis functions. The inhomogeneous boundary conditions at the belt-tensioner interface are treated as constraints and the Lagrange multiplier method is applied to impose them. This method overcomes the drawbacks of the first two methods and could be extended to models with bending stiffness. A result of the Lagrange multiplier approach is that the discretized matrices lose the symmetric/skew-symmetric properties of a conservative gyroscopic system, although this does not influence the accuracy of the results.

A different technique is developed in this work to solve the eigenvalue problem of the moving beam model. The key concepts are to reformulate the span deflections in terms of variables satisfying homogeneous boundary conditions, cast the equations into a structured symmetric/skew-symmetric extended operator form, and apply Galerkin discretiztion to this form. The reformulation is needed to transform the troublesome mixed continuum/discrete boundary conditions at the belt-tensioner interface, (14) and (16), into homogeneous boundary conditions.

First, the following coordinate transformations are applied:

$$y_1=w_1-\frac{r_t}{l_1}x\cos\beta_1\theta_t$$
$$y_2=w_2+\frac{r_t}{l_2}(x-1)\cos\beta_2\theta_t \tag{30}$$
$$y_3=w_3.$$

The new unknown functions $y_i$ satisfy the trivial boundary conditions

$$y_i(0,t)=0\quad y_i(1,t)=0\quad y_{i,xx}(0,t)=0\quad y_{i,xx}(1,t)=0,\quad i=1,2,3 \tag{31}$$

instead of the mixed continuum/discrete boundary conditions in (14) and (16). Substitution of (30) into (13)–(25) leads to a new set of equations. When directly rewritten in the extended operator form (26), however, these new equations do not lead to the requisite symmetric/skew-symmetric properties of the **M**, **G**, and **K** operators. To recover these operator properties, more manipulations are needed.

In the following derivation, the $w_i$ in (13)–(25) have been replaced by the $y_i$ through Eq. (30). Multiplying Eq. (13) for the first span by $r_t/l_1 x\cos\beta_1$ and integrating over the span yields

$$\left(\frac{l_1}{l}\right)^2\int_0^1 x\cos\beta_1 y_{1,tt}dx+\left(\frac{l_1}{l}\right)^2\left(\frac{r_t}{l_1}\right)\int_0^1(\cos\beta_1 x)^2dx\,\ddot{\theta}_t$$
$$-2s\left(\frac{l_1}{l}\right)\int_0^1 x\cos\beta_1 y_{1,xt}dx-2s\left(\frac{l_1}{l}\right)\left(\frac{r_t}{l_1}\right)\int_0^1 x\cos^2\beta_1 dx\,\dot{\theta}_t$$
$$-\overline{P}_1\int_0^1 x\cos\beta_1 y_{1,xx}dx+\varepsilon^2\left(\frac{l}{l_1}\right)^2\int_0^1 x\cos\beta_1 y_{1,xxxx}dx$$
$$-\gamma\left[-\frac{r_2}{l_1}\theta_2+\frac{r_1}{l_1}\theta_1-\frac{r_t}{l_1}\theta_t\sin\beta_1+\int_0^1 y_{1,x}w^*_{1,x}dx\right.$$
$$\left.+\int_0^1\left(\frac{r_t}{l_1}\right)\cos\beta_1\theta_t w^*_{1,x}dx\right]\int_0^1 x\cos\beta_1 w^*_{1,xx}dx=0. \quad (32)$$

Similar manipulations of Eq. (15) for the second span (first multiplying $-r_3/l_2(x-1)\cos\beta_2$ and then integrating) give

$$-\left(\frac{l_2}{l}\right)^2\int_0^1(x-1)\cos\beta_2 y_{2,tt}dx+\left(\frac{l_2}{l}\right)^2\cos^2\beta_2\int_0^1\left(\frac{r_t}{l_2}\right)(x-1)^2dx\,\ddot{\theta}_t+2s\left(\frac{l_2}{l}\right)\int_0^1(x-1)\cos\beta_2 y_{2,xt}dx$$
$$-2s\left(\frac{l_2}{l}\right)\left(\frac{r_t}{l_2}\right)\int_0^1(x-1)\cos^2\beta_2 dx\,\dot{\theta}_t+\overline{P}_2\int_0^1(x-1)\cos\beta_2 y_{2,xx}dx-\varepsilon^2\left(\frac{l}{l_2}\right)^2\int_0^1(x-1)\cos\beta_2 y_{2,xxxx}dx$$
$$+\gamma\left(-\frac{r_3}{l_2}\theta_3+\frac{r_2}{l_2}\theta_2+\frac{r_t}{l_2}\theta_t\sin\beta_2+\int_0^1 y_{2,x}w^*_{2,x}dx-\int_0^1\left(\frac{r_t}{l_2}\right)\cos\beta_2\theta_t w^*_{2,x}dx\right)\int_0^1(x-1)\cos\beta_2 w^*_{2,xx}dx=0. \quad (33)$$

Addition of (32), (33), and (25) leads to a new equation for the tensioner arm, which is not given here for the sake of brevity. This process is similar in spirit to pre-multiplying by the transpose of the transformation matrix to retain a symmetric form when transforming coordinates in symmetric, discrete equations of motion.

Equations (13)–(24) and this new tensioner equation can be expressed compactly in the following extended operator form:

$$\mathbf{M}\ddot{\mathbf{Y}}+\mathbf{G}\dot{\mathbf{Y}}+\mathbf{K}\mathbf{Y}=\mathbf{F} \quad (34)$$

$$\mathbf{Y}=\{y_1,y_2,y_3,\theta_1,\theta_2,\theta_3,\theta_t\}^T \quad (35)$$

$$\mathbf{MY}=\begin{bmatrix}\left(\frac{l_1}{r_t}\right)\left(\frac{l_1}{l}\right)^2 y_1+\left(\frac{l_1}{l}\right)^2\cos\beta_1 x\,\theta_t\\ \left(\frac{l_2}{r_t}\right)\left(\frac{l_2}{l}\right)^2 y_2-\left(\frac{l_2}{l}\right)^2\cos\beta_2(x-1)\,\theta_t\\ \left(\frac{l_3}{r_t}\right)\left(\frac{l_3}{l}\right)^2 y_3\\ m_1\left(\frac{r_1}{r_t}\right)\theta_1\\ m_2\left(\frac{r_2}{r_t}\right)\theta_2\\ m_3\left(\frac{r_3}{r_t}\right)\theta_3\\ \left(\frac{l_1}{l}\right)^2\int_0^1 x\cos\beta_1 y_1dx-\left(\frac{l_2}{l}\right)^2\int_0^1(x-1)\cos\beta_2 y_2dx+M_d\theta_t\end{bmatrix} \quad (36)$$

$$\mathbf{GY}=\begin{bmatrix}-2s\left(\frac{l_1}{l}\right)\left(\frac{l_1}{r_t}\right)y_{1,x}-2s\left(\frac{l_1}{l}\right)\cos\beta_1\theta_t\\ -2s\left(\frac{l_2}{l}\right)\left(\frac{l_2}{r_t}\right)y_{2,x}+2s\left(\frac{l_2}{l}\right)\cos\beta_2\theta_t\\ -2s\left(\frac{l_3}{l}\right)\left(\frac{l_3}{r_t}\right)y_{3,x}\\ 0\\ 0\\ 0\\ -s\left[\left(\frac{l_1}{l}\right)\int_0^1 2x\cos\beta_1 y_{1,x}dx-\left(\frac{l_2}{l}\right)\int_0^1 2(x-1)\cos\beta_2 y_{2,x}dx\right]\end{bmatrix} \quad (37)$$

$$\mathbf{KY}=\{K_1,K_2,K_3,K_4,K_5,K_6,K_7\}^T \tag{38}$$

$$K_1=-\left(\frac{l_1}{r_t}\right)\overline{P}_1 y_{1,xx}+\varepsilon^2\left(\frac{l}{l_1}\right)^2\left(\frac{l_1}{r_t}\right)y_{1,xxxx}-\gamma\left(\frac{l_1}{r_t}\right)\int_0^1 w^*_{1,x}y_{1,x}dx\,w^*_{1,xx}-\gamma\left(\frac{r_1}{r_t}\right)w^*_{1,xx}\theta_1+\gamma\left(\frac{r_2}{r_t}\right)w^*_{1,xx}\theta_2+\gamma\sin\beta_1 w^*_{1,xx}\theta_t-\gamma\cos\beta_1 w^*_1(1)w^*_{1,xx}\theta_t \tag{39}$$

$$K_2=-\left(\frac{l_2}{r_t}\right)\overline{P}_2 y_{2,xx}+\varepsilon^2\left(\frac{l}{l_2}\right)^2\left(\frac{l_2}{r_t}\right)y_{2,xxxx}-\gamma\left(\frac{l_2}{r_t}\right)\int_0^1 w^*_{2,x}y_{2,x}dx\,w^*_{2,xx}-\gamma\left(\frac{r_2}{r_t}\right)w^*_{2,xx}\theta_2+\gamma\left(\frac{r_3}{r_t}\right)w^*_{2,xx}\theta_3-\gamma\sin\beta_2 w^*_{2,xx}\theta_t-\gamma\cos\beta_2 w^*_2(0)w^*_{2,xx}\theta_t \tag{40}$$

$$K_3=-\left(\frac{l_3}{r_t}\right)\overline{P}_3 y_{3,xx}+\varepsilon^2\left(\frac{l}{l_3}\right)^2\left(\frac{l_3}{r_t}\right)y_{3,xxxx}-\gamma\left(\frac{l_3}{r_t}\right)\int_0^1 w^*_{3,x}y_{3,x}dx\,w^*_{3,xx}+\gamma\left(\frac{r_1}{r_t}\right)w^*_{3,xx}\theta_1-\gamma\left(\frac{r_3}{r_t}\right)w^*_{3,xx}\theta_3 \tag{41}$$

$$K_4=\gamma\left(\frac{r_1}{r_t}\right)\int_0^1 w^*_{1,x}y_{1,x}dx-\gamma\left(\frac{r_1}{r_t}\right)\int_0^1 w^*_{3,x}y_{3,x}dx+\gamma\left(\frac{r_1}{r_t}\right)\left(\frac{r_1}{l_1}+\frac{r_1}{l_3}\right)\theta_1-\gamma\left(\frac{r_1}{r_1}\right)\left(\frac{r_2}{l_1}\right)\theta_2-\gamma\left(\frac{r_1}{l_1}\right)[\sin\beta_1-\cos\beta_1 w^*_1(1)]\theta_t-\gamma\left(\frac{r_1}{r_t}\right)\left(\frac{r_3}{l_3}\right)\theta_3 \tag{42}$$

$$K_5=-\gamma\left(\frac{r_2}{r_t}\right)\int_0^1 w^*_{1,x}y_{1,x}dx+\gamma\left(\frac{r_2}{r_t}\right)\int_0^1 w^*_{2,x}y_{2,x}dx-\gamma\left(\frac{r_2}{r_t}\right)\times\left(\frac{r_1}{l_1}\right)\theta_1+\gamma\left(\frac{r_2}{r_t}\right)\left(\frac{r_2}{l_1}+\frac{r_2}{l_2}\right)\theta_2-\gamma\left(\frac{r_2}{r_t}\right)\left(\frac{r_3}{l_2}\right)\theta_3+\gamma\left(\frac{r_2}{l_1}\right)\times[\sin\beta_1-\cos\beta_1 w^*_1(1)]\theta_t+\gamma\left(\frac{r_2}{l_2}\right)[\sin\beta_2+\cos\beta_2 w^*_2(0)]\theta_t \tag{43}$$

$$K_6=-\gamma\left(\frac{r_3}{r_t}\right)\int_0^1 w^*_{2,x}y_{2,x}dx+\gamma\left(\frac{r_3}{r_t}\right)\int_0^1 w^*_{3,x}y_{3,x}dx-\gamma\left(\frac{r_3}{r_t}\right)\left(\frac{r_1}{l_3}\right)\theta_1-\gamma\left(\frac{r_3}{r_t}\right)\left(\frac{r_2}{l_2}\right)\theta_2-\gamma\left(\frac{r_3}{l_2}\right)[\sin\beta_2+\cos\beta_2 w^*_2(0)]\theta_t+\gamma\left(\frac{r_3}{r_t}\right)\left(\frac{r_3}{l_2}+\frac{r_3}{l_3}\right)\theta_3 \tag{44}$$

$$\begin{aligned}K_7=&-\gamma\sin\beta_1\int_0^1 w^*_{1,x}y_{1,x}dx+\gamma\cos\beta_1 w^*_{1,x}(1)\int_0^1 w^*_{1,x}y_{1,x}dx+\gamma\sin\beta_2\int_0^1 w^*_{2,x}y_{2,x}dx+\gamma\cos\beta_2 w^*_{2,x}(0)\int_0^1 w^*_{2,x}y_{2,x}dx\\&-\left[\gamma\left(\frac{r_1}{l_1}\right)\sin\beta_1-\gamma\left(\frac{r_1}{l_1}\right)\cos\beta_1 w^*_1(1)\right]\theta_1-\left[-\gamma\left(\frac{r_2}{l_1}\right)\sin\beta_1-\gamma\left(\frac{r_2}{l_2}\right)\sin\beta_2+\gamma\left(\frac{r_2}{l_1}\right)\cos\beta_1 w^*_1(1)-\gamma\left(\frac{r_2}{l_2}\right)\cos\beta_2 w^*_2(0)\right]\theta_2\\&+\left[\gamma\left(\frac{r_t}{l_1}\right)\sin^2\beta_1+\gamma\left(\frac{r_t}{l_2}\right)\sin^2\beta_2+k_s+\overline{P}_1\left(\frac{r_t}{l_1}\right)\cos^2\beta_1+\overline{P}_2\left(\frac{r_t}{l_2}\right)\cos^2\beta_2+\gamma\left(\frac{r_t}{l_1}\right)\cos^2\beta_1(w^*_1(1))^2\right.\\&\left.+\gamma\left(\frac{r_t}{l_2}\right)\cos^2\beta_2(w^*_2(0))^2-2\gamma\left(\frac{r_t}{l_1}\right)\sin\beta_1\cos\beta_1 w^*_1(1)+2\gamma\left(\frac{r_t}{l_2}\right)\sin\beta_2\cos\beta_2 w^*_2(0)\right]\theta_t+\left[\gamma\left(\frac{r_3}{l_2}\right)\sin\beta_2\right.\\&\left.+\gamma\left(\frac{r_3}{l_2}\right)\cos\beta_2 w^*_2(0)\right]\theta_t\end{aligned} \tag{45}$$

where $M_d=m_t+1/3[(r_t/l_1)(l_1/l)^2\cos^2\beta_1+(r_t/l_2)(l_2/l)^2\cos^2\beta_2]$. The external force vector **F** remains the same as (27). After these manipulations, the system seems more complicated. The key advantage, however, is that the new operators **M** and **K** are symmetric and **G** is skew-symmetric with an inner product analogous to (29).

## Galerkin Discretization

The mathematical structure of the extended operator form (34)–(45) and the trivial boundary conditions in (31) allow classical Galerkin discretization. The extended variable **Y** is expanded in a series of basis functions as

$$\mathbf{Y}=\sum_{k=1}^{N_1+N_2+N_3+4} a_k(t)\psi_k(x),$$

$$\begin{aligned}&\psi_k=\{\sin(k\pi x),0,0,0,0,0,0\}^T \quad k=1,2,\ldots N_1,\\&\psi_k=\{0,\sin(m\pi x),0,0,0,0,0\}^T \quad k=N_1+1,\ldots,N_1+N_2\\&\qquad m=k-N_1,\\&\psi_k=\{0,0,\sin(n\pi x),0,0,0,0\}^T \quad k=N_1+N_2+1,\ldots,N_1+N_2+N_3 \quad n=k-(N_1+N_2),\\&\psi_k=\{0,0,0,1,0,0,0\}^T \quad k=N_1+N_2+N_3+1,\\&\psi_k=\{0,0,0,0,1,0,0\}^T \quad k=N_1+N_2+N_3+2,\\&\psi_k=\{0,0,0,0,0,1,0\}^T \quad k=N_1+N_2+N_3+3,\\&\psi_k=\{0,0,0,0,0,0,1\}^T \quad k=N_1+N_2+N_3+4\end{aligned} \tag{46}$$

where $N_i$ is the number of basis functions for the $i$th span. The $\psi_k$ are global comparison functions where each one describes a deflection of the entire system and satisfy all boundary conditions.

**Table 1 Physical properties of the example system, from which nominal dimensionless parameters are calculated**

| | | | |
|---|---|---|---|
| Pulley radius $r_1$ | 0.0889 m | Pulley center $(x_1,y_1)$ | (0.5525,0.0556) m |
| Pulley radius $r_2$ | 0.0452 m | Pulley center $(x_2,y_2)$ | (0.3477,0.05715) m |
| Pulley radius $r_3$ | 0.02697 m | Pulley center $(x_3,y_3)$ | (0,0) |
| Tensioner arm $r_t$ | 0.097 m | Pulley center $(x_t,y_t)$ | (0.2508,0.0635) m |
| Rotational inertia $J_1$ | 0.07248 kg·m$^2$ | Belt modulus $EA$ | 120000N |
| Rotational inertia $J_2$ | 0.000293kg·m$^2$ | Initial tension $P_0$ | 300N |
| Rotational inertia $J_3$ | 0.000293kg·m$^2$ | Belt mass density $m$ | 0.1029kg/m |
| Rotational inertia $J_t$ | 0.001165kg·m$^2$ | Tensioner stiffness $k_r$ | 116.4N·m/rad |
| Span length $l_1$ | 0.1548 m | Alignment angle $\beta_1$ | 135.79° |
| Span length $l_2$ | 0.3449 m | Alignment angle $\beta_2$ | 178.74° |
| Span length $l_3$ | 0.5518 m | Tensioner rotation $\theta_{tr}$ | 0.1688 rad |

They form a complete set. After substitution of (46) into (26) (with $w\rightarrow y$), the error (residual) is constrained to be orthogonal to the $\psi_k$ using the inner product (29). This gives the equations of motion and eigenvalue problem

$$[\mathbf{M}]\ddot{\mathbf{A}}+[\mathbf{G}]\dot{\mathbf{A}}+[\mathbf{K}]\mathbf{A}=\mathbf{f} \tag{47}$$

$$-\omega^2[\mathbf{M}]\rho+i\omega[\mathbf{G}]\rho+[\mathbf{K}]\rho=\mathbf{0},\quad \mathbf{A}=\rho e^{i\omega t} \tag{48}$$

$$\rho=\{a_1,a_2,\ldots a_{N_1+N_2+N_3+4}\}^T \tag{49}$$

$$M_{ij}=\langle M\psi_j,\psi_i\rangle\quad G_{ij}=\langle G\psi_j,\psi_i\rangle\quad K_{ij}=\langle K\psi_j,\psi_i\rangle,\quad i,j=1\ldots N_1+N_2+N_3+4 \tag{50}$$

$$\mathbf{f}=\{f_1,f_2,\ldots f_{N_1+N_2+N_3+4}\}^T\quad f_i=\langle F,\psi_i\rangle,\quad i=1\ldots N_1+N_2+N_3+4 \tag{51}$$

where the inner product is an extended one similar to that in (29). The matrices [**M**], [**K**], and [***G***] inherit the symmetry/skew-symmetry of the corresponding differential operators. These properties ensure that the eigenvalues are purely imaginary, as required for a conservative gyroscopic system.

The present method has several advantages over continuum characteristic equation approaches, [5,8]: (1) It is easy to implement because of the simple basis functions and trivial boundary conditions. (2) It is efficient, accurate, and greatly reduces computational time. (3) It does not require a user-specified bandwidth to search for natural frequencies. (4) It is numerically robust and free of missing/false natural frequency concerns. (5) Because the method uses Galerkin discretization, all properties of that approach are retained, including convergence of the eigenvalues from above. (6) Dynamic response analysis is trivial to implement using (47).

## Results and Discussion

In this section, results are presented for a prototypical three-pulley system (Fig. 1); the physical properties are shown in Table 1. Because the motion of the crankshaft ($\theta_1$) is typically prescribed in practical applications, it is treated as a specified excitation source and $\theta_1=0$ in the following free-vibration analysis. Special attention is given to the interaction between span 3 and the rest of the system because this span is bounded by fixed pulleys, and its motion is decoupled from the rest of the system for vanishing bending stiffness.

Figures 2 and 3 show that when the belt bending stiffness is small ($\varepsilon=0.01$), there are two distinct types of modes: pulley rotationally dominant vibration modes and span transversely dominant vibration modes. These mode types are similar to the results computed with the string model except that here span 3 has some small transverse deflection (as opposed to being straight in the string model, [5]). These two figures also show that when bending stiffness increases, the magnitude of the span 3 deflection increases accordingly, and the relative magnitudes of the initially dominant components diminish. The coupling between the spans and pulleys becomes stronger for these modes.

Figure 4 describes a type of vibration mode not captured with the string model. When $\varepsilon$ is small ($\approx 0.01$), the dominant motion is the transverse motion of span 3 while all other components have small motions. But when $\varepsilon$ is appreciable, say $\varepsilon=0.07$ or $\varepsilon=0.1$, the modal amplitudes of other components are significant, indicating a strongly coupled mode. Note that as bending stiffness decreases, the span 3 deflection increases markedly relative to other deflections. In the limit as $\varepsilon\rightarrow 0$, span 3 is completely decoupled from the rest of the system, as in prior string model results, [5].

A key point of Figs. 2–4 is that bending stiffness induced modal coupling with spans connecting fixed center pulleys (such as span 3) provides an explanation for the observed vibration of these spans in vehicle applications. String models have no means to capture this known behavior except using parametric excitation models, [13,14], that are not relevant at the idle/low speed regions where span vibrations are commonly observed.

These figures also reveal another tendency for all types of

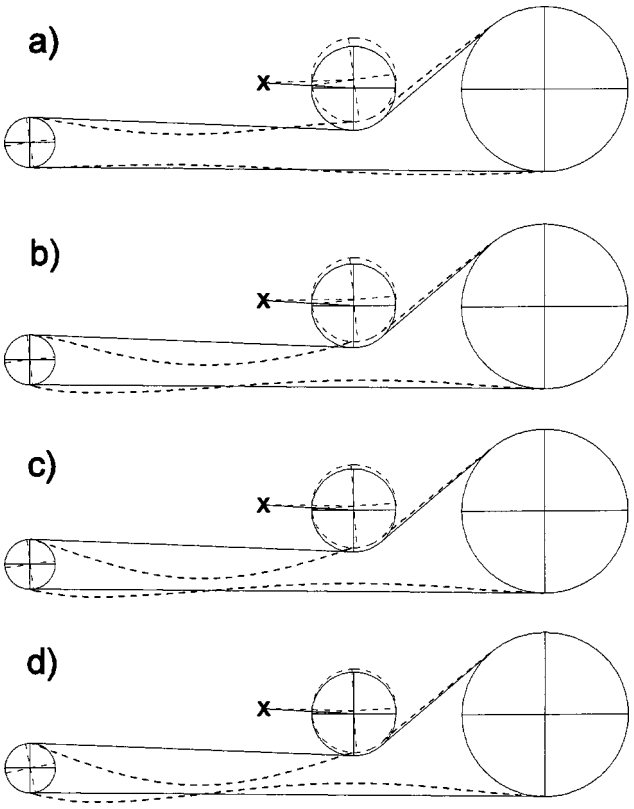


**Fig. 2 Rotationally dominant mode ($\varepsilon=0$) for increasing belt bending stiffness. The dimensionless natural frequency for $\varepsilon=0$ is $\omega=4.1205$. (*a*) $\varepsilon=0.01$, (*b*) $\varepsilon=0.04$, (*c*) $\varepsilon=0.07$, (*d*) $\varepsilon=0.1$. $s=0$, $k_s=4$, $\gamma=400$, $P_1=P_2=P_3=1$, $\beta_1=135.79°$, $\beta_2=178.74°$.**

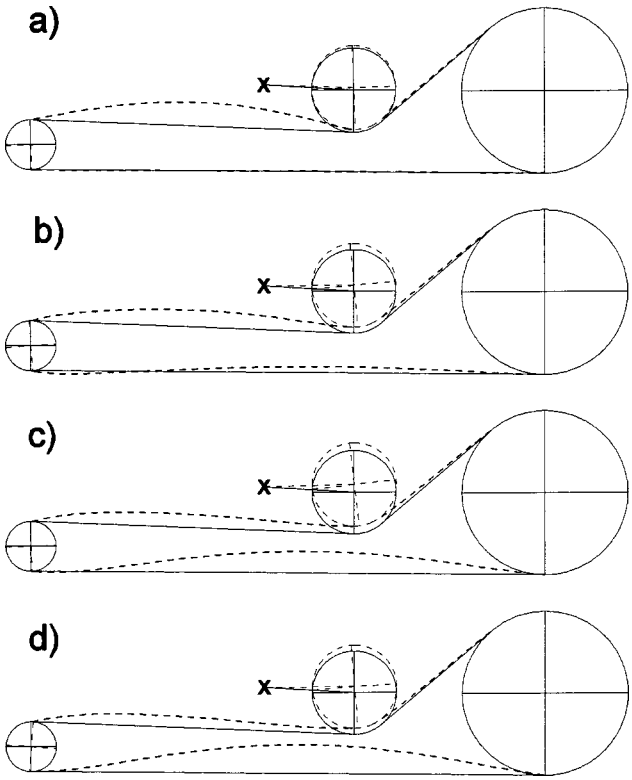


**Fig. 3 Span 2 transversely dominant mode ($\varepsilon=0$) for increasing belt bending stiffness. The dimensionless natural frequency for $\varepsilon=0$ is $\omega=3.0951$. (*a*) $\varepsilon=0.01$, (*b*) $\varepsilon=0.04$, (*c*) $\varepsilon=0.07$, (*d*) $\varepsilon=0.1$. $s=0$, $k_s=4$, $\gamma=400$, $P_1=P_2=P_3=1$, $\beta_1=135.79°$, $\beta_2=178.74°$.**

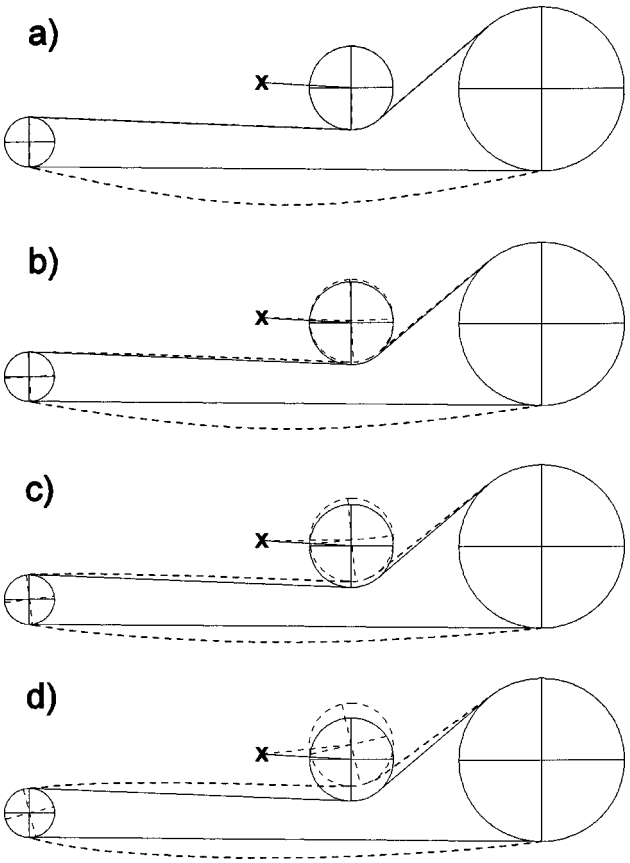


**Fig. 4 Span 3 transversely dominant mode ($\varepsilon=0$) for increasing belt bending stiffness. The dimensionless natural frequency for $\varepsilon=0$ is $\omega=1.9968$. (*a*) $\varepsilon=0.01$, (*b*) $\varepsilon=0.04$, (*c*) $\varepsilon=0.07$, (*d*) $\varepsilon=0.1$. $s=0$, $k_s=4$, $\gamma=400$, $P_1=P_2=P_3=1$, $\beta_1=135.79°$, $\beta_2=178.74°$.**

modes: When the belt bending stiffness increases or the span tensions decrease (that is, as $\varepsilon$ increases), the magnitude disparities between the dominant components and the other parts of the system decrease. In essence, the distinction between different types of modes becomes less pronounced. Eventually, this classification of vibration modes does not apply any more. This can be seen from the cases of $\varepsilon=0.1$ in Figs. 2–4 where all the spans and pulleys have nearly the same order amplitude. In this case, all the pulley and span vibrations are strongly coupled, and the system's dynamic operating condition response is quite different from that when belt bending stiffness is neglected. $\varepsilon=0.04$ and $\varepsilon=0.07$ fall into the transition region between the string and the beam models. For practical serpentine belt drives, manufacturers approximate the bending stiffness of a poly-ribbed belt typical of vehicle applications by $EI=(m-1)2.867\times10^{-3}\,\mathrm{N\cdot m^2}$ (where $m$ is the number of ribs). Notice that $\varepsilon$ depends on the relative magnitude of bending stiffness and belt tension because $\varepsilon^2=EI/P_0l^2$. For the range of belts and span tensions in use, reasonable values of $\varepsilon$ fall in the range $0.01\leqslant\varepsilon\leqslant0.12$.

Figure 5 shows the relationship between the natural frequencies and the bending stiffness. As bending stiffness increases, some natural frequencies decrease when the belt bending stiffness is small. This interesting phenomenon is inconsistent with the linear system requirement that natural frequencies increase with stiffness. The root cause is that although increased bending stiffness tends to increase the natural frequencies for a fixed steady state, the increased bending stiffness changes the steady state, which also influences the natural frequencies, as shown in the dynamic Eqs. (39)–(45). This change in the steady state causes some natural frequencies to decrease with increasing bending stiffness. The mechanism is that increased bending stiffness increases the steady state curvature, and correspondingly the coupling between the belt spans and pulleys also increases, [11]. The increased belt-pulley coupling causes the strange phenomenon because for transversely dominant modes the increased belt-pulley coupling is similar to relaxing constraints at the boundaries of the dominant span. Numerical experiments confirm that if the steady state is fixed (let the steady state terms marked by asterisk in the Eqs. (39)–(45) be

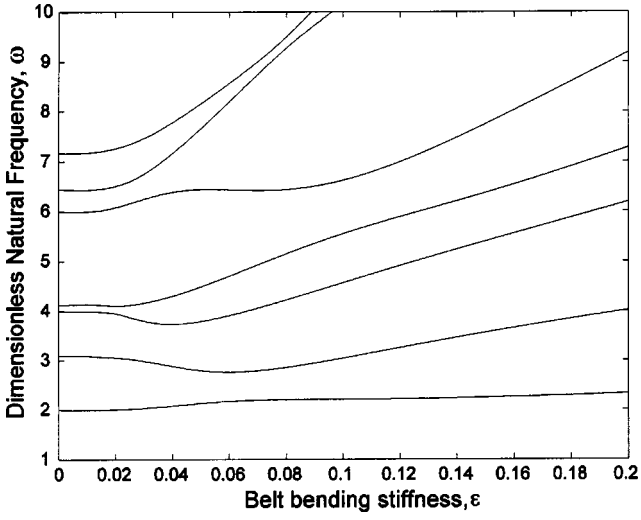


**Fig. 5 Natural frequency spectrum for varying belt bending stiffness. $s=0$, $k_s=4$, $\gamma=400$, $P_1=P_2=P_3=1$, $\beta_1=135.79°$, $\beta_2=178.74°$.**

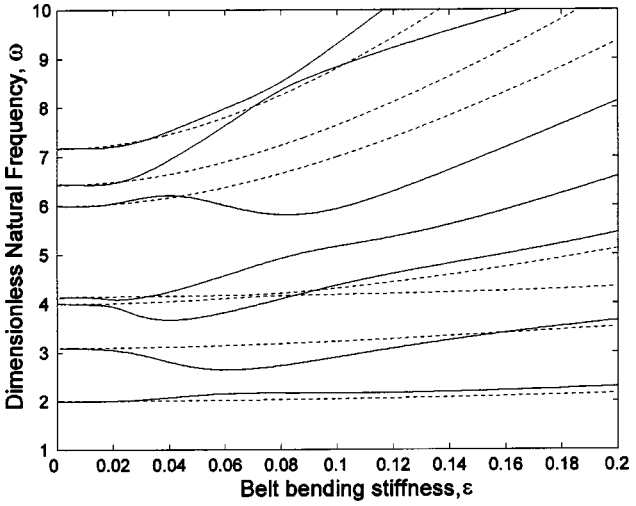


**Fig. 6 Natural frequency spectrum for varying belt bending stiffness. — — —, fix steady state; ——, fix bending stiffness value in (39)–(45). $s=0$, $k_s=4$, $\gamma=400$, $P_1=P_2=P_3=1$, $\beta_1=135.79°$, $\beta_2=178.74°$.**

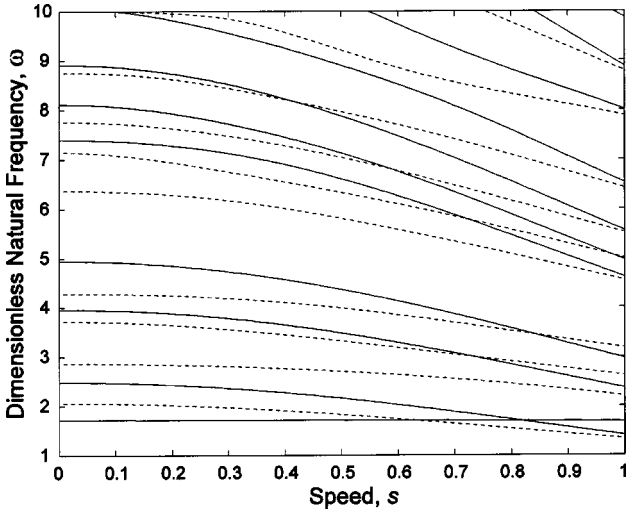


**Fig. 8 Natural frequency spectrum for varying belt speed. ——, $\eta=0$ ($\beta_1=68.53°$, $\beta_2=111.47°$); — — —, $\eta=0.78$ ($\beta_1=135.79°$, $\beta_2=178.74°$). $\varepsilon=0.04$, $k_s=4$, $\gamma=400$, $P_1=P_2=P_3=1$.**

assumed constant), then all the natural frequencies increase as the belt bending stiffness is increased (Fig. 6), which is consistent with our physical intuition. If the changing belt bending stiffness only influences the steady state while the value of $\varepsilon^2$ in (39)–(45) is held fixed, then Fig. 6 shows that some natural frequencies decrease due to the increased belt-pulley interactions. Eventually for large enough $\varepsilon$, further increases in bending stiffness lead to monotonic increases in all natural frequencies (Fig. 5).

The relationship between the dimensionless natural frequencies and belt speed is shown in Fig. 7. When the bending stiffness is small ($\varepsilon=0.01$), the spectrum is similar to the string model. The frequencies of transversely dominant modes decrease quickly with speed, but speed has little influence on the natural frequencies of rotationally dominant modes. As the bending stiffness increases to $\varepsilon=0.1$, the influence of speed on the natural frequencies is markedly smaller, and there is no clear distinction between rotationally dominant modes or transversely dominant modes. Notice that the natural frequencies do not decrease monotonically as they do for the single span moving string or beam systems.

Generally, only four or five basis functions per span are needed for all natural frequencies of practical importance to converge to within 3%. More terms are needed for increasing speed and higher natural frequencies, as discussed by Jha and Parker [21]. For the string model critical speed $s=1$ and $\omega<11$ in Fig. 7, six terms per span are needed for the eight natural frequencies to convergence to within 3% with $\varepsilon=0.1$; for $\varepsilon=0.01$, 16 terms per span are required for the 16 natural frequencies.

Through changing the orientation of the tensioner arm, the effects of the tensioner effectiveness $\eta$ on the natural frequencies are described in Figs. 8 and 9. $\eta$ is an indicator of the ability of the tensioner to maintain constant *tractive* belt tension despite changes in belt speed or accessory torques [7]. For a general $n$ pulley system with the tensioner pulley as pulley $i$, one has, [11],

$$\eta=\frac{1}{\dfrac{\Sigma_{j=1}^{n} l_j}{\gamma}\left[\dfrac{P_i\left(\dfrac{1}{l_{i-1}}\cos^2\beta_1+\dfrac{1}{l_i}\cos^2\beta_2\right)+k_s}{(\sin\beta_1-\sin\beta_2)^2}\right]+1} \tag{52}$$

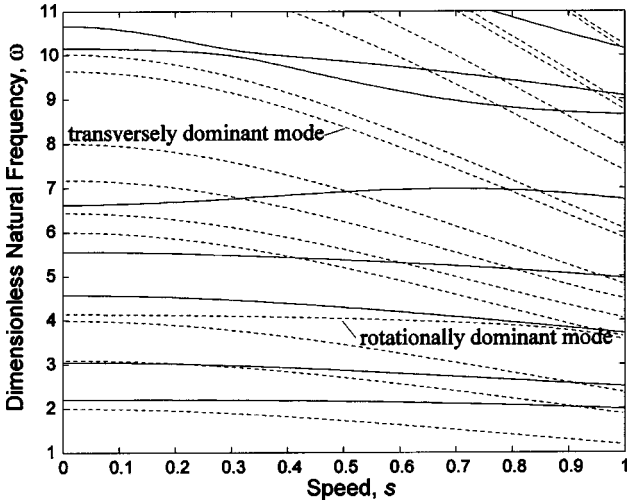


**Fig. 7 Natural frequency spectrum for varying belt speed. ——, $\varepsilon=0.1$; — — —, $\varepsilon=0.01$. $k_s=4$, $\gamma=400$, $P_1=P_2=P_3=1$, $\beta_1=135.79°$, $\beta_2=178.74°$.**

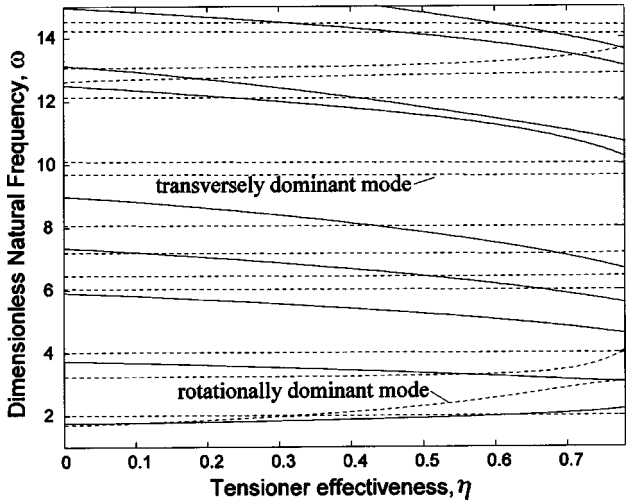


**Fig. 9 Natural frequency spectrum for varying tensioner effectiveness $\eta$. ——, $\varepsilon=0.1$; — — —, $\varepsilon=0.01$. $s=0$, $k_s=4$, $\gamma=400$, $P_1=P_2=P_3=1$.**

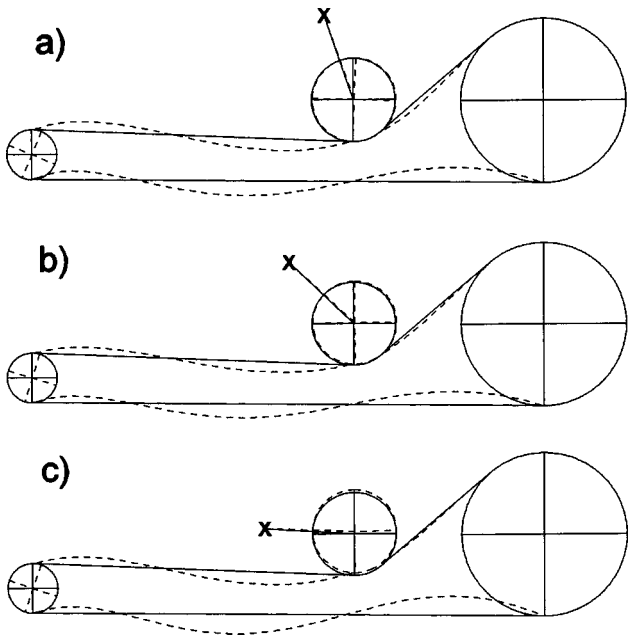


**Fig. 10 Fifth vibration mode for varying tensioner effectiveness $\eta$. (*a*) $\eta=0$ ($\beta_1=68.53°$, $\beta_2=111.47°$), (*b*) $\eta=0.5$ ($\beta_1=95.53°$, $\beta_2=138.47°$), (*c*) $\eta=0.78$ ($\beta_1=135.79°$, $\beta_2=178.74°$). $\varepsilon=0.1$, $s=0$, $k_s=4$, $\gamma=400$, $P_1=P_2=P_3=1$.**

For well-designed systems, $\eta$ is close to unity, while for poorly designed systems, $\eta$ is away from unity. Figure 8 shows how the tensioner effectiveness $\eta$ influences the relationship between natural frequencies and belt speed. For larger $\eta=0.78$, the decrease rate of the natural frequencies with belt speed is smaller than that for $\eta=0$ because of the stronger ability of the tensioner to compensate for the tension loss induced by belt speed due to centrifugal action ($\eta=0$ and $\eta=0.78$ can be visualized in Fig. 10). Similar behavior occurs with the string model, [5]. Further inspection of Figs. 7 and 8 reveals that for the properly designed system with $\eta=0.78$, the decrease rate of the natural frequencies with speed in Fig. 8 ($\varepsilon=0.04$) is between the two cases $\varepsilon=0.01$ and $\varepsilon=0.1$ in Fig. 7. This is because $\varepsilon=0.04$ falls in the transition region between the string and beam models. Speed has its strongest effect for small $\varepsilon$.

Figure 9 shows the relationship between natural frequencies and the tensioner effectiveness $\eta$ for different bending stiffness. The variation of $\eta$ is caused solely by changing the tensioner orientation $\beta_{1,2}$. For small bending stiffness, only rotationally dominant modes are influenced significantly while transverse dominant modes are insensitive to the orientation of the tensioner. This agrees with conclusions from the string model, [5,8]. As $\eta$ increases, the natural frequencies of rotationally dominant modes increase. Physically, this is because larger $\eta$ means the corresponding tensioner orientation provides increased resistance torque from the belts and makes it more difficult for the tensioner to rotate around its pivot (Fig. 10). This increases the effective rotational stiffness of the tensioner. Transverse dominant modes are insensitive to this effect.

For significant bending stiffness (or small tension), all natural frequencies are affected when the tensioner effectiveness $\eta$ is changed (Fig. 9). Furthermore, the dominant tendency of the natural frequencies is to decrease with $\eta$, in contrast with the small $\varepsilon$ case. These differences result because of the expanded vibration mode coupling that leads to all spans and pulleys deflecting in a given mode rather than the division into rotational and transverse dominant modes. For these coupled modes with modal deflections distributed throughout the system, there are two competing effects as $\eta$ increases. The first is described above for the small $\varepsilon$ case and tends to increase the natural frequencies for modes with appreciable tensioner rotation. With higher bending stiffness, the opposing effect is from the resistance of the tensioner to deflections of the endpoints of the spans adjacent to the tensioner. For small $\eta$, the tensioner orientation is such that it strongly resists translational deflection of the tensioner pulley in the radial direction that span deflections want to move it because the rigid tensioner arm can not be compressed (Fig. 10(*a*)). In contrast, for larger $\eta$ the tensioner resistance to span endpoint deflection comes primarily from the compliant tensioner spring (Fig. 10(c)). Consequently, this effect causes the natural frequencies of coupled belt-pulley modes to decrease for increasing $\eta$. This second effect tends to dominate the first one noted above as seen by the decreasing natural frequencies in Fig. 9. The exceptions are modes dominated by tensioner rotation such as the lowest natural frequency in Fig. 9. Still, the increase rate of this natural frequency is markedly smaller for $\varepsilon=0.1$ than $\varepsilon=0.01$ because of the additional coupling with the adjacent spans and the increased resistance to span endpoint deflection for small $\eta$.

## Summary and Conclusions

Dynamic analysis is conducted for serpentine belt systems when belt bending stiffness is modeled. Free vibration about nontrivial steady motions that result from belt bending stiffness are examined. A mathematical reformulation of the governing equations leads to an extended operator form that has the mathematical structure of a conservative gyroscopic system. In contrast to prior formulations, the mixed continuum/discrete boundary conditions at the interface between the belt and the tensioner pulley are replaced by trivial boundary conditions for all spans, including those adjacent to the tensioner. This transformation admits an efficient spatial discretization using Galerkin's method applied to the structured extended operator form. The method is numerically robust and free of missing/false natural frequency concerns, while at the same time preserving the conservative gyroscopic character of the discretized model. Dynamic response calculations using the discretized model follow naturally.

Belt bending stiffness introduces a linear coupling between the belts bounded by fixed pulleys and the rest of the system. For appreciable bending stiffness (or low tension), all modes are spatially distributed and involve transverse deflections of all spans in addition to the pulley rotations, in contrast to zero bending stiffness models where the modes divide into rotational pulley and transverse span modes. This modal coupling provides a mechanism whereby pulley rotation, which is directly excited by engine torque/speed fluctuations, couples to transverse vibration of all spans, including those bounded by fixed centers. This provides an explanation for the span vibrations observed in practice that potentially lead to noise and belt fatigue failure. This mechanism applies at engine idle speeds where parametric excitation mechanisms based on higher frequency excitation, [6,13,14], do not apply.

While the natural frequencies generally increase with bending stiffness, the changes are not monotonic. For small bending stiffness, some natural frequencies initially decrease. This unusual phenomenon results because the system steady state changes with bending stiffness in a way that tends to increase compliance for deflections about steady state.

Belt speed has reduced effect on the natural frequencies as bending stiffness increases within practical ranges. In contrast to the string model where only transverse dominant modes are affected by speed, all natural frequencies change with speed as bending stiffness induced modal coupling increases. Unlike single-span moving string and beam models, serpentine drive natural frequencies do not decrease monotonically with speed.

For systems with small bending stiffness, changing the tensioner orientation to increase the tensioner effectiveness $\eta$ *increases* the natural frequencies of rotationally dominant modes while having little influence on the natural frequencies of trans-

versely dominant modes. For systems of large bending stiffness, tensioner orientation influences all natural frequencies and, for the example system, tends to *decrease* them as $\eta$ increases.

## Acknowledgment

The authors thank Mark IV Automotive/Dayco Corporation and the National Science Foundation for support of this research.

## References

[1] Barker, C. R., Oliver, L. R., and Breig, W. F., 1991, ''Dynamic Analysis of Belt Drive Tension Forces During Rapid Engine Acceleration,'' SAE Paper 910687.
[2] Hawker, L. E., 1991, ''A Vibration Analysis of Automotive Serpentine Accessory Drives Systems,'' Ph.D. dissertation, University of Windsor, Ontario.
[3] Hwang, S. J., Perkins, N. C., Ulsoy, A. G., and Meckstroth, R. J., 1994, ''Rotational Response and Slip Prediction of Serpentine Belt Drives Systems,'' ASME J. Vibr. Acoust., **116**, pp. 71–78.
[4] Leamy, M. J., and Perkins, N. C., 1998, ''Nonlinear Periodic Response of Engine Accessory Drives With Dry Friction Tensioners,'' ASME J. Vibr. Acoust., **120**, pp. 909–916.
[5] Beikmann, R. S., Perkins, N. C., and Ulsoy, A. G., 1996, ''Free Vibration of Serpentine Belt Drive Systems,'' ASME J. Vibr. Acoust., **118**, pp. 406–413.
[6] Ulsoy, A. G., Whitesell, J. E., and Hooven, M. D., 1985, ''Design of Belt-Tensioner Systems for Dynamic Stability,'' ASME J. Vibr. Acoust., **107**, pp. 282–290.
[7] Beikmann, R. S., Perkins, N. C., and Ulsoy, A. G., 1996, ''Design and Analysis of Automotive Serpentine Belt Drive Systems for Steady State Performance,'' ASME J. Mech. Des., **119**, pp. 162–168.
[8] Zhang, L., and Zu, J. W., 1999, ''Modal Analysis of Serpentine Belt Drive Systems,'' J. Sound Vib., **222**(2), pp. 259–279.
[9] Zhang, L., Zu, J. W., and Hou, Z., 2001, ''Complex Modal Analysis of Non-Self-Adjoint Hybrid Serpentine Belt Drive Systems,'' ASME J. Vibr. Acoust., **123**(Apr.), pp. 150–156.
[10] Parker, R. G., 2002, ''Efficient Eigensolution, Dynamic Response, and Eigensensitivity of Serpentine Belt Drives,'' J. Sound Vib., in press.
[11] Kong, L., and Parker, R. G., 2003, ''Equilibrium and Belt-Pulley Vibration Coupling in Serpentine Belt Drives,'' ASME J. Appl. Mech., in press.
[12] Love, A. E. H., 1944, *A Treatise on the Mathematical Theory of Elasticity*, 4th Ed., Dover, New York.
[13] Parker, R. G., and Lin, Y., 2001, ''Parametric Instability of Axially Moving Media Subjected to Multifrequency Tension and Speed Fluctuations,'' ASME J. Appl. Mech., **68**, pp. 49–57.
[14] Mockensturm, E. M., Perkins, N. C., and Ulsoy, A. G., 1996, ''Stability and Limit Cycles of Parametrically Excited, Axially Moving Strings,'' ASME J. Vibr. Acoust., **118**, pp. 346–351.
[15] Pakdemirli, M., and Ulsoy, A. G., 1997, ''Stability Analysis of an Axially Accelerating String,'' J. Sound Vib., **203**(5), pp. 815–832.
[16] Wickert, J. A., and Mote, C. D., Jr., 1990, ''Classical Vibration Analysis of Axially Moving Continua,'' ASME J. Appl. Mech., **57**, pp. 738–744.
[17] Wang, K. W., and Mote, C. D., Jr., 1986, ''Vibration Coupling Analysis of Band/Wheel Mechanical Systems,'' J. Sound Vib., **109**, pp. 237–258.
[18] Mote, C. D., Jr., and Wu, W. Z., 1985, ''Vibration Coupling in Continuous Belt and Band Systems,'' J. Sound Vib., **102**, pp. 1–9.
[19] Turnbull, P. F., Perkins, N. C., and Schultz, W. W., 1995, ''Contact-Induced Nonlinearity in Oscillating Belts and Webs,'' J. Vib. Control, **1**, pp. 459–479.
[20] Sack, R. A., 1954, ''Transverse Oscillations in Traveling Strings,'' Br. J. Appl. Phys., **5**, pp. 224–226.
[21] Jha, R. K., and Parker, R. G., 2000, ''Spatial Discretization of Axially Moving Media Vibration Problems,'' ASME J. Vibr. Acoust., **122**, pp. 290–294.

# Aeroelastic Flutter Mechanisms of a Flexible Disk Rotating in an Enclosed Compressible Fluid

**Namcheol Kang**
Graduate Student

**Arvind Raman**
Assistant Professor,
e-mail: raman@ecn.purdue.edu

School of Mechanical Engineering,
Purdue University,
West Lafayette, IN 47907

*The aeroelastic stability of a thin, flexible disk rotating in an enclosed compressible fluid is investigated analytically through a discretization of the field equations of a rotating Kirchhoff plate coupled to the acoustic oscillations of the surrounding fluid. The discretization procedure exploits Green's theorem and exposes two different gyroscopic effects underpinning the coupled system dynamics: One describes the gyroscopic coupling between the disk and acoustic oscillations, and another arises from the disk rotation. The discretized dynamical system is cast in the compact form of a classical gyroscopic system and acoustic and disk mode coupling rules are derived. For the undamped system, coupled structure-acoustic traveling waves can destabilize through mode coalescence leading to flutter instability. A detailed investigation of the effects of dissipation arising from acoustic and disk damping predicts previously unknown instability mechanisms for this system. The results are expected to be relevant for the design of high speed, low vibration, low-noise hard disk drives, and optical data storage systems.* [DOI: 10.1115/1.1631034]

## 1 Introduction

The flow-induced vibrations of thin flexible rotating disk pose significant engineering challenges in the design of high-speed hard disk drives, optical disks, floppy disks, turbomachinery, and circular saws. In data storage applications, the drive towards increased rotation speeds to maximize data throughput are continually challenged by flow-induced and aeroelastic vibrations. These vibrations contribute directly to track positioning errors of the read/write head. Furthermore, the disks are efficient sound radiators, and under certain conditions the acoustic modes of the enclosure amplify disk vibrations leading to significant noise emission from the device.

The aeroelastic stability of unenclosed rotating disks was investigated in several previous works, [1–5]. However, the present article focuses on the flutter of rotating disks in enclosed fluids, a situation more commonly observed in practice. Some works use ad hoc rotating damping operators to model the surrounding fluid, [5–7]. However, a majority of the literature uses thin hydrodynamic lubrication theory to model the coupling of the disk with a thin air film, [8–12]. These models are well suited for floppy disks or circular saws with fluid bearings where the Reynolds number in the thin air film is very small. However, most other applications such as hard disk drives, CD-ROM's, and turbomachinery, involve larger enclosures and stiffer disks. In addition, the Reynolds numbers are very high, and the Ekman boundary layers on the disk are very small compared to the enclosure dimensions. Moreover acoustic oscillations in the enclosure can couple significantly to disk vibrations. For such applications, therefore, an appropriate initial model is that of a compressible potential flow (acoustics).

The aeroelastic stability of flexible disks rotating in an enclosed compressible potential flow was first investigated by Renshaw et al. [3]. Both theoretical predictions and experimental results were presented. A key conclusion in this work was that the use of compressible potential flow modeling of the surrounding fluid overestimates the experimentally observed flutter speeds by several orders of magnitude. Additionally, the underlying mechanisms of aeroelastic flutter and issues of modal coupling of acoustic and disk vibrations were not addressed. This work has led to a general opinion in the community that compressible potential flow is fundamentally incapable of predicting accurately aeroelastic flutter in these systems.

The present work re-examines the aeroelastic flutter of a disk rotating in an enclosed compressible fluid. The main contributions of this article are (i) to use discretization and computational techniques different from [3] that are better established in the acoustic-structure interaction community, and to present for the first time the discretized equations of motion governing the coupled rotating disk and acoustic oscillations, (ii) to explain clearly the coupling rules between disk vibration and fluid oscillation modes, and to describe the process of eigenvalue veering in this coupled structure-acoustic system, (iii) to include systematically in the compressible flow model the effects of acoustic and disk material damping which were neglected in [3], (iv) to demonstrate that there are not one but three distinct aeroelastic mechanisms for the onset of traveling wave flutter in such systems, and (v) to demonstrate that the predicted flutter speeds, and modes are very much in the range of known experimental results.

## 2 Coupled Field Equations

A uniform, thin annular disk, clamped at inner radius $R_i$ and free at outer radius $R_o$, rotates about its axis at a constant angular speed $\Omega_d$ in a compressible fluid filled cavity as shown in Fig. 1. The field equations for the small amplitude transverse vibrations of the rotating disk of thickness $H$ and mass density $\rho_d$ are formulated using the Kirchhoff plate theory for an isotropic, linearly elastic plate which is modified through a rotation speed dependent membrane stress field. Accordingly, $E$ and $\nu$ are the Young's modulus and Poisson's ratio of the disk material, respectively. The equations governing an Eulerian description of the time-dependent transverse deflection of the disk, $W$, and the compressible fluid oscillations are described in an inertial, ground-fixed coordinate frame $(R, \theta, Z)$. The undeflected disk is located in the plane $Z=0$. Radial and circumferential components $\sigma_R^*$ and $\sigma_\theta^*$ of the axisymmetric membrane stress field generated by steady rota-

Contributed by the Applied Mechanics Division of THE AMERICAN SOCIETY OF MECHANICAL ENGINEERS for publication in the ASME JOURNAL OF APPLIED MECHANICS. Manuscript received by the Applied Mechanics Division, February 11, 2003; final revision, June 4, 2003. Associate Editor: O. O'Reilly. Discussion on the paper should be addressed to the Editor, Prof. Robert M. McMeeking, Chair, Department of Mechanics and Environmental Engineering, University of California–Santa Barbara, Santa Barbara, CA 93106-5070, and will be accepted until four months after final publication in the paper itself in the ASME JOURNAL OF APPLIED MECHANICS.

  

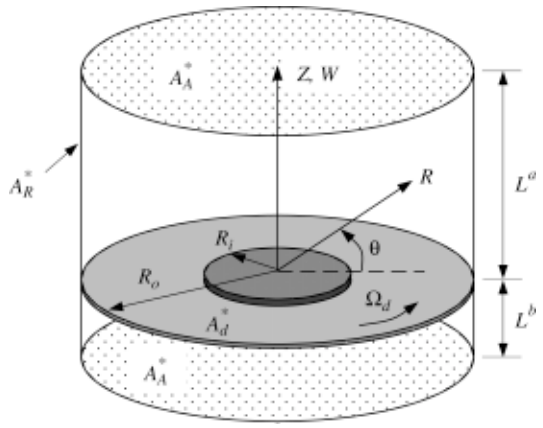


**Fig. 1 A schematic diagram of the rotating disk in an enclosed compressible, inviscid fluid**

tion are derived from classical plane-stress elasticity, [13]. An inviscid, compressible, irrotational fluid of mass density $\rho_f$ and acoustic speed $c_o$ surrounds the disk. Under the above modeling assumptions, the field equation for the rotating plate subject to an aerodynamic pressure differential $Q$ between the upper and lower face of the disk is, [4,12],

$$\rho_d H(W_{,TT}+2\Omega_d W_{,T\theta}+\Omega_d^2 W_{,\theta\theta})+\mathbf{C}[W_{,T}+\Omega W_{,\theta}]+D\nabla^4 W - \frac{H}{R}(R\sigma_r^* W_{,R})_{,R}-\frac{H}{R^2}(\sigma_\theta^* W_{,\theta})_{,\theta}=Q \tag{1}$$

where $\nabla^4$ is the biharmonic operator, a comma in the subscript denotes partial differentiation, and $D=EH^3/12(1-\nu^2)$ is the disk flexural rigidity. Note that the Eulerian description of the transverse disk deflection generates unsteady, gyroscopic, and Coriolis acceleration terms for each material particle. Further, the positive definite operator $\mathbf{C}[\cdot]$ models the disk material damping. Indeed in co-rotating coordinates the term $\mathbf{C}[W_{,T}+\Omega W_{,\theta}]$ represents a positive definite co-rotating damping. In this article we chose a simple viscoelastic model for a thin plate with $\mathbf{C}[\cdot]=\eta^* D\nabla^4(\cdot)$, where $\eta^*$ is a viscoelastic coefficient, [4]. The wave equation governing the propagation of infinitesimal disturbances in an initially quiescent, inviscid, compressible and irrotational fluid is given by

$$\nabla^2\Phi=\frac{1}{c_o^2}\Phi_{,TT} \tag{2}$$

where $\nabla^2$ is the Laplacian operator, and $\Phi(R,\theta,Z;T)$ is the velocity potential defined throughout the fluid domain. The velocity field $\mathbf{u}=\boldsymbol{\nabla}\Phi$, and the linearized fluid pressure $P(R,\theta,Z;T)$ at every point in the fluid is given by

$$P=-\rho_f\Phi_{,T} \tag{3}$$

Accordingly

$$Q=\rho_f\Phi_{,T}^a-\rho_f\Phi_{,T}^b|_{Z=0}\equiv\rho_f[[\Phi_{,T}]]_{Z=0} \tag{4}$$

where the superscripts $a$ and $b$ indicate the upper and lower cavities, respectively. Introduction of the dimensionless variables

$$r=\frac{R}{R_o},\quad z=\frac{Z}{R_o},\quad \kappa=\frac{R_i}{R_o},\quad w=\frac{W}{H},\quad l^{a,b}=\frac{L^{a,b}}{R_o},$$
$$t=\frac{T}{T_o},\quad \Omega=\Omega_d T_o,\quad T_o=\sqrt{\frac{\rho_d R_o^4 H}{D}},$$
$$\eta=\frac{\eta^*}{T_o},\quad \sigma_r=\frac{T_o^2}{\rho_d R_o^2}\sigma_r^*,\quad \sigma_\theta=\frac{T_o^2}{\rho_d R_o^2}\sigma_\theta^*,\quad \phi=\frac{T_o}{R_o H}\Phi \tag{5}$$

leads to the following coupled partial differential equations governing disk and acoustic oscillations:

$$w_{,tt}+2\Omega w_{,t\theta}+\Omega^2 w_{,\theta\theta}+\mathbf{C}_d[w_{,t}+\Omega w_{,\theta}]+\mathbf{K}_d[w]=\Lambda[[\phi_{,t}]]_{z=0} \tag{6}$$

$$\nabla^2\phi=\frac{1}{C^2}\phi_{,tt} \tag{7}$$

where

$$\mathbf{K}_d[w]=\nabla^4 w-\frac{1}{r}(r\sigma_r w_{,r})_{,r}-\frac{1}{r^2}\sigma_\theta w_{,\theta\theta}$$

$$\mathbf{C}_d[w_{,t}+\Omega w_{,\theta}]=n(\nabla^4 w_{,t}+\Omega\nabla^4 w_{,\theta}).$$

$\mathbf{K}_d[\cdot]$ is a self-adjoint and positive definite stiffness operator including membrane stress effects and $\mathbf{C}_d[w_{,t}+\Omega w_{,\theta}]$ contains a self-adjoint damping term and a circulatory term. Two key dimensionless parameters in Eq. (6) and Eq. (7) are:

(i) $\Lambda$, the weighted ratio of the fluid to disk mass density

$$\Lambda=\frac{\rho_f R_o}{\rho_d H} \tag{8}$$

Note that $\Lambda$ vanishes in vacuum implying that Eq. (6) reduces to the governing equation of a rotating disk without fluid coupling.

(ii) $C$, the ratio of acoustic speed of the fluid to a bending wave speed of the stationary disk, that is

$$C=\frac{c_o}{c_b} \tag{9}$$

where $c_b=R_o/T_o=\sqrt{D/\rho_d R_o^2 H}$ is the flexural wave speed of a flexural wave of wavelength $2\pi R_o$.

The boundary conditions for a clamped-free disk are posed in terms of the nondimensional variables as in [3]. For the surrounding compressible fluid, normal velocities satisfy the impermeability boundary conditions at the rigid walls over the area $A_R=2\pi(l^a+l^b)$, and the normal velocity matching condition on the disk surface over the area $A_d=\pi(1-\kappa^2)$. In addition, dissipation mechanisms of the acoustic oscillations are included through the introduction of a highly absorbent wall of the cavity over the area $A_A=\pi$ (Fig. 1). This boundary condition is often modeled as a simple point-impedance, $z_A^*$, [14]. The boundary conditions at each wall become

$$\boldsymbol{\nabla}\phi^{a,b}\cdot\mathbf{n}=\begin{cases}0 & on\ \ A_R\\ \mp\dot{w} & on\ \ A_d\\ -\dot{\phi}^{a,b}/z_A & on\ \ A_A\end{cases} \tag{10}$$

where, $\mathbf{n}$ is the unit normal vector on the surface, the $\mp$ sign indicates the opposing normal directions on the top and bottom side of the disk, and $z_A$ is the nondimensionalized acoustic impedance defined by $z_A=T_o z_A^*/\rho_f R_o$.

In this study, we consider the case when there is no radial gap between the disk and cylindrical rigid wall. The formulation presented here can be easily extended to the case with a radial gap. In this case, however, the Dirichlèt boundary conditions for the acoustic field in the radial gap make expensive the computations. Indeed, a much larger degree-of-freedom model for the discretized system would be needed for sufficient computational convergence. Moreover, it can be shown that the form of the disk-acoustic coupling in the discretized equations in this case remains similar to that of the present case. For this reason we restrict ourselves to the computationally simpler problem of a vanishing radial gap.

## 3 Coupled System Discretization

In what follows, the acousto-elasticity theory developed by of Dowell et al. [14] and others, is adapted to discretize the coupled disk-cavity system. The uncoupled acoustic normal modes $F_n$ of the upper and lower cavities correspond to the classical normal mode solutions for a rigid cylindrical acoustic cavity, [15]. These rigid wall-normal mode solutions satisfy the wave equation as well as the Neumann boundary conditions on all boundaries,

$$\nabla^2 F_n^{a,b} + \frac{\Lambda_n^2}{C^2} F_n^{a,b} = 0 \quad \text{with} \quad \nabla F_n^{a,b} \cdot \mathbf{n} = 0 \quad \text{on} \quad A = A_R + A_d + A_A \tag{11}$$

where $\Lambda_n$ is the $n$th uncoupled acoustical natural frequency and $F_n$ the corresponding normal mode. Application of Green's theorem to the scalar field $F_n^a \nabla^2 \phi^a - \phi^a \nabla^2 F_n^a$ defined in the upper cavity volume $V^a$ leads to, [14,16,17],

$$\int \int_{V^a} \int (F_n^a \nabla^2 \phi^a - \phi^a \nabla^2 F_n^a) dV = \int \int_A (F_n^a \nabla \phi^a \cdot \mathbf{n} - \phi^a \nabla F_n^a \cdot \mathbf{n}) dA. \tag{12}$$

Application of the boundary conditions and Eq. (11) yields

$$\frac{1}{C^2} \int_{V^a} [F_n^a \ddot{\phi}^a + (\Lambda_n^a)^2 \phi^a F_n^a] dV + \int_{A_A} F_n^a \frac{\dot{\phi}^a}{z_A} dA = -\int_{A_d} F_n^a \dot{w} dA. \tag{13a}$$

Similarly, accounting for the direction of the normal on the disk surface in the lower cavity,

$$\frac{1}{C^2} \int_{V^b} [F_n^b \ddot{\phi}^b + (\Lambda_n^b)^2 \phi^b F_n^b] dV + \int_{A_A} F_n^b \frac{\dot{\phi}^b}{z_A} dA = \int_{A_d} F_n^b \dot{w} dA. \tag{13b}$$

Equations (13) can be regarded as weak forms of the original partial differential Eq. (7). The velocity potentials and disk displacement are discretized using the rigid wall acoustic normal modes and the in vacuo structural modes, respectively, as the mutually orthogonal, complete basis functions.

$$\phi^a(r,\theta,z;t) = \sum_n a_n(t) F_n^a(r,\theta,z), \tag{14a}$$

$$\phi^b(r,\theta,z;t) = \sum_n b_n(t) F_n^b(r,\theta,z) \tag{14b}$$

$$w(r,\theta;t) = \sum_m q_m(t) \psi_m(r,\theta), \tag{15}$$

where $a_n$, $b_n$, and $q_m$ are the generalized coordinates of the upper, lower cavity and the disk, and $\psi_m$ are the in vacuo structural modes of the stationary disk, [18]. The subscript $(n_1, n_2, n_3)$ denotes $n_1$ nodal diameter, $n_2$ nodal circle, and $n_3$ $z$-directional node number of the cavity, and $(m_1, m_2)$ denotes a $m_1$ nodal diameter and $m_2$ nodal circle disk mode, respectively. Each triad $(n_1, n_2, n_3)$ is denoted simply by $n$ and each dyad $(m_1, m_2)$ is represented by $m$. Further, owing to the axisymmetry of the domain each asymmetric basis function ($n_1 \neq 0$ or $m_1 \neq 0$) is divided into the sine and cosine components. The sine and cosine components are denoted in the text and Appendix by the superscripts $S$ and $C$, respectively. Substitution of Eq. (14) and Eq. (15) into Eq. (13) and the use of the orthogonality of the rigid wall normal modes

$$\frac{1}{V^{a,b}} \int_{V^{a,b}} F_n^{a,b} F_r^{a,b} dV = \begin{cases} M_n^{a,b} & \text{when } n = r \\ 0 & \text{when } n \neq r \end{cases}$$

where

$$V^{a,b} = \pi l^{a,b} \tag{16}$$

leads to the discretized equations for the velocity potentials of the upper and lower acoustic cavities coupled to the disk:

$$\frac{V^a M_n^a}{C^2} [\ddot{a}_n + (\Lambda_n^a)^2 a_n] + A_A \sum_r \dot{a}_r C_{nr}^a = -A_d \sum_m \dot{q}_m L_{nm}^a \tag{17a}$$

$$\frac{V^b M_n^b}{C^2} [\ddot{b}_n + (\Lambda_n^b)^2 b_n] + A_A \sum_r \dot{b}_r C_{nr}^b = A_d \sum_m \dot{q}_m L_{nm}^b \tag{17b}$$

where

$$C_{nr}^{a,b} = \frac{1}{A_A} \int_{A_A} F_n^{a,b} F_r^{a,b} / z_A dA, \quad L_{nm}^{a,b} = \frac{1}{A_d} \int_{A_d} F_n^{a,b} \psi_m dA \tag{18}$$

are, respectively, the components of the acoustic damping and the disk-cavity coupling coefficient submatrices.

Galerkin discretization of the disk vibration using the in vacuo disk modes (Eq. (15)) and the substitution of Eq. (14) and Eq. (15) into Eq. (6) produces

$$\ddot{q}_m^C + 2m_1 \Omega \dot{q}_m^S + k_m q_m^C + \eta \omega_{ms}^2 (\dot{q}_m^C + m_1 \Omega q_m^S) = \Lambda A_d \left( \sum_n \dot{a}_n^C L_{nm}^{aC} - \sum_n \dot{b}_n^C L_{nm}^{bC} \right) \tag{19a}$$

$$\ddot{q}_m^S - 2m_1 \Omega \dot{q}_m^C + k_m q_m^S + \eta \omega_{ms}^2 (\dot{q}_m^S - m_1 \Omega q_m^C) = \Lambda A_d \left( \sum_n \dot{a}_n^S L_{nm}^{aS} - \sum_n \dot{b}_n^S L_{nm}^{bS} \right) \tag{19b}$$

where

$$k_m = \omega_{ms}^2 - \alpha_m - m_1^2 (\Omega^2 - \beta_m), \quad \omega_{ms}^2 = \pi \int_\kappa^1 (\tilde{\nabla}_r^4 R_m) R_m r dr$$

$$\alpha_m = \pi \int_\kappa^1 (r \sigma_r R_{m,r})_{,r} R_m dr, \ \beta_m = \pi \int_\kappa^1 \frac{1}{r} \sigma_\theta R_m^2 dr$$

and

$$\tilde{\nabla}_r^4 = \left( \frac{d^2}{dr^2} + \frac{1}{r} \frac{d}{dr} - \frac{m_1^2}{r^2} \right)^2.$$

$\omega_{ms}$ are the in vacuo natural frequencies of a stationary disk and $\alpha_m$ and $\beta_m$ are nondimensional parameters related to the speed dependence of the membrane stresses. Additionally, the disk radial eigenfunctions are normalized, $\pi \int_\kappa^1 R_m^2 r dr = 1$.

Combining Eq. (17) and Eq. (19) yields the gyroscopically coupled discretized equations governing the rotating disk and fluid oscillations in the cavity

$$\mathbf{M}\ddot{\mathbf{x}} + (\mathbf{C} + \mathbf{G})\dot{\mathbf{x}} + (\mathbf{K} + \mathbf{D})\mathbf{x} = \mathbf{0} \tag{20}$$

where

$$\mathbf{x} = [\mathbf{a}_n, \mathbf{b}_n, \mathbf{q}_m]^T$$

$$\mathbf{M} = \text{diag}[\mathbf{M}_a, \mathbf{M}_b, \mathbf{M}_q], \quad \mathbf{C} = \text{diag}[\mathbf{C}_a, \mathbf{C}_b, \mathbf{C}_q]$$

$$\mathbf{G} = [\mathbf{0}, \mathbf{0}, \mathbf{L}_{aq}; \mathbf{0}, \mathbf{0}, -\mathbf{L}_{bq}; -\mathbf{L}_{aq}^T, \mathbf{L}_{bq}^T, \mathbf{G}_q] \tag{21}$$

$$\mathbf{K} = \text{diag}[\mathbf{K}_a, \mathbf{K}_b, \mathbf{K}_q], \quad \mathbf{D} = \text{diag}[\mathbf{0}, \mathbf{0}, \mathbf{D}_q]$$

The components of the above submatrices are given in the Appendix. The mass and stiffness matrices are each composed of diag-

onal block matrices of upper, lower cavities and the rotating disk. Several unusual features of the coupled discretized dynamical system (Eq. (20)) are listed as follows:

1. The system features two intrinsically different gyroscopic effects in **G**: $(\mathbf{L}_{aq}, \mathbf{L}_{bq})$ describing the gyroscopic coupling between disk and upper and lower acoustic cavity oscillations and $\mathbf{G}_q$ arising from the disk rotation. The gyroscopic coupling between structural vibrations and acoustic oscillations of the surrounding enclosure is well known. Lord Rayleigh referred to this effect as ''gyrostatic'' coupling, [16].
2. The vanishing natural frequency of the fundamental acoustic mode renders positive semi-definite the system stiffness matrix. However the computational difficulties introduced by this singular stiffness matrix can be avoided through the introduction of a Helmholtz stiffness effect, [19].
3. The damping matrix, **C**, is composed of the symmetric acoustic and disk damping submatrices. Moreover they are diagonal so long as only the end covers of the cavity are absorbent.
4. The rotating damping arises from disk fixed material damping and leads to a skew-symmetric circulatory matrix, **D**. Note that the disk material damping also contributes to the symmetric **C** matrix.

## 4 Computational Issues

The coupled discretized equations governing disk and acoustic oscillations are a classical gyroscopic system with positive definite damping and circulatory terms. The resulting eigenvalue problem is conveniently solved using general solution techniques for gyroscopic systems, [20,21]. For simplicity, only the case of identical top and bottom enclosures is derived in this work.

The orthogonality conditions (Eq. (16)) and the expression for the coupling coefficients (Eq. (18)) lead immediately to two *disk-acoustic coupling rules*:

1. The sine modes of the disk couple only with the sine modes of cavity, and cosine modes of the disk couple only with the cosine modes of cavity.
2. A disk and an acoustic mode couple only if their nodal diameter numbers are identical.

These coupling rules are exploited in the subsequent computations by breaking down the general eigenvalue problem into several different sets of discretized equations. Each set or family of discretized equations governs the dynamics of disk and acoustic modes of a specific nodal diameter number. This partitioning of the discretized eigenvalue problem enables fast, accurate and inexpensive computations. Once the appropriate basis functions are chosen for discretization, the eigenvalues are computed in MATLAB using the state space form of the gyroscopic system, [20].

*A direct consequence of the coupled eigenvalue problem is that the system modes are no longer purely disk vibration or acoustic modes*. Coupled modes contain both disk vibration and acoustic or fluid oscillation components. Modes composed of mostly disk or acoustic components are referred to respectively as *disk* or *acoustic dominated* modes.

The convergence characteristics of the computed eigenvalues with increasing number of basis functions are now described. Representative results are now presented to determine the (2,0) disk-dominated mode frequency for a disk with parameters listed in Table 1, while rotating in an air filled cavity of $L^a = L^b = 1$ cm at supercritical speed, $\Omega_d = 40{,}000$ rpm. The disk parameters in Table 1 correspond to those of a commercial hard disk platter. Note, however, that cavity lengths in a disk drive are usually somewhat smaller than 1 cm. For a specific nodal diameter number mode, eigenvalues are calculated using as basis functions $N$ disk modes and $N^2$ acoustic modes possessing the same nodal diameter number. For example, to determine two nodal diameter modes of the system the (2,0), (2,1), . . . , (2,$N$) disk modes, and

**Table 1 Disk and acoustic cavity parameters used in most computations. These parameters correspond approximately to those of a hard disk drive platter.**

| | | |
|---|---|---|
| $R_o$ | 4.74 cm | Outer radius |
| $R_i$ | 1.56 cm | Inner radius |
| $H$ | 0.790 mm | Disk thickness |
| $\rho_d$ | 2700 kg/m$^3$ | Disk density |
| $\rho_f$ | 1.2 kg/m$^3$ | Air density |
| $E$ | 71 GPa | Young's modulus |
| $\nu$ | 0.33 | Poisson's ratio |
| $c_o$ | 343 m/sec | Speed of sound in air |

(2,0,0), (2,0,1), . . . , (2,0,$N$), . . . , (2,$N$,$N$) acoustic modes are used as basis functions in the computation. Furthermore, because both the sine and cosine modes in the upper and lower cavities are included in the discretization, the total number of basis functions considered in this computation becomes $2\times(N+2N^2)$. Figures 2(*a*) and (*b*) show the variation with $N$ of the (2,0) disk-dominated mode frequencies. Note that at supercritical speed the convergence of the (2,0) disk-dominated forward traveling wave (FTW) and that of the reflected traveling wave (RTW) are to be considered. The results show good convergence characteristics for both FTW and RTW frequencies. A choice of $N=5$ enables the prediction to within 0.02% of the asymptotic value of the (2,0) disk-dominated mode frequencies at $\Omega_d = 40{,}000$ rpm. Interestingly, predictions of RTW frequencies converge monotonically from below while those of the FTW converge from above. Similar results have also been reported recently in the literature with regard to supercritical gyroscopic systems, [22]. Computations were also performed to determine the convergence characteristics of other disk-dominated modes and also of acoustic-dominated modes at several speeds with similar results. Based on this detailed convergence study, $N=5$ was chosen for all subsequent computations. This choice enabled the prediction with sufficient accuracy of the lowest five disk and acoustic dominated modes. However, for very small air gaps increasing number of basis functions are needed to ensure sufficient accuracy.

## 5 Stationary Disk

Before investigating the dynamic behavior of a rotating disk, it is useful to understand the coupling between the stationary disk and the acoustic cavity. Although the gyroscopic term due to rotation ($\mathbf{G}_q$ in Eq. (21)) vanishes for the stationary disk, the disk couples with the acoustic modes due to acoustic-structure interaction. The frequencies of the disk and acoustic-dominated axisymmetric modes (zero nodal diameter modes) with respect to the nondimensional cavity length, $l$, (air gap) are shown in Fig. 3.

Several key observations can be made from Fig. 3. First, because the cavities on either side of the disk are identical ($l^a = l^b$

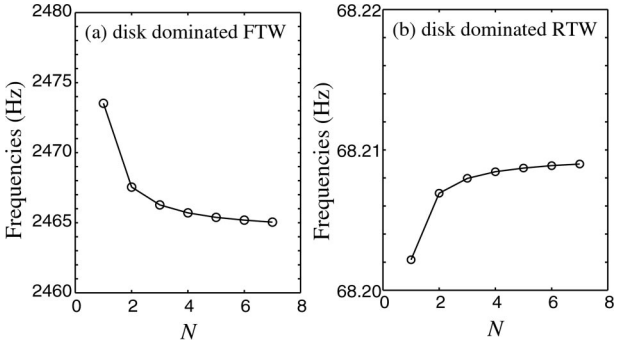


**Fig. 2 Convergence characteristics of the two nodal diameter mode at supercritical speed (40,000 rpm). Each *N* corresponds to use of $2(N+2N^2)$ basis functions in the discretization.**

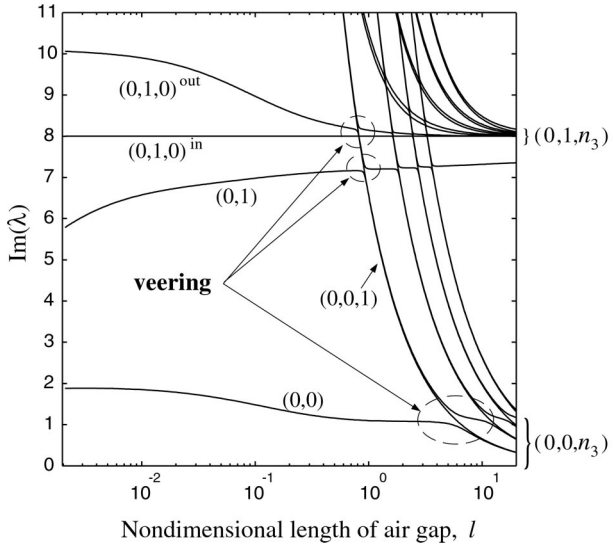


**Fig. 3 Coupled natural frequencies as a function of nondimensional cavity length, *l*, of the axisymmetric acoustic-structural modes of the stationary disk in a cylindrical acoustic cavity**

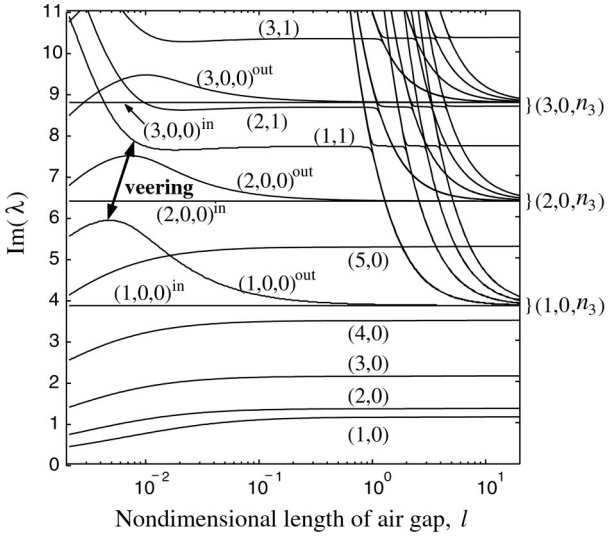


**Fig. 4 Coupled natural frequencies as a function of nondimensional cavity length, *l*, of the asymmetric acoustic-structural modes of the stationary disk in a cylindrical acoustic cavity. Note that all frequencies are repeated due to the axisymmetry of the domain.**

$=l$), there exist in-phase and out-of-phase acoustic modes (see for example the (0,1,0) acoustic mode in Fig. 3). In-phase modes describe synchronous variation of acoustic pressure in upper and lower cavities, and do not couple to disk vibration. On the other hand, out-of-phase acoustic modes couple directly to disk vibration. Clearly if the cavities are not identical, even the in-phase modes could couple to disk vibration.

Secondly, *eigenvalue veering phenomena occur whenever an out-of-phase acoustic mode frequency approaches a disk mode frequency of the same nodal diameter number*. For example the (0,0,1) acoustic-dominated mode frequency decreases with increasing air gap and veers with the (0,1) disk-dominated mode near $l \sim 0.8$. Following this the (0,1) disk-dominated mode resembles suddenly the (0,0,1) acoustic-dominated mode. The veered (0,0,1) mode in turn encounters the (0,0) disk dominated mode at $l \sim 5$ leading to yet another veering phenomenon.

Finally, the numerical results indicate that the disk-dominated zero-nodal diameter mode (0,0) frequency increases as air gaps decrease. This is because for small air gaps the uncoupled acoustic frequencies are very high and the acoustic coupling appears mainly as an added Helmholtz stiffness term. However, for large gaps, the (0,0) disk-dominated modes veer when they encounter the (0,0,1) acoustic-dominated mode. *Note that as a direct consequence of the coupling rules described earlier, the Helmholtz stiffness effects only the axisymmetric modes of the coupled system.*

In contrast to the axisymmetric modes, the variations of the natural frequencies with $l$ of the asymmetric modes of the coupled disk-cylindrical acoustic cavity system are shown in Fig. 4. First, the frequency of the (1,0) disk-dominated mode decreases with decreasing air gaps. Because such modes are not affected by the Helmhotz stiffness, they remain coupled weakly to acoustic modes of the same nodal diameter. However, because the frequencies of most acoustic modes increase with decreasing air gaps, this weak coupling appears as an added mass effect on the (1,0) disk-dominated mode. Second, in contrast to the asymmetric case, strong eigenvalue veering can occur at small air gaps. For instance the (1,1) disk dominated mode and the (1,0,0) acoustic dominated out-of-phase mode veer when $l \sim 10^{-2}$.

The presence of eigenvalue veering in such coupled structure-acoustic systems is of critical importance because small changes in system parameters can lead to the sudden change of a structure-dominated mode into an acoustic-dominated mode and vice versa. Such phenomena not only play an important role in the design of low-noise rotating disk systems but also in the onset of aeroelastic instabilities. The latter phenomenon is now discussed for the rotating disk system.

## 6 Rotating Disk (No Damping)

Disk rotation complicates significantly the coupling phenomena of the disk-cylindrical acoustic cavity system. The coupled eigenvalues depend on the gyroscopic terms arising from both disk rotation speed as well as acoustic-structure coupling. An air gap of 1 cm is chosen for all subsequent computations.

The speed dependence of the axisymmetric modes of the coupled disk-acoustic cavity system is shown in Fig. 5. Dashed lines indicating the uncoupled disk frequencies, that is disk frequencies in the absence of fluid-structure interaction ($\Lambda = 0$) are

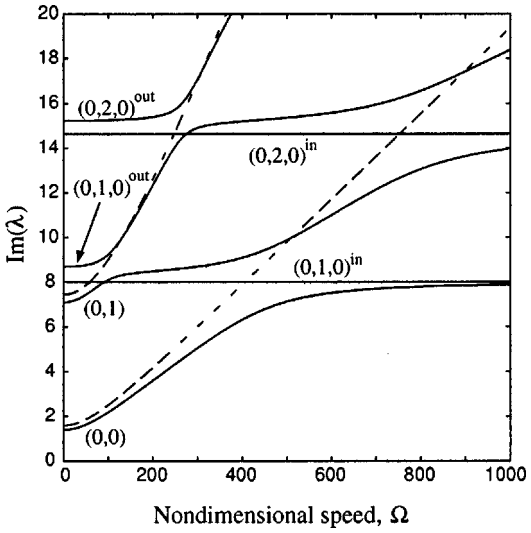


**Fig. 5 Variation with nondimensional speed of the natural frequencies of axisymmetric modes of the coupled rotating disk, acoustic cavity system. System parameters are listed in Table 1 and a cavity depth of 1 cm is chosen for the computation (solid line: coupled freq., dashed line: uncoupled freq.).**

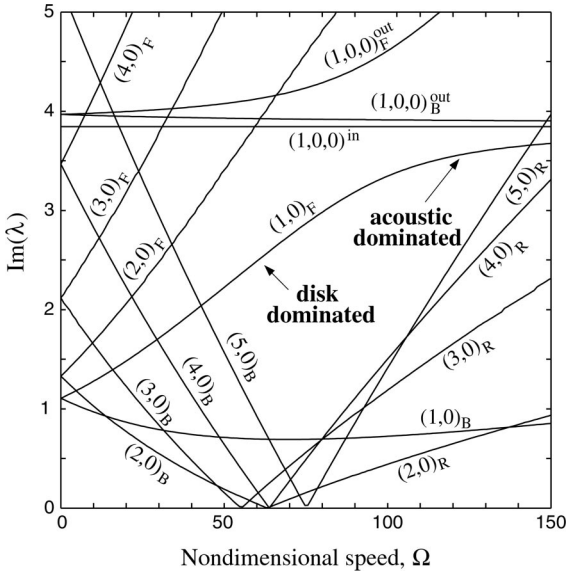


**Fig. 6 Variation with nondimensional speed ($0<\Omega<150$) of the natural frequencies of axisymmetric modes of the coupled rotating disk, acoustic cavity system. This computation is performed for the undamped system, with system parameters listed in Table 1 and a cavity depth of 1 cm is chosen for the computation.**

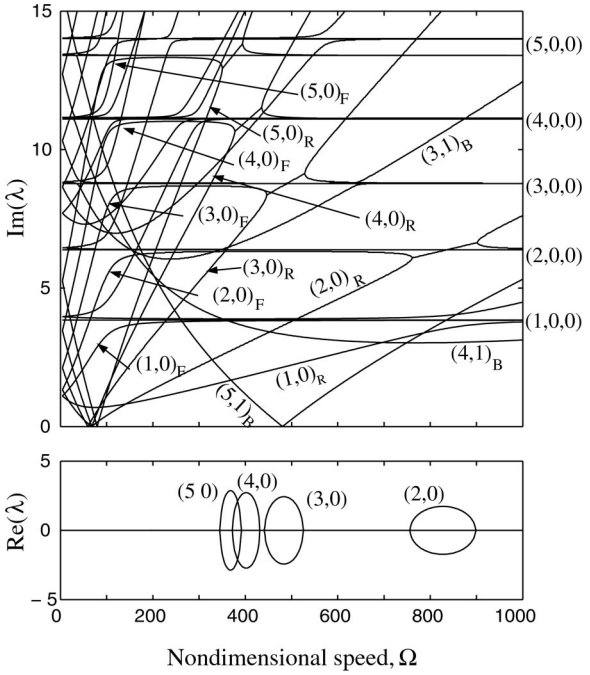


**Fig. 7 Variation with nondimensional speed ($0<\Omega<1000$) of the real and imaginary parts of the eigenvalues of axisymmetric modes of the coupled rotating disk, acoustic cavity system. This computation is performed for the undamped system, with system parameters listed in Table 1 and a cavity depth of 1 cm is chosen for the computation.**

also plotted in Fig. 5. The rotational stress terms in the stiffness operator ensure that the disk axisymmetric mode frequencies increase with increasing rotation speed. However, eigenvalue veering phenomena occur whenever a disk-dominated mode frequency approaches that of an out-of-phase acoustic-dominated mode. For instance the (0,1) disk-dominated mode veers with the (0,1,0) out-of-phase acoustic mode near $\Omega=100$. Other examples of eigenvalue veering can also be seen in Fig. 5. This implies that disk-dominated system modes can change suddenly at certain speeds into acoustic dominated modes and vice versa. Further the speeds at which eigenvalue veering occurs can be predicted in the following simple manner. Uncoupled axisymmetric disk frequencies increase with rotation speed while the uncoupled axisymmetric acoustic mode frequencies are independent of rotation speed. Therefore eigenvalue veerings of axisymmetric modes occur whenever the uncoupled disk frequencies nearly equal the uncoupled acoustic frequencies. In Fig. 5, this is indicated by the intersections of the uncoupled disk frequency loci with the in-phase acoustic frequency loci.

The variation with speed of the asymmetric mode frequencies of the system is shown in Fig. 6. As expected, the disk-dominated modes split into forward and backward traveling waves (FTW and BTW) and the BTW frequencies decrease and vanish at their respective critical speeds. The lowest critical speed at nondimensional $\Omega\sim55$ occurs for the (3,0) disk-dominated mode. At supercritical speed a BTW is referred to as a reflected traveling wave (RTW). The RTW frequencies increase from zero beyond the respective critical speeds. Several other unique features of the coupled system in Fig. 6 are now described.

First, the repeated out-of-phase acoustic modes are also split into FTW and BTW. For instance, the frequency of one of the (1,0,0) out-of-phase acoustic modes increases with rotation speed while the other frequency of the (1,0,0) mode decreases as the disk rotates. As in the case of disk modes, these can be interpreted as the forward and backward traveling waves of the acoustic cavity modes. The underlying physics of this phenomenon lies in the coupling between the out-of-phase acoustic dominated modes to disk dominated modes of the same nodal diameter number. If the disk dominated modes split into FTW and BTW so will the acoustic dominated modes.

Secondly, when the FTW frequency of a disk-dominated mode encounters an acoustic-dominated mode frequency of the same nodal diameter number, the disk-dominated mode veers into an acoustic-dominated mode. For example, the (1,0) FTW disk-dominated mode veers strongly at $\Omega\sim95$ into an acoustic-dominated (1,0,0) mode and its frequency approaches that of the uncoupled (1,0,0) acoustic mode. In other words, acoustic mode frequencies act as barriers for FTW disk dominated mode frequencies and force the disk-dominated FTW frequencies to veer into acoustic dominated FTWs.

Thirdly, as the rotation speed increases further in the supercritical range, the frequencies of the RTW coalesce with the acoustic-dominated mode frequencies (Fig. 7). For example the (2,0) disk-dominated RTW coalesces with the (2,0,0) acoustic-dominated FTW at $\Omega\sim770$, the (3,0) disk-dominated RTW with the (3,0,0) acoustic-dominated FTW at $\Omega\sim440$, and so on. This mode coalescence leads to the onset of traveling wave flutter over a certain speed range, and a pair of eigenvalues moves into the right half-complex plane.

Several conclusions can be made from Fig. 7 about the nature of the mechanism in the undamped system that induces traveling wave flutter:

1. For each nodal diameter number, the traveling wave flutter instability occurs over the range of speed beyond which the specific mode restabilizes.
2. The one nodal diameter mode does not undergo flutter instability. Because this mode has no critical speed and the system stiffness remains positive definite for all speeds in this mode, [23], the (0,1) mode remains stable for all rotation speeds.
3. The (2,0) mode has the largest speed range of instability and this range decreases with increase in nodal diameter number of the unstable wave.
4. Interestingly, the greater the nodal diameter number of the mode, the lower its flutter speed. The lowest speed at which

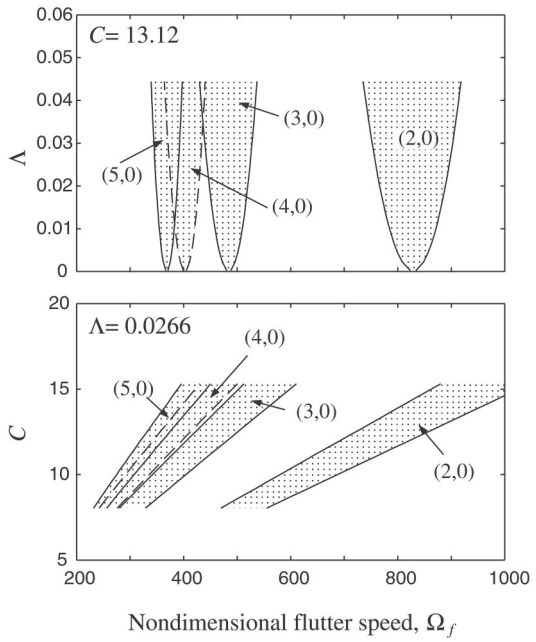


**Fig. 8 Variation of nondimensional flutter speed with Λ and *C*. These instability regions are plotted for the undamped system where $\eta=0$ and $z_A=$ infinity.**

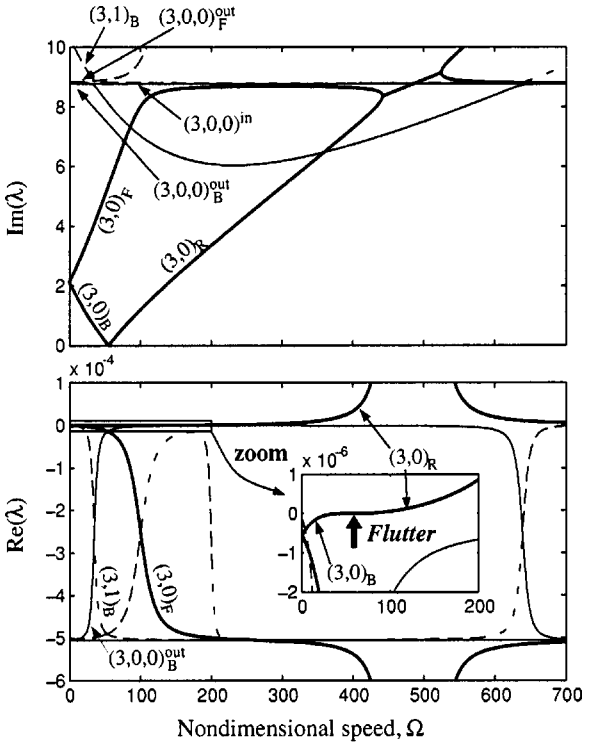


**Fig. 9 Variation with nondimensional speed ($0<\Omega<700$) of the real and imaginary parts of the eigenvalues of three nodal diameter modes of the coupled rotating disk, acoustic cavity system in the presence of acoustic damping alone induced by sound absorbing wall ($z_A=4.78\times10^5$). System parameters listed in Table 1 and a cavity depth of 1 cm is chosen for the computation.**

flutter occurs in this case seems to asymptote to $\Omega\sim320$. Note that the lowest critical speed of the disk is $\Omega\sim55$. This implies that while it is possible to describe a flutter speed beyond with the disk is unstable, it is impossible to say exactly which mode shape destabilizes first. From the computational results this first instability is likely to occur in a very high nodal diameter number mode.

5. Because the traveling wave instability occurs from the coalescence of acoustic and disk-dominated traveling waves, the unstable wave itself is neither disk nor acoustic dominated. The unstable wave then appears as a coupled structural-acoustic traveling wave rotating in the same direction as the disk, albeit slower than the disk.
6. Other instabilities caused by higher mode coalescence can also occur, although they are not shown in Fig. 7. For example, flutter instability caused by the mode coalescence of (5,0) and (5,1,0) waves occurs at a higher rotation speed than for the instability involving a coalescence of (5,0) and (5,0,0) waves.

The variation of the instability regions with respect to the nondimensional parameters Λ and *C* are shown in Fig. 8. At a particular value of Λ and *C*, a flutter instability of a traveling coupled acoustic-structural wave occurs over a finite speed range. The speed range is different for different nodal diameter modes. In the limiting case, in vacuum $\Lambda\rightarrow0$ and the instability regions vanish. On the other hand, the flutter speeds generally increase with increasing *C* values. This occurs because higher *C* values result in higher cavity frequencies relative to disk frequencies. The greater the *C* value, the higher the supercritical speed at which mode coalescence occurs.

This completes the discussion of the instability mechanisms of the rotating disk-cylindrical acoustic cavity system in the absence of dissipation.

## 7 Effects of Dissipation

In the presence of disk and acoustic damping, the system dynamics become more complicated than for undamped case discussed earlier. This is clearly a more practically relevant scenario. The effects of such dissipative mechanisms are now studied in detail in the following order (a) the effects of acoustic damping alone, (b) the effects of disk damping alone, and (c) the effects of combined disk and acoustic damping.

**7.1 Acoustic Damping Alone.** Acoustic damping arises in the model from the presence of a sound absorbing material on the top and bottom ends of the cylindrical enclosure (Eq. (10)). In the presence of acoustic damping only, the submatrices $\mathbf{C}_q$, $\mathbf{D}_q=\mathbf{0}$ and $\mathbf{C}_a=\mathbf{C}_b\neq\mathbf{0}$ in Eq. (21). This results in a classical gyroscopic system with positive definite damping. In the absence of this damping term, the system loses positive definiteness at its first critical speed and is gyroscopically stabilized immediately beyond critical speed. According the to the Kelvin-Tait-Chetaev theorem, [24], therefore the inclusion of the positive-definite acoustic damping destabilizes the system beyond its first critical speed. That is, the disk-dominated RTW undergoes a flutter instability exactly at critical speed. Once the flutter is initiated, the zero equilibrium remains unstable for all supercritical speeds. Also clearly, the first flutter speed of the coupled system corresponds to the first critical speed, in this case that of the (3,0) disk-dominated mode.

This prediction is confirmed numerically in Fig. 9, which shows the variation with rotation speed of the eigenvalues of the three nodal diameter modes. The system parameters are listed in Table 1 and the air gap is chosen to be 1 cm as before. A nondimensional impedance value of $z_A=4.78\times10^5$ is chosen for the computation. As expected the RTW of the (0,3) mode destabilizes exactly at critical speed. Further beyond this critical speed at least one pair of eigenvalues remains in the complex right half-plane. Several conclusions can be drawn from Fig. 9:

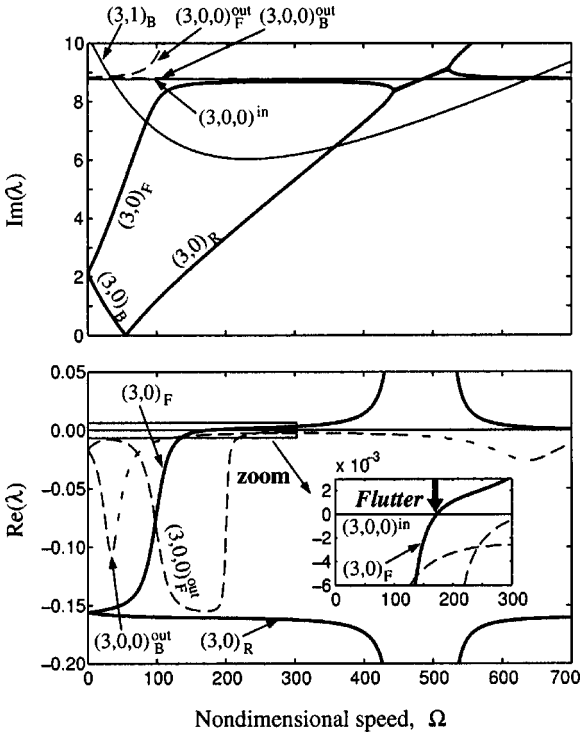


**Fig. 10 Variation with nondimensional speed ($0<\Omega<700$) of the real and imaginary parts of the eigenvalues of three nodal diameter modes of the coupled rotating disk, acoustic cavity system in the presence of disk damping alone induced by viscoelastic disk material ($\eta=1.766\times10^{-3}$). System parameters listed in Table 1 and a cavity depth of 1 cm is chosen for the computation.**

1. The disk destabilizes by a traveling wave flutter of a *disk dominated* (3,0) RTW. This corresponds to the mode with the lowest critical speed. Recall that in the absence of damping, the unstable wave contains both disk and acoustic components.
2. Unlike the undamped case, the zero equilibrium remains unstable for all supercritical speeds.
3. Interestingly, however, the instability at critical speed cannot be described as a classical Hopf bifurcation, for two reasons (i) a pair of eigenvalues moves into the right half-plane with zero imaginary parts, and (ii) the instability also violates the nonzero ''speed'' eigenvalue crossing condition for a Hopf bifurcation, because $d\lambda/d\Omega=0$ at the instability, [25].

In this mechanism, the system destabilizes through disk dominated flutter when the system stiffness matrix loses positive definiteness at the system critical speeds. Because the disk-fluid coupling does not appear in the stiffness matrix, the critical speed of the disk is independent of the properties of surrounding fluid. Thus the nondimensional flutter speed and mode do not change with respect to the nondimensional parameters $\Lambda$ and $C$.

**7.2 Disk Damping Alone.** In the absence of acoustic damping, the dissipation arises from disk material damping alone. The effect of this dissipation mechanism on the aeroelastic stability of the coupled disk-cavity system is now investigated. The real and imaginary parts of the eigenvalues of the three nodal diameter system modes as a function of $\Omega$ are shown in Fig. 10, with the viscoelastic coefficient $\eta=1.766\times10^{-3}$. The variation with $\Omega$ of the natural frequencies of the disk with material damping alone are nearly identical to those of the system with acoustic damping alone (Fig. 9). However, upon closer examination, the real part of the eigenvalues in Fig. 10 behave completely differently from that in Fig. 9. It is found that with increasing $\Omega$ the FTW disk dominated (3,0) mode frequency approaches the three nodal diameter acoustic dominated frequency. Near $\Omega\sim100$ the disk-dominated (3,0) mode veers to a near-speed independent natural frequency, and in the process of veering becomes an acoustic-dominated mode. Shortly thereafter, this acoustic dominated (3,0) FTW becomes unstable at $\Omega\sim180$.

The flutter instability in the presence of disk material damping alone is completely different from the instability mechanisms in the absence of dissipation or in the presence of acoustic damping alone:

1. In contrast to the other previous mechanisms, this flutter instability takes the form of an *acoustic-dominated* FTW. Once unstable, the equilibrium continues to remain unstable at higher speeds.
2. For the chosen system parameters, the instability occurs at an intermediate speed between the flutter speed of the same mode in the absence of any dissipation (Fig. 7) and in the presence of acoustic damping alone (Fig. 9).
3. This instability represents a classical Hopf bifurcation because at this flutter speed a pair of eigenvalues corresponding to an acoustic dominated FTW cross over to the right half-plane with nonzero imaginary part and nonzero ''speed.'' This is a particularly nonintuitive result given that disk material damping usually suppresses rotating disk instabilities.

To understand the underlying physics of this interesting result, consider the following argument. Disk material damping leads effectively to a damping that rotates with the disk, [12]. When viewed from a ground fixed reference frame, this damping contributes in Eq. (20) to the symmetric damping matrix **C** as well as to skew-symmetric circulatory matrix, **D**. However, upon recasting the discretized equations of motion (Eq. (20)) in a co-rotating frame, the disk material damping is essentially a symmetric positive definite damping. Two conclusions follow immediately. First, in the co-rotating frame, the acoustic cavity is no longer stationary but rotates in a direction opposite to that of the disk. This generates gyroscopic terms in the acoustic cavity oscillations. The rotating acoustic cavity then suffers critical speeds with vanishing traveling wave frequencies. Second, the disk material damping then provides a symmetric positive definite damping for the acoustic dominated traveling waves. Once again, invoking the Kelvin-Tait and Chetaev theorem, this implies that in the presence of disk material damping, an acoustic dominated traveling wave destabilizes at the critical speed of the rotating cavity. The implication therefore is that at $\Omega\sim180$ in Fig. 10 flutter occurs exactly at the critical speed of the acoustic dominated three nodal diameter mode.

To confirm this hypothesis the discretized equation (Eq. (20)) are recast in the co-rotating frame using the following time-dependent transformation

$$\begin{pmatrix} a^{C}_{n_1n_2n_3}(t) \\ a^{S}_{n_1n_2n_3}(t) \end{pmatrix} = \begin{pmatrix} \cos n_1\Omega t & -\sin n_1\Omega t \\ \sin n_1\Omega t & \cos n_1\Omega t \end{pmatrix} \begin{pmatrix} \bar{a}^{C}_{n_1n_2n_3}(t) \\ \bar{a}^{S}_{n_1n_2n_3}(t) \end{pmatrix} \tag{22a}$$

$$\begin{pmatrix} b^{C}_{n_1n_2n_3}(t) \\ b^{S}_{n_1n_2n_3}(t) \end{pmatrix} = \begin{pmatrix} \cos n_1\Omega t & -\sin n_1\Omega t \\ \sin n_1\Omega t & \cos n_1\Omega t \end{pmatrix} \begin{pmatrix} \bar{b}^{C}_{n_1n_2n_3}(t) \\ \bar{b}^{S}_{n_1n_2n_3}(t) \end{pmatrix} \tag{22b}$$

$$\begin{pmatrix} q^{C}_{m_1m_2}(t) \\ q^{S}_{m_1m_2}(t) \end{pmatrix} = \begin{pmatrix} \cos m_1\Omega t & -\sin m_1\Omega t \\ \sin m_1\Omega t & \cos m_1\Omega t \end{pmatrix} \begin{pmatrix} \bar{q}^{C}_{m_1m_2}(t) \\ \bar{q}^{S}_{m_1m_2}(t) \end{pmatrix} \tag{22c}$$

where the bar denotes coordinates in co-rotating frame, and the resulting eigenvalue dependence on $\Omega$ is plotted in Fig. 11 for the same system parameters as those used in Fig. 10. The subscripts $\overline{\text{F}}$

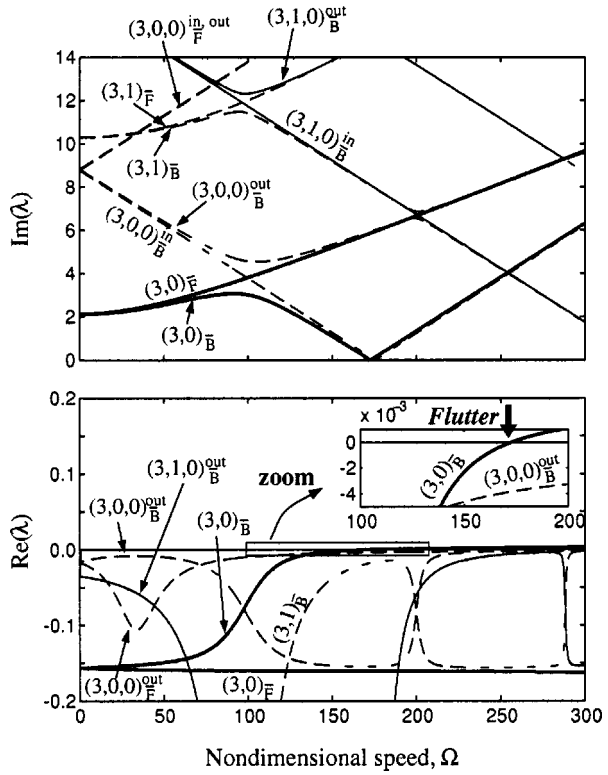


**Fig. 11 Variation with nondimensional speed ($0<\Omega<300$) of the real and imaginary parts of the eigenvalues of three nodal diameter modes in co-rotating frame, of the system in the presence of disk damping alone induced by viscoelastic disk material ($\eta=1.766\times10^{-3}$). System parameters listed in Table 1 and a cavity depth of 1 cm is chosen for the computation.**

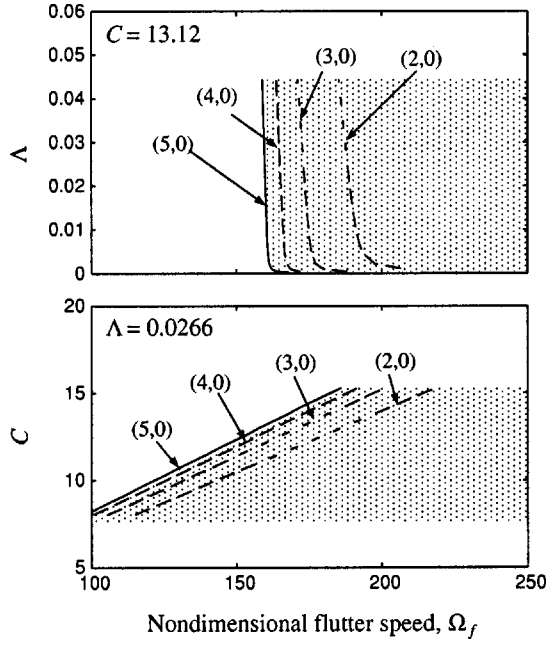


**Fig. 12 Variation of nondimensional flutter speed with $\Lambda$ and $C$. These instability regions are plotted for the case of $\eta=1.766\times10^{-3}$ and $z_A=$infinity.**

and $\overline{B}$ in Fig. 11 stand, respectively, for traveling waves rotating in the same sense as the acoustic cavity or opposed to it, when viewed in the co-rotating frame. For example, the $(3,0)_{\overline{B}}$ mode in Fig. 11 is essentially the same as the $(3,0)_F$ mode in Fig. 10. Similarly, the $(3,0,0)_F^{out}$ mode in ground-fixed frame is identical to the $(3,0,0)_{\overline{B}}^{out}$ mode in co-rotating frame.

From Fig. 11 it is clear that the acoustic modes split into FTW and BTW components. Further the three nodal diameter acoustic dominated traveling wave destabilizes exactly at the critical speed of this acoustic mode when viewed in a co-rotating frame. Interestingly therefore, the lowest flutter speed and corresponding flutter mode in the presence of disk material damping alone are dictated by the lowest critical speed of the acoustic cavity. Note that the natural frequencies of the acoustic modes and therefore their critical speeds also depend on cavity dimensions. Therefore the flutter speed and mode predicted by this instability mechanism can be modified significantly through variations in the enclosure geometry.

In addition, because the critical speed of the acoustic-dominated mode is dependent on the properties of surrounding fluid, the onset of flutter changes with respect to the nondimensional parameters $\Lambda$ and $C$. This dependence is described in Fig. 12. In vacuum as $\Lambda\rightarrow0$, flutter speed increase rapidly and occur at infinite rotating speeds while in a dense fluid the system becomes unstable at lower rotation speeds due to stronger disk-cavity couplings. Furthermore, because the uncoupled natural frequency of acoustic cavity is linearly proportional to the acoustic wave speed, the flutter speed in this mechanism varies linearly with the nondimensional wave speed, $C$. This completes the discussion of the flutter mechanism in the presence of disk damping alone.

**7.3 Combined Disk and Acoustic Damping.** In the presence of both disk and acoustic damping, flutter speed is controlled directly through interplay of acoustic cavity and disk damping. To investigate this effect, the flutter speeds of different nodal diameter modes of the system are plotted in Fig. 13 as a function of the parameter $z_A\eta$, the ratio of nondimensional disk material damping to nondimensional acoustic damping. The results are plotted for a fixed value of $z_A=4.78\times10^5$. When $\eta$ is small (low disk damping) or $z_A$ is small (high acoustic cavity damping), onset of flutter occurs in a disk-dominated RTW slightly above the lowest

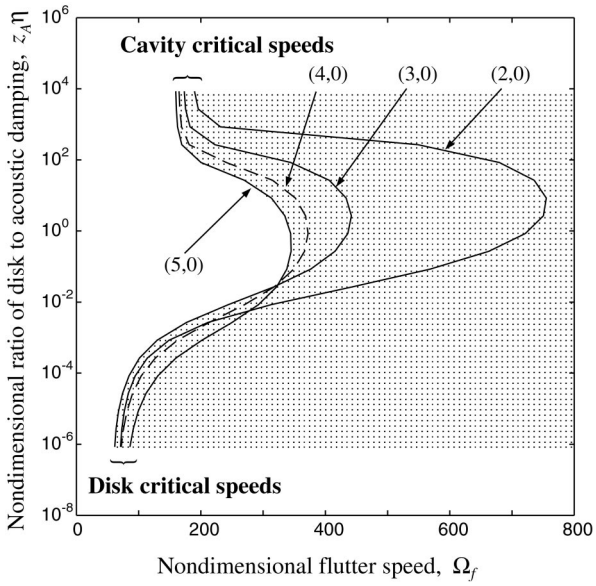


**Fig. 13 Variation of nondimensional flutter speed with the nondimensional ratio of disk to acoustic damping $z_A\eta$. These instability regions are plotted for $z_A=4.78\times10^5$.**

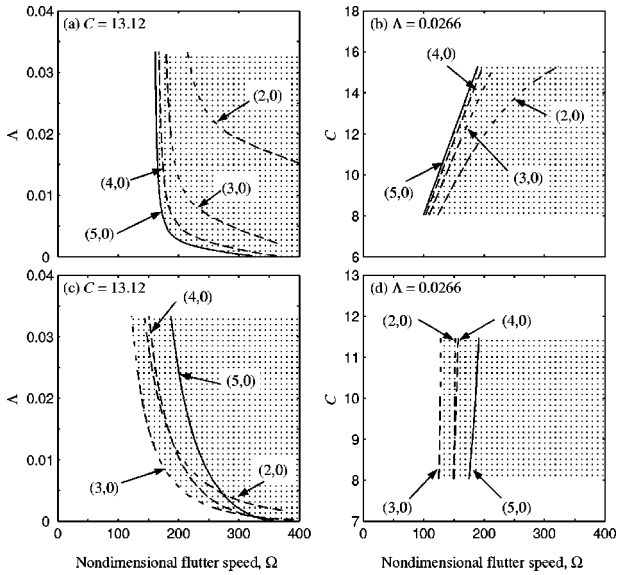


**Fig. 14 Variation of nondimensional flutter speed with $\Lambda$ and $C$ in the presence of both acoustic and disk damping. These instability regions are plotted for the case of $z_A^*=15\times10^6$ and $\eta^*=3.2\times10^{-6}$ (in a, b), and $\eta^*=3.2\times10^{-12}$ in ($c$, $d$). ($a$) and ($b$) correspond to a system where disk damping dominates acoustic damping while ($c$) and ($d$) correspond to a situation where acoustic damping effects are dominant.**

critical speed of the disk, and in the corresponding mode. This mechanism is identical to the flutter mechanism discussed earlier with acoustic damping alone. On the other hand, when $\eta$ is large (high disk damping) or $z_A$ is large (low acoustic cavity damping), the system flutters first in an acoustic dominated FTW with a very high nodal diameter number. For intermediate values of $z_A\eta$ the flutter speeds actually increase and approach the flutter speeds encountered from mode coalescence in the undamped system.

The variation of the instability regions with respect to the nondimensional parameters $\Lambda$ and $C$ are shown in Fig. 14. The results are plotted for fixed values of $z_A^*=15\times10^6$ while $\eta^*=3.2\times10^{-6}$ in Fig. 14($a$) and ($b$), and $\eta^*=3.2\times10^{-12}$ in Fig. 14($c$) and ($d$). The nondimensional ratios of disk to acoustic damping, $z_A\eta$, in Fig. 14($b$) and in Fig. 14($d$), are 844.17 and $8.441\times10^{-4}$, respectively. Note, however, that the nondimensional parameters $\Lambda$ and $z_A$ are related each other. For this reason as $\Lambda$ is varied in Fig. 14($a$) and ($c$), the value of $z_A$ also changes. Specifically the nondimensional ratio $z_A\eta$ varies in the range $675\sim1013$ in Fig. 14($a$) and from $6.7\times10^{-4}\sim0.101$ in Fig. 14($c$). In spite of this variation, Fig. 14($a$) corresponds to a situation where disk damping dominates acoustic damping and Fig. 14($c$) corresponds to the case where the acoustic damping dominates the disk damping. As expected the instability regions in Fig. 14($a$) and ($b$) are similar to the case of disk damping alone (Fig. 12). Similarly, the instability region in ($d$) resembles the case of acoustic damping alone. However, the instability region in Fig. 14($c$) is different from the case of acoustic damping alone. This is because the nondimensional acoustic impedance $z_A$ is increases as the $\Lambda$ is decreased and cannot be regarded as negligible at low fluid densities. It is interesting to note also that as $\Lambda$ decreases the first flutter mode can actually change from the (3,0) disk dominated to (4,0) disk-dominated RTW.

## 8 Conclusions and Discussion

The instability mechanisms of a flexible disk rotating in an enclosed compressible fluid are investigated in this study. Galerkin's method and Green's theorem are used to derive the discretized, linear equations governing rotating disk and fluid oscillations. The discretized dynamical system has the form of a classical gyroscopic system with positive damping and circulatory terms. Following a detailed convergence study, the coupled discretized eigenvalue problem is studied computationally.

The coupled rotating disk-acoustic cavity system oscillations are governed by two different gyroscopic couplings: one is due to acoustic-structure interaction and the other arises from disk rotation. The disk-acoustic cavity coupling generates in and out-of-phase acoustic modes. For a symmetrically placed disks in enclosure, out-of-phase acoustic modes couple to disk modes, and in-phase acoustic modes decouple from disk vibration. As the disk rotates, out-of-phase acoustic dominated as well as disk-dominated modes split into FTW and BTW. Further, eigenvalue veering between disk and acoustic modes leads to the sudden transformation of disk to acoustic-dominated modes at supercritical rotation speed. For the undamped system, the flutter instability is caused by mode coalescence over the certain speed range, leading to the flutter of a coupled acoustic-structural wave of high nodal diameter number. Further this wave propagates in the same direction as disk rotation, albeit slower than it.

The inclusion of acoustic damping from absorbent walls destabilizes a RTW of disk-dominated mode at the critical speed of the system. The flutter mode corresponds to the mode with the lowest critical speed. In addition, once initiated, the flutter instability persists for all higher speeds. In the presence of disk material damping alone, an acoustic dominated FTW destabilizes via flutter instability at supercritical speed. The flutter instability occurs in the form of a very high nodal diameter acoustic-dominated wave. This unstable wave propagates in the same direction as the disk, but travels slower than it. Further, this instability persists for all higher speeds. In the presence of both disk and acoustic damping, the flutter speed, mode, and mechanism are controlled by the ratio of disk to acoustic damping of the system.

It may be noted that the instabilities predicted in this article occur typically at supercritical speed. While these speeds are unlikely to be encountered in commercial hard disk drives, the disk-cavity coupling and veering issues discussed in this paper are of interest in the design of low-noise emission drives. Further, both the aeroelastic stability and cavity-disk coupling issues are likely to be important for optical or magneto-optical disks that operate currently near their critical speeds.

The verification of these different instability mechanisms requires further detailed experiments and is the subject of ongoing research. It is worthwhile, however, to compare qualitatively the present predictions to known experimental results on the flutter of disks in enclosed spaces with radial gaps. Especially the onset of flutter described for lightly damped steel disks in [2] is consistent with the dynamics predicted by the present study for systems with low disk to acoustic damping ratios (Figs. 13 and 14). However, to our best knowledge, the acoustic-dominated traveling wave flutter phenomenon has not yet been observed experimentally.

Finally we note that there is an interesting similarity between the flutter of infinitely long plates, [26,27], and the cavity damping dominated instability discussed in the present work. In both cases, the instability occurs as a traveling wave and the flutter mode wavelengths are of the order of twice the panel width or disk radial extent. However, the disk-cavity coupling and cavity-dominated instability phenomena described in the present study appear not to have been discussed yet in the literature on the flutter of infinitely long panels.

## Acknowledgments

The authors thank the Purdue Research Foundation and the National Science Foundation (NSF) for financial support provided under Award (CAREER) 0134455-CMS.

## Appendix

$$\mathbf{a}_n=[a_{000},\cdots,a_{0n_2n_3},a^C_{100},\cdots,a^C_{n_1n_2n_3},a^S_{100},\cdots,a^S_{n_1n_2n_3}]^T$$

$$\mathbf{b}_n=[b_{000},\cdots,b_{0n_2n_3},b^C_{100},\cdots,b^C_{n_1n_2n_3},b^S_{100},\cdots,b^S_{n_1n_2n_3}]^T$$

$$\mathbf{q}_m=[q_{00},\cdots,q_{0m_2},q^C_{10},\cdots,q^C_{m_1m_2},q^S_{10},\cdots,q^S_{m_1m_2}]^T$$

$$\mathbf{M}_{a,b}=\frac{\Lambda V^{a,b}}{C^2}\begin{bmatrix}\mathbf{M}_n & & \\ & \mathbf{M}^C_n & \\ & & \mathbf{M}^S_n\end{bmatrix}^{a,b},\quad \mathbf{M}_q=\begin{bmatrix}\mathbf{1} & & \\ & \mathbf{1} & \\ & & \mathbf{1}\end{bmatrix},$$

$$\mathbf{C}_{a,b}=\Lambda A_A\begin{bmatrix}\mathbf{C}_{nr} & & \\ & \mathbf{C}^C_{nr} & \\ & & \mathbf{C}^S_{nr}\end{bmatrix}^{a,b},$$

$$\mathbf{C}_q=\eta\begin{bmatrix}\boldsymbol{\omega}^2_{ms} & & \\ & \boldsymbol{\omega}^2_{ms} & \\ & & \boldsymbol{\omega}^2_{ms}\end{bmatrix},$$

$$\mathbf{L}_{aq,bq}=\Lambda A_d\begin{bmatrix}\mathbf{L}_{nm} & & \\ & \mathbf{L}^C_{nm} & \\ & & \mathbf{L}^S_{nm}\end{bmatrix}^{a,b},$$

$$\mathbf{G}_q=2\Omega\begin{bmatrix}\mathbf{0} & & \\ & & \boldsymbol{m}_1\\ & -\boldsymbol{m}_1^T & \end{bmatrix},$$

$$\mathbf{K}_{a,b}=\frac{\Lambda V^{a,b}}{C^2}\begin{bmatrix}\mathbf{M}_n\boldsymbol{\Lambda}^2_n & & \\ & \mathbf{M}^C_n\boldsymbol{\Lambda}^2_n & \\ & & \mathbf{M}^S_n\boldsymbol{\Lambda}^2_n\end{bmatrix}^{a,b},$$

$$\mathbf{K}_q=\begin{bmatrix}\boldsymbol{k}_m & & \\ & \boldsymbol{k}_m & \\ & & \boldsymbol{k}_m\end{bmatrix},$$

$$\mathbf{D}_q=\eta\Omega\begin{bmatrix}\mathbf{0} & & \\ & & \boldsymbol{m}_1\boldsymbol{\omega}^2_{ms}\\ & -(\boldsymbol{m}_1\boldsymbol{\omega}^2_{ms})^T & \end{bmatrix},$$

where all submatrices are diagonal except $\mathbf{C}_{nr}$ and $\mathbf{L}_{nm}$ and their each element is defined by the corresponding scalar variable in the text.

## References


[1] D'Angelo, C., and Mote, C. D., Jr., 1993, "Aerodynamically Excited Vibration and Flutter of a Thin Disk Rotating at Supercritical Speed," J. Sound Vib., **168**(1), pp. 15–30.

[2] D'Angelo, C., and Mote, C. D., Jr., 1993, "Natural Frequencies of a Thin Disk, Clamped by Thick Collars With Friction at the Contacting Surfaces, Spinning at High Rotating Speed," J. Sound Vib., **168**(1), pp. 1–14.

[3] Renshaw, A. A., D'Angelo, C., and Mote, C. D., Jr., 1994, "Aeroelastically Excited Vibration of a Rotating Disk," J. Sound Vib., **177**(5), pp. 577–590.

[4] Hansen, M. H., Raman, A., and Mote, C. D., Jr., 2001, "Estimation of Non-conservative Aerodynamic Pressure Leading to Flutter of Spinning Disks," J. Fluids Struct., **15**, pp. 39–57.

[5] Yasuda, K., Torii, T., and Shimizu, T., 1992, "Self-Excited Oscillations of a Circular Disk Rotating in Air," JSME Int. J., Ser. III, **35**, pp. 347–352.

[6] Kim, B. C., Raman, A., and Mote, C. D., Jr., 2000, "Prediction of Aeroelastic Flutter in a Hard Disk Drive," J. Sound Vib., **238**(2), pp. 309–325.

[7] Hansen, M. H., 1999, "*Aeroelasticity and Dynamics of Spinning Disks*," Ph.D. thesis, Department of Solid Mechanics, Technical University of Denmark.

[8] Huang, F. Y., and Mote, C. D., Jr., 1995, "On the Instability Mechanisms of a Disk Rotating Close to a Rigid Surface," ASME J. Appl. Mech., **62**, pp. 764–771.

[9] Huang, F. Y., and Mote, C. D., Jr., 1996, "Mathematical Analysis of Stability of a Spinning Disk Under Rotating, Arbitrarily Large Damping Forces," ASME J. Vibr. Acoust., **118**, pp. 657–662.

[10] Naganathan, G., Ramadhayani, S., and Bajaj, A. K., 2003, "Numerical Simulations of Flutter Instability of a Flexible Disk Rotating Close to a Rigid Wall," J. Vib. Control, **9**(1), pp. 95–118.

[11] Renshaw, A. A., 1998, "Critical Speed for Floppy Disks," ASME J. Appl. Mech., **65**, pp. 116–120.

[12] Hosaka, H., and Crandall, S. H., 1992, "Self-Excited Vibrations of a Flexible Disk Rotating on an Air Film Above a Flat Surface," Acta Mech., **3**, pp. 115–127.

[13] Love, A. E., 1944, *Treatise on the Mathematical Theory of Elasticity*, Dover, London.

[14] Dowell, E. H., Gorman, G. F., and Smith, D. A., 1977, "Acoustoelasticity: General Theory, Acoustic Natural Modes and Forced Response to Sinusoidal Excitation, Including Comparisons With Experiment," J. Sound Vib., **52**(4), pp. 519–542.

[15] Kinsler, L. E., Frey, A. R., Coppens, A. B., and Sanders, J. V., 2000, *Fundamentals of Acoustics*, Fourth Ed., John Wiley and Sons, New York, Chap. 9.

[16] Fahy, F., 1985, *Sound and Structural Vibration*, Academic Press, San Diego, CA, Chap. 6.

[17] Dowell, E. H., 1975, *Aeroelasticity of Plates and Shells*, Noordhoff International Publishing, Leyden, Chap. 4.

[18] Vogel, S. M., and Skinner, D. W., 1965, "Natural Frequencies of Transversely Vibrating Uniform Annular Plates," ASME J. Appl. Mech., **32**, pp. 926–931.

[19] Bokil, V. B., and Shirahatti, U. S., 1994, "A Technique for the Modal Analysis of Sound-Structure Interaction Problems," J. Sound Vib., **173**(1), pp. 23–41.

[20] Meirovitch, L., 1974, "A New Method of Solution of the Eigenvalue Problem for Gyroscopic Systems," AIAA J., **12**(10), pp. 1337–1342.

[21] Bai, Z., Demmel, J., Dongarra, J., Ruhe, A., and van der Vorst, H., 2000, *Templates for the Solution of Algebraic Eigenvalue Problems: A Practical Guide*, SIAM, Philadelphia.

[22] Jha, R. K., and Parker, R. G., 2000, "Spatial Discretization of Axially Moving Media Vibration Problems," ASME J. Vibr. Acoust., **122**, pp. 290–294.

[23] Renshaw, A. A., and Mote, C. D., Jr., 1992, "Absence of One Nodal Diameter Critical Speed Modes in an Axisymmetric Rotating Disk," ASME J. Appl. Mech., **59**, pp. 687–688.

[24] Merkin, D. R., 1997, *Introduction to the Theory of Stability*, Springer-Verlag New York, Chap. 6.

[25] Iooss, G., and Joseph, D. D., 1980, *Elementary Stability and Bifurcation Theory*, Second Ed., Springer-Verlag New York, Chap. VII.

[26] Dowell, E. H., 1966, "Flutter of Infinitely Long Plates and Shells. Part I: Plate," AIAA J., **4**(8), pp. 1370–1377.

[27] Epstein, R. J., Srinivasan, R., and Dowell, E. H., 1995, "Flutter of an Infinitely Long Panel in a Duct," AIAA J., **33**(1), pp. 109–115.

Journal of Applied Mechanics

# Brief Notes

A Brief Note is a short paper that presents a specific solution of technical interest in mechanics but which does not necessarily contain new general methods or results. A Brief Note should not exceed 2500 words *or equivalent* (a typical one-column figure or table is equivalent to 250 words; a one line equation to 30 words). Brief Notes will be subject to the usual review procedures prior to publication. After approval such Notes will be published as soon as possible. The Notes should be submitted to the Editor of the JOURNAL OF APPLIED MECHANICS. Discussions on the Brief Notes should be addressed to the Editorial Department, ASME International, Three Park Avenue, New York, NY 10016-5990, or to the Editor of the JOURNAL OF APPLIED MECHANICS. Discussions on Brief Notes appearing in this issue will be accepted until two months after publication. Readers who need more time to prepare a Discussion should request an extension of the deadline from the Editorial Department.

## On the Heavily Damped Response in Viscously Damped Dynamic Systems

**R. M. Bulatovic**
Faculty of Mechanical Engineering, University of Montenegro, 81 000 Podgorica, Yugoslavia

*Free motions of viscously damped linear systems are studied. A heavily damped multi-degree-of-freedom system is defined as one for which all its eigenvalues are real, negative, and semi-simple. Several results are obtained which state conditions for the heavy damping of the system. The conditions are given directly in terms of the coefficients of system matrices and these conditions may yield design constraints in terms of the physical parameters of the system. An example illustrates the validity and usefulness of the presented results.* [DOI: 10.1115/1.1629108]

### 1 Introduction and Previous Results

We consider a viscously damped linear mechanical system described by the equation

$$M\ddot{q}+B\dot{q}+Cq=0, \tag{1}$$

where $q$ is the $n$-dimensional position vector, and $M$, $B$, and $C$ are the inertia, damping, and stiffness matrices, assumed to be constant, real, symmetric, and positive definite. Since $M>0$ (positive definite), one can utilize the positive definite square root in a familiar way to transform Eq. (1) to the form

$$\ddot{x}+D\dot{x}+Kx=0, \tag{2}$$

where $D=M^{-1/2}BM^{-1/2}=D^T$, $K=M^{-1/2}CM^{-1/2}=K^T$ and $x=M^{1/2}q$.

The eigenvalue problem associated with (2) is

$$(\lambda^2 I+\lambda D+K)U=0, \tag{3}$$

where $I$ is the identity matrix, $U$ is an eigenvector of dimension $n$, and $\lambda$ is its eigenvalue. There are $2n$ eigenvalues $\lambda_i$ which are governed by the characteristic equation

$$\Delta(\lambda)=\det(\lambda^2 I+\lambda D+K)=0. \tag{4}$$

Contributed by the Applied Mechanics Division of THE AMERICAN SOCIETY OF MECHANICAL ENGINEERS for publication in the ASME JOURNAL OF APPLIED MECHANICS. Manuscript received by the ASME Applied Mechanics Division, Nov. 19, 1999; final revision, June 10, 2003. Associate Editor: V. K. Kinra.

If all eigenvalues are *distinct* (*simple*), the general solution of the equation of motion (2) has the form

$$x(t)=\sum_{1}^{2n} c_i U_i \exp(\lambda_i t), \tag{5}$$

where $c_i$ are the constants determined from the initial conditions. The expansion (5) is also valid for *semi-simple* eigenvalues, i.e., for the roots $\lambda_i$ of Eq. (4) having the multiplicity $k$, if the number of linearly independent eigenvectors corresponding to $\lambda_i$ is equal to $k$. It is well known that all eigenvalues of (3) have negative real parts and, consequently, the system (2) is asymptotically stable. The system (1) or (2) will be called *heavily damped* if all eigenvalues of (3) are real and semi-simple, and hence all solutions $q(t)$ of differential Eq. (1) do not oscillate. Characterization of the heavily damped system by its eigenvalues is not convenient for design purposes, since it requires a complete eigenvalue determination for every combination of various system parameters. Consequently, it is of interest to find conditions which are related in a simple way to the properties of the system matrices (see Inman [1]).

In the mechanics literature, particularly in ASME *Journal of Applied Mechanics* (see the list of references), some attention has been paid to the formulation of criteria which guarantee that all eigenvalues of the system are real and negative. There is a well-known definition of *overdamped* systems first used by Duffin [2] which ensures that a system (2) has real and semi-simple eigenvalues. Duffin's definition states that an overdamped system is one such that

$$(x^T Dx)^2>4x^T xx^T Kx \tag{6}$$

for all nonzero real $n$-vectors $x$. This is a sufficient condition for (3) to have real and semi-simple eigenvalues (but not necessary condition), i.e., (6) is sufficient for heavy damping in the sense of this paper. The following simple example of the system (2) illustrates this point. Let

$$D=\begin{pmatrix}4 & 0\\ 0 & 10\end{pmatrix} \quad \text{and} \quad K=\begin{pmatrix}3 & 0\\ 0 & 24\end{pmatrix}.$$

It is easy to verify that this uncoupled system is heavily damped (the eigenvalues are $\lambda_1=-1$, $\lambda_2=-3$, $\lambda_3=-4$, and $\lambda_4=-6$) but not overdamped (the condition (6) is not satisfied). Thus, the notions of heavy damping and of overdamping are different for multi-degree-of-freedom systems, although they are the same for single-degree-of-freedom systems. An overdamped system has some properties which cannot be generalized to less heavily damped systems (see Lancaster [3]). Notice also that (6) requires

  

substantial calculation to check its validity. Later Inman and Andry [4] proposed that the system is overdamped if

$$D > 2K^{1/2}, \tag{7}$$

where $K^{1/2}$ denotes the positive definite square root of the positive definite matrix $K$. Unfortunately, this condition does not guarantee real eigenvalues, as the example of Barkwell and Lancaster [5] subsequently illustrated. The fallacy in the proof of condition (7) has been recently discussed by Bhaskar [6]. Moreover, Barkwell and Lancaster [5] obtained the following result: The system (2) is overdamped if and only if there exists a positive number $k$ such that

$$D > kI + k^{-1}K. \tag{8}$$

The evaluation of this condition requires searches of the $k$ values by trial and error.

Beskos and Boley [7] proposed a method to determine a region in the parameter space such that each eigenvalue corresponding to the values of damping coefficients in that region is real and *distinct*. On the boundary of this region (''critical damping surface'') the eigenvalues are real and at least one is repeated. Unfortunately this method is cumbersome to use if the number of degrees-of-freedom is large, but it can be applied successfully for two-degree-of-freedom systems.

Thus, there is still a lack of simple and applicable conditions for heavy damping.

## 2 Simple Heavy Damping Conditions

We first formulate a lemma.

LEMMA 1. *The system (2) is heavily damped if and only if the following* $2n$*-dimensional conservative gyroscopic system*

$$\begin{pmatrix} I & 0 \\ 0 & I \end{pmatrix}\begin{pmatrix} \ddot{y} \\ \ddot{z} \end{pmatrix} + \begin{pmatrix} 0 & D \\ -D & 0 \end{pmatrix}\begin{pmatrix} \dot{y} \\ \dot{z} \end{pmatrix} - \begin{pmatrix} K & 0 \\ 0 & K \end{pmatrix}\begin{pmatrix} y \\ z \end{pmatrix} = \begin{pmatrix} 0 \\ 0 \end{pmatrix} \tag{9}$$

*is stable*.

*Proof*. The eigenvalue problem associated with (9) is

$$\begin{pmatrix} s^2 I - K & sD \\ -sD & s^2 I - K \end{pmatrix}\begin{pmatrix} Y \\ Z \end{pmatrix} = \begin{pmatrix} 0 \\ 0 \end{pmatrix}, \tag{10}$$

where $Y$ and $Z$ are $n$-dimensional vectors. The system (9) is stable if and only if all eigenvalues of (10) are purely imaginary and semi-simple. Note that if $(s = i\omega,\ V^T = (Y^T, Z^T))$, where $i = \sqrt{-1}$, is an eigenpair of (10), then $(\bar{s} = -i\omega, \bar{V}^T)$ is also an eigenpair.

If we substitute $s = i\omega$ in Eq. (10), we obtain

$$-(\omega^2 I + K)Y + i\omega DZ = 0, \tag{11}$$

and

$$-i\omega DY - (\omega^2 I + K)Z = 0. \tag{12}$$

From Eq. (11),

$$Z = -\frac{i}{\omega} D^{-1}(\omega^2 I + K)Y, \tag{13}$$

and substitution of this expression into Eq. (12) leads

$$(\omega^4 D^{-1} + \omega^2(D^{-1}K + KD^{-1} - D) + KD^{-1}K)Y = 0, \tag{14}$$

which is equivalent to

$$(\omega^2 I + \omega D + K)D^{-1}(\omega^2 I - \omega D + K)Y = 0. \tag{15}$$

Let $s = i\omega$, $\omega < 0$, be an eigenvalue of (10) with eigenvector $V^T = (Y^T, Z^T)$. From Eqs. (3) and (15), we deduce that $\lambda = \omega$ is eigenvalue of (3) with eigenvector $U = D^{-1}(\omega^2 I - \omega D + K)Y$. Conversely, if $\lambda = \omega < 0$ is an eigenvalue of (3) with eigenvector $U$, then $s = \pm i\omega$ are eigenvalues of (10) with eigenvectors

$$V = \begin{pmatrix} Y \\ \pm i\omega^{-1} D^{-1}(\omega^2 I + K)Y \end{pmatrix}, \tag{16}$$

where $Y = (\omega^2 I - \omega D + K)^{-1} DU$. □

THEOREM 1. *The system described by Eq. (2), with* $D = D^T > 0$ *and* $K = K^T > 0$*, is heavily damped if*

$$D^2 - 2(K + \omega_{\max}^2 I) > 0, \tag{17}$$

*where* $\omega_{\max}$ *is the highest frequency of the corresponding undamped system*.

*Proof*. According to Bulatovic [8], we introduce auxiliary function of the form

$$V = V_1(x, y) + V_1(y, -x) \tag{18}$$

with

$$V_1(\xi, \eta) = \xi^T(D^2 - K - \omega_{\max}^2 I)\xi + 2\xi^T DK\eta + \eta^T(K^2 + \omega_{\max}^2 K)\eta. \tag{19}$$

Here, $\xi$ and $\eta$ are $n$-dimensional real vectors and $\omega_{\max}^2$ is the largest eigenvalue of matrix $K$. The time derivative of $V$, along every solution of Eq. (9), becomes $\dot{V} = 0$. Now, we can rewrite $V_1$ as:

$$V_1 = \xi^T\left(\frac{1}{2}D^2 - K - \omega_{\max}^2 I\right)\xi + F(\xi, \eta), \tag{20}$$

where

$$2F = (D\xi + 2K\eta)^T(D\xi + 2K\eta) + 2\eta^T(\omega_{\max}^2 K - K^2)\eta. \tag{21}$$

From $\omega_{\max}^2 K - K^2 \geqslant 0$ and $K^2 + \omega_{\max}^2 K > 0$, according to (21), we see that $F$ is positive semi-definite and the set

$$\{(\xi, \eta) : \xi = 0, F = 0\} \tag{22}$$

is trivial. Consequently, according to (20), $V_1(\xi, \eta)$, as well as the function (18), are positive definite if the condition (17) holds. Therefore, Theorem 1 follows from Lyapunov's stability theorem and the previous lemma. □

For multi-degree-of-freedom systems the criterion (17) provides only sufficient and not necessary condition for heavy damping (unless either $K = \alpha I$ or $D = \alpha I$, where $\alpha$ is a positive scalar).

In the case of ''classical damping'' in which $D$ and $K$ commute a sharper result can be obtained:

THEOREM 2. *If* $DK = KD$*, then the system described by (2) is heavily damped if and only if*

$$D^2 > 4K. \tag{23}$$

*Proof*. If $DK = KD$, then (23) is necessary and sufficient for stability of the system (9). This follows immediately from a result of Bulatovic [9]. □

Notice that (23) is equivalent to (7), if $D$ and $K$ commute. We note also that the condition (23) may be easily established through the use of the modal matrix.

A simple necessary condition for heavy damping is given next.

THEOREM 3. *If all eigenvalues of (3) are real, then*

$$\|D\|^2 > 2\,\mathrm{Tr}(K) \tag{24}$$

*where* $\mathrm{Tr}(K)$ *is the trace of* $K$ *and* $\|D\|$ *is the Euclidean matrix norm of* $D$.

We note that $\mathrm{Tr}(K) = \Sigma_{i=1}^n k_{ii}$ and $\|D\|^2 = \Sigma_{i,j=1}^n d_{ij}^2$.

*Proof*. By proof of Lemma 1, it follows that all roots of characteristic Eq. (4) are real if and only if every eigenvalue of (10) is purely imaginary. If all eigenvalues of (10) are purely imaginary, then according to Theorem 2 of Lancaster and Zizler [10], the condition (24) holds. □

There is another way of establishing this result. Indeed, the eigenvalues $\lambda_i$ of (3) and eigenvalues of the state matrix

$$G = \left(\begin{array}{c|c} -D & -K \\ \hline I & 0 \end{array}\right)$$

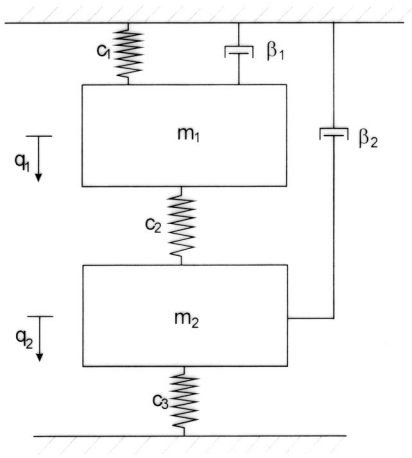


**Fig. 1 The system of example**

are the same. Consequently, using a well-known result of matrix theory (see Bellman [11]), we have

$$\sum_{i=1}^{2n} \lambda_i^2 = \mathrm{Tr}(G^2) = \mathrm{Tr}(D^2) - 2\,\mathrm{Tr}(K),$$

which is positive if all eigenvalues are real. From this and the fact that

$$\|D\|^2 = \mathrm{Tr}(D^2),$$

we obtain the result stated in (24).

Theorems 1–3 provide simple conditions for heavy damping, and they involve no undetermined parameters. The one-parameter criteria (i.e., conditions of the same type as (8) can be established by means of Lemma 1 and the results of Walker [12] for stability of conservative gyroscopic systems.

Finally, for completeness, the above results can be expressed in terms of the original matrices as follows:

(1) *If*

$$BM^{-1}B - 2(C + \omega_{\max}^2 M) > 0, \tag{25}$$

*the system described by (1) must be heavily damped.*

(2) *If* $BM^{-1}C = CM^{-1}B$, *then the system described by (1) is heavily damped if and only if*

$$BM^{-1}B - 4C > 0. \tag{26}$$

(3) *If the system described by (1) is heavily damped, then*

$$\mathrm{Tr}((M^{-1}B)^2) > 2\,\mathrm{Tr}(M^{-1}C). \tag{27}$$

## 3 Illustrative Example

To illustrate the usefulness of the above results consider the two-degree-of-freedom system shown in Fig. 1, where $c_i$ and $\beta_i$ stand for the spring constants and coefficients of viscous damping, respectively, and $q_1$ and $q_2$ are the displacements from equilibrium positions of masses $m_1$ and $m_2$. For simplicity, we take $c_1 = c_2 = c_3 = c$ and $m_1 = m_2 = m$. Such a model is described by the system (2) with

$$D = \begin{pmatrix} d_1 & 0 \\ 0 & d_2 \end{pmatrix}, \quad K = \begin{pmatrix} 2 & -1 \\ -1 & 2 \end{pmatrix} \tag{28}$$

where

$$d_i = \frac{\beta_i}{\sqrt{mc}}, \quad i = 1,2. \tag{29}$$

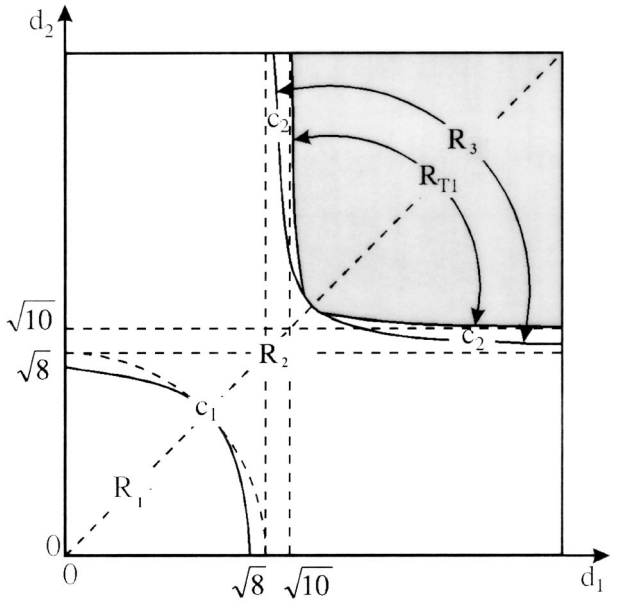


**Fig. 2 Weak ($R_1$), mixed ($R_2$), and heavy ($R_3$) damping regions, and the region $R_{T1}$ predicted by Theorem 1 for the system shown in Fig. 1**

The sufficient heavy damping criterion obtained here for a general case of damping is next applied to this system and the results are compared with the exact solution.

An elementary calculation shows that $\omega_{\max}^2 = \lambda_{\max}(K) = 3$. Condition (17) takes the form

$$D^2 - 2(K + \omega_{\max}^2 I) = \begin{pmatrix} d_1^2 - 10 & 2 \\ 2 & d_2^2 - 10 \end{pmatrix} > 0, \tag{30}$$

which yields

$$d_1^2 > 10 \tag{31}$$

and

$$d_1^2 d_2^2 - 10(d_1^2 + d_2^2) + 96 > 0. \tag{32}$$

If the parameters $d_1$ and $d_2$ are now chosen to satisfy (31) and (32), then (2), (28) will be heavily damped and the system will not oscillate when perturbed from equilibrium. The region $R_{T1}$ predicted by inequalities (31) and (32) is represented by shaded area in Fig. 2. The boundary of this region has asymptotes $d_1 = \sqrt{10}$ and $d_2 = \sqrt{10}$.

Next, a complete two-parameter $(d_1, d_2)$ damping analysis of the system, based on the discriminant of the characteristic polynomial and Theorem 3, is presented.

The characteristic equation for system (2), (28) is

$$\lambda^4 + a_1\lambda^3 + a_2\lambda^2 + a_3\lambda + a_4 = 0, \tag{33}$$

where

$$a_1 = d_1 + d_2, \quad a_2 = 4 + d_1 d_2, \quad a_3 = 2(d_1 + d_2), \quad a_4 = 3. \tag{34}$$

The discriminant of the polynomial (33) is defined as

$$\delta = \prod_{i>j}^{4} (\lambda_i - \lambda_j)^2, \tag{35}$$

where $\lambda_i$, $\lambda_j$ are the roots of the polynomial (multiple roots being counted as equal with different indices). On the other hand, the discriminant $\delta$ can be expressed by the coefficients of the polynomial (33), as follows (see, for example, Korn and Korn [13]):

$$\delta = \det\begin{pmatrix} 4 & s_1 & s_2 & s_3 \\ s_1 & s_2 & s_3 & s_4 \\ s_2 & s_3 & s_4 & s_5 \\ s_3 & s_4 & s_5 & s_6 \end{pmatrix}, \tag{36}$$

with

$$\left.\begin{aligned} s_1 &= -a_1 \\ s_2 &= a_1^2 - 2a_2 \\ s_3 &= -a_1^3 + 3a_1a_2 - 3a_3 \\ s_4 &= a_1^4 - 4a_1^2a_2 + 4a_1a_3 + 2a_2^2 - 4a_4 \\ s_5 &= -a_1^5 + 5a_1^3a_2 - 5a_1^2a_3 - 5a_1a_2^2 + 5a_2a_3 + a_1a_4 \\ s_6 &= a_1^6 - 6a_1^4a_2 + 6a_1^3a_3 + 9a_1^2a_2^2 - 12a_1a_2a_3 \\ &\quad - 2a_1^2a_4 - 2a_2^3 + 3a_3^2 + 6a_2a_4 \end{aligned}\right\}. \tag{37}$$

From (36), (37), and (34) we see that $\delta$ depends on the parameters $d_1$ and $d_2$. Since this expression is quite lengthy, it is omitted here.

It is evident from (35) that $\delta=0$ if (33) has multiple root; $\delta<0$ if (33) has two real distinct and two complex conjugate roots (mixed damped case); $\delta>0$ if (33) has either four real distinct (heavily damped case) or four complex conjugate distinct roots (weakly damped case). The question is now, whether the system is weakly damped (heavily damped) if $\delta>0$. An answer can be established by Theorem 2. According to this theorem, $\gamma=8-(d_1^2+d_2^2)\geqslant 0$ implies that (33), (34) has at least two complex conjugate roots. Consequently, when $\delta>0$, the system is weakly damped if and only if $\gamma\geqslant 0$. Summarizing these results we conclude that:

a. the system (2), (28) is weakly damped if $\delta(d_1,d_2)>0$ and $d_1^2+d_2^2\leqslant 8$;
b. the system (2), (28) is mixed damped if $\delta(d_1,d_2)<0$;
c. the system (2), (28) is heavily damped if $\delta(d_1,d_2)>0$ and $d_1^2+d_2^2>8$.

The equation $\delta(d_1,d_2)=0$ results in two curves $C_1$ and $C_2$, which have been depicted by MATLAB, see Fig. 2. Curve $C_1$ separates the weak damping region $R_1$ ($\delta>0, d_1^2+d_2^2\leqslant 8$) from the mixed damping region $R_2$ ($\delta<0$). Curve $C_2$, which has the asymptotes $d_1=\sqrt{8}$ and $d_2=\sqrt{8}$, separates the region $R_2$ from the heavy damping region $R_3$ ($\delta>0, d_1^2+d_2^2>8$).

Figure 2 shows that the region $R_3$ contains region $R_{T1}$ predicted by Theorem 1. Boundaries of these regions coincide at $d_1=d_2$ and the boundary of $R_{T1}$ slightly departs from $C_2$, more so as $d_1$ and $d_2$ increase. Thus, for this example the condition (17) gives a good result.

Finally, we note that another approach available to produce the critical damping curves $C_1$ and $C_2$ is given in Beskos and Boley [7] for a slightly different two-degree-of-freedom system. Their approach is based on a closed-form solution of the cubic polynomial which is obtained by differentiating the characteristic equation with respect to λ.

### 4 Concluding Remarks

We were interested in providing simple heavy damping criteria for multidimensional linear viscously damped systems with positive definite damping and stiffness matrices. Our primary intention was to avoid spectral (eigenvalue) analysis of the full, original damped system. Several results were derived. Theorem 1 provides sufficient condition for heavy damping, while Theorem 2 states necessary and sufficient condition when the damping is classical. Theorem 3 is a necessary condition. Both conditions (17) (or (25)) and (23) (or (26)) are presented in the form of the positive definiteness of certain combination of the system matrices. Condition (25) is not as simple as (26), since it requires the calculation of the maximal natural frequency which is not entirely trivial, but the check of (25) is much easier than solving the spectrum of the entire damped system. On the other hand, in contrast to the eigenvalue analysis, condition (25) yields inequalities amongst the various damping parameters, and these inequalities can be used to design a system or to adjust the damping constants in order to eliminate oscillation of the system. This was illustrated in Section 4. Moreover, a procedure to determine the nature of eigenvalues of two-degree-of-freedom system, as an alternative to the Beskos and Boley's approach, was presented based on Theorem 3 and on the discriminant of the characteristic polynomial. This leads to a complete two-parameter analysis, with the regions of weak, mixed, and heavy damping of the system shown in Fig. 1. Figure 2 illustrates the accomplished accuracy obtained by using Theorem 1.

### References


[1] Inman, D. J., 1989, *Vibration With Control, Measurement, and Stability*, Prentice-Hall, Englewood Cliffs, NJ.
[2] Duffin, R. J., 1955, "A Minimax Theory for Overdamped Networks," Journal of Rational Mechanics and Analysis, **4**, pp. 221–233.
[3] Lancaster, P., 1966, *Lambda-Matrices and Vibrating Systems*, Pergamon Press, Oxford, UK.
[4] Inman, D. J., and Andry, Jr., A. N., 1980, "Some Results on the Nature of Eigenvalues of Discrete Damped Linear Systems," ASME J. Appl. Mech., **47**, pp. 927–930.
[5] Barkwell, L., and Lancaster, P., 1992, "Overdamped and Gyroscopic Vibrating Systems," ASME J. Appl. Mech., **59**, pp. 176–181.
[6] Bhaskar, A., 1997, "Criticality of Damping in Multi-Degree-of-Freedom Systems," ASME J. Appl. Mech., **64**, pp. 387–393.
[7] Beskos, D. E., and Boley, B. A., 1980, "Critical Damping in Linear Discrete Dynamics Systems," ASME J. Appl. Mech., **47**, pp. 627–630.
[8] Bulatovic, R. M., 1997, "The Stability of Linear Potential Gyroscopic Systems When the Potential Energy has a Maximum," (in Russian) Prikl. Mat. Mekh. (PMM), **61**, pp. 385–389.
[9] Bulatovic, R. M., 1997, "On the Lyapunov Stability of Linear Conservative Gyroscopic Systems," C. R. Acad. Sci. **324**, pp. 679–683.
[10] Lancaster, P., and Zizler, P., 1998, "On the Stability of Gyroscopic Systems," ASME J. Appl. Mech., **65**, pp. 519–522.
[11] Belman, R., 1970, *Introduction to Matrix Analysis*, McGraw-Hill, New York.
[12] Walker, J. A., 1991, "Stability of Linear Conservative Gyroscopic Systems," ASME J. Appl. Mech., **58**, pp. 229–232.
[13] Korn, G. A., and Korn, T. M., 1961, *Mathematical Handbook for Scientists and Engineers*, McGraw-Hill, New York.


# On Viscoelastic Compliant Contact-Impact Models


**T. M. Atanackovic**
Professor

**D. T. Spasic**
Professor
Department of Mechanics, University of Novi Sad, POB 55, 21121 Novi Sad, Yugoslavia



*We study dynamics of a mass, moving on a straight line, and impacting against the rigid wall through a deformable body, that we model as a straight rod of negligible mass. The chosen constitutive model of the viscoelastic body comprises fractional derivatives of stress and strain and the restrictions on the coefficients that follow from Clausius Duhem inequality. We show that the dynamics of the problem is governed by a single differential equation of real order. The obtained equation was solved numerically. The comparison is made to the solution obtained by the Laplace transform and Post's inversion formula. The predictions of the*

*model concerning the duration of the impact, maximal values of the impacting force and deformation as well as the restitution coefficient are determined for several values of system parameters.*
[DOI: 10.1115/1.1629106]

## 1 Introduction

The impact of solid bodies is a complicated phenomena and could be studied by several different approaches. If impacting bodies are taken to be deformable then one has an advantage of being able to determine the impacting time, maximal deflections and impacting forces, see [1]. Special feature of viscoelastic impacting body is that there exist hysteresis-like behavior in force displacement diagram. Such a behavior was explained either by nonlinear models, [2], or by use of the standard linear viscoelastic model, as done recently by Butcher and Segalman [3]. As a matter of fact, in [3] besides the standard, the Kelvin-Voigt and Maxwell models of a viscoelastic body impacting against rigid obstacle were analyzed.

Our intention in this note is to use generalized model of a viscoelastic body that contains fractional derivatives of stress and strain for the study of impact. This model of a viscoelastic body with fractional derivatives (see [4,5]) was studied in [6–12], to mention just a few. We believe that generalized model of viscoelastic body used here is capable of describing impact in a more accurate way while still remaining in linear theory, [13]. Another feature of our approach is a consequent use of the restrictions on the coefficients of the model that follow from the Clausius Duhem inequality, [14]. The proposed model could be used for the study of polymers elastomers and other systems, [15].

## 2 The Models

Consider a mass $m$ moving on a straight line with constant velocity $v_0$ and impacting against the rigid wall (infinite mass), through a deformable body, that we model as a straight rod of negligible mass. We use $x$ to measure uniaxial deformation of that deformable body. This deformation is assumed to be isothermal. Let $f$ be the force between the body and the wall[1]. This force acts also on a mass $m$ so that its equation of motion reads

$$mx^{(2)}=-f, \quad x(0)=0, \quad x^{(1)}(0)=v_0, \quad f(0)=0, \tag{1}$$

where we used $(\cdot)^{(k)}=d^k(\cdot)/dt^k$ to denote the $k$th derivative with respect to time $t$. The relation between $f=f(t)$ and $x=x(t)$ (constitutive equation of the deformable body) may be taken in different forms. In order to motivate the approach to be followed attention is first focused on standard linear viscoelastic solid.

**2.1 Standard Linear Viscoelastic Solid: Zener Model.** In this case we have

$$f+\tau_f\cdot f^{(1)}=E(x+\tau_x\cdot x^{(1)}), \tag{2}$$

where $\tau_f$ and $\tau_x$ are the constants called relaxation times and $E$ is the modulus of elasticity. Note that in [3], Eq. (2) was written in slightly different form (our constants $E$, $\tau_f$ and $\tau_x$ are given as $E=m\omega_n^2$, $\tau_x=2\zeta/\omega_n$ and $\tau_f=2\zeta\eta/\omega_n$ where $\omega_n=\sqrt{k_1k_2/((k_1+k_2)m)}$, $\eta=k_2/(k_1+k_2)$ and $\zeta=k_1c/(2(k_1+k_2)m\omega_n)$ are introduced in [3]). A special case of (2) with $\tau_f=0$ represents the so-called Kelvin-Voigt model of a viscoelastic body. The *rheological* model corresponding to Kelvin-Voigt body is given in Fig. 1(*a*). In Fig. 1(*b*) the rheological model corresponding to standard linear viscoelastic solid, described by (2), is shown. Both models were used to study impact in [3]. Note, however, that there exists a fundamental restriction on the coefficients in (2) that follows from the second law of thermodynamics,

$$E>0, \quad \tau_f>0, \quad \tau_x>\tau_f \tag{3}$$

as proposed in [6] and [14]. Although the Kelvin-Voigt model $\tau_f=0$ does not satisfy the restrictions (3) it could be used for certain materials, and certain types of deformations, see [7]. Also note that there will be no damping if $\tau_x=\tau_f$ in (2), see [8].

As in [3], we consider that the body is separated when the contact force is equal to zero. It will be shown that this occurs before the deformation is recovered.

Introducing the dimensionless coordinate, force and time

$$\bar{x}=\frac{x}{v_0}\sqrt{\frac{E}{m}}, \quad \bar{f}=\frac{f}{v_0\sqrt{mE}}, \quad \bar{t}=t\sqrt{\frac{E}{m}}, \tag{4}$$

as well as the dimensionless relaxation times

$$\bar{\tau}_f=\tau_f\sqrt{\frac{E}{m}}, \quad \bar{\tau}_x=\tau_x\sqrt{\frac{E}{m}}, \tag{5}$$

from (1) and (2) we get the equations describing the impact of the system presented in Fig. 1(*b*):

$$x^{(2)}=-f, \quad x(0)=0, \quad x^{(1)}(0)=1, \quad f(0)=0, \tag{6}$$

and

$$f+\tau_f\cdot f^{(1)}=x+\tau_x\cdot x^{(1)}, \tag{7}$$

where we have omitted the bar, and where the derivatives are taken with respect to dimensionless time. In [3] the system (6), (7), was solved for $\tau_x=0.2$; $\tau_f=0.01$, 0.04 and 0.08. As we see the condition $\tau_x>\tau_f$ was satisfied in [3], although it was not explicitly stated.

To solve (6), (7) we use the Laplace transform technique. Introducing $X=X(s)=\mathcal{L}\{x(t)\}=\int_0^\infty e^{-st}x(t)dt$ and $F=F(s)=\mathcal{L}\{f(t)\}=\int_0^\infty e^{-st}f(t)dt$, from (6), (7) we get

$$F=\frac{1+\tau_x s}{1+\tau_f s}X, \tag{8}$$

and

$$X=\frac{1+\tau_f s}{\tau_f s^3+s^2+\tau_x s+1}, \quad F=\frac{1+\tau_x s}{\tau_f s^3+s^2+\tau_x s+1}. \tag{9}$$

An initial remark is that since $\lim_{s\to 0} sX(s)=0$ than certainly if $\lim_{t\to\infty}x(t)$ exists it tends to zero (as an expected consequence of viscosity). Second, the inverse transform of (8) yields the following relation between the force and the coordinate

$$f(t)=\frac{\tau_x}{\tau_f}x(t)+\frac{1}{\tau_f}\left(1-\frac{\tau_x}{\tau_f}\right)\int_0^t e^{-t-\xi/\tau_f}x(\xi)d\xi \tag{10}$$

which could be used if one wants to rewrite the impact model (6), (7) in the compact form of single integro-differential equation. Finally, with the help of standard software packages it is fairly straightforward to obtain the solution $x(t)$, $f(t)$ in the closed form. Namely, the inverse Laplace transform of (9) for $\tau_f=0.01$ and $\tau_x=0.2$ gives

$$\begin{aligned} x(t)&=0.0003e^{-24.84t}+e^{-0.08t}(1.006\sin t-0.0003\cos t),\\ f(t)&=-0.162e^{-24.84t}+e^{-0.08t}(\sin t+0.162\cos t). \end{aligned} \tag{11}$$

For the later use (when the inverse Laplace transform fails to proceed to a closed form) it is important to note that both $x(t)$ and $f(t)$ could be obtained by use of Post's inversion formula, see [16] p. 380, i.e.,

$$x(t)=\lim_{n\to\infty}\frac{(-1)^n\left(\frac{n}{t}\right)^{n+1}X^{(n)}\left(\frac{n}{t}\right)}{n!},$$

Contributed by the Applied Mechanics Division of THE AMERICAN SOCIETY OF MECHANICAL ENGINEERS for publication in the ASME JOURNAL OF APPLIED MECHANICS. Manuscript received by the ASME Applied Mechanics Division, Nov. 30, 2001; final revision, July 7, 2003. Associate Editor: K. R. Rajagopal.

[1]The force $f$ used here is given as $f=A\sigma$ where $A$ is the cross-sectional area and $\sigma$ is the stress. We assume that the cross sectional area remains the same during the deformation.

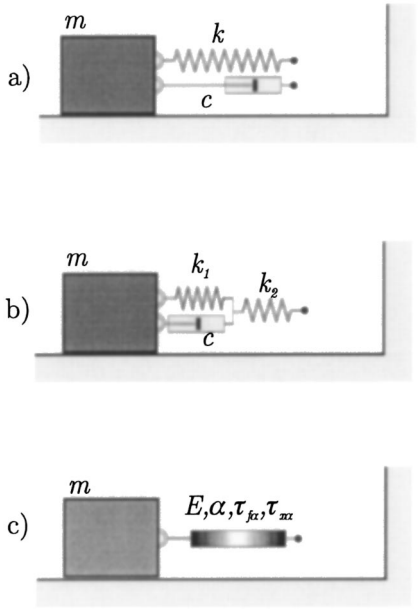


**Fig. 1 Systems under considerations**

$$f(t)=\lim_{n\to\infty}\frac{(-1)^n\left(\frac{n}{t}\right)^{n+1}F^{(n)}\left(\frac{n}{t}\right)}{n!}. \tag{12}$$

Although Post's formula, discovered in 1930 [17], may be regarded as an analytical result, very useful for applications, difficulties essentially technical in nature prevented its usage in practical problems. However, nowadays the $n$th derivatives of (9) needed for the right-hand sides of (12) could be easily calculated by use of standard software packages.

With this preparation completed we turn now to a discussion of the more general compliant contact impact model.

**2.2 Fractional Standard Linear Viscoelastic Solid: Modified Zener Model.** Once again we start with (1) but instead of (2) here we deal with the model incorporating fractional damping elements, Fig. 1(*c*),

$$f+\tau_{f\alpha}\cdot f^{(\alpha)}=E(x+\tau_{x\alpha}\cdot x^{(\alpha)}), \tag{13}$$

with $0<\alpha<1$ and where $(\cdot)^{(\alpha)}$ denotes the $\alpha$th derivative of a function $(\cdot)$ taken in Riemann-Liouville form as

$$\begin{aligned}\frac{d^\alpha}{dt^\alpha}g(t)=g^{(\alpha)}&\equiv\frac{d}{dt}\frac{1}{\Gamma(1-\alpha)}\int_0^t\frac{g(\xi)d\xi}{(t-\xi)^\alpha}\\&=\frac{d}{dt}\frac{1}{\Gamma(1-\alpha)}\int_0^t\frac{g(t-\xi)d\xi}{\xi^\alpha}\\&=\frac{g(0)t^{-\alpha}}{\Gamma(1-\alpha)}+\frac{1}{\Gamma(1-\alpha)}\int_0^t\frac{g^{(1)}(t-\xi)d\xi}{\xi^\alpha}\\&=\sum_{n=0}^{\infty}\binom{\alpha}{n}\frac{t^{n-\alpha}}{\Gamma(n+1-\alpha)}g^{(n)}(t),\end{aligned} \tag{14}$$

where $\Gamma$ denotes the Euler gamma function. Also in $(14)_4$ the binomial coefficients are $\binom{\alpha}{n}=(-1)^{n-1}\alpha\Gamma(n-\alpha)/\Gamma(1-\alpha)\Gamma(n+1)=(-1)^n(-\alpha)_n/n!$ and $(u)_n=u(u+1)\ldots(u+n-1)$, $n=1,2,\ldots,(u)_0\equiv1$. The dimension of the constants $\tau_{x\alpha}$ and $\tau_{f\alpha}$ is $[\text{time}]^\alpha$. Note that these constants no longer have the physical meaning they have in standard models. In (13) we assume that $E>0$, $\tau_{f\alpha}>0$, $\tau_{x\alpha}>\tau_{f\alpha}$ are satisfied and thus represent a thermodynamically well-behaved model.

Introducing the dimensionless quantities

$$\overline{\tau}_{x\alpha}=\tau_{x\alpha}\left(\frac{E}{m}\right)^{\alpha/2},\quad \overline{\tau}_{f\alpha}=\tau_{f\alpha}\left(\frac{E}{m}\right)^{\alpha/2}, \tag{15}$$

and using (4) we transform (13) into the following form (the bar is omitted):

$$f+\tau_{f\alpha}\cdot f^{(\alpha)}=x+\tau_{x\alpha}\cdot x^{(\alpha)}, \tag{16}$$

and find that the impact of the fractional standard linear solid is modeled by Eqs. (6) and (16). Note that this model, belongs to the class of continuous dynamics models of collision, i.e., collision dynamics is treated as a continuous time dynamics phenomena restricted to local deformations (vibration effects of the solid body are not taken into account). Compared to (7) in expression (16) the customary time derivatives of integer order are replaced by derivatives of real order $\alpha$ with $0<\alpha<1$. The justification for such models has resided in the fact that they are effective in describing the behavior of some real materials. Actually the study of considered fractional standard linear solid models possess an essential mathematical interest too.

Our main results concern the solution of (6), (16).

*2.2.1 Numerical Solution.* In order to compute the solution for the case of generalized constitutive equation we apply arguments presented in the book of Podlubny, [18], p. 223. First, we eliminate $f$ and remove the nonhomogeneous initial condition $(6)_3$. Namely, by introducing the variable

$$z(t)=x(t)-t, \tag{17}$$

and using basic properties of the Riemann-Liouville fractional differentiation, instead of (6), (16), we obtain the following differential equation of real order

$$\tau_{f\alpha}z^{(2+\alpha)}+z^{(2)}+z+\tau_{x\alpha}z^{(\alpha)}=-t-\frac{\tau_{x\alpha}\Gamma(2)}{\Gamma(2-\alpha)}t^{1-\alpha}, \tag{18}$$

with homogeneous boundary conditions

$$z^{(k)}(0)=0,\quad k=0,1,2. \tag{19}$$

Using the first-order approximation of problem (18), (19) we derive the following algorithm for obtaining the numerical solution, [18]:

$$z_0=0,\quad z_1=0,\quad z_2=0, \tag{20}$$

$$\begin{aligned}z_m=&\frac{1}{1+h^{-2}+\tau_{x\alpha}h^{-\alpha}+\tau_{f\alpha}h^{-2-\alpha}}\\&\times\left\{\frac{2z_{m-1}-z_{m-2}}{h^2}-\frac{\tau_{x\alpha}\Sigma_{j=1}^{m}\omega_{j,\alpha}z_{m-j}}{h^\alpha}\right.\\&\left.-\frac{\tau_{f\alpha}\Sigma_{j=1}^{m}\omega_{j,2+\alpha}z_{m-j}}{h^{2+\alpha}}-mh-\frac{\tau_{x\alpha}\Gamma(2)(mh)^{1-\alpha}}{\Gamma(2-\alpha)}\right\},\\&m=3,4,\ldots\end{aligned} \tag{21}$$

where $h$ is time step and where the coefficients $\omega_{j,\kappa}$, $\kappa=\alpha,2+\alpha$, are calculated by the recurrence relationships $\omega_{0,\kappa}=1$; $\omega_{j,\kappa}=(1-(\kappa+1)/j)\omega_{j-1,\kappa}$, $j=1,2,3,\ldots$. Noting that $z_m=z(t_m)=z(mh)$ from (17) we obtain

$$x(t_m)=mh+z_m. \tag{22}$$

Finally, by use of second-order backward differences from (6) we find

$$f(t_m)=-\frac{(z_m-2z_{m-1}+z_{\kappa-2})}{h^2}. \tag{23}$$

**Table 1 Impact materials for specific materials**

| Material Description | Impact Description | |
|---|---|---|
| $\alpha=1$ | | $T=2.962$ |
| | $f_{\max}(1.289)=0.887$ | |
| $\tau_f=0.01$ | | $x=0.144$ |
| | $x_{\max}(1.480)=0.869$ | |
| $\tau_x=0.2$ | | $x^{(1)}=-0.756$ |
| $\alpha=1$ | | $T=2.981$ |
| | $f_{\max}(1.330)=0.907$ | |
| $\tau_f=0.04$ | | $x=0.126$ |
| | $x_{\max}(1.490)=0.890$ | |
| $\tau_x=0.2$ | | $x^{(1)}=-0.792$ |
| $\alpha=1$ | | $T=3.013$ |
| | $f_{\max}(1.388)=0.933$ | |
| $\tau_f=0.08$ | | $x=0.100$ |
| | $x_{\max}(1.507)=0.918$ | |
| $\tau_x=0.2$ | | $x^{(1)}=-0.842$ |
| $\alpha=0.95$ | | $T=2.945$ |
| | $f_{\max}(1.289)=0.899$ | |
| $\tau_{f\alpha}=0.01$ | | $x=0.144$ |
| | $x_{\max}(1.475)=0.870$ | |
| $\tau_{x\alpha}=0.2$ | | $x^{(1)}=-0.762$ |
| $\alpha=0.95$ | | $T=3.141$ |
| | $f_{\max}(1.570)=0.999$ | |
| $\tau_{f\alpha}=0.01$ | | $x=0$ |
| | $x_{\max}(1.571)=0.998$ | |
| $\tau_{x\alpha}=0.011$ | | $x^{(1)}=-0.997$ |
| $\alpha=0.49$ | | $T=2.151$ |
| | $f_{\max}(0.832)=1.140$ | |
| $\tau_{f\alpha}=5\times10^{-8}$ | | $x=0.232$ |
| | $x_{\max}(1.110)=0.642$ | |
| $\tau_{x\alpha}=0.886$ | | $x^{(1)}=-0.596$ |
| $\alpha=0.23$ | | $T=2.025$ |
| | $f_{\max}(0.910)=1.356$ | |
| $\tau_{f\alpha}=0.004$ | | $x=0.135$ |
| | $x_{\max}(1.034)=0.632$ | |
| $\tau_{x\alpha}=1.183$ | | $x^{(1)}=-0.771$ |

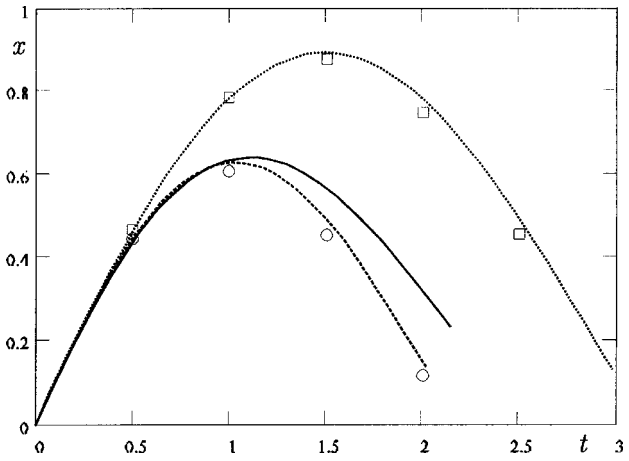


**Fig. 2 Curves $x(t)$ for standard linear solid $\alpha=1$, $\tau_f=0.04$, $\tau_x=0.2$, (dotted), fractional standard solid with $\alpha=0.49$, $\tau_{f\alpha}=5\times10-8$, $\tau_{x\alpha}=0.886$, (solid line) and for $\alpha=0.23$, $\tau_{f\alpha}=0.004$, $\tau_{x\alpha}=1.183$, (dashed)**

The described numerical method was experimentally verified on a number of test problems by comparing it (when it was possible) with analytical solutions, see [18]. In the case of Eq. (18), and therefore Eqs. (22), (23), the concept of Post's formula although less accurate for small $n$ could be very useful.

*2.2.2 The Laplace Transform and Post's Inversion Formula Applied to (6), (16).* Using the standard procedure together with the standard expression for the Laplace transform of $g^{(\alpha)}$, given as $\mathcal{L}\{g^{(\alpha)}\}=s^\alpha G-[(\int_0^t g(\xi)d\xi/(t-\xi)^\alpha)]_{t=0}$, where $\mathcal{L}\{g(t)\}=G=G(s)$ and where the term in brackets vanishes if $\lim_{t\to0}+g(t)$ is bounded (see [4]), from (6), (16) we find that

$$F=\frac{1+\tau_{x\alpha}s^\alpha}{1+\tau_{f\alpha}s^\alpha}X, \tag{24}$$

and

$$X=\frac{1+\tau_{f\alpha}s^\alpha}{\tau_{f\alpha}s^{2+\alpha}+s^2+\tau_{x\alpha}s^\alpha+1}, \quad F=\frac{1+\tau_{x^\alpha}s^\alpha}{\tau_{f\alpha}s^{2+\alpha}+s^2+\tau_{x\alpha}s^\alpha+1}. \tag{25}$$

As before, since $\lim_{s\to0} sX\to0$ we conclude that the motion will vanish as expected. Also note that the model incorporating fractional damping elements (25) does not admit closed form solution. As the matter of fact the inversion of (24) yields the following relation between $f(t)$ and $x(t)$

$$f(t)=\frac{\tau_{x\alpha}}{\tau_{f\alpha}}x(t)+\frac{1}{\tau_{f\alpha}}\left(1-\frac{\tau_{x\alpha}}{\tau_{f\alpha}}\right)\int_0^t e_{\alpha,\alpha}\left(t-\xi,\frac{1}{\tau_{f\alpha}}\right)x(\xi)d\xi, \tag{26}$$

where $e_{\alpha,\beta}(t;\lambda)$ stands for the generalized Mittag-Leffler function, that is $e_{\alpha,\beta}(t;\lambda)\equiv E_{\alpha,\beta}(-\lambda t^\alpha)/t^{1-\beta}$ with $E_{\alpha,\beta}(t)=\Sigma_{n=0}^\infty t^n/\Gamma(\alpha n+\beta)$. The corresponding integro-differential equation as a compliant contact impact model could be obtained easily from (6). Note also that (26) generalizes (10) as expected.

Finally we apply Post's inversion formula. This procedure could be used for error estimation of the numerical solution. Also by using (12) with $X$ and $F$ given by (25) we could obtain an analytical approximation for the solution $x(t)$ and $f(t)$.

In the next section we illustrate all the results of above.

## 3 The Predictions

In Table 1 we present the duration of impact $T$, determined by the condition $f(T)=0$ as proposed in [3], maximal values of $x$ and $f$ for several values of dimensionless relaxation times in case of standard linear (viscoelastic) solids and for several values of constants $\alpha$, $\tau_{f\alpha}$, and $\tau_{x\alpha}$ (see (4) and (5) for definitions). The values of dimensionless time corresponding to these maximums are given in parenthesis. The values $x$ and $x^{(1)}$ at $T$ ($x^{(1)}(T)$ determines the restitution coefficient) are also presented.

The numerical values of constants $0<\alpha<1$, $\tau_{f\alpha}$ and $\tau_{x\alpha}$ were taken from the paper of Fenander where the railpad models were investigated, [8].

For $\alpha=1$ we apply the inverse Laplace transform to (9). For $\alpha<1$ we apply numerical procedure (21) and then (22), (23). In all the calculations the time step was $h=10^{-3}$.

In Fig. 2 we present some solutions $x(t)$. The values obtained by applying Post's inversion formula (12) to (9) for $\alpha=1$, $\tau_f=0.04$ and $\tau_x=0.2$ are also presented (squares in Fig. 2). The difference between the exact solution (11) and the solution obtained by Post's formula for $n=70$, is less than $5\times10^{-2}$. Also, the values calculated by Post's formula (12) applied to (25) for $\alpha=0.23$, $\tau_{f\alpha}=0.004$, $\tau_{x\alpha}=1.183$ for $n=40$ are also marked by circles in Fig. 2. In this case the differences between the numerical solution and these values are less than $5\times10^{-2}$. In both cases the derivatives were calculated with the help of SciWorkPlace (TCI Software Research) and Mathematica (Wolfram Research, Inc.). It is worth noting that modern computers allow larger $n$ and thus more accuracy.

Finally the hysteresis diagrams corresponding to the solutions presented in Fig. 2 are shown in Fig. 3.

Note that when compared to standard linear viscoelastic solid the solid described by fractional derivatives exhibits shorter duration of impact, smaller maximal deformation and larger maximal force.

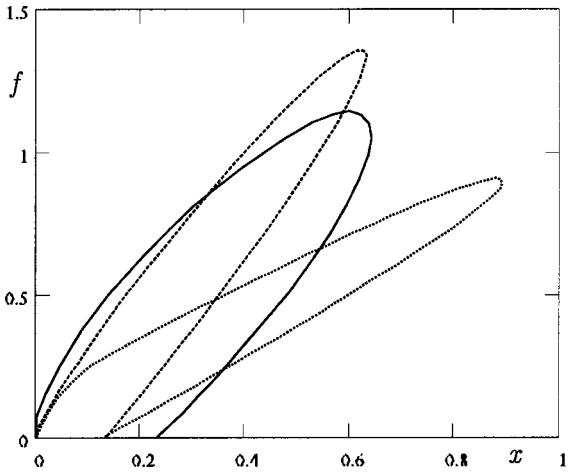


**Fig. 3 Hysteresis diagrams for standard linear solid $\alpha=1$, $\tau_f=0.04$, $\tau_x=0.2$, (dotted), fractional standard solid with $\alpha=0.49$, $\tau_{f\alpha}=5\times10^{-8}$, $\tau_{x\alpha}=0.886$, (solid line) and for $\alpha=0.23$, $\tau_{f\alpha}=0.004$, $\tau_{x\alpha}=1.183$, (dashed)**

## 4 Analysis of the Results

From the values presented in Table 1 we conclude that for the case when $\alpha\to1$ the solutions for the fractional standard linear solid are very close, and tend to the ones, that describe the standard linear solid (for $\alpha=1$ and the same values of the constants describing material). Also when $\tau_x\to\tau_f$ there is no damping as expected, i.e., velocity after the rebound is almost of the same intensity as before the impact. In such a case the presented values of $T$ and $x_{\max}$ could be compared with the case of nonlinear spring as presented in [19]. Namely, in [19] the impact is modeled by the equation

$$x^{(2)}=-\rho x^{3/2},\quad x(0)=0,\quad x^{(1)}(0)=1. \tag{27}$$

For example, if the we take $\rho=1$ we obtain $T=3.218$, $x^{(1)}(T)=-1$ and $x_{\max}=1.093$. However, it should be noted that in tackling the compliant impact problem by use of nonlinear elastic spring one methodological anomaly is encountered. Namely, if the body is released from rest in a vertical plane and impinges the horizontal surface it will bounce forever. In reality this is not the case due to damping.

Our final remark concerns the thermodynamical restrictions. Violating them could pose severe problems. Roughly speaking putting $\tau_{f\alpha}>\tau_{x\alpha}$ will lead to the rebound velocity which is higher then the approaching velocity, i.e., $|x^{(1)}(T)|>x^{(1)}(0)=1$. In the former example if the body falls a distance $h$ it will bounce to the distances higher then $h$ and bounce forever as well.

## 5 Conclusions

In this paper we have analyzed the elastic compliant contact impact model with fractional derivative type of dissipation. Thermodynamical restrictions on constitutive equations are taken into account. We show that the dynamics of the problem is governed by a single differential equation of real order. The obtained equation was solved numerically. The comparison is made to the solution obtained by the Laplace transform and Post's inversion formula. The predictions of the model concerning the duration of the impact, maximal values of the impacting force and deformation as well as the restitution coefficient are determined for several values of system parameters.

## References


[1] Brogliato, B., 1999, *Nonsmooth Dynamics*, Springer, London.
[2] Hunt, K. H., and Crossley, F. R. E., 1975, "Coefficient of Restitution Interpreted as Damping in Vibroimpact," ASME J. Appl. Mech., **42**, pp. 440–445.
[3] Butcher, E. A., and Segalman, D. J., 2000, "Characterizing Damping and Restitution in Compliant Impact via Modified K-V and Higher Order Linear Viscoelastic Models," ASME J. Appl. Mech., **67**, pp. 831–834.
[4] Oldham, K. B., and Spanier, J., 1974, *The Fractional Calculus*, Academic Press, San Diego, CA.
[5] Samko, S. G., Kilbas, A. A., and Marichev, O. I., 1993, *Fractional Integrals and Derivatives*, Gordon and Breach, Amsterdam.
[6] Bagley, R. L., and Torvik, P. J., 1986, "On the Fractional Calculus Model of Viscoelastic Behaviour," J. Rheol., **30**, pp. 133–155.
[7] Pritz, T., 1996, "Analysis of Four-Parameter Fractional Derivative Model of Real Solid Materials," J. Sound Vib., **195**, pp. 103–115.
[8] Fenander, Å., 1998, "A Fractional Derivative Railpad Model Included in a Railway Track Model," J. Sound Vib., **212**, pp. 889–903.
[9] Baclic, B. S., and Atanackovic, T. M., 2000, "Stability and Creep of a Fractional Derivative Order Viscoelastic Rod," Bull. T. CXXI Serb. Acad. Sci. Arts, (25), pp. 115–131.
[10] Suarez, L. E., and Shokooh, A., 1997, "An Eigenvector Expansion Method for the Solution of Motion Containing Fractional Derivatives," ASME J. Appl. Mech., **64**, pp. 629–635.
[11] Enelund, M., and Lesieutre, G. A., 1999, "Time Domain Modeling of Damping Using Anelastic Displacement Fields and Fractional Calculus," Int. J. Solids Struct., **36**, pp. 4447–4472.
[12] Haupt, P., Lion, A., and Backhaus, E., 2000, "On the Dynamic Behaviour of Polymers Under Finite Strains: Constitutive Modeling and Identification of Parameters," Int. J. Solids Struct., **37**, pp. 3633–3646.
[13] Bagley, R. L., 1989, "Power Law and Fractional Calculus Model of Viscoelasticity," AIAA J., **27**, pp. 1412–1417.
[14] Atanackovic, T. M., 2001, "A Modified Zener Model of a Viscoelastic Body," Continuum Mech. Thermodyn., in press.
[15] Palade, L. I., Verney, V., and Attane, P., 1996, "A Modified Fractional Model to Describe the Entire Viscoelastic Behaviour of Polybutadienes From Flow to Glassy Regime," Rheol. Acta, **35**, pp. 265–273.
[16] Mikusiński, J., 1959, *Operational Calculus*, Pergamon Press, New York.
[17] Post, E. L., 1930, "Generalized Differentiation," Trans. Am. Math. Soc., **32**, pp. 723–781.
[18] Podlubny, I., 1999, *Fractional Differential Equations*, Academic Press, San Diego, CA.
[19] Kilchevski, N. A., 1976, *Dynamic Contact of Solid Bodies*, Naukova Dumka, Kiev.


# Surface Instability of a Semi-Infinite Elastic Body Under Surface van der Waals Forces


**C. Q. Ru**
Department of Mechanical Engineering, University of Alberta, Edmonton, AL T6G 2G8, Canada
e-mail: c.ru@ualberta.ca



*It is shown that the surface of a semi-infinite linear elastic body attracted by a rigid flat through van der Waals-like forces is always unstable. The wavelength of the surface wrinkling is finite and decreases with the van der Waals interaction coefficient. In particular, this result implies that the deformation field of the semi-infinite linear elastic body attracted by a rigid flat cannot be determined uniquely.* [DOI: 10.1115/1.1636791]


## Introduction

Intermolecular and surface forces, [1], have a crucial effect on mechanical behavior of deformable bodies at micro/nanoscale. One well-known example is the contact mechanics of elastic bodies in the presence of van der Waals-like interaction, [2]. Despite extensive research, however, it appears that surface instability of elastic bodies under van der Waals-like attractive forces has not


Contributed by the Applied Mechanics Division of THE AMERICAN SOCIETY OF MECHANICAL ENGINEERS for publication in the ASME JOURNAL OF APPLIED MECHANICS. Manuscript received by the ASME Applied Mechanics Division, June 19, 2001; final revision, May 5, 2003. Associate Editor: B. M. Moran.

been widely recognized. Very recently, surface instability of a compliant rubber-like elastic layer attracted by a rigid flat has been studied in [3,4]. This new type of surface instability is elastic in nature and does not rely on the existence of a surface compressive prestress. Therefore, it is essentially different from other known surface instability due to surface compressive stress, [5–7], negative surface modulus, [6], or surface diffusion, [8].

The analysis given in [3,4] has been restricted to surface instability of a thin elastic film bonded on a rigid substrate, although the thickness of interacting deformable bodies is often large compared to their other characteristic sizes (such as the gap width between the interacting bodies, the wavelength, and even the size of the interacting zone). For an elastic film on a rigid substrate, it is found, [3,4], that the wavelength of the surface instability mode is proportional to the thickness of the elastic film. Obviously, this result cannot be directly applied to a semi-infinite elastic body by treating it as a limit case of an elastic layer, because it would predict an infinite wavelength and thus surface wrinkling of a semi-infinite elastic body would not occur. It is the aim of this note to analyze surface instability of a semi-infinite elastic body. Here, we shall confine ourselves to plane strain and thus consider an elastic half-plane attracted by a rigid flat through van der Waals-like interaction, as depicted in Fig. 1.

## Surface Instability

When the rigid flat is brought into contact with the elastic half-plane, van der Waals forces come into play if the gap width between the two surfaces is, say, below 100 nm, [1,3]. For instance, a simple general expression for the van der Waals attraction between two flat surfaces, as function of the distance, can be found in [3]. Thus, the present problem, depicted in Fig. 1, admits a total potential energy, just like [3,4], and is a conservative system. Hence, surface instability of the elastic half-plane can be studied by the conventional method of examining the existence of nontrivial deformation state in the neighborhood of the uniform deformation state of the elastic half-plane.

Therefore, surface instability is defined by the existence of a nontrivial infinitesimal perturbation which satisfies all linearized governing equations and zero boundary conditions. Since the van der Waals attractive forces only cause a surface normal stress on the elastic half-plane, and the value of the surface normal stress at any point can be assumed to be a function of the distance between the two surface at that point, it follows that the perturbed surface shear stress $\sigma_{xy}$ vanishes, and the perturbed surface normal stress $\sigma_{yy}$ depends linearly on the perturbed surface normal displacement, $v$, of the elastic half-plane. Thus the surface conditions for the perturbed elastic half-plane can be written as

$$\sigma_{yy}=-\beta v-\gamma v_{,xx}, \quad \sigma_{xy}=0, \quad y=0^{+} \tag{1}$$

where the interaction coefficient $\beta$ is determined by the second derivative of the van der Waals interaction energy at the equilibrium distance between two flat surfaces, and $\gamma(>0)$ is the surface energy of the elastic half-plane. In particular, the coefficient $\beta$ depends on the equilibrium distance between two flat surfaces prior to surface instability, and is not equal to the Hamaker constant of the van der Waals law, [1,3]. Here, because the van der Waals attractive force at any point is a decreasing function of the distance at that point, the perturbed surface normal stress $\sigma_{yy}$ at a point is tensile (or compressive) if the perturbed surface normal displacement $v$ at that point is negative (or positive), see Fig. 1. This explains the sign "$-$" for the coefficient $\beta$. Therefore, the van der Waals interaction on the perturbed surface acts like a uniform distributed linear spring with negative spring constant, and becomes a driving force for surface instability. Based on this fact, it is anticipated that the surfaces of the elastic half-plane would become unstable when the van der Waals attractive interaction, characterized by the coefficient $\beta$, is sufficiently strong. It is stressed that the present analysis based on the surface conditions (1) is valid not only for van der Waals interaction, but also for electrostatic interaction between two oppositely charged solid bodies, [9].

The perturbed stresses and displacements have to meet the equations of plane elastostatics. Thus, in the upper half-plane ($y>0$), the perturbed stresses and displacements $(u,v)$ can be given in terms of a single complex potential $\Omega(z)$ (see, e.g., [10], pp. 52–54) as follows:

$$\begin{aligned} &2\mu(u+iv)=\kappa\Omega(z)+\Omega(\overline{z})+(\overline{z}-z)\overline{\Omega'(z)},\\ &\sigma_{xx}+\sigma_{yy}=2[\Omega'(z)+\overline{\Omega'(z)}],\\ &\sigma_{yy}-i\sigma_{xy}=\Omega'(z)-\Omega'(\overline{z})+(z-\overline{z})\overline{\Omega''(z)}, \quad z=x+iy, \quad y\geqslant 0 \end{aligned} \tag{2}$$

where $\Omega(z)$ is an analytic function defined in the upper and lower half-planes, respectively, $\kappa=(3-4\nu)$ for plane strain and $\kappa=(3-\nu)/(1+\nu)$ for plane stress, and $\mu$ and $\nu$ are the shear modulus and Poisson's ratio of the elastic half-plane. Since admissible perturbations must meet zero boundary conditions, all perturbed displacements and stresses must vanish when $y$ tends to infinity, and thus $\Omega(z)$ and its derivatives approach zero when $y$ tends to infinity.

Let us now examine the existence of a nonzero perturbation. It follows from (2) that the second surface condition of (1) gives

$$[\Omega'(x)+\overline{\Omega'}(x)]^{+}=[\Omega'(x)+\overline{\Omega'}(x)]^{-}, \quad y=0.$$

Because $\Omega(z)$ approaches zero when $y$ tends to infinity, the above condition implies, [10],

$$\Omega(z)+\overline{\Omega}(z)=0 \tag{3}$$

in the entire $z$-plane, where the second term on LHS is the symmetric continuation of $\Omega(z)$ defined in the opposite half-plane with respect to the real axis. On using (2) and (3), the first surface condition of (1) is given by

$$\begin{aligned} &4i\mu[\Omega'^{+}(x)-\Omega'^{-}(x)]\\ &\quad=-\beta[\kappa\Omega(z)+\Omega(\overline{z})]^{+}+\beta\overline{[\kappa\Omega(z)+\Omega(\overline{z})]^{+}}\\ &\qquad-\gamma[[\kappa\Omega''(z)+\Omega''(\overline{z})]^{+}-\overline{[\kappa\Omega''(z)+\Omega''(\overline{z})]^{+}}]\\ &\quad=-\beta(\kappa+1)[\Omega^{+}(x)+\Omega^{-}(x)]-\gamma(\kappa+1)\\ &\qquad\times[\Omega''^{+}(x)+\Omega''^{-}(x)], \quad y=0 \end{aligned}$$

which leads to

$$\begin{aligned} &[4i\mu\Omega'(x)+\beta(\kappa+1)\Omega(x)+(\kappa+1)\gamma\Omega''(x)]^{+}\\ &\quad=[-(\kappa+1)\beta\Omega(x)-(\kappa+1)\gamma\Omega''(x)+4i\mu\Omega'(x)]^{-},\\ &\quad y=0. \end{aligned} \tag{4}$$

Here, LHS of (4) can be understood as the boundary value of an analytic function in the upper half-plane, while RHS as the boundary value of another analytic function in the lower half-plane. Because $\Omega(z)$ and its derivatives approach zero when $y$ tends to infinity, it follows from (4) that

$$\begin{aligned} &[4i\mu\Omega'(z)+\beta(\kappa+1)\Omega(z)+(\kappa+1)\gamma\Omega''(z)]=0, \quad y>0;\\ &[-\beta(\kappa+1)\Omega(z)+4i\mu\Omega'(z)-(\kappa+1)\gamma\Omega''(z)]=0, \quad y<0. \end{aligned} \tag{5}$$

Thus, $\Omega(z)$ can be determined by the two differential equations in the upper and lower half-planes, respectively. It can be verified that a nonzero solution $\Omega(z)$ which approaches zero when $y$ tends to infinity exists if and only if $\beta>0$. When $\beta>0$, we have

$$\begin{aligned} &\Omega(z)=A\exp[i\lambda z], \quad y>0;\\ &\Omega(z)=B\exp[-i\lambda z], \quad y<0 \end{aligned} \tag{6}$$

with

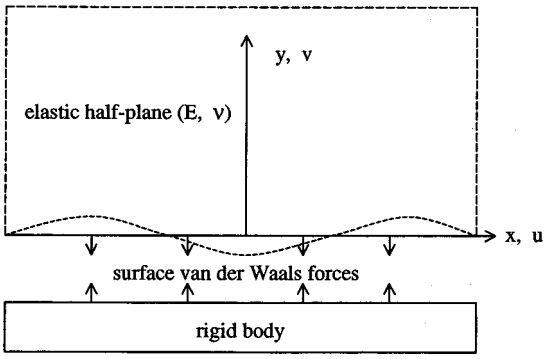


**Fig. 1 Surface instability of an elastic half-plane under surface van der Waals forces**

$$\lambda = \frac{-2\mu + \sqrt{4\mu^2 + \beta\gamma(\kappa+1)^2}}{\gamma(\kappa+1)} \tag{7}$$

where the positive sign "+" has been chosen because $\lambda$ must be positive. Further, in view of (3), one finds

$$B = -\bar{A} \tag{8}$$

where $A = a + ib$, and $a$ and $b$ are two arbitrary real numbers.

## Discussions

In contrast to surface instability of an elastic film on a rigid substrate, [3,4], or the so-called "tip-surface" instability, [11], which occurs only when the interaction exceeds a certain critical value, the above results indicate that surface instability of an elastic half-plane occurs whenever $\beta > 0$. In particular, this means that the deformation field of the elastic half-plane cannot be determined uniquely. The perturbed surface displacements caused by the surface instability are given by

$$\begin{aligned} 2\mu u &= (\kappa-1)[a\cos\lambda x - b\sin\lambda x], \\ 2\mu v &= (\kappa+1)[b\cos\lambda x + a\sin\lambda x] \end{aligned} \tag{9}$$

where $a$ and $b$ are two arbitrary real numbers. The ratio of the magnitude of the surface normal displacement to the magnitude of the surface tangential displacement is $(\kappa+1)/(\kappa-1)$, and thus the surface tangential displacement vanishes in plane strain when $\nu = 1/2$.

Surface wrinkling is significant especially for compliant solids, such as rubble-like materials. For instance, for elastomeric materials, [3,4], we have $\mu = 1$ M Pa, $\gamma = 0.01$–$0.1$ J/m$^2$, and $\beta = 10^8 - 10^{11}$ J/m$^4$. In this case, it is verified that the ratio $(\beta\gamma/\mu^2)$ is a few orders of magnitude smaller than unity, and thus (7) is simplified approximately to

$$\lambda \approx \frac{\beta(\kappa+1)}{4\mu}. \tag{10}$$

The wavelength of surface wrinkling predicted by (10) for the above material constants falls within the range from 100 $\mu$m to 10 cm. Obviously, it is much larger than typical wavelengths of rubble thin films of thickness less than 10 $\mu$m, [3,4]. In particular, the wavelength obtained from (10) or (7) also determines the rate of decay of surface perturbation in the $y$-direction. Here, it is noted that the $\lambda$-$\beta$ relation (10) differs from a similar relation derived in [3,4] for an elastic film on a rigid substrate by a factor of about 1.5. This also indicates that the present results cannot be obtained from those derived in [3,4] as a limit case of an elastic layer on a rigid substrate.

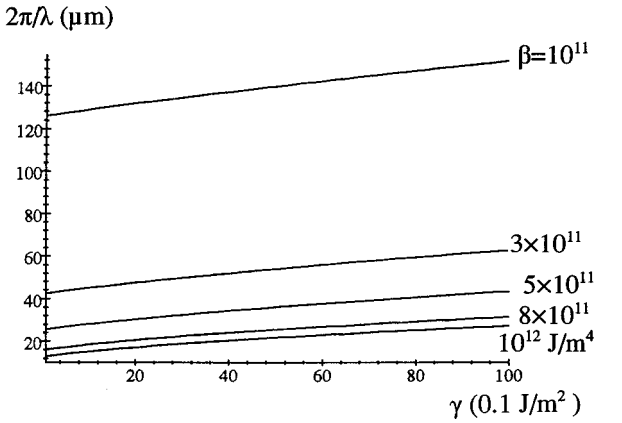


**Fig. 2 The dependence of the wavelength of surface wrinkling on the interaction coefficient $\beta$ and the surface energy $\gamma$ (when $\mu = 1$ MPa, $\nu = 1/2$)**

When $\gamma$ or $\beta$ is much larger than the above material constants, the dependence of the wavelength, defined by $(2\pi/\lambda)$ through (7), on both $\beta$ and $\gamma$ is shown in Fig. 2 (where $\mu = 1$ MPa, $\nu = 1/2$) for $\beta = 10^{11}$, $3\times10^{11}$, $5\times10^{11}$, $8\times10^{11}$, and $10^{12}$ J/m$^4$, respectively. It is seen from Fig. 2 that the wavelength of surface wrinkling is very sensitive to the interaction coefficient $\beta$, but not to the surface energy $\gamma$. In particular, the wavelength of surface wrinkling decreases when the interaction coefficient $\beta$ increases. Because surface wrinkling becomes significant usually only when the wavelength is sufficiently small, the surface instability studied here would become significant only when the interaction coefficient $\beta$ is sufficiently large. It would happen usually only when the distance between two interacting bodies downs to the nanoscale.

Finally, the present results are based on a simple linearized analysis of nontrivial infinitesimal perturbations, without consulting the total potential energy of the system. For instance, we have not compared the total potential energy between the uniform state and the perturbed nonuniform state. Indeed, detailed analysis of post-bifurcation based on total potential energy of the system could be an interesting subject for future work.

## References

[1] Israelachvili, J., 1992, Intermolecular and Surface Forces, 2nd Ed., Academic Press, San Diego, CA.
[2] Johnson, K. L., 1996, "Continuum Mechanics Modeling of Adhesion and Friction," Langmuir, **12**, pp. 4510–4513.
[3] Monch, W., and Herminghaus, S., 2001, "Elastic Instability of Rubber Films Between Solid Bodies," Europhys. Lett., **53**, pp. 525–531.
[4] Shenoy, V., and Sharma, A., 2001, "Pattern Formation in a Thin Solid Film With Interactions," Phys. Rev. Lett., **86**, pp. 119–122.
[5] Nowinski, J. L., 1969, "Surface Instability of a Half-Space Under Highly Two-Dimensional Compression," J. Franklin Inst., **228**, pp. 367–376.
[6] Andreussi, F., and Gurtin, M. E., 1977, "On the Wrinkling of a Free Surface," J. Appl. Phys., **48**, pp. 3798–3799.
[7] Gent, A. N., and Cho, I. S., 1999, "Surface Instability in Compressed or Bent Rubber Blocks," Rubber Chem. Technol., **72**, pp. 253–262.
[8] Srolovitz, D. J., 1989, "On the Stability of Surfaces of Stressed Solids," Acta Metall., **37**, pp. 621–624.
[9] Schaffer, E., Albrecht, T. T., Russell, T. P., and Steiner, U., 2000, "Electrically Induced Structure Formation and Pattern Transfer," Nature (London), **403**, pp. 874–877.
[10] England, A. E., 1971, "Complex-Variable Methods in Elasticity," Wiley Intersecience, London.
[11] Pethica, J. B., and Sutton, A. P., 1988, "On the Stability of a Tip and Flat at Very Small Separation," J. Vac. Sci. Technol., **A6**, pp. 2490–2494.

# Nonlinear Elasticity for Modeling Fracture of Isotropic Brittle Solids

**K. Y. Volokh**
Faculty of Civil and Environmental Engineering,
Technion, Haifa 32000, Israel

*A softening hyperelastic continuum model is proposed for analysis of brittle fracture. Isotropic material is characterized by two standard parameters—shear and bulk modulus—and an additional parameter of the volumetric separation work. The model can be considered as a volumetric generalization of the concept of the cohesive surface. The meaning of the proposed constitutive equations is clarified by the examples of simple shear and hydrostatic pressure. It is emphasized that the proposed constitutive model includes only smooth functions and the necessary computational techniques are those of nonlinear elasticity.*
[DOI: 10.1115/1.1636795]

## 1 Introduction

The idea to describe fracture as a material separation across a surface was pioneered by Barenblatt [1]. It appears by name of the cohesive zone model (CZM) in the modern literature. The cohesive zone is a surface in a bulk material where displacement discontinuities occur. Thus, continuum is enhanced with discontinuities. The latter requires an additional constitutive description. Equations relating normal and tangential displacement jumps across the cohesive surfaces with the proper tractions define a specific CZM. There is a plenty of proposals of the ''cohesive'' constitutive equations (for example, Barenbaltt [1], Rice and Wang [2], Tvergaard and Hutchinson [3], and Xu and Needleman [4]). All these models are constructed qualitatively as follows: tractions increase, reach a maximum, and then approach zero with increasing separation. This scenario is in harmony with our intuitive understanding of the rupture process. It is qualitatively analogous to atomic interactions.

Needleman [5] lifted the cohesive zone models to computational practice. Since then CZMs are used increasingly in finite element simulations of crack-tip plasticity and creep; crazing in polymers; adhesively bonded joints; interface cracks in bimaterials; delamination in composites and multilayers; fast crack propagation in polymers, etc. Cohesive zones can be inside finite elements or along their boundaries (de Borst [6], Xu and Needleman [4], and Belytschko et al. [7]). Crack nucleation, propagation, branching, kinking, and arrest are a natural outcome of the computations where the discontinuity surfaces are spread over the bulk material. This is in contrast to the traditional approach of fracture mechanics where stress analysis is separated from a description of the actual process of material failure.

The CZM approach is natural for simulation of fracture at the material interface in composites and multilayers. It is less natural for modeling fracture of the bulk material because it leads to the simultaneous use of two material models for the same real material. One model describes the bulk material, while the other model describes the cohesive zones imbedded in the bulk material. Such two-model approach is rather artificial physically. It seems preferable to incorporate a material failure law directly in the constitutive description of the bulk material. Such volumetric models of the material failure via strain localization are usually based on inelastic constitutive equations, including damage theories, where the strain softening takes place (see the survey article by de Borst [6]). An interesting hyperelastic softening model based on the microstructural concept of the virtual internal bond has been proposed recently by Gao and Klein [8].

The computational efficiency of both volumetric and surface fracture models can suffer from two general problems. The first problem is mesh sensitivity. It takes place when the deformed finite element model reaches a critical point, which is a limit and multiple bifurcation point. This happens when a number of finite elements in various areas of the structure reach the cohesive strength simultaneously. The multiplicity of the bifurcation point and, consequently, the sensitivity of computations increase with the refinement of the mesh. The mesh refinement can be limited by introducing the characteristic length like in Bazant and Planas [9] or Gao and Ji [10]. This will provide the upper bound for the bifurcation multiplicity. It does not resolve the problem of the bifurcation multiplicity as a whole, however. A more radical way in circumventing the mesh sensitivity issue is the introduction of the second displacement gradients and conjugate higher order stresses (de Borst and van der Giessen [11] and Hutchinson [12]). This augmented initial boundary value problem can avoid the troubling critical point of the finite element model at all. The price for that is high because the enhanced model requires the additional boundary conditions which are not readily interpreted in simple physical terms.

The bifurcation multiplicity and the related mesh sensitivity are inherent in *any* softening material model for a *specific* loading of the considered structure. Another computational problem of the separation constitutive models is more universal. It is related to the use of inequalities, like in damage or plasticity theories, and vertex—hidden bifurcation—points, like in some compound elastic models of debonding. These undesirable features significantly sophisticate numerical procedures and require informal experience from their user.

We aim at formulating a volumetric material failure model, which is both analytically and computationally simpler than the existing fracture models. For this purpose a nonlinear softening hyperelastic continuum model is considered. Isotropic material is characterized by two standard parameters—shear and bulk modulus—and an additional parameter of the *volumetric separation work*. This model can be considered as a volumetric generalization of the concept of the cohesive surface. The meaning of the proposed constitutive equations is clarified by the examples of simple shear and hydrostatic pressure. It is emphasized that the proposed constitutive model includes only smooth functions and the necessary computational techniques are those of nonlinear elasticity.

## 2 Constitutive Equations

We set the strain energy per unit volume in the form

$$W=\Phi-\Phi\left(1+3\sqrt{\frac{K}{\Phi}}\varepsilon\right)\exp\left\{-3\sqrt{\frac{K}{\Phi}}\varepsilon-\frac{G}{\Phi}e_{ij}e_{ij}\right\}, \tag{2.1}$$

where the standard volumetric/deviatoric decomposition of the strain tensor is used,

$$\varepsilon=\varepsilon_{ii}/3, \tag{2.2}$$

$$e_{ij}=\varepsilon_{ij}-\varepsilon\,\delta_{ij}. \tag{2.3}$$

Coefficients $K$ and $G$ are the usual bulk and shear modulus respectively, while $\Phi$ is a new constant of the isotropic brittle solid. This is the *volumetric separation work*. Its dimension is work per unit volume, i.e., it is the same as the dimension of $K$ and $G$ and the dimension of stress. It is worth emphasizing that the introduced volumetric separation work is different from the separation work traditionally used in the cohesive surface approach to fracture. The dimension of the latter is work per unit area.

For a hyperelastic material stresses are defined as follows:

Contributed by the Applied Mechanics Division of THE AMERICAN SOCIETY OF MECHANICAL ENGINEERS for publication in the ASME JOURNAL OF APPLIED MECHANICS. Manuscript received by the ASME Applied Mechanics Division, October 21, 2002; final revision, August 18, 2003. Associate Editor: H. Gao.

  

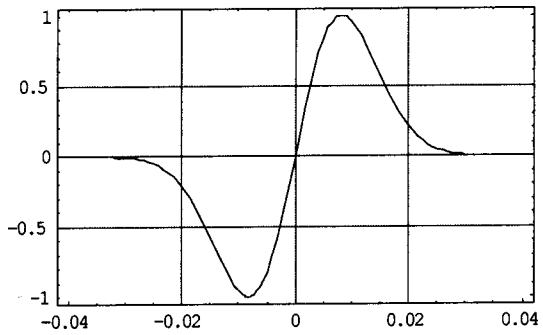


**Fig. 1 Simple shear. Normalized traction (vertical axis) versus shear deformation (horizontal axis) as defined by Eq. (3.7).**

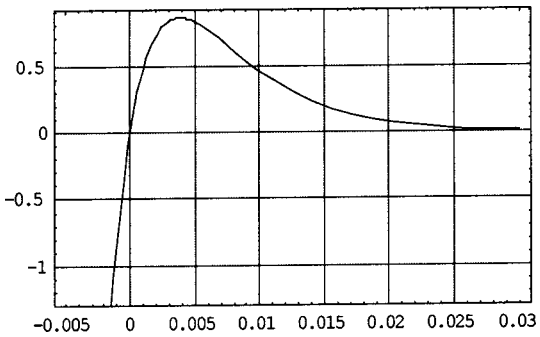


**Fig. 2 Hydrostatic pressure. Normalized pressure (vertical axis) versus volumetric deformation (horizontal axis) as defined by Eq. (4.3).**

$$\sigma_{ij}=\frac{\partial W}{\partial \varepsilon_{ij}}=\frac{\partial W}{\partial e_{mn}}\frac{\partial e_{mn}}{\partial \varepsilon_{ij}}+\frac{\partial W}{\partial \varepsilon}\frac{\partial \varepsilon}{\partial \varepsilon_{ij}}. \tag{2.4}$$

All entries on the right-hand side of this equation are readily computed accounting for the strain energy expression:

$$\frac{\partial W}{\partial e_{mn}}=2Ge_{mn}\left(1+3\sqrt{\frac{K}{\Phi}}\varepsilon\right)\exp\left\{-3\sqrt{\frac{K}{\Phi}}\varepsilon-\frac{G}{\Phi}e_{ij}e_{ij}\right\}, \tag{2.5}$$

$$\frac{\partial e_{mn}}{\partial \varepsilon_{ij}}=\delta_{mi}\delta_{jn}-\delta_{ij}\delta_{mn}/3, \tag{2.6}$$

$$\frac{\partial W}{\partial \varepsilon}=9K\varepsilon\exp\left\{-3\sqrt{\frac{K}{\Phi}}\varepsilon-\frac{G}{\Phi}e_{ij}e_{ij}\right\}, \tag{2.7}$$

$$\frac{\partial \varepsilon}{\partial \varepsilon_{ij}}=\delta_{ij}/3. \tag{2.8}$$

By using the volumetric/deviatoric decomposition of the stress tensor,

$$\sigma_{ij}=\sigma\delta_{ij}+s_{ij}\quad,\quad \sigma=\sigma_{kk}/3, \tag{2.9}$$

we have

$$s_{ij}=\frac{\partial W}{\partial e_{ij}}=2Ge_{ij}\left(1+3\sqrt{\frac{K}{\Phi}}\varepsilon\right)\exp\left\{-3\sqrt{\frac{K}{\Phi}}\varepsilon-\frac{G}{\Phi}e_{mn}e_{mn}\right\}, \tag{2.10}$$

$$\sigma=\frac{\partial W}{3\partial \varepsilon}=3K\varepsilon\exp\left\{-3\sqrt{\frac{K}{\Phi}}\varepsilon-\frac{G}{\Phi}e_{mn}e_{mn}\right\}. \tag{2.11}$$

Linearized Eqs. (2.10) and (2.11) present the classical Hooke's law.

In order to justify and clarify the specific choice of the strain energy we consider two limit cases in the following two sections.

## 3 Simple Shear

Assume that only the following strain and stress components are nonzero:

$$\tau=s_{12}=s_{21}\quad,\quad \gamma=e_{12}=e_{21}. \tag{3.1}$$

In this case the constitutive law (2.10) takes the form

$$\tau=2G\gamma\exp\left\{-\frac{2G}{\Phi}\gamma^2\right\}. \tag{3.2}$$

The shape of this curve appears in Fig. 1. Qualitatively, this means that the magnitude of the shear traction increases linearly with the shear strain, reaches a maximum, and then approaches zero with increasing separation. It does not matter what the sign of the traction is.

The local maximum of the curve is at point

$$\gamma=\pm\sqrt{\frac{\Phi}{4G}}. \tag{3.3}$$

The corresponding absolute magnitude of the maximum traction is

$$\tau_{\max}=\sqrt{G\Phi}\exp\{-1/2\}. \tag{3.4}$$

Assume that for the given material the maximum traction is known:

$$\tau_{\max}=G/100. \tag{3.5}$$

Then we have

$$\Phi=\frac{G}{10^4\exp(-1)}. \tag{3.6}$$

Substituting Eq. (3.6) in Eq. (3.2) and normalizing the latter with respect to $\tau_{\max}$ we obtain

$$\frac{\tau}{\tau_{\max}}=200\gamma\exp\{-2\cdot 10^4\exp(-1)\gamma^2\}. \tag{3.7}$$

The graph of this function is shown in Fig. 1.

## 4 Hydrostatic Pressure

Assume that the deformation under a uniform hydrostatic pressure is purely volumetric

$$\sigma_{ij}=\sigma\delta_{ij}\quad,\quad \varepsilon_{ij}=\varepsilon\delta_{ij}. \tag{4.1}$$

In this case the constitutive law (2.11) takes the form

$$\sigma=3K\varepsilon\exp\left\{-3\sqrt{\frac{K}{\Phi}}\varepsilon\right\}. \tag{4.2}$$

The shape of this curve appears in Fig. 2. Qualitatively, it can be interpreted as the linear increase of the magnitude of the tension pressure with the increase of the material volume at the point, it reaches a maximum, and then approaches zero with increasing separation. The latter is nothing but the void nucleation. For the compression pressure the situation is different, however. There is no separation!

Assume that the material is defined by Eq. (3.5) and $K/G=2$, then Eq. (4.2) normalized with respect to $\tau_{\max}$ takes the following form:

$$\frac{\sigma}{\tau_{\max}}=600\varepsilon\exp\{-300\sqrt{2\exp(-1)}\varepsilon\}. \tag{4.3}$$

The graph of this function is shown in Fig. 2.

## 5 Conclusions

A novel constitutive model of an isotropic brittle solid has been proposed. The exponential hyperelastic constitutive law describes this model. The material bulk modulus and the shear modulus are completed with a new constant—the volumetric separation work. The proposed constitutive equations are cohesive, that is they naturally allow for the material separation–strain localization. These equations may be interpreted on the basis of the simple shear and hydrostatic pressure examples. The distortional (deviatoric) deformation at the given point exhibits behavior analogous to the simple shear, which graph is shown in Fig. 1. The dilatational (volumetric) deformation at the given point exhibits behavior analogous to the hydrostatic pressure, which graph is shown in Fig. 2.

Adding the momentum conservation laws and the proper boundary and initial conditions to the constitutive equations described in Section 2 of our work, it is possible to set the initial boundary value problem of *nonlinear elasticity*. The latter means that the standard and well established numerical procedures are available. When a brittle solid is loaded quasi-statically then the crack nucleation means passing a limit point in the state space of the discretized IBVP. Well-developed techniques of the arc-length continuation can be used (Crisfield [13] and Riks [14]). The loss of the positive definiteness of the tangent stiffness matrix (the Jacobian of the total discrete energy) means static instability. If the equilibrium path does not become stable again, then the dynamic crack propagation takes place and dynamic integration procedures should be used (Belytschko et al. [15] and Xu and Needleman [4]). It is worth emphasizing that only smooth functions are used in the constitutive equations. The latter allows for circumventing the problems of inequalities and vertex points, which are typical of most separation models.


## Acknowledgment

This research was supported by the Fund for the Promotion of Research at the Technion.


## References


[1] Barenblatt, G. I., 1959, "The Formation of Equilibrium Cracks During Brittle Fracture—General Ideas and Hypotheses. Axially Symmetric Cracks," J. Appl. Math. Mech., **23**, pp. 622–636.

[2] Rice, J. R., and Wang, J. S., 1989, "Embrittlement of Interfaces by Solute Segregation," Mater. Sci. Eng., A, **107**, pp. 23–40.

[3] Tvergaard, V., and Hutchinson, J. W., 1992, "The Relation Between Crack Growth Resistance and Fracture Process Parameters in Elastic-Plastic Solids," J. Mech. Phys. Solids, **40**, pp. 1377–1397.

[4] Xu, X. P., and Needleman, A., 1994, "Numerical Simulations of Fast Crack Growth in Brittle Solids," J. Mech. Phys. Solids, **42**, pp. 1397–1434.

[5] Needleman, A., 1987, "A Continuum Model for Void Nucleation by Inclusion Debonding," ASME J. Appl. Mech., **54**, pp. 525–531.

[6] de Borst, R., 2001, "Some Recent Issues in Computational Failure Mechanics," Int. J. Numer. Methods Eng., **52**, pp. 63–95.

[7] Belytschko, T., Moes, N., Usiu, S., and Parimi, C., 2001, "Arbitrary Discontinuities in Finite Elements," Int. J. Numer. Methods Eng., **50**, pp. 993–1013.

[8] Gao, H., and Klein, P., 1998, "Numerical Simulation of Crack Growth in an Isotropic Solid With Randomized Internal Cohesive Bonds," J. Mech. Phys. Solids, **46**, pp. 187–218.

[9] Bazant, Z. P., and Planas, J., 1998, *Fracture and Size Effect of Concrete and Other Quasibrittle Materials*, CRC Press, Boca Raton, FL.

[10] Gao, H., and Ji, B., 2003, "Modeling Fracture of Nanomaterials via a Virtual Internal Bond Method," Eng. Fract. Mech., **70**, pp. 1777–1791.

[11] de Borst, R., and van der Giessen, E., 1998, *Material Instabilities in Solids*, John Wiley and Sons, Chichister, UK.

[12] Hutchinson, J. W., 2000, "Plasticity at the Micron Scale," Int. J. Solids Struct., **37**, pp. 225–238.

[13] Crisfield, M. A., 1991, 1997, *Non-linear Finite Element Analysis of Solids and Structures*, Vols. 1, 2, John Wiley and Sons, Chichester, UK.

[14] Riks, E., 1998, "Buckling Analysis of Elastic Structures: A Computational Approach," Adv. Appl. Mech., **34**, pp. 1–76.

[15] Belytschko, T., Liu, W. K., and Moran, B., 2000, *Nonlinear Finite Elements for Continua and Structures*, John Wiley and Sons, New York.


# Flutter of Rotating Shells With a Co-rotating Axial Flow[1]


**L. Cortelezzi**

**A. Pong**

**M. P. Païdoussis**
Fellow ASME

Department of Mechanical Engineering, McGill University, Montreal, QC H3A 2K6, Canada



*It is shown that, in certain regions of parameter space, travelling wave solutions in rotating shells containing co-rotating inviscid fluid become indeterminate. This may render the determination of the flutter speed impossible, or the solution nonphysical.*


[DOI: 10.1115/1.1636794]


## Introduction

The dynamics and stability of a shell containing fluid in matched (solid body) rotation and also flowing axially was examined by Lai and Chow [1], inspired by fluid-structure interactions in "the thrust chamber and the pipelines in the liquid propellant feed system of a spinning rocket." In contrast to Srinivasan [2], Dowell et al. [3] and related studies which are connected to a real system and need to face the complications attendant thereto, the problem studied by Lai and Chow is very idealized. A closely similar study was made by Chen and Bert [4] in which the shell is stationary but the fluid is rotating as in the foregoing; thus, the physical system is closer to engineering applications, but the use of inviscid flow theory is less justifiable—see Païdoussis [5] for a review.

This note presents new results which show that some of those by Lai and Chow and Bert and Chen are questionable.

## Equations of Motion and Analysis

Consider both the shell and the fluid to be rotating with angular velocity $\Omega$, and the fluid to have an axial velocity $U$, relative to the shell. The shell is assumed to be very thin and its motions to be governed by the Donnell equations, [1], which in operator form in terms of coordinates rotating with the shell are

$$\mathbf{L}_{\mathrm{D}}\begin{Bmatrix} u \\ v \\ w \end{Bmatrix} = \gamma\begin{Bmatrix} \partial^2 u/\partial t^2 \\ \partial^2 v/\partial t^2 - \Omega^2 v + 2\Omega(\partial w/\partial t) \\ -\partial^2 w/\partial t^2 + \Omega^2 w + 2\Omega(\partial v/\partial t) + p/\rho_s h \end{Bmatrix}, \quad (1)$$

where $u$, $v$, and $w$ are the axial, circumferential, and radial displacements of the shell, and the other symbols are as in standard thin-shell theory. The fluid velocities, $v_x$, $v_r$, and $v_\theta$, are related to the pressure $p$ by

$$\frac{\mathrm{D}v_x}{\mathrm{D}t} = -\frac{1}{\rho}\frac{\partial p}{\partial x},$$

$$\frac{\mathrm{D}v_r}{\mathrm{D}t} - \frac{v_\theta^2}{r} - 2\Omega v_\theta - \Omega^2 r = -\frac{1}{\rho}\frac{\partial p}{\partial r}, \quad (2)$$


[1]This work was supported by the Natural Sciences and Engineering Research Council of Canada and FCAR of Québec.

Contributed by the Applied Mechanics Division of THE AMERICAN SOCIETY OF MECHANICAL ENGINEERS for publication in the ASME JOURNAL OF APPLIED MECHANICS. Manuscript received by the ASME Applied Mechanics Division, January 16, 2003; final revision, June 9, 2003. Associate Editor: R. C. Benson.

$$\frac{Dv_\theta}{Dt}+\frac{v_r v_\theta}{r}+2\Omega v_r=-\frac{1}{\rho}\frac{1}{r}\frac{\partial p}{\partial \theta},$$

assuming the fluid to be inviscid and incompressible, D/D$t$ being the material derivative.

Considering traveling wave solutions, the velocities are expressed as

$$\{v_x,\ v_r,\ v_\theta\}=\{U,\ 0,\ 0\}+\{\hat{v}_x(r),\ \hat{v}_r(r),\ \hat{v}_\theta(r)\}e^{i\alpha}, \quad (3)$$

$$\alpha=\omega t-kx-n\theta, \quad (4)$$

where $k$ is the axial wavenumber; similarly,

$$p=P+p^*, \quad p^*=\hat{p}e^{i\alpha}, \quad (5)$$

in which $p^*$ is the perturbation pressure, while $P$ is the mean pressure.

Utilizing these equations and continuity, one eventually finds

$$\frac{d^2\hat{p}}{dr^2}+\frac{1}{r}\frac{d\hat{p}}{dr}+\left[k^2(\lambda^2-1)-\frac{n^2}{r^2}\right]\hat{p}=0, \quad (6)$$

$$\lambda=\frac{2\Omega}{(\omega-kU)}, \quad (7)$$

for small perturbations. Equation (6) admits solutions of three different types, depending on $\lambda^2$. The perturbation pressure is related to the perturbation radial displacement via the impermeability boundary condition,

$$v_r|_{r=a}=i\overline{w}(\omega-kU)e^{i\alpha}, \quad (8)$$

where the shell displacements are taken to be

$$\{u,\ v,\ w\}=\{\overline{u},\ \overline{v},\ \overline{w}\}e^{i\alpha}. \quad (9)$$

Using these equations, the solutions to (6) may be written as

$$\hat{p}=\frac{\rho a(\omega-kU)^2(1-\lambda^2)I_n(kr\sqrt{1-\lambda^2})}{ka\sqrt{1-\lambda^2}I_{n-1}(ka\sqrt{1-\lambda^2})-n(1+\lambda)I_n(ka\sqrt{1-\lambda^2})}\overline{w}, \quad \lambda^2<1, \quad (10a)$$

$$=\frac{8\rho(n+1)\Omega^2 r^n}{a^{n+1}[n(n+1)+k^2a^2]}\overline{w}, \quad \lambda^2=1, \quad (10b)$$

$$=\frac{\rho a(\omega-kU)^2(1-\lambda^2)J_n(kr\sqrt{\lambda^2-1})}{ka\sqrt{\lambda^2-1}J_{n-1}(ka\sqrt{\lambda^2-1}-n(1+\lambda)J_n(ka\sqrt{\lambda^2-1})}\overline{w}, \quad \lambda^2>1, \quad (10c)$$

where $J_n$ and $I_n$ are Bessel and modified Bessel functions of the first kind and order $n$. These expressions, evaluated at $r=a$, together with (9) are then substituted into (1), giving three homogeneous ODEs in $\overline{u}$, $\overline{v}$, and $\overline{w}$, solution of which yields the desired frequency $\omega$.

The results are presented in terms of the following dimensionless parameters:

$$\tilde{\omega}=\omega a\sqrt{\frac{\rho_s(1-\nu^2)}{E}}, \quad \tilde{\Omega}=\Omega a\sqrt{\frac{\rho_s(1-\nu^2)}{E}},$$

$$\tilde{U}=U\sqrt{\frac{\rho(1-\nu^2)}{E}}, \quad \kappa=ka, \quad (11)$$

where $\nu$ is the Poisson ratio, $E$ Young's modulus, $a$ the shell radius, and $\rho_s$ and $\rho$ the shell and fluid densities.

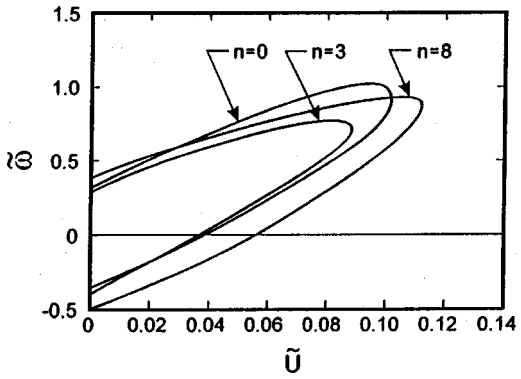


**Fig. 1 The dimensionless frequency $\tilde{\omega}$ versus $\tilde{U}$ for different $n$, as given by Lai and Chow**

## Typical Results

Typical results from Lai and Chow's [1] work are shown in Fig. 1 for a rotating elastomer shell with co-rotating and axially flowing fluid. It is seen that, at a fixed $\tilde{\Omega}=0.1$ (1 820 r.p.m.) and a given wave number, $\kappa=10$, the system first loses stability in the $n=3$ mode at $\tilde{U}=0.089$ ($U=3.3$ m/s)—at the "nose" of the curve shown. When $\tilde{\Omega}=0$ (not shown), one obtains flutter in the $n=6$ mode, at a higher critical $\tilde{U}$, by about 11%.

Similar results have been obtained for Chen and Bert's, [4], system. The analysis is similar, and so is the form of the solution.

## Newer Work

The authors decided to extend this analysis to take real fluid effects into account. The first step was to reproduce Lai and Chow's results, using the same Eqs. (1)–(11). This was found to be impossible, at least for part of the solutions (such as those shown in Fig. 1). Specifically, in most cases it was found impossible to "close the curve" at the nose, and hence to determine the critical $\tilde{U}=\tilde{U}_f$.

At first it was thought that the difficulties were numerical, and several different root-finding methods were tried, but they all gave similar results. The problem is real, and it is the following. Referring to Eqs. (10 *a,b,c*), it is noted that (i) to trace each of the curves of Fig. 1 fully, one generally needs all forms for $\hat{p}$, Eqs. (10 *a,b,c*); (ii) the denominator of (10c) is a functional of the $J_n$ Bessel functions, each of which crosses zero an infinite number of times, and so does the denominator as a whole. For example, by inspection, for the $n=0$ case the denominator becomes zero at every value of $ka\sqrt{\lambda^2-1}$ for which $J_{-1}(ka\sqrt{\lambda^2-1})=0$. As a result, the perturbation pressure at these points is indeterminate and the solution becomes impossible.

A typical set of results for the $n=0$ case of Fig. 1 are shown in Fig. 2. The two straight lines limit the domain within which exist islets where a solution is not feasible. Thus, it becomes impossible to properly "close the curve" and determine $\tilde{U}_f$. Generally, the width and orientation of the no-solution band is parameter-dependent; thus, the band could well disappear completely or it could cover most of the stability curve.

In this regard, a valuable suggestion was made by a reviewer of an earlier version of this paper. The original eigenvalue problem of Eq. (1) may symbolically be written as $\mathbf{Lw}=\mathbf{p}$, where $\mathbf{p}=A\mathbf{w}$ with $A=A_N/A_D$. If this is recast in terms of pressure, one obtains the equivalent eigenvalue problem $\mathbf{L}A_D\mathbf{p}=A_N\mathbf{p}$, which may well circumvent the numerical difficulties associated with $A_D=0$ at some frequencies. The infinite pressure points could then be viewed as points of zero displacement amplitude.[2] However, although this could mean that closed curves similar to Fig. 1

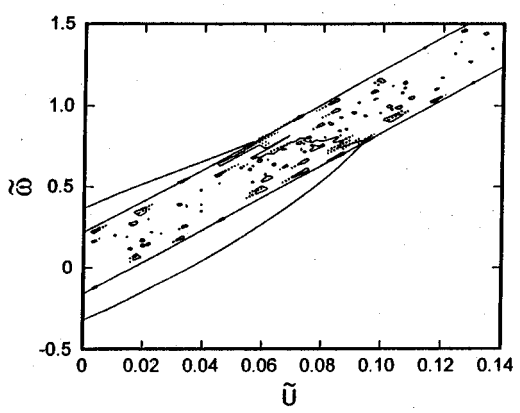


**Fig. 2 The recalculated $\tilde{\omega}$ versus $\tilde{U}$ plot for $n=0$**

could then be obtained, it does not truly solve the problem; solutions of zero displacement amplitude are as strange as solutions of infinite pressure for this linear homogeneous problem. Thus, instead of islets of nonsolution (infinite pressure) we would have islets of zero-amplitude solutions.

The same applies to Chen and Bert's results, in view of the similarities in the expressions for the perturbation pressures.

## Conclusion

It is not known how the two sets of previous authors have overcome these difficulties and have presented full curves.[3] It is of course possible to ignore the islets of nonsolution and join the valid regions with a trusty French curve, though *any* solution within the no-solution band is really questionable. Alternatively, the previous authors may have used the device suggested by the reviewer. In either case a mathematical/physical difficulty exists.

Fundamentally, the question is this: does the mathematical difficulty have the physical meaning that flutter of arbitrary amplitude in such cases is impossible, even though its existence seems physically reasonable? Of course, the whole analysis of the physical system is highly idealized by ignoring viscous effects. Their incorporation, however, is anything but trivial. Perhaps, as is often the case, added realism will also overcome the mathematical difficulties. This line of research is being pursued.

It was nevertheless thought that the research community should be made aware that the results of the 1970s analyses may be flawed in some regions of the parameter space.

[2]As suggested by the same reviewer, at these points the fluid would then behave as a vibration absorber.

[3]All of those who actually did the calculations being unreachable.

## References


[1] Lai, Y.-C., and Chow, C.-Y., 1973, "Stability of a Rotating Thin Elastic Tube Containing a Fluid Flow," Zeitschrift für angewande Mathematik und Mechanik, **53**, pp. 511–517.

[2] Srinivasan, A. V., 1971, "Flutter Analysis of Rotating Cylindrical Shells Immersed in a Circular Helical Flowfield of Air," AIAA J., **9**, pp. 394–400.

[3] Dowell, E. H., Srinivasan, A. V., McLean, J. D., and Ambrose, J., 1974, "Aeroelastic Stability of Cylindrical Shells Subjected to a Rotating Flow," AIAA J., **12**, pp. 1644–1651.

[4] Chen, T. L. C., and Bert, C. W., 1977, "Dynamic Stability of Isotropic or Composite-Material Cylindrical Shells Containing Swirling Fluid Flow," ASME J. Appl. Mech., **44**, pp. 112–116; *ibid.* **44**, p. 513.

[5] Païdoussis, M. P., 2003, *Fluid-Structure Interactions: Slender Structures and Axial Flow*, **2**, Elsevier, Oxford.


# Reciprocity Theorems for Diffusion, Flow, and Waves


**Kees Wapenaar and Jacob Fokkema**
Centre for Technical Geoscience, Delft University of Technology, P. O. Box 5028, 2600 GA Delft, The Netherlands



*Diffusion, flow, and wave phenomena can each be captured by a unified differential equation in matrix-vector form. This equation forms the basis for the derivation of unified reciprocity theorems for diffusion, flow and wave phenomena.*


[DOI: 10.1115/1.1636792]


## Introduction

Diffusion, flow, and wave phenomena can each be captured by the following differential equation in matrix-vector form:

$$\underset{\sim}{\mathbf{A}}\frac{D\mathbf{u}}{Dt}+\mathbf{B}\mathbf{u}+\mathbf{D}_x\mathbf{u}=\mathbf{s}, \tag{1}$$

where $\mathbf{u}=\mathbf{u}(\mathbf{x},t)$ is a vector containing space and time-dependent field quantities, $\mathbf{s}=\mathbf{s}(\mathbf{x},t)$ is a source vector, $\mathbf{A}=\mathbf{A}(\mathbf{x})$ and $\mathbf{B}=\mathbf{B}(\mathbf{x})$ are matrices containing space-dependent material parameters, and $\mathbf{D_x}$ is a matrix containing the spatial differential operators $\partial/\partial x_1$, $\partial/\partial x_2$, and $\partial/\partial x_3$. Finally, $D/Dt$ denotes the material time derivative, defined as $D/Dt=\partial/\partial t+\mathbf{v}\cdot\boldsymbol{\nabla}=\partial/\partial t+v_k\partial/\partial x_k$, where $\partial/\partial t$ denotes the time derivative in the reference frame and $\mathbf{v}=\mathbf{v}(\mathbf{x})$ is the space-dependent flow velocity of the material; $v_k$ denotes the $k$th component of $\mathbf{v}$. Throughout this paper the summation convention applies to repeated subscripts; lowercase Latin subscripts run from 1 to 3. The vectors and matrices in Eq. (1) are further defined in the appendices for diffusion (Appendix A), acoustic wave propagation in moving fluids (Appendix B), momentum transport (Appendix C), and coupled elastodynamic and electromagnetic wave propagation in porous solids (Appendix D). In this paper we use Eq. (1) as the basis for deriving unified reciprocity theorems for these phenomena. In general, a reciprocity theorem interrelates the quantities that characterize two admissible physical states that could occur in one and the same domain, [1]. One can distinguish between convolution type and correlation type reciprocity theorems, [2]. Generally speaking, these two types of reciprocity theorems find their applications in forward and inverse problems, respectively. Both types of reciprocity theorems will be derived for the field vector $\mathbf{u}$.

## The Differential Equation in the Frequency Domain

Reciprocity theorems can be derived in the time domain, the Laplace domain and the frequency domain, [3]. Here we only consider the frequency domain. We define the Fourier transform of a time-dependent function $f(t)$ as $\hat{f}(\omega)=\int_{-\infty}^{\infty}f(t)\exp(-j\omega t)\mathrm{d}t$, where $j$ is the imaginary unit and $\omega$ denotes the angular frequency. We apply the Fourier transform to all terms in Eq. (1), under the assumption that this equation is linear in $\mathbf{u}$. Hence, we only consider those cases in which the field quantities in $\mathbf{u}$ do not appear in any of the matrices or operators in Eq. (1). In particular, this is why the term $D\mathbf{u}/Dt$ in the momentum transport Eq. (*C*7) is replaced by $\partial\mathbf{u}/\partial t$ in (C10). Transforming Eq. (1) to the frequency domain yields


Contributed by the Applied Mechanics Division of THE AMERICAN SOCIETY OF MECHANICAL ENGINEERS for publication in the ASME JOURNAL OF APPLIED MECHANICS. Manuscript received by the ASME Applied Mechanics Division, Aug. 8, 2002; final revision, May 3, 2003. Associate Editor: D. A. Siginer.

$$\mathbf{A}(j\omega+\mathbf{v}\cdot\boldsymbol{\nabla})\hat{\mathbf{u}}+\mathbf{B}\hat{\mathbf{u}}+\mathbf{D}_x\hat{\mathbf{u}}=\hat{\mathbf{s}}, \tag{2}$$

where $\hat{\mathbf{u}}=\hat{\mathbf{u}}(\mathbf{x},\omega)$ is the space and frequency-dependent field vector and $\hat{\mathbf{s}}=\hat{\mathbf{s}}(\mathbf{x},\omega)$ is the space and frequency-dependent source vector. The term $\mathbf{v}\cdot\boldsymbol{\nabla}$ should be dropped for linearized momentum transport (Appendix C) as well as for wave phenomena in nonmoving media (Appendix D). Finally we remark that in a number of cases matrix $\mathbf{B}$ contains temporal convolution kernels in the time domain (Appendix B) or, equivalently, complex frequency-dependent material parameters in the frequency domain (Appendices B and D).

## Modification of Gauss' Divergence Theorem

The reciprocity theorem will be derived for a volume $\mathcal{V}$ enclosed by surface $\partial\mathcal{V}$ with outward pointing normal vector $\mathbf{n}$. Note that $\partial\mathcal{V}$ does not necessarily coincide with a physical boundary. Gauss' divergence theorem plays a central role in the derivation. For a scalar field $a(\mathbf{x})$, this theorem reads

$$\int_{\mathcal{V}}\frac{\partial a(\mathbf{x})}{\partial x_i}\mathrm{d}^3\mathbf{x}=\oint_{\partial\mathcal{V}}a(\mathbf{x})n_i\mathrm{d}^2\mathbf{x}, \tag{3}$$

where $n_i$ denotes the $i$th component of $\mathbf{n}$. In this section we will modify this theorem for the differential operator matrix $\mathbf{D}_x$ appearing in Eqs. (1) and (2). Note that $\mathbf{D}_x=\mathbf{D}_x^T$ for all forms of $\mathbf{D}_x$ appearing in the appendices (here superscript $^T$ denotes matrix transposition only; it does not denote operator transposition). Let $D_{IJ}$ denote the operator in row $I$ and column $J$ of matrix $\mathbf{D}_x$. The symmetry of $\mathbf{D}_x$ implies $D_{IJ}=D_{JI}$. We define a matrix $\mathbf{N}_\mathbf{x}$ which contains the components of the normal vector $\mathbf{n}$, organized in a similar way as matrix $\mathbf{D}_x$, see the appendices for details. Hence, if $N_{IJ}$ denotes the element in row $I$ and column $J$ of matrix $\mathbf{N}_x$, we have $N_{IJ}=N_{JI}$. For example, for matrices $\mathbf{D}_x$ and $\mathbf{N}_x$ in Eqs. (A3) and (A5) we have $D_{12}=D_{21}=\partial/\partial x_1$ and $N_{12}=N_{21}=n_1$. If we now replace the scalar field $a(\mathbf{x})$ by $a_I(\mathbf{x})b_J(\mathbf{x})$, we may generalize Eq. (3) to

$$\int_{\mathcal{V}}D_{IJ}[a_I(\mathbf{x})b_J(\mathbf{x})]\mathrm{d}^3\mathbf{x}=\oint_{\partial\mathcal{V}}a_I(\mathbf{x})b_J(\mathbf{x})N_{IJ}\mathrm{d}^2\mathbf{x}, \tag{4}$$

where the summation convention applies for repeated capital Latin subscripts (which may run from 1 to 4, 12 or 22, depending on the choice of operator $\mathbf{D}_x$). Applying the product rule for differentiation and using the symmetry property $D_{IJ}=D_{JI}$, we obtain for the integrand in the left-hand side of Eq. (4)

$$D_{IJ}(a_Ib_J)=a_ID_{IJ}b_J+(D_{JI}a_I)b_J=\mathbf{a}^T\mathbf{D}_x\mathbf{b}+(\mathbf{D}_x\mathbf{a})^T\mathbf{b}, \tag{5}$$

where $\mathbf{a}$ and $\mathbf{b}$ are vector functions, containing the scalar functions $a_I(\mathbf{x})$ and $b_J(\mathbf{x})$, respectively. Rewriting the integrand in the right-hand side of Eq. (4) in a similar way, we thus obtain

$$\int_{\mathcal{V}}[\mathbf{a}^T\mathbf{D}_x\mathbf{b}+(\mathbf{D}_x\mathbf{a})^T\mathbf{b}]\mathrm{d}^3\mathbf{x}=\oint_{\partial\mathcal{V}}\mathbf{a}^T\mathbf{N}_x\mathbf{b}\mathrm{d}^2\mathbf{x}. \tag{6}$$

Finally we consider a variant of this equation. We replace $\mathbf{a}$ by $\mathbf{Ka}$, where $\mathbf{K}$ is a diagonal matrix with the following property:

$$\mathbf{D}_x\mathbf{K}=-\mathbf{K}\mathbf{D}_x, \tag{7}$$

see the appendices for details. With this replacement, Eq. (6) becomes

$$\int_{\mathcal{V}}[\mathbf{a}^T\mathbf{K}\mathbf{D}_x\mathbf{b}-(\mathbf{D}_x\mathbf{a})^T\mathbf{K}\mathbf{b}]\mathrm{d}^3\mathbf{x}=\oint_{\partial\mathcal{V}}\mathbf{a}^T\mathbf{K}\mathbf{N}_x\mathbf{b}\mathrm{d}^2\mathbf{x}. \tag{8}$$

## Reciprocity Theorem of the Convolution Type

We consider two physical states in volume $\mathcal{V}$. The field quantities, the material parameters, the flow velocity as well as the source functions may be different in both states and they will be distinguished with subscripts $A$ and $B$ (of course the summation convention does not apply for these subscripts). We substitute $\hat{\mathbf{u}}_A$ and $\hat{\mathbf{u}}_B$ for $\mathbf{a}$ and $\mathbf{b}$ in Eq. (8), apply Eq. (2) for states $A$ and $B$ and use the symmetry properties

$$\mathbf{A}_A^T\mathbf{K}=\mathbf{K}\mathbf{A}_A \quad \text{and} \quad \mathbf{B}_A^T\mathbf{K}=\mathbf{K}\mathbf{B}_A \tag{9}$$

(see the appendices). This yields

$$\begin{aligned}\oint_{\partial\mathcal{V}}\hat{\mathbf{u}}_A^T\mathbf{K}\mathbf{N}_x\mathbf{u}_B\mathrm{d}^2\mathbf{x}=&\int_{\mathcal{V}}[\mathbf{u}_A^T\mathbf{K}\hat{\mathbf{s}}_B-\mathbf{s}_A^T\mathbf{K}\mathbf{u}_B\mathrm{d}^3\mathbf{x}\\&+\int_{\mathcal{V}}\mathbf{u}_A^T\mathbf{K}[j\omega(\mathbf{A}_A-\mathbf{A}_B)+(\mathbf{B}_A-\mathbf{B}_B)]\mathbf{u}_B\mathrm{d}^3\mathbf{x}\\&+\int_{\mathcal{V}}[((\mathbf{v}_A\cdot\boldsymbol{\nabla})\mathbf{u}_A)^T\mathbf{K}\mathbf{A}_A\\&-\mathbf{u}_A^T\mathbf{K}\mathbf{A}_B(\mathbf{v}_B\cdot\boldsymbol{\nabla})]\mathbf{u}_B\mathrm{d}^3\mathbf{x}.\end{aligned} \tag{10}$$

The first term in the last integral can be written as

$$\begin{aligned}((\mathbf{v}_A\cdot\boldsymbol{\nabla})\mathbf{u}_A{}^T\mathbf{K}\mathbf{A}_A\hat{\mathbf{u}}_B=&\boldsymbol{\nabla}\cdot(\mathbf{v}_A\hat{\mathbf{u}}_A^T\mathbf{K}\mathbf{A}_A\mathbf{u}_B\\&-\hat{\mathbf{u}}_A^T\mathbf{K}\frac{\partial(v_{i,A}\mathbf{A}_A)}{\partial x_i}\mathbf{u}_B-\mathbf{u}_A^T\mathbf{K}\mathbf{A}_A(\mathbf{v}_A\cdot\boldsymbol{\nabla})\mathbf{u}_B.\end{aligned} \tag{11}$$

For diffusion (Appendix A) the term $\partial(v_{i,A}\mathbf{A}_A)/\partial x_i$ vanishes on account of the equation of continuity. For acoustic wave propagation this term (with $v_{i,A}$ replaced by $v_{i,A}^0$, Appendix B) is negligible in comparison with the spatial derivatives of the wave fields $\hat{\mathbf{u}}_A$ and $\hat{\mathbf{u}}_B$. For the other situations considered in the appendices, $v_{i,A}$ is taken equal to zero. Hence, the term containing $\partial(v_{i,A}\mathbf{A}_A)/\partial x_i$ will be dropped. Substituting the remainder of the right-hand side of Eq. (11) into Eq. (10) and applying the theorem of Gauss for the term containing the divergence operator, yields

$$\begin{aligned}\oint_{\partial\mathcal{V}}\hat{\mathbf{u}}_A^T\mathbf{K}\mathbf{N}_x\hat{\mathbf{u}}_B\mathrm{d}^2\mathbf{x}=&\int_{\mathcal{V}}[\hat{\mathbf{u}}_A^T\mathbf{K}\hat{\mathbf{s}}_B-\hat{\mathbf{s}}_A^T\mathbf{K}\hat{\mathbf{u}}_B]\mathrm{d}^3\mathbf{x}\\&+\int_{\mathcal{V}}\hat{\mathbf{u}}_A^T\mathbf{K}[j\omega(\mathbf{A}_A-\mathbf{A}_B)+(\mathbf{B}_A-\mathbf{B}_B)]\hat{\mathbf{u}}_B\mathrm{d}^3\mathbf{x}\\&-\int_{\mathcal{V}}\hat{\mathbf{u}}_A^T\mathbf{K}[\mathbf{A}_A(\mathbf{v}_A\cdot\boldsymbol{\nabla})+\mathbf{A}_B(\mathbf{v}_B\cdot\boldsymbol{\nabla})]\hat{\mathbf{u}}_B\mathrm{d}^3\mathbf{x}\\&+\oint_{\partial\mathcal{V}}(\hat{\mathbf{u}}_A^T\mathbf{K}\mathbf{A}_A\hat{\mathbf{u}}_B)\mathbf{v}_A\cdot\mathbf{n}\mathrm{d}^2\mathbf{x}.\end{aligned} \tag{12}$$

This is the unified reciprocity theorem of the convolution type (we speak of convolution type, because the multiplications in the frequency domain correspond to convolutions in the time domain). It interrelates the field quantities (contained in $\hat{\mathbf{u}}_A$ and $\hat{\mathbf{u}}_B$), the material parameters (contained in $\mathbf{A}_A$, $\mathbf{B}_A$, $\mathbf{A}_B$, and $\mathbf{B}_B$), the flow velocities ($\mathbf{v}_A$ and $\mathbf{v}_B$) as well as the source functions (contained in $\hat{\mathbf{s}}_A$ and $\hat{\mathbf{s}}_B$) of states $A$ and $B$. The left-hand side is a boundary integral which contains a specific combination of the field quantities of states $A$ and $B$ at the boundary of the volume $\mathcal{V}$. The first integral on the right-hand side interrelates the field quantities and the source functions in $\mathcal{V}$. The second integral contains the differences of the medium parameters in both states; obviously this integral vanishes when the medium parameters in both states are identical. The third integral on the right-hand side contains the flow velocities in $\mathcal{V}$; this integral vanishes when the medium parameters in both states are identical and the flow velocities in both states are opposite to each other. The last integral on the right-hand side is a boundary integral containing the normal component of the flow velocity in state $A$; it vanishes when this flow velocity is tangential to the boundary $\partial\mathcal{V}$. Depending on the type of application, states $A$ and $B$ can be both physical states, or both mathematical states (e.g., Green's states), or one can be a physical state

and the other a mathematical state (the latter situation leads to representation integrals). For further discussions on convolution-type reciprocity theorems in different fields of application we refer to Lyamshev [4], De Hoop and Stam [1], Fokkema and Van den Berg [3], Allard et al. [5], Pride and Haartsen [6], and Belinskiy [7].

## Reciprocity Theorem of the Correlation Type

We substitute $\hat{\mathbf{u}}_A^*$ and $\hat{\mathbf{u}}_B$ for **a** and **b** in Eq. (6), where* denotes complex conjugation. Following the same procedure as in the previous section, using the symmetry property

$$\mathbf{A}_A^H = \mathbf{A}_A\,, \tag{13}$$

where $^H$ denotes complex conjugation and transposition, we obtain

$$\begin{aligned}\oint_{\partial\mathcal{V}} \hat{\mathbf{u}}_A^H \mathbf{N}_x \hat{\mathbf{u}}_B \mathrm{d}^2\mathbf{x} = &\int_{\mathcal{V}} [\hat{\mathbf{u}}_A^H \hat{\mathbf{s}}_B + \hat{\mathbf{s}}_A^H \hat{\mathbf{u}}_B]\mathrm{d}^3\mathbf{x} \\ &+ \int_{\mathcal{V}} \hat{\mathbf{u}}_A^H [j\omega(\mathbf{A}_A - \mathbf{A}_B) - (\mathbf{B}_A^H + \mathbf{B}_B)]\hat{\mathbf{u}}_B \mathrm{d}^3\mathbf{x} \\ &+ \int_{\mathcal{V}} \hat{\mathbf{u}}_A^H [\mathbf{A}_A(\mathbf{v}_A\cdot\boldsymbol{\nabla}) - \mathbf{A}_B(\mathbf{v}_B\cdot\boldsymbol{\nabla})]\hat{\mathbf{u}}_B \mathrm{d}^3\mathbf{x} \\ &- \oint_{\partial\mathcal{V}} (\hat{\mathbf{u}}_A^H \mathbf{A}_A \hat{\mathbf{u}}_B)\mathbf{v}_A\cdot\mathbf{n}\mathrm{d}^2\mathbf{x}. \end{aligned} \tag{14}$$

This is the unified reciprocity theorem of the correlation type (we speak of correlation type, because the multiplications in the frequency domain correspond to correlations in the time domain). The term $\hat{\mathbf{u}}_A^H$ contains ''back-propagating'' field quantities in state *A*, [2]. When we compare this reciprocity theorem with Eq. (12), we observe that, apart from the complex conjugation, the diagonal matrix **K** is absent in all integrals and that some plus and minus signs have been changed. In particular, the term $(\mathbf{B}_A - \mathbf{B}_B)$ has been replaced by $(\mathbf{B}_A^H + \mathbf{B}_B)$, which means that the second integral on the right-hand side no longer vanishes when the medium parameters in both states are identical. Moreover, the term $[\mathbf{A}_A(\mathbf{v}_A\cdot\boldsymbol{\nabla}) + \mathbf{A}_B(\mathbf{v}_B\cdot\boldsymbol{\nabla})]$ has been replaced by $[\mathbf{A}_A(\mathbf{v}_A\cdot\boldsymbol{\nabla}) - \mathbf{A}_B(\mathbf{v}_B\cdot\boldsymbol{\nabla})]$, which means that the third integral on the right-hand side vanishes when the medium parameters contained in matrix **A** as well as the flow velocities are identical in both states. For a discussion on the application of correlation-type reciprocity theorems to inverse problems we refer to Fisher and Langenberg [8] and De Hoop and Stam [1].

## Conclusions

We have formulated a general differential equation in matrix-vector form (equation (1)), which applies to diffusion (Appendix A), acoustic wave propagation in moving fluids (Appendix B), momentum transport (Appendix C) and coupled elastodynamic and electromagnetic wave propagation in fluid-saturated porous solids (Appendix D). For linear phenomena (which excludes non-linear momentum transport) we have transformed the general equation from the time domain to the frequency domain (Eq. (2)). Based on this general equation as well as the symmetry properties (7), (9), and (13) we have derived unified reciprocity theorems of the convolution type (Eq. (12)) and of the correlation type (Eq. (14)), respectively.


## Acknowledgments

We thank our colleague David Smeulders for his advice on the theoretical aspects of wave propagation in porous media. This work is part of the research program of the Netherlands research center for Integrated Solid Earth Science (ISES).


## Appendix A

**Mass Diffusion.** The equation of continuity for species *k* in a mixture of fluids reads

$$\varrho\,\frac{DY^{(k)}}{Dt} + \frac{\partial J_j^{(k)}}{\partial x_j} = \dot{\omega}^{(k)}, \tag{A1}$$

where $Y^{(k)}$ is the mass fraction of species *k*, $J_j^{(k)}$ its mass flux relative to the mixture, $\varrho$ is the mass density of the mixture and $\dot{\omega}^{(k)}$ the mass production rate density of species *k* (due to chemical reactions). Fick's first law of diffusion reads

$$J_j^{(k)} + \varrho\,\mathcal{D}^{(k)}\frac{\partial Y^{(k)}}{\partial x_j} = 0, \tag{A2}$$

where $\mathcal{D}^{(k)}$ is the diffusion coefficient for species *k*. Equations (*A*1) and (*A*2) can be combined to yield Eq. (1), with

$$\mathbf{u} = \begin{pmatrix} Y^{(k)} \\ J_1^{(k)} \\ J_2^{(k)} \\ J_3^{(k)} \end{pmatrix}, \quad \mathbf{s} = \begin{pmatrix} \dot{\omega}^{(k)} \\ 0 \\ 0 \\ 0 \end{pmatrix},$$

$$\mathbf{D}_x = \begin{pmatrix} 0 & \frac{\partial}{\partial x_1} & \frac{\partial}{\partial x_2} & \frac{\partial}{\partial x_3} \\ \frac{\partial}{\partial x_1} & 0 & 0 & 0 \\ \frac{\partial}{\partial x_2} & 0 & 0 & 0 \\ \frac{\partial}{\partial x_3} & 0 & 0 & 0 \end{pmatrix}, \tag{A3}$$

$$\mathbf{A} = \begin{pmatrix} \varrho & 0 & 0 & 0 \\ 0 & 0 & 0 & 0 \\ 0 & 0 & 0 & 0 \\ 0 & 0 & 0 & 0 \end{pmatrix} \quad \text{and}$$

$$\mathbf{B} = \begin{pmatrix} 0 & 0 & 0 & 0 \\ 0 & \frac{1}{\varrho\,\mathcal{D}^{(k)}} & 0 & 0 \\ 0 & 0 & \frac{1}{\varrho\,\mathcal{D}^{(k)}} & 0 \\ 0 & 0 & 0 & \frac{1}{\varrho\,\mathcal{D}^{(k)}} \end{pmatrix}. \tag{A4}$$

Matrices $\mathbf{N}_x$ and **K**, appearing in the modified divergence theorems (6) and (8), read

$$\mathbf{N}_x = \begin{pmatrix} 0 & n_1 & n_2 & n_3 \\ n_1 & 0 & 0 & 0 \\ n_2 & 0 & 0 & 0 \\ n_3 & 0 & 0 & 0 \end{pmatrix} \quad \text{and}$$

$$\mathbf{K} = \begin{pmatrix} 1 & 0 & 0 & 0 \\ 0 & -1 & 0 & 0 \\ 0 & 0 & -1 & 0 \\ 0 & 0 & 0 & -1 \end{pmatrix}. \tag{A5}$$

Note that matrices $\mathbf{D}_x$, **A** and **B** obey Eqs. (7), (9), and (13). Other diffusion phenomena can be formulated in a similar way.

## Appendix B

**Acoustic Wave Propagation in Moving Fluids.** The linearized equation of motion in a moving fluid reads

$$\varrho \frac{Dv_i}{Dt} + b^v * v_i + \frac{\partial p}{\partial x_i} = f_i, \tag{B1}$$

with

$$\frac{D}{Dt} = \frac{\partial}{\partial t} + v_k^0 \frac{\partial}{\partial x_k}, \tag{B2}$$

where $p$ is the acoustic pressure, $v_i$ the particle velocity associated to the acoustic wave motion (which is to be distinguished from the flow velocity $v_k^0$ in the operator $D/Dt$), $\varrho$ the mass density of the medium in equilibrium, $f_i$ the volume density of external force, and $b^v$ a causal loss function ($*$ denotes a temporal convolution). The linearized stress-strain relation reads

$$\frac{1}{K}\frac{Dp}{Dt} + b^p * p + \frac{\partial v_i}{\partial x_i} = q, \tag{B3}$$

where $K$ is the bulk compression modulus, $q$ the volume injection rate density, and $b^p$ a causal loss function.

Equations (*B*1) and (*B*3) can be combined to yield the general matrix-vector Eq. (1), with $D/Dt$ defined in Eq. (*B*2) and

$$\mathbf{u} = \begin{pmatrix} p \\ v_1 \\ v_2 \\ v_3 \end{pmatrix}, \quad \mathbf{s} = \begin{pmatrix} q \\ f_1 \\ f_2 \\ f_3 \end{pmatrix},$$

$$\mathbf{A} = \begin{pmatrix} \frac{1}{K} & 0 & 0 & 0 \\ 0 & \varrho & 0 & 0 \\ 0 & 0 & \varrho & 0 \\ 0 & 0 & 0 & \varrho \end{pmatrix} \quad \text{and} \tag{B4}$$

$$\mathbf{B} = \begin{pmatrix} b^p * & 0 & 0 & 0 \\ 0 & b^v * & 0 & 0 \\ 0 & 0 & b^v * & 0 \\ 0 & 0 & 0 & b^v * \end{pmatrix}.$$

Matrices $\mathbf{D}_x$, $\mathbf{N}_x$, and $\mathbf{K}$ are the same as in Appendix A. The symmetry properties described by Eqs. (7), (9), and (13) are easily confirmed. Finally, note that in the frequency domain formulation, the temporal convolution kernels $b^p(\mathbf{x},t)*$ and $b^v(\mathbf{x},t)*$ in matrix $\mathbf{B}$ are replaced by complex frequency-dependent functions $\hat{b}^p(\mathbf{x},\omega)$ and $\hat{b}^v(\mathbf{x},\omega)$, respectively.

## Appendix C

**Momentum Transport.** The nonlinear equation of motion for a viscous fluid reads

$$\varrho \frac{Dv_i}{Dt} - \frac{\partial \tau_{ij}}{\partial x_j} = f_i, \tag{C1}$$

where $v_i$ is the particle velocity, $\tau_{ij}$ the stress tensor, $\varrho$ the mass density, and $f_i$ the volume density of external force. Stoke's stress-strain rate relation reads

$$-\tau_{ij} + \eta_{ijkl}\frac{\partial v_k}{\partial x_l} = p\,\delta_{ij}, \tag{C2}$$

where $\eta_{ijkl}$ is the anisotropic viscosity tensor and $p$ the hydrostatic pressure. The viscosity tensor obeys the following symmetry relation $\eta_{ijkl} = \eta_{jikl} = \eta_{ijlk} = \eta_{klij}$. For isotropic fluids the viscosity tensor reads $\eta_{ijkl} = \eta(-2/3\delta_{ij}\delta_{kl} + \delta_{ik}\delta_{jl} + \delta_{il}\delta_{jk})$, where $\eta$ is the isotropic viscosity parameter. Equations (*C*1) and (*C*2) can be combined to yield the general matrix-vector Eq. (1). To this end we first rewrite these equations as

$$\varrho \frac{D\mathbf{v}}{Dt} - \frac{\partial \boldsymbol{\tau}_j}{\partial x_j} = \mathbf{f}, \tag{C3}$$

$$-\boldsymbol{\tau}_j + \mathbf{h}_{jl}\frac{\partial \mathbf{v}}{\partial x_l} = p\,\boldsymbol{\delta}_j, \tag{C4}$$

with

$$\mathbf{v} = \begin{pmatrix} v_1 \\ v_2 \\ v_3 \end{pmatrix}, \quad \mathbf{f} = \begin{pmatrix} f_1 \\ f_2 \\ f_3 \end{pmatrix} \boldsymbol{\tau}_j = \begin{pmatrix} \tau_{1j} \\ \tau_{2j} \\ \tau_{3j} \end{pmatrix}, \quad \boldsymbol{\delta}_j = \begin{pmatrix} \delta_{1j} \\ \delta_{2j} \\ \delta_{3j} \end{pmatrix} \quad \text{and}$$
$$\mathbf{h}_{jl} = \begin{pmatrix} \eta_{1j1l} & \eta_{1j2l} & \eta_{1j3l} \\ \eta_{2j1l} & \eta_{2j2l} & \eta_{2j3l} \\ \eta_{3j1l} & \eta_{3j2l} & \eta_{3j3l} \end{pmatrix}. \tag{C5}$$

Note that

$$\mathbf{h}_{jl} = \mathbf{h}_{lj}^T \tag{C6}$$

on account of the symmetry properties of $\eta_{ijkl}$. Hence, we obtain

$$\overline{\mathbf{A}}\frac{D\mathbf{u}}{Dt} + \overline{\mathbf{B}}\mathbf{u} + \mathbf{C}\mathbf{D}_x\mathbf{u} = \overline{\mathbf{s}}, \tag{C7}$$

with

$$\mathbf{u} = \begin{pmatrix} \mathbf{v} \\ -\boldsymbol{\tau}_1 \\ -\boldsymbol{\tau}_2 \\ -\boldsymbol{\tau}_3 \end{pmatrix}, \quad \overline{\mathbf{s}} = \begin{pmatrix} \mathbf{f} \\ p\,\boldsymbol{\delta}_1 \\ p\,\boldsymbol{\delta}_2 \\ p\,\boldsymbol{\delta}_3 \end{pmatrix},$$

$$\overline{\mathbf{A}} = \begin{pmatrix} \varrho\mathbf{I} & \mathbf{O} & \mathbf{O} & \mathbf{O} \\ \mathbf{O} & \mathbf{O} & \mathbf{O} & \mathbf{O} \\ \mathbf{O} & \mathbf{O} & \mathbf{O} & \mathbf{O} \\ \mathbf{O} & \mathbf{O} & \mathbf{O} & \mathbf{O} \end{pmatrix}, \quad \overline{\mathbf{B}} = \begin{pmatrix} \mathbf{O} & \mathbf{O} & \mathbf{O} & \mathbf{O} \\ \mathbf{O} & \mathbf{I} & \mathbf{O} & \mathbf{O} \\ \mathbf{O} & \mathbf{O} & \mathbf{I} & \mathbf{O} \\ \mathbf{O} & \mathbf{O} & \mathbf{O} & \mathbf{I} \end{pmatrix}, \tag{C8}$$

$$\mathbf{C} = \begin{pmatrix} \mathbf{I} & \mathbf{O} & \mathbf{O} & \mathbf{O} \\ \mathbf{O} & \mathbf{h}_{11} & \mathbf{h}_{12} & \mathbf{h}_{13} \\ \mathbf{O} & \mathbf{h}_{21} & \mathbf{h}_{22} & \mathbf{h}_{23} \\ \mathbf{O} & \mathbf{h}_{31} & \mathbf{h}_{32} & \mathbf{h}_{33} \end{pmatrix},$$

$$\mathbf{D}_x = \begin{pmatrix} \mathbf{O} & \mathbf{D}_1 & \mathbf{D}_2 & \mathbf{D}_3 \\ \mathbf{D}_1 & \mathbf{O} & \mathbf{O} & \mathbf{O} \\ \mathbf{D}_2 & \mathbf{O} & \mathbf{O} & \mathbf{O} \\ \mathbf{D}_3 & \mathbf{O} & \mathbf{O} & \mathbf{O} \end{pmatrix} \quad \text{and} \tag{C9}$$

$$\mathbf{D}_j = \begin{pmatrix} \frac{\partial}{\partial x_j} & 0 & 0 \\ 0 & \frac{\partial}{\partial x_j} & 0 \\ 0 & 0 & \frac{\partial}{\partial x_j} \end{pmatrix},$$

for $j = 1, 2, 3$, $\mathbf{I}$ being the $3\times3$ identity matrix and $\mathbf{O}$ the $3\times3$ null matrix. Multiplication of all terms in Eq. (*C*7) by the inverse of $\mathbf{C}$ and linearization of the term $D\mathbf{u}/Dt$ yields

$$\mathbf{A}\frac{\partial \mathbf{u}}{\partial t} + \mathbf{B}\mathbf{u} + \mathbf{D}_x\mathbf{u} = \mathbf{s}, \tag{C10}$$

with

$$\mathbf{A} = \mathbf{C}^{-1}\overline{\mathbf{A}} = \overline{\mathbf{A}}, \quad \mathbf{B} = \mathbf{C}^{-1}\overline{\mathbf{B}} \quad \text{and} \quad \mathbf{s} = \mathbf{C}^{-1}\overline{\mathbf{s}}. \tag{C11}$$

Matrices $\mathbf{N}_x$ and $\mathbf{K}$, appearing in the modified divergence theorems (6) and (8), read

$$\mathbf{N_x}=\begin{pmatrix} \mathbf{O} & \mathbf{N}_1 & \mathbf{N}_2 & \mathbf{N}_3 \\ \mathbf{N}_1 & \mathbf{O} & \mathbf{O} & \mathbf{O} \\ \mathbf{N}_2 & \mathbf{O} & \mathbf{O} & \mathbf{O} \\ \mathbf{N}_3 & \mathbf{O} & \mathbf{O} & \mathbf{O} \end{pmatrix} \quad \text{and} \quad \mathbf{N}_j=\begin{pmatrix} n_j & 0 & 0 \\ 0 & n_j & 0 \\ 0 & 0 & n_j \end{pmatrix}, \tag{C12}$$

for $j=1, 2, 3$ and

$$\mathbf{K}=\mathrm{diag}(\mathbf{1},-\mathbf{1},-\mathbf{1},-\mathbf{1}), \quad \text{with } \mathbf{1}=(1,1,1). \tag{C13}$$

Based on the structure of the matrices $\overline{\mathbf{A}},\overline{\mathbf{B}},\mathbf{C}$, $\mathbf{D_x}$, and $\mathbf{K}$ as well as the symmetry relation (C6), we find that the symmetry properties described by Eqs. (7), (9), and (13) are obeyed.

## Appendix D

**Coupled Elastodynamic and Electromagnetic Wave Propagation in Porous Solids.** We briefly review the theory for elastodynamic waves coupled to electromagnetic fields in a dissipative inhomogeneous anisotropic fluid-saturated porous solid, [6,9]. The linearized equations of motion read in the frequency domain (using the vector notation introduced in Appendix C)

$$j\omega\varrho^b\hat{\mathbf{v}}^s+j\omega\varrho^f\hat{\mathbf{w}}-\frac{\partial\hat{\boldsymbol{\tau}}^b_j}{\partial x_j}=\hat{\mathbf{f}}^b, \tag{D1}$$

$$j\omega\varrho^f\hat{\mathbf{v}}^s+\eta\hat{\mathbf{k}}^{-1}(\hat{\mathbf{w}}-\hat{\mathbf{L}}\hat{\mathbf{E}})+\nabla\hat{p}=\hat{\mathbf{f}}^f, \tag{D2}$$

with $\hat{\mathbf{w}}=\phi(\hat{\mathbf{v}}^f-\hat{\mathbf{v}}^s)$. Here $\hat{\mathbf{v}}^s$ and $\hat{\mathbf{v}}^f$ are the averaged solid and fluid particle velocities associated to the wave motion, $\hat{\mathbf{w}}$ is the filtration velocity, $\phi$ the porosity, $\hat{\boldsymbol{\tau}}^b_j$ the averaged bulk stress, $\hat{p}$ the averaged fluid pressure, and $\hat{\mathbf{E}}$ the averaged electric field strength. The source functions $\hat{\mathbf{f}}^b$ and $\hat{\mathbf{f}}^f$ are the volume densities of external force on the bulk and on the fluid, respectively. The constitutive parameters $\varrho^b$ and $\varrho^f$ are the anisotropic bulk and fluid mass densities, respectively, [10]. In the following we assume that these tensors are symmetric, according to $\varrho^b=(\varrho^b)^T$ and $\varrho^f=(\varrho^f)^T$, which is for example the case when the anisotropy is the result of parallel fine layering at a scale much smaller than the wavelength. The complex frequency-dependent tensor $\hat{\mathbf{k}}$ is the dynamic permeability tensor of the porous material, with $\hat{\mathbf{k}}=\hat{\mathbf{k}}^T$, and $\eta$ is the fluid viscosity parameter. Finally, the complex frequency-dependent tensor $\hat{\mathbf{L}}$ accounts for the coupling between the elastodynamic and electromagnetic waves. In the following we will assume that this tensor is symmetric as well, according to $\hat{\mathbf{L}}=\hat{\mathbf{L}}^T$ (Pride and Haartsen [6] discuss the conditions for this symmetry).

The linearized stress-strain relations read

$$-j\omega\hat{\boldsymbol{\tau}}^b_j+\mathbf{c}_{jl}\frac{\partial\hat{\mathbf{v}}^s}{\partial x_l}+\mathbf{d}_j\nabla\cdot\hat{\mathbf{w}}=\mathbf{0}, \tag{D3}$$

$$j\omega\hat{p}+\mathbf{d}^T_l\frac{\partial\hat{\mathbf{v}}^s}{\partial x_l}+M\nabla\cdot\hat{\mathbf{w}}=0, \tag{D4}$$

with $\mathbf{0}$ a $3\times1$ null vector and $\mathbf{d}_j$ and $\mathbf{c}_{jl}$ defined similar as $\boldsymbol{\delta}_j$ and $\mathbf{h}_{jl}$ in Eq. (C5), i.e., $(\mathbf{d}_j)_i=d_{ij}$, with $d_{ij}=d_{ji}$, and $(\mathbf{c}_{jl})_{ik}=c_{ijkl}$, with $c_{ijkl}=c_{jikl}=c_{ijlk}=c_{klij}$. Note that $\mathbf{c}_{jl}=\mathbf{c}^T_{lj}$. $M$, $d_{ij}$ and $c_{ijkl}$ are the stiffness parameters of the porous solid.

Maxwell's electromagnetic field equations read

$$j\omega\boldsymbol{\epsilon}\hat{\mathbf{E}}+\hat{\mathbf{J}}-\nabla\times\hat{\mathbf{H}}=-\hat{\mathbf{J}}^e, \tag{D5}$$

$$j\omega\boldsymbol{\mu}\hat{\mathbf{H}}+\nabla\times\hat{\mathbf{E}}=-\hat{\mathbf{J}}^m, \tag{D6}$$

where $\hat{\mathbf{H}}$ is the averaged magnetic field strength, $\hat{\mathbf{J}}$ the averaged induced electric current density, $\boldsymbol{\epsilon}$ and $\boldsymbol{\mu}$ are the anisotropic permittivity and permeability, with $\boldsymbol{\epsilon}=\boldsymbol{\epsilon}^T$ and $\boldsymbol{\mu}=\boldsymbol{\mu}^T$, and $\mathbf{J}^e$ and $\mathbf{J}^m$ are source functions in terms of the external electric and magnetic current densities. The induced electric current density is coupled to the elastodynamic wave motion, according to

$$\hat{\mathbf{J}}=\hat{\boldsymbol{\sigma}}\hat{\mathbf{E}}-\hat{\mathbf{L}}[\nabla\hat{p}+j\omega\varrho^f\hat{\mathbf{v}}^s-\hat{\mathbf{f}}^f], \tag{D7}$$

where $\hat{\boldsymbol{\sigma}}$ is the complex frequency dependent conductivity, with $\hat{\boldsymbol{\sigma}}=\hat{\boldsymbol{\sigma}}^T$. Substituting the constitutive relation (D7) into the Maxwell Eq. (D5), and adding $\hat{\mathbf{L}}$ times Eq. (D2) to Eq. (D5) in order to compensate for the term $-\hat{\mathbf{L}}[\nabla\hat{p}+j\omega\varrho^f\hat{\mathbf{v}}^s-\hat{\mathbf{f}}^f]$, yields

$$j\omega\boldsymbol{\epsilon}\hat{\mathbf{E}}+(\hat{\boldsymbol{\sigma}}-\eta\hat{\mathbf{L}}\hat{\mathbf{k}}^{-1}\hat{\mathbf{L}})\hat{\mathbf{E}}+\eta\hat{\mathbf{L}}\hat{\mathbf{k}}^{-1}\hat{\mathbf{w}}-\nabla\times\hat{\mathbf{H}}=-\hat{\mathbf{J}}^e. \tag{D8}$$

Equations (D8) and (D6), together with Eqs. (D1), (D2), (D3), and (D4) can be combined to yield

$$j\omega\overline{\mathbf{A}}\hat{\mathbf{u}}+\overline{\mathbf{B}}\hat{\mathbf{u}}+\mathbf{C}\mathbf{D}_x\hat{\mathbf{u}}=\hat{\hat{\mathbf{s}}}, \tag{D9}$$

where

$$\hat{\mathbf{u}}=\begin{pmatrix}\hat{\mathbf{u}}_1\\ \hat{\mathbf{u}}_2\\ \hat{\mathbf{u}}_3\end{pmatrix}, \quad \hat{\hat{\mathbf{s}}}=\begin{pmatrix}\hat{\hat{\mathbf{s}}}_1\\ \hat{\hat{\mathbf{s}}}_2\\ \hat{\hat{\mathbf{s}}}_3\end{pmatrix}, \quad \overline{\mathbf{A}}=\begin{pmatrix}\overline{\mathbf{A}}_{11} & \mathbf{O} & \mathbf{O}\\ \mathbf{O} & \overline{\mathbf{A}}_{22} & \overline{\mathbf{A}}_{23}\\ \mathbf{O} & \overline{\mathbf{A}}^T_{23} & \overline{\mathbf{A}}_{33}\end{pmatrix}, \tag{D10}$$

$$\overline{\mathbf{B}}=\begin{pmatrix}\overline{\mathbf{B}}_{11} & \mathbf{O} & \overline{\mathbf{B}}_{13}\\ \mathbf{O} & \mathbf{O} & \mathbf{O}\\ -\overline{\mathbf{B}}^T_{13} & \mathbf{O} & \overline{\mathbf{B}}_{33}\end{pmatrix},$$

$$\mathbf{C}=\begin{pmatrix}\mathbf{I} & \mathbf{O} & \mathbf{O}\\ \mathbf{O} & \mathbf{C}_{22} & \mathbf{C}_{23}\\ \mathbf{O} & \mathbf{C}^T_{23} & \mathbf{C}_{33}\end{pmatrix} \quad \text{and} \quad \mathbf{D}_x=\begin{pmatrix}\mathbf{D}_{11} & \mathbf{O} & \mathbf{O}\\ \mathbf{O} & \mathbf{D}_{22} & \mathbf{O}\\ \mathbf{O} & \mathbf{O} & \mathbf{D}_{33}\end{pmatrix}, \tag{D11}$$

where $\mathbf{I}$ and $\mathbf{O}$ are identity and null matrices of appropriate size and

$$\hat{\mathbf{u}}_1=\begin{pmatrix}\hat{\mathbf{E}}\\ \hat{\mathbf{H}}\end{pmatrix}, \quad \hat{\mathbf{u}}_2=\begin{pmatrix}\hat{\mathbf{v}}^s\\ -\hat{\boldsymbol{\tau}}^b_1\\ -\hat{\boldsymbol{\tau}}^b_2\\ -\hat{\boldsymbol{\tau}}^b_3\end{pmatrix}, \quad \hat{\mathbf{u}}_3=\begin{pmatrix}\hat{\mathbf{w}}\\ \hat{p}\end{pmatrix},$$

$$\hat{\hat{\mathbf{s}}}_1=\begin{pmatrix}-\hat{\mathbf{J}}^e\\ -\hat{\mathbf{J}}^m\end{pmatrix}, \quad \hat{\hat{\mathbf{s}}}_2=\begin{pmatrix}\hat{\mathbf{f}}^b\\ \mathbf{0}\\ \mathbf{0}\\ \mathbf{0}\end{pmatrix}, \quad \hat{\hat{\mathbf{s}}}_3=\begin{pmatrix}\hat{\mathbf{f}}^f\\ 0\end{pmatrix}, \tag{D12}$$

$$\overline{\mathbf{A}}_{11}=\begin{pmatrix}\boldsymbol{\epsilon} & \mathbf{O}\\ \mathbf{O} & \boldsymbol{\mu}\end{pmatrix}, \quad \overline{\mathbf{A}}_{22}=\begin{pmatrix}\varrho^b & \mathbf{O} & \mathbf{O} & \mathbf{O}\\ \mathbf{O} & \mathbf{I} & \mathbf{O} & \mathbf{O}\\ \mathbf{O} & \mathbf{O} & \mathbf{I} & \mathbf{O}\\ \mathbf{O} & \mathbf{O} & \mathbf{O} & \mathbf{I}\end{pmatrix}, \tag{D13}$$

$$\overline{\mathbf{A}}_{23}=\begin{pmatrix}\varrho^f & \mathbf{0}\\ \mathbf{O} & \mathbf{0}\\ \mathbf{O} & \mathbf{0}\\ \mathbf{O} & \mathbf{0}\end{pmatrix}, \quad \overline{\mathbf{A}}_{33}=\begin{pmatrix}\mathbf{O} & \mathbf{0}\\ \mathbf{0}^T & 1\end{pmatrix},$$

$$\overline{\mathbf{B}}_{11}=\begin{pmatrix}(\hat{\boldsymbol{\sigma}}-\eta\hat{\mathbf{L}}\hat{\mathbf{k}}^{-1}\hat{\mathbf{L}}) & \mathbf{O}\\ \mathbf{O} & \mathbf{O}\end{pmatrix},\quad \overline{\mathbf{B}}_{13}=\begin{pmatrix}\eta\hat{\mathbf{L}}\hat{\mathbf{k}}^{-1} & \mathbf{0}\\ \mathbf{O} & \mathbf{0}\end{pmatrix},$$
$$\overline{\mathbf{B}}_{33}=\begin{pmatrix}\eta\hat{\mathbf{k}}^{-1} & \mathbf{0}\\ \mathbf{0}^T & 0\end{pmatrix}, \tag{D14}$$

$$\mathbf{C}_{22}=\begin{pmatrix}\mathbf{I} & \mathbf{O} & \mathbf{O} & \mathbf{O}\\ \mathbf{O} & \mathbf{c}_{11} & \mathbf{c}_{12} & \mathbf{c}_{13}\\ \mathbf{O} & \mathbf{c}_{21} & \mathbf{c}_{22} & \mathbf{c}_{23}\\ \mathbf{O} & \mathbf{c}_{31} & \mathbf{c}_{32} & \mathbf{c}_{33}\end{pmatrix},\quad \mathbf{C}_{23}=\begin{pmatrix}\mathbf{O} & \mathbf{0}\\ \mathbf{O} & \mathbf{d}_1\\ \mathbf{O} & \mathbf{d}_2\\ \mathbf{O} & \mathbf{d}_3\end{pmatrix},$$
$$\mathbf{C}_{33}=\begin{pmatrix}\mathbf{I} & \mathbf{0}\\ \mathbf{0}^T & M\end{pmatrix}, \tag{D15}$$

$$\mathbf{D}_{11}=\begin{pmatrix}\mathbf{O} & \mathbf{D}_0^T\\ \mathbf{D}_0 & \mathbf{O}\end{pmatrix},\quad \mathbf{D}_0=\begin{pmatrix}0 & -\dfrac{\partial}{\partial x_3} & \dfrac{\partial}{\partial x_2}\\ \dfrac{\partial}{\partial x_3} & 0 & -\dfrac{\partial}{\partial x_1}\\ -\dfrac{\partial}{\partial x_2} & \dfrac{\partial}{\partial x_1} & 0\end{pmatrix},$$
$$\mathbf{D}_{33}=\begin{pmatrix}\mathbf{O} & \boldsymbol{\nabla}\\ \boldsymbol{\nabla}^T & 0\end{pmatrix} \tag{D16}$$

and $\mathbf{D}_{22}$ equal to $\mathbf{D}_x$ in Eq. (*C*9). Multiplying all terms in Eq. (*D*9) by the inverse of $\mathbf{C}$ finally yields

$$j\omega\mathbf{A}\hat{\mathbf{u}}+\mathbf{B}\hat{\mathbf{u}}+\mathbf{D}_x\hat{\mathbf{u}}=\hat{\mathbf{s}}, \tag{D17}$$

with $\mathbf{A}=\mathbf{C}^{-1}\overline{\mathbf{A}}$, $\mathbf{B}=\mathbf{C}^{-1}\overline{\mathbf{B}}=\overline{\mathbf{B}}$ and $\hat{\mathbf{s}}=\mathbf{C}^{-1}\hat{\bar{\mathbf{s}}}=\hat{\bar{\mathbf{s}}}$. Matrices $\mathbf{N}_\mathbf{x}$ and $\mathbf{K}$, appearing in the modified divergence theorems (6) and (8), read

$$\mathbf{N}_\mathbf{x}=\begin{pmatrix}\mathbf{N}_{11} & \mathbf{O} & \mathbf{O}\\ \mathbf{O} & \mathbf{N}_{22} & \mathbf{O}\\ \mathbf{O} & \mathbf{O} & \mathbf{N}_{33}\end{pmatrix},\quad \mathbf{N}_{11}=\begin{pmatrix}\mathbf{O} & \mathbf{N}_0^T\\ \mathbf{N}_0 & \mathbf{O}\end{pmatrix},$$
$$\mathbf{N}_0=\begin{pmatrix}0 & -n_3 & n_2\\ n_3 & 0 & -n_1\\ -n_2 & n_1 & 0\end{pmatrix},\quad \mathbf{N}_{33}=\begin{pmatrix}\mathbf{O} & \mathbf{n}\\ \mathbf{n}^T & 0\end{pmatrix}, \tag{D18}$$

$$\mathbf{K}=\mathrm{diag}(-\mathbf{1},\mathbf{1},\mathbf{1},-\mathbf{1},-\mathbf{1},-\mathbf{1},\mathbf{1},-1), \tag{D19}$$

and $\mathbf{N}_{22}$ equal to $\mathbf{N}_x$ in Eq. (*C*12). Based on the structure of the matrices $\overline{\mathbf{A}}$, $\overline{\mathbf{B}}$, $\mathbf{C}$, $\mathbf{D}_x$, and $\mathbf{K}$ as well as the symmetry relations discussed above, we find that the symmetry properties described by Eqs. (7), (9), and (13) are obeyed.

Finally, note that when the coupling tensor $\hat{\mathbf{L}}$ is zero, the matrix $\overline{\mathbf{B}}_{13}$ vanishes and hence equation (*D*9) decouples into the electromagnetic wave equation for the wave vector $\hat{\mathbf{u}}_1$ and Biot's poroelastic wave equation for the wave vector $(\hat{\mathbf{u}}_2^T,\hat{\mathbf{u}}_3^T)^T$, [11]. For a nonporous solid the matrices $\overline{\mathbf{A}}_{23}$ and $\mathbf{C}_{23}$ vanish as well, so Biot's wave equation reduces to the elastodynamic wave equation for the wave vector $\hat{\mathbf{u}}_2$. Obviously the symmetry properties described by Eqs. (7), (9), and (13) are obeyed for the matrices appearing in the electromagnetic wave equation, Biot's poroelastic wave equation and the elastodynamic wave equation, respectively.

## References


[1] De Hoop, A. T., and Stam, H. J., 1988, "Time-Domain Reciprocity Theorems for Elastodynamic Wave Fields in Solids With Relaxation and Their Application to Inverse Problems," Wave Motion, **10**, pp. 479–489.

[2] Bojarski, N. N., 1983, "Generalized Reaction Principles and Reciprocity Theorems for the Wave Equations, and the Relationship Between the Time-Advanced and Time-Retarded Fields," J. Acoust. Soc. Am., **74**, pp. 281–285.

[3] Fokkema, J. T., and Van den Berg, P. M., 1993, *Seismic Applications of Acoustic Reciprocity*, Elsevier, Amsterdam.

[4] Lyamshev, L. M., 1961, "On Some Integral Relationships in Acoustics of Moving Medium," Dokl. Akad. Nauk, **138**, pp. 575–578.

[5] Allard, J. F., Brouard, B., and Lafarge, D., 1993, "Reciprocity and Antireciprocity in Sound Transmission Through Layered Materials Including Elastic and Porous Media," Wave Motion, **17**, pp. 329–335.

[6] Pride, S. R., and Haartsen, M. W., 1996, "Electroseismic Wave Properties," J. Acoust. Soc. Am., **100**, pp. 1301–1315.

[7] Belinskiy, B. P., 2001, "On Some General Mathematical Properties of the System Elastic Plate-Acoustic Medium. Acoustic Interactions With Submerged Elastic Structures, Part II," Ser. Stab. Vib. Control Syst. Ser. B, **5**, pp. 193–218.

[8] Fisher, M., and Langenberg, K. J., 1984, "Limitations and Defects of Certain Inverse Scattering Theories," IEEE Trans. Antennas Propag., **32**, pp. 1080–1088.

[9] Pride, S., 1994, "Governing Equations for the Coupled Electromagnetics and Acoustics of Porous Media," Phys. Rev. B, **50**, pp. 15,678–15,696.

[10] Schoenberg, M., and Sen, P. N., 1983, "Properties of a Periodically Stratified Acoustic Half-Space and Its Relation to a Biot Fluid," J. Acoust. Soc. Am., **73**, pp. 61–67.

[11] Biot, M. A., 1956, "Theory of Propagation of Elastic Waves in Fluid-Saturated Porous Solid: I. Low Frequency Range," J. Acoust. Soc. Am., **28**, pp. 168–178.

Journal of Applied Mechanics

# ERRATUM

## Erratum: "On the Mechanical Modeling of Functionally Graded Interfacial Zone With a Griffith Crack: Anti-Plane Deformation" [ASME J. Appl. Mech., 2003, 70, pp. 676–680]

**Y. S. Wang, G.-Y. Huang, and D. Gross**

---

The name of the third author should read D. Gross.

  